

Durham E-Theses

The role of clay mineral diagenesis in overpressure generation and compaction of siliciclastic mudstones

ANDRAS, PETER

How to cite:

ANDRAS, PETER (2018) *The role of clay mineral diagenesis in overpressure generation and compaction of siliciclastic mudstones*, Durham theses, Durham University. Available at Durham E-Theses Online: <http://etheses.dur.ac.uk/12531/>

Use policy

The full-text may be used and/or reproduced, and given to third parties in any format or medium, without prior permission or charge, for personal research or study, educational, or not-for-profit purposes provided that:

- a full bibliographic reference is made to the original source
- a [link](#) is made to the metadata record in Durham E-Theses
- the full-text is not changed in any way

The full-text must not be sold in any format or medium without the formal permission of the copyright holders.

Please consult the [full Durham E-Theses policy](#) for further details.

Academic Support Office, Durham University, University Office, Old Elvet, Durham DH1 3HP
e-mail: e-theses.admin@dur.ac.uk Tel: +44 0191 334 6107
<http://etheses.dur.ac.uk>

The role of clay mineral diagenesis in overpressure generation and compaction of siliciclastic mudstones

Péter András

**This thesis is submitted in partial fulfilment of the requirements for the degree of
Doctor of Philosophy at Durham University**

**Department of Earth Sciences
University of Durham**

2017

Abstract

Clay mineral diagenesis has a considerable effect on the physical properties of siliciclastic mudstones, with important implications for pore pressure prediction. The dominant clay mineral reaction, the conversion of smectite to illite, involves a series of dissolution and reprecipitation reactions which results in a significant change in the orientation of the clay mineral fabric. Unloading is a direct result of clay mineral diagenesis and concomitant fabric destabilisation, due to the local transfer of load from dissolving detrital clay grains to fluid. Pore pressure is then a function of the rate at which it is generated by clay mineral diagenesis (and other mechanisms such as disequilibrium compaction) and the rate at which it is dissipated by compaction and fluid flow.

Clear evidence has been found for chemical compaction (porosity loss/sediment volume reduction) associated with illitization of smectite in Miocene mudstones in the Central Malay Basin, in Cretaceous mudstones at Haltenbanken, offshore mid-Norway, in Cretaceous to Tertiary mudstones in the Sergipe-Alagoas Basin, offshore Brazil and in Triassic mudstones in the North Sea Central Graben from measured physical, textural, and mineralogical properties, and from log responses. In addition to this diagenetically mature, illitized mudstones continue to compact mechanically with increasing effective stress. The newly presented data have been interpreted to discriminate between two models for the chemical compaction of diagenetically altered mudstones proposed by previous researchers: (effective) stress-independent chemical compaction and chemically-enhanced mechanical compaction. Key evidence in favour of the chemically-enhanced mechanical compaction model comes from density logs of Cretaceous mudstones at the Halten Terrace, offshore mid-Norway in association with the pore pressure history inferred by previous pore pressure analysis. This model is also consistent with the petrographic evidence that clay-rich siliciclastic mudstones have a clay-supported matrix both before and after illitization. Established methods of pore pressure estimation do not correctly account for the mechanical and chemical contributions to mudstone compaction, except empirically or in favourable circumstances where use can be made of data from offset wells with similar lithology, burial history and temperature history.

Contents

| | |
|---|-------|
| Abstract | ii |
| Contents | iii |
| List of illustrations | x |
| List of tables | xxxii |
| Declarations | xxxiv |
| Acknowledgements | xxxv |
| Quote | xxxvi |
| Chapter 1 | 1 |
| <i>Introduction</i> | |
| 1.1 Introduction | 2 |
| 1.2 Basic concepts and terminology | 4 |
| 1.2.1 Mudstones and shales | 4 |
| 1.2.2 Clay minerals | 5 |
| 1.2.3 Organic matter | 14 |
| 1.2.4 Porosity | 14 |
| 1.2.5 Permeability | 16 |
| 1.2.6 Pore pressure | 17 |
| 1.3 Research objectives | 20 |
| 1.4 Thesis organisation | 21 |
| 1.5 List of publications | 23 |
| Chapter 2 | 25 |
| <i>Chemical reactions and physical changes in mudstones during burial diagenesis and their relation to overpressure generation and prediction: a review</i> | |
| 2.1 Introduction | 26 |
| 2.2 Early diagenesis | 26 |
| 2.3 Mechanical compaction | 27 |

| | | |
|--------------------|---|----|
| 2.3.1 | Porosity stress relationship | 28 |
| 2.4 | Clay mineral diagenesis | 31 |
| 2.4.1 | Smectite illitization..... | 32 |
| 2.5 | Clay mineral fabric alignment | 39 |
| 2.6 | Chemical compaction | 41 |
| 2.7 | Overpressure generation and prediction in siliciclastic mudstones | 44 |
| 2.7.1 | Influence of clay diagenesis on wireline log properties..... | 51 |
| 2.7.2 | Influence of clay diagenesis on pore fluid pressure | 58 |
| 2.7.3 | Summary | 63 |
| Chapter 3..... | | 65 |
| <i>Methodology</i> | | |
| 3.1 | Introduction..... | 66 |
| 3.2 | Sampling | 66 |
| 3.3 | Sample characterization procedures..... | 67 |
| 3.3.1 | Quantitative bulk fraction X-ray diffraction (QXRD) | 68 |
| 3.3.2 | Quantitative clay fraction X-ray diffraction | 69 |
| 3.3.3 | Cation exchange capacity (CEC) | 70 |
| 3.3.4 | Total organic carbon (TOC) | 71 |
| 3.3.5 | Major-element and trace-element chemical analyses | 71 |
| 3.3.6 | Grain density | 74 |
| 3.3.7 | Total porosity | 75 |
| 3.3.8 | Mercury Injection Core Porosimetry (MICP) | 75 |
| 3.3.9 | Permeability calculations | 79 |
| 3.3.10 | High Resolution X-Ray Textural Goniometry (HRXTG)..... | 79 |
| 3.3.11 | Scanning Electron Microscopy (SE, BSEM) | 82 |
| 3.4 | Wireline log analysis..... | 82 |

| | | |
|---|--|-----|
| 3.4.1 | Wireline data quality check..... | 82 |
| 3.4.2 | Wireline log-based mudstone discrimination..... | 83 |
| 3.4.3 | Log-based porosity calculations..... | 88 |
| 3.5 | One dimensional basin modelling..... | 88 |
| Chapter 4..... | | 90 |
| <i>Mechanical compaction in diagenetically altered mudstones: an example from the Central Malay Basin</i> | | |
| 4.1 | Introduction..... | 91 |
| 4.2 | Geological background | 92 |
| 4.2.1 | Overpressure distribution | 96 |
| 4.3 | Supplied data..... | 98 |
| 4.4 | Well locations, local geology and overall lithology | 98 |
| 4.5 | Pore pressure-depth profile and geothermal gradient..... | 102 |
| 4.6 | Mudstone sample characterization results..... | 104 |
| 4.6.1 | Bulk mineralogical properties | 105 |
| 4.6.2 | Clay mineralogical properties | 110 |
| 4.6.3 | Total organic carbon content..... | 113 |
| 4.6.4 | Bulk inorganic chemical properties..... | 114 |
| 4.6.5 | Clay mineral fabric alignment | 121 |
| 4.6.6 | Mudstone petrography | 122 |
| 4.6.7 | Mudstone porosity..... | 124 |
| 4.6.8 | Mudstone permeability | 126 |
| 4.7 | Discussion | 127 |
| 4.7.1 | Sediment provenance and paleoweathering reconstruction from major and trace element geochemistry | 127 |
| 4.7.2 | Mudstone mineralogy | 133 |

| | | |
|--|--|-----|
| 4.7.3 | Evaluation with wireline log-based compaction profiles and implication for overpressure development..... | 136 |
| 4.7.4 | Implications for mudstone compaction processes..... | 140 |
| 4.8 | Summary and conclusions..... | 143 |
| Chapter 5..... | | 144 |
| <i>Overpressure generation as a result of clay mineral diagenesis in Lower Cretaceous mudstones on the Halten Terrace, offshore mid-Norway</i> | | |
| 5.1 | Introduction..... | 145 |
| 5.2 | Geological background..... | 148 |
| 5.2.1 | Overpressure distribution..... | 152 |
| 5.3 | Cretaceous overpressures, maximum burial temperatures and mudstone porosities..... | 153 |
| 5.4 | Mudstone sample material..... | 158 |
| 5.4.1 | Bulk mineralogical properties..... | 162 |
| 5.4.2 | Clay mineralogical properties..... | 168 |
| 5.4.3 | Total organic carbon content..... | 171 |
| 5.4.4 | Bulk inorganic chemical properties..... | 172 |
| 5.4.5 | Clay mineral fabric alignment..... | 179 |
| 5.4.6 | Mudstone petrography..... | 182 |
| 5.4.7 | Mudstone porosity and permeability..... | 189 |
| 5.5 | One-dimensional basin modelling..... | 193 |
| 5.6 | Discussion..... | 201 |
| 5.6.1 | Sediment provenance and paleoweathering reconstruction from major and trace element geochemistry..... | 201 |
| 5.6.2 | Mudstone mineralogy..... | 209 |
| 5.6.3 | The effect of rapid Plio-Pleistocene burial on the extent of smectite illitization..... | 212 |

| | | |
|---|---|-----|
| 5.6.4 | The role of rapid Plio-Pleistocene burial in overpressure development | 212 |
| 5.6.5 | Evaluation with wireline log-based compaction profiles and implications for the mechanisms of overpressure generation | 217 |
| 5.6.6 | Implications for mudstone compaction processes | 223 |
| 5.7 | Summary and conclusions | 228 |
| Chapter 6 | | 230 |
| <i>Clay mineralogical control on compaction properties of Albian to Miocene mudstones of the Sergipe-Alagoas Basin, offshore eastern Brazil</i> | | |
| 6.1 | Introduction | 231 |
| 6.2 | Geological background | 232 |
| 6.3 | Supplied data | 235 |
| 6.4 | Well locations, local geology and overall lithology | 235 |
| 6.5 | Pore pressure-depth profiles and geothermal gradient | 238 |
| 6.6 | Mudstone sample characterization results | 240 |
| 6.6.1 | Bulk mineralogical properties | 242 |
| 6.6.2 | Clay mineralogical properties | 253 |
| 6.6.3 | Total organic carbon content | 257 |
| 6.6.4 | Bulk inorganic chemical properties | 258 |
| 6.6.5 | Mudstone porosity and permeability | 264 |
| 6.7 | Discussion | 268 |
| 6.7.1 | Sediment provenance and paleoweathering reconstruction from major and trace element geochemistry | 268 |
| 6.7.2 | Mudstone mineralogy | 275 |
| 6.7.3 | Evaluation with wireline log-based compaction profiles and implication for overpressure development | 278 |
| 6.7.4 | Implications for mudstone compaction processes | 282 |
| 6.8 | Summary and conclusions | 285 |

| | |
|---|-----|
| Chapter 7..... | 286 |
| <i>Diagenesis and compaction of Triassic mudstones in the HPHT fields of the North Sea, Cenrtal Graben</i> | |
| 7.1 Introduction..... | 287 |
| 7.2 Samples and geological setting | 289 |
| 7.2.1 Overpressure distribution | 292 |
| 7.3 Mudstone sample characterization results..... | 294 |
| 7.3.1 Bulk mineralogical properties | 294 |
| 7.3.2 Clay mineralogical properties | 298 |
| 7.3.3 Total organic carbon content..... | 299 |
| 7.3.4 Clay mineral fabric alignment | 300 |
| 7.3.5 Mudstone petrography | 302 |
| 7.3.6 Mudstone porosity and permeability | 306 |
| 7.4 Discussion | 310 |
| 7.4.1 Mudstone mineralogy..... | 310 |
| 7.4.2 Implications for mudstone compaction processes..... | 312 |
| 7.5 Summary and conclusions..... | 314 |
| Chapter 8..... | 315 |
| <i>Chemical compaction or chemically enhanced mechanical compaction: a discussion on compaction processes in diagenetically altered mudstones</i> | |
| 8.1 Evidence for chemical compaction | 316 |
| 8.2 Clay diagenetic control on mudstone microfabric revealed by High Resolution X-ray Texture Goniometry..... | 321 |
| 8.3 Discriminating between compaction models..... | 328 |
| 8.4 Implications for pore pressure prediction in diagenetically altered mudstones..... | 331 |
| 8.5 Project conclusions..... | 338 |
| 8.6 Recommendations for future work..... | 339 |

| | |
|--------------------|-----|
| Appendix I | 341 |
| Appendix II | 347 |
| Appendix III | 352 |
| Appendix IV | 356 |
| Appendix V | 370 |
| Appendix VI | 373 |
| References..... | 375 |

List of illustrations

| | |
|--|----|
| Figure 1.1. Basic structural models of most common clay mineral groups found in siliciclastic mudstones. R: Exchangeable cations; F: Fixed cations. Based on Moore and Reynolds (1997) | 9 |
| Figure 1.2. Mixed layer illite/smectite as interpreted by MacEwan crystallite model and fundamental particle model. After Moore and Reynolds (1997) | 10 |
| Figure 1.3. TEM lattice fringe image modified after Veblen et al. (1990) showing variable spacings between smectite interlayer surfaces (dark fringes, marked with green lines) in R>1 illite/smectite sample. Digits refer to number of 2:1 layers in fundamental particles. The inset cartoon illustrates one 40Å (4nm) thick (4 layer) fundamental particle with interlayer charge values shown on the left. | 12 |
| Figure 1.4. Schematic illustrations of adsorbed and double-layer water (a) and water associated with external and internal clay mineral surfaces (b). SEM image shows kaolinite; TEM image shows smectite with a collapsed (1nm) layer. From Passey et al. (2010) | 14 |
| Figure 1.5. Schematic representations of different porosity types in siliciclastic mudstones and their relations with different measurement techniques. Modified after Eslinger and Pevear (1988) | 15 |
| Figure 1.6. Variations of stress magnitudes with depth in different Andersonian faulting/stress and pore pressure regimes. Pp: pore pressure; Sv: lithostatic (overburden) stress; S_{Hmax} : maximum horizontal stress; S_{Hmin} : minimum horizontal stress (From Zoback, 2010) | 18 |
| Figure 2.1. Published porosity-depth trends for shales from different sedimentary basins worldwide (From Mondol et al. 2007) | 27 |
| Figure 2.2. Experimental porosity-stress/depth trends for clays (from Chilingar and Knight, 1960) in comparison with observed mudstone compaction trends (From Bjørlykke, 1998) | 29 |
| Figure 2.3. Experimental compaction curves of brine-saturated smectite and kaolinite (From Mondol et al., 2007) in comparison with the compaction trends of Yang and Aplin (2004) | 30 |

| | |
|--|----|
| Figure 2.4. Common diagenetic pathways for clay minerals in sandstones and shales. I: illite; S: smectite; D: dickite; C: chlorite (From Worden and Morad, 2003) | 31 |
| Figure 2.5. Model of the mechanism of smectite illitization based on Srodon et al. (2000). Refer to text for explanation | 34 |
| Figure 2.6. Published examples of illitization profiles. 1: Colorado River Delta, US (Jennings and Thompson, 1986); 2: Gulf Coast, US (Perry and Hower, 1972); 3: Gulf Coast, US (Hower et al., 1976); 4: North Sea (Srodon and Eberl, 1984); 5: Campos Basin, Brazil (Anjos, 1986); 6: Douala Basin, North Africa (Srodon and Eberl, 1984); 7: Central Poland (Srodon and Eberl, 1984)..... | 36 |
| Figure 2.7. Model predictions for illitization illustrating the roles of different drivers (modified after Huang et al. 1993). Refer to text for more explanation..... | 37 |
| Figure 2.8. Evolution of the clay mineral fabric during burial diagenesis and early metamorphism (modified after Haines et al., 2009). Thick black line represents clay mineral fabric anisotropy evolution in sedimentary basins from deposition to low grade metamorphism as inferred from natural data | 40 |
| Figure 2.9. Chemical compaction models for mudstones. Left: the stress-independent chemical compaction model for mudstones undergoing diagenesis at temperatures above ~100°C. Right: the chemically-enhanced mechanical compaction model for mudstones undergoing diagenesis at all temperatures above ~70°C | 43 |
| Figure 2.10. (a) Porosity-stress (b) Porosity-depth and (c) Pressure-depth profiles where overpressure is due to disequilibrium compaction. Points A, B and C show porosity, vertical effective stress and pore pressure in arbitrary mudstone beds buried to different depths. OP: overpressure, ES: effective stress..... | 45 |
| Figure 2.11. Porosity-stress/depth and pressure-depth profiles where overpressure is due to unloading mechanism. Points A, B and C show porosity, vertical effective stress and pore pressure in arbitrary mudstone beds buried to different depths. OP: overpressure, ES: effective stress..... | 47 |
| Figure 2.12. Demonstration of shale normal compaction (blue trend) and elastic rebound/unloading behaviour (From Bowers 2001) | 48 |
| Figure 2.13. Pore structure model used to explain shale compaction behaviour (From Bowers and Katsube, 2002) | 49 |

| | |
|--|----|
| Figure 2.14. Schematic Cartesian diagram for normal compaction and unloading of siliciclastic mudstones according to geomechanics principles showing dependence of vertical effective stress on velocity and density as used in the methodology of Bowers (2001). Axes are sonic (or seismic) P-wave velocity, density and vertical effective stress (From Goult and Ramdhan 2012)..... | 50 |
| Figure 2.15. Density and velocity log responses from Well A. (a) velocity vs density (b) velocity and density vs effective stress (c) velocity and density vs depth (modified after Lahann et al., 2001). | 52 |
| Figure 2.16. Density and velocity log responses from Well B. (a) velocity and density vs depth (b) velocity vs effective stress (c) density vs effective stress (d) velocity vs density (modified after Lahann et al., 2001). | 53 |
| Figure 2.17. Schematic illustration of the idea proposed by Lahann (2002) for chemically-enhanced mechanical compaction. (a) Compaction at hydrostatic conditions. (b) Compaction at constant effective stress. (c) Compaction as effective stress decreases (i.e., during unloading). Refer to text for further explanation. | 54 |
| Figure 2.18. Mudstone compaction trend (arrowed curve) on a sonic-density crossplot based on results obtained by Dutta (2002) in the Gulf of Mexico. | 55 |
| Figure 2.19. Velocity-density crossplot illustrating different mudstone compaction pathways based on results obtained by Hoesni (2004) and Swarbrick (2012) (Modified after Swarbrick 2012). | 57 |
| Figure 2.20. Overpressure generation by load transfer in maturing source rocks. Transforming some of the kerogen into oil would increase the porosity of the mudstone (Point A to B) if no pore-fluid can escape. This would have the effect of transferring some of the overburden load supported by the original kerogen onto the pore fluid. The rock now has the same porosity as when it was buried to point C thus it would be overpressured if the effective stress remains constant. K: kerogen (From Osborne and Swarbrick 1997)..... | 59 |
| Figure 3.1. Example of MICP pore throat size distribution and cumulative porosity data representation | 78 |
| Figure 3.2. Left: HRXTG machine with two rotation axes indicated (refer to text for explanation). Right: Close-up of the detached custom build goniometer head with magnetic sample holder | 80 |

| | |
|--|-----|
| Figure 3.3. Example of 2 θ scan result with peak positions of characteristic clay minerals. | 81 |
| Figure 3.4. (a) Schematic diagram of variation of sand vs clay mineral content (increasing left to right) (b) Associated response on a plot of density versus the difference between neutron porosity and density porosity (based on Katahara, 2008). | 84 |
| Figure 3.5. Schematic crossplot of density porosity vs neutron porosity illustrating a simple quartz-clay-water model. The clay mineral volume (red arrow) is proportional to the neutron porosity minus density porosity, if both are on a sandstone matrix (From Katahara, 2006b). | 85 |
| Figure 4.1. Location map of the Malay Basin (modified after Madon, 2007). The XY line is a cross section in Figure 34. | 92 |
| Figure 4.2. Stratigraphic framework and structural history of the Malay Basin (modified after Madon 2007). | 95 |
| Figure 4.3. Cross section of the Malay Basin along XY (Figure 32). The top of overpressure is shown as the blue dashed line (modified after Madon 2007). | 96 |
| Figure 4.4. The present-day state of overpressure in the Malay Basin as proposed by Madon (2007). The main overpressure compartment with a convex-up top-of-overpressure in the basin centre is maintained by the hydraulic conductivity of the sediment column and the presence of a regional shale seal (Units F and L). Secondary pressure compartments are the result of pressure transfer from the main compartment and are sealed by transgressive shale units (from Madon, 2007). | 97 |
| Figure 4.5. Location map for wells Bravo-L, Bravo-X and Bravo-Y in Central Malay Basin (courtesy of Petronas). The black lines represent faults. The red dashed line outlines a gas cloud observed on seismic data (Figure 4.6). | 98 |
| Figure 4.6. Vertical slice passing through wells Bravo-X and Bravo-Y from the provided 3D seismic cube. Note the presence of a gas cloud and the possibility of a fault between the two wells (reflections are obscured by the presence of gas). | 99 |
| Figure 4.7. Bravo-Y gamma (a), neutron (b), sonic (c) and density (d) logs through the working interval prior to mudstone discrimination. Encircled sections display anomalously low sonic transit time compared to neighbouring intervals. | 101 |
| Figure 4.8. Pore pressure-depth profiles for (a) Bravo-X, (b) Bravo-Y and (c) Bravo-L. (d) estimated local linear geothermal gradient and RFT measured temperatures plotted against depth for Bravo-X and Bravo-Y. | 103 |

| | |
|--|-----|
| Figure 4.9. Washed cutting samples (a)XM8 (b)XM6 (c) XM1 and (d) XM9. Scale bar is 5cm. | 104 |
| Figure 4.10. Bulk mineral composition of mudstone samples obtained from QXRD | 106 |
| Figure 4.11. Bulk mineralogy versus depth for (a)(c)(e)(g) Bravo-L and (b)(d)(f)(h) Bravo-Y. | 107 |
| Figure 4.12. Bravo-Y bulk rock CEC plotted against QXRD-based (a) illite-smectite content, (b) total clay content, (c) barite content and (d) measured TOC content. The dashed line represents the expected CEC values for a given illite-smectite and clay content. Encircled samples are having anomalously high CEC values for their illite-smectite content based on the estimated trend. | 111 |
| Figure 4.13. Experimental and simulated XRD patterns for ethylene glycol-saturated samples XM1 and XM-8. | 112 |
| Figure 4.14. Calculated smectite equivalent % in illite-smectite for Bravo-Y mudstone samples plotted against depth. (a) smectite equivalent content calculated using the CEC results as described in 3.3.3. (b) smectite equivalent content calculated using the combination of the bulk QXRD and <0.2 μm fraction modelling results. | 113 |
| Figure 4.15. TOC (%) results for Bravo-Y mudstones. | 114 |
| Figure 4.16. $\text{SiO}_2\text{-Al}_2\text{O}_3\text{-TOC}$ ternary diagram showing mixing relationships of the main sediment components in Bravo-Y samples (red dots). Green and brown stars indicate the average compositions of smectite and illite respectively; the field outlined by dashed lines represents the compositional variation of illites and smectites (based on Weaver, 1989). | 115 |
| Figure 4.17. Strong positive correlation between calculated Chemical Index of Alteration (CIA) and Chemical Index of Weathering (CIW) values of Bravo-Y mudstones. | 116 |
| Figure 4.18. Variation of (a) Si/Al, (c) K/Al and (e)Na/Al with depth in comparison with the variation of (b) quartz, (d) illite-smectite and (f) plagioclase content. | 117 |
| Figure 4.19. Measured clay mineral fabric anisotropy values of Bravo-Y mudstone samples. Representative illite/mica and chlorite/kaolinite pole figures are displayed to the right. The letters of these samples are shown on the left figure. | 122 |
| Figure 4.20. SEM images of XM7. (a)(b) Low-magnification BSEM images showing abundant silt-sized grains. (c) (d) BSEM images showing examples of well-developed planar clay mineral fabric. Silt-sized quartz grains locally disturb the fabric | |

| | |
|--|-----|
| alignment. Arrows show examples of compactional bending of clays around resistant larger grains. Q: quartz, M: mica, Sid: siderite, Py: pyrite. All images are from sections perpendicular to the bedding..... | 123 |
| Figure 4.21. BSEM images showing examples for pore filling euhedral siderite cement in XM7. Arrows show examples of compactional bending of clays around resistant larger grains. Q: quartz, Sid: siderite. Both images are from sections perpendicular to the bedding. | 123 |
| Figure 4.22. Density log derived porosity for Bravo-Y mudstones. Smoothed density log porosity is in grey with best fitting exponential porosity trend in red. | 124 |
| Figure 4.23. Calculated bedding perpendicular permeability (after Yang and Aplin 2010) for Bravo-Y mudstones. | 126 |
| Figure 4.24. Multi element spider diagrams for Bravo-Y mudstones. Major and trace element composition normalised to post-Archean Australian average shale (PAAS; values of Taylor and McLennan 1985) and to average upper continental crust (UCC; values from McLennan 2001)..... | 128 |
| Figure 4.25. Chondrite-normalised (values of Taylor and McLennan 1985) REE patterns for Bravo-Y mudstones..... | 129 |
| Figure 4.26. Selected trace element plots indicating the average bulk composition of the source. (a) Th versus Sc (b) Th/Sc versus Sc (c) discrimination plot of La/Th versus Hf (after Floyd and Leveridge 1987) (d) discrimination plot of Th/Sc versus Zr/Sc (after McLennan et al 1993) monitoring sediment sorting and recycling processes. UCC, PAAS (values from Taylor and McLennan 1985, McLennan 2001) and average Phanerozoic granite, granodiorite, andesite and basalt (values from Condie 1993) are additionally plotted for reference. | 129 |
| Figure 4.27. Discrimination plot of La-Th-Sc (after Bhatia and Crook 1986) indicating the average bulk composition of the source. UCC, PAAS (values from Taylor and McLennan 1985, McLennan 2001) and average Phanerozoic granite, granodiorite, andesite and basalt (values from Condie 1993) are additionally plotted for reference..... | 130 |
| Figure 4.28. A-CN-K (A=Al ₂ O ₃ ; CN= CaO*+Na ₂ O; K=K ₂ O; all in molecular proportions; refer to 3.3.5 for more detail) ternary diagram of the Bravo-Y mudstone sample set with associated chemical index of alteration (CIA) values (after Nesbitt and Young 1982). | |

| | |
|---|-----|
| Dashed arrow represents the estimated weathering trend. Average compositions of granite, granodiorite, andesite, basalt (from Condie 1993), post-Archean Australian average shale (PAAS, Taylor and McLennan 1985), average upper continental crust (UCC, McLennan 2001) and average composition of illites and smectites are plotted for reference. Refer to text for further explanation. | 131 |
| Figure 4.29. Plot of chemical index of alteration (CIA) against index of compositional variability (ICV) (after Potter et al 2005) illustrating relationships between the degree of source area weathering and original detrital mineralogy in the Bravo-Y mudstones. Dashed lines represent weathering trends. Average compositions of granite (Gr), granodiorite (Grd), andesite (And), basalt (Ba) (from Condie 1993), PAAS (Taylor and McLennan 1985) and UCC (McLennan 2001) are plotted for reference. Refer to text for further explanation. | 132 |
| Figure 4.30. Published examples of illite % in illite-smectitie with new results from the Central Malay Basin Bravo-Y well plotted against maximum burial depth (a) and maximum burial temperature (b)..... | 135 |
| Figure 4.31. Smoothed density (blue) and sonic (red) logs through the mudstone intervals for (a) Bravo-X, (b) Bravo-Y and (c) Bravo-L. Top of overpressure is indicated by horizontal black dotted line..... | 137 |
| Figure 4.32. Sonic-density crossplots for Bravo-X (a), Bravo-Y (b) and Bravo-L (c) with smoothed logs. Colour coding is by depth below seafloor (m).Blue and red dots denote the last hydrostatic RFT and the first overpressured RFT respectively. Red and Green line is the illitic and smectitic line from Dutta (2002). | 138 |
| Figure 4.33. Central Malay Basin Bravo-Y density porosity (grey curve) plotted against calculated hydrostatic vertical effective stress. The density reversal near TD is interpreted as a result of higher porosity due to early overpressure generated by disequilibrium compaction. Red curve – the normal compaction curve fitted to the mudstone density data where pore pressure is hydrostatic. Dashed blue and black trends – experimentally compacted kaolinite (from Mondol et al. 2007) and mechanically compacted mudstone with 40% clay content (from Yang & Aplin 2004)..... | 141 |

| | |
|---|-----|
| Figure 5.1. Location map of the study area, offshore mid-Norway (modified after Goulty et al., 2016) with locations of the studied wells. The XY line marks the location of the geoseismic section shown in Figure 5.3. | 147 |
| Figure 5.2. Structural elements in the Halten Terrace area (modified after Cicchino et al., 2015)..... | 149 |
| Figure 5.3. Geoseismic section along profile XY (see Figure 65 for location). Key picked horizons: BPia – Base Upper Pliocene; IMo – Intra Miocene; ; TPal – Top Paleocene; BPal – Base Paleocene; ICmp – Intra-Campanian; TCen – Top Cenomanian; ILK – Intra-Lower Cretaceous; BK – Base Cretaceous; BJ – Base Jurassic; IP? – Intra-Permian(?). The Lange Formation lies between the Top Cenomanian and Base Cretaceous horizons. The Kvitnos Formation immediately overlies the Top Cenomanian horizon (from Goulty et al., 2016)..... | 150 |
| Figure 5.4. Chronostratigraphy and lithostratigraphy of the Halten Terrace area (from Cicchino et al., 2015). | 151 |
| Figure 5.5. Multi-well pressure-depth plot showing pore pressure measurements as reported by O'Connor et al. (2012) from isolated turbidite sandstone bodies within the Cretaceous mudstones. The single outlier deep pressure measurement from well 6506/11-6 is in the lowest acceptable data category (O'Connor et al., 2012) and is probably erroneous. The lithostatic stress shown here is an average profile for the wells with good density logs (from Goulty et al., 2016)..... | 154 |
| Figure 5.6. Spatial variation of the density log porosity (%) at a common depth of 2700m below seafloor in the Haltenbanken study area as reported by Cicchino et al. (2015) | 155 |
| Figure 5.7. Spatial variation of calculated linear geothermal gradients (°C/km) in the Haltenbanken study area as reported by Cicchino et al. (2015) | 156 |
| Figure 5.8. X Washed cutting samples (a) 6406/2-3; 3254 mbs; (b) 6507/2-3; 2515 m bsf. | 159 |
| Figure 5.9. Examples of the four most common mudstone lithology types from (a) 6507/2-3, ~2513m bsf; (b) 6506/11-4S, ~3964.9m bsf (c) 6506/11-3, 3642m bsf (d) 6506/11-3, 2815m bsf (e) 6607/5-1, 3025m bsf (f) 6506/3-1, 2773-74m bsf. Refer to text for further explanation..... | 161 |
| Figure 5.10. Bulk mineral composition of mudstone samples obtained from QXRD | 162 |

| | |
|---|-----|
| Figure 5.11. Bulk mineralogy versus depth trends in the studied Cretaceous mudstones | 163 |
| Figure 5.12. Bulk rock CEC plotted against QXRD measured barite content..... | 168 |
| Figure 5.13. (a) Calculated smectite equivalent % in illite-smectite for Cretaceous mudstone samples plotted against depth below seafloor. Smectite equivalent content was calculated using CEC results as described in 3.3.3. (b) QXRD measured K-feldspar content versus depth below seafloor. | 169 |
| Figure 5.14. Experimental and simulated XRD patterns for ethylene glycol-saturated samples from wells 6406/2-3 and 6507/6-2. | 170 |
| Figure 5.15. Smectite equivalent (%) in illite-smectite versus depth for samples from wells 6406/2-3 and 6507/6-2. Smectite equivalent content was calculated using the combination of the bulk QXRD and <0.2µm fraction modelling results. | 171 |
| Figure 5.16. TOC (wt%) results for Cretaceous mudstones. | 172 |
| Figure 5.17. Variation of (a) Si/Al, (c) Na/Al and (e) K/Al with depth in comparison with the variation of (b) quartz, (d) plagioclase and (f) illite-smectite..... | 174 |
| Figure 5.18. Correlation between calculated CIA and CIW values for cuttings and core samples. | 178 |
| Figure 5.19. Measured illite-smectite (001) maximum intensity values of Cretaceous mudstone samples. Representative illite-smectite pole figures are displayed to the right..... | 179 |
| Figure 5.20. Post depositional, soft sediment deformation structure (slump) in a mudstone sample at 4020 m bsf in well 6406/2-3 and associated illite-smectite (001) pole figure. Picture source: Norwegian Petroleum Directorate (NPD)..... | 180 |
| Figure 5.21. Illite-smectite (001) maximum intensity values shown in correlation with the maximum intensity values of chlorite (002)+kaolinite (001) for the Cretaceous mudstone samples..... | 181 |
| Figure 5.22. Illite-smectite maximum intensity values shown in correlation with (a) total clay and (b) quartz content of the Cretaceous mudstone samples. | 181 |
| Figure 5.23. BSE images of Lower Cretaceous mudstone samples from wells (a)(b)(d) 6406/2-3 at 4003m and (c) 6507/2-3 at 2878m depths below seafloor, showing examples of well-developed clay mineral fabric. Q: quartz, M: mica, OM: organic | |

matter, Py: pyrite, Sid: siderite. All sections imaged are perpendicular to the bedding.....182

Figure 5.24. BSE images of Lower Cretaceous mudstone samples from well 6507/2-3 at 2508 (a)(c)(d) and 2878m (b) depths below seafloor and, showing examples of poor sorting (a)(b) and of silt-sized quartz grains locally disturbing the clay mineral fabric (c)(d). Q: quartz, M: mica, Fp: detrital feldspar Sid: siderite. All sections imaged are perpendicular to the bedding.....183

Figure 5.25. BSE images of Lower Cretaceous mudstone sample from wells 6406/2-3 at 4003m (f) 6507/2-3 at 2508 (c) and 2878 m (a)(b)(d)(e) depths below seafloor showing examples of strongly altered and mechanically deformed detrital mica grains (a)(b); sand-sized detrital feldspar grain (c); partially dissolved detrital feldspar grain with authigenic chlorite inside its dissolution voids (d); Completely altered remnants of detrital grains of unknown origin (e) and detrital feldspar grains completely replaced by authigenic kaolinite (e)(f). Q: quartz, M: mica, Py: pyrite, Fp: detrital feldspar Sid: authigenic siderite, Kaol Rep: authigenic kaolinite replacing detrital feldspar, Chl: authigenic chlorite, Adt: completely altered remnants of detrital grains of unknown origin (likely feldspar). All sections imaged are perpendicular to the bedding.....184

Figure 5.26. BSE images of a siderite concretion in Lower Cretaceous mudstone sample from well 6507/2-3 at 2878 m depth below seafloor with early diagenetic pore filling euhedral siderite cement and abundant foraminifer fossils, showing examples of early diagenetic kaolinite preserved inside foram fossil cavities (a,c), late diagenetic chlorite replacing early diagenetic kaolinite (c) and locally preserved isotropic clay fabrics (b,c,d,e,f). Cal: calcite, Py: pyrite, Sid: authigenic siderite Kaol: authigenic kaolinite Chl: authigenic chlorite. All sections imaged are perpendicular to the bedding.....185

Figure 5.27. BSE images of a siderite concretion in Lower Cretaceous mudstone sample from well 6507/2-3 at 2878m depth below seafloor with (a) abundant pore filling euhedral siderite and authigenic kaolinite, (b) example of a larger void inside a planktonic foraminifer fossil that has been filled by authigenic phases (pyrite, siderite, kaolinite and chlorite). Cal: calcite, Py: pyrite, Sid: siderite Kaol: kaolinite Chl: chlorite Q: quartz. All sections imaged are perpendicular to the bedding.....186

| | |
|--|-----|
| Figure 5.28. BSE images of a Lower Cretaceous mudstone sample from well 6507/2-3 at 2878m depth below seafloor, showing examples of authigenic quartz overgrowth cement on detrital grains. White arrows denote euhedral crystal terminations resulting in inter-grown composite grains. | 188 |
| Figure 5.29. BSE images of Lower Cretaceous mudstone samples from wells (a) 6507/2-3 at 2878m and (b) 6406/2-3 at 4003m depths below seafloor, showing examples of (a) compactionally deformed organic matter (likely wood fragments) with abundant framboidal pyrite, (b) example of a mudstone sample with abundant detrital organic matter with characteristic arcuate shapes indicating continental origin and woody material..... | 188 |
| Figure 5.30. (a) Measured grain densities and (b) corrected total porosities of selected Cretaceous mudstone samples plotted against depth below seafloor..... | 189 |
| Figure 5.31. (a) Correlation between corrected total porosity and illite-smectite (001) fabric intensity; (b) correlation between mean pore throat radius and illite-smectite (001) fabric intensity..... | 190 |
| Figure 5.32. Calculated bedding perpendicular permeability (after Yang and Aplin, 2010) of selected Cretaceous mudstone samples..... | 191 |
| Figure 5.33. Corrected pore throat size distribution (left) and corrected cumulative porosity (right) (from MICP) of selected Cretaceous mudstone samples. Dashed lines on right figures denote mean pore throat radius. | 192 |
| Figure 5.34. 1D burial-temperature history plot for wells 6406/2-3 and 6507/2-3. Depth is displayed relative to sea surface (m)..... | 197 |
| Figure 5.35. Pore fluid overpressure and vertical effective stress (VES) development for the Lower Cretaceous Lange Formation (middle part) in wells 6406/2-3 and 6507/2-3. | 198 |
| Figure 5.36. Porosity and permeability of the modelled formation units in wells 6406/2-3 and 6507/2-3. Depth is displayed relative to sea surface (m). | 199 |
| Figure 5.37. Modelled formation pressures caused by disequilibrium compaction and measured RFT pressures (from O'Connor et al., 2012) within the Lange Formation in wells 6406/2-3 and 6507/2-3. Pore pressure measurements exceed the modelled fluid pressures by 5-10MPa which suggest the presence of pressure generating | |

| | |
|---|-----|
| mechanisms other than disequilibrium compaction within the Cretaceous mudstones. Depth is displayed relative to sea surface (m). | 200 |
| Figure 5.38. Multi element spider diagram for Cretaceous mudstones. Major and trace element composition is normalised to post-Australian average shale (PAAS; values of Taylor and McLennan 1985). | 202 |
| Figure 5.39. Multi element spider diagram for Cretaceous mudstones. Major and trace element composition is normalised to average upper continental crust (UCC; values from McLennan, 2001). | 202 |
| Figure 5.40. Chondrite-normalised (values of Taylor and McLennan, 1985) REE patterns for Cretaceous mudstones. | 204 |
| Figure 5.41. Selected trace element plots indicating the average composition of the source. (a) Th versus Sc (b) Th/Sc versus Sc (c) discrimination plot of La/Th versus Hf (after Floyd and Leveridge, 1987) (d) discrimination plot of Th/Sc versus Zr/Sc (after McLennan et al., 1993) monitoring sediment sorting and recycling processes. UCC, PAAS (values from Taylor and McLennan, 1985 and McLennan, 2001) and average Phanerozoic granite, granodiorite, andesite and basalt (values from Condie, 1993) are additionally plotted for reference. | 205 |
| Figure 5.42. Discrimination plot of La-Th-Sc (after Bhatia and Crook, 1986) indicating the average bulk composition of the source. UCC, PAAS (values from Taylor and McLennan, 1985 and McLennan, 2001) and average Phanerozoic granite, granodiorite, andesite and basalt (values from Condie, 1993) are additionally plotted for reference. | 206 |
| Figure 5.43. A-CN-K ($A=Al_2O_3$; $CN=CaO^*+Na_2O$; $K=K_2O$; all in molecular proportions; refer to 3.3.5 for more detail) ternary diagram of the Cretaceous mudstone sample set with associated chemical index of alteration (CIA) values (after Nesbitt and Young, 1982). Dashed arrow represents the estimated weathering trend. Average compositions of granite, granodiorite, andesite and basalt (values from Condie, 1993), post-Archean Australian average shale (PAAS, Taylor and McLennan, 1985), average upper continental crust (UCC, McLennan, 2001) and average composition of illites and smectites are additionally plotted for reference. Refer to text for further explanation. | 207 |

| | |
|--|-----|
| Figure 5.44. Plot of chemical index of alteration (CIA) against index of compositional variability (ICV) (after Potter et al., 2005) illustrating relationships between the degree of source area weathering and original detrital mineralogy in the Cretaceous mudstones. Dashed lines represent weathering trends. Average compositions of granite, granodiorite, andesite and basalt (values from Condie, 1993), post-Archean Australian average shale (PAAS, Taylor and McLennan, 1985), average upper continental crust (UCC, McLennan, 2001) are additionally plotted for reference. Refer to text for further explanation..... | 208 |
| Figure 5.45. Published examples of illite % in illite-smectite with new results from Cretaceous mudstones of the Halten Terrace, offshore mid-Norway plotted against maximum burial temperature. Illite % in illite-smectite was calculated using the CEC results as described in 3.3.3. | 210 |
| Figure 5.46. Depths of the top of the Kvitnos and base of the Lange formations at present day (filled circles) and prior to deposition of the Naust Formation (empty circles) in all studied wells. Red dashed line represents the 70°C isotherm which is the likely temperature of the onset of illitization. Temperature is calculated using a common linear geothermal gradient of 38°C/km from the seafloor which is assumed to be at 5°C..... | 211 |
| Figure 5.47. (a) Multi well pressure-depth plot of Figure 69 colour-coded according to the porosity classification of Cicchino et al. (2015). Separate trends are drawn through pressure measurements from the Lange Fm sands in the shallower low porosity wells and in the deeper high porosity wells (modified after Cicchino et al., 2015). Lateral variations in mudstone porosity show correlation with the (b) present day top Kvitnos depth, (c) base Lange depth, (d) Cretaceous interval thickness and (e) overpressure estimated from mud weight. Plots coloured according to the porosity classification of Cicchino et al. (2015). Correlation plots were constructed using data presented by Cicchino et al. (2015)..... | 214 |
| Figure 5.48. Smoothed density (blue) and sonic (red) logs through the mudstone intervals for (a) 6406/2-3 and (b) 6507/2-3. | 218 |
| Figure 5.49. Sonic-density crossplots for 6406/2-3 (a) and 6507/2-3 (b). Colour coding is by depth relative to sea surface. Red and green line is the illitic and smectitic line from Dutta (2002)..... | 219 |

| | |
|--|-----|
| Figure 5.50. Sonic-density crossplots for nine wells (including 6406/2-3; 6507/2-3 and 6506/3-1; locations of the rest is shown in Goulty et al. 2016) using lithology-corrected sonic transit times and smoothed logs. Vertical arrows denote picked onsets of unloading in each well (from Goulty et al., 2016). | 221 |
| Figure 5.51. Pressure-depth profiles within the Cretaceous formations for ten wells (including 6406/2-3; 6507/2-3 and 6506/3-1; locations of the rest is shown in Goulty et al. 2016). Depths are displayed relative to mean sea level. Trends were estimated by fitting to direct measurements. Dashed line denotes maximum disequilibrium compaction overpressure at ~1.5Ma when bulk of the Naust Fm was deposited (Rise et al., 2005). The depths of unloading were picked on sonic-density crossplots as shown in Figure 5.50 (from Goulty et al., 2016)..... | 222 |
| Figure 5.52. (a) Multi well pressure-depth plot showing pressure measurements from isolated turbidite sandstone bodies in the Cretaceous. (b) Evidence for continued compaction at reduced effective stresses associated with smectite illitization in the Cretaceous mudstones in well 6406/2-3. Density porosity was calculated from smoothed logs using 2.75g/cm ³ for grain density and 1.05g/cm ³ for fluid density. Mercury intrusion porosity denotes corrected total porosity which was determined according to 3.3.7. The exponential normal compaction trend of Hansen (1996) for hydrostatically pressured Tertiary and Cretaceous mudstones on the Norwegian Shelf is shown here (from Andras et al., 2016). | 223 |
| Figure 5.53. Best-fitting exponential trends for the density porosity values in the Kvitnos and Lange mudstones penetrated by 48 wells at Haltenbanken (locations shown in Cicchino et al. 2015), coloured according to the value of density porosity at 2700m depth below seafloor: blue – low porosity of 9-16%; green – intermediate porosity of 16-18%; red – high porosity of 18-25%. Cuttings from the four named wells with dashed trend lines were sampled for XRD analysis, as reported by Cicchino et al. (2015). The linear normal compaction trend of Hansen (1996) for hydrostatically pressured Tertiary and Cretaceous mudstones on the Norwegian shelf is shown here. (From Cicchino et al., 2015). | 225 |
| Figure 6.1. Location map of the Sergipe-Alagoas Basin..... | 232 |
| Figure 6.2. Stratigraphic framework and structural history of the Sergipe-Alagoas Basin (modifie after Mohriak et al., 2000). Red square marks the study interval. | |

| | |
|--|-----|
| Abbreviations of formation units: EST, Estância; BAT, Batinga; ARA, Aracaré; BAN, Bananeiras; SER, Serraria; BIT, Barra de Itiúba; PDO, Penedo; CSO, Coqueiro Seco; MAC, Maceió; MUR, Muribeca; RIA, Riachuelo; TQR, Taquari; COT, Cotinguiba; AJU, Aracaju; CAL, Calumbi; MOS, Mosquero; MRT, Marituba..... | 233 |
| Figure 6.3. Location map for wells A, C, D and E in the Sergipe Sub-Basin. | 235 |
| Figure 6.4. Schematic NW-SE cross section of the Sergipe Sub-Basin (Based on Feijo, 2014)..... | 236 |
| Figure 6.5. Pore pressure-depth profiles for wells A, C, D and E. Blue dots are direct formation pressure measurements and dashed lines denote mudweights. | 237 |
| Figure 6.6. Measure formation temperatures in the shelfal wells. Red dots: direct readings; Green dots: extrapolated readings; and black dots: modelled temperatures (modified after Sargent et al., 2015). | 238 |
| Figure 6.7. Washed cutting samples (a) Well A; 1098m bsf (b) Well E; 3259m bsf..... | 240 |
| Figure 6.8. Examples of mudstone lithology types from (a) Well C; ~2910-2913m bsf and (b) Well E; ~2752-53m bsf. | 241 |
| Figure 6.9. Bulk mineral composition of mudstone samples obtained from QXRD. | 242 |
| Figure 6.10. Bulk mineralogy versus depth trends for Well A mudstones. | 244 |
| Figure 6.11. Bulk mineralogy versus depth trends for Well C mudstones. | 245 |
| Figure 6.12. Bulk mineralogy versus depth trends for Well D mudstones. | 246 |
| Figure 6.13. Bulk mineralogy versus depth trends for Well E mudstones..... | 247 |
| Figure 6.14. Bulk rock CEC plotted against QXRD measured barite content..... | 254 |
| Figure 6.15. (a) Calculated smectite equivalent % in illite-smectite for the studied mudstone samples plotted against depth below seafloor. Smectite equivalent content was calculated using CEC results as described in 3.3.3. (b) QXRD measured K-feldspar content versus depth below seafloor. | 255 |
| Figure 6.16. Experimental and simulated XRD patterns for ethylene glycol-saturated samples from Well C..... | 256 |
| Figure 6.17. Smectite equivalent (%) in illite-smectite versus depth for the studied samples. Smectite equivalent content was calculated using the combination of the bulk QXRD, <2 μ m and <0.2 μ m fraction modelling results..... | 257 |
| Figure 6.18. TOC (wt%) results for the studied mudstones..... | 258 |

| | |
|--|-----|
| Figure 6.19. Variation of (a) Si/Al, (c) K/Al and (e) Na/Al with depth in comparison with the variation of (b) quartz, (d) illite-smectite and (f) plagioclase. | 260 |
| Figure 6.20. Strong positive correlation between calculated CIA and CIW values of the studied mudstones. | 264 |
| Figure 6.21. (a) Measured grain densities and (b) corrected total porosities of selected mudstone samples plotted against depth below seafloor. | 265 |
| Figure 6.22. Calculated bedding perpendicular permeability (after Yang and Aplin, 2010) of selected mudstone samples. | 266 |
| Figure 6.23. Corrected pore throat size distribution (left) and corrected cumulative porosity (right) (from MICP) of selected mudstone samples. Dashed lines on right figures denote mean pore throat radius. | 267 |
| Figure 6.24. Multi element spider diagrams for Sergipe Alagoas Basin mudstones. Major and trace element composition normalised to post-Archean Australian average shale (PAAS; values of Taylor and McLennan 1985) and to average upper continental crust (UCC; values from McLennan 2001). | 269 |
| Figure 6.25. Chondrite-normalised (values of Taylor and McLennan, 1985) REE patterns for Sergipe Alagoas Basin mudstones. | 270 |
| Figure 6.26. Selected trace element plots indicating the average composition of the source. (a) Th versus Sc (b) Th/Sc versus Sc (c) discrimination plot of La/Th versus Hf (after Floyd and Leveridge, 1987) (d) discrimination plot of Th/Sc versus Zr/Sc (after McLennan et al., 1993) monitoring sediment sorting and recycling processes. UCC, PAAS (values from Taylor and McLennan, 1985 and McLennan, 2001) and average Phanerozoic granite, granodiorite, andesite and basalt (values from Condie, 1993) are additionally plotted for reference. | 271 |
| Figure 6.27. Discrimination plot of La-Th-Sc (after Bhatia and Crook, 1986) indicating the average bulk composition of the source. UCC, PAAS (values from Taylor and McLennan, 1985 and McLennan, 2001) and average Phanerozoic granite, granodiorite, andesite and basalt (values from Condie, 1993) are additionally plotted for reference. | 272 |
| Figure 6.28. A-CN-K ($A=Al_2O_3$; $CN=CaO^*+Na_2O$; $K=K_2O$; all in molecular proportions; refer to 3.3.5 for more detail) ternary diagram of the Sergipe Alagoas Basin mudstone sample set with associated chemical index of alteration (CIA) values (after Nesbitt | |

and Young, 1982). Dashed arrow represents the estimated weathering trend. Average compositions of granite, granodiorite, andesite and basalt (values from Condie, 1993), post-Archean Australian average shale (PAAS, Taylor and McLennan, 1985), average upper continental crust (UCC, McLennan, 2001) and average composition of illites and smectites are additionally plotted for reference. Refer to text for further explanation.....273

Figure 6.29. Plot of chemical index of alteration (CIA) against index of compositional variability (ICV) (after Potter et al., 2005) illustrating relationships between the degree of source area weathering and original detrital mineralogy in the Sergipe Alagoas Basin mudstones. Dashed lines represent weathering trends. Average compositions of granite, granodiorite, andesite and basalt (values from Condie, 1993), post-Archean Australian average shale (PAAS, Taylor and McLennan, 1985), average upper continental crust (UCC, McLennan, 2001) are additionally plotted for reference. Refer to text for further explanation.274

Figure 6.30. Published examples of illite % in illite-smectite with new results from the studied mudstones of the Sergipe Alagoas Basin, offshore Brazil plotted against maximum burial temperature. Illite % in illite-smectite was calculated using the combination of the bulk QXRD, <2µm and <0.2µm fraction modelling results.276

Figure 6.31. Smoothed (a) sonic and (b) density logs through the mudstone intervals for Wells A, C, D and E.279

Figure 6.32. Sonic-density crossplot for Well D. Colour coding is by depth relative to seafloor. Red and green line is the illitic and smectitic line from Dutta (2002).280

Figure 6.33. Sedimentation rate vs age in the four studied wells based on 1D basin modelling (courtesy of Petrobras).281

Figure 6.34. (a) Variation of smectite equivalent (%) in illite-smectite (calculated using the combination of the bulk QXRD, <2µm and <0.2µm fraction modelling results) with increasing depth for the studied samples in comparison with (b) the variation of mudstone porosity with depth. Smoothed lines are calculated density porosity (calculated from smoothed logs using 2.75g/cm³ for grain density and 1.05g/cm³ for fluid density) and coloured dots are corrected total porosity (determined according to 3.3.7).283

| | |
|--|-----|
| Figure 6.35. Calculated density porosity (calculated from smoothed logs using 2.75g/cm ³ for grain density and 1.05g/cm ³ for fluid density) for Sergipe-Alagoas Basin mudstones plotted against calculated hydrostatic vertical effective stress. Coloured dots are corrected total porosity (determined according to 3.3.7). Dashed purple and black trends – experimentally compacted kaolinite (from Mondol et al. 2007) and mechanically compacted mudstone with 50% clay content (from Yang and Aplin 2004). | 284 |
| Figure 7.1. (A) Location map of the Central North Sea showing quad 30,22 and the Norwegian block 6 (red outline); grey colouring shows the distribution of the Triassic sediments. (B) Map of the Central Graben with major structures showing Triassic fields and well locations in UK quadrants 22 and 30 and Norwegian quadrant 6 (modified after Stricker, 2016). | 288 |
| Figure 7.2. Regional lithostratigraphy of the Central Graben, North Sea (from Stricker and Jones, 2016). | 290 |
| Figure 7.3. Multi well pressure-depth plot for Triassic formations in United Kingdom quad 30. Plotted data displays pressure measurements obtained from modular formation dynamics tester (MDT) and drill stem tests (DST) from 41 wells (from Nguyen et al., 2013). | 292 |
| Figure 7.4. Temperature measurements (courtesy of ConocoPhillips) and estimated linear geothermal gradient plotted against depth for the Jade field in block 30. | 293 |
| Figure 7.5. Bulk mineral composition of mudstone samples obtained from QXRD. | 294 |
| Figure 7.6. Bulk mineralogy versus depth trends in the studied Triassic mudstones. | 295 |
| Figure 7.7. Calculated smectite equivalent % in illite-smectite for Triassic mudstone samples plotted against depth relative to Kelly bushing. Smectite equivalent content was calculated using the CEC results as described in 3.3.3. | 298 |
| Figure 7.8. TOC (wt%) results for Triassic mudstones. | 299 |
| Figure 7.9. Measured illite-smectite (001) maximum intensity values of Triassic mudstone samples. Representative illite-smectite pole figures are displayed to the right. | 300 |
| Figure 7.10. Illite-smectite (001) maximum intensity values shown in correlation with (a) total clay and (b) quartz content of the Triassic mudstone samples. | 301 |

| | |
|---|-----|
| Figure 7.11. Illite-smectite (001) maximum intensity values shown in correlation with the maximum intensity values of chlorite (002)+kaolinite (001) for the Triassic mudstone samples..... | 302 |
| Figure 7.12. BSE images of Triassic mudstone samples from wells 22/29-1 (c)(d)(e)(f)(g) and 30/7a-7 (a)(b)(h) at 4624 m and 3414 m depths below seafloor respectively, showing examples of poor sorting and of silt-sized mineral grains locally disturbing the clay mineral fabric (d)(e)(f), and examples of locally well-developed clay mineral fabric (g). Q: quartz, M: mica, Dol: dolomite, Chl: chlorite, Py: pyrite and Hal: halite. All sections imaged are perpendicular to the bedding. | 303 |
| Figure 7.13. BSEM images showing examples for pore filling euhedral and poikilitic halite cement in Well 22/29-1 at 4624m. Q: quartz, M: mica, Dol: dolomite, Chl: chlorite, Py: pyrite, Ank: ankerite, Hal: halite and Kaol: kaolinite. All sections imaged are perpendicular to the bedding..... | 304 |
| Figure 7.14. BSE image of a Triassic mudstone sample from Well 22/29-1 at 4624m depth below seafloor, showing example of authigenic quartz overgrowth cement on detrital grains. White arrows denote euhedral crystal terminations resulting in intergrown composite grains. Q: quartz, Dol: dolomite, Chl: chlorite, Ank: ankerite, Hal: halite. Imaged section is perpendicular to the bedding..... | 305 |
| Figure 7.15. (a) Measured grain densities and (b) corrected total porosities of selected Triassic mudstone samples plotted against depth relative to Kelly bushing. | 306 |
| Figure 7.16. (a) Correlation between corrected total porosity and illite-smectite (001) fabric intensity; (b) correlation between mean pore throat radius and illite-smectite (001) fabric intensity..... | 307 |
| Figure 7.17. Calculated bedding perpendicular permeability (after Yang and Aplin, 2010) of selected Triassic mudstone samples. | 308 |
| Figure 7.18. Corrected pore throat size distribution (left) and corrected cumulative porosity (right) (from MICP) of selected Triassic mudstone samples. Dashed lines on right figures denote mean pore throat radius..... | 309 |
| Figure 7.19. Published examples of illite % in illite-smectite with new results from Triassic mudstones of the North Sea Central Graben plotted against maximum burial temperature..... | 311 |

Figure 7.20. Corrected total porosities (coloured dots; determined according to 3.3.7) plotted against burial depth below seafloor. The exponential normal compaction trend of Hansen (1996) for hydrostatically pressured Tertiary and Cretaceous mudstones on the Norwegian Shelf is shown here. Empty dots denote mudstone porosities recalculated using the combination of the model of Yang and Aplin (2004) and the maximum effective stress values estimated by Stricker and Jones (2016).
.....313

Figure 8.1. Published examples of measured total porosities with new results from Halten Terrace, offshore mid-Norway, Sergipe Alagoas Basin and the Central North Sea plotted against maximum burial depth. Experimental compaction curves for brine-saturated smectite and kaolinite (from Mondol et al., 2007) are plotted in comparison. All depth are measured relative to sea floor.....317

Figure 8.2. Published examples of measured total porosities with new results from Halten Terrace, offshore mid-Norway, Sergipe Alagoas Basin and the Central North Sea plotted against maximum burial temperature.....318

Figure 8.3. 2:1 Al clay (illite + illite-smectite) (001) fabric alignment in MRD plotted against temperature for samples from the mid-Norwegian, Central Malay Basin and Central North Sea case studies and previous studies. At any temperature, there is substantial scatter which is at least partly a reflection of variations in the clay:silt (i.e. plate:sphere) ratio of the samples. Note the sharp increase in alignment at temperatures associated with the onset of illitization (70–100°C). The only anomalous dataset which does not show this abrupt change is that of Aplin et al. (2006), which is interpreted as the result of the highly overpressured slope setting and the presence of pure smectite in those mudstones.....322

Figure 8.4. Illite-smectite (001) fabric alignment shown in correlation with chlorite (002)+kaolinite (001) fabric alignment. Alignment is given in MRD. The strong correlation suggests at least partial mechanical realignment of the clay matrix during clay diagenesis.....323

Figure 8.5. Alignment of illite-smectite (001), measured by HRXTG, as a function of porosity. At any porosity, there is substantial scatter which is at least partly a reflection of variations in the clay:silt (i.e. plate:sphere) ratio of the samples.324

| | |
|---|-----|
| Figure 8.6. BSE image of a Lower Cretaceous mudstone sample, from well from 6507/2-3 at 2878m depth below seafloor, showing an example of silt-sized quartz grains in contact creating pressure shadows in which the phyllosilicates are uncompacted and locally have an isotropic fabric. The section imaged is perpendicular to the bedding. | 326 |
| Figure 8.7. BSE image of a Lower Cretaceous mudstone sample, from well 6507/2-3 at 2878 m depth below seafloor, showing an example of local isotropic chlorite fabric inside a foraminifer fossil. The section imaged is perpendicular to the bedding. ... | 327 |
| Figure 8.8. BSE image of a Lower Cretaceous mudstone sample, from well from 6507/2-3 at 2878 m depth below seafloor, showing an example of isotropic chlorite fabric inside a partially dissolved feldspar grain. The section imaged is perpendicular to the bedding. | 327 |
| Figure 8.9. Schematic illustration of the evolution of mudstone porosity (blue), clay mineral fabric (black) and illite-smectite mineralogy (reddish brown) during burial diagenesis as inferred from natural data presented in this thesis. Refer to text for further explanation..... | 330 |
| Figure 8.10. Pore pressure estimation for Bravo-Y in the Central Malay Basin using the equivalent depth method (red line) and Eaton's method (brown line) with measured pore pressures (blue diamonds). The equivalent depth method uses the exponential normal compaction trend fitted to the smoothed density porosity log as shown in Figure 4.33. Eaton's method uses a linear normal compaction trend fitted to the sonic log data in the hydrostatically pressured shallower section and a standard exponent of three..... | 332 |
| Figure 8.11. (a) Interpretation of the mudstone compaction trend (arrowed curve) on a sonic-density crossplot based on results presented in this thesis. Numbers correspond to three stages of mudstone compaction displayed on Figure 8.9. The green and orange lines are Dutta's (2002) trends for smectite-rich and illite-rich mudstones, respectively. (b) The fan of arrows illustrates possible depth trends for a specific mudstone lithology undergoing diagenesis accompanied by unloading. Different models of velocity-stress and density-velocity dependence of mudstones during illitization is displayed on the bottom figures. Letters show the evolutionary pathway of an arbitrary chosen mudstone bed reaching the same density/porosity | |

| | |
|---|-----|
| value (c) via load transfer and (d) via fluid expansion. Refer to text for more explanation. | 335 |
|---|-----|

List of tables

| | |
|---|-----|
| Table 1.1. Classification of planar hydrous phyllosilicates after Guggenheim et al. (2006) .. | 7 |
| Table 3.1. Pressure steps used during mercury intrusion porosimetry | 77 |
| Table 3.2. Classification for alignment measured in multiples of random distribution (MRD) (from Day-Stirrat, 2006) | 81 |
| Table 4.1. List of mudstone samples selected for study | 105 |
| Table 4.2. Correlation matrix showing values of Pearson's correlation coefficient for Bravo-L mineralogy | 108 |
| Table 4.3. Correlation matrix showing values of Pearson's correlation coefficient for Bravo-Y mineralogy | 109 |
| Table 4.4. Correlation matrix showing values of Pearson's correlation coefficient for major elements of Bravo-Y mudstones. | 118 |
| Table 4.5. Correlation matrix showing values of Pearson's correlation coefficient for selected trace elements of Bravo-Y mudstones | 119 |
| Table 4.6. Correlation matrix showing values of Pearson's correlation coefficient for REE of Bravo-Y mudstones. | 120 |
| Table 5.1. List of Cretaceous mudstone samples selected for study | 158 |
| Table 5.2. Correlation matrix showing values of Pearson's correlation coefficient for mineralogy of the Cretaceous mudstones (all samples). | 164 |
| Table 5.3. Correlation matrix showing values of Pearson's correlation coefficient for 6406/2-3 mineralogy. | 165 |
| Table 5.4. Correlation matrix showing values of Pearson's correlation coefficient for 6507/6-2 mineralogy. | 166 |
| Table 5.5. Correlation matrix showing values of Pearson's correlation coefficient for major elements of Cretaceous mudstones | 175 |
| Table 5.6. Correlation matrix showing values of Pearson's correlation coefficient for REE of Cretaceous mudstones | 176 |
| Table 5.7. Correlation matrix showing values of Pearson's correlation coefficient for selected trace elements of Cretaceous mudstones. | 177 |

| | |
|--|-----|
| Table 5.8. Basic model parameters, with estimated depositional periods in millions of years, layer thicknesses and lithology for the 6406/2-3 1D burial history model. Based on Dalland et al. (1988) and Ottesen et al. (2009). | 195 |
| Table 5.9. Basic model parameters, with estimated depositional periods in millions of years, layer thicknesses and lithology for the 6507/2-3 1D burial history model. Based on Dalland et al. (1988) and Ottesen et al. (2009). | 196 |
| Table 6.1. List of mudstone samples selected for study..... | 240 |
| Table 6.2. Correlation matrix showing values of Pearson's correlation coefficient for Well A mineralogy..... | 248 |
| Table 6.3. Correlation matrix showing values of Pearson's correlation coefficient for Well C mineralogy. | 249 |
| Table 6.4. Correlation matrix showing values of Pearson's correlation coefficient for Well D mineralogy..... | 250 |
| Table 6.5. Correlation matrix showing values of Pearson's correlation coefficient for Well E mineralogy. | 251 |
| Table 6.6. Correlation matrix showing values of Pearson's correlation coefficient for major elements of the studied mudstones..... | 261 |
| Table 6.7. Correlation matrix showing values of Pearson's correlation coefficient for selected trace elements of the studied mudstones. | 262 |
| Table 6.8. Correlation matrix showing values of Pearson's correlation coefficient for REE of the studied mudstones..... | 263 |
| Table 7.1. List of Triassic mudstone samples selected for study..... | 291 |
| Table 7.2. Correlation matrix showing values of Pearson's correlation coefficient for Triassic mudstone mineralogy..... | 296 |

Declarations

I declare that this thesis, which I submit for the degree of Doctor of Philosophy at Durham University, is my own work, except where acknowledgement is made in the text, and not substantially the same as any work which has previously been submitted at this or any other university for any degree, diploma or other qualification.

September, 2017

© Copyright, Péter András, 2017

The copyright of this thesis rests with the author. No quotation from it should be published in any form without the author's prior written consent. All information derived from this thesis must be acknowledged appropriately.

Acknowledgements

The project was part of the GeoPOP Joint Industry Project and has been made possible through the funding of its sponsors who are hereby gratefully acknowledged. This study benefited from the working materials (samples, log data) provided by Petronas, Petrobras and ConocoPhillips. In addition, the British Geological Survey and the Norwegian Petroleum Directorate provided samples, well log data and the guidance of their technical staff.

I am very grateful to my academic supervisors Andrew Aplin, Neil Goulty and Stuart Jones for all the insight and assistance they have provided throughout the project. Firstly, I would like to thank Andy for providing me with the opportunity to take part in this project and for the helpful scientific discussions and advices. I would like to thank him for his assistance and patience during the long write-up period too. I would like to thank Neil for our long discussions on mudstone compaction processes which largely contributed to the completion of this thesis. I would like to thank Stuart for his great support during this project.

I extend my gratitude to all staff, technicians and researchers I have worked with over the course of the project whilst at Durham University, Newcastle University, Polish Academy of Sciences in Krakow and the University of Michigan. These include: Arkadiusz Derkowski, Tomasz Topór (Research Centre in Krakow); Prof. Ben Van Der Pluijm, Austin Boles (University of Michigan); Philip Green, Joshua Obradors Prats (Newcastle University); Colin Sargent, Shanvas Sathar, Chris Saville, Jon Gluyas, Chris Greenwell, Stephan Stricker, Mark Brodie, Sean O’Neil, Ian Chaplin, Leon Bowen (Durham University).

Finally, I would like to thank my wonderful wife, my family and all my friends for all the love and support they have given me throughout this time – I couldn’t have done it without you.

Quote

"Possibly many may think that the deposition and consolidation of fine-grained mud must be a very simple matter, and the results of little interest. However, when carefully studied experimentally it is soon found to be so complex a question, and the results dependent on so many variable conditions, that one might feel inclined to abandon the inquiry, were it not that so much of the history of our rocks appears to be written in this language."

Henry Clifton Sorby, 1908

Chapter 1

Introduction

1.1 Introduction

Fine-grained siliciclastics like muds, mudstones and shales are the most common sediments and sedimentary rock types, constituting two thirds of the sedimentary rock record. They contain the most complete record of earth history (Schieber, 1998). Yet, in spite of their ubiquity, study of mudstones and shales lags behind that of sandstones and carbonates (Schieber and Zimmerle, 1998; Aplin et al., 1999). This apparent “lack of interest” can be (at least partially) attributed to the lack of available shale core samples from deeper (>1km) boreholes. A key reason for this is that shales are generally not the primary targets in petroleum exploration and the additional cost related to coring in deep boreholes is very high.

The recent success of shale gas and shale oil plays generated a renewed interest in shale-related research. Considerable effort has been made to better understand their physical properties (with porosity and permeability being key) and the basic principles controlling their behaviour (e.g. Passey et al., 2010; Milner et al., 2010; Milliken et al., 2013; Loucks et al., 2009). However, most attention was paid to the special cases, to those rocks which act as economic reserves of shale gas or shale oil. The more general/common varieties (usually with TOC <2wt.%), those comprising 70% of the sediments deposited in sedimentary basins worldwide, have received much less attention. Knowledge of their composition, physical properties and compaction behaviour is essential not just from an academic point of view, but also crucial for the petroleum industry, holding importance for basin modelling, seismic interpretation, borehole stability problems and determining the seal capacity of caprocks (e.g. Banik, 1984; Giles et al., 1998; Armitage et al., 2010).

Due to their low permeability, mudstones have a profound effect on the fluid flow in sedimentary basins. Rapid burial of these fine grained, low permeability lithologies can lead to pore fluid overpressure via compaction disequilibrium (Hart et al., 1995). Overpressure has been observed and reported from many sedimentary basins worldwide (e.g. Huffman and Bowers, 2002). Overpressure development affects ground-water circulation at a basin scale (Harrison and Summa, 1991). It also affects the state of stress in the subsurface (Zoback, 2010), thereby influencing both small and large scale structural patterns (e.g. Bruce, 1973; Cartwright, 1994)

Knowledge of overpressure in the subsurface is critical for the petroleum industry since it poses a severe risk during drilling. However, direct pore pressure measurements are only available from permeable reservoir formations. In mudrock sequences pore pressures can only be estimated indirectly, by empirical methods from seismic and wireline log (e.g. velocity, resistivity and density) responses, which capture porosity changes during compaction (Mann and Mackenzie, 1990). For these methods to be effective it is important to understand the relationship between effective stress, lithology, porosity and log responses. It is also essential to understand the nature of the overpressure generating mechanisms in order to choose the best method for pore pressure prediction (Bowers, 1995, 2001).

Although pore pressure prediction in shallower (<2 km), lower temperature (<70°C) sedimentary environments can be done fairly accurately (Eaton, 1975; Bowers, 1995; Yang and Aplin, 2004), these methods fail to deliver accurate predictions in higher temperature environments (Hoesni, 2004; Swarbrick, 2012). The reason for this is our limited understanding of how diagenesis affects the physical properties of fine-grained sediments.

The most important chemical diagenetic processes in siliciclastic mudstones are clay mineral transformations, the most common of which is the smectite-to-illite transformation. Although the illitization reaction has been extensively studied from a mineralogical perspective, its effect on the physical properties of mudstones, and on porosity loss in particular, is not well quantified (e.g. Hower et al., 1976; Bjorlykke and Hoeg, 1997).

There are contrasting views on how clay diagenesis affects mudstone porosity (e.g. Bjorlykke and Hoeg, 1997; Lahann and Swarbrick, 2011). These conflicting ideas concerning the physical processes associated with the transformations have consequences for predicting porosity and pore pressure. Similarly, there has been substantial disagreement about the extent to which clay mineral reactions can generate overpressure and, if they do, the mechanisms involved (e.g. Plumley, 1980; Dutta, 1986; Harrison and Summa, 1991; Audet, 1995; Osborne and Swarbrick, 1997; Lahann and Swarbrick, 2011).

These controversies generated the motivation to study the compaction behaviour of these fine grained lithologies and to unravel the key mineralogical, textural and physical changes during diagenesis. An additional aim was to relate these changes to pore pressure generation and prediction.

This thesis details integrated research studies of mudstone samples and wireline log data from four different case studies in which mudstones have undergone chemical diagenesis in a range of pore pressure environments. Results allow testing of the extent to which mineralogical changes lead to porosity loss and the extent to which pore pressure signatures are retained by mudstone fabrics.

1.2 Basic concepts and terminology

In the following section the basic concepts regarding mudstones, their physical properties and pore pressure are explained.

There are various terminologies used for fine-grained siliciclastic sediments and their properties. These are often not well defined and slackly used. This can lead to confusion since different terminologies are often used for the same thing or conversely the same terminology is used for different things or properties. The next section also explains the terminology which will be used in this thesis.

1.2.1 Mudstones and shales

Mudstones are fine-grained clastic sedimentary rocks comprising grains smaller than 62.5 μm . They are classified as siltstones if >50 % of the grains are 2–63 μm in diameter and claystones, if >50 % of the grains are <2 μm in diameter. They are further defined as shales, if they exhibit some degree of fissility (e.g. Folk, 1974; Schieber, 1998; Potter et al., 2005). The term mudstone and shale is widely used to include all different kinds of fine-grained rock types with different mineralogies (e.g., chalk, diatomites) without restriction to siliciclastic lithologies (Aplin and Macquaker, 2011). In this thesis, I restrict attention to organic-lean (with TOC <2wt.%) siliciclastic mudstones comprised primarily of clay minerals, quartz and feldspars, and will use the term mudstone in the broad sense to include all fine-grained siliciclastic rocks comprising >50% silt and/or clay-sized grains.

1.2.2 Clay minerals

Clay minerals are the most important components in siliciclastic mudstones. They are most commonly weathering products of other silicate minerals and are composed of very small crystallites, usually (but not always) less than 2 μm in diameter. Clay minerals exert a significant effect on the physical characteristics of mudstones and also are at the heart of most diagenetic reactions (e.g. Potter et al., 1980; Velde, 1995; Schieber, 1998; Potter et al., 2005).

Clay minerals are hydrous aluminium silicates belonging to the group of layer silicates ("phyllosilicates"). The silicate layers are the fundamental units of the clay mineral structure, composed of one or two tetrahedral sheets and one octahedral sheet. The tetrahedral sheet is made of Si^{4+} and/or Al^{3+} (sometimes Fe^{3+}) coordinated by oxygen ions forming a tetrahedron. In the octahedral sheet, the cations Al^{3+} , Mg^{2+} , Fe^{2+} and Fe^{3+} are coordinated by oxygen ions and hydroxyl groups to form octahedra. They can be classified by the number and type of the sheets making up the structure. If the silicate layers are composed of one tetrahedral and one octahedral sheet, the structure is denoted as a 1:1 layer silicate structure (e.g. kaolinite). If the structure is composed of one octahedral sheet sandwiched between two tetrahedral sheets, it is called a 2:1 layer type (e.g., illite, smectites). The sheets can be further classified based on the number of occupied octahedral cation sites in the basic structural unit, which contains three octahedral cation sites. If all three octahedral sites are occupied by cations, the sheet is called trioctahedral; if only two out of the three, it is called dioctahedral. Cation substitution in the tetrahedral and/or octahedral sheets can produce charge deficiency that is compensated by the incorporation of mono- or divalent cations in the interlayer position (Bailey, 1980; Guggenheim et al., 2006). The bonding within the layers is strong (ionic-covalent type), whereas between the layers it is relatively weak (van der Waals forces if the layer charge is 0; ionic type if the layer charge >0), which results in the characteristic platy habit of clay crystals. These layers are tens to thousands of nanometers in the X and Y directions and a few to tens of layers are stacked on top of each other in the Z* or [001] crystallographic direction forming clay crystals (Moore and Reynolds, 1997).

Classification of planar hydrous phyllosilicates based on the recommendations of the Association Internationale pour l'Etude des Argiles (AIPEA) Nomenclature Committee is shown in Table 1.1 (Guggenheim et al., 2006).

Clay minerals containing identical layers and interlayers are termed end-member or discrete clay minerals. In this case the strict periodicity of the clay structure along the direction of the Z^* -axis is preserved. Clay minerals may hybridise via mixed layering, in which case the strict periodicity is violated by differences in layer type or in interlayer material along the Z^* -axes. These mineral species are termed mixed layer or interstratified clay minerals (Moore and Reynolds, 1997; Środoń, 1999).

| Layer type | Interlayer material | Group | Octahedral character | Species (not an exhaustive list) |
|--------------------------|--|---------------------------|----------------------|--|
| 1:1 | None or only H ₂ O (x~0) | Serpentine-kaolin | Trioctahedral | Lizardite, berthierine |
| | | | Diocahedral | Kaolinite, dickite, nacrite, halloysite (planar) |
| | | | Di, trioctahedral | Odinite |
| 2:1 | None (x~0) | Talc-pyrophyllite | Trioctahedral | Talc, willemseit |
| | Hydrated exchangeable cations (x~0.2-0.6) | Smectite | Diocahedral | Pyrophyllite |
| | | | Trioctahedral | Saponite, hectorite |
| | Hydrated exchangeable cations (x~0.6-0.9) | Vermiculite | Trioctahedral | Montmorillonite, beidellite, nontronite |
| | | | Diocahedral | Tri vermiculite |
| | Non-hydrated monovalent cations (x~1.0*) | True mica | Trioctahedral | Biotite, annite, phlogopite, lepidolite |
| | | | Diocahedral | Muscovite, celadonite, paragonite |
| | Non-hydrated mono or divalent cations (x~0.6-0.9*) | Interlayer-deficient mica | Trioctahedral | Illite, glauconite |
| | | | Diocahedral | |
| | Non-hydrated divalent cations (x~2.0*) | Brittle mica | Trioctahedral | Margarite |
| | | | Diocahedral | |
| 2:1 (Interstratified) | Hydroxide sheet (x~variable) | Chlorite | Trioctahedral | Chamosite, clinocllore |
| | | | Diocahedral | Donbassite |
| | | | Di, trioctahedral | Sudoite, cookeite |
| | Regularly interstratified (x~variable) | Chlorite-smectite | Tri, Tri | Corrensite (low charge) |
| | | Chlorite-vermiculite | Tri, Tri | Corrensite (high charge) |
| | | Mica-smectite | Di, Di | Rectorite, tosudite |

Table 1.1. Classification of planar hydrous phyllosilicates after Guggenheim et al. (2006)

x: charge/formula unit; Tri: trioctahedral; Di: Dioctahedral

*: values taken from Środoń (1999)

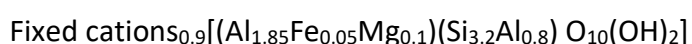
Mixed layering can be characterized based on the stacking order using the term Reichweite, R , as it was originally proposed by Jagodzinski (1949). Reichweite is defined in terms of the probability of finding privileged stacking sequences. Random ordering, when there is no preferred sequence in stacking of layers is characterized by $R = 0$. If there is some preferred sequence in layer stacking than the mixed layering is called ordered. Preferred sequences of single layers of components (e.g. ABABAB..) is characterized by $R = 1$ (short-range ordering).

In case the proportion of the component layers does not equal 1:1 (i.e. ABBBAB..) ordering is defined with respect to one of the components (e.g. in the above case with respect to A). Sequences of two layers of one component with single layers of another (i.e. AABAAB..) is characterized with $R = 2$ (long-range ordering) (Moore and Reynolds, 1997).

$R = 1$ ordering is called regular when the proportion of the component layers equals 1:1 (i.e. ABABAB..). Such species of mixed layer clay minerals are treated as “special cases” and are considered as separate minerals (e.g. rectorite is regular interstratification of dioctahedral mica and dioctahedral smectite). The most common regularly interstratified 2:1 minerals are shown in Table 1.1. Other mixed layer species got their names from a combination of their components’ names (e.g. illite/smectite). The convention is to put the name of the component with smaller d_{001} first (Środoń, 1999).

The four most common clay mineral groups are represented in Figure 1.1. The illite-smectite group (illite, smectite and mixed layer illite/smectite) is by far the most abundant in sedimentary environments, accounting for 30% of the mass of the Earth’s sedimentary cover (Garrels and Mackenzie, 1971).

The key difference between illite and smectite arises from the ion substitution in the tetrahedral and octahedral sheets, resulting in different layer charge magnitudes. According to Srodon et al. (1992) illite interlayers have a stable charge of $0.9/\text{O}_{10}(\text{OH})_2$ and smectite interlayers typically have a layer charge close to $0.4/\text{O}_{10}(\text{OH})_2$. The authors suggested the following structural formula for illite:



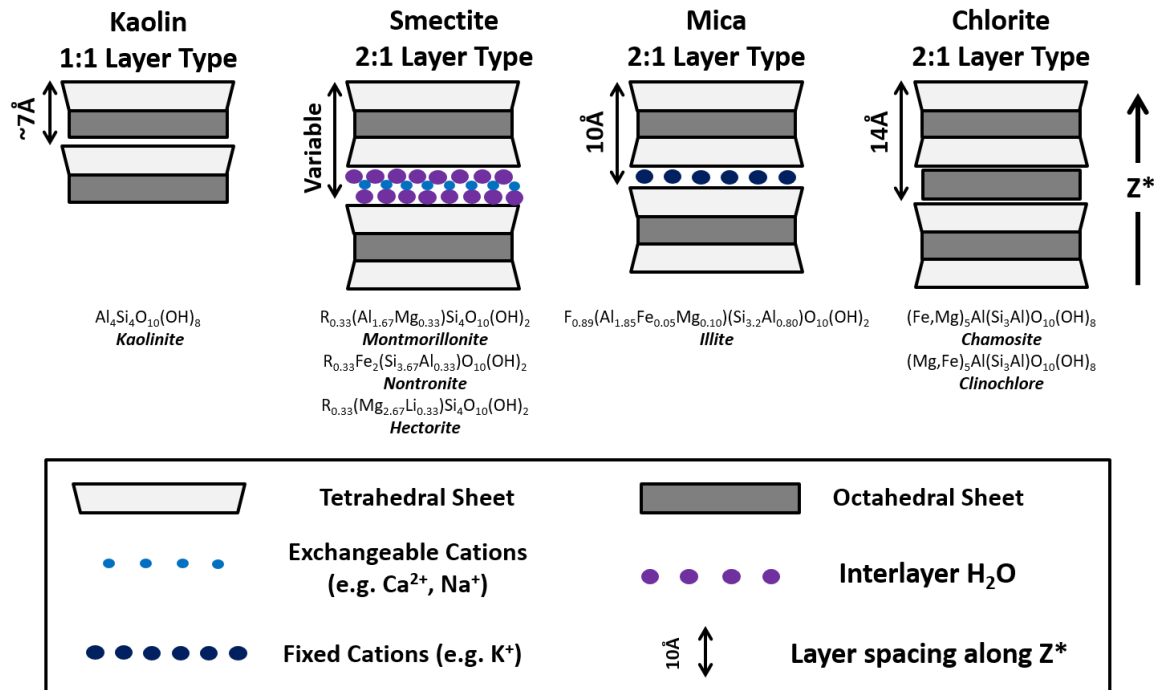
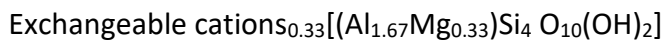


Figure 1.1. Basic structural models of most common clay mineral groups found in siliciclastic mudstones. R: Exchangeable cations; F: Fixed cations. Based on Moore and Reynolds (1997)

An ideal structural formula for dioctahedral smectite (montmorillonite) can be written as the following (Moore and Reynolds, 1997):



The layer charge is lower for smectites resulting in the unique ability of expansion when water or other polar molecules enter the interlayer space. Water can be incorporated in the interlayer space as single, double or triple sheets, depending on relative humidity, salinity, temperature and also pressure (Colten-Bradley, 1987).

Mixed layer illite/smectites are more common than either discrete illite or discrete smectite (Moore and Reynolds, 1997). They are products of progressive illitization of smectite at high temperatures during burial diagenesis (e.g. Hower et al., 1976) or during hydrothermal alteration or contact metamorphism (e.g. Inoue and Kitagawa, 1994). Mixed layer illite/smectite can also form at surface temperatures as a result of wetting and drying processes (Eberl et al., 1987). However, the majority of the mixed layer illite/smectite found in sedimentary environments forms as a result of burial diagenesis, which is discussed in more detail in the next chapter.

Identification and quantification of mixed layering is most commonly done by XRD and the nature of mixed-layering is assessed from the (00l) XRD patterns of separated clay fractions. This creates a problem when dealing with clays containing expandable interlayer surfaces, because there is a lack of consistency between the structural and operational (i.e. based on XRD $d_{(001)}$ spacing under specified conditions) definitions of smectite and illite. Characteristics of expandable clays determined by XRD are only valid for specific exchangeable cation and relative humidity (Środoń, 1999).

The crystal structure of mixed layer illite/smectite can be described by two seemingly contradictory models, the MacEwan crystallite model and the fundamental particle model. These are shown in Figure 1.2.

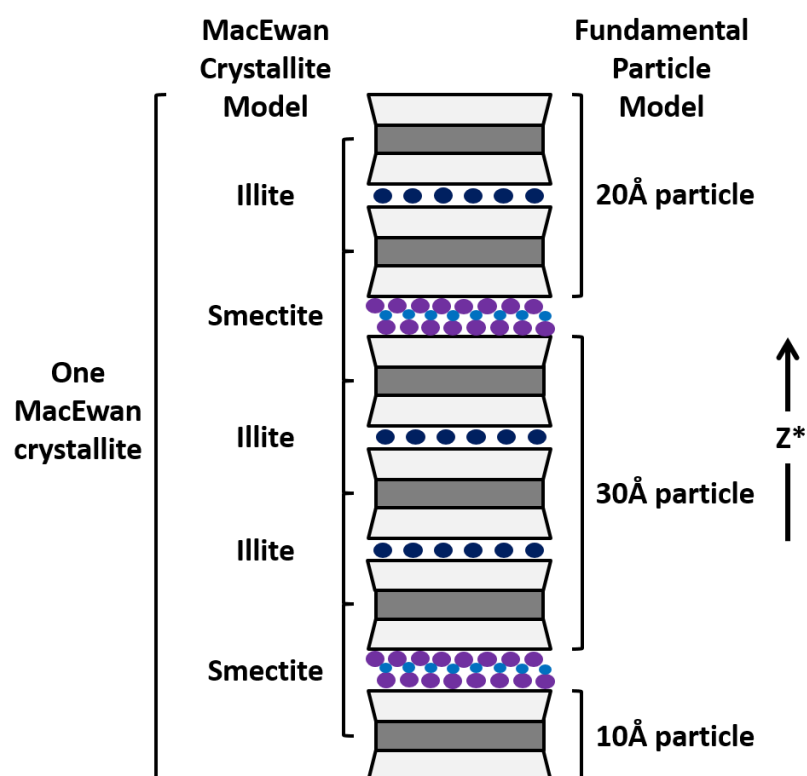


Figure 1.2. Mixed layer illite/smectite as interpreted by MacEwan crystallite model and fundamental particle model. After Moore and Reynolds (1997)

The MacEwan crystallite model is based on the Markov theory of interlayer order in mixed layer clays, which was introduced by Hendricks and Teller (1942) and MacEwan (1956, 1958). Their theory describes diffraction in one-dimension from infinitely thick

interstratifications of two types of layers. This theory was later applied to calculate XRD patterns of illite/smectite (Reynolds and Hower, 1970).

According to the MacEwan crystallite model illite/smectite crystals are 10 nm thick or greater and are composed of stacked illite and smectite interlayers. These interlayers are stacked along the Z^* axis to form MacEwan crystallites (this name was introduced by Altaner et al. 1988) with different ordering types. In this model the layers are stacked together coherently and are characterized by crystallographic continuity (Figure 1.2). The proportion and sequence of these interlayers are the main controls on illite:smectite ratio (usually given as expandability or smectite% in illite/smectite) and on interlayer ordering determined by XRD (Reynolds, 1980).

In contrast to the MacEwan crystallite model which was derived from XRD studies of illite/smectite, the fundamental particle model is based on observations made by transmission electron microscopy (Pt-shadowing technique). This concept was introduced by Nadeau et al. (1984a; 1984b; 1984c) and it views illite/smectite as an aggregate of much thinner crystallites termed fundamental particles. These are individual particles that yield single-crystal electron diffraction patterns from the X-Y plane.

Nadeau et al. (1984a) distinguished three types of fundamental particles:

1. Smectite fundamental particle is a 10 Å (or 1 nm) thick, single 2:1 silicate layer
2. Illite fundamental particle must be at least 20 Å (or 2 nm) thick and it is composed of two to five 2:1 silicate layers held together by potassium ions
3. Chlorite fundamental particle is minimum 24 Å (or 2.4 nm) thick and composed of two 2:1 silicate layers joined by a (Mg, Fe) hydroxide sheet

Fundamental particles corresponding to the thinnest structural unit possible for a given mineral are referred to as elementary particles (e.g. smectite monolayer or illite bilayer).

These fundamental particles on their own would produce XRPD patterns characteristic of end-member clay minerals. Nadeau et al. (1984c) proposed that the mixed layer XRD character is a result of the phenomenon called interparticle diffraction. According to the

authors these particles are not grown together (do not have crystallographic continuity) as for the MacEwan crystallite model but rather stacked together randomly and form a group of particles that diffract X-rays. The interfaces between these small particles can absorb water or organic molecules, which then would be perceived by XRD as a smectite or expandable component. According to this smectitic behaviour (expandability) occurs at the interfaces between fundamental particles, but these interfaces do not necessarily have a smectitic charge (Nadeau and Bain, 1986). Thus, the proportion and thickness of the fundamental particles are the main controls on the illite:smectite ratio or expandability and on the interlayer ordering determined by XRD. In this model expandability is inversely proportional to the mean fundamental particle thickness.

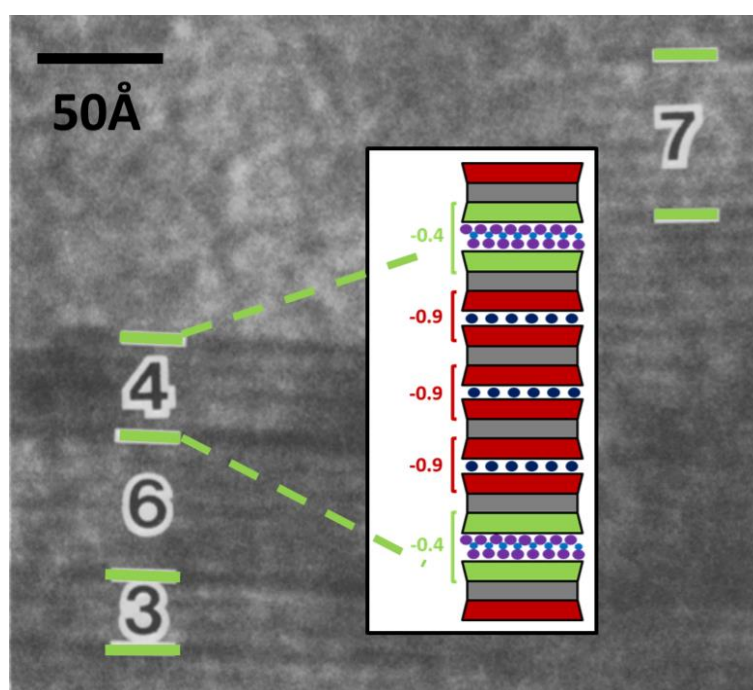


Figure 1.3. TEM lattice fringe image modified after Veblen et al. (1990) showing variable spacings between smectite interlayer surfaces (dark fringes, marked with green lines) in $R > 1$ illite/smectite sample. Digits refer to number of 2:1 layers in fundamental particles. The inset cartoon illustrates one 40 Å (4 nm) thick (4 layer) fundamental particle with interlayer charge values shown on the left.

The fundamental particle model interprets disordered ($R=0$) illite/smectites as mixture of two phases but sees ordered ($R \geq 1$) illite/smectite as a single phase (illite fundamental particles of various sizes). In contrast to this, the MacEwan crystallite model interprets

illite/smectite as two separate phases with different compositions. However, the distinction between these phases is unclear, because of the location of the phase boundaries within the crystallites (Figure 1.2). This is a result of the inability of the XRD analysis to determine the composition of the tetrahedral sheet on the top and bottom of the MacEwan crystallites (Altaner et al., 1988; Eberl and Srodon, 1988; Srodon et al., 1992).

Later studies involving HRTEM lattice fringe observations on in situ, undisturbed illite/smectite samples revealed crystal thicknesses more similar to MacEwan crystallites (J. H. Ahn and Peacor, 1986; Srodon et al., 1990; Veblen et al., 1990). One example taken from Veblen et al. (1990) is shown in Figure 1.3. Srodon et al. (1990) showed that illite/smectite crystals in natural rocks can be up to 15 layers thick and they commonly form nearly parallel face-to-face groupings hundreds of Ångstroms (tens of nm) thick and thousands of Ångstroms (hundreds of nm) long, which the authors called “quasi-crystals”.

In addition Altaner et al. (1988) presented convincing evidence using ^{29}Si -NMR (nuclear magnetic resonance) data that the top and bottom of both MacEwan crystallites and fundamental particles have a smectitic composition. The authors further suggested that mixed layer illite/smectite crystals separate along smectitic surfaces due to osmotic swelling during sample preparation for TEM which involves considerable dilution in water. This liability of illite/smectite crystals was later confirmed by Clauer et al. (1997). Presently, most researchers consider fundamental particles as fragments of MacEwan crystallites and accept a model for interstratified crystals which can be considered as a reconciliation of the two concepts (e.g. Ahn and Peacor, 1986b; Altaner et al., 1988; Srodon et al., 1990, 1992; Środoń et al., 2000). This concept is illustrated in Figure 1.3 which shows fundamental particles with different numbers of layers. In accord with Srodon et al. (1992) there are no smectite interlayers in fundamental particles, but their tetrahedral sheets facing the outside world have smectitic layer charges. This means that there is one smectite interlayer per fundamental particle (each tetrahedral sheet counts as $\frac{1}{2}$ smectite interlayer). The same assumption is made in this thesis.

1.2.3 Organic matter

Organic components can have considerable effect on the physical properties of some mudstones; however, this thesis focuses on the more common, organic matter poor varieties. Because of this I refrain from a more detailed discussion on the terminology related to organic components in mudstones and shales.

In this thesis, the term organic matter is used as general term for all types of organic components. Further terms like kerogen or bitumen will be avoided since these are usually based upon their solubility in organic solvents.

1.2.4 Porosity

Porosity can have different meaning for different disciplines and its numerical value also depends on the technique used to measure it (Pearson, 1999).

The definition of porosity in petrophysics is “the ratio of void volume to total volume of the body considered” (Zinszner and Pellerin, 2007). In natural environments pore voids are usually saturated by a fluid (mostly water), which makes this straightforward definition much more complicated when applied to fine grained lithologies containing considerable amounts of clay minerals. In clay minerals water plays a considerable role in the definition of the material, which makes the definition of a well-defined and invariant total volume and void volume very difficult (Zinszner and Pellerin, 2007).

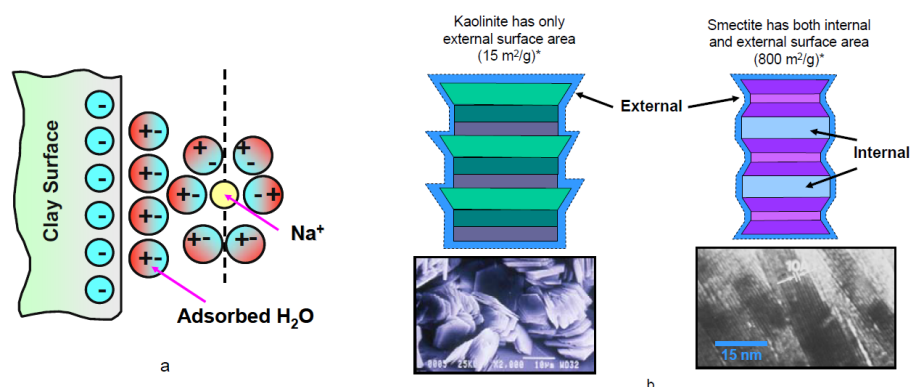


Figure 1.4. Schematic illustrations of adsorbed and double-layer water (a) and water associated with external and internal clay mineral surfaces (b). SEM image shows kaolinite; TEM image shows smectite with a collapsed (1 nm) layer. From Passey et al. (2010)

In expandable clay minerals (e.g. smectites) exchangeable cations can hold variable amounts of strongly bound shells of water molecules depending on water activity. In addition to this, water is also associated with clay mineral surfaces, either as adsorbed water, double-layer water or strongly held capillary-bound water (e.g. Passey et al., 2010). This is illustrated in Figure 1.4.

The term clay-bound water is used for the volume of water adsorbed on internal (associated with expandable clay minerals) and/or external clay mineral surfaces. Total (or physical) porosity is defined as the total water-accessible porosity, which includes the water content interacting with clay mineral surfaces plus the free water in the open pore and capillary spaces. The term effective porosity is used for total porosity minus clay-bound water, which only includes the free water content. These definitions are used in this thesis.

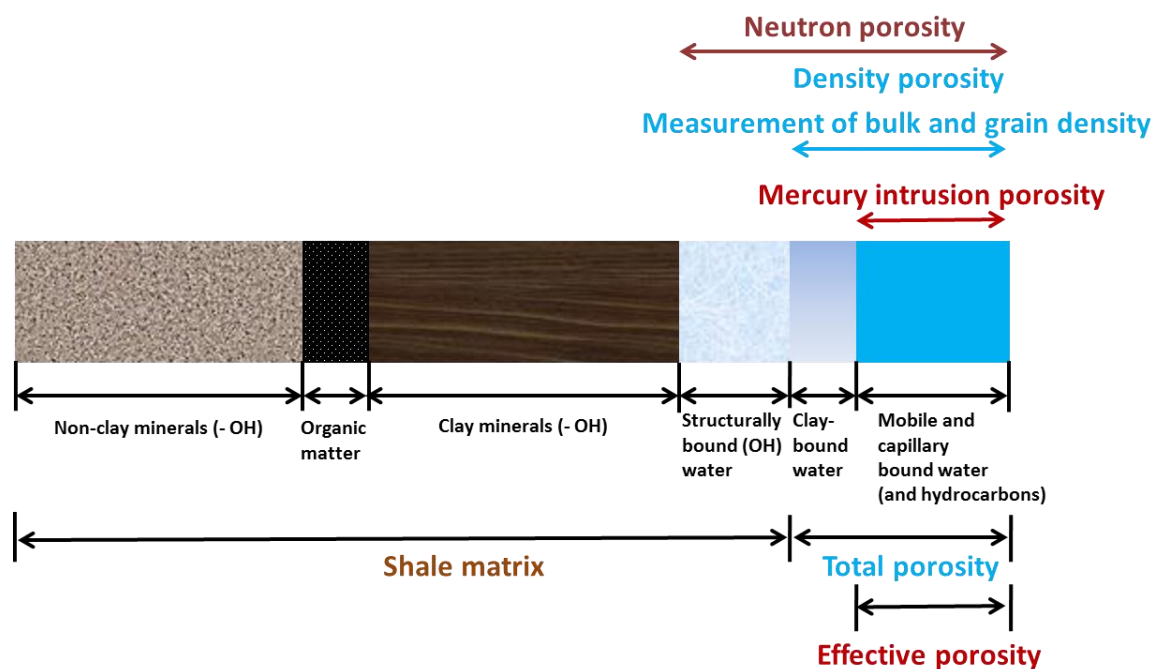


Figure 1.5. Schematic representations of different porosity types in siliciclastic mudstones and their relations with different measurement techniques. Modified after Eslinger and Pevear (1988)

Figure 1.5 illustrates these terms and how they relate to the measurement techniques applied in this thesis.

A single porosity value cannot represent the heterogeneity of pore-structures in natural mudstones. Pore size distribution is used to quantify the relative volumes associated with different pore sizes. In reality mudstone pore networks are highly irregular and

heterogeneous, so the term pore size does not have a precise definition. In addition different techniques record the pore structure differently and convert the raw data into quantitative pore structure description based on model assumptions (e.g. Kuila and Prasad, 2013). In this thesis, a one-dimensional approximation is used with the assumption of cylindrical pore geometry and the term pore size will refer to equivalent cylindrical pore diameter.

Several different pore size classification nomenclatures exist in the literature (e.g. Loucks et al., 2012). In this thesis, the pore size classification scheme recommended by the International Union of Pure and Applied Chemistry (IUPAC) is applied. They define micropores as pores with pore sizes below 2 nm; mesopores as pores with pore sizes between 2 nm and 50 nm; and macropores as pores with pore-size greater than 50 nm (Rouquerol et al., 1994)

1.2.5 Permeability

Permeability is a measure of the ease with which fluid can flow through a porous medium. It is a constant for a given porous medium and fluid type. Absolute or specific permeability is defined to separate the influence of the fluid from that of the porous medium (Leonards, 1962).

Absolute permeability is given as:

$$K = \frac{k \times \mu}{\rho} \quad (1)$$

Where

K absolute permeability (m²)

k hydraulic conductivity from Darcy's law (m/s)

μ coefficient of dynamic viscosity of the fluid (Ns/m²)

ρ unit weight of the fluid (g/cm³)

This term is used in this thesis (further used simply as permeability) in relation to the mudstone matrix; permeability of faults and fractures will not be considered.

1.2.6 Pore pressure

Hydrostatic or normal pressure is equivalent to the pressure associated with the weight of an overlying column of fluid from mean sea level to any given depth. It implies an open and interconnected pore or fracture network from the surface to the depth of interest.

Pore fluid pressure different from hydrostatic at any given depth is considered to be abnormal. Overpressure refers to pore fluid pressure in excess of the normal or hydrostatic pressure at a given depth. Pore pressure less than hydrostatic at a given depth is referred to as underpressure (e.g. Mouchet and Mitchell, 1989).

Hydrostatic pore fluid pressure is given by:

$$P_{hydro} = \int_0^z \rho_w(z) g dz \quad (2)$$

Where

P_{hydro} = hydrostatic pore fluid pressure (MPa)

ρ_w = fluid density (g/cm³)

g = gravitational acceleration (m/s²)

z = depth of interest (m)

Hydrostatic pore pressure increases with depth at a rate around 10 MPa/km (0.44 psi/ft), but its gradient also depends on pore fluid salinity (i.e. density).

Lithostatic pore pressure means that the pore pressure equals the vertical stress corresponding to the total weight of the overlying sediments and their fluids i.e. the overburden stress or lithostatic stress.

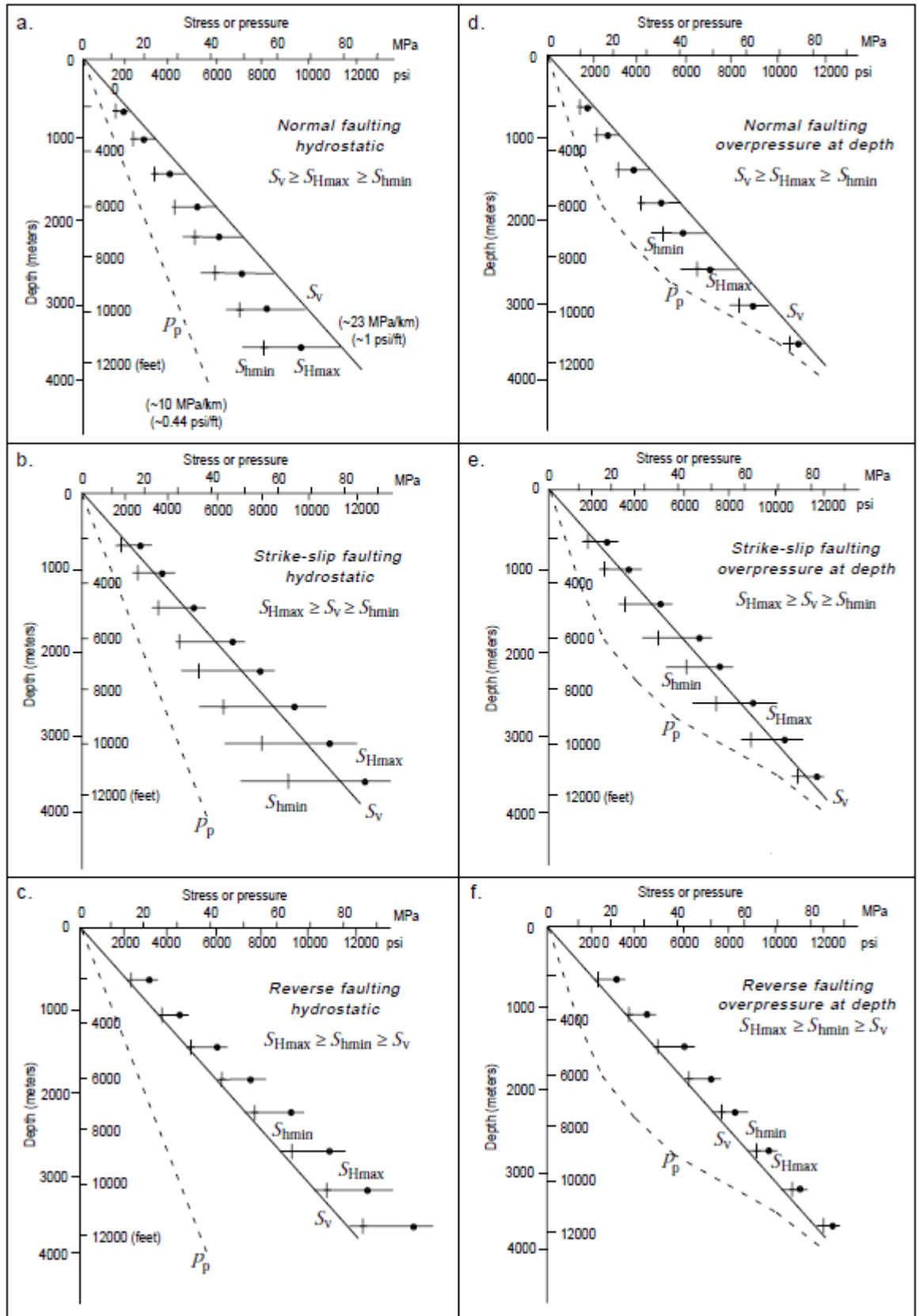


Figure 1.6. Variations of stress magnitudes with depth in different Andersonian faulting/stress and pore pressure regimes. P_p : pore pressure; S_v : lithostatic (overburden) stress; S_{Hmax} : maximum horizontal stress; S_{Hmin} : minimum horizontal stress (From Zoback, 2010)

Lithostatic pressure is given by:

$$S_v = (\rho_w g z_w) + \int_{z_w}^z \rho_r(z) g dz \quad (3)$$

Where

S_v = lithostatic pressure (MPa) ρ_w = fluid density (g/cm³) (in offshore areas)

ρ_r = bulk rock density (g/cm³) z_w = water depth (m) (in offshore areas)

g = gravitational acceleration (m/s²) z = depth of interest (m)

The lithostatic pressure gradient is often taken as 23 MPa/km (1 psi/ft), corresponding to an average bulk rock density of 2.3 g/cm³. In reality the pressure gradient varies with depth, corresponding to changes of rock and fluid density.

It is commonly assumed that the vertical stress is a principal stress and that pore pressure cannot exceed the vertical stress (pore pressure will always be less than or equal to the least principal stress). However, where there is topography, the vertical stress is generally not a principal stress; and even where the vertical stress is the minimum principal stress, pore pressure could exceed it by an amount equal to the tensile strength of the rock.

Figure 1.6 which shows the variation of stress magnitudes with depth in different stress regimes in both hydrostatic and overpressured conditions. The difference between the principal stresses increases with depth in a hydrostatic regime and decreases due to overpressure (e.g. Zoback, 2010). The difference between the principal stresses decreases due to the poroelastic effect of increased horizontal stresses in response to overpressure under zero strain conditions and due to the faulting induced by severe overpressure.

Fracture pressure is defined as the amount of pore pressure that is needed to exceed the sum of the minimum principal stress and the tensile strength of the rock and cause hydraulic fracturing. The fracture pressure is generally (in most settings) lower than the lithostatic stress, typically 70-90% of the overburden stress (e.g. Rouchet, 1981).

1.3 Research objectives

The overall objective of this project is to investigate the link between chemical diagenesis, the consolidation state of mudrocks and their physical properties as determined by wireline logs. The main research questions are the implications of clay mineral reactions for (a) the structural fabric of mudstones, (b) porosity changes resulting from the reactions (c) the possibility that porosity continues to be lost mechanically, after the main clay mineral reactions have occurred and (d) the implications for pore pressure generation and prediction.

Four case studies have been identified to investigate diagenesis and chemical compaction in clastic mudstones selected from single Formations but buried to a range of temperatures (60-150°C), in different pore pressure regimes. The four selected case studies are the Miocene mudstones in the Central Malay Basin, Cretaceous mudstones at Haltenbanken, offshore mid-Norway, Cretaceous to Tertiary mudstones in the Sergipe-Alagoas Basin, offshore Brazil and Triassic mudstones in the North Sea Central Graben. These have been specifically selected to test hypotheses put forward for the chemical compaction of diagenetically altered mudstones proposed by previous researchers: (effective) stress-independent chemical compaction and chemically-enhanced mechanical compaction (refer to 2.6). Sample sets have been chosen which allowed to investigate the impact of pore pressure on chemical compaction: in essence, do high pressures inhibit porosity loss in clastic mudstones subjected to diagenetic mineralogical change?

The main research objectives addressed in this thesis are as follows:

- Defining the key mineralogical and textural changes during diagenesis using quantitative mineral phase analysis, X-ray goniometry and petrography
- Evaluating the impact of chemical diagenesis on the physical properties by relating the established mineralogical and textural changes to physical properties measured on the samples and inferred from wireline logs
- Evaluating the impact of clay mineral diagenesis on the compaction properties of mudstones using the wireline log responses and textural observations on the samples

- Evaluating the role of clay mineral diagenesis on pore pressure generation using the wireline logs (e.g. sonic transit time vs density log s) and 1D basin modelling.

1.4 Thesis organisation

This thesis is divided into eight chapters which can be organized into four distinct sections. The first two chapters introduce the main research problem and discuss the present state of the relevant research, respectively. The third chapter focuses on methodology. The following four chapters detail results from four different case studies. The last chapter summarizes key observations, brings together key results from individual case studies and compares these with preexisting ideas in the published literature.

The details of each individual chapters are as follows:

Chapter 2. Chemical reactions and physical changes in mudstones during burial diagenesis and their relation to overpressure generation and prediction: a review

This chapter presents a summary of the present state of the scientific literature regarding clay diagenesis, compaction, overpressure generation and prediction in siliciclastic mudstones. The main research problem is also introduced and discussed in light of the literature.

Chapter 3. Methodology

This chapter details the research methodologies used for this thesis. Details for various analytical equipment and variety of rock property techniques which had been applied during the course of this research are also discussed. Error minimising practices and calibrations are also presented.

Chapter 4. Mechanical compaction in diagenetically altered mudstones: an example from the Central Malay Basin

This chapter details and discusses mineralogical, geochemical, petrographic and wireline log data from Miocene mudstones of the Central Malay Basin. A summary of the geology of the Malay Basin is also presented. The main focus is on the role of mechanical compaction in these diagenetically mature mudstones at temperatures above 100°C.

Chapter 5. Overpressure generation as a result of clay mineral diagenesis in Lower Cretaceous mudstones on the Halten Terrace, offshore mid-Norway

This chapter details and discusses mineralogical, geochemical, petrographic, porosity and wireline log data from Lower Cretaceous mudstones on the Halten Terrace. A brief summary of the geological history of the area is also presented. The main focus in this chapter is on the role of clay mineral diagenesis in overpressure generation in these mudstones.

Chapter 6. Clay mineralogical control on compaction properties of Albian to Miocene mudstones of the Sergipe-Alagoas Basin, offshore eastern Brazil

This chapter details and discusses mineralogical, geochemical, porosity and wireline log data from Albian to Miocene mudstones of the Sergipe-Alagoas Basin. A brief summary of the geology of the Sergipe-Alagoas Basin is also presented. The main focus is on the effects of clay mineralogy and diagenesis on the compaction properties of these mudstones.

Chapter 7. Diagenesis and compaction of Triassic mudstones in the HPHT fields of the North Sea Central Graben

This chapter details and discusses mineralogical, petrographic and porosity data from Triassic mudstones of the North Sea Central Graben. A summary of the geology of the Malay Basin is also presented. The main focus is on the effects of clay mineralogy and diagenesis on the compaction properties of these mudstones.

Chapter 8. Chemical compaction or chemically enhanced mechanical compaction: a discussion on compaction processes in diagenetically altered mudstones

This chapter presents a discussion of the main research problem in light of the presented new evidence. The main focus is on the role of mechanical compaction processes in diagenetically altered mudstones. The consequences with regards to overpressure generation and prediction are also discussed. The main conclusions drawn in this thesis are summarised and areas for future research are revealed.

1.5 List of publications

Published in peer reviewed journals

Goult, N.R., Sargent, C., Andras, P., Aplin, A.C., 2016. Compaction of diagenetically altered mudstones – Part 1: Mechanical and chemical contributions. Mar. Pet. Geol. doi:10.1016/j.marpetgeo.2016.07.015

Conference Proceedings and Abstracts

Andras, P., Aplin, A.C., Goult, N.R., Sargent, C., Derkowski, A., van der Pluijm, B.A., 2016. Clay Mineral Transformations and Associated Compaction of Siliciclastic Mudstones, in: Fifth EAGE Shale Workshop, Extended abstract. doi:10.3997/2214-4609.201600396. Oral presentation at fifth EAGA Shale Workshop, 2nd May, 2016, Catania, Italy.

Andras, P., Aplin, A.C., Goult, N.R., Sargent, C., 2015. Clay mineral transformations, compaction and overpressure generation in siliciclastic mudstones, 54th Annual general Meeting, BSRG, Abstract Volume, p. 16. Oral presentation at 54th BSRG AGM, 21st December 2015, Keele, UK.

Andras, P., Aplin, A.C., Derkowski, A., van der Pluijm, B.A., 2015. Diagenesis and chemical compaction in Lower Cretaceous mudstones on the Halten Terrace, offshore mid-Norway, Department of Earth Sciences Conference, Durham University, Abstract Volume, p. 37. Poster presentation at 4th Department of Earth Sciences Conference, 7th June, 2015, Durham, UK.

Andras, P., Aplin, A.C., Derkowski, A., van der Pluijm, B.A., 2015. Chemical compaction in overpressured mudrocks: an example from the Lower Cretaceous on the Halten Terrace, offshore mid-Norway, Geopressure 2015, Abstract Volume, p. 19. Oral presentation at Geopressure 2015, 14th April, 2015, Durham, UK.

Andras, P., Aplin, A.C., Goult, N.R., Jones, S., 2014. Chemical compaction of overpressured shales, 5th ISGC, Acta Mineralogica-Petrographica Abstract Series, p. 1. Oral presentation at 5th ISGC, 26th April, 2014, Budapest, Hungary.

Andras, P., Aplin, A.C., Goult, N.R., Jones, S., 2013. Diagenesis and non-mechanical compaction of overpressured shales, 52nd Annual General Meeting, BSRG, Abstract Volume, p. 22. Oral presentation at 52nd BSRG AGM, 20th December, 2013, Hull, UK.

In preparation

Andras, P., Aplin, A.C., Goult, N.R., Sargent, C., Derkowski, A., van der Pluijm, B.A., Overpressure generation as a result of clay mineral diagenesis in Lower Cretaceous mudstones on the Halten Terrace, offshore mid-Norway

Andras, P., Aplin, A.C., Derkowski, A., van der Pluijm, B.A., Clay diagenetic control on mudstone microfabric revealed by High Resolution X-ray Texture Goniometry

Andras, P., Aplin, A.C., Goult, N.R., Sargent, C., Derkowski, A., Hoesni, M.J., Mechanical compaction in diagenetically altered mudstones: an example from the Central Malay Basin

Andras, P., Aplin, A.C., Goult, N.R., Sargent, C., Derkowski, A., Carvalho, J.G., Clay mineralogical control on compaction properties of Albian to Miocene mudstones of the Sergipe-Alagoas Basin, offshore eastern Brazil

Andras, P., Aplin, A.C., Goult, N.R., Chemical compaction or chemically enhanced mechanical compaction: a discussion on compaction processes in diagenetically altered mudstones.

Chapter 2

Chemical reactions and physical changes in mudstones during burial diagenesis and their relation to overpressure generation and prediction: a review

2.1 Introduction

The main goal of this chapter is to introduce the main research problem by reviewing relevant literature on mechanical compaction, clay diagenesis, chemical compaction, overpressure generation and prediction in mudstones. Particular focus is given to detail both physical and chemical changes during diagenesis and to discuss their effect on porosity, permeability and pore pressure.

Sections 2.2, 2.3, 2.4, 2.5 and 2.6 describe the main physical, chemical and textural changes established in the literature so far and section 2.7 discusses their relation to pore pressure generation and prediction.

2.2 Early diagenesis

At deposition, muds comprise thermodynamically unstable mineral assemblages derived from terrestrial weathering and biological productivity in the overlying water column. They become lithified, transforming into mudstones, as a result of a range of physical, chemical and biological processes, collectively termed diagenesis. Diagenesis is preconditioned by the depositional mineral assemblages, which are functions of provenance, detrital input, primary production, chemical conditions at the sediment-water interface, and rates of sediment deposition (C. Weaver, 1989).

Early diagenetic processes are contemporaneous with deposition. They can have significant effects on the subsequent diagenetic pathways, as early diagenetic minerals can fill the depositional porosity. These early cementation processes affect physical properties, stiffening the rock, and make it resistant to mechanical compaction. These early processes are typically redox processes where organic matter becomes oxidized by microbes, influencing the preservation of organic carbon. Significant early cementation is usually associated with organic-rich mudstones or condensed sections because it requires organic matter and oxidants, and enough time before significant burial takes place (Macquaker et al., 2010; Aplin and Macquaker, 2011).

2.3 Mechanical compaction

When deposited, muds have 80–90% porosity, but after 6 km burial ($>200^{\circ}\text{C}$) porosity is usually reduced to less than 5%. By then, the mineral assemblage is dominated in siliciclastic mudstones by quartz, illite and chlorite. The lithification of mudstone is driven by the physical and chemical processes of compaction, grain reorientation, mineral dissolution, cementation and recrystallization (Rieke and Chilingarian, 1974; Bjørlykke and Høeg, 1997; Bjørlykke, 1999).

At temperatures below $\sim 70^{\circ}\text{C}$, compaction (i.e., reduction of sediment volume by elimination of pore space) is dominated by mechanical processes, with the fastest rate of compaction in mudstones occurring within the first kilometre of burial (Hedberg, 1936; Rieke and Chilingarian, 1974). Pore space reduction is associated with grain rotation and breakage which results in closer packing of the particles, a reduction in pore size and thus permeability (Dewhurst et al., 1998; Yang and Aplin, 1998).

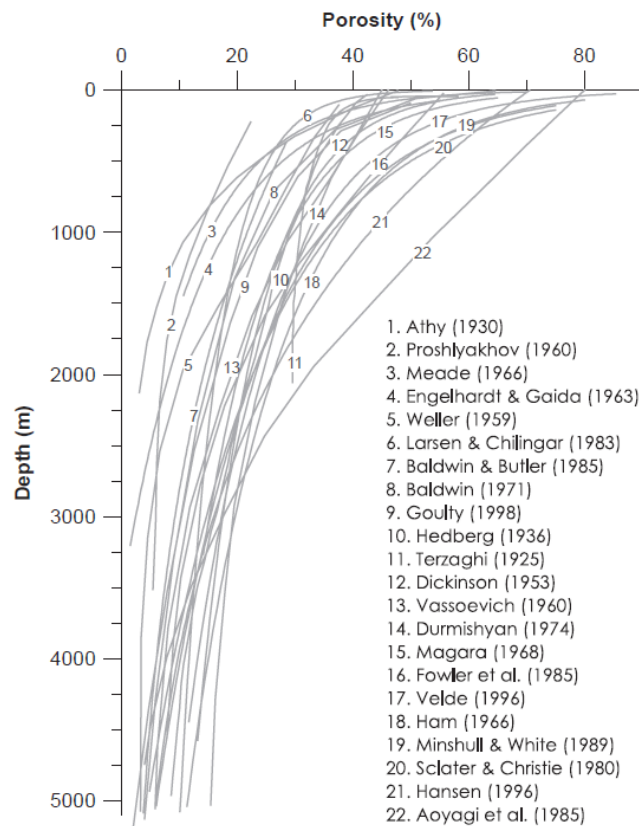


Figure 2.1. Published porosity-depth trends for shales from different sedimentary basins worldwide (From Mondol et al. 2007)

2.3.1 Porosity stress relationship

Considerable effort has been made to develop quantitative models for mechanical compaction. These are mostly empirical, using exponential or power law functions and are focusing on the relationship between porosity and depth (e.g. Athy, 1930; Sclater and Christie, 1980; Hansen, 1996).

The most commonly used model is that of Athy, (1930), which relates porosity φ at depth z to an initial porosity φ_0 :

$$\varphi = \varphi_0 e^{-bz} \quad (4)$$

In this equation b is a calibration constant.

The large variety of compaction trends shown in Figure 2.1 clearly illustrates the problem with this purely empirical approach. Such a model cannot be used to predict porosity for mudstones with different lithology (grain size and mineralogy) and burial (stress) history. These empirical trends can only be useful as a reference in a given sedimentary basin with known burial history and geology.

Another approach to compaction modelling comes from the field of soil mechanics. This is based on Terzaghi's (1925) effective stress principle. Vertical effective stress (effective overburden stress; σ'_v) is defined as the difference between the total vertical stress (overburden stress; σ_v) and pore fluid pressure (u):

$$\sigma'_v = \sigma_v - u \quad (5)$$

In this approach the soil mechanics developed relationship between void ratio (defined as the difference between void and solid volume; e) and vertical effective stress (portion of the overburden stress carried by the rock framework) is used to describe one dimensional compaction (Terzaghi, 1943; Skempton, 1969; Burland, 1990):

The relationship between void ratio (e) and porosity (φ) is given as:

$$e = \frac{\varphi}{1 - \varphi} \quad (6)$$

Void ratio can be calculated using equation (7):

$$e = e_{100} - \beta \ln \left(\frac{\sigma'_v}{100} \right) \quad (7)$$

In this equation e_{100} is the void ratio at 100 kPa effective stress and β (compression coefficient) is the slope of the linear relationship between void ratio and the natural logarithm of vertical effective stress.

These parameters are strongly correlated to the Atterberg liquid limit (see definition in Atterberg, 1911; Casagrande, 1932), which is related to the grain size and mineralogy of the sediment. The degree of compaction for a given effective stress is, therefore, also dependent on the grain size distribution and mineralogy; with finer grained muds having higher depositional porosity, but being more compressible (Skempton, 1969; Burland, 1990; Aplin et al., 1995). Experimental studies like those of Chilingar and Knight (1960) and Mondol et al. (2007) have shown that mineralogy also influences compaction, with smectite being substantially less compressible compared to illite or kaolinite (Figure 2.2 and 2.3).

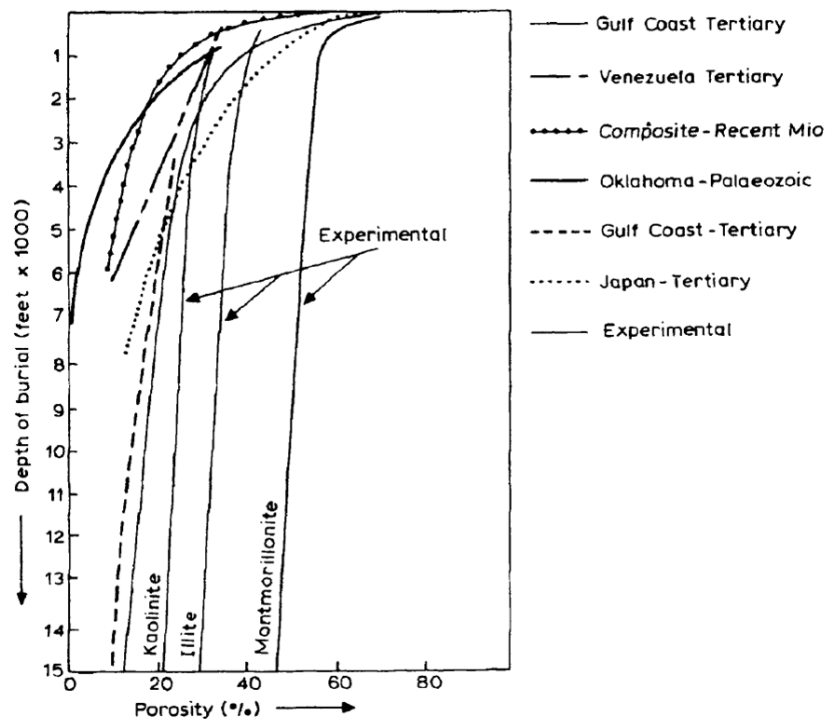


Figure 2.2. Experimental porosity-stress/depth trends for clays (from Chilingar and Knight, 1960) in comparison with observed mudstone compaction trends (From Bjørlykke, 1998)

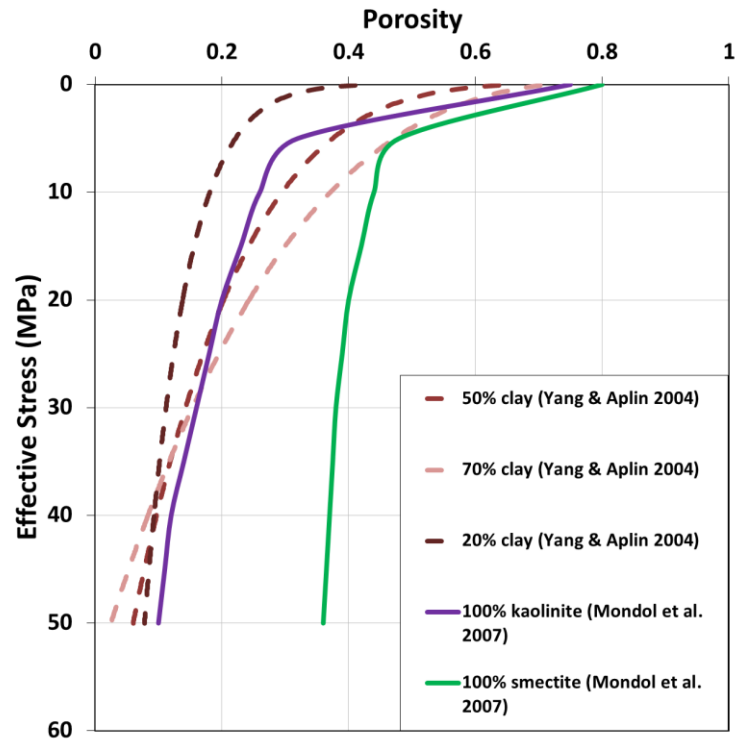


Figure 2.3. Experimental compaction curves of brine-saturated smectite and kaolinite (From Mondol et al., 2007) in comparison with the compaction trends of Yang and Aplin (2004)

Similarly, permeability shows considerable variability as a function of lithology. As shown by Neuzil (1994), mudstone permeabilities vary by three orders of magnitude at a given porosity value.

Permeability closely relates to pore-size distribution, which is controlled by grain size and mineralogy (e.g. Yang and Aplin, 1998, 2007), consequently much of this variation can be explained by variations in grain size and mineralogy. At a given porosity finer grained mudstones have lower permeabilities than coarser grained ones.

2.4 Clay mineral diagenesis

As burial progresses, changes resulting from inherited disequilibrium mineral assemblages dominate diagenesis. These involve both biogenic (opal, carbonate; not the subject of this study) and siliciclastic components, in particular clay minerals. At temperatures above ~70°C, clay diagenetic reactions become progressively more active as drivers of physical changes in mudstones.

Smectites and mixed-layer illite-smectite are commonly the most abundant detrital components in mudstones by volume (Garrels and Mackenzie, 1971), which is why smectite illitization is considered to be the dominant clay diagenetic reaction in mudstones. This reaction releases water, silica and cations that can react with kaolinite and calcite to produce chlorite and ankerite (Boles and Franks, 1979). In addition, most detrital plagioclase becomes albitized as a result of reacting with sodium ions released from the transforming smectite (Milliken, 1992).

Other clay diagenetic reactions include the transformation of kaolinite to illite, usually starting around 120°C, provided that potassium is still available (Bjørlykke, 1998). Figure 2.4 illustrates several possible clay diagenetic pathways established for sandstones, which also thought to generally apply for shales (Worden and Morad, 2003).

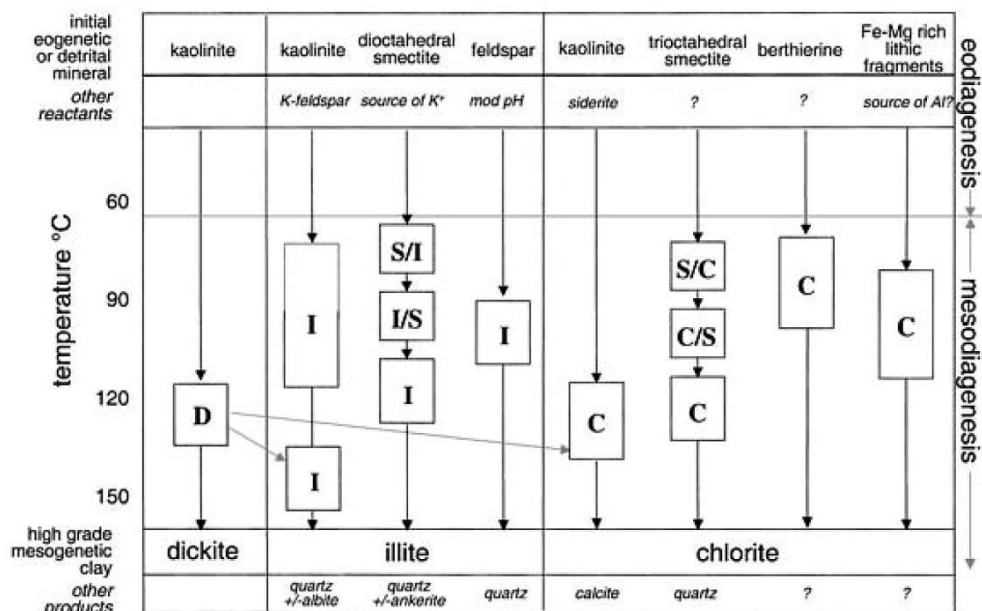


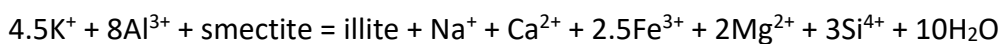
Figure 2.4. Common diagenetic pathways for clay minerals in sandstones and shales. I: illite; S: smectite; D: dickite; C: chlorite (From Worden and Morad, 2003)

2.4.1 Smectite illitization

Studies on mudstone burial diagenesis started in the US Gulf Coast (e.g., Burst 1959; Powers 1967), which included the first extensive work on smectite illitization by Perry & Hower (1970), Reynolds & Hower (1970) and Hower et al. (1976).

Hower et al. (1976) suggested the following general diagenetic reaction for mudstones during illitization:

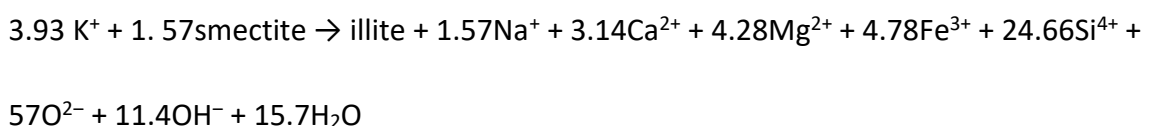
K-feldspar (+ mica) + smectite → illite + chlorite + quartz



The reaction implies that the main compositional change to smectite is the substitution of Al for Si in tetrahedral sheets, loss of octahedral Mg and Fe, gain of interlayer K and expulsion of interlayer Ca and Na, all resulting in the increase of the layer charge and formation of illite. The source of Al and K is the breakdown of K-feldspar and possibly mica. Mg and Fe lost from smectite form chlorite and excess Si released from K-feldspar, mica and smectite precipitates as quartz. This reaction is approximately isovolumetric and would result in lowering of the pH level in the pore fluid (Hower et al. 1976; Boles & Franks 1979).

Hower et al. (1976) reported that at a depth of about 3000 m (approx. 90°C) and at expandability values around 45 to 35 % smectite the interlayer ordering in illite/smectite changed from random (R0) to short range ordering (R1). At expandability values around 25% smectite R>1 ordering was observed. Expandability in the Gulf Coast sediments stopped changing around 20% smectite in illite/smectite.

Boles & Franks (1979) proposed an alternative reaction model for illitization:



This reaction assumes Al conservation between the smectite and newly forming illite layers, therefore suggesting dissolution and recycling ('cannibalization') of smectite layers and associated volume reduction of the illite/smectite. This would result in reducing the mass of the illite/smectite phase by more than 30%; would produce large amounts of

quartz and would also increase the pH level of the pore fluid. Potassium needed for the reaction to take place comes from breakdown of K-feldspar.

The exact reaction mechanism of the smectite-to-illite transition in natural systems is still debated. Possible physicochemical mechanisms for this reaction can be classified into two main categories: (a) solid-state transformation, involving layer by layer replacement of smectite by illite; and (b) dissolution and crystallization, involving dissolution of smectite and nucleation and crystallization of illite (Altaner and Ylagan, 1997).

A solid state transformation mechanism was inferred from Hower et al. (1976). This model predicts similar grain sizes, shapes and fabrics for illite daughter crystals to their parent smectite. Another consequence of this model is that R2 ordering is not allowed, R1 evolves directly into R3 (Altaner and Ylagan, 1997).

This model was later challenged by Nadeau et al. (1985), who used a dissolution and crystallization mechanism to explain the continuous evolution of fundamental particle thickness distributions in their study. The same transformation mechanism was assumed by Boles and Franks (1979). This model predicts that the original morphological characteristics of the parent smectite would be completely lost during illitization (Altaner and Ylagan, 1997).

Eberl and Srodon (1988), Inoue et al. (1988) and Eberl et al. (1990) suggested that Ostwald ripening is the mechanism during illitization. Ostwald ripening is a dissolution and recrystallization process characterized by simultaneous dissolution and growth of mineral in a single medium, during which the smallest crystallites dissolve and reprecipitates onto larger crystals (Eberl et al., 1990).

This was later challenged by Środoń et al. (2000), who showed that distributions of fundamental particle thickness evolve in a unique way during illitization. These particle distribution shapes are different than known shapes resulting from Ostwald ripening. In addition to this Ostwald ripening is also inconsistent with the large chemical and mineralogical changes associated with illitization (Altaner and Ylagan, 1997).

Srodon et al. (2000) proposed a model for illitization based on analysis of fundamental particle thickness distributions. This model is illustrated in Figure 2.5.

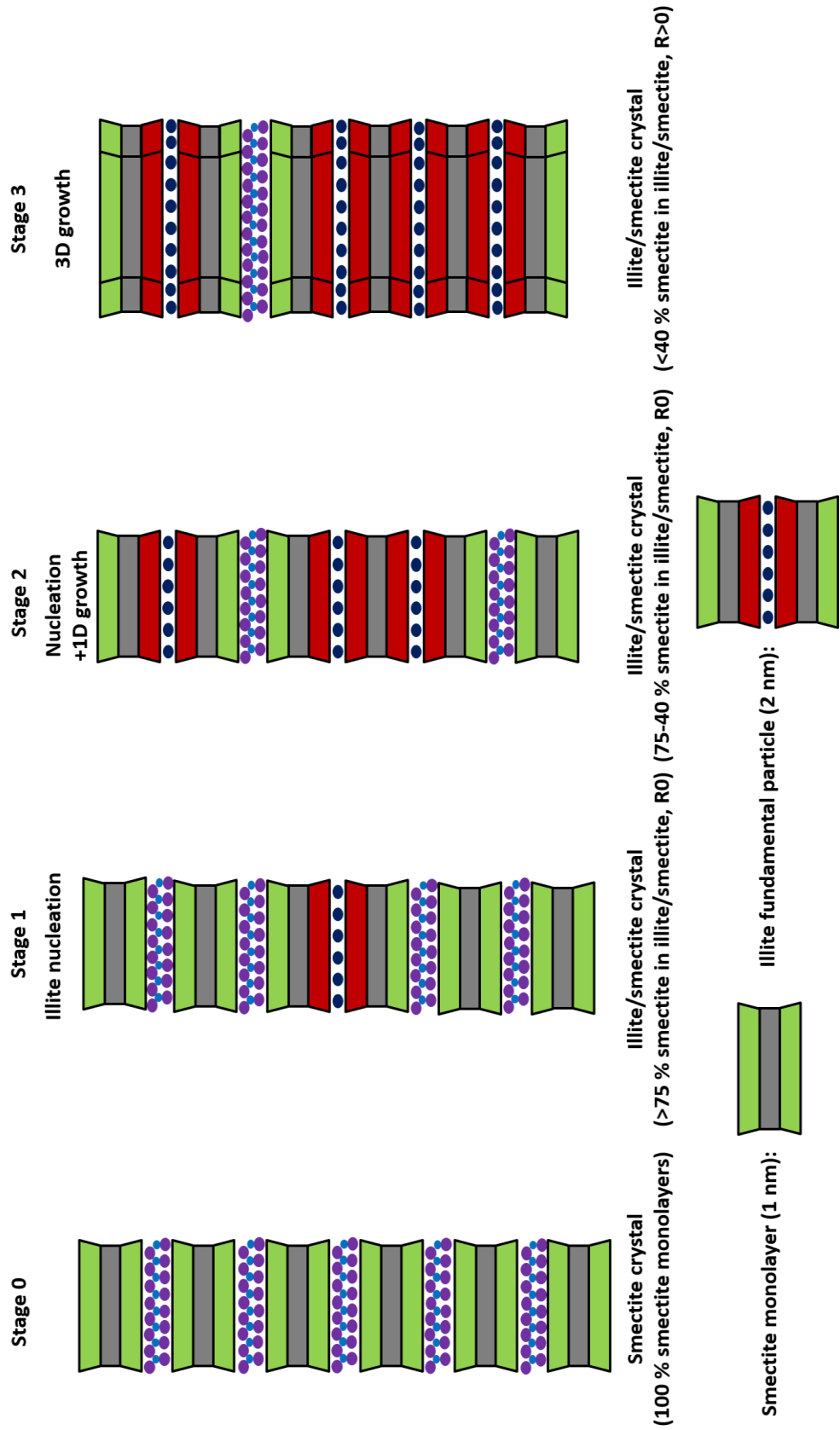


Figure 2.5. Model of the mechanism of smectite illitization based on Srodon et al. (2000). Refer to text for explanation

According to the authors there are three stages of the illitization process:

- It starts with dissolution of smectite monolayers and nucleation of illite fundamental particles (2 nm thick) until illite/smectite contains 70% smectite monolayers (>75% smectite in illite/smectite and R0 ordering)
- Nucleation of illite fundamental particles in decaying rate accompanied by their one-dimensional (along the Z* direction) growth until all smectite monolayer is consumed (mean illite particle size of 3 nm; 75-40% smectite in illite/smectite and R0 ordering)
- Surface controlled growth of illite fundamental particles in one-dimension until mean particle size is 3 nm, then three-dimensional growth of illite particles (mean illite particle size from 3 nm to 10 nm; <40% smectite in illite/smectite; R>0 ordering)

The dissolving smectite layers provide chemical elements for illite fundamental particles, but do not serve as nuclei of illite crystals.

The shape of the illitization profile (smectite in illite/smectite vs. depth/temperature) predicted by this model (i.e. marked decrease in smectite % with depth at onset of the process and negligible/immeasurable decrease below approximately 20-15% smectite) is in good agreement with reported examples of illitization profiles from shales (Figure 2.6).

Illitization has been reported in sedimentary basins from all over the world. Reported examples of the transition generally seem to follow the scheme originally described by Hower et al. (1976) from the Gulf Coast. Several reported examples are shown in Figure 2.6.

In overall, illitization seems to proceed through mixed layer intermediates with increasing percentage of illite in illite/smectite. As illite/smectite becomes more illitic the interlayer order changes from random (R0) to short range ordered (R1) and then to long range ordered (R2, R3) (Srodon and Eberl, 1984).

One interesting exception is that reported by Anjos (1986), (shown as the fifth trend on Figure 2.6), where the smectite is nontronite and it does not appear to change with increasing depth and temperature.

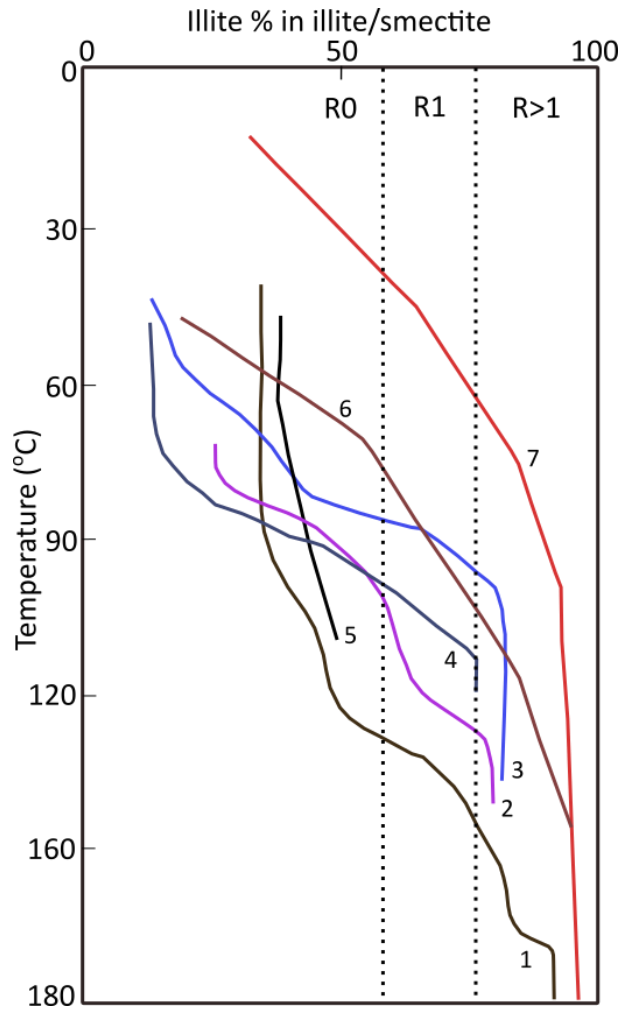


Figure 2.6. Published examples of illitization profiles. 1: Colorado River Delta, US (Jennings and Thompson, 1986); 2: Gulf Coast, US (Perry and Hower, 1972); 3: Gulf Coast, US (Hower et al., 1976); 4: North Sea (Srodon and Eberl, 1984); 5: Campos Basin, Brazil (Anjos, 1986); 6: Douala Basin, North Africa (Srodon and Eberl, 1984); 7: Central Poland (Srodon and Eberl, 1984)

It should be noted however that recent work on smectite illitization (e.g. Claret et al., 2004; McCarty et al., 2008, 2009) which applied the multi-specimen X-ray diffraction profile fitting method developed by Drits et al. (1997) and Sakharov et al. (1999) suggest that the models which are assuming a statistically homogeneous and continuous reaction, with steadily increasing illite interlayers in illite/smectite with increasing depth and temperature may be too simplistic. These studies showed that clay fractions of the early diagenetic Callovo-Oxfordian formations of the Paris Basin (Claret et al., 2004) and Oligocene Frio Formation of the Gulf of Mexico (McCarty et al., 2008) contains a physical mixture of smectite and randomly interstratified (R0) illite/smectite with a considerably high illite interlayer content (65% Illite). In addition to this the interlayer content does not

appear to change in the studied depth interval. These findings are also consistent with TEM observations reported by Dong (2005).

Lanson et al. (2005, 2009) presented data from two onshore wells in the Texas Gulf Coast, which extend through most of the smectite to illite transition zone. In accord with the shallower studies the authors reported the coexistence of different phases at different stages of diagenesis.

These results strongly indicate a heterogeneous reaction via a sequence of intermediate phases and possibly new reaction mechanisms (Lanson et al., 2009).

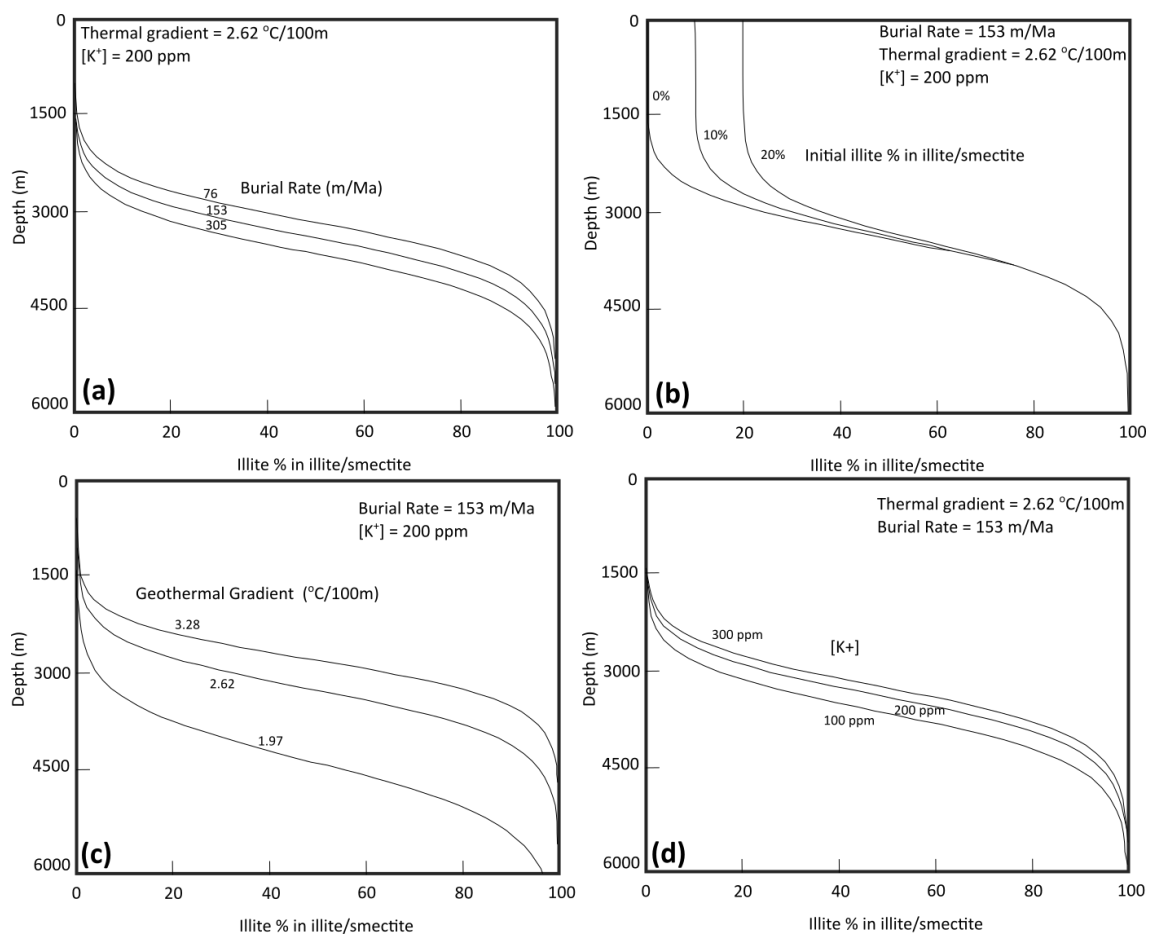


Figure 2.7. Model predictions for illitization illustrating the roles of different drivers (modified after Huang et al. 1993). Refer to text for more explanation

Key drivers behind illitization are temperature and geologic time (e.g. Hower et al., 1976; Velde and Vasseur, 1992), but additional factors like potassium concentration (Huang et al., 1993) and water/rock ratio (Whitney, 1990) have also been shown to influence the

reaction progress. However temperature is considered to be the most important controlling factor (Pollastro, 1993; Clauer et al., 1997).

Several kinetic models have been proposed for illitization (e.g. Huang et al., 1993; Cuadros and Linares, 1996; Cuadros, 2006), which are based on laboratory experiments and field observations. In Figure 2.7 the kinetic model proposed by Huang et al. (1993) is shown which employs a third-order empirical kinetic equation. The figure illustrates the roles of different drivers by showing model predictions of illitization profiles for different burial rates (a), initial smectite compositions (b), thermal gradients (c) and potassium concentrations (d).

The availability of potassium is a prerequisite for illitization (Hower et al., 1976). Different potassium sources either from within (mainly from K-feldspar) or outside an argillaceous whole-rock system may give rise to different rates of illitization (Berger et al., 1999).

The chemical mass balance aspect of illitization is another debated issue which has considerable consequence regarding the reaction model, reaction kinetic rates and overall volume change.

In the “classic trilogy” of Aronson and Hower (1976), Hower et al. (1976) and Yeh and Savin (1977), the authors concluded that the investigated Gulf of Mexico shales behaved as a closed system (on a large or formation scale). Several later studies like that of Jennings and Thompson (1986) reached similar conclusion.

In contrast, studies like that of Boles and Franks (1979), Awwiller (1993), Lynch (1997), van de Kamp (2008) and Day-Stirrat et al. (2010) argued for an open system chemical behaviour in shales during diagenesis based on mass balance calculations and observations of potassium enrichment with depth in some shale sections.

However these arguments were later questioned by Bjørlykke (1997), Bjørlykke (1998), Bjørlykke (1999), Bjørlykke and Jahren (2012) and Bjørlykke (2014), who showed that the bulk chemical composition of mudstones and shales remain nearly constant during progressive burial. The reason for this is that elemental transport by either advective or diffusive flow in these low permeability lithologies is extremely slow. However, diffusion might be important on a small scale (over short distances).

In accordance with a closed geochemical system Peltonen et al. (2009), Thyberg et al. (2009, 2010) and Thyberg and Jahren, (2011) showed evidence for authigenic silica retained in the mudstones following clay mineral reactions.

In addition to this, the observed potassium enrichment in shale sections was shown to be a result of depositional variations rather than open system K metasomatism (Hutcheon et al., 1998).

In overall, shales appear to behave as a closed system (although not in a true thermodynamic sense) at least at large scales, implying that clay diagenetic reactions can be predicted based on initial mineralogy and burial history.

Whilst there is copious literature on the mineralogy and chemistry of clay mineral diagenesis, considerably less is known about the physical changes occurring during clay diagenesis and how diagenesis affects the physical properties of mudstones. In the following sections a brief review and discussion are given about reported physical changes associated with clay diagenesis.

2.5 Clay mineral fabric alignment

Muds and mudstones are predominantly made of grains smaller than 63 μm . However, these mineral grains can have a variety of shapes and sizes. As a general rule clay minerals are lath shaped and mainly <10 μm in diameter. In contrast minerals like quartz and feldspar are more equidimensional and mainly > 10 μm . There are exceptions to this rule e.g. clay minerals like mica, kaolinite and chlorite can have diameters >10 μm and conversely non-clay minerals can be <10 μm .

It is generally thought that in marine environments larger grains (>10 μm diameter) tend to settle as single grains and smaller grains (<10 μm diameter) tend to settle as flocs or biologically produced aggregates (Kranck and Milligan, 1985; Kranck et al., 1996). This model implies that initial depositional processes in most fine grained siliciclastic lithologies produce an essentially isotropic clay mineral fabric. This is also supported by visual observations made on recent sediments (Bennett et al., 1991). However, a more anisotropic fabric is expected for silt-grade phyllosilicates (>10 μm , e.g. mica) and during very low sedimentation rates (Matenaar, 2002).

This initial depositional fabric is profoundly transformed by burial diagenesis and early (low-grade) metamorphism, at which stage clay minerals are reoriented normal to the maximum effective stress (parallel to bedding in tectonically-relaxed settings) and form a strongly aligned fabric (Oertel, 1983; Ho et al., 1999; Jacob et al., 2000).

Mechanical compaction can increase the alignment of clay minerals due to mechanical particle reorientation. This process was shown to be important during the early stages of compaction (e.g. Meade, 1966; Bennett et al., 1981). The overall orientation of the clay mineral fabric is also dependent on the initial composition (i.e. the ratio of the platy vs spherical mineral grains) of the mudstone (e.g. Voltolini et al., 2009; Day-Stirrat et al., 2011). However solely mechanical reorientation of clay particles (without mineralogical changes) can only result in a small fabric alignment increase as it was shown e.g. by Ho et al. (1999) and Aplin et al. (2006).

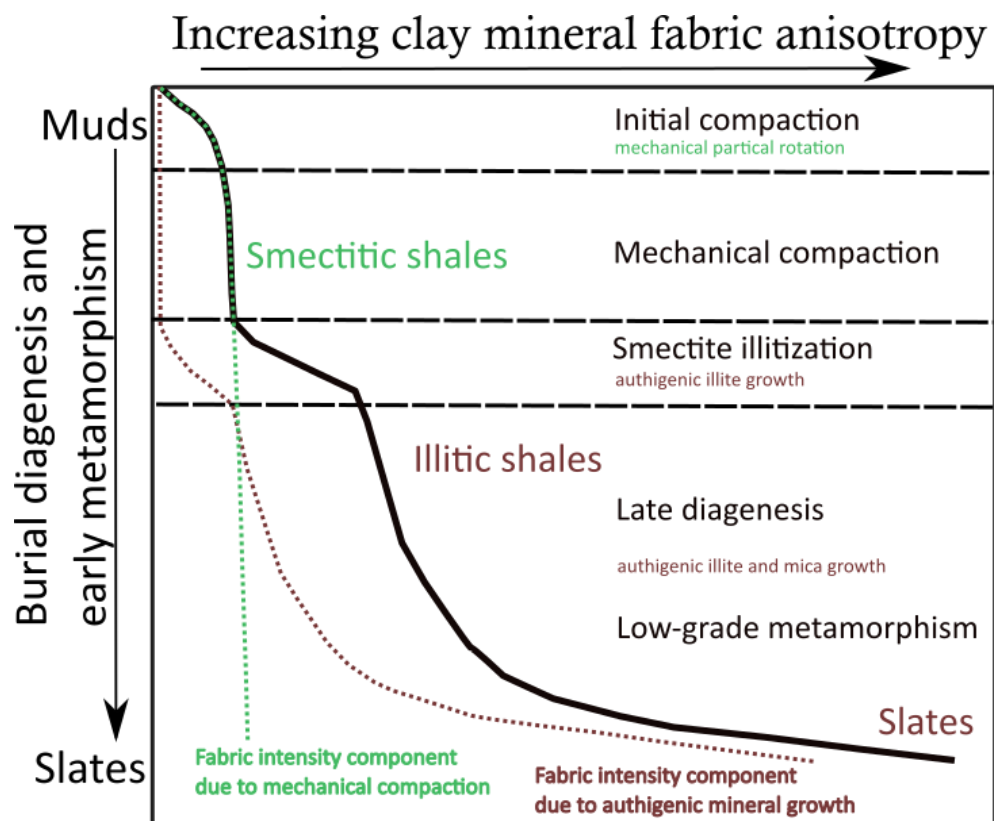


Figure 2.8. Evolution of the clay mineral fabric during burial diagenesis and early metamorphism (modified after Haines et al., 2009). Thick black line represents clay mineral fabric anisotropy evolution in sedimentary basins from deposition to low grade metamorphism as inferred from natural data

Quantitative studies on clay mineral alignment have shown that illitization leads to a more aligned fabric, where authigenic illite grows normal to the maximum effective stress (Ho et al., 1999, Worden et al., 2005, Day-Stirrat et al., 2008). This fabric change has a considerable effect on the physical properties of mudstones by reducing the porosity (Ho et al., 1999, Day-Stirrat et al., 2008), changing the pore structure (Bowers and Katsube 2002) and creating permeability anisotropy. These changes also affect the sonic and velocity logs and the seismic responses, by changing compressional and shear-wave velocities (e.g. Banik, 1983, Johnston and Christensen 1995).

Figure 2.8 shows a schematic illustration of the clay fabric evolution during burial, as inferred from published data. This model assumes that strong clay fabric anisotropy is primarily a result of authigenic mineral growth during illitization. In contrast Day-Stirrat et al. (2008) argued for the combined effect of mechanical particle reorientation and authigenic mineral growth. They proposed that water released by the reaction may act as lubricant and facilitate further rotation of the platy minerals into nanoporosity. In overall the relative roles of mechanical grain rotation and authigenic mineral growth have only been partly resolved.

2.6 Chemical compaction

Chemical compaction (also called ‘non-mechanical compaction’) is a term commonly used to describe the dissolution of quartz or carbonate at grain-to-grain contacts in sandstones and limestones, with concomitant mineral precipitation and porosity loss (e.g. Worden and Burley, 2003). This is an inappropriate conceptual model for mudstones in which the main diagenetic reactions involve the dissolution and reprecipitation of clay minerals. Key questions are the implications of the dissolution-precipitation reactions on the structural fabric of the mudstones and the resulting changes in both porosity and pore pressure.

As Bjørlykke (1998) pointed out, there is a clear difference between published porosity–stress/depth trends of experimentally compacted clay mixtures and those of natural mudstones (Figure 2.2), implying that the greater degree of compaction in natural mudstones is due to chemical processes.

Bjørlykke & Hoeg (1997) and Bjørlykke (1998, 1999) related chemical compaction (porosity reduction) in mudstones to the dissolution of smectite and, at greater temperatures, also kaolinite and to the precipitation of illite and other authigenic phases (quartz and chlorite) in the pore space. They proposed that compaction in mudstones takes place in three stages: initially by mechanical compaction where porosity is a function of the effective stress and lithology; then by a transitional stage where both mechanical and chemical compaction take place; and subsequently by chemical compaction where porosity reduction is controlled by the kinetics of mineral reactions, and thus by temperature and time. By implication, porosity loss by chemical compaction at the third stage is independent, or nearly independent, of effective stress. The top of the transitional stage is the depth of the onset of smectite-to-illite transformation, usually at temperatures around 70°C. The boundary between the transitional and chemical compaction stage is set to higher temperatures, around 100°C, depending on mineralogical composition and thermal history. This model, which will be referred to as the (effective) stress-independent chemical compaction model (Figure 2.9), was later adopted by several authors (e.g. Draege et al., 2006).

If mudstone compaction above ~100°C is purely chemical, the implication is that mechanical compaction does not take place which in turn implies that mudstones become stronger through diagenesis, such that their stress state lies inside the yield envelope even, if pore pressure is hydrostatic (“framework stiffening”, e.g. Draege et al. 2006). This assumption implies that porosity loss during chemical compaction becomes almost independent of the effective stress. Since porosity reduction/volume loss can only proceed, if pore water can escape (Cicchino et al. 2015), porosity reduction cannot be completely independent of the effective stress, even in mudstones at the chemical compaction stage. Nevertheless, in this model, porosity and permeability at the chemical compaction stage are primarily a function of temperature history and mineralogy.

In contrast, Dutta (1986, 2002, 2016) proposed a temperature-dependent compaction behaviour for mudstones, in which porosity is a complex function of clay type, time, temperature and effective stress (see also 2.7.1; Figure 2.18). Lahann (2002) developed this idea by proposing that in reducing the amount of smectite-associated bound water in the system, illitization reduces the equilibrium porosity associated with a given effective

stress. Lahann (2002) modelled the effect of illitization of smectite on the compaction properties of mudstones by using two end-member compaction curves, one for smectitic (pre-illitization) and one for illitic (post-illitization) mudstones (see also 2.7.1, Figure 2.17).

In connection with this model, Katahara (2006) proposed that illitization of smectite can be considered as a failure process in which the microstructure surrounding transforming smectite platelets is disrupted, provided that the smectite grains are load-bearing. Lahann and Swarbrick (2011) coined the term “framework weakening” to describe this behaviour, although their alternative description of the mudstones as “more compactable” is preferable. In geomechanical terms, the idea is that the yield envelope shrinks during clay diagenesis at constant volume, and pore pressure increases. If pore fluid escapes such that the stress state and pore pressure are unchanged, the volume occupied by the mudstone reduces (see also 2.7.2). In the following of this thesis this model will be referred to as the chemically-enhanced mechanical compaction (Figure 2.9).

In summary, according to Dutta (2002) and Lahann (2002), chemical reactions drive changes in the mechanical properties of the mudstones, so porosity loss is dependent on time and temperature as well as on effective stress.

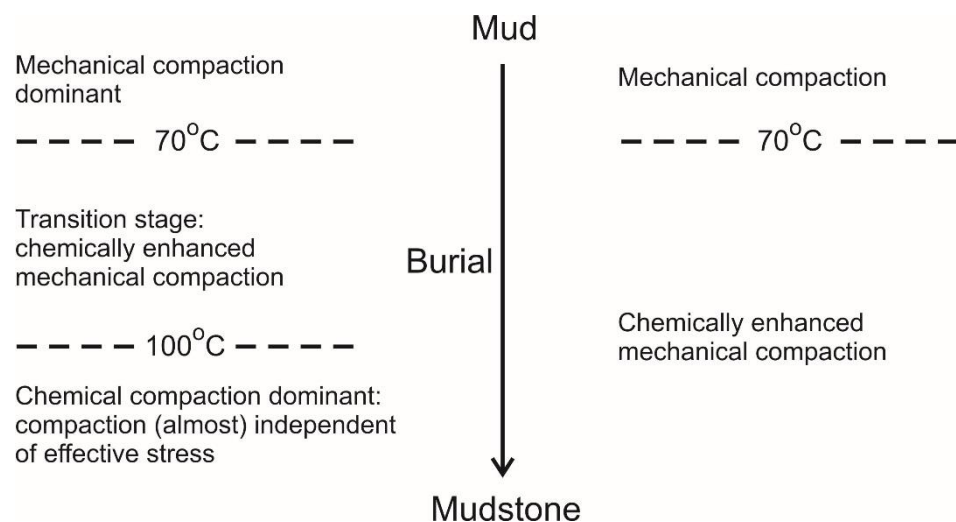


Figure 2.9. Chemical compaction models for mudstones. Left: the stress-independent chemical compaction model for mudstones undergoing diagenesis at temperatures above ~100 °C. Right: the chemically-enhanced mechanical compaction model for mudstones undergoing diagenesis at all temperatures above ~70 °C

These models are assuming very different physical processes associated with the transformations, which will have very different consequence on how to predict porosity and the pore pressure. However, these different proposed processes also having different consequences regarding mudstone porosity, texture and log responses which can be tested with real life data.

2.7 Overpressure generation and prediction in siliciclastic mudstones

Pore fluid overpressure is common in many sedimentary basins worldwide (Hunt, 1990). It is usually recorded during drilling operations, using wireline tools like Repeat Formation Tester or inferred from drilling parameters such as mud weight. However, pore pressure can only be measured directly from permeable sedimentary rock units. In low-permeability rocks, such as siliciclastic mudstones pore pressure has to be inferred from adjacent permeable rocks or from wireline log-based interpretations of rock properties (e.g. Mouchet and Mitchell, 1989).

Wireline log responses depend directly on lithological, textural, mineralogical and pore fluid properties. These properties are the combined result of burial history, effective stress history, temperature history and diagenesis of the sediments (e.g. Dutta and Khazanehdari, 2006).

At shallow depths (at temperatures below $\sim 70^{\circ}\text{C}$) overpressure may be generated when fine grained sediments undergo rapid burial. During burial and compaction, water is expelled from the pore network and increasing effective stress drives the grains closer together, thereby reducing porosity and permeability. Overpressure is generated when permeability becomes so low that water can no longer be expelled fast enough to remain in hydrostatic equilibrium as burial proceeds and some of the overburden stress is borne by the fluid. The retention of excess water necessarily means that the porosity is greater than it would be if the pore water were in hydrostatic equilibrium, hence the name of this process is disequilibrium compaction or undercompaction. It is thought to be the most common cause of overpressure in sedimentary basins worldwide (e.g. Swarbrick et al., 2002).

Horizontal compression due to tectonic forces can also generate overpressure in a similar way (Rubey and Hubbert, 1959; Yassir and Addis, 2002), however it should be noted that in tectonically active environments compaction is no longer controlled by the vertical effective stress alone (Goult, 2004).

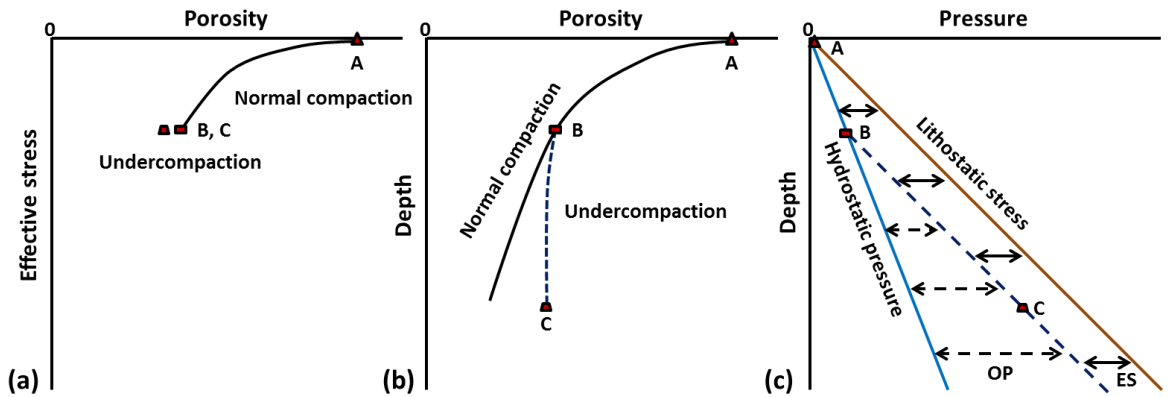


Figure 2.10. (a) Porosity-stress (b) Porosity-depth and (c) Pressure-depth profiles where overpressure is due to disequilibrium compaction. Points A, B and C show porosity, vertical effective stress and pore pressure in arbitrary mudstone beds buried to different depths. OP: overpressure, ES: effective stress

It is commonly observed in many sedimentary basins that during disequilibrium compaction the pressure-depth profile is sub-parallel to the lithostatic stress-depth profile (e.g. Dickinson, 1953; Swarbrick and Osborne, 1998) as it is illustrated in Figure 2.10c. In Figure 2.10 below point B both the vertical effective stress and the porosity is constant. Note that the rock is normally compacted for the ambient confining stress and pore pressure (“normally consolidated” mudstones; Terzaghi, 1943). This has the consequence that pore pressure can be directly estimated from porosity data for example as a function of mudstone lithology (e.g. Yang and Aplin, 2004) using the soil mechanics established quantitative relationship between effective stress and porosity (refer to 2.3.1).

Equivalent depth methods are based on the same principle and rely on a well-defined “normal” or hydrostatic compaction curve which then can be compared with actual mudstone porosities (derived from wireline logs) to determine an equivalent depth for the vertical effective stress (Figure 2.10). This method is deterministic and relies on the assumption that mudstones with equal porosity and same composition have been

subjected to the same maximum vertical effective stress. This assumption is only valid, if overpressure was created solely by disequilibrium compaction and the ratios between the principal effective stresses do not vary with depth (Goult, 2004).

The most widely applied method of pore pressure estimation is probably the method of Eaton (1975) which commonly uses sonic transit time, resistivity and seismic interval velocity data. This method also relies on a normal compaction curve and uses the ratio of the observed log reading and the expected log value for normally pressured rocks to estimate the pore pressure. This method is empirical, and the established normal compaction trend can be fitted to match pressure measurements from offset wells. It can be used to predict overpressures generated by mechanisms other than disequilibrium compaction; however it commonly does not provide accurate results unless modified empirically to fit offset well data. The problem with Eaton's method from a theoretical point of view is that it is not scientifically based.

Overpressure can also be generated by other mechanism commonly categorized as unloading processes. Unloading is defined as any process that reduces the effective stress acting on sediments or rocks (Bowers 1995). Unloading can be a result of erosion (removal of overburden load) or pore fluid expansion where overpressure results from the rock matrix constraining the fluid as it tries to increase in volume (pore pressure increase without concomitant increase in confining stress). Unloading processes include kerogene maturation, gas generation, volume changes during mineral diagenesis (e.g. gypsum to anhydrite, smectite to illite transformation), aquathermal expansion, potentiometric head, hydrocarbon buoyancy, osmosis and pressure transfer by lateral or vertical fluid flow (Osborne and Swarbrick 1997). In order to generate overpressure by any of these processes, the adjacent strata need to sufficiently restrict the pore fluid expulsion.

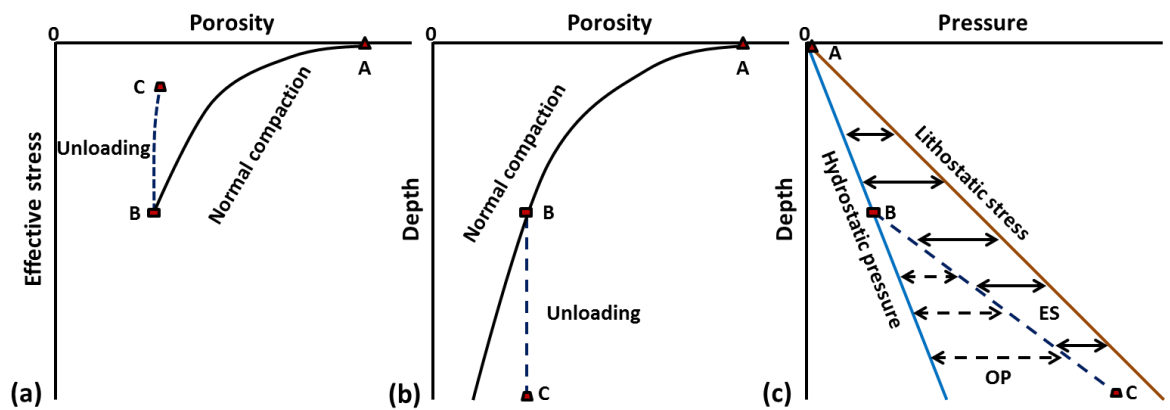


Figure 2.11. Porosity-stress/depth and pressure-depth profiles where overpressure is due to unloading mechanism. Points A, B and C show porosity, vertical effective stress and pore pressure in arbitrary mudstone beds buried to different depths. OP: overpressure, ES: effective stress

Mudstone compaction is essentially irreversible, since this deformation is dominantly a plastic process and most of the deformation is not recovered during unloading (i.e. effective stress reduction). Such unloaded mudstones are “over-consolidated”, since the current effective stress is lower than the maximum they have ever experienced (Terzaghi, 1943; Skempton, 1969). This has the consequence that the soil mechanics based relationship between effective stress and porosity cannot be used to predict the pore pressure. As shown in Figure 2.11, mudstones buried to points B and C have the same porosity despite having considerable different vertical effective stresses.

During unloading mudstones will follow a considerably different porosity (or related log response) effective stress path, corresponding to elastic rebound (Figures 2.11a, 2.12). As demonstrated by the laboratory compaction data of (Tosaya, 1982), wireline log responses which are dependent on transport properties; such as sonic velocity (or transit time) and resistivity, are more sensitive to elastic rebound compared to log responses that measure bulk properties, such as bulk density or neutron logs (Figure 2.12). Therefore effective stress reduction during fluid expansion will result in an anomalously low velocity or resistivity (velocity/resistivity reversal) compared to minor or no changes in density (Hermanrud et al., 1998; Bowers and Katsube 2002).

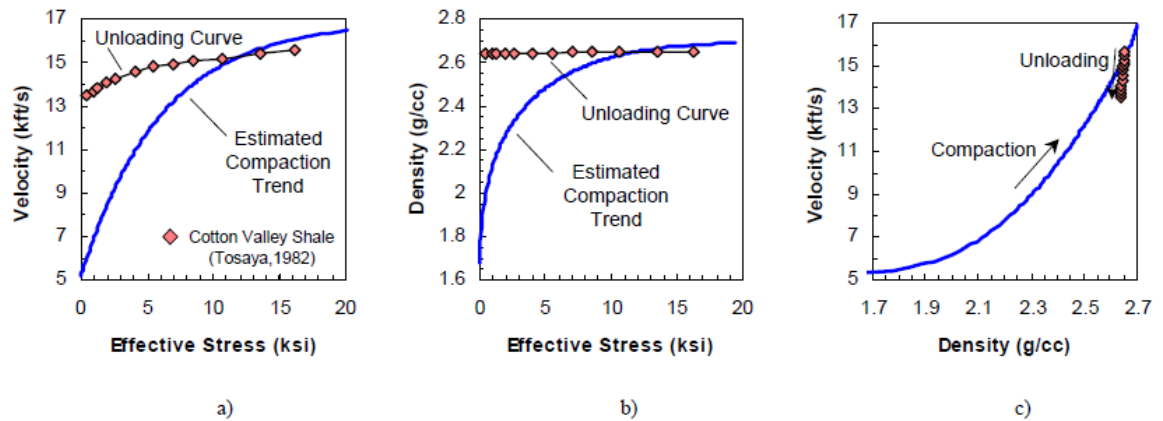


Figure 2.12. Demonstration of shale normal compaction (blue trend) and elastic rebound/unloading behaviour (From Bowers 2001)

Hermanrud et al. (1998) proposed that the observed decrease in sonic velocity during unloading results from reduction in intergranular contact stresses and resistivity decrease can be attributed to enhanced fluid connectivity due to microfracturing.

Bulk properties are dependent on total pore volume, while transport properties are more related to pore sizes, shapes and connectivity (Bowers and Katsube, 2002). Bowers and Katsube (2002) proposed that shale pore structure can be characterized by a storage-connecting pore system where the volume fraction of storage pores plus connecting pores equals the effective porosity. Storage pores are relatively large void spaces that can only be accessed through smaller connecting pores (Figure 2.13). In this model, the flow of fluids and electrical current is assumed to be controlled by the network of sheet like connecting pores with low aspect ratios. Consequently, connecting pores undergo more elastic rebound during unloading compared to storage pores. This will have a much greater effect on the transport properties than on the bulk properties which explain why wireline logs which are dependent on transport properties (e.g. sonic velocity or resistivity) are more impacted by elastic rebound.

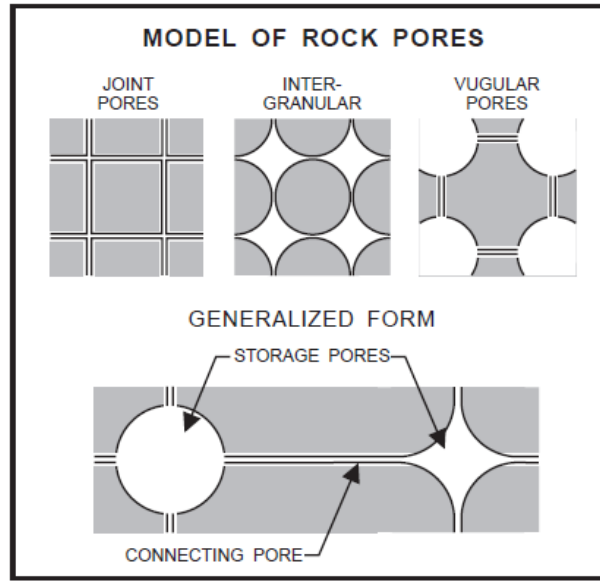


Figure 2.13. Pore structure model used to explain shale compaction behaviour (From Bowers and Katsube, 2002)

Plots of velocity against density or sonic transit time against density have been used to infer whether mudstones are on the normal compaction curve or not (Figure 2.12c). Where compaction is purely mechanical and sediments are on the normal compaction trend, velocity-density crossplots define an envelope in which the location of any particular sample is related to porosity and thus pore pressure (Bowers, 2001); the precise location also depends on lithology, e.g. clay content (Katahara, 2008).

A state-of-the-art method to estimate pore pressure where unloading mechanisms of overpressure generation are active is the method of Bowers (2001), which was developed in two papers by Bowers (1995, 2001). This method accounts for unloading as well as disequilibrium compaction in mudstones by using the sonic and density log data to estimate the vertical effective stress which is then subtracted from the overburden stress.

As shown by Goult (2015) Bower's method can be reduced to a power-law relation between vertical effective stress, sonic velocity and density as shown in equation 8 and illustrated in Figure 2.14.

$$\sigma = \frac{a(V - 5000)^b}{(\rho - 1.5)^c} \quad (8)$$

V is velocity in units of m/s, ρ is density in units of g/cm³, stress and pore pressure is in units of MPa; a , b and c are empirical constants which can be determined empirically using datasets with pore pressure measurements.

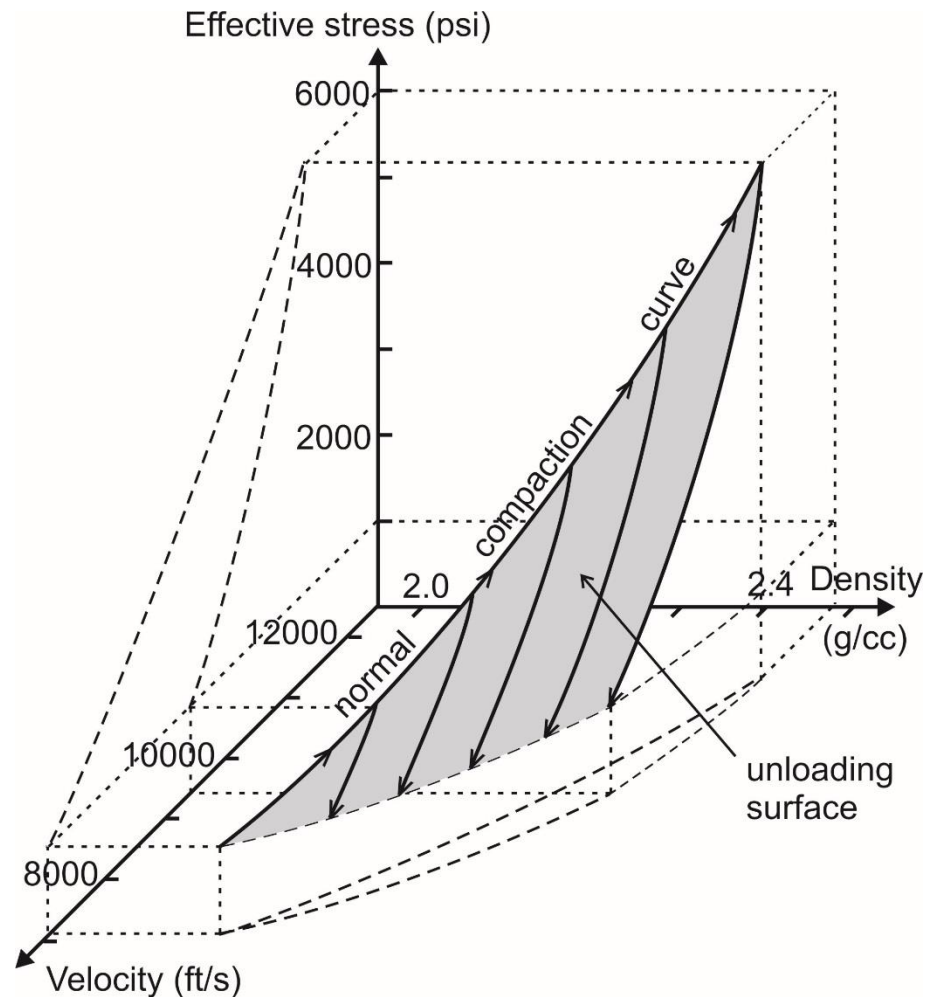


Figure 2.14. Schematic Cartesian diagram for normal compaction and unloading of siliciclastic mudstones according to geomechanics principles showing dependence of vertical effective stress on velocity and density as used in the methodology of Bowers (2001). Axes are sonic (or seismic) P-wave velocity, density and vertical effective stress (From Goult and Ramdhan 2012)

The main assumption here is that there is a single normal compaction trend for mudstones at hydrostatic pore pressure, which bounds an unloading surface (Figure 2.14). The normal compaction trend governs compaction at yield, typically for one-dimensional consolidation, and the unloading surface governs poroelastic behaviour. As shown in Figure 2.14 there is a reversible unloading path associated with every point on

the normal compaction curve forming an unloading surface in this three-dimensional space.

2.7.1 Influence of clay diagenesis on wireline log properties

In their classic paper Hermanrud et al. (1998) showed that bulk density and neutron log responses of deeply buried intra-reservoir Jurassic shales on the Halten Terrace, offshore mid-Norway are not noticeably different in hydrostatically pressured and highly overpressured compartments. The authors concluded that porosity reduction in these mudstones proceeded independently of the effective stress and hence independently of overpressuring.

The lack of relationship between overpressure and (log based) porosity in deeply buried mudstones in the North Sea and Haltenbanken led Teige et al. (1999) and Nordgård Bolås et al. (2004) reach the same conclusion.

Lahann et al. (2001) presented crucial evidence by incorporating mineralogical characterization into the interpretation of wireline log responses. The authors showed a combination of X-ray diffraction-based mineralogy, pore pressure data, density and sonic velocity log responses from two wells (Well A and Well B). They observed an unreactive illite-smectite suite with no discernible change in the expandability of the illite-smectite phase with increasing depth and temperature in Well A. The absence of illitization was attributed to the lack of a potassium source in these mudstones (lack of potassium feldspar). In contrast to this, illitization occurred progressively with depth in Well B. As shown in Figure 2.15 the unreactive illite-smectite in Well A yielded a single stress-density, stress-velocity (Figure 2.15b) and velocity-density (Figure 2.15a) relationship where samples from the velocity reversal zone have the same stress-density, stress-velocity or velocity-density relationships as do samples from shallower depths. The single stress-velocity relationship also indicates that disequilibrium compaction is the primary cause of overpressure in this well (refer to Figure 2.14). In contrast to this, ongoing illitization in Well B yielded a more complex stress-density (Figure 2.16c), stress-velocity (Figure 2.16b) and velocity-density (Figure 2.16d) relationship. Figure 2.16a shows the variation of bulk density and sonic velocity with depth. Note that there is a zone of

constant velocity at around 11,500 feet (3505.2 m) followed by a distinct zone of velocity reversal. The onset of illitization is around 7600 feet (2316.48 m). The zone of illitization has a slightly faster sonic velocity compared to shallower zones until the depth of around 11,500 feet (3505.2 m). Below this depth both the velocity and the effective stress decreases.

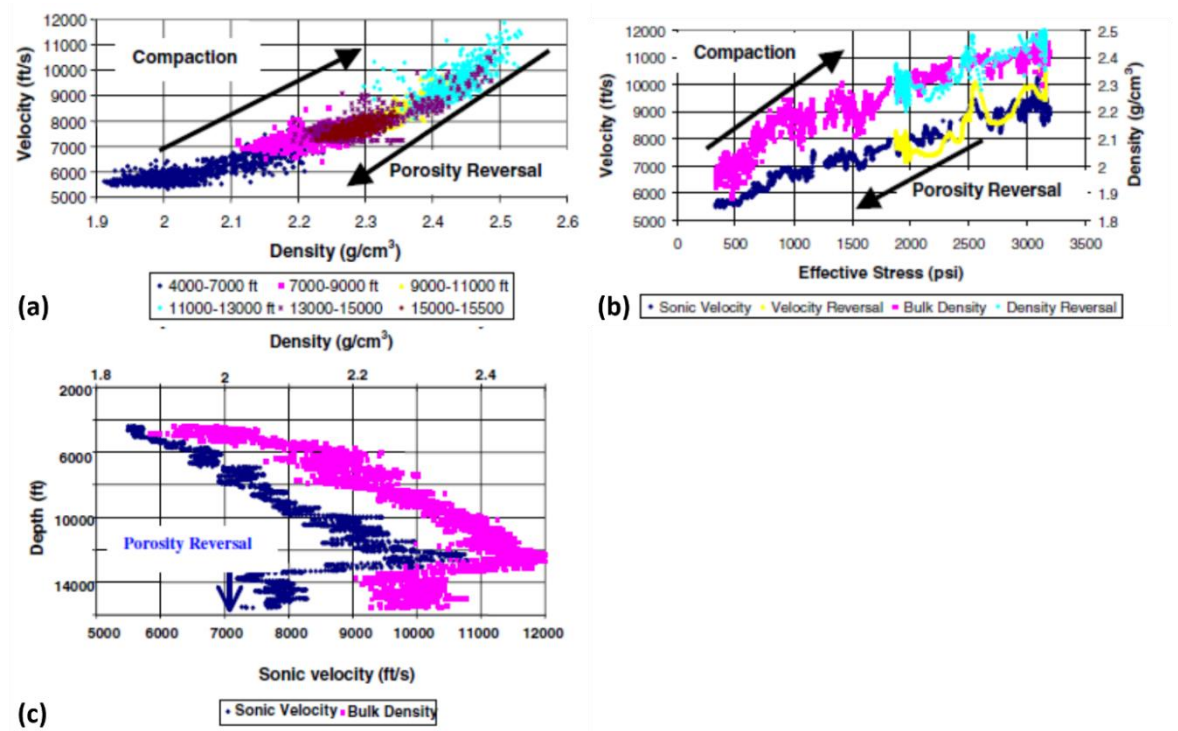


Figure 2.15. Density and velocity log responses from Well A. (a) velocity vs density (b) velocity and density vs effective stress (c) velocity and density vs depth (modified after Lahann et al., 2001).

Note that the velocity-effective stress relationship in the zone of the reversal is considerably different than the velocity-stress trend at shallower depth (primary compaction/loading curve). This characteristic clearly suggests unloading (Bowers 1995; refer to Figure 2.14). As shown in Figures 2.16c and d, the density continues to increase even in the zone of unloading. The authors proposed that ongoing illitization in a system that is open to fluid loss would result in an increase in density (loss of porosity) at constant stress. Small increase in density in the zone of unloading is interpreted as ongoing illitization in a system that allows some fluid loss only the pore fluid escape is not fast enough to maintain constant stress. Note that this interpretation is in accordance with Lahann's (2002) chemically enhanced mechanical compaction model (Figure 2.17).

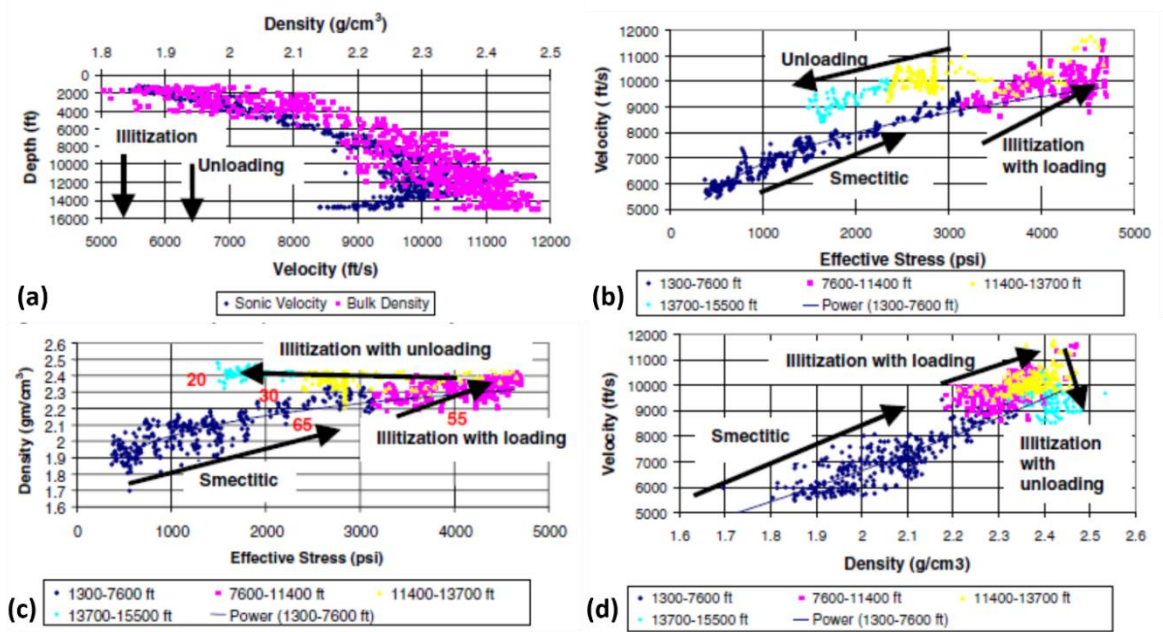


Figure 2.16. Density and velocity log responses from Well B. (a) velocity and density vs depth (b) velocity vs effective stress (c) density vs effective stress (d) velocity vs density (modified after Lahann et al., 2001).

The cartoons in Figure 2.17 are constructed to further explain this behaviour. Figure 2.17a illustrates illitization at hydrostatic conditions. The lighter green trend is the smectitic compaction trend, the solid red arrow shows the porosity change during illitization, and the darker green trend shows the illitic compaction trend, based on the model proposed by Lahann (2002). Figure 2.17b illustrates illitization at constant effective stress and Figure 2.17c illustrates illitization during unloading (reduction in effective stress). Note that the amount of porosity loss (density increase) during ongoing diagenesis is dependent on the maximum effective stress at the onset of clay diagenesis and on the subsequent effective stress history.

Dutta (2002) introduced the crossplot of sonic transit time against density for analysing pore pressure in mudstones which has since been adopted by several authors (e.g. Katahara, 2006b; Ramdhan and Goult, 2010, 2011) and has also been adopted in this thesis. In principle, there is no difference compared to plotting velocity against density, other than the form of the compaction trends (Figures 2.18, 2.19).

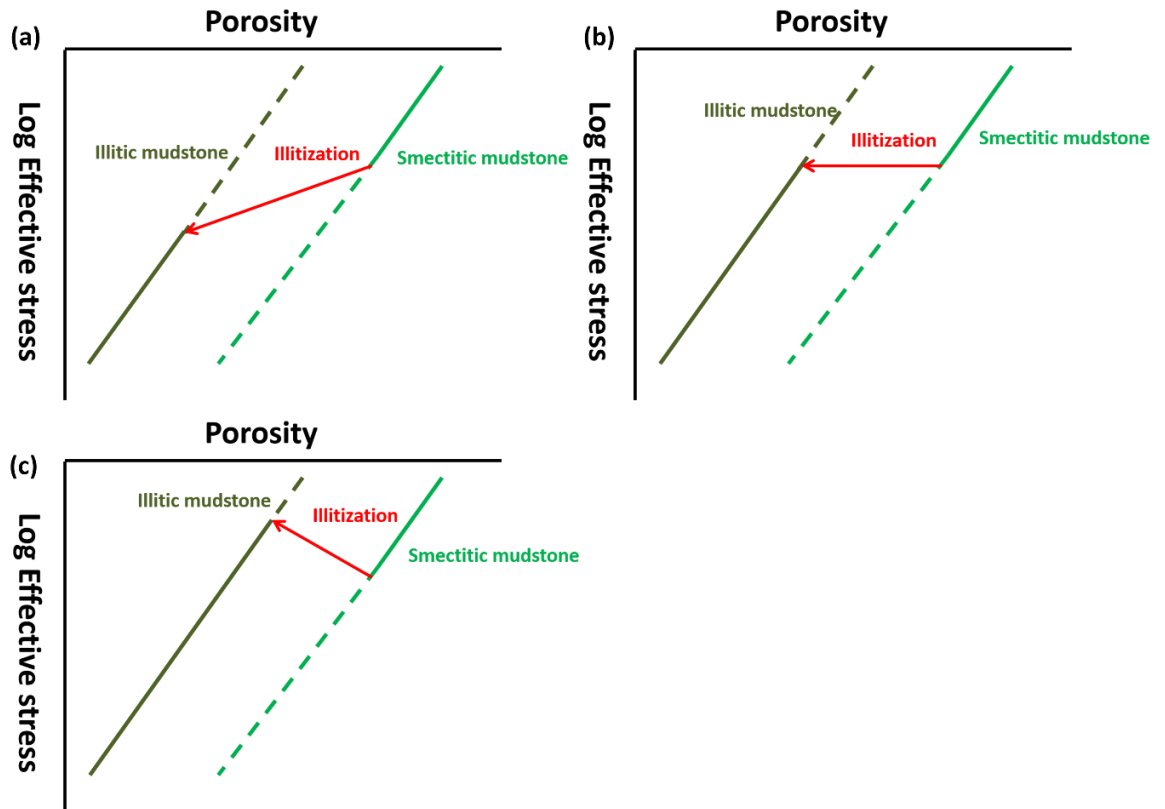


Figure 2.17. Schematic illustration of the idea proposed by Lahann (2002) for chemically-enhanced mechanical compaction. (a) Compaction at hydrostatic conditions. (b) Compaction at constant effective stress. (c) Compaction as effective stress decreases (i.e., during unloading). Refer to text for further explanation.

Dutta (2002) used crossplots of sonic transit time against density to demonstrate the effects of clay diagenesis on the compaction properties of mudstones in the Gulf of Mexico. He identified two bounding linear compaction trends which he originally labelled “eodiagenesis”, for early mechanical compaction of smectite-rich mudstones, and “telodiagenesis”, for the compaction of diagenetically altered illitic mudstones. Diagenesis caused an increase in bulk density for a given transit time and shifted the overall compaction trend of a given mudstone from the smectitic (“eodiagenetic”) trend towards the illitic (“telodiagenetic”) trend (Figure 2.18).

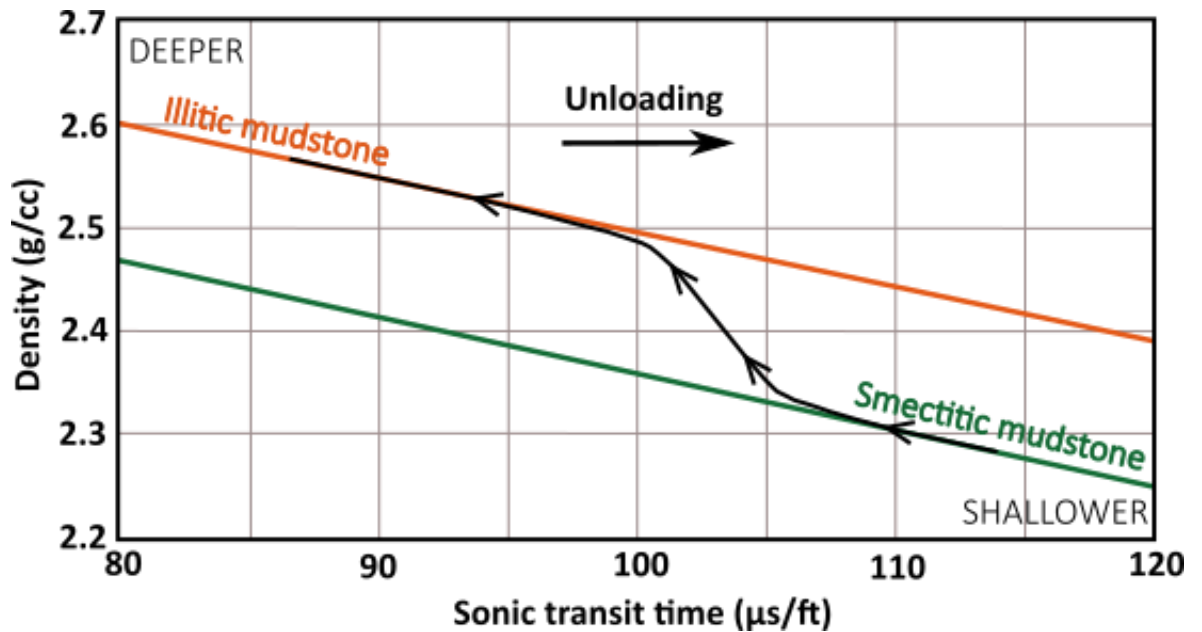


Figure 2.18. Mudstone compaction trend (arrowed curve) on a sonic-density crossplot based on results obtained by Dutta (2002) in the Gulf of Mexico.

The author concluded that mudstone compaction is temperature-dependant and porosity is a function of clay type, effective stress, time and temperature. As shown in Figure 2.18 the overall compaction trend on the crossplot is from bottom right to top left (towards decreasing transit time and increasing density) with increasing depth. The black curve marked with arrows shows the typical compaction trend for mudstones undergoing progressive burial and compaction without unloading. Clay mineral diagenesis depends on both temperature and time therefore the onset of the transitional section of the black curve depends on the time-temperature history of the mudstone. Disequilibrium compaction occurring at the mechanical compaction stage would slow or even halt compaction along the smectitic line. Disequilibrium compaction occurring after the onset of clay diagenesis would result in the transitional section of the compaction trend approaching the illitic line at lower density and for illitized mudstones compaction would slow progress along the illitic trend but would not deviate from it. Unloading at any depth would cause a shift to the right on the cross plot. If, however unloading occurs with clay diagenesis, the trend on the cross plot would lie somewhere between the compaction trend and the pure unloading response (shift toward the right).

Note that Dutta's (2002) findings are in agreement with Lahann's (2002) chemically enhanced mechanical compaction model.

Hoesni (2004) reported velocity-bulk density trends in the Malay Basin in which both velocity and density continued to increase after the onset of overpressure. The observed wireline log trends consisted of two distinct parts: (1) a sharp increase in density with minor change in velocity, (2) followed by sharp increase in velocity with minor change in density. The absence of velocity and density reversals with increasing depth suggests that neither disequilibrium compaction nor unloading can explain this behaviour on its own. The author interpreted these trends as ongoing clay diagenesis and chemical compaction and proposed that sequential filling of the pore space by authigenic cementing phases can explain the observed log responses. According to this model a sharp increase in density with minor change in velocity is the result of preferential cementation in the storage pores. This has a considerable effect on the density but only minor effect on sonic velocity since the connection pores are largely unaffected. In contrast, a sharp increase in velocity with minor change in density can be explained by cementation of the crack like connecting pores which would result in minor density change but considerable increase in sonic velocity.

Additionally, Swarbrick (2012) noted that when bulk densities reach values in excess of 2.60-2.65 g/cm³ the rate of velocity change increases. This is most likely the result of ultralow porosities and bulk density approaching rock matrix values.

Ramdhan and Goult (2010, 2011) investigated overpressure in Miocene mudstones of the Mahakam Delta in the shelfal area of the Lower Kutai Basin, Indonesia and showed that despite the sonic and resistivity logs displaying reversals at the top of the transition zone into hard overpressure, the density continues to increase despite of effective stress decreasing monotonically. Goult et al. (2012) explained this behaviour by invoking Bjørlykke & Høeg's (1997) stress independent chemical compaction model. The authors proposed that porosity reduction in the chemical compaction regime proceeds almost independently of the effective stress, at least until pore pressures reaches extremely high values. They provided an explanation for this behaviour suggesting that clay diagenesis will result in enhanced horizontal clay mineral alignment which will create sub-horizontal

flat pores. These, due to their flexibility tend to close even under low values of effective stress resulting in further compaction unless the fluid expulsion is restricted sufficiently for these pores to be held open (pore pressure approaches the lithostatic stress).

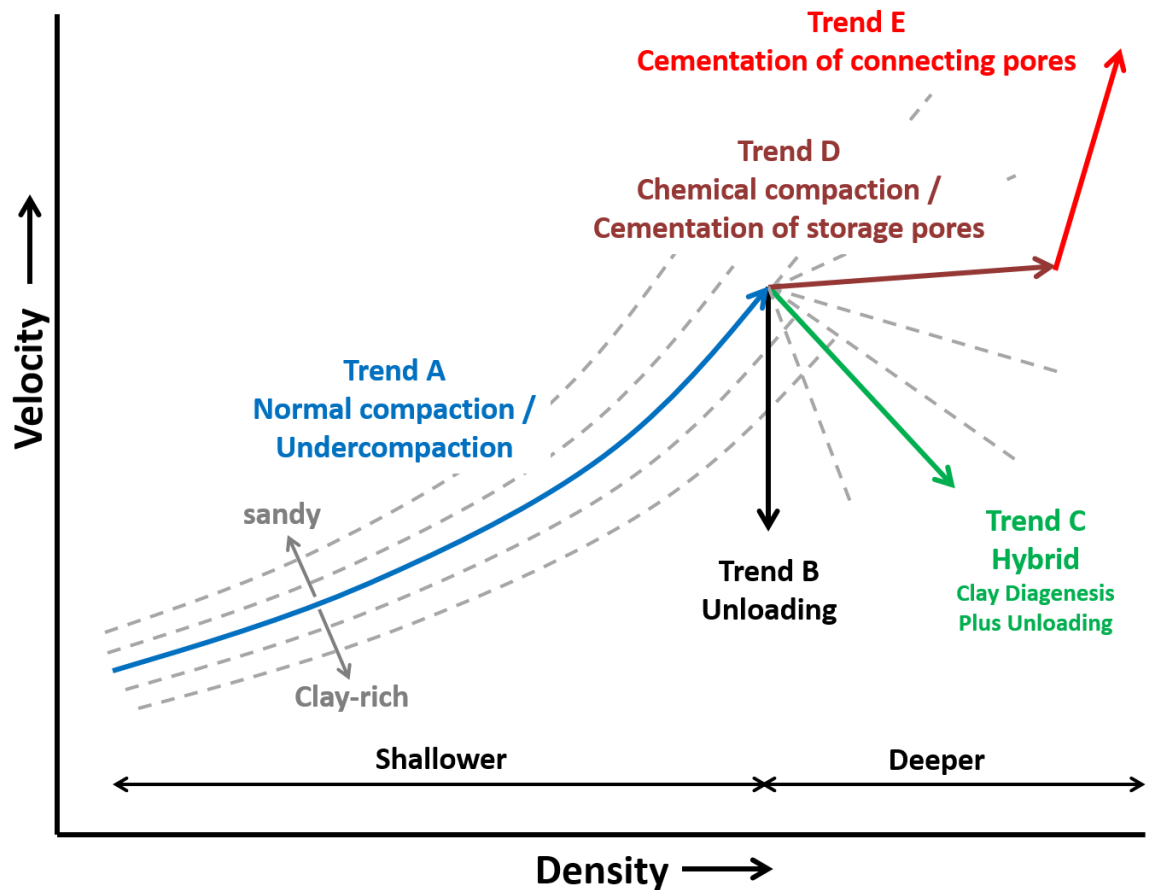


Figure 2.19. Velocity-density crossplot illustrating different mudstone compaction pathways based on results obtained by Hoesni (2004) and Swarbrick (2012) (Modified after Swarbrick 2012).

Figure 2.19 illustrates the previously discussed various evolutionary pathways of mudstone compaction in a velocity-density space. Mechanical compaction with increasing effective stress moves the compaction trend toward higher velocity and density (Trend A). Development of overpressure due to disequilibrium compaction will slow the increase of velocity and reduce bulk density. Even if there's a rapid change in overpressure and both velocity and density show reversals, mudstone data points will remain on or near the normal compaction trend or Trend A. Unloading will move the trend towards lower velocity with negligible change in bulk density (Trend B). Ongoing clay diagenesis and chemical compaction will move the trend towards higher density with small increase in

velocity (Trend D). However, if unloading occurs with diagenesis the trend will move towards lower velocity while density keeps increasing (Trend C). Cementation of connecting pores will result in a sharp increase in velocity with minor change in density (Trend E) (Hoesni 2004; Swarbrick 2012).

2.7.2 Influence of clay diagenesis on pore fluid pressure

Clay diagenesis, especially smectite illitization has long been considered as a possible source of overpressure in mudstones (e.g. Burst, 1959; Powers, 1967; Swarbrick et al., 2002).

According to Powers (1967) and Burst (1959) smectite dehydration can generate overpressure due to volume expansion when interlayer water is expelled into the pore space. In addition, they proposed that the release of interlayer water from smectite is instrumental in driving hydrocarbons out from the source rocks into traps. Bruce (1984) showed that theoretically smectite dehydration could increase the amount of pore fluid by up to 6.6 wt.%. However, based on thermodynamic considerations Colten-Bradley (1987) suggested that overpressure would inhibit smectite dehydration, because increasing fluid pressure would elevate the dehydration temperatures. Additionally, Osborne and Swarbrick (1997) calculated that the overall volume increase associated with simple dehydration is only maximum 4.0 vol.%.

The frequent association of the illitization reaction and the onset of overpressuring in the Gulf Coast sequences were reported by several authors (Plumley, 1980; Berg and Habeck, 1982; Bruce, 1984). However, as it was noted by Osborne and Swarbrick (1997) this relationship on its own does not prove that illitization can generate overpressure.

As it was shown in 2.4.1 the overall volume change involved with the illitization reaction is not known which makes it very difficult to evaluate its role in overpressure generation. According to Audet (1995) the reaction could increase the pore pressure by as much as 30%. In contrast, Osborne and Swarbrick (1999) calculated the volume change of the entire reacting system using ten possible reaction pathways and concluded that illitization cannot generate significant amount of overpressure by pore fluid expansion.

Freed and Peacor (1989) and Bjorkum and Nadeau (1998) emphasised the role of the sealing effect of the precipitating authigenic phases in the pore space. They argued that the coincidence of overpressure with illitization can be attributed to the reduction in the permeability of the mudstones. Reduction of permeability however would only help to retain fluids and thus preserve overpressure created by other mechanisms, but this would not generate extra overpressure (Swarbrick and Osborne, 1998).

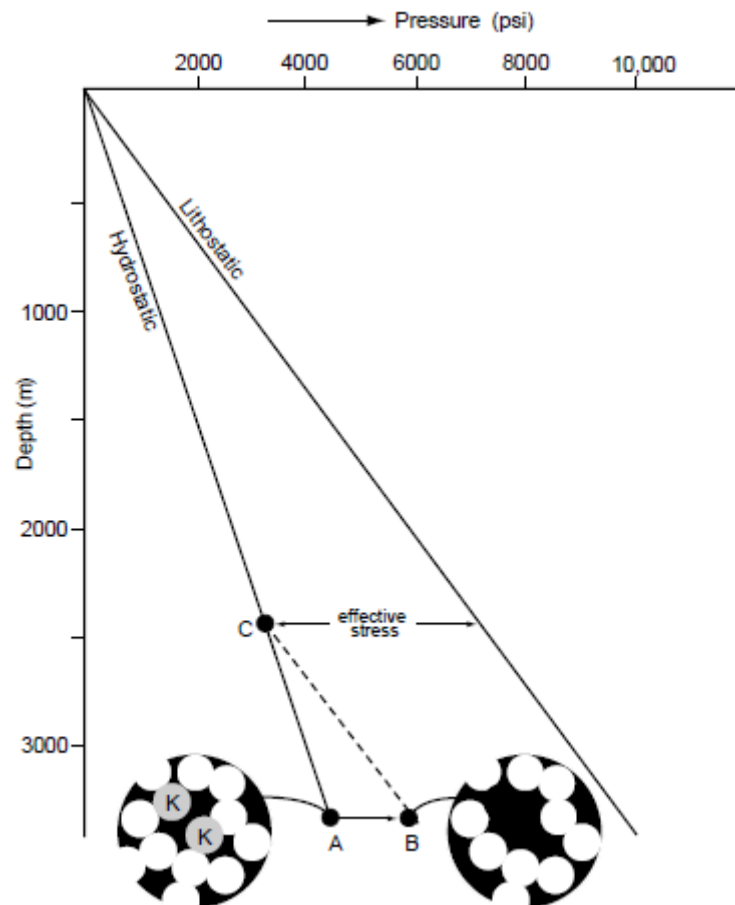


Figure 2.20. Overpressure generation by load transfer in maturing source rocks. Transforming some of the kerogen into oil would increase the porosity of the mudstone (Point A to B) if no pore-fluid can escape. This would have the effect of transferring some of the overburden load supported by the original kerogen onto the pore fluid. The rock now has the same porosity as when it was buried to point C thus it would be overpressured if the effective stress remains constant. K: kerogen (From Osborne and Swarbrick 1997).

Swarbrick and Osborne (1998) proposed that the frequently observed coincidence of overpressure with illitization might be related to the accompanying changes of the physical characteristics of the mudstones. Osborne and Swarbrick (1997) suggested that

chemical compaction processes may be able to generate significant amount of overpressure when part of the load-bearing framework is transformed into liquid and where diagenesis radically alters the compressibility of the rock framework. They also gave an example for this mechanism from an organic rich source rock (Figure 2.10). As shown in Figure 2.10, if some of the kerogen is transformed into liquid products and there is no pore fluid loss then the porosity of the mudstone would increase and some of the overburden load would be transferred to the fluid phase. Originally the authors referred to this pressure generating mechanism as disequilibrium compaction induced by mineral diagenesis but later Lahann (2002) and Lahann and Swarbrick (2011) coined the term load transfer.

Lahann et al. (2001) and Lahann (2002) suggested that smectite illitization can generate overpressure in similar manner. Lahann (2002) proposed that illitization changes the equilibrium porosity associated with an effective stress (Figure 2.17), thus if pore water escape is inhibited during the transformation than overpressure would be generated due to load transfer. Note that this pressure generating mechanism is independent of the volume change associated with the illitization reaction. However, any volume increase resulting from the reaction would increase the amount of the total generated overpressure.

Based on this idea, Lahann (2002) introduced smectitic and illitic compaction models to interpret pore pressure variation with depth in Gulf Coast mudstones. He used Corbet and Bethke's (1992) modified Athy expression in the form:

$$\varphi = \varphi_m + \varphi_0 e^{-\beta \sigma} \quad (9)$$

Where φ is total porosity; φ_m is the porosity term for clay bound water ("irreducible porosity"); β and φ_0 are empirical constants; σ is vertical effective stress.

Note that in contrast to Athy's (1930) original version (refer back to 2.3.1) this equation allows the porosity to decline to a minimum value rather than to approach 0 with increasing stress/depth.

Lahann (2002) determined the values for β and φ_0 for the smectitic model empirically by model fitting to measured and log-based porosity data from the shallow, hydrostatically pressured sections. φ_m value for the smectitic model was fixed at 12% which is consistent with the retention of two smectitic interlayer water layers in these mudstones. The illitic model was derived in part from the smectitic model by reducing the φ_m term to 3%. This value is based on the estimated volume of smectitic water content in typical illitized Gulf of Mexico mudstones. The φ_0 term was assumed to be identical for illitic and smectitic mudstones. The β term for the illitic model was derived empirically by calibration with observed pore fluid pressures in deeper, overpressured sections. The author proposed that the required increase in the β term indicates that these mudstones become more compactable which is consistent with the reported increase in clay fabric orientation coincident with illitization (refer to section 2.5). Lahann and Swarbrick (2011) coined the term framework weakening to describe this behaviour and proposed that conversion of bound water to mobile water, dissolution of load bearing grains and increasing clay mineral preferred orientation during diagenesis would create a weaker (more compactable) mudstone framework. This process can generate considerable amount of overpressure by load transfer if fluid export from the mudstone is sufficiently inhibited. Lahann (2002) suggested that overpressure contribution due to smectite illitization in smectite rich mudstones can be 1500-3000psi (~10-20 MPa).

Lahann and Swarbrick (2011) also presented relationships between mudstone density and calculated effective stress from the Gulf of Mexico shelf, which support these changes in mudstone properties. They showed examples for increasing density with constant or decreasing effective stress which cannot be explained by fluid-expansion or prediagenetic compaction. The authors proposed that these observations are inconsistent with unloading due to fluid expansion as originally described by Bowers (1994) which would result in substantial velocity reduction with minor or no change in bulk density but are consistent with overpressure generation by load transfer following framework weakening. Trends for unloaded mudstones when plotted on velocity-density plot matched Dutta's (2002) illitic trend (Figure 2.18).

Katahara (2006) made similar observations in the Gulf of Mexico and suggested that unloading due to illitization is inelastic, thus an increase in effective stress after unloading

would not result in a return along the same curve as for elastic unloading (fluid expansion) but would result in compaction along a different curve.

Dutta (1986, 1988, 2002) presented a model for pore pressure in mudstones which incorporated the effects of chemical diagenesis. His model employed a generalised compaction model, chemical kinetic theory and a simple thermal history model to predict the pore pressure. More recently an updated version of this model was presented in Dutta et al. (2014) and Dutta (2016).

The authors presented a generalised compaction model by proposing the following relationship between vertical effective stress (σ) and void ratio (e):

$$\sigma = \sigma_0 \exp(-\beta e) \quad (10)$$

Where σ_0 is a lithology-dependent coefficient describing the effective stress needed to reduce the porosity to zero and β is a lithology dependant modulating function termed the “diagenesis function” by Dutta (2016) that incorporates thermal history into this model. Its explicit form can be found in Dutta et al. (2014) and Dutta (2016). Illitization is modelled using a first-order rate theory and Arrhenius rate equation. The parameters (e.g. activation energy etc.) for this model were derived from published X-ray diffraction data.

In addition, Dutta et al. (2014) proposed the following relationship between sonic transit time ($\Delta\tau$), effective stress (σ) and the “diagenesis function” (β):

$$\Delta\tau = \Delta\tau_m (1 + \beta^{-1} \ln(\sigma_0/\sigma))^x \quad (11)$$

Where m denotes the rock matrix and x is a lithology dependant coefficient as discussed by Issler (1992). The above relationship is only valid for load bearing sediments with porosities less than the critical porosity (Issler 1992, Dutta et al. 2014).

The above relation relates sonic transit time directly to effective stress for a given mudstone lithology and thermal history. The effective stress is then related to pore pressure according to Therzaghi's principle (equation (5)).

A more pragmatic approach to pore pressures prediction in diagenetically altered mudstones was presented by Sargent et al. (2015) and Goult and Sargent (2016). Their method makes use of the sonic-density and Dutta's (2002) illitic (late diagenetic) trend (Figure 2.18). The fundamental assumption underlying their ("Budge-Fudge") method is that there is a unique sonic-density trend for diagenetically altered mudstones of a given lithology, for temperatures above $\sim 100^{\circ}\text{C}$, provided they are not unloaded, even though neither density nor velocity is uniquely related to effective stress at that stage. That assumption permits estimation of the amount of unloading overpressure present in the mudstones using Bower's (2001) unloading relation (Sargent et al. 2015). The limitation is that the maximum effective stress experienced by the mudstones has to be estimated in an independent operation.

2.7.3 Summary

Standard log- and seismically-based pressure prediction methods require a normal compaction curve that is a relationship between porosity and effective stress. More advanced methods define a range of lithologically constrained porosity-effective stress relationships (e.g. Yang and Aplin, 2004). Such methods will only continue to work at higher temperatures if porosity continues to be lost as a function of effective stress.

A purely empirical method such as Eaton (1975) can provide accurate results even in diagenetically mature mudrocks provided that it is properly calibrated using data from offset wells. Bowers' method assumes that the vertical effective stress is a unique function of sonic velocity and bulk density for a given mudstone lithology, nevertheless in common with other empirical methods it can give satisfactory prediction results in high temperature settings if calibrated with neighbouring wells that are good analogues (Goult and Ramdhan 2012). However even these empirical approaches are liable to give inaccurate results in frontier areas when there is a lack of local calibration.

Any pore pressure prediction method incorporating the effects of chemical diagenesis make certain assumptions regarding how clay diagenesis affects the physical properties of mudstones. These assumptions are mostly based on theoretical considerations (e.g.

Bjørlykke & Hoeg 1997; Draege et al. 2006) or inferred from trends in wireline log responses (e.g. Hoesni 2004; Lahann and Swarbrick 2011).

One key question is the way in which porosity is lost in mudstones during mineral diagenesis. If porosity loss becomes independent of the effective stress, as it is assumed for the chemical compaction model (refer back to 2.6; Figure 2.9) then all porosity-based pressure prediction methods will become useless at high temperatures. On the other hand, if porosity continues to be lost as a function of the effective stress as it is postulated for the chemically enhanced mechanical compaction model (Figure 2.9) then the nature of the porosity-effective stress relationship has to be established and quantified for diagenetically mature mudstones in order to make accurate pore pressure predictions.

Other key issue is whether clay mineral transformations can actually generate overpressures and if they do, what are the mechanisms involved.

In this thesis, I set out to test these assumptions and hypotheses using a combination of mudstone sample characterization and wireline log analysis with the aim to increase the understanding of how clay diagenesis affects the compaction and pore fluid properties of dominantly siliciclastic mudstones.

Chapter 3

Methodology

3.1 Introduction

This study involves a combined analysis of mudstone sample material and wireline log data from four different localities. These were specifically selected to test hypotheses regarding compaction and overpressure generation in diagenetically consolidated mudstones.

This chapter describes the various techniques and methodologies used to study the effects of mineral diagenesis on the physical properties of siliciclastic mudstones.

A wide range of techniques were employed in analysing the mineralogical, chemical, textural and physical properties of the rock samples. However, most of these techniques are standard procedures so only a brief description is given about their general aims and technical points.

Section 3.2 describes the sampling procedures; 3.3 describes the sample characterization methodologies; detailing the various techniques used to analyse the mineralogical, chemical and physical properties. Section 3.4 details the wireline log editing, log-based mudrock discrimination and log-based porosity calculation procedures. Section 3.5 describes the details of the one-dimensional basin modelling.

3.2 Sampling

Mudstone samples examined in this study are from single formations buried to a range of temperatures (60-170°C), in different pore pressure regimes. Localities were selected where the chosen formation were assumed to be at their maximum depth of burial. This study relies on the assumptions that the mineralogy of the primary sediments for a given formation was broadly uniform. With this in mind I chose formations with relatively invariable lithological characteristics and wells located relatively close to one another (as far as it was possible). The four selected case studies, more-or-less meet these criteria.

Cuttings were collected from depths intervals which were previously checked using the wireline logs (Gamma ray and NPHI-DPHI) to make sure these are made of dominantly mudstones. Care was taken to pick thick mudstone sections in order to minimise contamination from other lithologies.

Core samples were collected from volumetrically significant fine grained lithologies. Sampling points for dominant fine grained lithologies were selected based on the need to select a range of materials from the discernible heterogeneity; rock types that dominate over significant core intervals; and core material that are homogeneous within the actual sample size so that analyses made on subsamples can be correlated. Care was taken to collect samples from homogeneous and uncemented mudstone-rich intervals.

Depth intervals have been chosen to cover the whole illitization profile.

3.3 Sample characterization procedures

Both dry cuttings and mudstone core samples were used in this study. Cutting samples were provided as both washed and unwashed samples of variable size and quality.

All cutting samples were thoroughly washed to remove any remaining drilling mud. Water based drilling mud was removed by placing the samples in an orbital shaker overnight and washing through a sieve with 150-micron mesh size. For cuttings contaminated by oil-based drilling mud, 100 ml of 5% teepol washing solution was added to each sample. Particles that passed through the sieve were discarded. Particles retained in the sieve were kept for analyses.

Apart from the fact that they were either water-based or oil-based muds, no further information was available regarding the chemical composition of the drilling muds. The barite content was used as a proxy for drilling mud contamination (see also 4.6.2) since it is the dominant component in most drilling muds. When there was a strong correlation between the barite and any other component, it was considered as clear indication of drilling mud contamination.

In order to effectively integrate whole-rock mineralogy, chemistry and cation exchange capacity, the samples selected for these analyses were first crushed in a mortar to pass through a 0.4 mm sieve (< 40 mesh) then homogenised and split into chemically and mineralogically equivalent aliquots (McCarty, 2002; Omotoso et al., 2006).

Details of the sample characterization techniques and procedures are presented in the following sections.

3.3.1 Quantitative bulk fraction X-ray diffraction (QXRD)

Mineral quantification in bulk mudrock samples was performed using X-ray diffraction analysis.

Quantitative analysis of all mudstone samples from Haltenbanken; all samples from Central North Sea; all samples from Bravo-Y well from Central Malay Basin; and XSA1-13, XSC1 samples from Sergipe Alagoas Basin was done at the Institute of Geological Sciences, Krakow, Poland, following the methodology of Środoń et al. (2001). Analysis of the Bravo-L well samples from Malay Basin and ASA1-13, ASE1-10, ASC1-11 and ASD1-8 samples from Sergipe Alagoas Basin was done at the Hutton Institute, Aberdeen, Scotland following the normalized full pattern reference intensity ratio (RIR) method of Hillier (2000, 2003) and Omotoso et al. (2006).

In Krakow, the X-ray diffraction data were collected from randomly oriented (side loaded) sample powders spiked with 10 wt.% ZnO on a Thermo X'TRA diffractometer equipped with a SiLi solid state detector. XRD patterns were collected from 5-65°2θ, 2s counting/0.02°2θ step using CuKα radiation with 40 kV applied voltage and 40 mA current.

Mineral quantification was done by analysing the X-ray diffractograms using the Quanta computer program (Środoń et al., 2001; Mystkowski et al., 2002; Chevron ETC proprietary). Quanta use a combination of single-peak and whole-pattern fitting approaches to quantitative XRD analysis. In this method clay minerals are quantified from their 060 reflections and the total dioctahedral Al-rich 2:1 clays (illite, muscovite, dioctahedral smectite, mixed layer illite/smectite) are quantified together as illite+smectite group minerals. Errors in accuracy are low with < 2 wt.% deviation from actual values. No normalisation is applied, and the analysis is tested by the departure of the sum of all measured components from 100% (Środoń et al. 2001). Further details regarding the accuracy of this method can be found in Środoń et al. (2001) and Omotoso et al. (2006).

In Aberdeen, the X-ray diffraction data were collected from randomly oriented (spray dried) sample powders on a Siemens D5000 diffractometer equipped with a scintillation

point detector. XRD patterns were recorded from $2-75^{\circ}2\theta$, 2 s counting/ $0.02^{\circ}2\theta$ step using $\text{CoK}\alpha$ radiation with 40 kV applied voltage and 40 mA current.

Mineral quantification was done using the Diffrac Plus Evaluation - EVA software following the RIR method. This method has an uncertainty of ± 3 wt.% at 95 % confidence level for all the phases analysed (Hillier 2000). Further details regarding the accuracy of this method can be found in Hillier (2000, 2003) and Omotoso et al. (2006).

3.3.2 Quantitative clay fraction X-ray diffraction

Structural details of clay minerals were identified and quantified on selected samples using the XRD patterns collected on oriented specimens of separated clay fractions.

In Krakow the clay fractions ($<0.2 \mu\text{m}$) were separated following Jackson's (1969) standard procedure by chemical purification including removal of carbonates, Fe-(oxy-)hydroxides and organic matter followed by centrifugation.

XRD patterns were collected from oriented samples of extracted and Ca-exchanged $<0.2 \mu\text{m}$ size fractions in air-dried state and following saturation with ethylene glycol on a Thermo X'TRA diffractometer equipped with SiLi solid state detector. XRD data was collected from $5-52^{\circ}2\theta$, 4s counting/ $0.02^{\circ}2\theta$ step using $\text{CuK}\alpha$ radiation with 40 kV applied voltage and 40 mA current.

Quantitative clay mineral analyses were performed by full XRD pattern computer simulation method (Drits et al., 1997; Sakharov et al., 1999) with Sybilla software (Chevron ETC proprietary), employing the formalism described by Drits and Tchoubar (1990).

In Aberdeen, the clay fractions ($<2 \mu\text{m}$) were separated using timed sedimentation and prepared as oriented mounts using the filter peel transfer technique. XRD patterns were collected from oriented samples in the air-dried state, after glycolation and after heating to 300°C for one hour on a Panalytical Xpert Pro diffractometer equipped with X'celerator Position Sensitive Detector. XRD data was collected from $3-45^{\circ}2\theta$, 4 s counting/ $0.02^{\circ}2\theta$ using $\text{CuK}\alpha$ radiation with 40 kV applied voltage and 40 mA current. Quantitative clay mineral analyses were done using a mineral intensity factor approach based on calculated

XRPD patterns (Hillier, 2000, 2003). For clay minerals present in amount >10 wt% uncertainty is better than ± 5 wt.% at the 95% confidence level (Hillier, 2000, 2003).

3.3.3 Cation exchange capacity (CEC)

Cation exchange capacity (CEC) of bulk mudrock samples was measured using the cobalt hexamine trichloride method following Orsini and Remy (1976), Bardon et al. (1983) and the ISO 23470 Standard. 0.5 – 1 g of powdered sample was mixed with 25 ml of the $[\text{Co}(\text{NH}_3)_6]\text{Cl}_3$ solution (at pH 7-8) at known absolute concentration, sonicated for 2 minutes and shaken for 1 hour, then centrifuged for 10 minutes at approx. 4000 X g. Absorbance of the supernatant solutions was analysed with a VIS spectrometer at wavelength of 470 nm. The amount of $[\text{Co}(\text{NH}_3)_6]^{3+}$ cation remaining in the solution after adsorption by the sample linearly correlates with the supernatant absorbance. CEC values are reported on a dry sample weight basis in meq/100g and $\text{cmol}_{(+)}/\text{kg}$, after drying the samples overnight at 200°C. Further details regarding the accuracy of this method can be found in Derkowski and Bristow (2012).

Bulk rock CEC of typical (organic-lean) mudstones is primarily controlled by the clay mineral content (i.e., the type and quantity of the clay minerals present in a sample). The overall CEC contribution of clay minerals can be expressed as smectite-equivalent content, defined as the theoretical weight fraction of pure smectite in the bulk sample that would have the same CEC contribution (Środoń, 2009; Środoń et al., 2009; Derkowski and Bristow, 2012; Derkowski and Marynowski, 2016).

The smectite equivalent represents the sum of all mineral surfaces available for cation exchange, which is dominated by the clay mineral (external and internal) surfaces in most organic-lean mudstones. Clay minerals contribute to the smectite-equivalent proportionally to their expandability. Non-expandable clay minerals like illite, mica, kaolinite and chlorite have minor or negligible impact on the smectite-equivalent. In general, the quantity and expandability of the illite/smectite are the main factors determining bulk rock CEC in most mudrocks. Other expandable mixed layer species like chlorite/smectite or kaolinite/smectite are uncommon in most settings (Środoń, 2009; Środoń et al., 2009).

In this study, the CEC measurement was used to refine the 2:1 mineral composition in the bulk rock samples, as determined by bulk QXRD. The CEC value was used to calculate the smectite-equivalent component in the bulk rock illite+smectite mineral group. This calculation is based on the assumption that pure illite end member has a CEC value of 15meq/100g and that pure smectite end member has a CEC value of 100meq/100g (Środoń and McCarty, 2008). The smectite-equivalent (%S_{IS}) component is calculated using the following relationship:

$$\%S_{IS} = \frac{measCEC_{IS} - CEC_I}{CEC_S - CEC_I} \times 100 \quad (12)$$

Where $measCEC_{IS}$ is the measured bulk rock CEC value, CEC_I and CEC_S are the CEC values for end member illite and smectite respectively.

3.3.4 Total organic carbon (TOC)

Total organic carbon (TOC) content was measured using Eltra CS-500 IR-analyzer with total inorganic carbon (TIC) module.

Total carbon was measured as CO₂ gas content, which evolved by total combustion under oxygen atmosphere. TIC content was determined as CO₂ released from reaction with 15% HCl solution. TOC was calculated as the difference between total C and TIC.

3.3.5 Major-element and trace-element chemical analyses

Major and trace-element chemical analyses on the bulk mudstone samples were obtained from ActLabs, Ontario, Canada (www.actlabs.com).

Samples were pulverized to <200 mesh and then prepared by lithium metaborate/tetraborate fusion. Samples were analysed by inductively coupled plasma optical emission spectrometry (ICP OES) and inductively coupled plasma mass spectrometry (ICP MS) for major and trace elements respectively. Detection limit is better than 0.01% for major and trace elements. Reproducibility was checked by repeating measurements on selected samples. Details of accuracy and precision can be found in Appendix IV.

Major and trace elemental composition of bulk mudstone samples was used in conjunction with bulk mineralogy to interpret compositional differences between the samples. Additionally, major and trace elements were used to make inferences about the sediment source and about the extent of paleo-weathering.

There are various factors controlling the mineralogical and chemical composition of siliciclastic sediments, including source rock composition, weathering (e.g. intensity and duration), transportation mechanisms, depositional environment (e.g. marine or fresh water) and post depositional processes (e.g. diagenesis and metamorphism) (e.g. McLennan et al., 1993). Numerous investigations applied geochemical approaches to study the above aspects (e.g. Bhatia, 1985; McLennan et al., 1993b; Cullers, 1994; Nesbitt and Markovics, 1997; McLennan, 2001; Hofer et al., 2013). In overall, fine-grained siliciclastics like mudstones are preferentially used to identify the average composition of the source and to identify paleo-weathering and depositional conditions. This is because mudstones usually cover a longer and more continuous time period compared to coarser-grained lithologies. In addition, mudstones more reliably retain near-original chemical and mineralogical signatures of the source (McLennan et al., 1993a; Hofmann et al., 2001; Hofer et al., 2013). It should be noted that diagenesis can substantially change the original depositional mineralogy and in some cases possibly the chemical composition as well (Fedó et al., 1995). However, in most cases diagenetic processes in mudstones are isochemical (e.g. Hower et al., 1976) and bulk chemical composition of deeply buried mudstone samples can be used to interpret compositional differences in the source or to identify paleo-weathering conditions. Thus, in this thesis the assumption has been made that after deposition mudstones are behaving as a chemically closed system (refer back to 2.4.1).

Major and trace elemental composition of the mudstone samples was compared to those of the post-Archean Australian average shale (PAAS) of Taylor and McLennan (1985) and average upper continental crust (UCC) of Taylor and McLennan (1985) and McLennan (2001). These are well established and often used geochemical references for clastic sediments. Chondrite-normalized patterns of rare earth elemental (REE) composition were calculated using chondrite REE values presented by Taylor and McLennan (1985).

Oxid and elemental ratios of major elements were used as indicators of original detrital mineralogy. Si/Al (proxy for quartz content), K/Al (proxy for illite content), and Na/Al (proxy for smectite content) ratios were used to identify compositional variation within the samples (Hofmann et al., 2001).

The Index of Compositional Variability (ICV) was calculated following Cox et al. (1995) as shown in equation (13):

$$ICV = (Fe_2O_3 + K_2O + Na_2O + CaO + MgO + MnO)/Al_2O_3 \quad (13)$$

ICV measures the abundance of alumina relative to other major cations in the mudstone samples. This can be used as a measure of compositional maturity. In general non-clay silicates contain lesser amount of Al_2O_3 than clay minerals and tend to have a higher ICV. Clay mineral ICV values are in the range of 0.03-0.78, and feldspar ICV values are in the range of 0.54-0.87 (Cox et al., 1995).

The degree of source rock weathering was quantified by calculating weathering indices using the molecular proportions of mobile and immobile element oxides. The Chemical Index of Alteration (CIA) was calculated following the method of Nesbitt and Young (1982) as shown below:

$$CIA = \{Al_2O_3 / (Al_2O_3 + Na_2O + CaO * + K_2O)\} \times 100 \quad (14)$$

Oxides are in molecular proportions. CaO^* represents CaO in the silicate fraction. Corrections for carbonate and apatite content was made by making the assumption that CaO^* is equivalent or less than Na_2O . The measured sample CaO contents were used when $CaO \leq Na_2O$. When CaO content of the samples were higher than the Na_2O content, then measured contents of the latter were used as an approximation (McLennan et al., 1993a).

Weathering trends were established using the A-CN-K ($A=Al_2O_3$; $CN=CaO^*+Na_2O$; $K=K_2O$; all in molecular proportions) ternary diagram of Nesbitt and Young (1982).

To further minimise errors related to the unknown CaO content of silicate fraction the Chemical Index of Weathering (CIW) was also calculated using the method of Cullers (2000) as shown in the below section (oxides are in molecular proportions):

$$CIW = \{Al_2O_3 / (Al_2O_3 + Na_2O)\} \times 100 \quad (15)$$

Ratios of low-solubility trace elements (e.g. REEs, Th, Sc) were used for provenance analysis. Th/Sc and Zr/Sc ratios were used as proxies for compositional variation within the source and sediment recycling respectively (McLennan et al., 1993b). REE fractionation was quantified using the chondrite normalised La_N/Yb_N ratio. The degree of Eu anomaly was quantified using the chondrite normalised Eu/Eu^* ratio (McLennan and Taylor, 1991).

3.3.6 Grain density

Grain density of mudstone samples was measured using the “Small Pycnometer Method” (British Standards 733: Part 2: 1987).

In this method, the mass of the oven-dry sample is determined by weighing and its volume is calculated from the mass of water displaced by the sample in a pycnometer. Quartz was used as a standard reference material.

Grain density is calculated using the equation:

$$G_s = \frac{m_s}{v_s} \quad (16)$$

Where G_s is the grain density (g/cm^3), m_s is the mass of the oven-dry particles of the sample (g) and v_s is their volume (cm^3).

Grain density is used to calculate the total porosity of the samples. Note that samples are dried at 105°C prior to the measurement to remove free water. This might result in removing some of the interlayer water in smectite, thereby increasing the grain density of this mineral and the calculated total porosity.

3.3.7 Total porosity

Total porosity (\emptyset) is determined from dry bulk density (ρ_b) and grain density (G_s):

$$\emptyset = 1 - \frac{\rho_b}{G_s} \quad (17)$$

Grain density is measured as described in 3.3.6. Dry bulk density is calculated from the bulk volume of a sample with known mass that is used in the process of pore size distribution measurement as described in 3.3.8.

3.3.8 Mercury Injection Core Porosimetry (MICP)

Mercury intrusion porosimetry was used to measure the porosity and pore size distribution of selected samples. In reality this technique measures the largest pore entrance and not the actual inner pore size and only determines the pore throat size distribution (Giesche, 2006).

Pore throat size distributions were determined using a Micromeritics Corporation, Autopore II 9220 Porosimeter, with penetrometers of capacity 5mL.

During this procedure, an oven dried (at 105°C for 24 hours), weighed sample is placed inside the penetrometer, which is then loaded into the pressure system of the porosimeter. To ensure that only applied pressure is acting on the sample the pressure system is evacuated to less than 30 μ m Hg. After this mercury is introduced into the penetrometer and a range of pressures are applied to the mercury according to pre-programmed pressure steps. First a range of low pressures is applied after which the penetrometer is removed and weighed (mass of penetrometer plus mercury plus sample).

The bulk volume of the sample is derived from this mass using equation (18).

$$V = V_p - \frac{m_{psHg} - m_{ps}}{G_{Hg}} \quad (18)$$

V is bulk volume of sample (cm^3); V_p is the volume of the penetrometer (cm^3); m_{psHg} is the mass of penetrometer loaded with sample and filled with mercury (g); m_{ps} is the mass of penetrometer plus sample (g); G_{Hg} is the density of mercury (g/cm^3)

Afterwards the penetrometer is loaded into the high-pressure system and series of high pressures is applied to the mercury. At each applied step the volume of mercury that penetrated the sample is determined by measuring the electrical capacitance of the penetrometer through transducers connected to each end of the penetrometer. These values are recorded as a series of intrusion pressures and volumes. Table 3.1 shows the pressure steps that were used in this study.

Pore size can be calculated assuming a cylindrical pore geometry using Washburn's (1921) equation (19):

$$P_c = \frac{2\sigma\cos(\theta)}{r} \quad (19)$$

Where P_c is capillary pressure (N/m^2), σ is interfacial tension (N/m), θ is the contact angle between the solid and mercury and r is the radius of the cylindrical pore (m). It is assumed that the surface tension of mercury is $0.485 \text{ N}/\text{m}$ and the contact angle between mercury and the pore surface is 141° (e.g. Wardlaw and McKellar, 1981).

| Step | Pressure psi | Step | Pressure psi | Step | Pressure psi | Step | Pressure psi |
|------|-----------------|------|-----------------|------|-----------------|------|-----------------|
| 1 | 3 | 22 | 600 | 43 | 5500 | 64 | 21000 |
| 2 | 5 | 23 | 700 | 44 | 6000 | 65 | 22000 |
| 3 | 7 | 24 | 800 | 45 | 6500 | 66 | 23000 |
| 4 | 10 | 25 | 900 | 46 | 7000 | 67 | 24500 |
| 5 | 14 | 26 | 1000 | 47 | 7500 | 68 | 26000 |
| 6 | 18 | 27 | 1100 | 48 | 8000 | 69 | 27500 |
| 7 | 25 | 28 | 1250 | 49 | 8500 | 70 | 29000 |
| 8 | 40 | 29 | 1400 | 50 | 9000 | 71 | 30500 |
| 9 | 60 | 30 | 1600 | 51 | 9500 | 72 | 32000 |
| 10 | 80 | 31 | 1800 | 52 | 10000 | 73 | 33500 |
| 11 | 100 | 32 | 2000 | 53 | 10700 | 74 | 35000 |
| 12 | 130 | 33 | 2200 | 54 | 11400 | 75 | 36500 |
| 13 | 160 | 34 | 2400 | 55 | 12100 | 76 | 38000 |
| 14 | 190 | 35 | 2700 | 56 | 13000 | 77 | 40000 |
| 15 | 220 | 36 | 3000 | 57 | 14000 | 78 | 42000 |
| 16 | 250 | 37 | 3300 | 58 | 15000 | 79 | 44000 |
| 17 | 300 | 38 | 3600 | 59 | 16000 | 80 | 46000 |
| 18 | 350 | 39 | 3900 | 60 | 17000 | 81 | 48000 |
| 19 | 400 | 40 | 4200 | 61 | 18000 | 82 | 50000 |
| 20 | 450 | 41 | 4500 | 62 | 19000 | 83 | 53000 |
| 21 | 500 | 42 | 5000 | 63 | 20000 | 84 | 56000 |

Table 3.1. Pressure steps used during mercury intrusion porosimetry

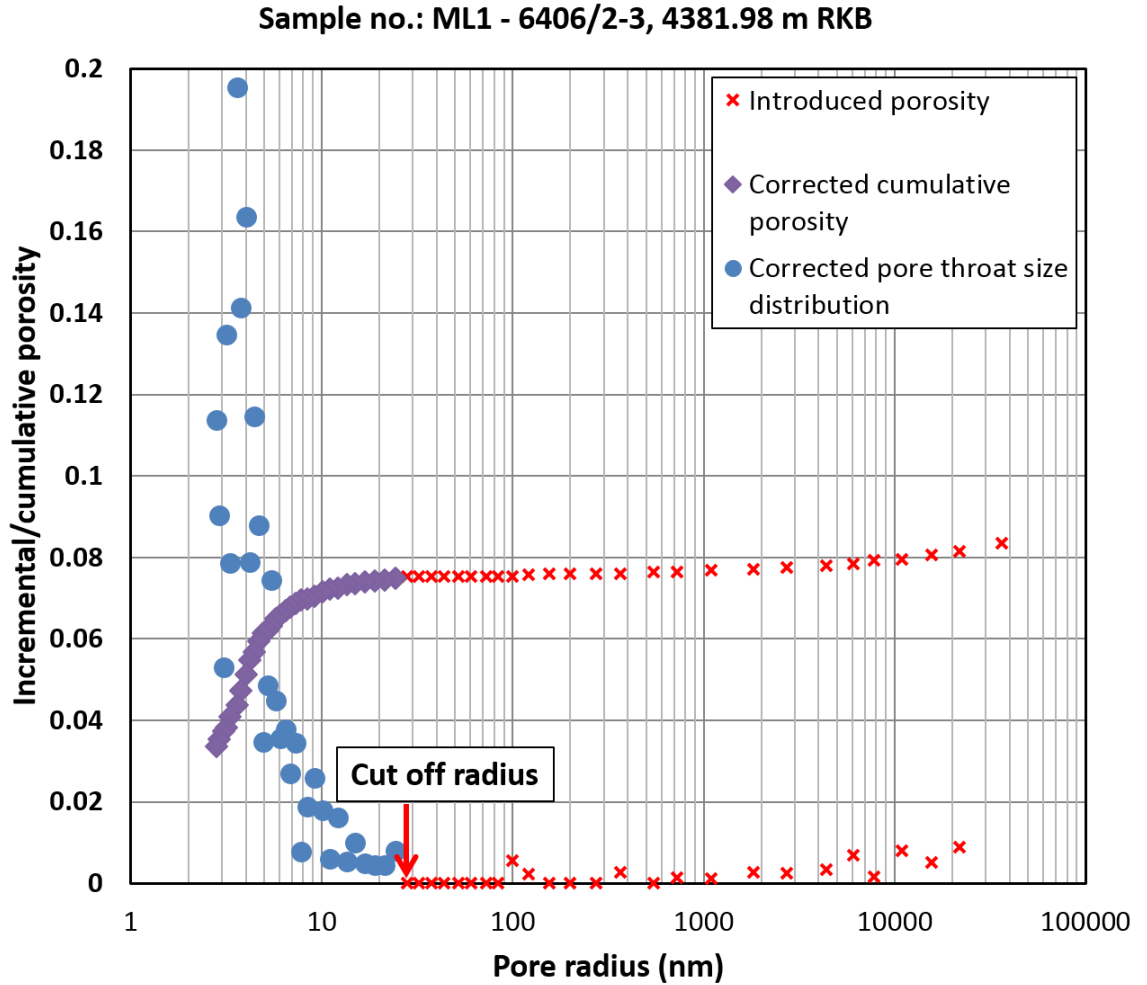


Figure 3.1. Example of MICP pore throat size distribution and cumulative porosity data representation

A frequently used representation of the pore throat size distribution and cumulative porosity data is shown in Figure 3.1. Cumulative porosity refers to the fraction of porosity contributed by pores with a throat radius smaller than a given value.

The MICP measured pore volume is different from the total porosity since MICP cannot measure isolated pores and pore throats smaller than 2.8 nm. Therefore, the pore size distribution shown in Figure 3.1 does not start at zero porosity and the total porosity is determined from bulk volume and grain density as it is described in 3.3.7.

Porosity must be corrected for damage which may arise during sample preparation. Figure 3.1 shows an example of a pore size distribution curve where this correction has been applied. As shown, with increasing pore throat radius the incremental (frequency)

value gradually approaches to a minimum value and then arises once again above this value. The radius corresponding to the minimum incremental value is defined as the cut off radius. All measured pores that have a radius greater than the cut off radius are subjectively defined as fractures introduced during sample preparation. A corrected porosity value is calculated using only the volume of the sample corrected for damage.

No standards were used during measurements; however repeat measurements taken on selected samples show repeatability.

3.3.9 Permeability calculations

Direct permeability measurement techniques were not part of this study. Instead of measurements, calculations were made utilising grain density, clay content and pore size distribution data. These are based on the models of Yang and Aplin (1998, 2010).

3.3.10 High Resolution X-Ray Textural Goniometry (HRXTG)

High resolution X-ray textural goniometry was used to quantitatively measure the clay mineral fabric orientation in selected mudstone samples. This technique was developed at the University of Michigan, USA by van der Pluijm et al. (1994). Detailed description of the method can be found in Day-Stirrat (2006).

Mudstone samples were mounted on a glass slide and cut perpendicular to bedding. The bedding orientation was known for the core samples, for cutting samples the sections were cut perpendicular to any visible primary bedding structure or lamination. The sections were sliced into approximately 0.2 mm sections and mounted into a magnetic sample holder which was placed over an open circular window on the custom-made goniometer head, as shown on the right-side picture in Figure 3.2.

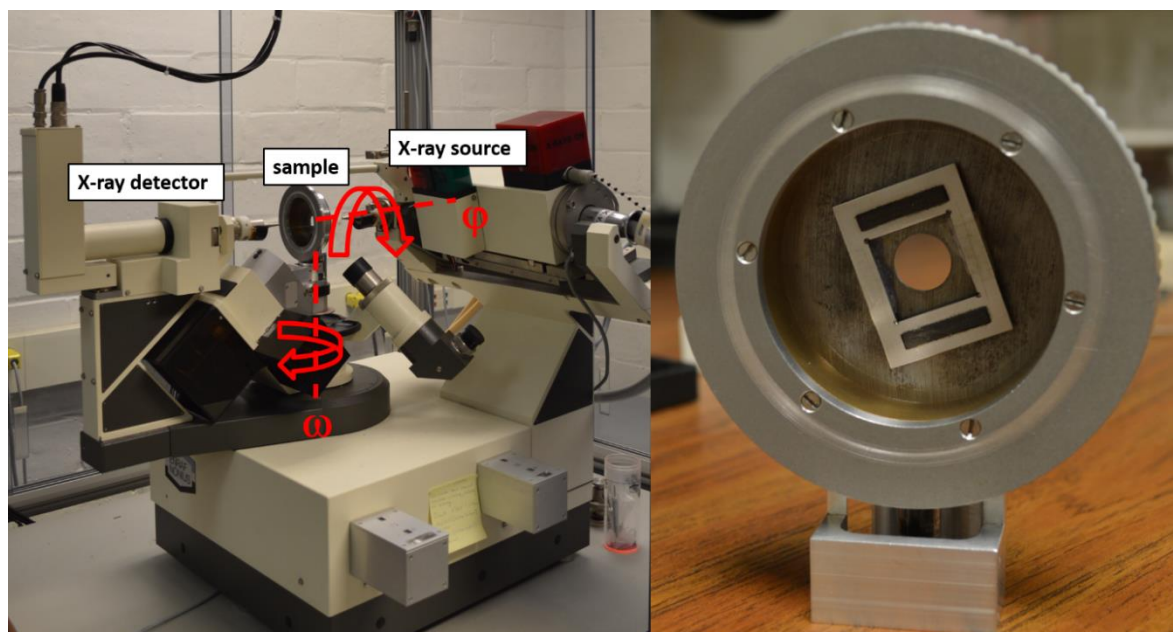


Figure 3.2. Left: HRXTG machine with two rotation axes indicated (refer to text for explanation). Right: Close-up of the detached custom build goniometer head with magnetic sample holder

The goniometer head is attached to an automated Enraf-Nonius CAD4 single-crystal diffractometer with MoK α – radiation source and scintillation detector. The measurement is done in transmission mode and in two steps. In transmission mode, the X-ray passes through the sample. At first the detector is positioned at pre-set 2θ angles over the range $0.5\text{--}6.0^\circ 2\theta$ Mo ($1\text{--}13^\circ 2\theta$ Cu) to detect which clay minerals are present and to determine the exact diffraction angles at which textural data should be collected. This is followed by the measurement of the orientation of previously selected clay mineral phases (“pole figure scan”). The detector is set to a given 2θ angle corresponding to the d spacing of the 001 or 002 reflection of the selected clay mineral phase. Figure 3.3 shows examples for the most commonly used phases like chlorite 001/14Å or illite 001/10Å. The sample is then rotated around two axes to capture a grid of diffracted intensity and orientations. One axis is parallel to an imaginary line connecting the goniometer and detector (ϕ), the other one is normal to it (ω) (left picture in Figure 3.2). Intensity data is collected every 2.5° between 0 and 360° around the ϕ axis and in nine steps between 0 and 40° around the ω axis, thus in total 1296 measurements were made on each sample.

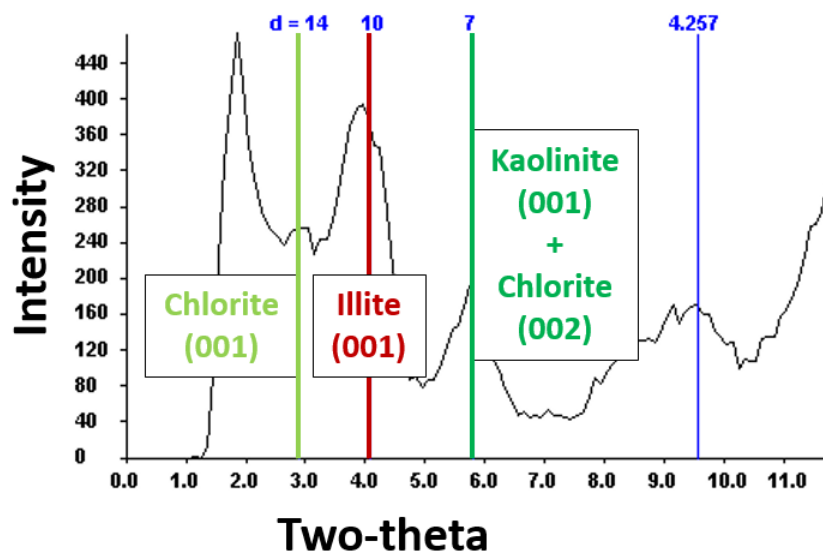


Figure 3.3. Example of 2θ scan result with peak positions of characteristic clay minerals

The results are corrected for background and absorption then normalized to ensure concentration-independence (van der Pluijm et al., 1994).

The degree of alignment is determined from the intensity distribution of diffracted X-rays which is displayed as pole-figure diagrams showing the distribution of crystallographic orientation in the form of poles to crystallographic planes. More aligned clay fabrics correspond to pole figures that can be contoured as concentric rings. Isotropic clay fabric on the other hand will result in pole figures with no poles. The degree of alignment is expressed as maximum pole density in multiples of random distribution or MRD where greater values represent greater alignment (Wenk, 1985). Alignment classifications corresponding to values measured in MRD are given in Table 3.2.

| MRD Value | Alignment Classification |
|-----------|----------------------------------|
| <1.8 | No alignment/very weak alignment |
| 2-3 | Weak alignment |
| 3-4 | Moderate alignment |
| 4-5 | Strong alignment |
| >5 | Very strong alignment |

Table 3.2. Classification for alignment measured in multiples of random distribution (MRD) (from Day-Stirrat, 2006)

3.3.11 Scanning Electron Microscopy (SE, BSEM)

Electron microscopy (both SE and BSE) was used on selected samples to examine the mudstone textures and to have a qualitative estimate of clay mineral fabric orientation.

Selected mudstone samples were cut perpendicular to bedding and prepared into polished thin sections (300 μm) and polished slabs which were carbon coated and analysed using a Hitachi SU-70 Scanning Electron Microscope. Operating conditions for the machine were 15 KeV accelerating voltage and 2-4 nA filament current with working distance of approximately 15 mm.

3.4 Wireline log analysis

In addition to sample analyses, wireline logs and pore pressure data were also employed to study mudstone compaction. Wireline logs and mudstone sample analysis data complement each other, since wireline log data on its own lacks information regarding detailed lithology and diagenesis.

Wireline logs were provided in digital form. Additional data such as end well reports, pore pressure and temperature data (BHT, DST), mudlogs and drilling logs were also used.

Wireline data quality checking, editing and log based mudrock discrimination as part of the research was undertaken by Colin Sargent.

3.4.1 Wireline data quality check

To remove inherent noise from raw wireline data large data spikes relative to the median of neighbouring data values were rejected. This was done by applying a moving median filter across the working interval in all the wells. The window length and threshold value for the median filter were selected independently for each log type (see also 3.4.2). Additionally, manual editing was occasionally required over short intervals, where the spliced log data included part of a run through a cased section.

Caliper logs were used to discriminate sections with poor borehole conditions and to filter the density and neutron data, since these logs are short-range tools and require smooth

borehole walls for good measurement. Filtering was done by rejecting any sample reading where the caliper value is greater than the normal bit size plus one inch. Because of the poor borehole conditions of most studied wells in the Sergipe Alagoas Basin a caliper threshold limit of normal bit size plus two inches was chosen to maximise selection of density and neutron data.

3.4.2 Wireline log-based mudstone discrimination

Definitions of mudstone like that in 1.2.1 are not practical when using the wireline logs as mudstone discriminator. A more practical, operational definition is needed for this purpose. The most commonly applied method uses the gamma-ray log as a standalone mudstone-sandstone discriminator. This method estimates the rocks shale volume from the gamma-ray log by using either a linear or a non-linear model for shale volume as a function of the gamma-ray log signal. Thus, an arbitrarily chosen cut-off value can be assigned to discriminate mudstones and sandstones (Heslop, 1974).

The gamma-ray log detects natural gamma rays emitted from radioactive isotopes of uranium, thorium and potassium. Since these elements (especially Th and K) tend to concentrate in clay minerals this is used as an indicator of clay mineral content. Therefore, the above method defines mudstones as a function of the clay mineral content and not of the clay size fraction (Heslop, 1974; Katahara, 2008).

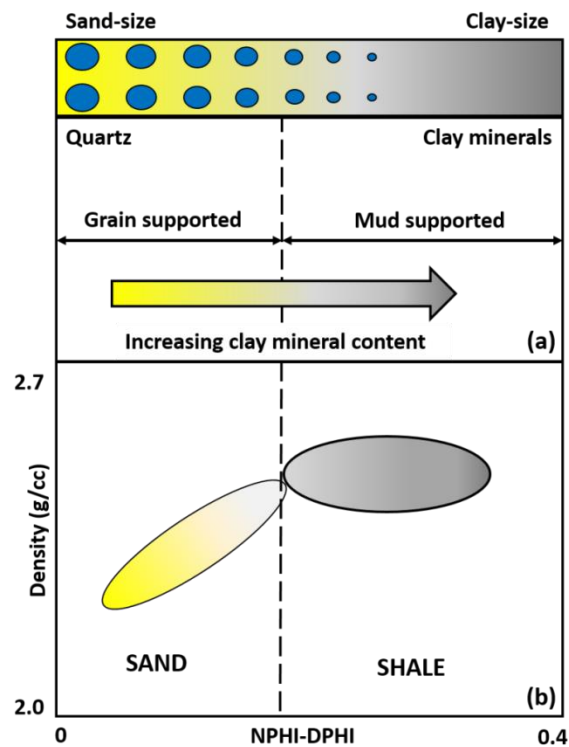


Figure 3.4. (a) Schematic diagram of variation of sand vs clay mineral content (increasing left to right) (b) Associated response on a plot of density versus the difference between neutron porosity and density porosity (based on Katahara, 2008).

Heslop (1974) showed that several log properties exhibit a change in slope when plotted against clay content (Figure 3.4b). The author proposed that with increasing clay content, eventually the clay matrix becomes load-bearing and that the change in slope is at the boundary between grain-supported sands and clay-matrix supported mudstones, thus it is a lithological boundary (Figure 3.4a). Katahara (2008) concluded that the clay content (and associated log response) at this slope discontinuity is the only reliable reference to discriminate mudstones from sandstones.

Another commonly applied method for estimating the clay mineral content uses the difference between neutron porosity (NPHI) and density porosity (DPHI).

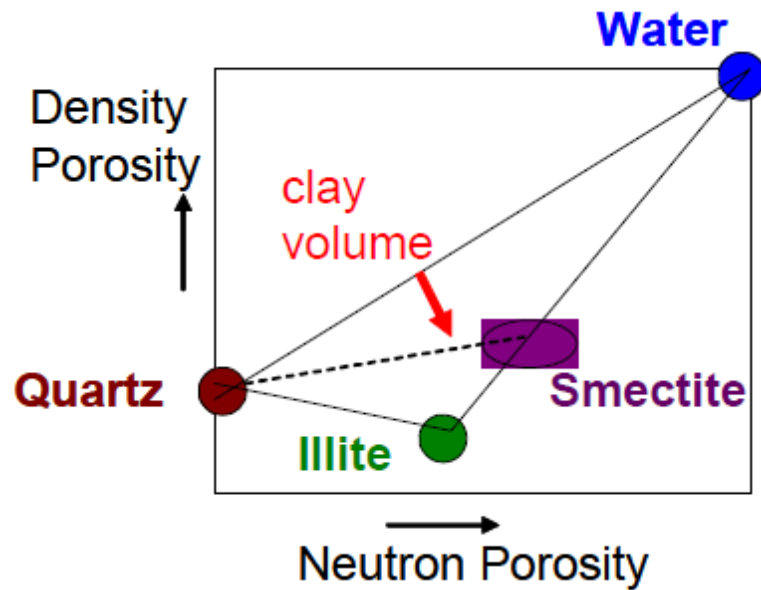


Figure 3.5. Schematic crossplot of density porosity vs neutron porosity illustrating a simple quartz-clay-water model. The clay mineral volume (red arrow) is proportional to the neutron porosity minus density porosity, if both are on a sandstone matrix (From Katahara, 2006b)

The density tool measures electron density, by emitting and detecting gamma rays. The electron density for most minerals and fluids found in natural sediments and rocks is directly proportional to their bulk density. Therefore, the average electron density correlates with average bulk density. Density porosity is calculated by assuming a density for the pore fluid and for the rock matrix. The neutron tool emits high-energy neutrons and measures how effectively the formations scatter and absorb these. This measurement relates to hydrogen concentration. Analysts use lithology dependent transform to convert this to neutron porosity. Since clay minerals have hydrogen in the form of hydroxyls in their crystal structure, neutron porosity in shales depends directly on clay mineral content (e.g. “Schlumberger Oilfield Glossary,” 2016).

As it is shown in Figure 3.5 the clay mineral volume (red arrow) is proportional to neutron porosity minus density porosity. If we assume very simple quartz-clay-water model of mudstone composition, then mudstones will plot within the triangle bounded by those three points (Figure 3.5). Clean sandstone points are on the line connecting quartz and water. Clay minerals are below the clean sandstone line and for a given clay mineral, lines of constant clay content are parallel to it. This will be true for all clay minerals, although the proportionality will vary for different clay mineral types (Katahara, 2006, 2008).

According to Katahara (2006, 2008) the difference between neutron porosity and density porosity is a better measure of clay mineral content than the gamma-ray log because mudstones in a limited range of neutron-density difference show a much tighter trend on a sonic-density than mudstones in a limited gamma-ray range.

In most of the studied wells (excluding the Haltenbanken) in this thesis a two-step process involving the gamma ray, density and neutron logs had been applied to discriminate mudstone data points from non-mudstone data in the wireline logs, which was followed by a moving median filter. This method is broadly similar to that of Katahara (2006).

It should be noted that in most of the wells' log data no clear boundary could be recognised between the grain supported (sandstones) and mud supported (mudstones) lithologies. Cut off values for the gamma-ray log and NPHI-DPHI were chosen individually based on local lithological characteristics for all three case studies. The lack of a clear slope discontinuity in the wireline log data with increasing clay content can most likely be attributed to the overall fine-grained and clay-rich nature of the studied sections.

Mudstone discrimination in the Malaysian wells was done in two steps. The first step involved the gamma-ray log and calculating the mean of all the gamma log samples across the working intervals in all three wells. Samples with gamma log values less than 85% or greater than 130% of the calculated mean were discarded. The second step involved calculating the mean of the difference between the neutron porosity and density porosity (NPHI-DPHI) across the same intervals. The density log porosity was calculated as described in 3.4.3 using a fluid density of 1.015 g/cm^3 and mudstone grain density of 2.75 g/cm^3 . Sample values of NPHI-DPHI less than 45% or greater than 250% of the calculated mean were discarded. A moving median filter was applied to remove any remaining spikes from the density and sonic logs. The window size was set to 41 samples and the threshold level to 0.05 g/cm^3 for the density log and to 21 samples and to $4 \text{ } \mu\text{s}$ for the sonic log. If the difference between the central and the median value in the window exceeds the threshold, the central value is removed from the log. Additional smoothing of the sonic and density logs was done using a Hanning window of length 100 m.

Mudstone discrimination in the Norwegian wells was done using the natural gamma-ray log. The mean values of all the gamma log samples across the working intervals were calculated in all of the wells. Samples with gamma log values less than 85% of the calculated mean were discarded. In addition, a moving median filter was used to remove remaining spikes and smoothing was done using a Hanning window of length 100 m. Density porosity was calculated according to 3.4.3 using a fluid density of 1.05 g/cm^3 and mudstone grain density of 2.75 g/cm^3 .

Mudstone discrimination in the Brazilian wells was done in two steps. The first step involved the gamma-ray log and calculating the mean of all the gamma log samples across the working intervals in all four wells. Samples with gamma log values less than 78% of the calculated mean were discarded. The second step involved calculating the mean of the difference between the neutron porosity and density porosity (NPHI-DPHI) across the same intervals. The density log porosity was calculated as described in 3.4.3 using a fluid density of 1.05 g/cm^3 and mudstone grain density of 2.75 g/cm^3 . Sample values of NPHI-DPHI less than 95% of the calculated mean were discarded. A moving median filter was applied to remove any remaining spikes from the density and sonic logs. The window size was set to 21 samples and the threshold level to 0.05 g/cm^3 for the density log and to $4 \mu\text{s}$ for the sonic log. If the difference between the central and the median value in the window exceeds the threshold, the central value is removed from the log. Additional smoothing of the sonic and density logs was done using a Hanning window of length 100 m.

3.4.3 Log-based porosity calculations

Mudstone porosities were calculated using the density log by assuming a pore fluid density and a matrix density. Density porosity ($D\phi$) is calculated using the below equation:

$$D\phi = \frac{(\rho_m - \rho_b)}{(\rho_m - \rho_f)} \quad (20)$$

Where

ρ_m = Matrix density (g/cm³)

ρ_b = Bulk density (g/cm³)

ρ_f = Fluid density (g/cm³)

3.5 One dimensional basin modelling

Pore pressure in the Lower Cretaceous mudstones on the Halten Terrace, offshore mid-Norway was modelled in one dimension using Schlumberger's PetroMod (version 2014.1) software. One-dimensional modelling was used to estimate the magnitude of overpressure build-up by disequilibrium compaction. It should be noted that this model does not include other mechanism for generating excess pore pressures, such as lateral transfer or hydrocarbon cracking and is only able to take vertical stress into account. Similarly, any influence of clay mineral diagenesis on fluid pressure generation is ignored.

PetroMod uses a forward modelling approach to calculate the geological evolution of a basin from the burial history. The one-dimensional burial model was built up using present-day well stratigraphy, well log lithology and lithological descriptions of the modelled formation units (Tables 5.8 and 5.9; based on Dalland et al. 1988 and Ottesen et al. 2009). Heat flow was assumed to be 0.0065 W/m² following Ritter et al. (2004) and was assumed to be constant through time. This value is commonly used for the mid-Norwegian Continental shelf and is consistent with present day geothermal gradients as estimated by Cicchino et al. (2015). In addition, present day surface temperature (assumed to be 5 °C) and present-day water depth was assumed to be constant through

time. Solely default PetroMod lithology types, chosen on the basis of well log descriptions were used in this model.

Chapter 4

Mechanical compaction in diagenetically altered mudstones: an example from the Central Malay Basin

4.1 Introduction

Compaction of fine grained siliciclastics is driven by both mechanical and chemical processes. Mechanical compaction dominates during the first 1 or 2 km of burial, where temperature is too low to cause significant chemical changes. These mechanical processes are relatively well understood so mechanical compaction can be modelled fairly accurately (e.g. Mondol et al 2007). Significantly less is known about the processes in the so called chemical compaction regime, where porosity is seriously underestimated by mechanical compaction models alone (Bjørlykke 1998). This suggests that chemical diagenetic changes can cause further porosity loss in addition to the mechanical compaction processes.

The Malay Basin provides a unique opportunity to study the effects of high temperature on the compaction properties of siliciclastic mudstones and to test the previously proposed hypotheses regarding chemical compaction. It is characterized by high heat flow and a geothermal gradient which can be as high as 60°C/km in the central part of the basin. This has the consequence that temperatures of 70-100°C, generally thought to be associated with the onset of clay diagenesis (e.g. Hower et al., 1976; Bjørlykke, 1998), occur at a relatively shallow depth of only around 1000 m. At this depth mudstones still retain a relatively high amount of porosity so any effects due to temperature-related processes such as clay diagenesis are much easier to detect.

Additionally, previous studies looking at well log and sample data observed anomalous rock properties and proposed that diagenetic changes are the main cause behind these. Hoesni (2004) presented wireline log evidence for ongoing diagenesis and chemical compaction (refer to 2.7.1). He observed velocity-density trends in which both velocity and density continued to increase after the onset of overpressure. Pore pressures were underestimated in these sections when using traditional pressure prediction models. Sample data was later presented by Duffy (2011) who showed that measured porosities in these diagenetically mature mudstones were anomalously low when compared to existing mechanical compaction models. These findings provided the basis for further investigation.

Well log data were provided by Petronas from 3 wells (Bravo-X; Bravo-L; Bravo-Y) and samples from two wells (Bravo-L and Bravo-Y) in the Central Malay Basin. Mineralogical

and chemical properties of the samples were analysed and compared with physical properties such as porosity derived from well log responses. The key aim was to assess the role of clay mineral diagenesis on the compaction properties of Miocene Formation E mudstones. In addition to this, the secondary objective was to evaluate the role of clay mineral diagenesis on pore pressure generation in the Central Malay Basin.

This chapter details these results following a brief introduction to the geological history of the Malay Basin.

4.2 Geological background

The Malay Basin is located on the Sunda shelf, offshore east of Peninsular Malaysia in Southeast Asia (Figure 4.1). It is one of the most prolific hydrocarbon basins in Southeast Asia having hydrocarbon reserves in excess of 2.4 billion barrels of oil and 36.6 trillion cubic feet of gas (Zainul et al., 1999).

The Malay Basin is a Northwest-Southeast trending extensional rift basin, formed during the late Eocene to early Oligocene and filled with continental to shallow-marine siliciclastic sediments. The basin is ~500 km long and ~200 km wide and has an asymmetrical profile (Figure 4.1). Regionally the basin overlies the pre-Late Cretaceous tectonic core, “Sundaland”, which lies beneath much of Indochina, Thailand and Western Indonesia (Doust and Sumner, 2007).

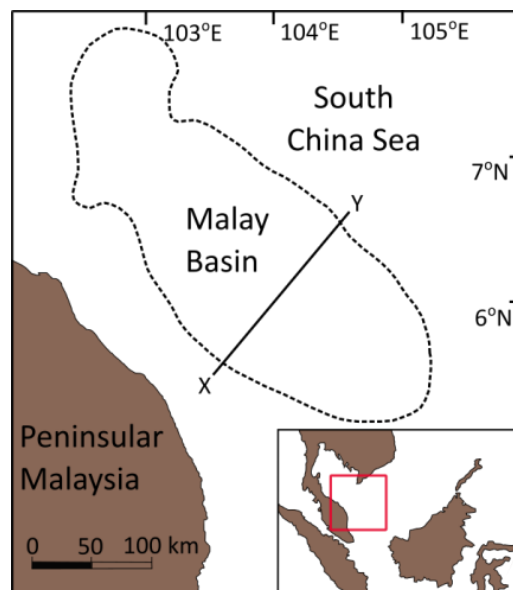


Figure 4.1. Location map of the Malay Basin (modified after Madon, 2007). The XY line is a cross section in Figure 34.

Tectonic models explaining the origin of the basin range from a simple pull-apart (Tapponnier et al., 1982) to a complex oblique rifting scenario (Ngha et al., 1996). According to Tapponnier et al. (1982) the basin formed as a result of reactivation of a major left-lateral strike-slip fault zone caused by the eastward extrusion of Indochina in response to collision of India with Eurasia. This pull-apart model was later challenged by structural evidence from seismic data which showed proof of transtensional extension of the basement. This provided the basis for the oblique rifting model (Ngha et al., 1996; Tjia, 1998). In addition to these others also suggested a back-arc basin model related to subduction of the Indian-Australian Plate along the West Burma-Sumatra-Java trench (Kingston et al., 1983; Morley, 2001).

Madon and Watts (1998) showed that crustal extension and thinning is also associated with the rifting event. The Malay Basin is characterized by high heat flow and geothermal gradient as a consequence of crustal thinning. Yusoff (1993) and Halim (1994) reported very high basement heat flow values, above 100 mW/m². Halim (1994) recorded an average geothermal gradient of 51.8°C/km for the basin; however geothermal gradient varies with location.

The early extensional phase resulted in East-West trending grabens and half-grabens. As a result of the alteration of the regional stress field during the middle to late Miocene the main axial fault became dextral (Figure 4.2). This caused basin inversion and reactivation of the basement extensional faults. These thrust faults propagated into the overlying strata, forming anticlines that later became potential traps for hydrocarbons (Madon, 2007).

Sedimentation began during the initial syn-rift phase in the Late Eocene-Early Oligocene times with sedimentation rates in excess of 1000 m/Ma. These early sediments are mainly fluvial and lacustrine deposits. This initial phase is followed by the post-rift, thermal subsidence phase with exponentially decaying sedimentation rates. These deposits are mainly comprised of coastal plain sediments. Middle-Late Miocene inversion resulted in a major unconformity which is distinguishable on wireline logs and seismic sections. With the exception of some erosion during Pleistocene lowstands, sediment deposition has resumed from Pliocene onwards as a result of continued, gentle subsidence. The youngest formations were deposited at an average rate of 160 m/Ma. The overall

thickness of deposited sediments varies between <3000 m and >12000 m and the present-day surface lies under a water column of <200 m (Bishop, 2002; Madon, 2007). Figure 4.2 shows the stratigraphic subdivision which is used in this thesis. This subdivision uses lettered groups which were identified using seismic stratigraphy, where the seismic sequence boundaries represent erosional surfaces.

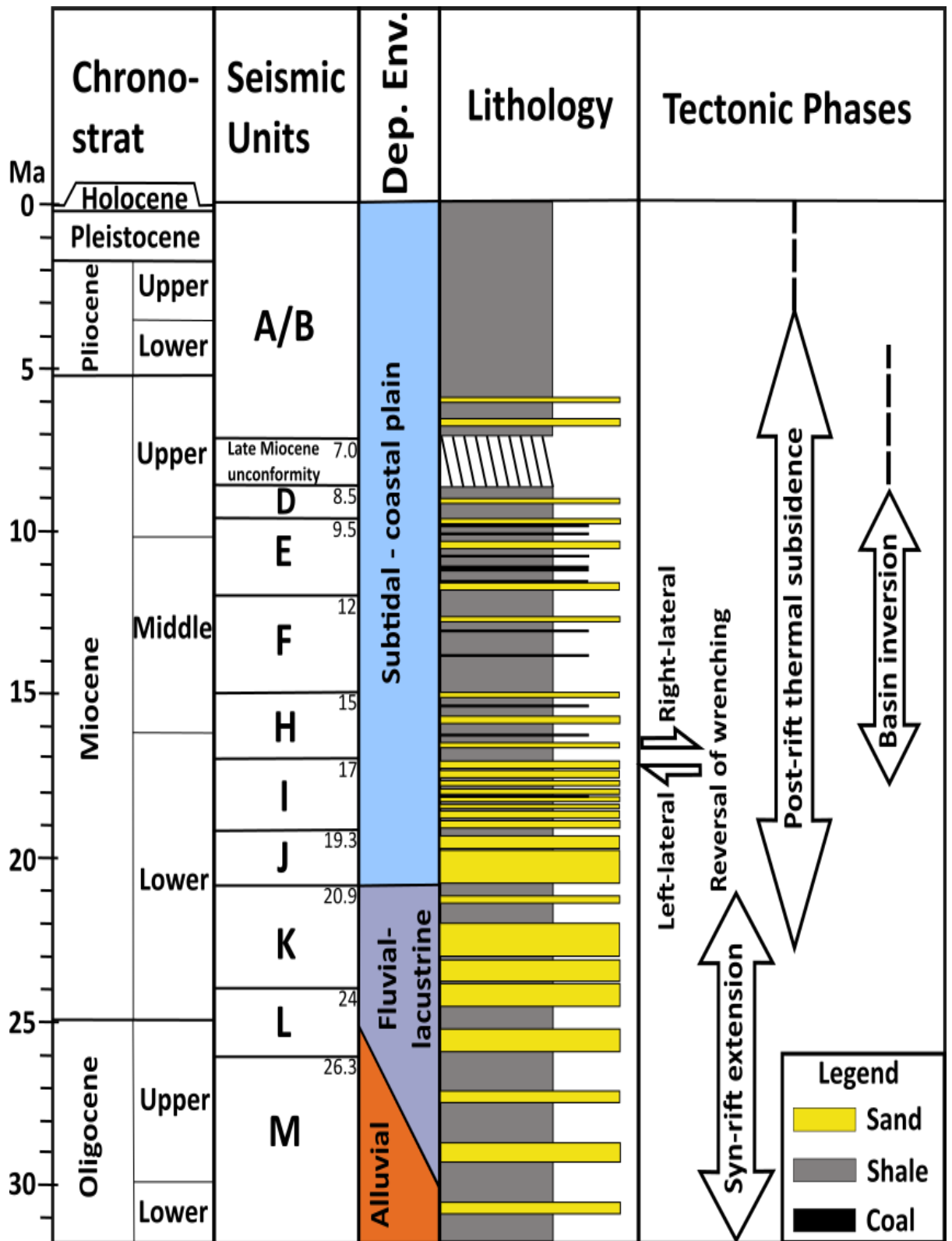


Figure 4.2. Stratigraphic framework and structural history of the Malay Basin (modified after Madon 2007).

The Malay Basin is subdivided into formations from M (oldest) to A (youngest) as shown in Figure 4.2 (Madon, 2007). The figure also shows the chronostratigraphy, tectonic phases and the overall lithology.

The main source rocks are the Oligocene-Lower Miocene lacustrine shales (groups K to M) and Middle-Upper Miocene coaly shales (groups E and I). The Lacustrine shales are thought to be the oil-prone source rocks. The main reservoirs are mostly found in fluvial channels (groups K to M) and shoreface and subtidal shelf sands (groups J and I) (Madon, 2007; Ghosh et al., 2010).

4.2.1 Overpressure distribution

Overpressure causes significant problems for the hydrocarbon industry in the Malay Basin with 80% of exploration and appraisal wells terminated because of pressure issues (Madon, 2007). However, several new discoveries of oil plays in deep overpressured zones clearly show the need for a better understanding of the pressure generating mechanisms and its controlling factors. This knowledge is crucial for future discoveries and for the utilization of these overpressured plays (Hoesni, 2015).

As shown in Figure 4.3, the top of overpressure in the Malay Basin has a domal profile. It is observed to be shallower in the centre at a depth of around 1400 m within formation unit E. It then gradually deepens towards the basin flanks and cross-cuts the stratigraphy (Hoesni, 2004; Madon, 2007).

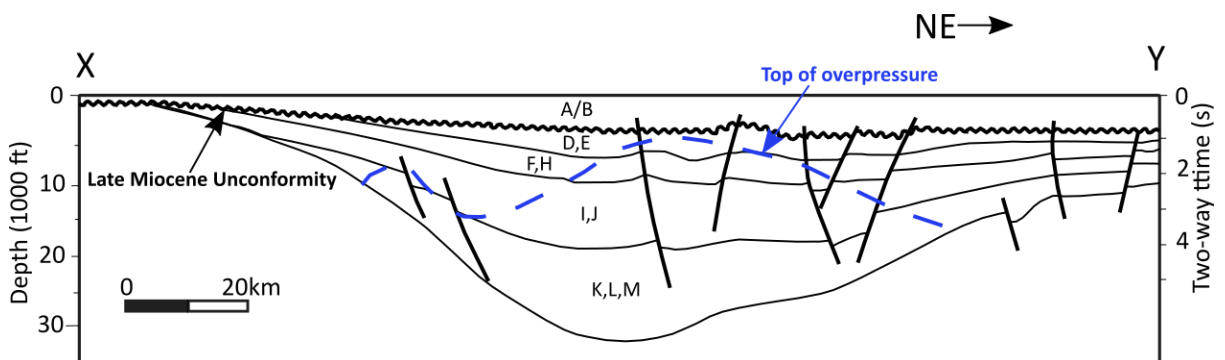


Figure 4.3. Cross section of the Malay Basin along XY (Figure 32). The top of overpressure is shown as the blue dashed line (modified after Madon 2007).

According to Madon (2007) the primary cause of overpressure in the Malay Basin is disequilibrium compaction. He reported at least two major overpressure compartments that are sealed by regional shale units (unit F and unit L). In his model overpressure development is the consequence of high initial subsidence and sedimentation rates during basin extension. According to this model sedimentation rates during the post-rift phase were not high enough to generate overpressure and interpret the origin of the observed overpressure in the post rift strata as secondary, derived from excess pressure dissipated from the underlying syn-rift strata. The domal shape of the top of overpressure is thus interpreted as a result of different rates of subsidence and sedimentation across the basin (Madon, 2007). This model is illustrated in Figure 4.4.

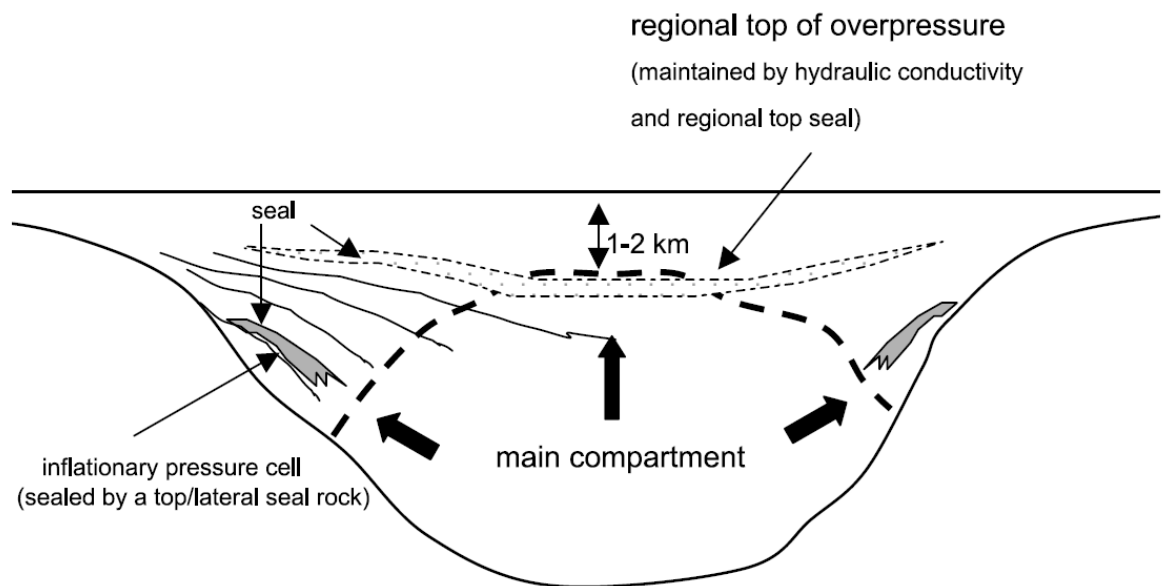


Figure 4.4. The present-day state of overpressure in the Malay Basin as proposed by Madon (2007). The main overpressure compartment with a convex-up top-of-overpressure in the basin centre is maintained by the hydraulic conductivity of the sediment column and the presence of a regional shale seal (Units F and L). Secondary pressure compartments are the result of pressure transfer from the main compartment and are sealed by transgressive shale units (from Madon, 2007).

Hoesni (2004) reported log-based evidence for additional processes contributing to overpressure such as clay diagenesis and chemical compaction. More recently however Hoesni (2015) presented new results from basin modelling which suggest that chemical compaction itself does not contribute directly to effective stress reduction. Instead it

enhances the sealing effectiveness of the mudstones leading to a more effective pressure build-up due to disequilibrium compaction with contributions from other secondary sources.

In addition to this Tingay et al. (2011, 2013) showed evidence for overpressure contribution from kerogen to gas maturation in the northern Malay Basin.

4.3 Supplied data

The dataset provided by Petronas included wireline data from three wells, Bravo-L, Bravo-X and Bravo-Y in the Central Malay Basin. The provided wireline data comprised density, sonic, gamma ray, resistivity, neutron and caliper logs. In addition to this, drilling summaries, mudlogs, repeat formation tester (RFT) pressure and temperature measurements and a 3D seismic volume were also provided. Mudstone cuttings were provided from Bravo-L and Bravo-Y.

4.4 Well locations, local geology and overall lithology

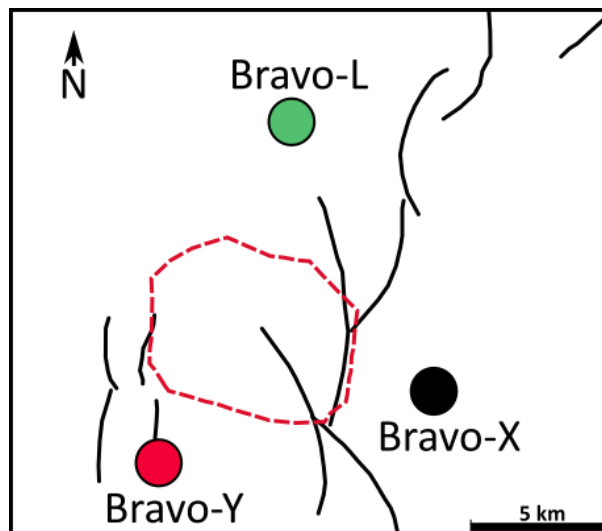


Figure 4.5. Location map for wells Bravo-L, Bravo-X and Bravo-Y in Central Malay Basin (courtesy of Petronas). The black lines represent faults. The red dashed line outlines a gas cloud observed on seismic data (Figure 4.6).

Well locations are shown relative to one another in Figure 36. Bravo-X and Bravo-Y are separated by ~10 km; Bravo-L is located ~3 km further to the north. Water depths in wells Bravo-L, X and Y are 70, 71 and 65 m respectively. The slice through the provided 3D

seismic cube, as shown in Figure 4.6, illustrates that the wells are located on a local structural high. The main fault zone shown in Figure 4.5 can be interpreted in the seismic data however it is slightly masked by the presence of a gas cloud (Figure 4.6).

After initial inspection of the provided dataset the stratigraphic interval from the top of the late Miocene Formation D to the depth of well terminations near the base of Formation E was chosen for further study. The reason for this was the lack of any available sample data from Units A and B and the generally poor quality of the shallow wireline log data due to poor borehole conditions as indicated by the caliper logs.

The lithology in the studied interval consists of 70-75% mudstones with some thinner silty and sandy sections and several coal seams, up to 5 m thick, as indicated by the log responses (Figure 4.7) and the provided mudlogs. As a representation of the overall lithology Figure 4.7 shows (a) gamma ray, (b) neutron, (c) sonic and (d) density log responses prior to mudstone discrimination from Bravo-Y. Coal seams are responsible for anomalously low density ($\sim 1.2\text{-}1.3 \text{ g/cm}^3$), high sonic transit time ($\sim 150 \text{ } \mu\text{s/ft}$), high neutron porosity ($\sim 70\%$) and low natural gamma values ($< 50 \text{ api}$).

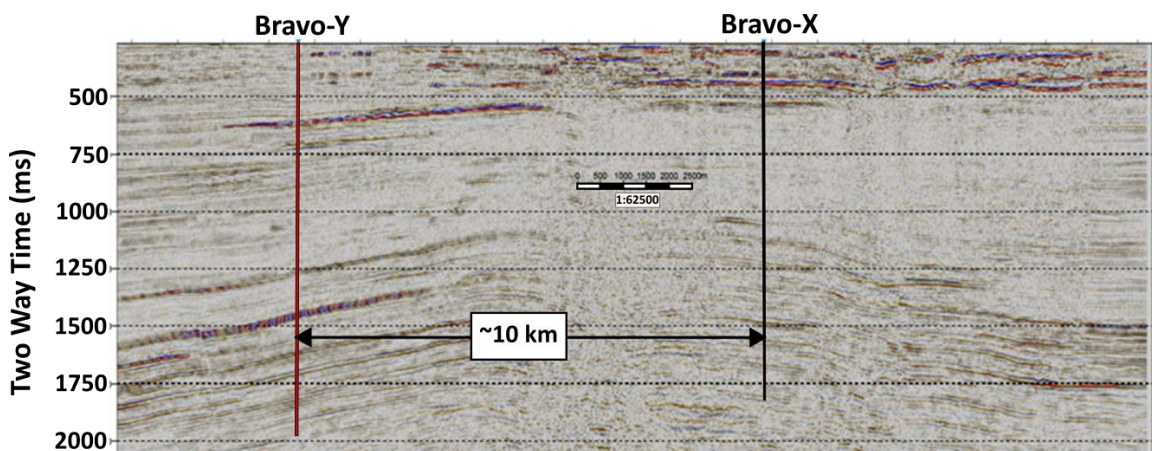


Figure 4.6. Vertical slice passing through wells Bravo-X and Bravo-Y from the provided 3D seismic cube. Note the presence of a gas cloud and the possibility of a fault between the two wells (reflections are obscured by the presence of gas).

In contrast to this, high spikes in the natural gamma logs are associated with organic matter rich mudstone intervals, as inferred from their high uranium content shown by the spectral gamma log readings. Note the presence of 10-20 m thick intervals with anomalously low sonic transit time (circled in Figure 4.7c). Similar intervals can be observed in all three wells and are identified as consisting of mainly mudstones. The

anomalously low sonic transit time would indicate cemented layers; however interestingly no other logs show similar excursions at these depths (see also 4.7.3).

Based on the information provided by Petronas, all sediments in these three wells are now at their maximum burial depth. This is also supported by the observation that there is only minor change in the sonic log response passing through the top of Formation Unit D.

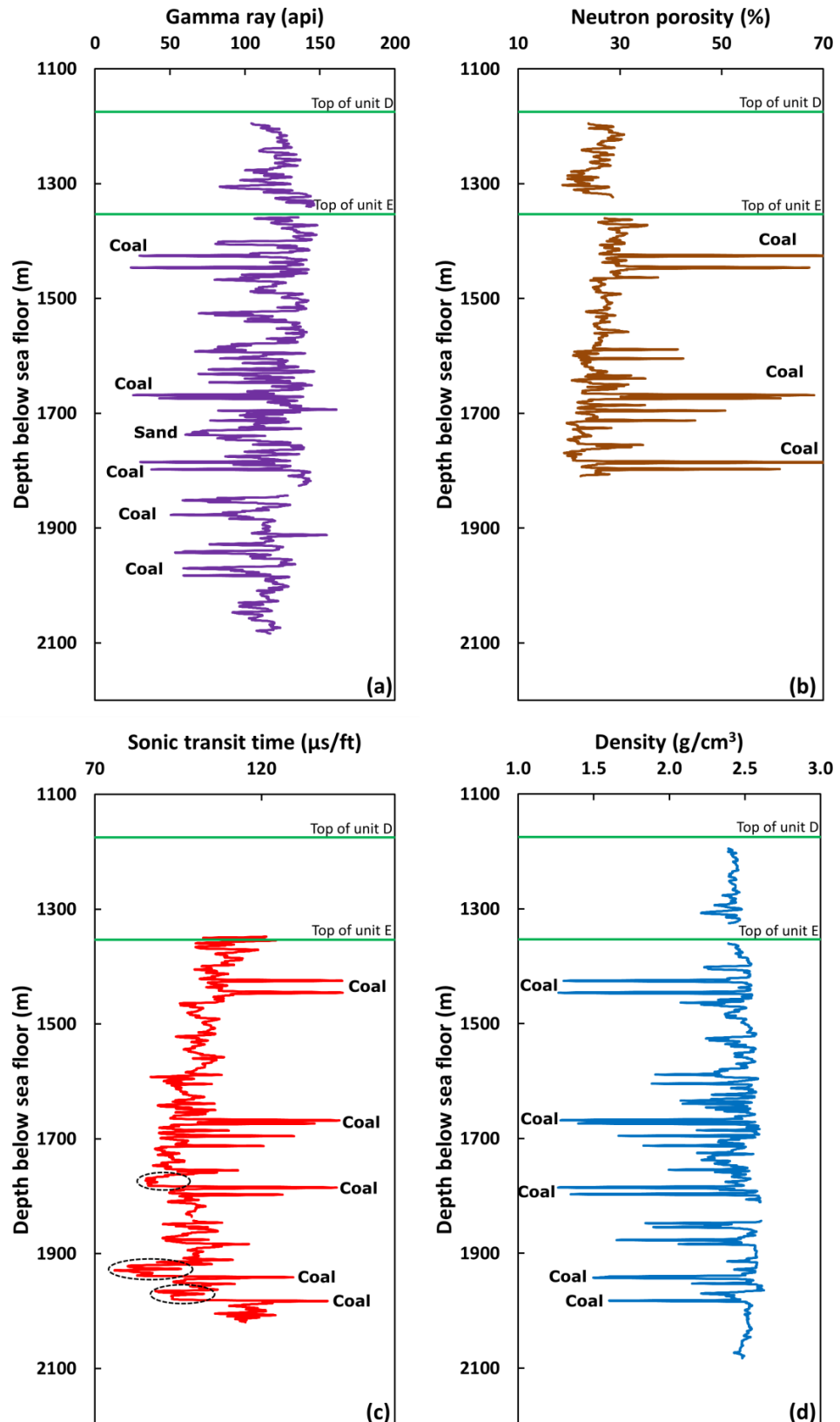


Figure 4.7. Bravo-Y gamma (a), neutron (b), sonic (c) and density (d) logs through the working interval prior to mudstone discrimination. Encircled sections display anomalously low sonic transit time compared to neighbouring intervals.

4.5 Pore pressure-depth profile and geothermal gradient

Measured pore pressures and temperatures are shown in Figure 4.8. The shallowest RFT pressure measurements in Bravo-L and Bravo-X (Figures 4.8a, c) indicate low overpressure in Unit B and part of Unit D. The pore pressure gradually goes back to hydrostatic in Unit D and remains hydrostatic until the top of overpressure deeper within Unit E.

In contrast pressure measurements in Bravo-Y indicate hydrostatic pressure across Units A/B and D until the top of overpressure in Unit E.

The depths of the top of overpressure were estimated at 1730 m below sea surface in Bravo-X, at 1760 m below sea surface in Bravo-L and at 1825 m below sea surface in Bravo-Y; between the deepest recorded hydrostatic and shallowest overpressured RFT pressure value. Below this depth overpressure steeply increases until the base of the well in all three cases (Figures 4.8a-c).

Figure 4.8 (d) shows the measured temperatures in Bravo-X and Bravo-Y. A local linear geothermal gradient was estimated using only the Bravo-X data since it appeared to be more consistent. Following Hermanrud et al. (1990) who showed that RFT measured temperatures underestimate the true formation temperatures due to cooling effect of the drilling mud; a line was taken through the upper envelope of the RFT temperature values, yielding 60°C/km. This is also consistent with the thermal gradient reported by Halim (1994) for the Central Malay Basin.

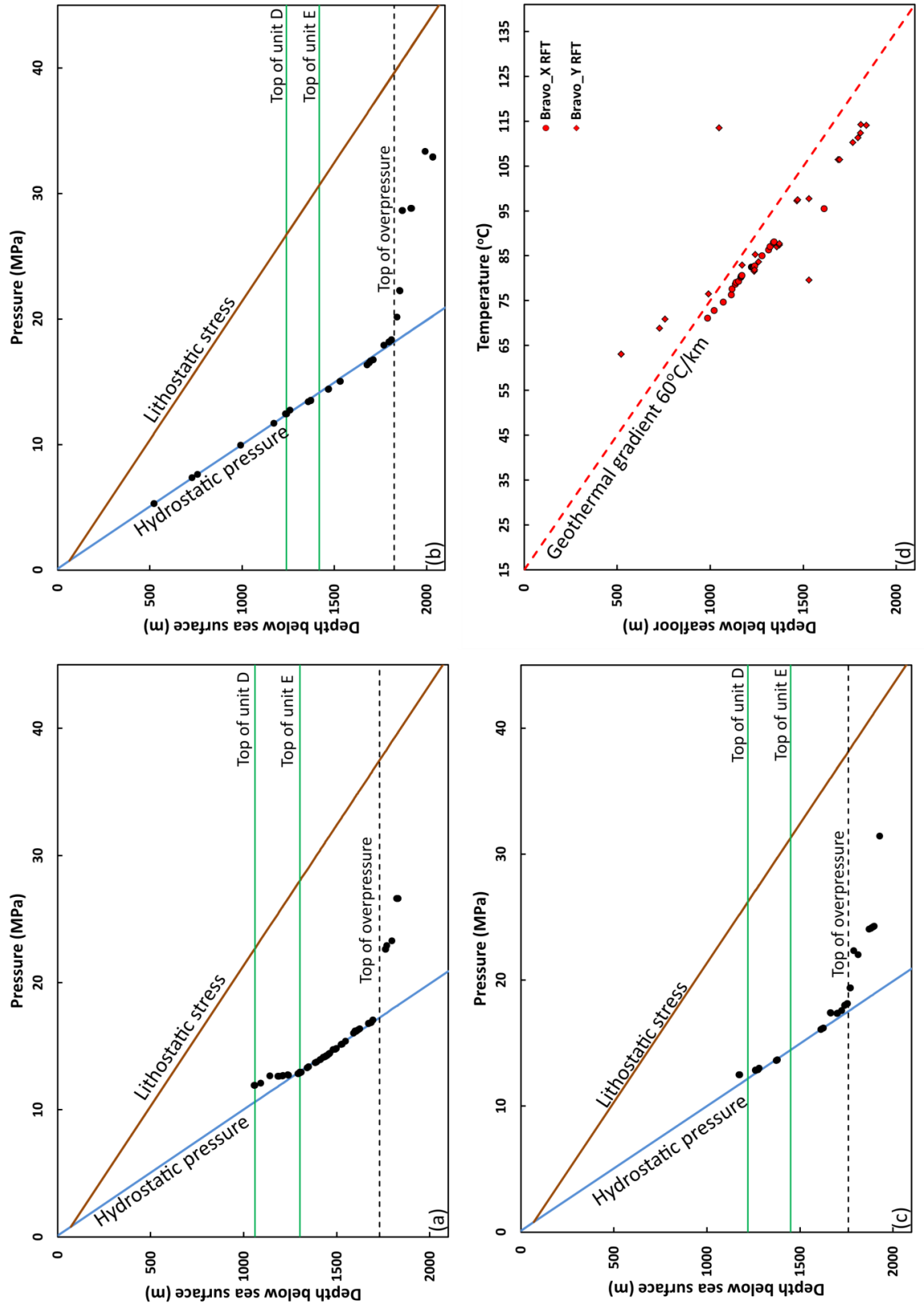


Figure 4.8. Pore pressure-depth profiles for (a) Bravo-X, (b) Bravo-Y and (c) Bravo-L. (d) estimated local linear geothermal gradient and RFT measured temperatures plotted against depth for Bravo-X and Bravo-Y.

4.6 Mudstone sample characterization results

Mudstone samples were provided as cuttings of variable size and quality (Figure 4.9). Based on quality and amount of remaining washed sample material, 16 samples were selected for further study. Due to the small amount of Bravo-Y sample material, samples from adjacent depth intervals were mixed to create XM1, XM3, XM4 and XM8. The complete list of the studied samples is shown in Table 4.1. The selected samples were from depths in the range of 1453-2093 m below seafloor, corresponding to Formation Unit E.

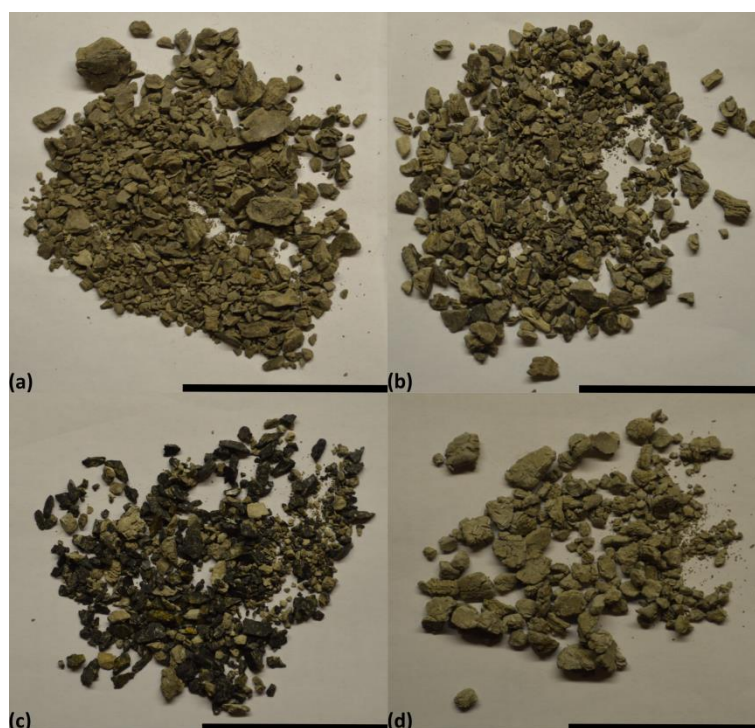


Figure 4.9. Washed cutting samples (a)XM8 (b)XM6 (c) XM1 and (d) XM9. Scale bar is 5 cm.

Cuttings were mainly small (sub-millimetre to centimetre scale), dark grey, greenish-grey or black pieces of sub-angular to sub-rounded material (Figure 4.9). There was considerable amount of dark, organic rich material, most likely coal in samples XM1 and XM3.

| Sample | Sample type | Well | Depth interval below seafloor (m) | Average depth below seafloor (m) | Temperature (°C) |
|--------|-------------|---------|---|--|---------------------|
| XL1 | cuttings | Bravo-L | 1523-1528 | 1525.5 | 107 |
| XL2 | cuttings | Bravo-L | 1618-1623 | 1620.5 | 112 |
| XL3 | cuttings | Bravo-L | 1763-1768 | 1765.5 | 121 |
| XL4 | cuttings | Bravo-L | 1863-1868 | 1865.5 | 127 |
| XL5 | cuttings | Bravo-L | 1928-1933 | 1930.5 | 131 |
| XL6 | cuttings | Bravo-L | 1998-2003 | 2000.5 | 135 |
| XM1 | cuttings | Bravo-Y | 1453-1468 | 1460.5 | 103 |
| XM2 | cuttings | Bravo-Y | 1513-1518 | 1515.5 | 106 |
| XM3 | cuttings | Bravo-Y | 1628-1638 | 1633.0 | 113 |
| XM4 | cuttings | Bravo-Y | 1668-1698 | 1683.0 | 116 |
| XM5 | cuttings | Bravo-Y | 1723-1728 | 1725.5 | 119 |
| XM6 | cuttings | Bravo-Y | 1753-1758 | 1755.5 | 120 |
| XM7 | cuttings | Bravo-Y | 1863-1868 | 1865.5 | 127 |
| XM8 | cuttings | Bravo-Y | 1933-1958 | 1945.5 | 132 |
| XM9 | cuttings | Bravo-Y | 2013-2018 | 2015.5 | 136 |
| XM10 | cuttings | Bravo-Y | 2088-2093 | 2090.5 | 140 |

Table 4.1. List of mudstone samples selected for study.

4.6.1 Bulk mineralogical properties

Quantitative bulk XRD shows a very consistent bulk mineral composition (Figure 4.10). Quartz, K-feldspar, plagioclase, siderite, kaolinite, 2:1 clays (illite-smectite) and chlorite were detected in all of the samples. The average clay content (kaolinite + mica + illite + illite-smectite + chlorite) is ~45 wt%. The dominant components are quartz (average ~40 wt%) and 2:1 clay minerals (illite-smectite; average ~30 wt%). There is an average of ~ 8 wt% siderite, ~10 wt% kaolinite and ~ 1.6 wt% barite in the samples. There are traces of K-feldspar in all of the samples, traces of anatase (XL1-6, XM1-XM9) and pyrite (XL1-XL6, XM1, XM4, XM6-XM10) in most of them, and in some of them traces of iron oxide

(hematite+goethite) (XM1-XM3, XM5), and gypsum (XM3, XM5-XM8). The quantitative bulk fraction XRD results from Bravo-L and Bravo-Y can be found in Appendix I.

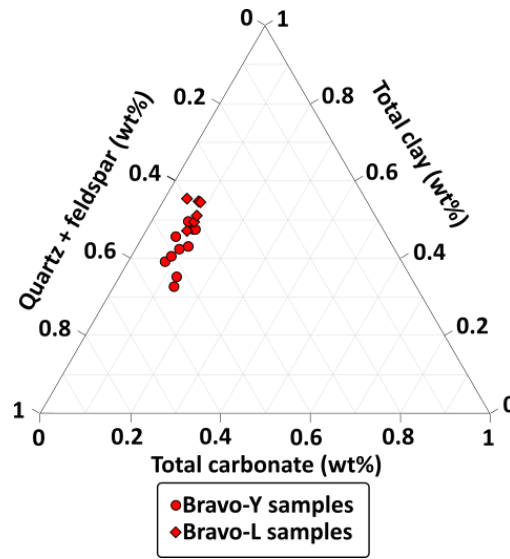


Figure 4.10. Bulk mineral composition of mudstone samples obtained from QXRD

Figure 4.10 was constructed using the quantitative XRD determined mineral weight percentages. Total clay content is defined here as the sum of all the XRD determined clay minerals including all 2:1 clays (illite, mica and illite-smectite). Bravo-L samples appear to be slightly more clay-rich; however, the overall mineralogy in the samples is fairly similar. No trend can be seen when plotting individual mineralogy with depth. The detected mineral composition is very monotonous (Figure 4.11). It should be noted however that sampled depth intervals lie in the range of 5-30 m and the results only show averaged mineralogy.

The variability of quartz with increasing depth shows a good negative correlation with the variability of the sum of clay minerals (Figure 4.11a, b) indicating that quartz is predominantly sedimentary in origin. The variability of kaolinite with increasing depth shows a weak negative correlation with the variability of illite-smectite (Figure 4.11c, d). No other mineral shows such a relationship. Tables 4.2 & 4.3 shows correlation coefficient values for individual mineral phases. Quartz shows a very strong negative correlation with illite-smectite (I+I/S). Kaolinite shows a very strong positive correlation with quartz in the Bravo-L samples (Table 4.2) but interestingly no such relationship can be seen in the Bravo-Y samples (Table 4.3). Another interesting feature of the Bravo-L samples is the strong negative correlation between plagioclase and quartz, but once again no such relationship can be seen in Bravo-Y.

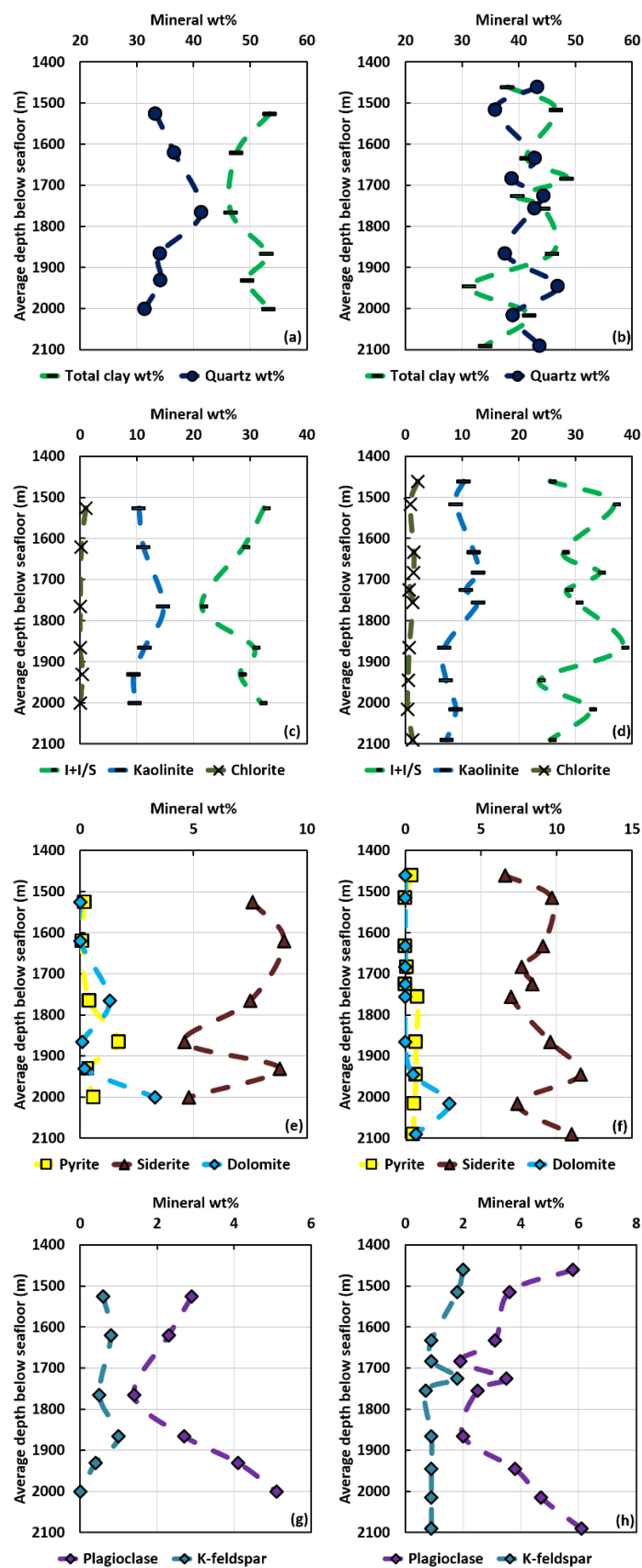


Figure 4.11. Bulk mineralogy versus depth for (a)(c)(e)(g) Bravo-L and (b)(d)(f)(h) Bravo-Y.

| | <i>Quartz</i> | <i>Plagioclase</i> | <i>K-feldspar</i> | <i>Calcite</i> | <i>Dolomite</i> | <i>Siderite</i> | <i>Pyrite</i> | <i>Barite</i> | <i>Muscovite</i> | <i>I+I/S-ML</i> | <i>Chlorite</i> | <i>Kaolinite</i> |
|--------------------|---------------|--------------------|-------------------|----------------|-----------------|-----------------|---------------|---------------|------------------|-----------------|-----------------|------------------|
| Quartz | 1.00 | | | | | | | | | | | |
| Plagioclase | -0.85 | 1.00 | | | | | | | | | | |
| K-feldspar | 0.28 | -0.68 | 1.00 | | | | | | | | | |
| Calcite | 0.20 | -0.29 | 0.36 | 1.00 | | | | | | | | |
| Dolomite | -0.20 | 0.53 | -0.82 | -0.30 | 1.00 | | | | | | | |
| Siderite | 0.42 | -0.33 | 0.11 | 0.50 | -0.53 | 1.00 | | | | | | |
| Pyrite | -0.20 | 0.02 | 0.40 | -0.37 | 0.01 | -0.80 | 1.00 | | | | | |
| Barite | -0.18 | -0.13 | 0.68 | 0.73 | -0.67 | 0.29 | 0.08 | 1.00 | | | | |
| Muscovite | -0.32 | 0.55 | -0.53 | -0.89 | 0.52 | -0.57 | 0.43 | -0.66 | 1.00 | | | |
| I+I/S-ML | -0.94 | 0.63 | -0.04 | -0.01 | 0.01 | -0.36 | 0.19 | 0.37 | 0.04 | 1.00 | | |
| Chlorite | -0.29 | 0.03 | 0.06 | -0.08 | -0.47 | 0.43 | -0.47 | 0.12 | -0.22 | 0.41 | 1.00 | |
| Kaolinite | 0.92 | -0.84 | 0.29 | 0.01 | -0.04 | 0.06 | 0.06 | -0.33 | -0.18 | -0.84 | -0.37 | 1.00 |

Table 4.2. Correlation matrix showing values of Pearson's correlation coefficient for Bravo-L mineralogy.

| | <i>Quartz</i> | <i>Plagioclase</i> | <i>K-feldspar</i> | <i>Calcite</i> | <i>Dolomite</i> | <i>Siderite</i> | <i>Pyrite</i> | <i>Barite</i> | <i>I+I/S</i> | <i>Chlorite</i> | <i>Kaolinite</i> |
|--------------------|---------------|--------------------|-------------------|----------------|-----------------|-----------------|---------------|---------------|--------------|-----------------|------------------|
| Quartz | 1.00 | | | | | | | | | | |
| Plagioclase | 0.35 | 1.00 | | | | | | | | | |
| K-feldspar | -0.05 | 0.36 | 1.00 | | | | | | | | |
| Calcite | -0.03 | 0.55 | 0.30 | 1.00 | | | | | | | |
| Dolomite | -0.11 | 0.39 | -0.28 | 0.24 | 1.00 | | | | | | |
| Siderite | 0.21 | 0.10 | -0.22 | -0.04 | -0.08 | 1.00 | | | | | |
| Pyrite | 0.20 | 0.09 | -0.52 | 0.23 | 0.33 | 0.06 | 1.00 | | | | |
| Barite | 0.26 | 0.57 | 0.01 | 0.77 | 0.15 | 0.55 | 0.22 | 1.00 | | | |
| I+I/S | -0.94 | -0.59 | -0.05 | -0.15 | 0.00 | -0.18 | -0.11 | -0.40 | 1.00 | | |
| Chlorite | 0.14 | 0.25 | 0.27 | 0.28 | -0.47 | -0.43 | -0.22 | 0.08 | -0.30 | 1.00 | |
| Kaolinite | 0.02 | -0.39 | -0.01 | -0.47 | -0.30 | -0.69 | -0.39 | -0.70 | 0.00 | 0.49 | 1.00 |

Table 4.3. Correlation matrix showing values of Pearson`s correlation coefficient for Bravo-Y mineralogy.

In addition, plagioclase also shows a relatively strong positive correlation with illite-smectite and a relatively strong negative correlation with Kfeldspar in the Bravo-L samples. This correlation strongly suggests a secondary (authigenic) origin of plagioclase in the Bravo-L mudstones. Siderite shows a strong negative correlation with pyrite in Bravo-L, however no such correlation exists in Bravo-Y.

The origin of the detected barite is uncertain due to the nature of the cutting samples. Barite is commonly used in drilling muds as heavyweight additive. It occurs naturally in sedimentary environments; however, it is relatively uncommon in most settings so it was assumed to have come from the drilling mud, and barite-free normalized mineral concentrations have been calculated. Traces of halite and sylvite are probably precipitates from pore solutions.

4.6.2 Clay mineralogical properties

Cation exchange capacity (CEC) measurements of the Bravo-Y mudstone samples range from 5.4 to 10.7 meq/100g. These results are fairly consistent and suggest that the dioctahedral 2:1 mineral fraction is dominated by illite (average of 25% smectite equivalent in illite-smectite). However, any contamination by clay components of the drilling fluid can affect the CEC results. Bentonite is one such component and could have influenced the CEC results. Organic matter from an organic-based drilling fluid is another possible source of contamination. The barite content is usually the best indicator of drilling mud contamination since it is the dominant component in most drilling muds. Overall, the low (average of 1.6 wt%) barite content suggests that contamination was not significant. Figure 4.12 was constructed to check for any drilling mud contamination. No clear correlation can be seen between the measured CEC values and the barite content (Figure 4.12c). Similarly, no correlation can be found between the CEC and the TOC content (Figure 4.12d). However, the measured CEC of samples XM8 and XM10 (inside the dashed circle) appears to be anomalously high considering their estimated total illite-smectite content (Figure 4.12a, b).

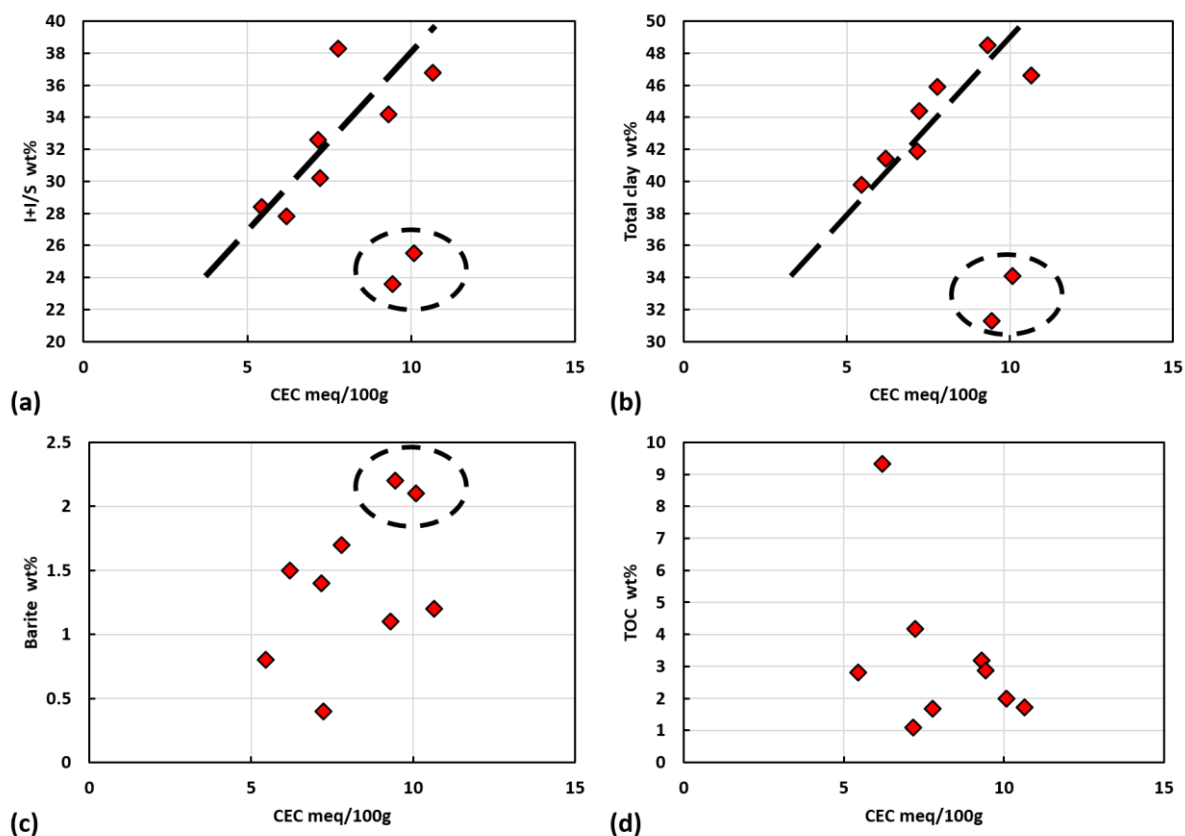


Figure 4.12. Bravo-Y bulk rock CEC plotted against QXRD-based (a) illite-smectite content, (b) total clay content, (c) barite content and (d) measured TOC content. The dashed line represents the expected CEC values for a given illite-smectite and clay content. Encircled samples are having anomalously high CEC values for their illite-smectite content based on the estimated trend.

Since these results do not show any evidence for ongoing clay mineral transformations, the CEC value should correspond to the total illite-smectite content in a given sample, meaning that those anomalous values should plot on or close to the linear trend in Figure 4.12a, b. These anomalously high CEC values are interpreted as a result of contamination by drilling mud. Figure 4.14a shows the calculated smectite equivalent content in illite-smectite for the individual samples (excluding the samples with anomalous CEC values). If we do not consider the samples with anomalously high CEC values, these results indicate approximately 20% smectite equivalent in illite-smectite for all of the Bravo-Y mudstone samples (Figure 4.14a). Complete CEC data and calculated smectite equivalent contents for individual samples can be found in Appendix I.

The authigenic (<0.2 μm fraction) clay fraction XRD results correlate well with the CEC results by showing illite-dominated clays. Overall the samples contain illite, illite-smectite,

kaolinite and chlorite. The clay fraction is dominated by mixed-layer illite-smectite with ordered interstratification ($R > 1$) (Figure 4.13).

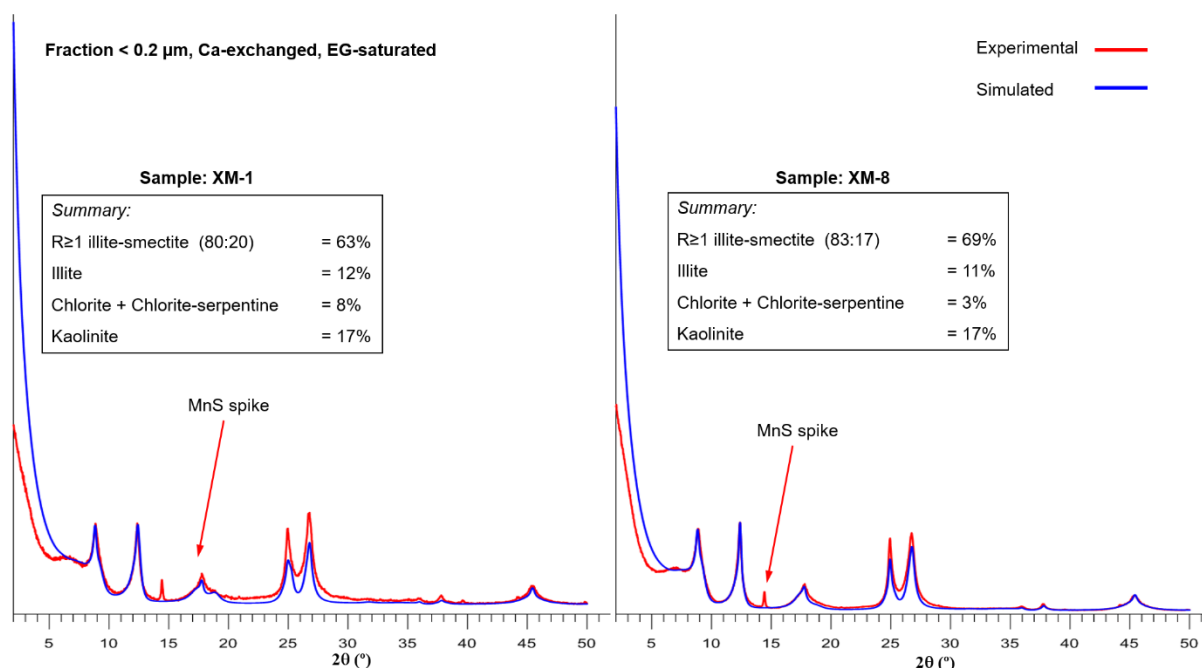


Figure 4.13. Experimental and simulated XRD patterns for ethylene glycol-saturated samples XM1 and XM-8.

The estimated smectite% in illite-smectite is approximately 20% in all samples. No pure smectite or disordered (R_0) illite-smectite phase has been detected. Full <0.2 μ m fraction XRD data and modelling results can be found in Appendix II.

Figure 4.14 shows the calculated smectite equivalent content of the illite-smectite for the individual samples. Smectite equivalent values shown in Figure 4.14a were calculated using the CEC results as previously described in 3.3.3. Smectite equivalent values shown in Figure 4.14b were calculated using the clay fraction XRD modelling results in combination with the bulk fraction estimated total illite-smectite content.

Based on these results, either the mudstones in Bravo-Y were initially smectite-poor or all the smectite has already been transformed to illite (diagenesis approaching “completion”). It should be noted that the dominance of an ordered mixed-layer illite-smectite phase strongly suggests a diagenetically mature assemblage (refer to 1.2.2).

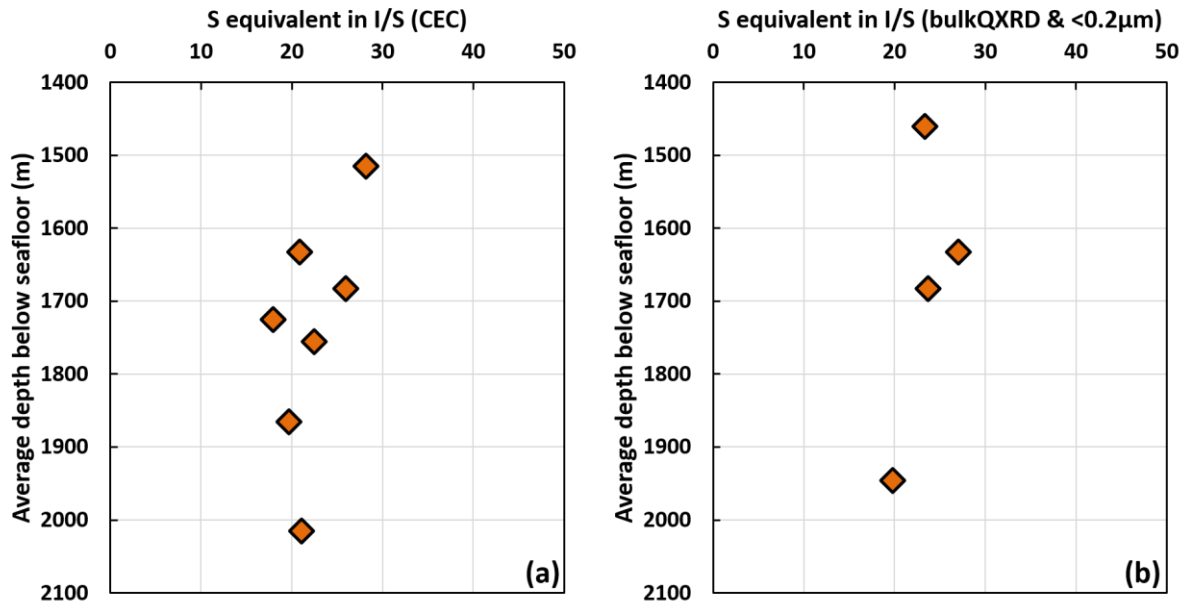


Figure 4.14. Calculated smectite equivalent % in illite-smectite for Bravo-Y mudstone samples plotted against depth. (a) smectite equivalent content calculated using the CEC results as described in 3.3.3. (b) smectite equivalent content calculated using the combination of the bulk QXRD and <0.2 μm fraction modelling results.

4.6.3 Total organic carbon content

Total organic carbon content (TOC) was estimated from all Bravo-Y mudstone samples. Complete TOC data and calculated organic matter contents for individual samples are given in Appendix III.

Figure 4.15 shows the estimated TOC content of individual mudstone samples. These results are considered anomalously high for these mudstones. The anomalous results are a consequence of the heterogeneous sample material and contamination with organic-based drilling mud. The unusually high TOC values in the shallower samples, especially those of XM1 and XM3 correspond to the presence of dark, organic-rich material, most probably coal. Due to the low quantity of sample material, a preferential selection of a more homogeneous sample material was not possible.

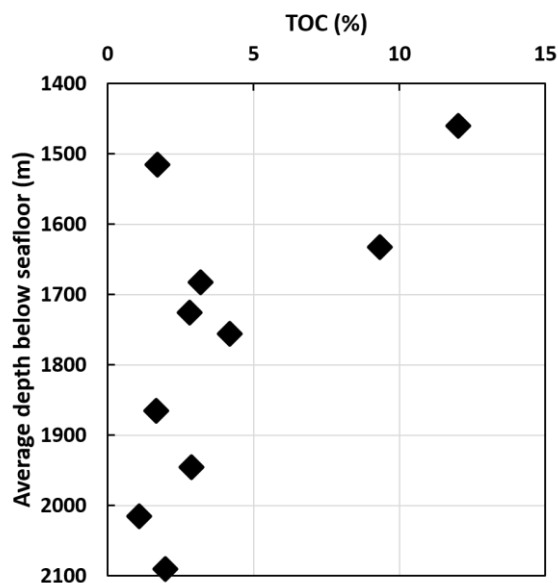


Figure 4.15. TOC (%) results for Bravo-Y mudstones.

4.6.4 Bulk inorganic chemical properties

Bravo-Y mudstone samples were analysed for their major and trace elemental composition. Complete major and trace element concentrations of the individual mudstone samples along with the ratios of selected pairs of major and trace elements and calculated weathering indices can be found in Appendix IV. Overall, in accord with the consistent bulk mineralogy major and trace elements show relatively little variability among the samples.

The amount of SiO_2 varies between 48.88 and 62.83% (average of 55.65%), Al_2O_3 varies between 12.38 and 18.48% (average of 15.78%), TiO_2 varies between 0.59 and 0.79% (average of 0.71%), Fe_2O_3 varies between 5.41 and 7.18% (average of 6.28%), MnO varies between 0.08 and 0.14% (average of 0.11%), MgO varies between 1.22 and 2.09% (average of 1.57%), CaO varies between 0.52 and 2.05% (average of 0.88%), Na_2O varies between 0.5 and 0.94% (average of 0.68%), K_2O varies between 1.93 and 2.93% (average of 2.49%) and P_2O_5 varies between 0.08 and 0.12% (average of 0.10). Total iron is expressed as Fe_2O_3 . The anomalously high loss on ignition (LOI) values of the samples XM1 and XM3 can be attributed to the presence of organic rich, coaly material in the cutting samples. Further evidence is presented in Table 4.4 which shows strong correlation between the measured LOI and TOC values.

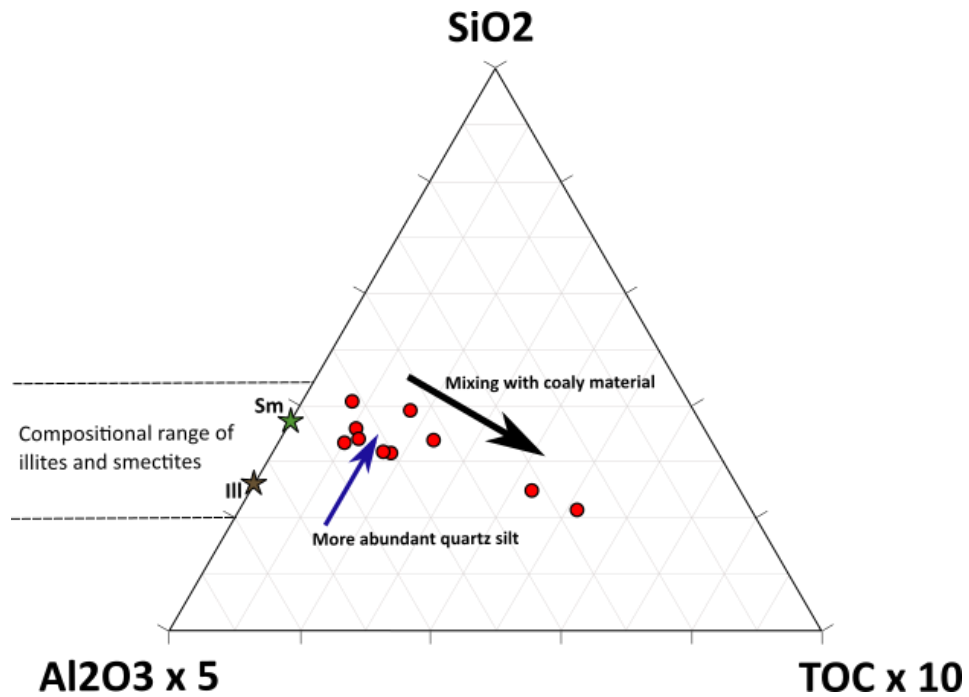


Figure 4.16. SiO_2 - Al_2O_3 -TOC ternary diagram showing mixing relationships of the main sediment components in Bravo-Y samples (red dots). Green and brown stars indicate the average compositions of smectite and illite respectively; the field outlined by dashed lines represents the compositional variation of illites and smectites (based on Weaver, 1989).

It should be noted that due to the heterogenous nature of the provided Bravo-Y mudstone cuttings these samples are not truly representatives of “pure”, homogeneous mudstones. Hence these results only represent an average composition of the fine-grained lithologies present in the sampled depth intervals. Figure 4.16 was constructed to show the mixing relationships of the main sediment components in Bravo-Y samples. The relatively high $\text{SiO}_2/\text{Al}_2\text{O}_3$ ratios (average of 3.6) of the samples (considering that the dominant aluminosilicate phase is illite) can be attributed to the relatively high detrital quartz content.

Correlation coefficient values for major elements are given in Table 4.4. Al_2O_3 shows good positive correlations with K_2O and TiO_2 . This indicates that both potassium and titanium reside primarily in clay minerals and are dominantly terrigenous components. K_2O and TiO_2 also show weak positive correlation with SiO_2 that can be attributed to small amounts of detrital feldspar and anatase. Positive correlation between Fe_2O_3 and Al_2O_3 indicates that iron was transported to the basin with clay minerals either as primary constituents in the crystal structure or on crystal surfaces as oxides and oxyhydroxides

(Carroll, 1958; Hofstetter et al., 2003). MnO shows positive correlation with Fe_2O_3 indicating that Mn primarily resides in siderite. Good correlation between CaO and MgO can be attributed to the presence of dolomite. Correlation between K_2O and MgO can be attributed to the presence of chlorite.

Values of $\text{K}_2\text{O}/\text{Al}_2\text{O}_3$ ratio of the Bravo-Y samples show very little variation between 0.14 and 0.18 (average of 0.16). These values are consistent with the preponderance of clay minerals (illite) over K-feldspar in these samples (Cox et al., 1995).

Similarly values of Si/Al, K/Al and Na/Al show relatively little variation and correlate well with QXRD established mineral abundances (Figure 4.18). In accordance with an illite dominated clay mineralogy Na/Al shows strong correlation with the plagioclase content. This indicates that sodium resides almost exclusively in plagioclase feldspar (Figure 4.18e, f).

Calculated Index of Compositional Variability (ICV) values of the samples range from 0.72 to 0.94. Calculated Chemical Index of Alteration (CIA) and Chemical Index of Weathering (CIW) values range from 72 to 79 and 90 to 96 respectively. Calculated CIA and CIW values show strong positive correlation indicating that the two indices are matchable (Figure 4.17).

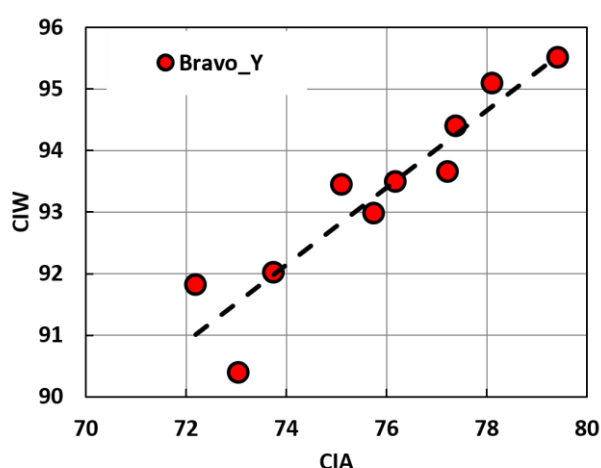


Figure 4.17. Strong positive correlation between calculated Chemical Index of Alteration (CIA) and Chemical Index of Weathering (CIW) values of Bravo-Y mudstones.

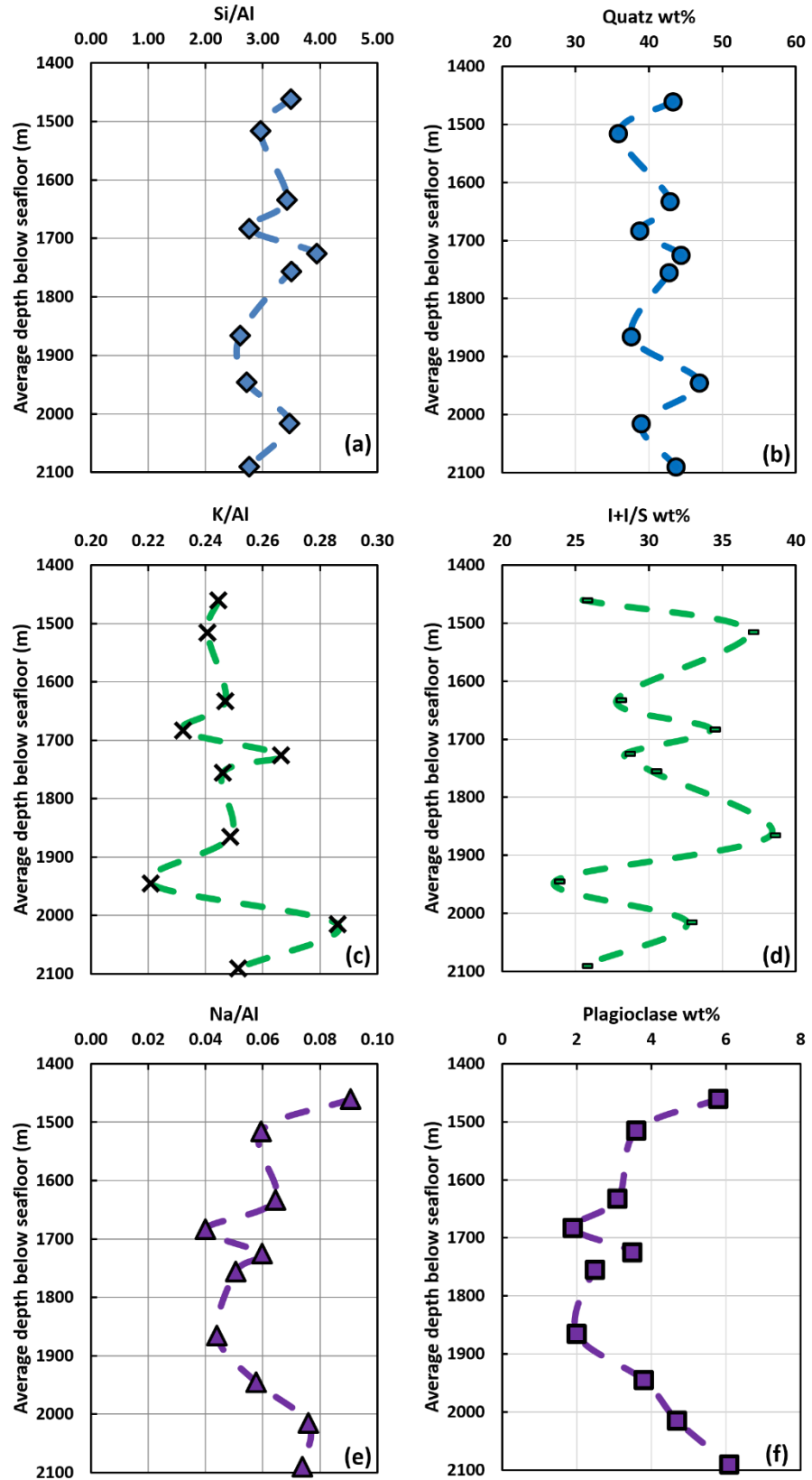


Figure 4.18. Variation of (a) Si/Al, (c) K/Al and (e) Na/Al with depth in comparison with the variation of (b) quartz, (d) illite-smectite and (f) plagioclase content.

| | <i>SiO₂</i> | <i>Al₂O₃</i> | <i>Fe₂O₃(T)</i> | <i>MnO</i> | <i>MgO</i> | <i>CaO</i> | <i>Na₂O</i> | <i>K₂O</i> | <i>TiO₂</i> | <i>P₂O₅</i> | <i>LOI</i> | <i>TOC</i> |
|---------------------------------------|------------------------|------------------------------------|---------------------------------------|------------|------------|------------|------------------------|-----------------------|------------------------|-----------------------------------|------------|------------|
| SiO₂ | 1.00 | | | | | | | | | | | |
| Al₂O₃ | 0.06 | 1.00 | | | | | | | | | | |
| Fe₂O₃(T) | -0.31 | 0.64 | 1.00 | | | | | | | | | |
| MnO | -0.43 | 0.09 | 0.66 | 1.00 | | | | | | | | |
| MgO | -0.11 | 0.53 | 0.11 | -0.46 | 1.00 | | | | | | | |
| CaO | 0.06 | 0.11 | -0.20 | -0.49 | 0.74 | 1.00 | | | | | | |
| Na₂O | -0.28 | -0.05 | -0.12 | -0.37 | 0.65 | 0.39 | 1.00 | | | | | |
| K₂O | 0.32 | 0.85 | 0.29 | -0.34 | 0.74 | 0.45 | 0.09 | 1.00 | | | | |
| TiO₂ | 0.52 | 0.78 | 0.41 | 0.07 | 0.12 | 0.03 | -0.54 | 0.72 | 1.00 | | | |
| P₂O₅ | -0.44 | 0.70 | 0.93 | 0.61 | 0.35 | 0.06 | 0.01 | 0.40 | 0.38 | 1.00 | | |
| LOI | -0.77 | -0.62 | -0.09 | 0.38 | -0.42 | -0.36 | 0.09 | -0.82 | -0.80 | -0.10 | 1.00 | |
| TOC | -0.62 | -0.72 | -0.20 | 0.31 | -0.54 | -0.48 | 0.04 | -0.87 | -0.81 | -0.26 | 0.97 | 1.00 |

Table 4.4. Correlation matrix showing values of Pearson`s correlation coefficient for major elements of Bravo-Y mudstones.

| | <i>SiO2</i> | <i>Al2O3</i> | <i>CaO</i> | <i>TiO2</i> | <i>Sc</i> | <i>V</i> | <i>Ba</i> | <i>Sr</i> | <i>Y</i> | <i>Zr</i> | <i>Cr</i> | <i>Co</i> | <i>Ni</i> | <i>Zn</i> | <i>Rb</i> | <i>Nb</i> | <i>Pb</i> | <i>Th</i> | <i>U</i> |
|--------------|-------------|--------------|------------|-------------|-----------|----------|-----------|-----------|----------|-----------|-----------|-----------|-----------|-----------|-----------|-----------|-----------|-----------|----------|
| SiO2 | 1.00 | | | | | | | | | | | | | | | | | | |
| Al2O3 | 0.06 | 1.00 | | | | | | | | | | | | | | | | | |
| CaO | 0.06 | 0.11 | 1.00 | | | | | | | | | | | | | | | | |
| TiO2 | 0.52 | 0.78 | 0.03 | 1.00 | | | | | | | | | | | | | | | |
| Sc | 0.05 | 0.91 | 0.38 | 0.68 | 1.00 | | | | | | | | | | | | | | |
| V | 0.03 | 0.91 | 0.43 | 0.62 | 0.97 | 1.00 | | | | | | | | | | | | | |
| Ba | -0.26 | 0.49 | 0.70 | 0.05 | 0.64 | 0.69 | 1.00 | | | | | | | | | | | | |
| Sr | -0.08 | 0.38 | 0.54 | 0.14 | 0.64 | 0.59 | 0.77 | 1.00 | | | | | | | | | | | |
| Y | 0.46 | 0.39 | -0.53 | 0.70 | 0.18 | 0.06 | -0.35 | -0.16 | 1.00 | | | | | | | | | | |
| Zr | 0.92 | -0.10 | -0.14 | 0.43 | -0.18 | -0.22 | -0.46 | -0.36 | 0.57 | 1.00 | | | | | | | | | |
| Cr | -0.75 | -0.09 | 0.06 | -0.46 | 0.03 | 0.09 | 0.25 | 0.31 | -0.64 | -0.86 | 1.00 | | | | | | | | |
| Co | -0.21 | 0.56 | 0.26 | 0.17 | 0.75 | 0.68 | 0.69 | 0.82 | 0.00 | -0.40 | 0.22 | 1.00 | | | | | | | |
| Ni | -0.31 | 0.29 | 0.05 | 0.10 | 0.52 | 0.42 | 0.23 | 0.65 | -0.10 | -0.49 | 0.57 | 0.71 | 1.00 | | | | | | |
| Zn | -0.31 | 0.26 | 0.08 | 0.14 | 0.27 | 0.20 | 0.33 | 0.42 | 0.03 | -0.31 | 0.21 | 0.32 | 0.38 | 1.00 | | | | | |
| Rb | 0.18 | 0.90 | 0.43 | 0.72 | 0.96 | 0.98 | 0.60 | 0.56 | 0.12 | -0.08 | 0.03 | 0.59 | 0.41 | 0.22 | 1.00 | | | | |
| Nb | 0.62 | 0.58 | 0.17 | 0.82 | 0.50 | 0.50 | 0.11 | 0.23 | 0.48 | 0.40 | -0.35 | 0.00 | -0.06 | -0.03 | 0.61 | 1.00 | | | |
| Pb | -0.15 | 0.51 | 0.06 | 0.43 | 0.40 | 0.45 | 0.34 | 0.22 | 0.11 | -0.18 | 0.37 | 0.10 | 0.18 | 0.57 | 0.53 | 0.33 | 1.00 | | |
| Th | 0.31 | 0.89 | 0.01 | 0.96 | 0.80 | 0.74 | 0.17 | 0.21 | 0.64 | 0.22 | -0.31 | 0.35 | 0.25 | 0.17 | 0.80 | 0.69 | 0.48 | 1.00 | |
| U | 0.70 | 0.41 | -0.03 | 0.77 | 0.26 | 0.20 | -0.20 | -0.25 | 0.76 | 0.76 | -0.89 | -0.15 | -0.41 | -0.20 | 0.28 | 0.60 | -0.05 | 0.66 | 1.00 |

Table 4.5. Correlation matrix showing values of Pearson`s correlation coefficient for selected trace elements of Bravo-Y mudstones.

| | <i>SiO2</i> | <i>Al2O3</i> | <i>CaO</i> | <i>TiO2</i> | <i>La</i> | <i>Ce</i> | <i>Pr</i> | <i>Nd</i> | <i>Sm</i> | <i>Eu</i> | <i>Gd</i> | <i>Tb</i> | <i>Dy</i> | <i>Ho</i> | <i>Er</i> | <i>Tm</i> | <i>Yb</i> |
|--------------|-------------|--------------|------------|-------------|-----------|-----------|-----------|-----------|-----------|-----------|-----------|-----------|-----------|-----------|-----------|-----------|-----------|
| <i>SiO2</i> | 1.00 | | | | | | | | | | | | | | | | |
| <i>Al2O3</i> | 0.06 | 1.00 | | | | | | | | | | | | | | | |
| <i>CaO</i> | 0.06 | 0.11 | 1.00 | | | | | | | | | | | | | | |
| <i>TiO2</i> | 0.52 | 0.78 | 0.03 | 1.00 | | | | | | | | | | | | | |
| <i>La</i> | 0.60 | 0.73 | 0.07 | 0.98 | 1.00 | | | | | | | | | | | | |
| <i>Ce</i> | 0.61 | 0.71 | 0.03 | 0.97 | 1.00 | 1.00 | | | | | | | | | | | |
| <i>Pr</i> | 0.59 | 0.73 | 0.04 | 0.99 | 0.99 | 0.99 | 1.00 | | | | | | | | | | |
| <i>Nd</i> | 0.54 | 0.72 | 0.02 | 0.96 | 0.99 | 0.99 | 0.98 | 1.00 | | | | | | | | | |
| <i>Sm</i> | 0.55 | 0.73 | -0.11 | 0.97 | 0.95 | 0.95 | 0.97 | 0.93 | 1.00 | | | | | | | | |
| <i>Eu</i> | 0.43 | 0.07 | -0.41 | 0.46 | 0.52 | 0.58 | 0.54 | 0.56 | 0.56 | 1.00 | | | | | | | |
| <i>Gd</i> | 0.33 | 0.75 | -0.05 | 0.96 | 0.91 | 0.90 | 0.92 | 0.90 | 0.93 | 0.47 | 1.00 | | | | | | |
| <i>Tb</i> | 0.54 | 0.52 | -0.09 | 0.86 | 0.89 | 0.91 | 0.91 | 0.92 | 0.90 | 0.76 | 0.83 | 1.00 | | | | | |
| <i>Dy</i> | 0.67 | 0.41 | -0.20 | 0.80 | 0.84 | 0.87 | 0.85 | 0.86 | 0.82 | 0.76 | 0.76 | 0.89 | 1.00 | | | | |
| <i>Ho</i> | 0.62 | 0.51 | -0.13 | 0.85 | 0.87 | 0.89 | 0.88 | 0.90 | 0.84 | 0.57 | 0.81 | 0.87 | 0.95 | 1.00 | | | |
| <i>Er</i> | 0.52 | 0.58 | -0.17 | 0.88 | 0.91 | 0.93 | 0.91 | 0.94 | 0.86 | 0.72 | 0.86 | 0.91 | 0.96 | 0.94 | 1.00 | | |
| <i>Tm</i> | 0.68 | 0.64 | -0.08 | 0.95 | 0.96 | 0.97 | 0.97 | 0.95 | 0.96 | 0.60 | 0.88 | 0.92 | 0.93 | 0.95 | 0.93 | 1.00 | |
| <i>Yb</i> | 0.74 | 0.51 | -0.10 | 0.91 | 0.92 | 0.94 | 0.93 | 0.90 | 0.91 | 0.61 | 0.86 | 0.86 | 0.91 | 0.92 | 0.90 | 0.96 | 1.00 |

Table 4.6. Correlation matrix showing values of Pearson`s correlation coefficient for REE of Bravo-Y mudstones.

Correlation coefficient values for selected trace elements and rare earth elements (REE) are shown in Table 4.5 and 4.6 respectively. Among the analysed trace elements Sc, V, Rb, Nb and Th show strong positive correlation with Al_2O_3 indicating that their closely related to clay minerals either as primary constituents or as adsorbed components on clay mineral surfaces. Zirconium and uranium show strong positive correlation with SiO_2 indicating the presence of zircon. Yttrium and niobium shows positive correlation with TiO_2 and are likely associated with anatase. Strontium positively correlates with CaO and is most likely related to carbonate (calcite and dolomite). Chromium, cobalt and nickel are most likely associated with mafic mineral components. Rare earth elements show strong positive correlations with TiO_2 and Al_2O_3 indicating that their mostly associated with clay minerals.

Th/Sc ratios of the Bravo-Y samples range from 0.98 to 1.20 (average of 1.08). Zr/Sc ratios range from 8.93 to 17.53 (average of 10.89). La/Sc ratios of the samples range from 2.3 to 3.03 (average of 2.55). La/Th ratios range from 2.24 to 2.50 (average of 2.35). Zr/Cr ratios range from 0.91 to 3.8 (average of 1.64) and Y/Ni ratios range from 0.57 to 1 (average of 0.72).

4.6.5 Clay mineral fabric alignment

Quantitative assessment of the phyllosilicate alignment of the Bravo-Y mudstone samples was carried out using high-resolution X-ray textural goniometry (HRXTG) as described in 3.3.10.

Ideally the degree of preferred orientation is measured in a bedding-parallel direction. However, due to the inherent uncertainty of mudstone cuttings (often no indication where the bedding is), most of the results were considered erroneous. Features such as colour variations or preferred breakage were used to estimate the bedding direction. Figure 4.19 shows the results considered least erroneous.

Complete HRXTG data of individual samples (including the chosen 2theta angles) can be found in Appendix V.

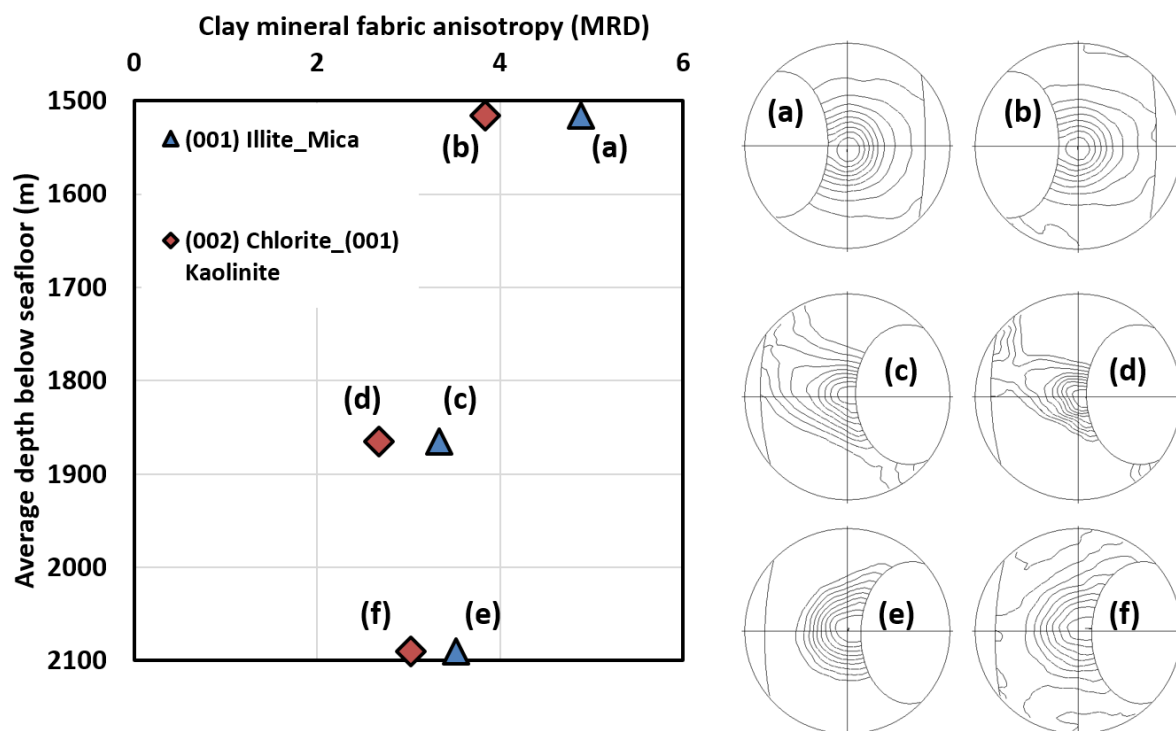


Figure 4.19. Measured clay mineral fabric anisotropy values of Bravo-Y mudstone samples. Representative illite/mica and chlorite/kaolinite pole figures are displayed to the right. The letters of these samples are shown on the left figure.

The results shown in Figure 4.19 indicate moderate/strong alignment, even in the shallowest sample (XM2; 1515 m below seafloor). Even if we ignore possible error (real MRD values may be higher), overall these results indicate moderate to strong alignment in Bravo-Y mudstones.

4.6.6. Mudstone petrography

Support for the results shown in 4.6.5 is provided by petrographic observations made by SEM (Figure 4.20), which suggest an overall well-developed clay mineral fabric in the Bravo-Y mudstone samples. However, SEM observations also revealed considerable variability of the clay mineral fabric on a millimetre-scale.

Overall BSEM observations suggest that the fine-grained clay mineral matrix is well aligned where quartz or other silt sized spherical grains (e.g. quartz, pyrite etc) do not disrupt the fabric. Where silt sized equidimensional grains are present the clay fabric is locally disrupted (Figures 4.20d&4.21a).

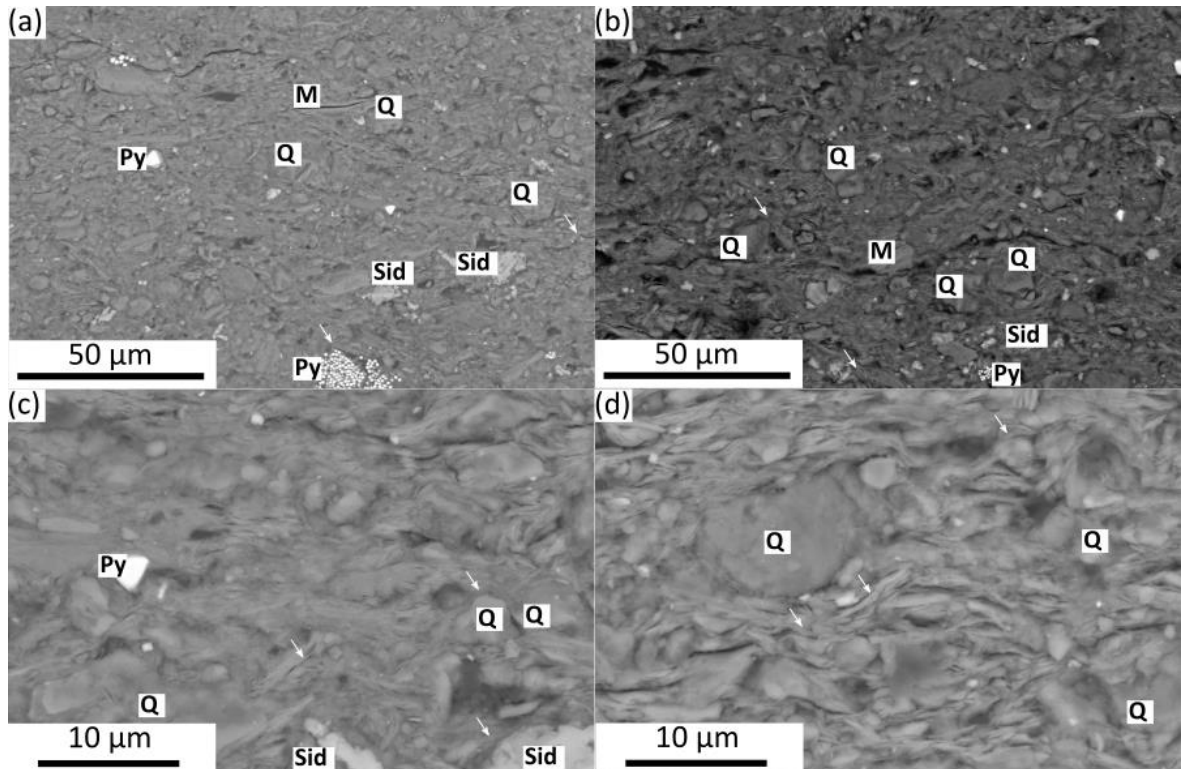


Figure 4.20. SEM images of XM7. (a)(b) Low-magnification BSEM images showing abundant silt-sized grains. (c) (d) BSEM images showing examples of well-developed planar clay mineral fabric. Silt-sized quartz grains locally disturb the fabric alignment. Arrows show examples of compactional bending of clays around resistant larger grains. Q: quartz, M: mica, Sid: siderite, Py: pyrite. All images are from sections perpendicular to the bedding.

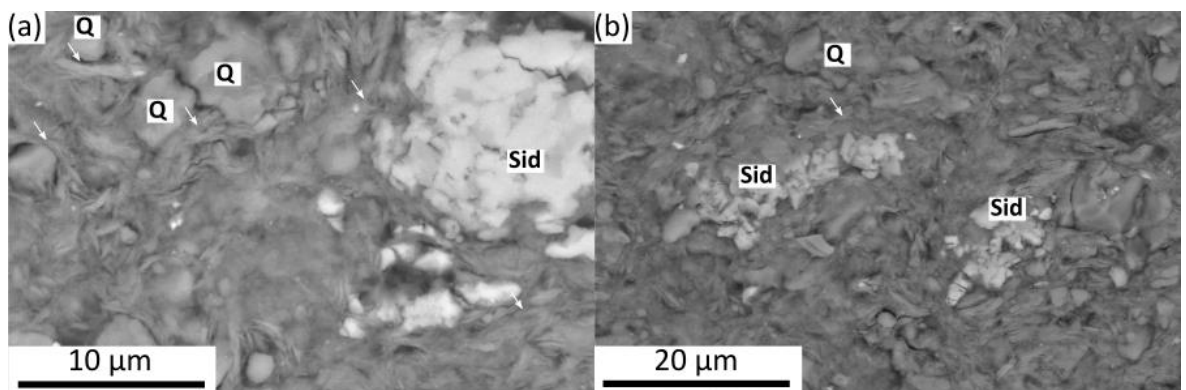


Figure 4.21. BSEM images showing examples for pore filling euhedral siderite cement in XM7. Arrows show examples of compactional bending of clays around resistant larger grains. Q: quartz, Sid: siderite. Both images are from sections perpendicular to the bedding.

All samples contain a mixture of silt- and clay-sized particles (Figure 4.20). Overall sorting of the samples is poor, and the silt particles are mixed with the clay-sized particles (Figure

4.20). Silt-sized mineral grains are dominantly quartz and siderite with lesser amounts of mica and pyrite. Mechanical features such as bending of clays around more resistant mineral grains were also commonly observed features within these mudstones (marked by arrows in Figures 4.20&4.21).

Siderite is present as patchy euhedral pore filling cement (Figure 4.21). Pyrite was present in both framboidal and euhedral forms (Figure 4.20a).

These results further suggest a diagenetically mature and highly compacted clay mineral assemblage in the Bravo-Y mudstones.

4.6.7 Mudstone porosity

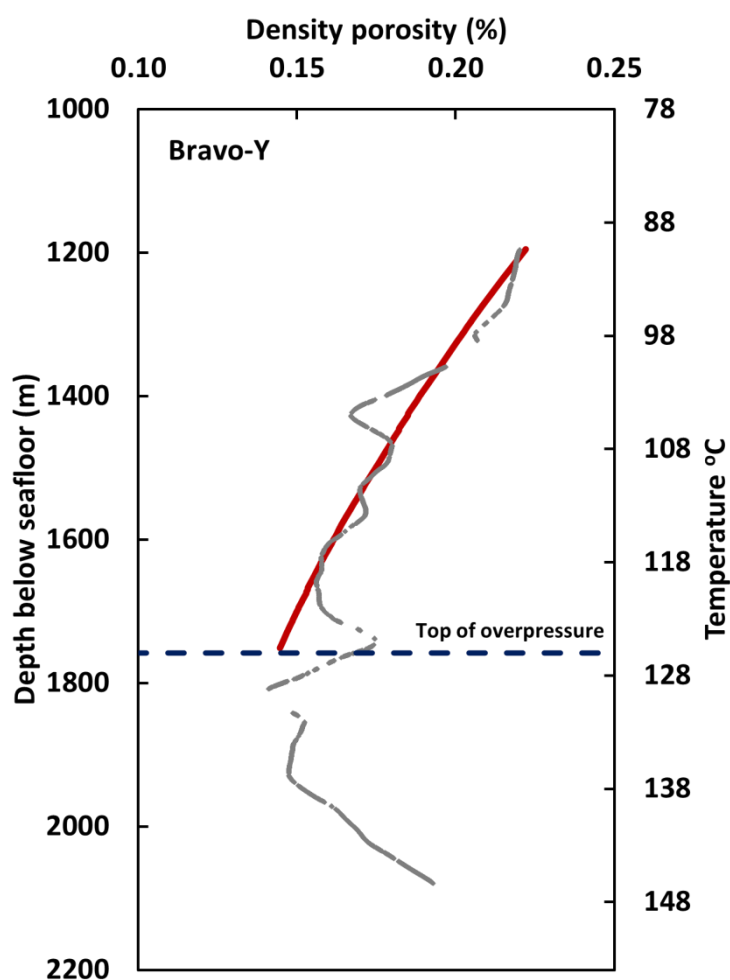


Figure 4.22. Density log derived porosity for Bravo-Y mudstones. Smoothed density log porosity is in grey with best fitting exponential porosity trend in red.

Due to the nature of the provided cutting samples (heterogeneous material and low quantity) porosity measurements have not been carried out. Mudstone porosities through the working interval in Bravo-Y were calculated using the density log as described in 3.4.3. Fluid density was assumed to be 1.015 g/cm³ and the grain density to be 2.82 g/cm³. Average grain density was calculated from the bulk QXRD mineralogy using grain density values for minerals identified by XRD. Mineral grain density values were obtained from www.webmineral.com. The estimated value of pore fluid density corresponds to a hydrostatic fluid pressure gradient of 9.9553 MPa/km obtained from hydrostatic pore pressure measurements in Formation Units A, B and E. An exponential curve was fitted by least squares through the computed density porosity in the hydrostatically pressured interval (Figure 4.22) in the form of equation 9.

The calculated density porosity trend for Bravo-Y shows approximately 8% porosity loss (from 24% to 14%) between 1200 and 1800 m below seafloor (Figure 4.22). It should be noted that the calculated density porosities are considered as the highest possible porosities for these mudstones. This is because average grain density was calculated assuming zero organic matter content due to the uncertainty of the anomalous TOC results. In reality mudstone porosities can be considerably lower depending on the total organic matter content.

4.6.8 Mudstone permeability

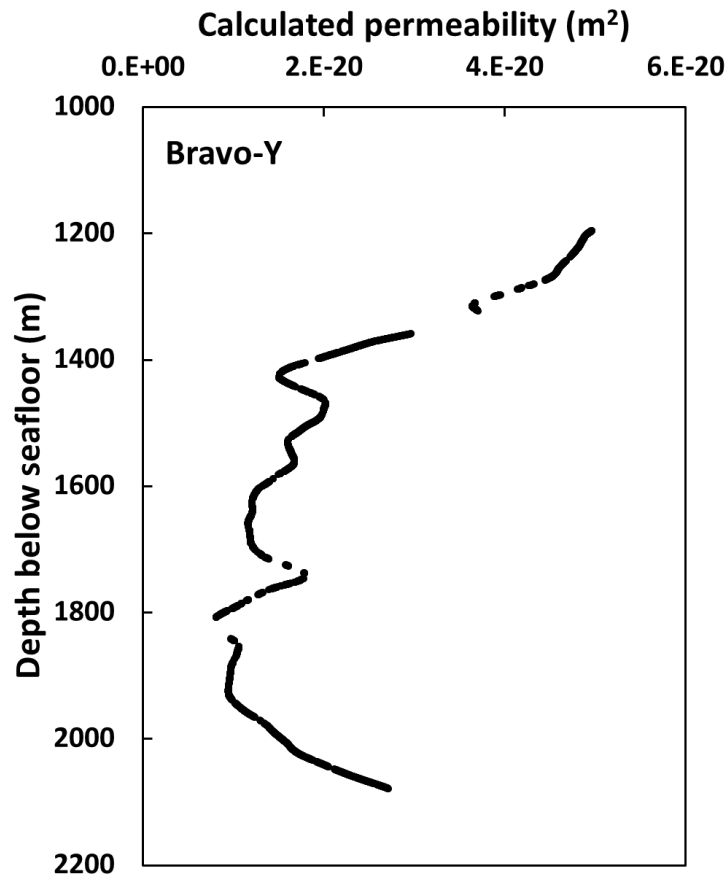


Figure 4.23. Calculated bedding perpendicular permeability (after Yang and Aplin 2010) for Bravo-Y mudstones.

Mudstone permeability through the working interval in Bravo-Y was calculated based on the model of Yang and Aplin (2010) utilising bulk QXRD estimated average total clay mineral content and calculated density porosities. Total clay mineral content was used as a proxy for the mass fraction of particles less than two microns since no grain size distribution measurements have been made and it was assumed to be 40% through the whole working interval.

The calculated mudstone permeabilities are low (in the nD range) and except for a slight increase below the top of overpressure around 1760 m below seafloor show an overall decreasing permeability-depth trend (Figure 4.23).

4.7 Discussion

4.7.1 Sediment provenance and paleoweathering reconstruction from major and trace element geochemistry

Figure 4.24 shows major and trace elemental distributions of the Bravo-Y mudstone samples normalized to post-Archaean Australian Shale (PAAS; from Taylor and McLennan 1985) (Figure 4.24a&c) and to average upper continental crust (UCC; from McLennan 2001) (Figure 4.24b&d).

In comparison to PAAS the Bravo-Y mudstones appear to be slightly depleted in Ti, Mg, Ca, Na, K and P (Figure 4.24a). Depletion of Mg, Ca and Na in the Bravo-Y mudstones can be attributed to lesser amount of dolomite, calcite and plagioclase in these samples compared to PAAS. Note that the only sample showing a slight positive Ca anomaly is XM9 which has 3 wt% dolomite (Figure 4.11; Appendix I). Depletion in Ti and K indicate lesser amount of clay minerals (silty mudstones) in these mudstones compared to PAAS. Phosphorus depletion is the result of lesser amount of accessory phases such as apatite compared to PAAS.

The plot of major elements normalized to UCC values indicate significant depletion of Ca and Na and slight depletion of Mg, K and P. Iron and manganese show a slight enrichment compared to UCC (Figure 4.24b). Depletion of Ca and Na in these samples compared to UCC is clearly the result of chemical weathering of the source material during erosion, transport and deposition of these sediments (e.g. Nesbit et al. 1980, Nesbit and Young 1982, McLennan et al. 1993). Slight depletion of Mg, K and P compared to UCC can be attributed to the relatively small amount of clay minerals (silty mudstones) and apatite. Enrichment in Fe and Mn is the result of relatively high amount of authigenic siderite.

Trace elemental composition of the samples is fairly similar to both PAAS and UCC (Figure 4.24c&d) with the exception of Ba, Pb, Zn and Sr. Significant enrichment in Ba, Pb and Zn compared to both PAAS and UCC is clearly the result of contamination by drilling mud. Barium can be attributed to barite. However, in addition to barite other weighting additives such as galena are also commonly used. Zinc can be attributed to drilling fluid components such as zinc bromide (ZnBr_2). Slight depletion of strontium compared to UCC

can be attributed to weathering since strontium along with Ca and Na tend to be leached during chemical weathering (Nesbit et al. 1980).

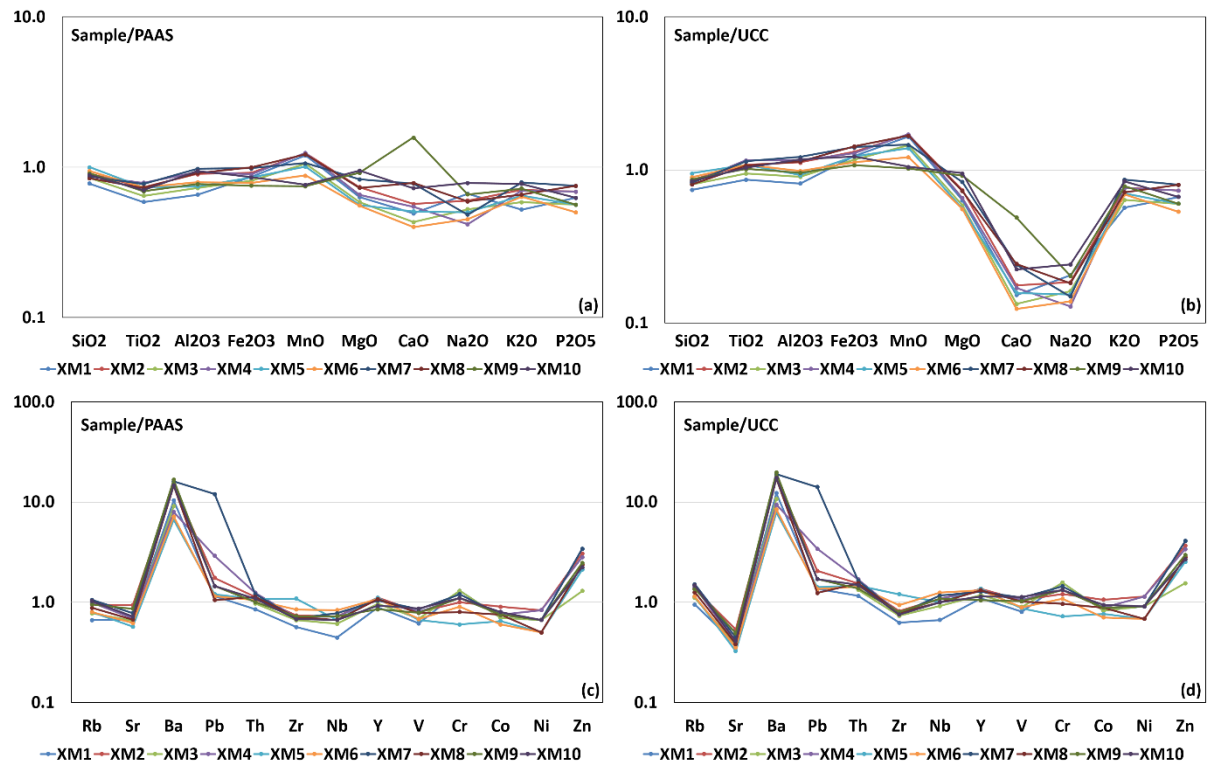


Figure 4.24. Multi element spider diagrams for Bravo-Y mudstones. Major and trace element composition normalised to post-Archean Australian average shale (PAAS; values of Taylor and McLennan 1985) and to average upper continental crust (UCC; values from McLennan 2001).

Uniform K_2O/Al_2O_3 and TiO_2/Al_2O_3 ratios of the Bravo-Y samples indicate a source area of similar bulk composition throughout their deposition. This is also supported by the relatively little variation in the ratios of low-solubility trace elements (such as Th, Hf, REEs etc.) which are generally considered inert during the sediment cycle (Taylor and McLennan 1985).

Figure 4.25 shows chondrite-normalized REE patterns of Bravo-Y mudstones. REE patterns display LREE enrichments and variable degrees of development of a negative Eu anomaly. The chondrite normalized ratio of Eu/Eu^* of mudstone samples ranges from 0.34 to 0.67 (average of 0.48). These values are close to but somewhat lower than PAAS (0.66). Since europium is not fractionated during weathering or diagenesis relative to other REE (McLennan 1989) the size of the Eu anomaly reflects the Eu anomaly in the source rocks. The chondrite normalized La_N/Yb_N ratios vary from 8.36 to 9.21 (average of 8.84). Once again these values are similar to that of PAAS (9.2). In overall, patterns like LREE

enrichment, flat HREE and negative Eu anomaly indicate that these mudstones were derived from a dominantly felsic continental source region (Bhatia 1985, McLennan et al. 1993).

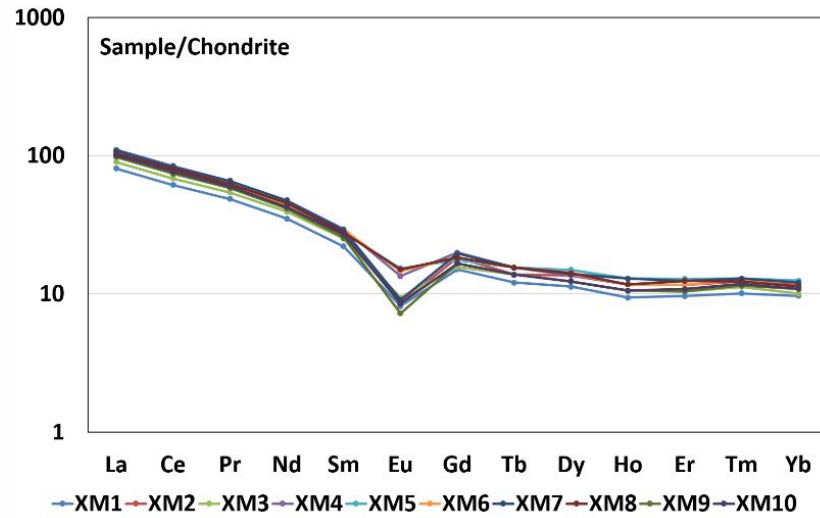


Figure 4.25. Chondrite-normalised (values of Taylor and McLennan 1985) REE patterns for Bravo-Y mudstones.

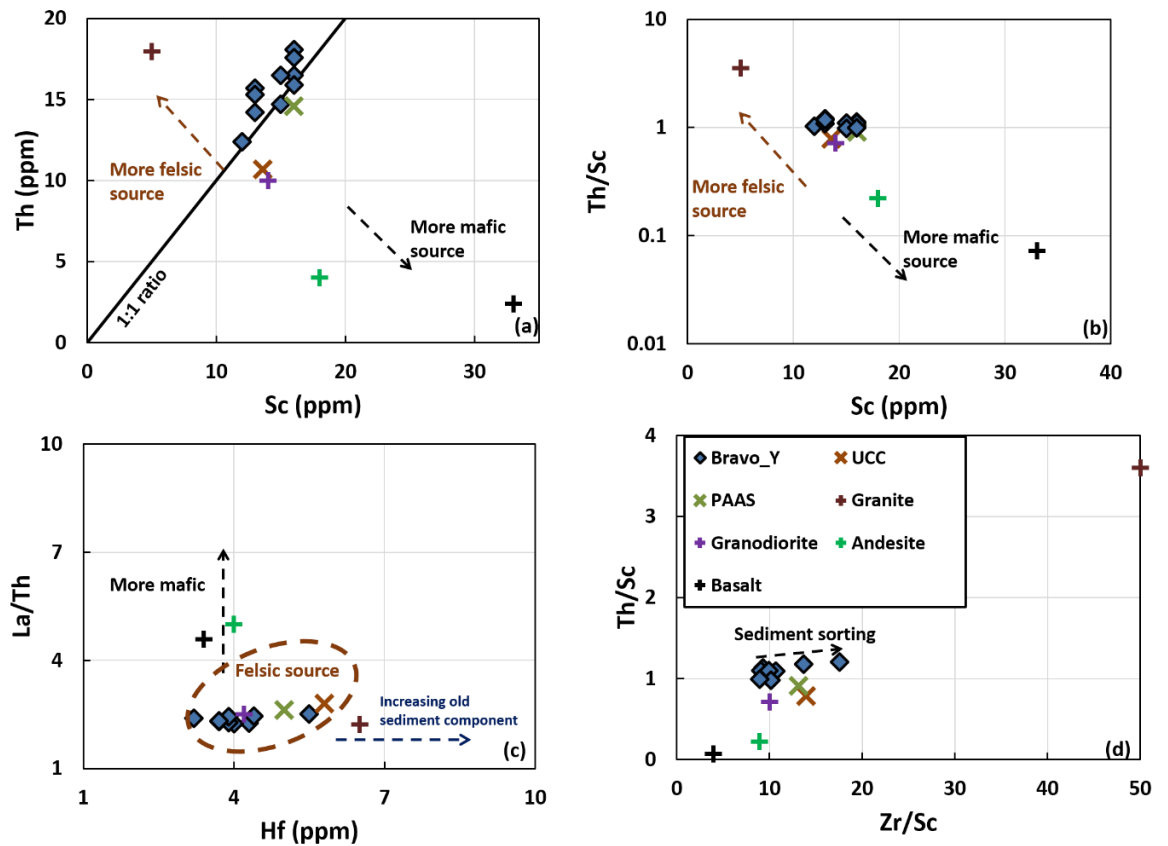


Figure 4.26. Selected trace element plots indicating the average bulk composition of the source. (a) Th versus Sc (b) Th/Sc versus Sc (c) discrimination plot of La/Th versus Hf (after Floyd and

Leveridge 1987) (d) discrimination plot of Th/Sc versus Zr/Sc (after McLennan et al 1993) monitoring sediment sorting and recycling processes. UCC, PAAS (values from Taylor and McLennan 1985, McLennan 2001) and average Phanerozoic granite, granodiorite, andesite and basalt (values from Condie 1993) are additionally plotted for reference.

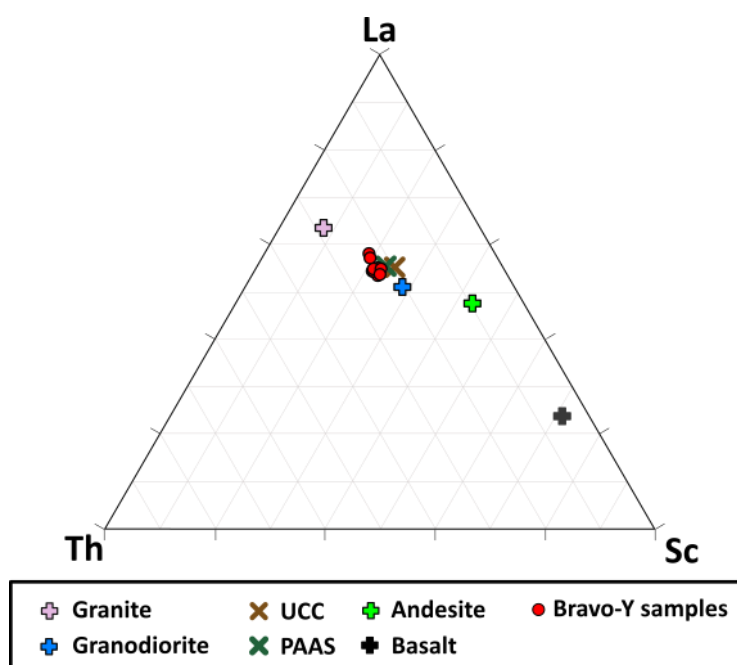


Figure 4.27. Discrimination plot of La-Th-Sc (after Bhatia and Crook 1986) indicating the average bulk composition of the source. UCC, PAAS (values from Taylor and McLennan 1985, McLennan 2001) and average Phanerozoic granite, granodiorite, andesite and basalt (values from Condie 1993) are additionally plotted for reference.

Similarly, ratios of La/Th (average of 2.35), Th/Sc (average of 1.08) and relatively large Hf contents (average of 4.03) of the mudstone samples also indicate derivation from a continental crust of largely granitic/granodioritic composition (Bhatia and Taylor 1981, McLennan et al 1993) (Figures 4.25&4.26).

Figure 4.26a&b show the ratios of Th/Sc in Bravo-Y mudstones. The Th/Sc ratio of the samples is a sensitive index of average source composition (Taylor and McLennan 1985). Rocks with mafic and intermediate compositions tend to have considerably higher Sc than do rocks with felsic compositions. This is illustrated in Figure 4.26 by showing the Th/Sc ratios for average Phanerozoic granite, granodiorite, andesite and basalt (values taken from Condie 1993) and also for average upper continental crust (UCC, values from McLennan 2001) and for post-Archean Australian average shale (PAAS, values from Taylor

and McLennan 1985). The average Th/Sc ratio in the Bravo-Y mudstones (1.08) is somewhat higher than that of PAAS (0.91) and considerably higher than that of granodiorite (0.71) and UCC (0.78). Figure 4.26c shows a plot of La/Th against Hf which also provides a useful discrimination between different source compositions. As shown in Figure 4.26c sediments derived from a dominantly felsic source region have relatively low and uniform La/Th ratios and Hf contents in the range of approximately 3-7 ppm. Erosion of ancient metasedimentary rocks will result in an increase in the Hf contents due to the release of zircon which is the main host mineral phase for Hf (Floyd and Leveridge 1987). Figure 4.26d shows a plot of Th/Sc versus Zr/Sc which can be used to monitor sediment recycling and sorting processes (McLennan et al 1993). In overall, the relatively high Th/Sc ratios and relatively low Zr/Sc ratios of the Bravo-Y samples indicates no or only minor sediment recycling. The only two samples (XM5&XM6) having relatively higher Zr/Sc ratios are the ones with the highest Si/Al ratio (Figure 4.18) indicating that this minor zircon enrichment is probably due to the presence of slightly more abundant coarse-grained material (sediment sorting).

On the discrimination plot of La-Th-Sc the samples plot close to PAAS and to the average composition of the upper continental crust (UCC) (Figure 4.27).

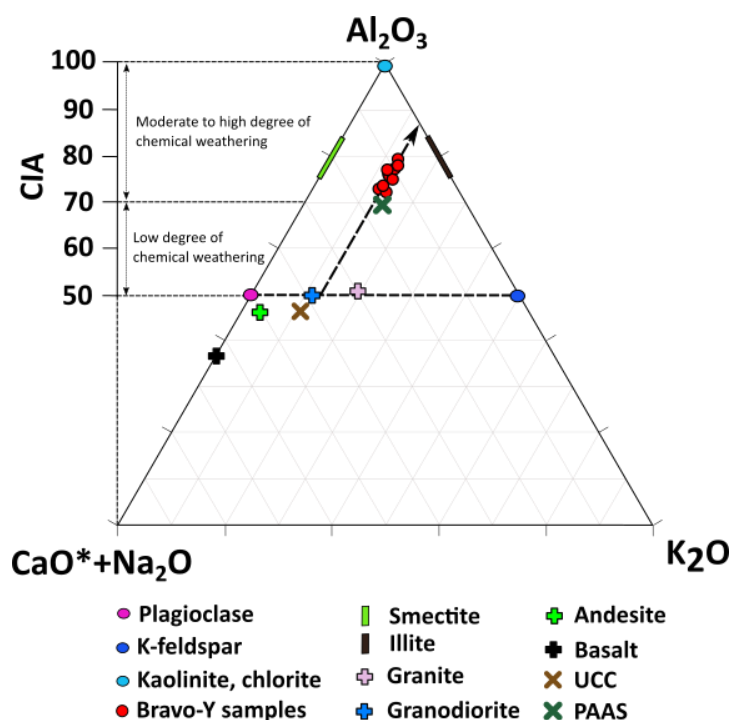


Figure 4.28. A-CN-K ($A=Al_2O_3$; $CN=CaO^*+Na_2O$; $K=K_2O$; all in molecular proportions; refer to 3.3.5 for more detail) ternary diagram of the Bravo-Y mudstone sample set with associated chemical

index of alteration (CIA) values (after Nesbitt and Young 1982). Dashed arrow represents the estimated weathering trend. Average compositions of granite, granodiorite, andesite, basalt (from Condie 1993), post-Archean Australian average shale (PAAS, Taylor and McLennan 1985), average upper continental crust (UCC, McLennan 2001) and average composition of illites and smectites are plotted for reference. Refer to text for further explanation.

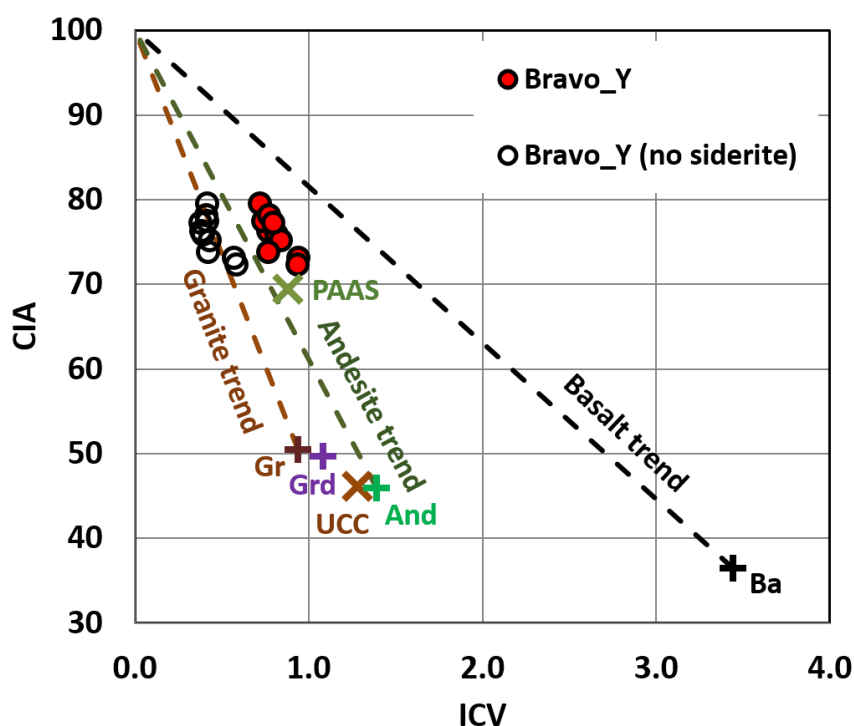


Figure 4.29. Plot of chemical index of alteration (CIA) against index of compositional variability (ICV) (after Potter et al 2005) illustrating relationships between the degree of source area weathering and original detrital mineralogy in the Bravo-Y mudstones. Dashed lines represent weathering trends. Average compositions of granite (Gr), granodiorite (Grd), andesite (And), basalt (Ba) (from Condie 1993), PAAS (Taylor and McLennan 1985) and UCC (McLennan 2001) are plotted for reference. Refer to text for further explanation.

The degree of source area weathering was quantified using the chemical index of alteration (CIA) following the method of Nesbitt and Young (1982) as described in 3.3.5. CIA values for Bravo-Y mudstones indicate moderate to high degree of chemical weathering (Figure 4.28). Bravo-Y mudstones plot as a distinct linear array in A-CN-K space as shown in Figure 4.28. A straight line through the mudstone data projects onto the feldspar join at a point which indicates the proportion of plagioclase to Kfeldspar in the source. This indicates an average composition of the source close to that of an

average granodiorite (Figure 4.28). The estimated weathering trend shown in Figure 58 is subparallel to the A-CN join and is marked by the dashed line with an arrowhead. It is extending from a composition close to granodiorite towards illite (Figure 4.28).

Figure 4.29 shows a crossplot of CIA against ICV values which would suggest evolution from an andesitic source and intermediate/mafic source composition. However, it should be noted that the ICV values of the Bravo-Y mudstones are anomalously high (> 0.7). Such high ICV would indicate the presence of a large nonclay (e.g. feldspars, mafic minerals) fraction (Cox et al. 1995), which is not supported by previous results (e.g. QXRD). The high ICV values can however be explained by the presence of authigenic siderite and high associated Fe_2O_3 content. This is illustrated in Figure 4.29 which shows the ICV values for Bravo-Y mudstones after correction for Fe_2O_3 content of the siderite (empty symbols).

Overall, inferences from major and trace element geochemistry are in accordance with the geological setting and tectonic history of the Malay Basin (refer to 4.2). The most likely provenance areas of these mudstones were the Khorat Swell to the northeast and ancestral Peninsular Malaysia to the southwest of the Malay Basin. These areas are mostly composed of granite and metamorphic rocks (Shing, 1992).

4.7.2 Mudstone mineralogy

The primary sediment composition and the early diagenetic reactions determine subsequent diagenetic pathways. Early diagenetic processes are contemporaneous with deposition and can locally affect the physical properties by cementing depositional porosity and make the mudstone locally resistant to mechanical compaction. These early diagenetic processes are typically redox processes where organic matter becomes oxidised by microbes (Aplin and Macquaker, 2011).

Sulphate reduction was locally important during early diagenesis in the studied Formation E mudstones as evidenced by the common occurrence of framboidal pyrite. Framboidal pyrite likely precipitated from iron-rich porewaters near sites of sulphide supply, usually near organic matter as a result of bacterial sulphate reduction, where sulphide production rates were high enough to reach supersaturation with respect to FeS. Euhedral pyrite likely precipitated directly from iron-rich porewaters when FeS_2 saturation was reached near sites where FeS saturation levels were not reached at the

sites of sulphide supply due to lower sulphide production rates from organic matter (Taylor and Macquaker, 2000).

The presence of siderite indicates that Fe(III) reduction was also important (at least locally) during early diagenesis (Taylor, 1998). Cementation by siderite is likely to have occurred prior to compaction as a result of bacterially mediated respiratory processes. This indicates that sites of cementation were close to the sediment-water interface for prolonged periods of times in order to allow for cementation to take place (e.g. Taylor and Macquaker, 2000, 2014). Although siderite precipitation had locally affected mudstone porosities its overall effect on porosity reduction in the studied Formation E mudstones is negligible.

The Bravo-Y CEC and clay fraction XRD results reveal a diagenetically mature clay mineral assemblage consistent with the high geothermal gradient. It should be noted that the question whether the illitic nature of the samples is depositional or diagenetic in origin cannot be comprehensively answered by this study as shallower samples were not available. However, the observed negative correlation of plagioclase with quartz and with Kfeldspar and its positive correlation with illite-smectite in Bravo-L mudstone samples does give some indication of a diagenetically mature clay mineral assemblage. Since in these mudstones sodium resides exclusively in the plagioclase feldspar (Figure 4.18e, f) positive correlation between plagioclase and illite-smectite strongly suggest that sodium was originally a constituent in the clay minerals most likely in smectites or in smectitic interlayers in illite-smectite. The lack of such correlation in Bravo-Y might be attributed to the presence of small amounts of detrital plagioclase in those samples since Bravo-Y mudstones are slightly more silt-rich. Bravo-Y mudstone samples are also more heterogeneous due to the poor quality of the provided cuttings which might be another contributing factor.

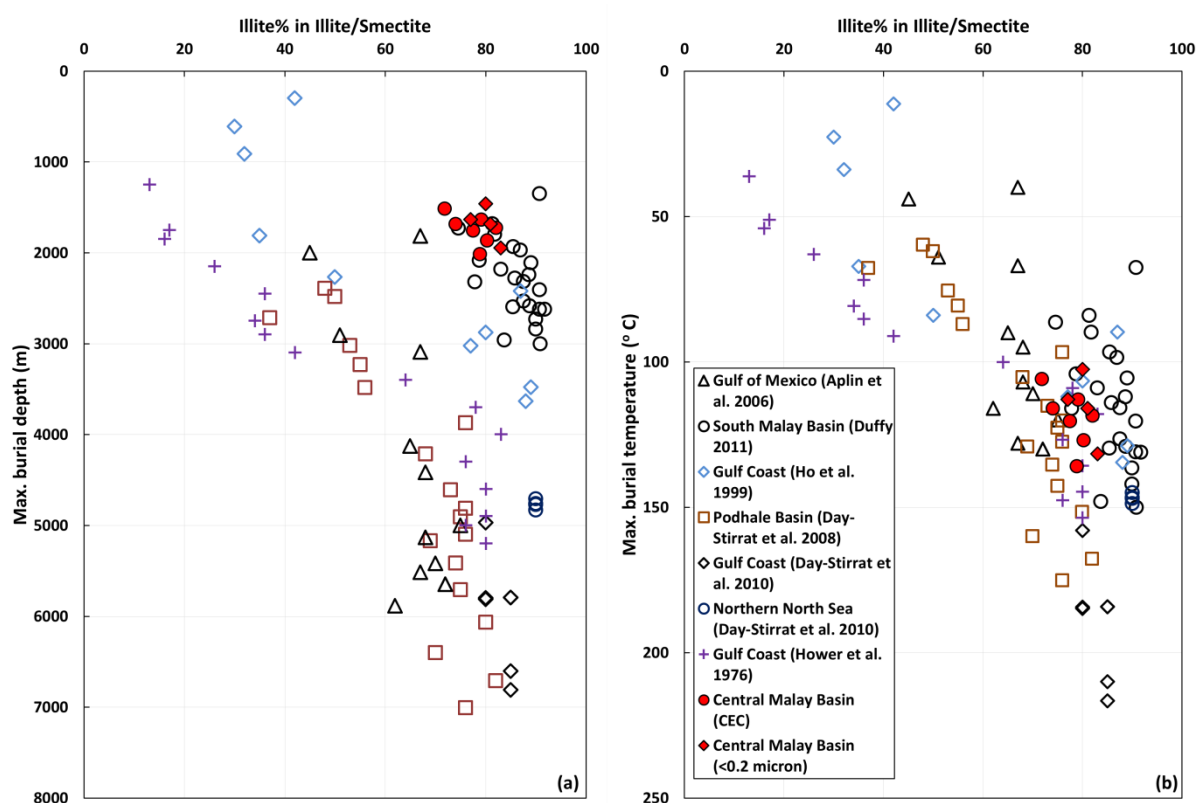


Figure 4.30. Published examples of illite % in illite-smectite with new results from the Central Malay Basin Bravo-Y well plotted against maximum burial depth (a) and maximum burial temperature (b).

Another indication which shows that clay mineral diagenesis in the Bravo-Y mudstone samples is in the final stages is the lack of pure smectite and smectitic illite-smectite, and additionally the dominance of an ordered ($R > 1$) mixed layer illite-smectite phase. As it is shown in Figure 4.30a when plotted against maximum burial depth the Central Malay Basin mudstones appear considerably more mature than those from other locations. Note that illite-smectites in mudstone samples reported from the Gulf of Mexico and Podhale Basin at similar burial depth are considerably more smectitic and are all pre-transition (R_0 to R_1). However, when plotted against temperature as opposed to burial depth the Central Malay Basin mineralogy results fit in with reported examples from different locations (Figure 4.30b).

The Bravo-Y results correlate well with clay mineralogy data from Duffy (2011) (Figure 4.30), from two south Malay Basin wells, from Formations H,I,J,K and L. The bulk mineralogy of those mudstones is fairly similar to Formation E with the only main difference being the lack of siderite from the older formations (K and L) which were

deposited in a fluvial-lacustrine environment. The illitic nature of those South Malay mudstones was interpreted to be a result of diagenesis based on the presence of a glycolated 16.8 Å peak (expandable/smectitic interlayer) in the shallowest samples. The presence of smectitic layers in the shallowest South Malay samples and the slightly more illite % in illite-smectite in the deeper samples (Figure 4.30) compared to Formation E mudstones can be attributed to differences in geothermal gradient (present day geothermal gradient in the South Malay Basin is 45-50°C/km) in combination with differences in starting mineralogy (e.g. smectite content, Kfeldspar content) and age. In overall the mineral composition of the studied Formation E mudstones show limited variation and is consistent throughout with a diagenetically mature assemblage in which smectite has been illitized.

4.7.3 Evaluation with wireline log-based compaction profiles and implication for overpressure development

Figure 4.31 shows smoothed cosine-weighted density and sonic log responses through the mudstone intervals for wells Bravo L, X&Y. Below the top of Formation Unit D sonic transit time decreases and density increases monotonously with increasing depth until the top of overpressure in all three wells indicating ongoing compaction. Small fluctuations in the smoothed data are the result of changing lithology, most likely related to variations in grain size, heavy mineral and/or clay mineral content. These changes cannot be resolved by the mineralogical results presented in 4.6.1 due to the poor resolution. Small lithological changes cannot be seen since the presented results represent averaged mineralogical composition of several meters of mudstones.

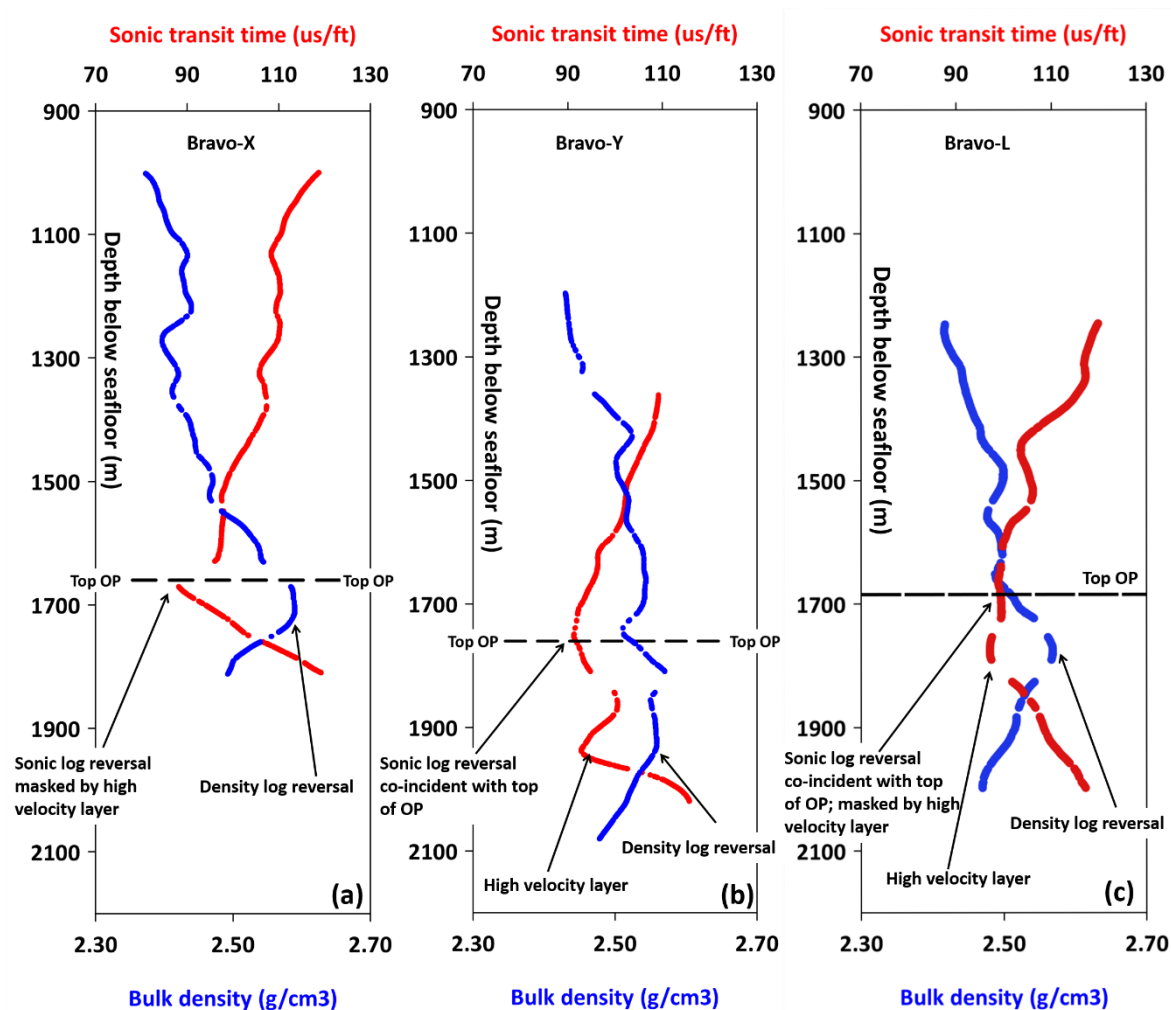


Figure 4.31. Smoothed density (blue) and sonic (red) logs through the mudstone intervals for (a) Bravo-X, (b) Bravo-Y and (c) Bravo-L. Top of overpressure is indicated by horizontal black dotted line.

The onset of overpressure is associated with rapid increase of the sonic log response (sonic reversal) while density continues to increase below the top of overpressure in all the wells which is indicative of unloading. Note that the sonic reversal is slightly masked in Bravo-X and L due to the presence of an approximately 15-20 m thick mudstone layer with anomalously low sonic transit time (“high velocity layer”; Figure 4.31a,c and 4.32a,c). Similar layers can be observed in Bravo-Y although slightly below the top of overpressure (Figure 4.31b). High velocity layers are shown in Figure 4.7c from Bravo-Y prior to mudstone discrimination and smoothing. Without prior evidence, they might be interpreted as evidence for lateral drainage, but no other log types show similar

excursions. The nature of these layers is uncertain because of the lack of available mudstone samples from these depth intervals.

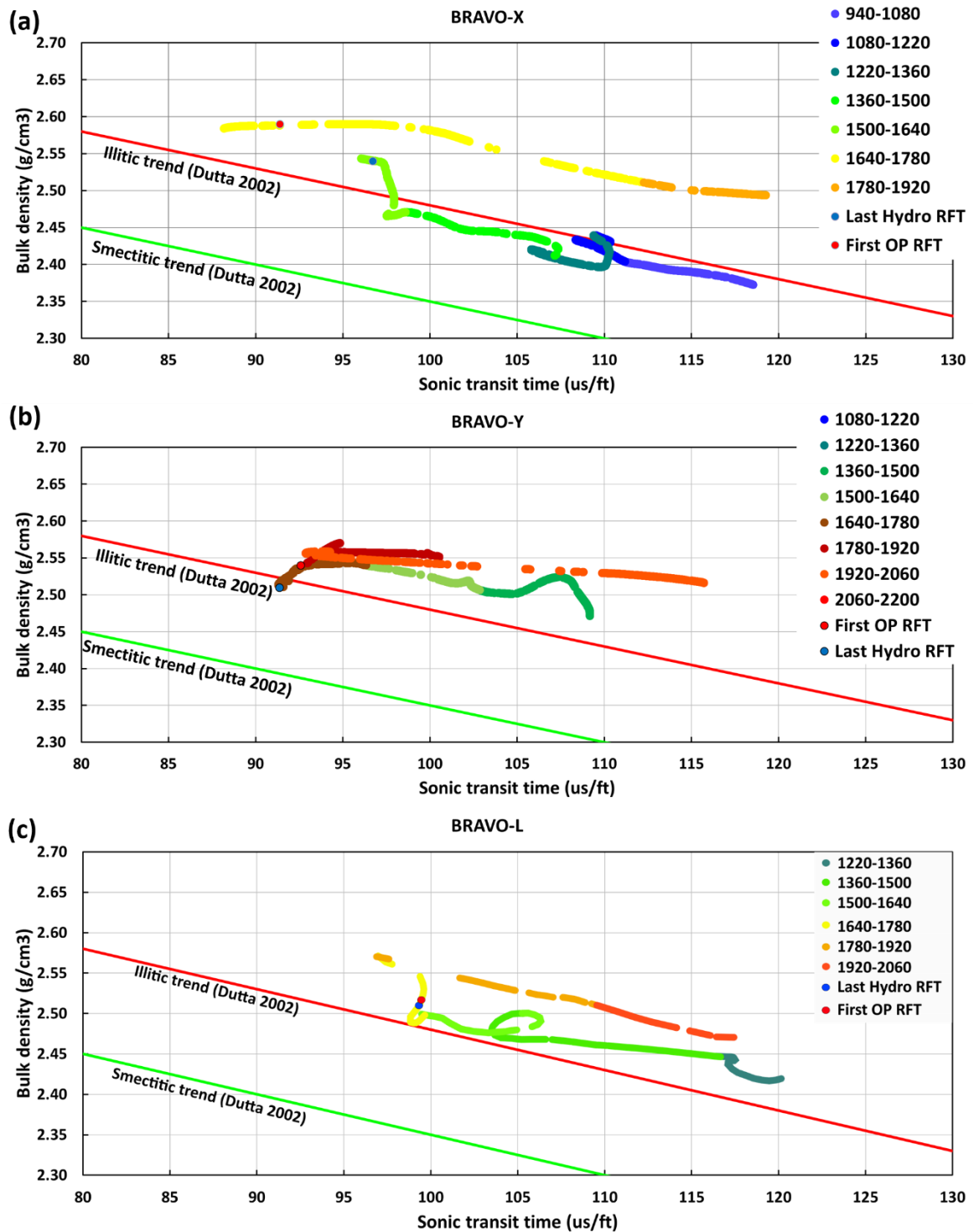


Figure 4.32. Sonic-density crossplots for Bravo-X (a), Bravo-Y (b) and Bravo-L (c) with smoothed logs. Colour coding is by depth below seafloor (m). Blue and red dots denote the last hydrostatic RFT and the first overpressured RFT respectively. Red and Green line is the illitic and smectitic line from Dutta (2002).

Possibilities include cementation by carbonate or silica, however if the cause of the excursion had been carbonate, an excursion on the resistivity log would also be expected and there is none.

Figure 4.32 shows crossplots of smoothed sonic transit time against smoothed density in the studied mudstone intervals for Bravo-X, Bravo-Y and Bravo-L. Dutta's (2002) reference lines for smectite rich and illite rich mudstones are also shown. At shallow depth, the sonic-density path is a linear trend in all three wells which runs parallel with the illitic line. The sonic-density path in Bravo-Y is slightly above the illitic line (Figure 4.32b). This relatively high density may be due to the siderite content and illite dominated clay mineralogy. Changes in the siderite content may also explain the upward step in density from 2.47 g/cm³ to 2.54 g/cm³ seen on the crossplot for Bravo-X (Figure 4.32a) but cannot be confirmed in the absence of mineralogical data. A similar upward step can be seen on the crossplot of Bravo-L (Figure 4.32c) however its interpretation is unclear since it is located below the top of overpressure and might be the result of unloading. There is a clear trend of increasing sonic transit time with (initially) constant density associated with the top of overpressure in Bravo-X and Bravo-Y. The same trend is masked in Bravo-L due to the presence of a high velocity layer (Figure 4.32c). This trend is typical of severe unloading due to rapid increase in pore pressure. Fluctuations and various switchbacks on the crossplot trends are attributed to lithological variation.

There are clear reversals in the density logs too, however in all three wells these are below the top of present-day overpressure (Figures 4.31 and 4.32). Since the bulk mineralogy results show consistent mineralogy with no apparent depth variation, density reversals are most easily explained as retention of higher porosity from early overpressure generated by disequilibrium compaction. Another possible interpretation of density reversal would be opening of microcracks associated with incipient hydrofracturing (e.g. Ramdhan and Goult, 2011). However, opening of microcracks is only expected in the zone of hard overpressure where the pore pressure is approximately equal to the lithostatic stress. Also, the opening of microcracks on its own would not be able to explain the observed reduction in density, equivalent to a porosity increase of approximately 5% (Goult et al., 2012)(Figure 4.33).

In overall, the following interpretation can be drawn based on the wireline logs. Early overpressure was generated by disequilibrium compaction and subsequent development of strong overpressure is due to unloading.

According to Madon (2007) the primary cause of overpressure in the Central Malay Basin is disequilibrium compaction. Similar conclusion has been reached by Hoesni (2004, 2015) who also suggested that overpressure generation by disequilibrium compaction was enhanced by clay diagenesis and associated chemical compaction. However sharp pressure ramps into high overpressure –such as those observed in these three wells— are generally considered to be the result either of gas generation or load transfer or lateral/vertical pressure transfer (Swarbrick et al., 2002). Clay diagenesis and load transfer are not viable pressure generating mechanisms in the Formation E mudstones based on the observation that illitization is already in its final stages at a depth of ~1400 m below seafloor. Furthermore, the present-day top of overpressure is at considerably greater depth and shows no correlation with clay mineralogy. The temperature is high enough (>120 °C) at the top of overpressure for gas generation to be a viable pressure generating mechanism. In addition, gas may be migrating upwards through conduits from deeper sources. This is further supported by the existence of a large gas cloud observed on seismic sections adjacent to the studied wells (Figure 4.6). Although clay diagenesis did not contribute directly to effective stress reduction, chemical compaction likely resulted in anomalously low mudstone porosities (see also 4.7.4). This might have contributed indirectly to overpressure generation by creating a more effective seal.

In addition to this, at the present day, Formation D is ~100 m shallower in Bravo-L and Bravo-X where the top of overpressure is also ~100 m shallower than in Bravo-Y (Figure 4.8), suggesting that there may be a local stratigraphic control on the depth to the top of overpressure.

4.7.4 Implications for mudstone compaction processes

Figure 4.33 shows the calculated density porosity of Bravo-Y mudstones in comparison with Mondol et al's. (2007) experimental mechanical compaction curve for 100% kaolinite and with Yang and Aplin's (2004) compaction curve for mudstone with 40% clay content. The experimental compaction curve of pure kaolinite was selected since it represents the

lowest porosities achieved by experimental mechanical compaction of clays and silt-clay mixtures. Pure illite or mixtures of silt and clays would be a closer representation of the Bravo-Y mudstone mineralogy however these all have considerably higher porosities than pure kaolinite (Mondol et al., 2007; Mondol, 2009a). Yang and Aplin's (2004) relationship between porosity and effective stress was chosen to represent real life mechanical compaction since it was derived from natural mudstone porosity data and it is based on solid soil mechanical principles.

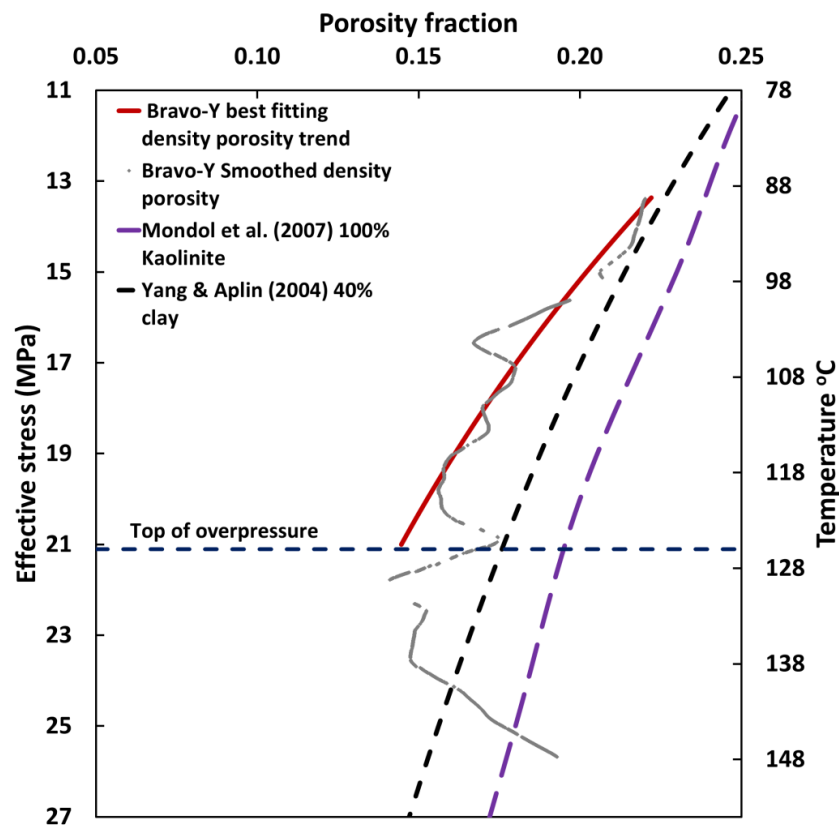


Figure 4.33. Central Malay Basin Bravo-Y density porosity (grey curve) plotted against calculated hydrostatic vertical effective stress. The density reversal near TD is interpreted as a result of higher porosity due to early overpressure generated by disequilibrium compaction. Red curve – the normal compaction curve fitted to the mudstone density data where pore pressure is hydrostatic. Dashed blue and black trends – experimentally compacted kaolinite (from Mondol et al. 2007) and mechanically compacted mudstone with 40% clay content (from Yang & Aplin 2004).

Total clay mineral content as estimated by QXRD was used as a proxy for the mass fraction of particles less than two microns and the average clay mineral content in the studied samples was chosen to represent the whole working interval. An exponential curve was fitted by least squares through the computed density porosity in the

hydrostatically pressured interval in the form of equation 9. Note that the calculated density porosity of the Bravo-Y mudstones is lower, and that porosity is lost considerably faster than on either of the mechanical compaction trends. Considering that density porosity was calculated by assuming no organic matter and that consequently real mudstone porosities might be considerably lower (refer to 4.6.6) this observation strongly suggests that there are compaction mechanisms at work in the studied mudstone section of the Central Malay Basin that are not included in these purely mechanical compaction models. Similar observations have been made by Duffy, (2011) in the South Malay Basin who showed that the measured total porosities of Formation H,I,J,K and L mudstone samples are considerably lower than most previously published compaction trends from other sedimentary basins. Reported porosities of those mudstones are similar to calculated Formation E density porosities.

These observations suggest that illitization during ongoing compaction resulted in anomalously low porosities compared to solely mechanically compacted mudstones. Even though illitization has reached a plateau (>80% illite in mixed-layer illite-smectite) at depths greater than 1400 m below seafloor, porosity continues to decrease with depth in all three cases. Perhaps these chemically altered mudstones continue to compact mechanically, and/or there are ongoing mineralogical changes which cannot be resolved in our XRD results for the reasons advanced by Srodon et al. (2000) (see 2.4) but which continue to allow chemical compaction to occur. However, inferences made based on the wireline logs (see 4.7.3) indicate that early overpressure was generated by disequilibrium compaction, with top of overpressure at ~1300-1400 m depth below seafloor (Figures 4.22 and 4.33) when they were subject to the maximum effective stress they have experienced during their burial history. At these depths (i.e. the depths of top of overpressure ~1300-1400 m depth below seafloor) temperatures were already higher than 90°C thus early overpressure generated by disequilibrium compaction was able to preserve higher porosity in diagenetically mature and fully illitized mudstones.

4.8 Summary and conclusions

Previous studies have observed anomalously low porosities in mudstone buried to the diagenetic regime. These mudstone porosities are considerably lower compared to what would be predicted by purely mechanical compaction models. These observations indicate that chemical diagenetic changes can cause further porosity loss in addition to the mechanical compaction processes (e.g. Bjørlykke 1998).

Complementing the observations of Bjørlykke and Høeg (1997) and Bjørlykke (1998), Duffy (2011) found that porosities in diagenetically mature Miocene mudstones in the South Malay Basin were anomalously low when compared to existing mechanical compaction models.

Evidence presented here shows that Miocene mudstones in the Central Malay Basin have considerable lower porosities than the experimentally compacted kaolinite-smectite and silt-kaolinite mixtures of Mondol et al. (2007) and Mondol (2009), respectively. These porosities are also low compared to the compaction trend of Yang and Aplin (2004) for mechanically compacted mudstones with similar clay content. Bulk QXRD results indicate diagenetically mature (illitized) mudstone assemblage in the studied Central Malay Basin wells. These results are in agreement with previous findings and suggest that illitization during ongoing compaction results in anomalously low porosity compared to solely mechanical compaction.

Previous studies have also observed the lack of a relationship between porosity and effective stress in deeply buried, diagenetically mature mudstones (Hermanrud et al., 1998; Teige et al., 1999) (refer to 2.6 and 2.7).

In contrast, evidence presented here suggests that diagenetically mature, Miocene mudstones in the Central Malay Basin continue to compact mechanically with increasing effective stress at temperatures above 100°C. Trends in Figure 4.33 indicate that the effects of disequilibrium compaction have been clearly preserved in these mudstones.

These observations appear to contradict the stress independent “non-mechanical” chemical compaction model of Bjørlykke and Høeg (1997) and Bjørlykke (1998) and provide strong evidence in favour of continued mechanical compaction in diagenetically mature siliciclastic mudstones above 100°C.

Chapter 5

Overpressure generation as a result of clay mineral diagenesis in Lower Cretaceous mudstones on the Halten Terrace, offshore mid-Norway

5.1 Introduction

According to the stress independent chemical compaction model of Bjørlykke and Høeg, (1997), mudstone compaction below 2-3 km ($>70^{\circ}\text{C}$) is mainly chemical, involving dissolution and reprecipitation of minerals. Implicit in this model is that overpressured mudstones at depths where chemical compaction is dominant should not be expected to have significantly higher porosity than normally pressured mudstones. In contrast, according to the chemically enhanced mechanical compaction model (refer to 2.6) the porosity of diagenetically altered mudstones depends on both effective stress and the temperature history, thus mechanical compaction does not become negligible at temperatures above $\sim 100^{\circ}\text{C}$. These assumptions can be tested with carefully selected real life sample and datasets.

Lower Cretaceous mudstones on the Halten Terrace, offshore mid-Norway provide an ideal sample set with which to study the processes of chemical compaction in an overpressured regime. These mudstones are buried to a depth of 2 to 4 km below sea floor corresponding to a temperature range of $80\text{-}160^{\circ}\text{C}$. They are at maximum burial depth at the present day. They are overpressured, with pore pressure increasing gradually from near hydrostatic pressure towards the lithostatic gradient, whilst showing very little lateral variation from well to well.

Previous studies investigating the cause of overpressure suggested that these mudstones were likely to have been hydrostatically pressured prior to the geologically recent rapid deposition of Plio-Pleistocene glaciogenic sediments due to the limited amount of Cenozoic burial before 3 Ma (Skar et al., 1999; O'Connor et al., 2012). In addition to this, several studies looking at pore pressure and wireline log data argued that the magnitude of present day overpressure in the Cretaceous strata cannot be explained solely by disequilibrium compaction due to rapid Plio-Pleistocene burial and attributed the present day overpressure to the combination of disequilibrium compaction and clay mineral diagenesis (O'Connor et al., 2012; C Sargent et al., 2015; Goult et al., 2016). These findings provided the basis for further investigation.

Mudstone samples, pore pressure and well log data were provided by the Norwegian Petroleum Directorate. Mudstone samples were collected from nine wells (6507/6-2, 6507/2-3, 6406/2-3, 6407/10-2, 6506/3-1, 6506/11-3, 6607/5-1, 6506/11-2, 6506/11-4S). Textural, mineralogical and chemical properties of the samples were analysed and compared with physical properties such as porosity measured on the samples and derived from well log responses. The key aim was to assess the role of clay mineral diagenesis in overpressure generation in the Cretaceous mudstones on the Halten Terrace, offshore mid-Norway.

This chapter details these results following a brief introduction to the geological history of the Halten Terrace, offshore mid-Norway.

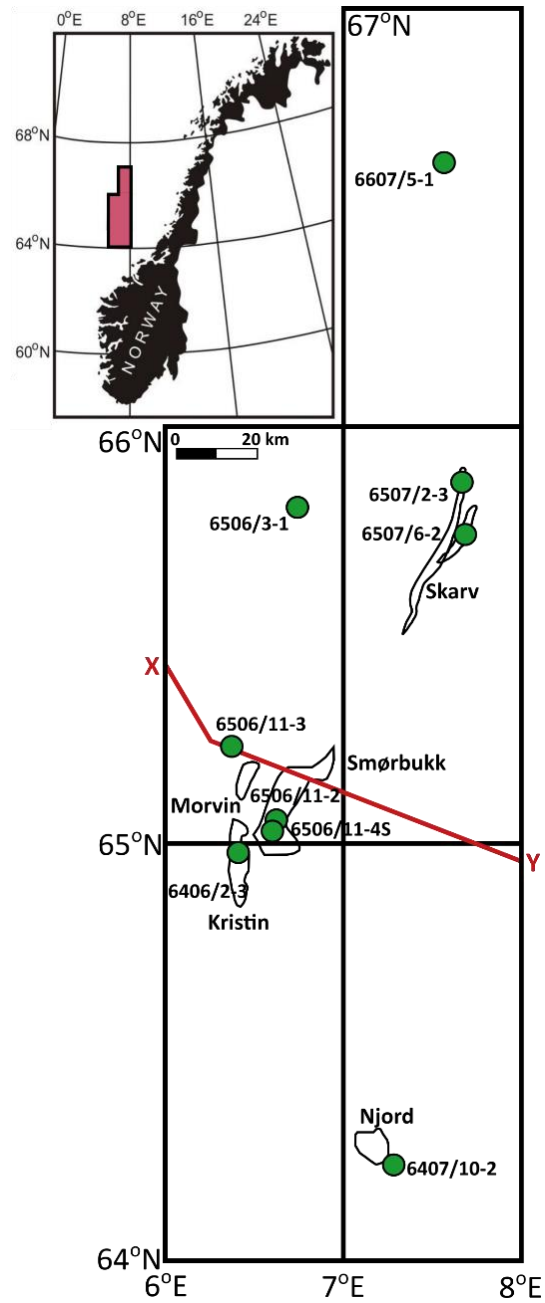


Figure 5.1. Location map of the study area, offshore mid-Norway (modified after Goultly et al., 2016) with locations of the studied wells. The XY line marks the location of the geoseismic section shown in Figure 5.3.

5.2 Geological background

The Halten Terrace is located between 64° and 66° N on the Norwegian shelf, offshore mid-Norway (Figure 5.1). It is situated between the Trøndelag Platform which lies to the east and the Vøring Basin which lies to the west (Figure 5.2). It is a highly prospective geological province in the Norwegian Sea with several giant HC accumulations which are mostly located in tilted Jurassic fault blocks.

Present day structural configuration of the Norwegian Sea continental margin is the combined result of multiple rift events in the Early-Middle Devonian, Carboniferous, Late Permian-Early Triassic, Jurassic-Early Cretaceous and Late Cretaceous-Palaeocene (Blystad et al., 1995). Major, regional structural elements were created by extensional tectonics related to Devonian to Early Cretaceous rifting events. The last major rift episode was related to the opening of the North Atlantic Ocean.

The Halten Terrace is a structural element involving Jurassic and older sediments that developed during a Jurassic-Early Cretaceous rift episode (Blystad et al., 1995). It is bounded to the west by the Klakk Fault Complex and to the east by the Bremstein Fault Complex which are separating it from the Vøring Basin and from the Trøndelag Platform respectively (Figures 5.2 and 5.3). Following the Jurassic-Early Cretaceous rift episode the Cretaceous period was a time of tectonic quiescence with post-rift thermal subsidence until the onset of the Late Cretaceous rifting. However, some structural features developed during this period due to the mobility of the underlying Triassic evaporites. The initial topographic relief of the rifting episode was largely levelled in the Santonian thereby causing the Early Cretaceous depocenters to merge into a wider depocenter (Figure 5.3) (Færseth and Lien, 2002).

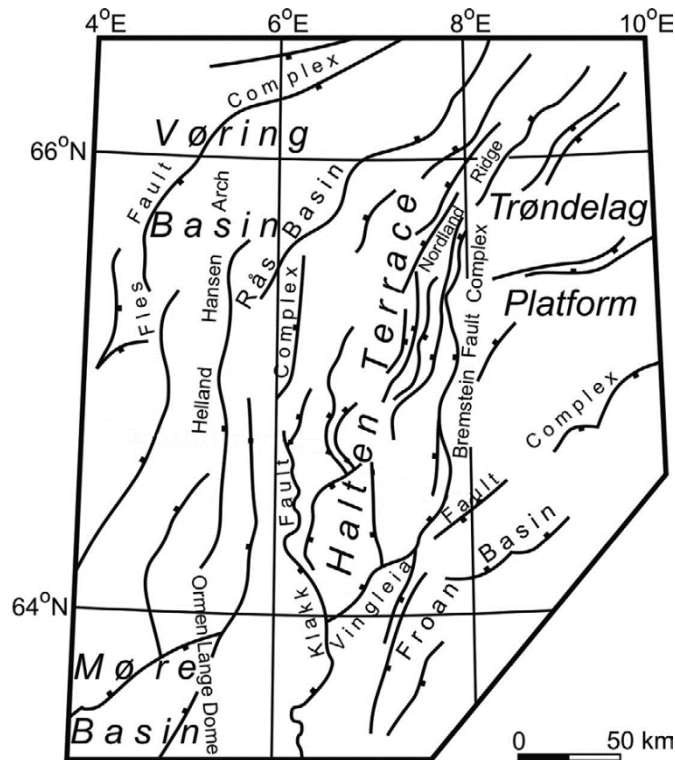


Figure 5.2. Structural elements in the Halten Terrace area (modified after Cicchino et al., 2015)

The period of tectonic quiescence was ended with the start of a new rift episode in the Early Campanian which resulted in regional uplift and created an unconformity across the Vøring Basin (Brekke et al., 1999). This was followed by continental break-up which culminated with the final opening of the North Atlantic. Continental break-up resulted in the eruption of basaltic lavas in the Late Palaeocene to Early Eocene times. Tectonic compression in the middle Miocene created arches and domes and late Pliocene-Pleistocene uplift of mainland Norway caused westward tilt and erosion (Stuevold and Eldholm, 1996).

Throughout the Early and Middle Jurassic laterally extensive sandstones of deltaic to shallow marine origin were deposited interbedded with mudstones in the Halten Terrace area. These are overlain by the open marine mudstones of the Middle Jurassic Melke Formation and the Upper Jurassic Spekk Formation each reaching around 100m thickness at the Halten Terrace (Figure 5.4) (Dalland et al., 1988).

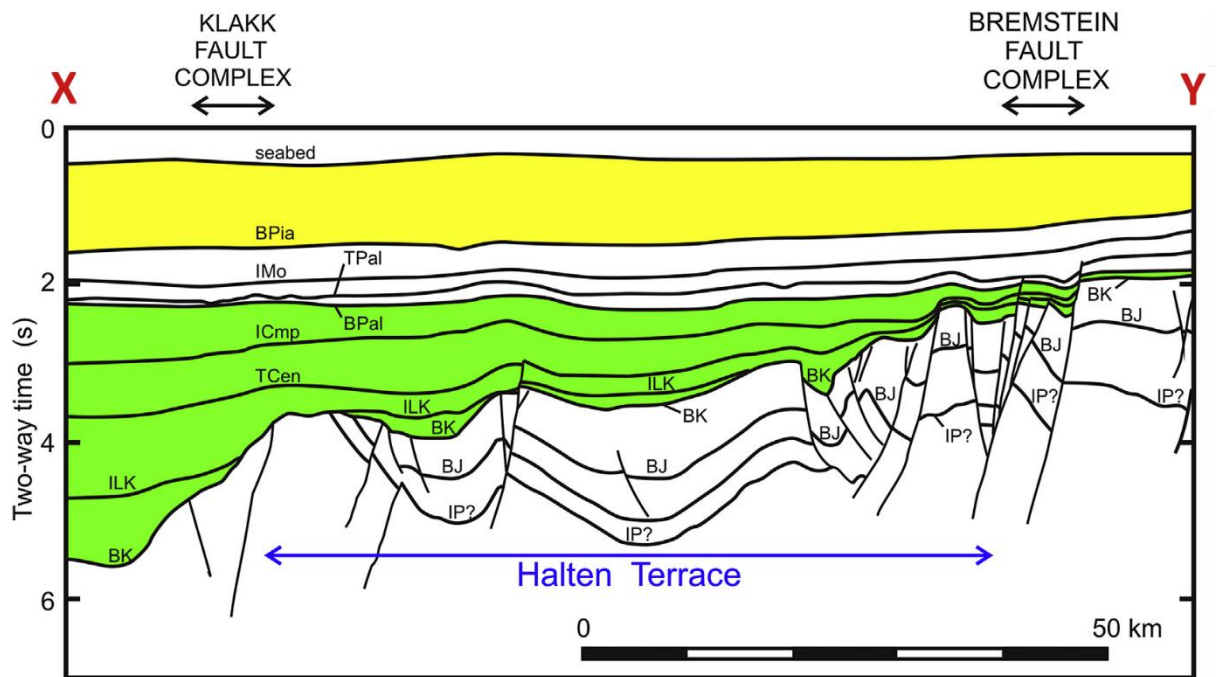


Figure 5.3. Geoseismic section along profile XY (see Figure 65 for location). Key picked horizons: BPia – Base Upper Pliocene; IMo – Intra Miocene; ; TPal – Top Paleocene; BPal – Base Paleocene; ICmp – Intra-Campanian; TCen – Top Cenomanian; ILK – Intra-Lower Cretaceous; BK – Base Cretaceous; BJ – Base Jurassic; IP? – Intra-Permian(?). The Lange Formation lies between the Top Cenomanian and Base Cretaceous horizons. The Kvitnos Formation immediately overlies the Top Cenomanian horizon (from Goulty et al., 2016).

The Cretaceous, post-rift sediments are dominated by mudstones which were deposited in a relatively deep marine palaeo-environment (Dalland et al., 1988). Turbidite sandstone bodies — such as the Lysing Formation which is coeval with the youngest mudstones of the Lange Formation (Figure 5.4) — punctuating the mudstones have become increasingly important as exploration targets. The Lyr Formation consists of interbedded marls and calcareous mudstones deposited under open marine conditions. Where it is present, it marks the base of the Cretaceous sequence. It is typically less than 100 m thick at the Halten Terrace.

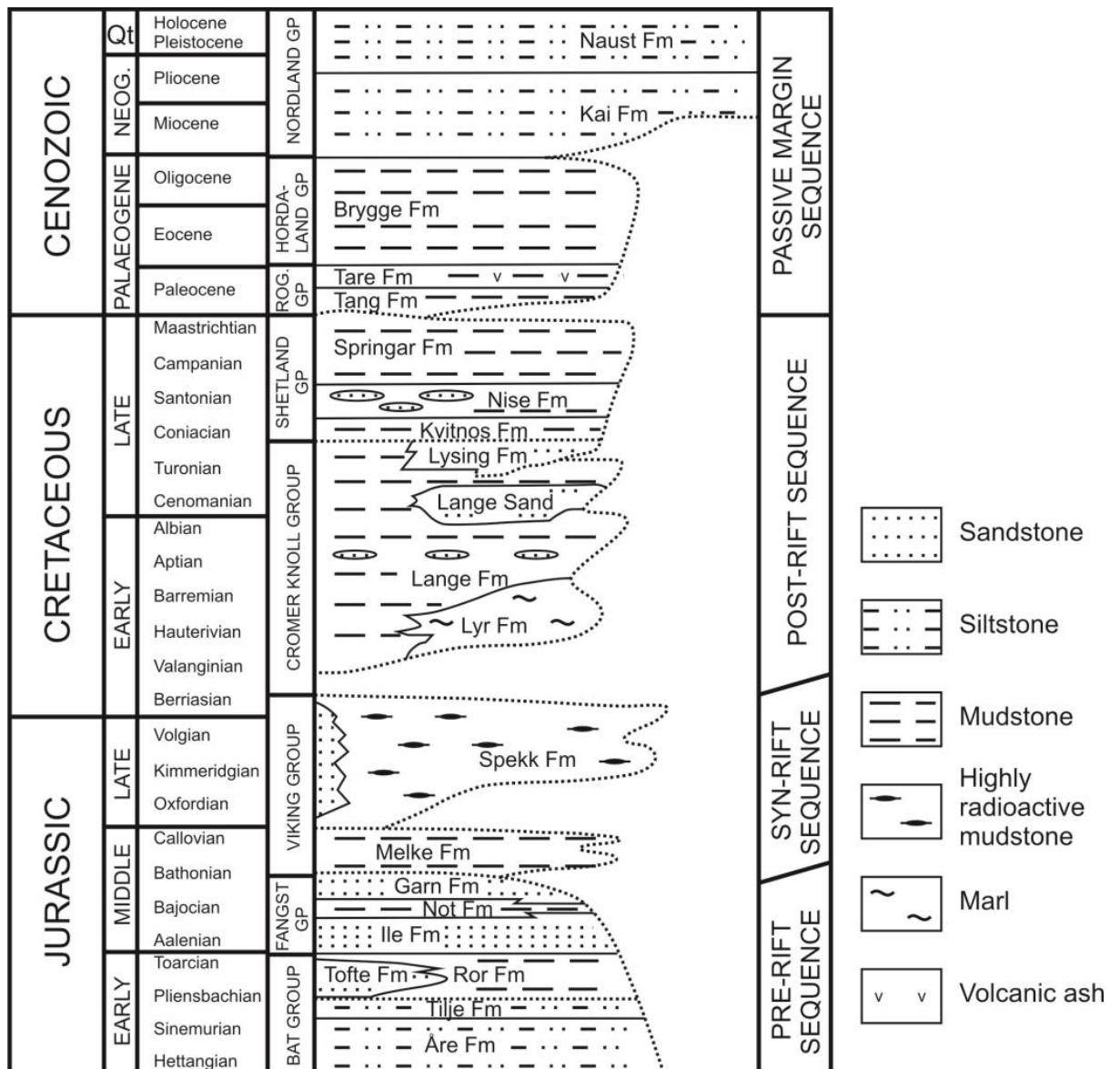


Figure 5.4. Chronostratigraphy and lithostratigraphy of the Halten Terrace area (from Cicchino et al., 2015).

The regionally extensive Lange Formation mostly comprises mudstone, with a few stringers of limestone in the lower part of the formation and several sandstone members in the upper part. At the Halten Terrace it has a maximum recorded thickness of 1300 m. The Kvitnos, Nise and Springar formations are predominantly claystones interbedded with stringers of carbonate and sandstone (Figure 5.4). At the Halten Terrace the Kvitnos Formation has a thickness of around 500 m. The overlying Nise and Springar formations have a combined thickness of only about 100-200 m.

The Palaeocene Rogaland Group (Tang and Tare formations) consists of deep marine claystones with thin siltstone beds and tuffs deposited by sub-aerial volcanism associated with the opening of the North Atlantic. These mudstones contain significant amount of smectite (Thyberg et al., 2000). The two formations have a combined thickness of around 130 m across the Halten Terrace. The Tertiary Hordaland Group (Brygge Formation) is composed of claystones with few stringers of sandstone, siltstone, limestone and marl deposited in an open marine environment. The Brygge Formation is 450 m thick in the type well, 6407/10-3. The Tertiary-Quaternary Nordland Group (Kai and Naust formations) consist of alternating claystone, siltstone and sandstone deposited in marine environment. The early-Miocene-late Pliocene Kai Formation comprises alternating beds of claystone, siltstone and sandstone and is around 270 m thick across the Halten Terrace. The Naust Formation comprises glacially derived material of alternating grey clay and poorly sorted sand, with a few layers of very coarse sand towards the top of the formation (Dalland et al., 1988). The age of the Naust Formation is late Pliocene-present (Ottesen et al., 2009), however it was mostly deposited between 2.7 and 1.7 Ma in a series of east-to-west prograding wedges (Rise et al., 2005) and can be up to 1300 m thick in the Halten Terrace area.

5.2.1 Overpressure distribution

At Haltenbanken, the top of overpressure is encountered in the Paleogene formations at a depth of around 2.3 km below sea surface. The dominant lithology in these formations is mudstone and overpressure build-up within them coincide with a high smectite content (Peltonen et al., 2008) which tend to reduce permeability. Overpressure in the Paleogene formations has been attributed to disequilibrium compaction due to the rapid deposition of the Naust Formation (Hermanrud et al., 1998; Skar et al., 1999; O'Connor et al., 2012).

Sparse pressure measurements within the Cretaceous formations show fairly constant fluid pressures in the upper Cretaceous and gradually increasing pore pressures in the lower Cretaceous formations with little lateral variation across the Haltenbanken (Figure 69) (Skar et al., 1999; O'Connor et al., 2012). Overpressure in the Cretaceous mudstones

have been attributed to the combination of disequilibrium compaction and clay diagenesis (O'Connor et al., 2012) (see also 5.3).

Overpressure in the Jurassic formations vary considerably across the Halten Terrace (Hermanrud et al., 1998). In the west of the Halten Terrace Lower and Middle Jurassic sandstones are highly overpressured. In contrast, pore pressures in the same formations at the eastern part are near hydrostatic. These two pressure cells are baffled by a north-south fault system. A third pressure cell with moderate overpressure has also been recognised (Hermanrud et al., 1998). The Jurassic formations sub-crop at the seabed to the east, near the Norwegian coast, thereby providing an obvious pathway for lateral reservoir drainage. Gas generation (Vik et al., 1991), lateral transfer of fluids from the Vøring Basin across the Klakk Fault system (Skar et al., 1999) and clay diagenesis (O'Connor et al., 2012) has all been proposed as possible overpressure generating mechanisms.

The Jurassic pressure system is baffled from the Cretaceous formations by the Upper Jurassic mudstones of the Melke and Spekk Formations (Figure 5.4).

5.3 Cretaceous overpressures, maximum burial temperatures and mudstone porosities

Figure 5.5 shows a multi-well pressure-depth plot for pressure measurements in the Cretaceous formations. These measurements were taken in sandstones within the Cretaceous formations and are thought to be representative of the pressures in the mudstones. This is because these sandstones are isolated within the mudstones and there is no evidence for lateral drainage such as marked reduction in overpressure along drainage pathways or shoulder effects on well logs (O'Connor et al., 2012). Overall, pressure measurements are sparsely distributed and imply little lateral pore pressure variation along the Halten Terrace.

Overpressures within the Upper Cretaceous Springar, Nise and Kvitnos formations are usually estimated from mudweights used in drilling. Only two direct measurements are available towards the base of the Kvitnos Formation (Figure 5.5). Direct RFT and DST measurements made in the Lysing Formation and in the sandstone members of the Lange

porosity values at that depth. High porosity wells have porosity in excess of 18%, intermediate porosity wells have porosity between 18-16% and low porosity wells have porosity less than 16% at 2700 m depth below seafloor. They suggested that the lateral variation in porosity is the result of lateral variations in the efficacy of pore water escape following rapid Plio-Pleistocene burial. They also proposed that lateral variations in overpressure may have been greater immediately after the deposition of the Naust Formation and have since been reduced by lateral fluid flow. Their proposal was later confirmed by the pore pressure interpretation of Sargent et al. (2015).

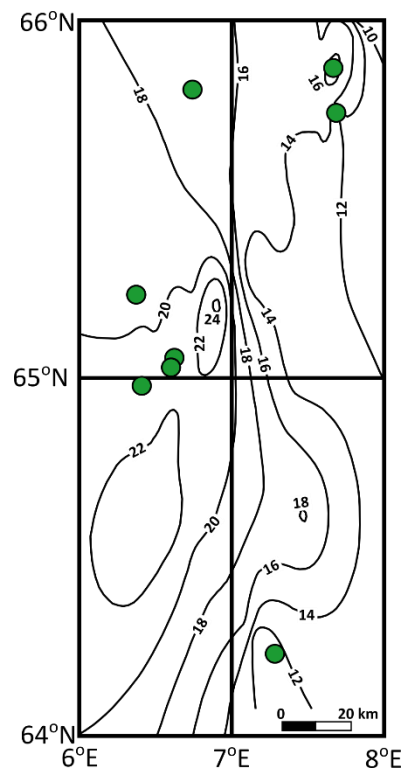


Figure 5.6. Spatial variation of the density log porosity (%) at a common depth of 2700 m below seafloor in the Haltenbanken study area as reported by Cicchino et al. (2015)

Based on these findings the stratigraphic interval from the top of the Kvitnos Formation to the base of the Lange Formation was chosen for this study, although mudstone samples were almost exclusively collected from the Lower Cretaceous Lange Formation. Mudstone samples were collected from nine wells across the Halten Terrace in order to represent the full range of the reported density porosity variation (Figure 5.6).

With the only exception of well 6407/10-2 located in the Njord Field (Figure 5.1), where sediments might have experienced some uplift in the late Quaternary, Cretaceous

mudstones are at their maximum burial depth at the present day in all of the studied wells (Cicchino et al., 2015).

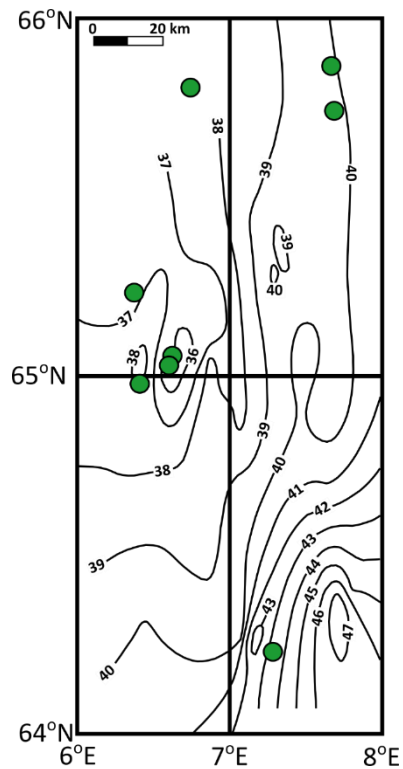


Figure 5.7. Spatial variation of calculated linear geothermal gradients ($^{\circ}\text{C}/\text{km}$) in the Haltenbanken study area as reported by Cicchino et al. (2015)

Cicchino et al. (2015) used DST temperature measurements to calculate linear geothermal gradients in wells across the Haltenbanken area and reported on the spatial variation in geothermal gradient which is shown in Figure 5.7. Their estimated geothermal gradients were used in this thesis.

| Well | Sample type | Depth below seafloor (m) | Temperature ($^{\circ}\text{C}$) |
|----------|-------------|--------------------------|------------------------------------|
| 6406/2-3 | cuttings | 3054.0 (+/- 3m) | 121 |
| 6406/2-3 | cuttings | 3254.0 (+/- 3m) | 129 |
| 6406/2-3 | cuttings | 3454.0 (+/- 3m) | 136 |
| 6406/2-3 | cuttings | 3655.0 (+/- 3m) | 144 |
| 6406/2-3 | cuttings | 3790.0 (+/- 3m) | 149 |
| 6406/2-3 | core | 3986.0 | 156 |
| 6406/2-3 | core | 3997.8 | 157 |
| 6406/2-3 | core | 4002.7 | 157 |
| 6406/2-3 | core | 4003.0 | 157 |
| 6406/2-3 | core | 4010.8 | 157 |
| 6406/2-3 | core | 4020.0 | 158 |

| | | | |
|----------|----------|-----------------|-----|
| 6406/2-3 | core | 4025.0 | 158 |
| 6406/2-3 | core | 4025.9 | 158 |
| 6406/2-3 | cuttings | 4078.0 (+/- 3m) | 160 |

| Well | Sample type | Depth below seafloor (m) | Temperature (°C) |
|------------|-------------|--------------------------|------------------|
| 6406/2-3 | cuttings | 4218.0 (+/- 3m) | 165 |
| 6407/10-2 | cuttings | 2051.0 (+/- 3m) | 93 |
| 6407/10-2 | cuttings | 2246.0 (+/- 3m) | 102 |
| 6407/10-2 | cuttings | 2386.0 (+/- 3m) | 108 |
| 6506/11-2 | cuttings | 3350.0 (+/- 3m) | 126 |
| 6506/11-2 | cuttings | 3500.0 (+/- 3m) | 131 |
| 6506/11-2 | cuttings | 3698.0 (+/- 3m) | 138 |
| 6506/11-2 | cuttings | 3791.0 (+/- 3m) | 141 |
| 6506/11-2 | cuttings | 3815.0 (+/- 3m) | 142 |
| 6506/11-3 | core | 2795.4 | 106 |
| 6506/11-3 | core | 2815.0 | 106 |
| 6506/11-3 | core | 3576.9 | 134 |
| 6506/11-3 | core | 3588.6 | 134 |
| 6506/11-3 | core | 3592.5 | 134 |
| 6506/11-3 | core | 3593.4 | 134 |
| 6506/11-3 | core | 3636.5 | 136 |
| 6506/11-3 | core | 3636.7 | 136 |
| 6506/11-3 | core | 3637.5 | 136 |
| 6506/11-3 | core | 3640.9 | 136 |
| 6506/11-3 | core | 3644.0 | 136 |
| 6506/11-4S | core | 3935.3 | 162 |
| 6506/11-4S | core | 3954.8 | 163 |
| 6506/11-4S | core | 3955.8 | 163 |
| 6506/11-4S | core | 3958.6 | 163 |
| 6506/11-4S | core | 3959.8 | 163 |
| 6506/11-4S | core | 3962.0 | 163 |
| 6506/11-4S | core | 3964.9 | 164 |
| 6506/3-1 | core | 2756.9 | 107 |
| 6506/3-1 | core | 2765.6 | 107 |
| 6506/3-1 | core | 2777.2 | 108 |
| 6506/3-1 | core | 2786.8 | 108 |
| 6507/2-3 | core | 2495.6 | 105 |
| 6507/2-3 | core | 2501.0 | 105 |
| 6507/2-3 | core | 2501.8 | 105 |
| 6507/2-3 | core | 2505.8 | 105 |
| 6507/2-3 | core | 2507.6 | 105 |
| 6507/2-3 | core | 2508.0 | 105 |
| 6507/2-3 | core | 2508.8 | 105 |
| 6507/2-3 | core | 2512.9 | 106 |

| 6507/2-3 | core | 2513.8 | 106 |
|----------|-------------|--------------------------|------------------|
| 6507/2-3 | core | 2513.9 | 106 |
| 6507/2-3 | core | 2878.0 | 120 |
| Well | Sample type | Depth below seafloor (m) | Temperature (°C) |
| 6507/2-3 | core | 2878.6 | 120 |
| 6507/6-2 | cuttings | 2332.0 (+/- 3m) | 98 |
| 6507/6-2 | cuttings | 2442.0 (+/- 3m) | 103 |
| 6507/6-2 | cuttings | 2537.0 (+/- 3m) | 106 |
| 6507/6-2 | cuttings | 2637.0 (+/- 3m) | 110 |
| 6507/6-2 | cuttings | 2747.0 (+/- 3m) | 115 |
| 6507/6-2 | cuttings | 2812.0 (+/- 3m) | 117 |
| 6607/5-1 | core | 3016.0 | 98 |
| 6607/5-1 | core | 3017.4 | 99 |

Table 5.1. List of Cretaceous mudstone samples selected for study.

5.4 Mudstone sample material

Well data and samples were publicly available from the Norwegian Petroleum Directorate. Mudstone samples were collected from nine wells 6507/6-2, 6507/2-3, 6406/2-3, 6407/10-2, 6506/3-1, 6506/11-3, 6607/5-1, 6506/11-2 and 6506/11-4S. Collected samples included both core samples and cuttings. The complete list of the studied samples is shown in Table 5.1. In total 65 (21 cuttings and 44 core) were selected for further study. Studied samples were from depth in the range of 2051-4218 m below seafloor, corresponding to a temperature range of 90-170°C. Both cuttings and the core samples were collected from the NPD core store in Stavanger.

Cuttings were collected from depths intervals which were previously checked using the wireline logs (Gamma ray and NPHI-DPHI) to make sure these are made of dominantly mudstones. Care was taken to pick thick mudstone sections in order to minimise contamination from other lithologies.

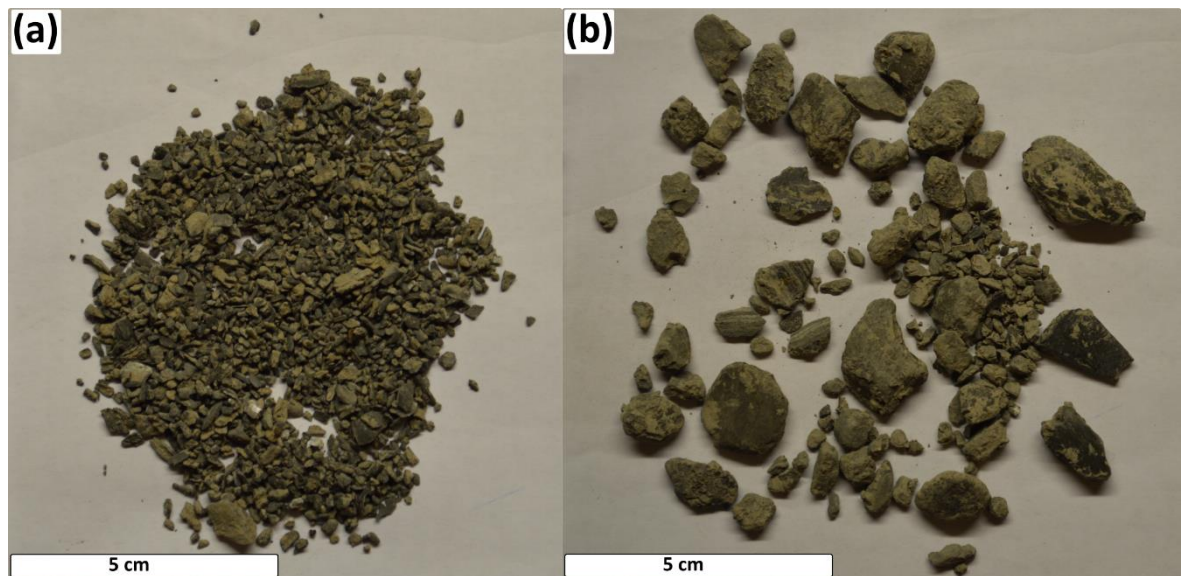


Figure 5.8. X Washed cutting samples (a) 6406/2-3; 3254 mbs; (b) 6507/2-3; 2515 m bsf.

Cuttings were mainly small (sub-millimetre to centimetre scale), dark grey pieces of sub-angular to sub-rounded material (Figure 5.8).

Core samples were obtained from the mudstone intervals of the cored sandstone members of the Lange Formation in wells 6507/2-3, 6406/2-3, 6506/3-1, 6506/11-3, 6607/5-1 and 6506/11-4S. Sampling mostly covered volumetrically significant fine grained lithologies. Four visually recognisable and common fine-grained lithology types were identified in the cores which are represented in Figure 5.9. These are as follows:

- Silt-bearing mudstones with strong or diffuse parallel laminations, dark grey to black with few/no fossils (Figure 5.9a, b).
- Highly bioturbated silt bearing mudstones with abundant carbonaceous fossil assemblages (mostly bivalves) and abundant zones of localised cementation with calcite or siderite, grey to grey-brown (Figure 5.9c, d).
- Variably bioturbated, interbedded mud, silt and fine sand with lenticular bedding, dark grey (Figure 5.9e, f)
- Carbonate concretions, cemented with calcite and siderite, grey and reddish-brown (Figure 5.9f)

Sampling points for dominant fine grained lithologies were selected based on the need to select a range of materials from the discernible heterogeneity; rock types that dominate over significant core intervals; and core material that are homogeneous within the actual sample size so that analyses made on subsamples can be correlated. Care was taken to collect samples from homogeneous and uncemented mudstone-rich intervals except for a few samples from siderite concretions. Visually discernible differential compaction around the siderite concretions (Figure 5.9f) indicated that they were formed relatively early (pre-compaction) in the burial history, so samples were taken as representatives of the preserved early diagenetic textures.

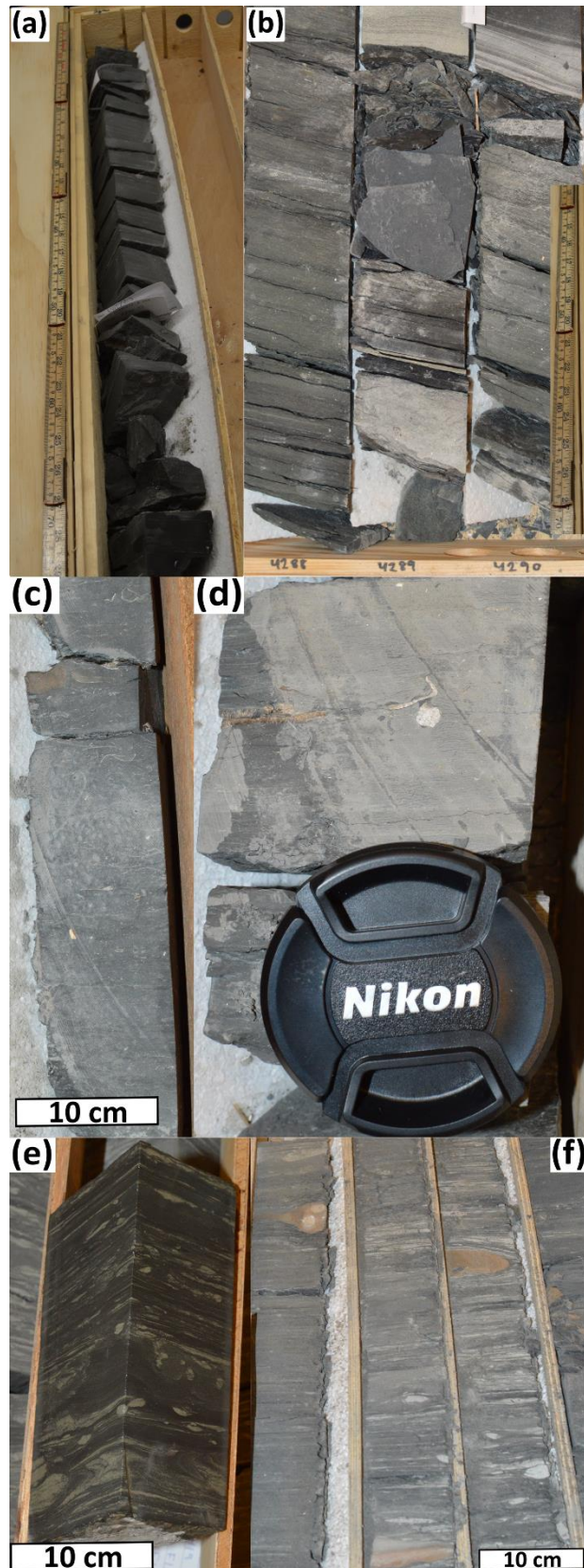


Figure 5.9. Examples of the four most common mudstone lithology types from (a) 6507/2-3, ~2513 m bsf; (b) 6506/11-4S, ~3964.9 m bsf (c) 6506/11-3, 3642 m bsf (d) 6506/11-3, 2815 m bsf (e) 6607/5-1, 3025 m bsf (f) 6506/3-1, 2773-74 m bsf. Refer to text for further explanation.

5.4.1 Bulk mineralogical properties

Quantitative bulk XRD show consistent bulk mineral composition (Figure 5.10). Quartz, plagioclase, 2:1 clays (illite-smectite), kaolinite and chlorite were detected in all of the samples. The average clay content (kaolinite + mica + illite + illite-smectite + chlorite) is ~60 wt%. The dominant components are quartz (average ~ 20 wt%) and 2:1 clay minerals (illite-smectite; average ~ 40 wt%). There is an average of ~ 12 wt% kaolinite, ~ 6 wt% chlorite and ~ 6 wt% plagioclase in the samples. Minor amounts (average ~1-4 wt%) of calcite, pyrite, siderite, K-feldspar and barite were detected in most of the samples. There are traces of iron oxide (hematite + goethite) and anatase in most of the samples, and in some of them traces of anhydrite and gypsum. Bulk quantitative XRD data of the studied samples can be found in Appendix I.

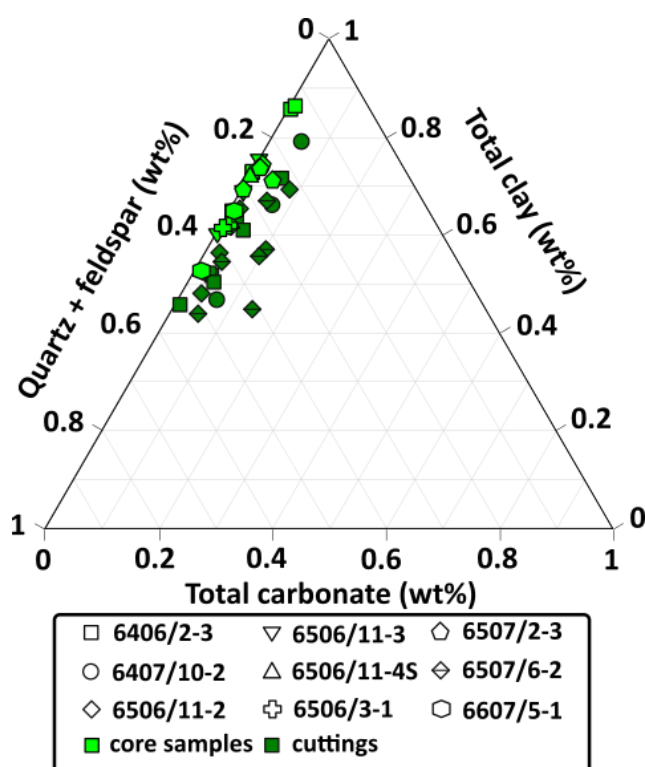


Figure 5.10. Bulk mineral composition of mudstone samples obtained from QXRD

Figure 5.10 was constructed using the quantitative XRD determined mineral weight percentages. Total clay content is defined here as the sum of all the XRD determined clay minerals including all 2:1 clays (illite, mica and illite-smectite). Overall, mineralogy in the

studied wells, is fairly similar, however core samples appear to be slightly more clay-rich and contain less carbonate.

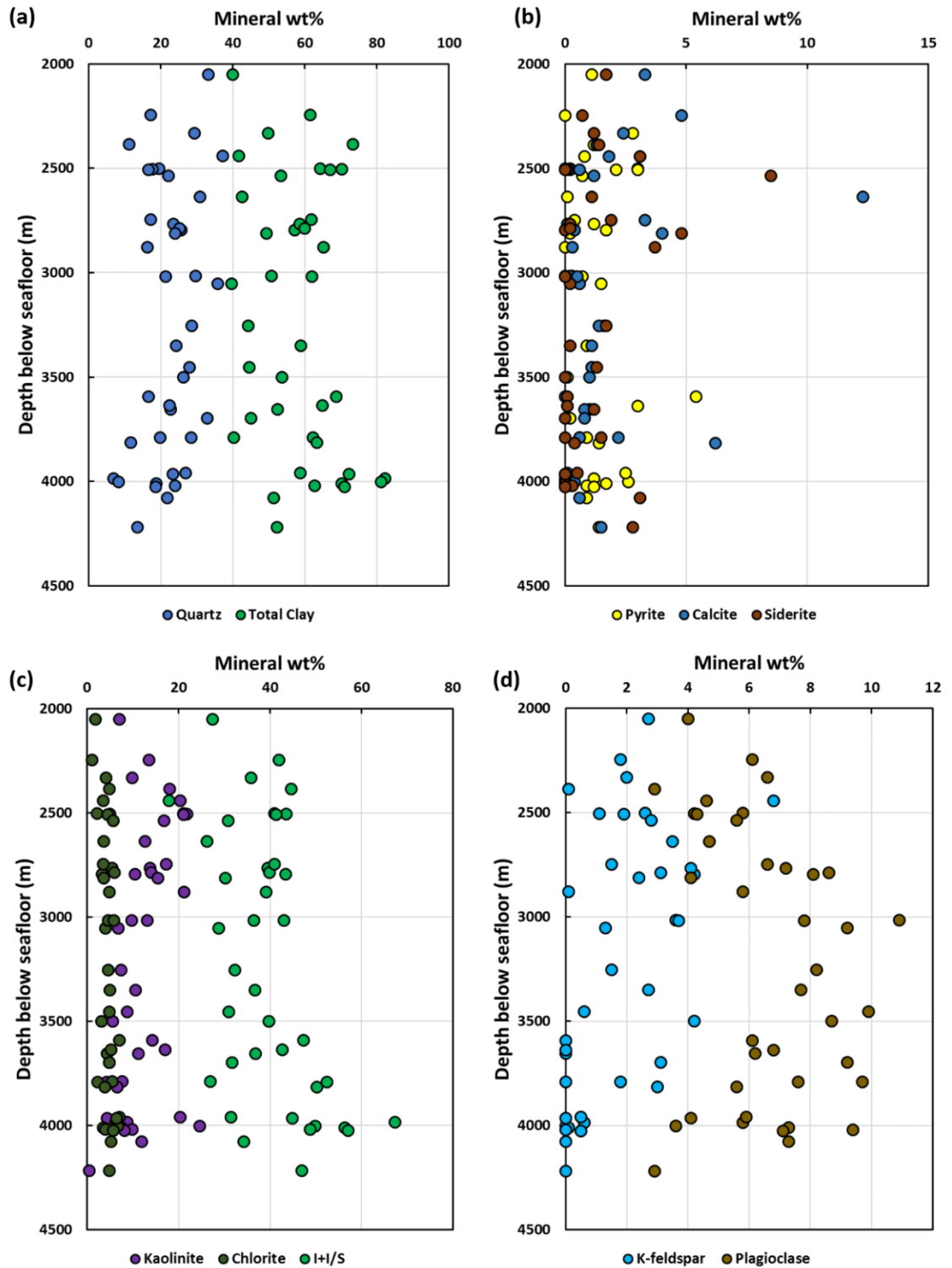


Figure 5.11. Bulk mineralogy versus depth trends in the studied Cretaceous mudstones

| | <i>Quartz</i> | <i>Kspar</i> | <i>Plagioclase</i> | <i>Calcite</i> | <i>Pyrite</i> | <i>Siderite</i> | <i>Barite</i> | <i>Kaolin</i> | <i>I+I/S</i> | <i>Chlorite</i> |
|--------------------|---------------|--------------|--------------------|----------------|---------------|-----------------|---------------|---------------|--------------|-----------------|
| Quartz | 1.00 | | | | | | | | | |
| Kspar | 0.47 | 1.00 | | | | | | | | |
| Plagioclase | 0.42 | 0.16 | 1.00 | | | | | | | |
| Calcite | 0.14 | 0.26 | -0.27 | 1.00 | | | | | | |
| Pyrite | -0.24 | -0.28 | -0.19 | -0.28 | 1.00 | | | | | |
| Siderite | 0.07 | 0.05 | -0.30 | 0.18 | -0.26 | 1.00 | | | | |
| Barite | 0.15 | -0.25 | -0.08 | 0.21 | -0.19 | 0.41 | 1.00 | | | |
| Kaolin | -0.24 | 0.04 | -0.40 | -0.07 | 0.31 | 0.17 | -0.38 | 1.00 | | |
| I+I/S | -0.79 | -0.41 | -0.03 | -0.31 | 0.23 | -0.43 | -0.36 | -0.14 | 1.00 | |
| Chlorite | -0.11 | -0.21 | -0.17 | -0.17 | -0.17 | -0.18 | -0.21 | -0.25 | 0.18 | 1.00 |

Table 5.2. Correlation matrix showing values of Pearson's correlation coefficient for mineralogy of the Cretaceous mudstones (all samples).

| | <i>Quartz</i> | <i>Kspar</i> | <i>Plagioclase</i> | <i>Calcite</i> | <i>Pyrite</i> | <i>Siderite</i> | <i>Barite</i> | <i>Kaolin</i> | <i>I+I/S</i> | <i>Chlorite</i> |
|--------------------|---------------|--------------|--------------------|----------------|---------------|-----------------|---------------|---------------|--------------|-----------------|
| Quartz | 1.00 | | | | | | | | | |
| Kspar | 0.47 | 1.00 | | | | | | | | |
| Plagioclase | 0.79 | 0.44 | 1.00 | | | | | | | |
| Calcite | 0.40 | 0.04 | -0.03 | 1.00 | | | | | | |
| Pyrite | -0.41 | 0.16 | -0.46 | -0.30 | 1.00 | | | | | |
| Siderite | 0.16 | -0.16 | -0.16 | 0.63 | -0.36 | 1.00 | | | | |
| Barite | 0.40 | 0.00 | -0.11 | 0.84 | -0.37 | 0.81 | 1.00 | | | |
| Kaolin | -0.33 | -0.25 | -0.19 | -0.33 | 0.53 | -0.33 | -0.48 | 1.00 | | |
| I+I/S | -0.82 | -0.25 | -0.44 | -0.70 | 0.29 | -0.51 | -0.70 | 0.09 | 1.00 | |
| Chlorite | -0.72 | -0.30 | -0.49 | -0.28 | 0.45 | -0.33 | -0.48 | 0.44 | 0.59 | 1.00 |

Table 5.3. Correlation matrix showing values of Pearson's correlation coefficient for 6406/2-3 mineralogy.

| | <i>Quartz</i> | <i>Kspar</i> | <i>Plagioclase</i> | <i>Calcite</i> | <i>Pyrite</i> | <i>Siderite</i> | <i>Barite</i> | <i>Kaolin</i> | <i>I+I/S</i> | <i>Chlorite</i> |
|--------------------|---------------|--------------|--------------------|----------------|---------------|-----------------|---------------|---------------|--------------|-----------------|
| Quartz | 1.00 | | | | | | | | | |
| Kspar | 0.82 | 1.00 | | | | | | | | |
| Plagioclase | -0.44 | -0.55 | 1.00 | | | | | | | |
| Calcite | 0.19 | -0.03 | -0.33 | 1.00 | | | | | | |
| Pyrite | 0.24 | -0.15 | 0.59 | -0.41 | 1.00 | | | | | |
| Siderite | -0.31 | 0.01 | -0.22 | -0.48 | -0.25 | 1.00 | | | | |
| Barite | -0.59 | -0.45 | -0.32 | -0.05 | -0.48 | 0.26 | 1.00 | | | |
| Kaolin | 0.00 | 0.56 | -0.32 | -0.39 | -0.56 | 0.41 | 0.14 | 1.00 | | |
| I+I/S | -0.83 | -0.93 | 0.77 | -0.15 | 0.25 | -0.11 | 0.32 | -0.41 | 1.00 | |
| Chlorite | -0.28 | -0.19 | 0.23 | -0.38 | 0.17 | 0.79 | -0.20 | -0.03 | 0.12 | 1.00 |

Table 5.4. Correlation matrix showing values of Pearson's correlation coefficient for 6507/6-2 mineralogy.

The detected mineral composition is monotonous, however quartz, illite-smectite, K-feldspar and plagioclase contents show considerable variability among the studied mudstone samples (Figure 5.11). It should be noted however that collected samples included both cores and cuttings which also contributes to this variability. Cuttings represent sampled depth intervals in the range of 5 m and these results only show averaged mineralogy.

Figure 5.11 shows mineralogy-depth trends in the studied Cretaceous section by using individual mineralogy data from all nine wells. The variability of quartz with increasing depth shows a good negative correlation with the variability of the sum of clay minerals (Figure 5.11a) indicating that quartz is predominantly sedimentary in origin. The K-feldspar content decreases with depth in all wells implying ongoing clay mineral diagenesis. Concomitant with the disappearance of K-feldspar, the plagioclase content appears to be increasing with depth, however this trend seems to be somewhat obscured below ~3000 m bsf (Figure 5.11d) most likely due to the variability of initial detrital mineralogy between wells and/or samples (cuttings vs core). In addition, the chlorite content appears to be increasing while the kaolinite content is decreasing with increasing depth (Figure 5.11c).

Tables 5.2-5.4 show correlation coefficient values for individual mineral phases. Table 5.2 was constructed by using mineralogy data from all nine wells while Tables 5.3 and 5.4 were constructed by only using data from wells 6406/2-3 and 6507/6-2 respectively. These two individual wells have been selected because they contained most of the collected samples. As it can be seen quartz shows a very strong negative correlation with illite-smectite in all wells. In addition to this, K-feldspar and plagioclase content correlates positively with quartz. However, the correlation between plagioclase and quartz is much weaker in 6507/6-2 compared to 6406/2-3 and vice versa correlation between K-feldspar and quartz is much weaker in 6406/2-3 than in 6507/6-2. Other interesting features of the 6507/6-2 samples are the strong negative correlation between K-feldspar and illite-smectite and the strong positive correlation between plagioclase and illite-smectite. The positive correlation between plagioclase and illite-smectite indicates a secondary (authigenic) origin of plagioclase in 6507/6-2. Such differences between samples from

different wells can be attributed to local differences in depositional mineralogy and grain size (differences in the relative amounts of detrital and authigenic minerals).

The origin of the detected barite is uncertain. Barite is commonly used in drilling muds as heavyweight additive. It occurs naturally in sedimentary environments; however, it is relatively uncommon in most settings. It was also detected in some of the core samples however only in trace amounts. Comparatively large amounts of barite in the cuttings are clearly the result of contamination with drilling mud components so it was assumed to have come from drilling mud, and barite free normalized mineral concentrations have been calculated. Traces of halite and sylvite are probably precipitates from pore solutions.

5.4.2 Clay mineralogical properties

Cation exchange capacity (CEC) measurements of Cretaceous mudstone samples range from 5.2 to 21.2 meq/100g and show an overall decreasing CEC-depth trend. These results are consistent with ongoing smectite illitization. However, any contamination by clay components of the drilling fluid can affect the CEC results of cutting samples. Bentonite is one such component and could have influenced the CEC results. Organic matter from an organic-based drilling fluid is another possible source of contamination. The barite content is usually the best indicator of drilling mud contamination since it is the dominant component in most drilling muds. Large amounts of barite in most of the cuttings would indicate contamination, however the comparatively similar CEC of the core samples and the lack of any discernible correlation between the CEC and the barite content (Figure 5.12) suggest that the CEC results are largely unaffected.

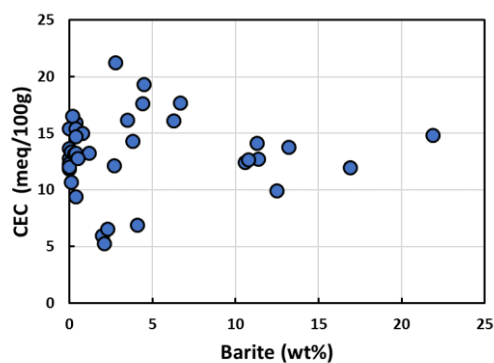


Figure 5.12. Bulk rock CEC plotted against QXRD measured barite content.

Figure 5.13a shows the calculated smectite equivalent contents in illite-smectite for the individual samples. These results show ongoing illitization of smectite in the Cretaceous mudstones. Smectite content is decreasing with increasing depth from ~60% smectite in illite-smectite at ~2500 m below seafloor to ~20% smectite in illite-smectite at ~4000 m below seafloor. As it is shown in Figure 5.13b K-feldspar is decreasing concomitantly and disappearing at ~4000 m below seafloor. It should be noted that the shallowest samples shown in Figure 5.13a at ~2000 m below seafloor are from well 6407/10-2 and might have been uplifted.

Complete CEC data and calculated smectite equivalent contents for individual samples can be found in Appendix I.

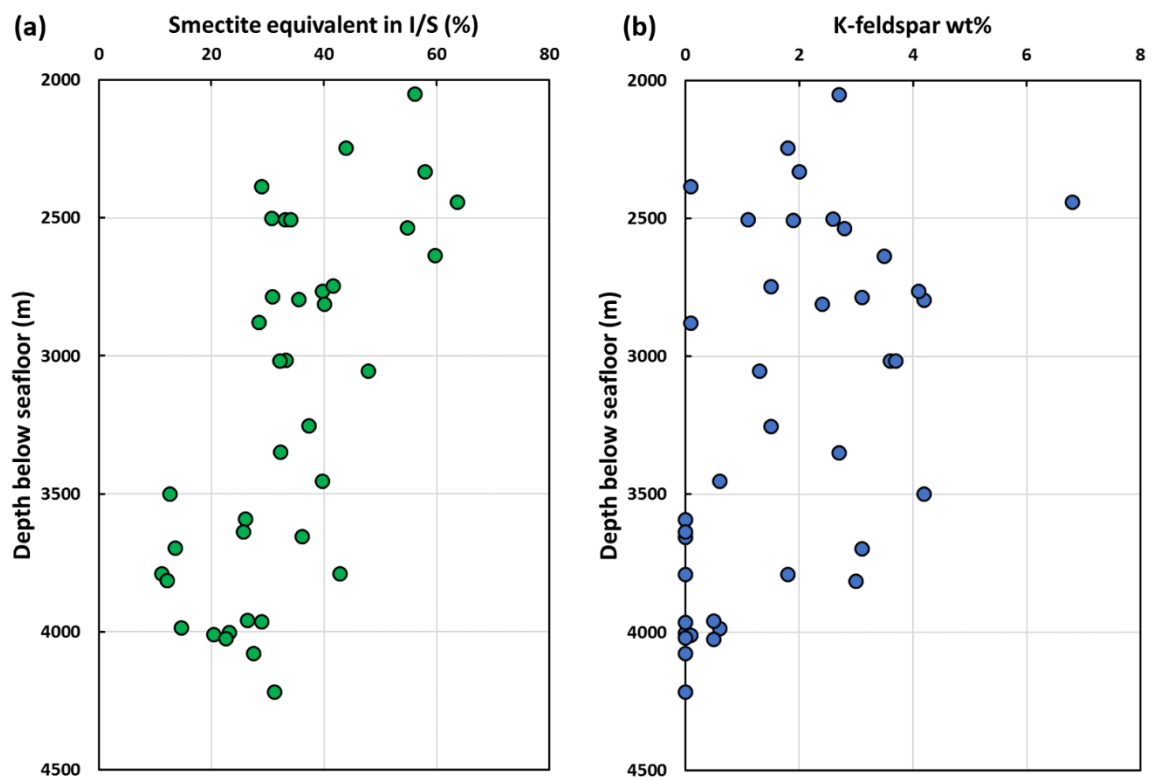


Figure 5.13. (a) Calculated smectite equivalent % in illite-smectite for Cretaceous mudstone samples plotted against depth below seafloor. Smectite equivalent content was calculated using CEC results as described in 3.3.3. (b) QXRD measured K-feldspar content versus depth below seafloor.

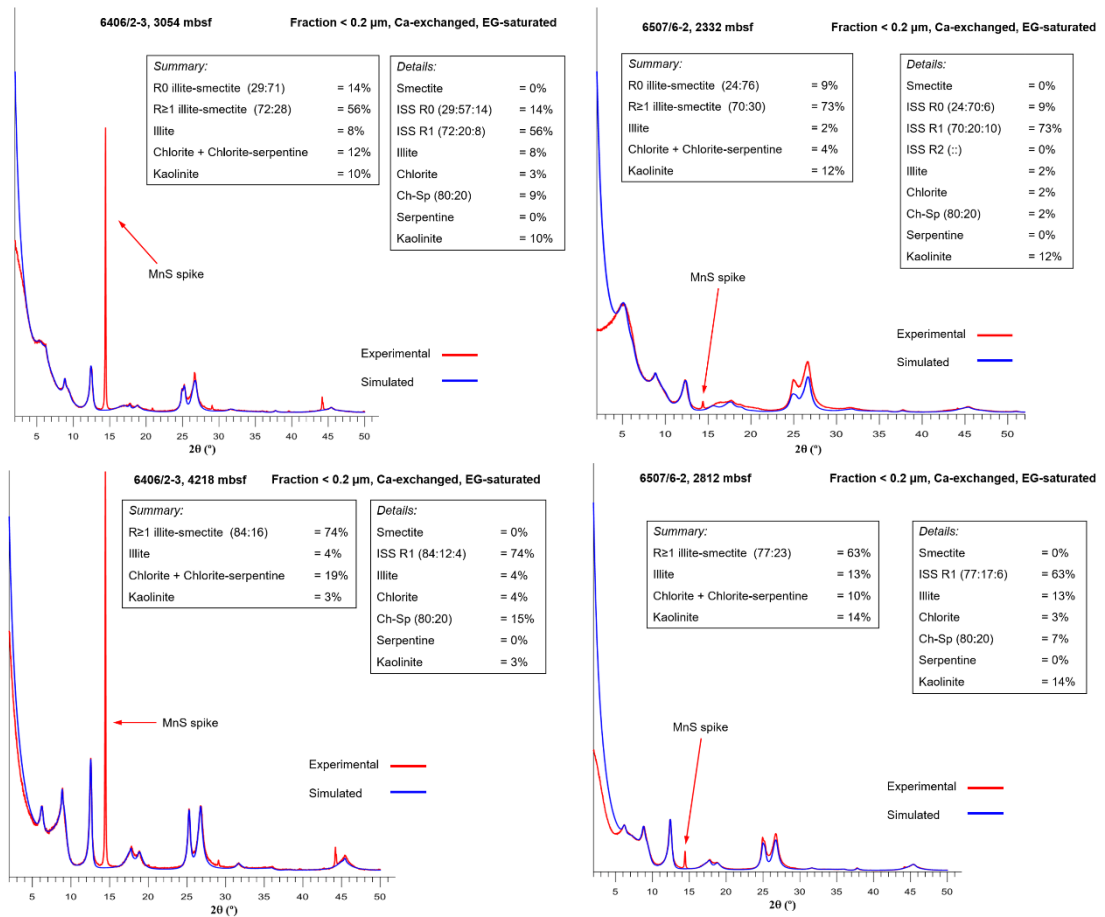


Figure 5.14. Experimental and simulated XRD patterns for ethylene glycol-saturated samples from wells 6406/2-3 and 6507/6-2.

The authigenic (<0.2 μ m fraction) clay fraction XRD results confirm ongoing illitization of smectite by showing decreasing smectite content with increasing depth (Figure 5.15). In overall the mudstone samples contain illite, illite-smectite, kaolinite and chlorite. The <0.2 μ m clay fraction is dominated by mixed-layer illite-smectite with ordered interstratification (R>1) (Figure 5.14). A disordered (R0) illite-smectite phase population with >70% smectite in illite-smectite has been detected in the shallower samples from both 6507/6-2 and 6406/2-3 (Figure 5.14). However, this population disappears with increasing depth in both wells. No pure smectite has been detected in the samples. Full <0.2 μ m fraction XRD data and modelling results can be found in Appendix II.

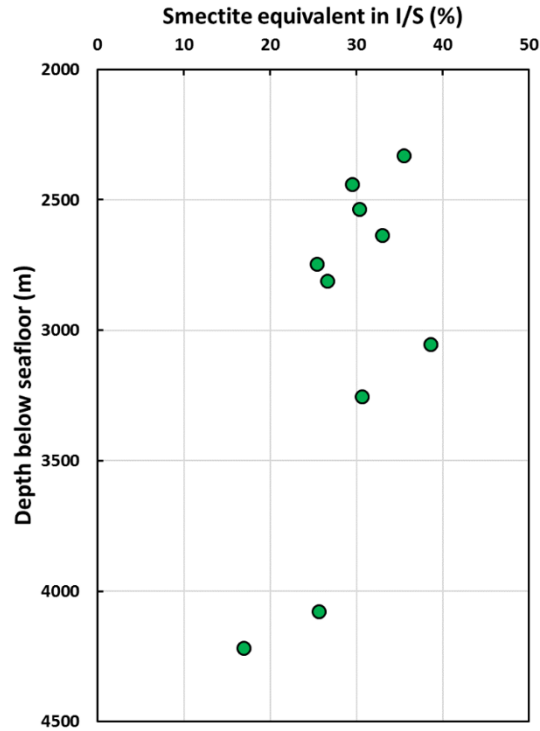


Figure 5.15. Smectite equivalent (%) in illite-smectite versus depth for samples from wells 6406/2-3 and 6507/6-2. Smectite equivalent content was calculated using the combination of the bulk QXRD and $<0.2\ \mu\text{m}$ fraction modelling results.

5.4.3 Total organic carbon content

Total organic carbon content (TOC) was estimated in mudstone samples from all nine wells. Complete TOC data and calculated organic matter contents for individual samples are given in Appendix III.

Figure 5.16 shows the measured TOC content of individual mudstone samples. The TOC values are consistent, mostly being less than 2 wt%. Samples with anomalously high TOC values have high amount of detrital plant material as it was shown by SEM (see also 5.4.5). In overall, these TOC values are considered typical for siliciclastic mudstones.

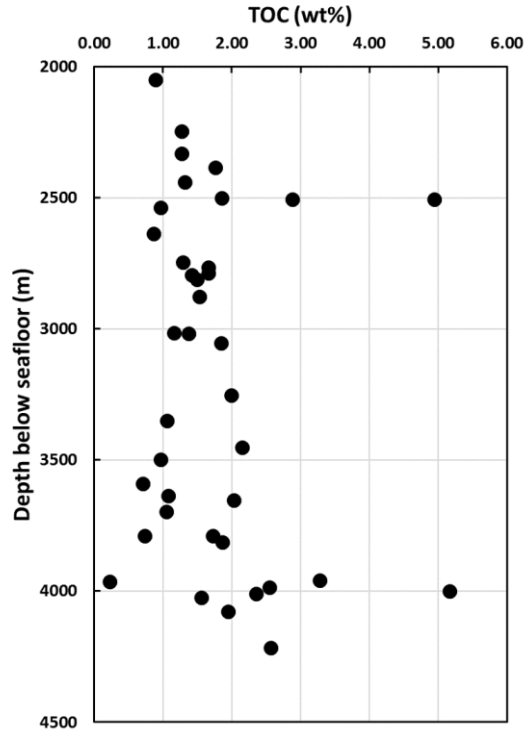


Figure 5.16. TOC (wt%) results for Cretaceous mudstones.

5.4.4 Bulk inorganic chemical properties

Cretaceous mudstones were analysed for their major and trace elemental composition. Complete major and trace element concentrations of the individual mudstone samples along with the ratios of selected pairs of major and trace elements and calculated weathering indices can be found in Appendix IV.

The amount of SiO_2 varies between 37.48 and 61.13% (average of 50.84%), Al_2O_3 varies between 11.47 and 20.86% (average 17.12%), TiO_2 varies between 0.50 and 1.06% (average 0.79%), Fe_2O_3 varies between 5.05 and 11.52% (average 7.41%), MnO varies between 0.03 and 1.32% (average 0.30%), MgO varies between 1.16 and 2.04% (average 1.59%), CaO varies between 0.25 and 7.51% (average 1.73%), Na_2O varies between 0.55 and 1.68% (average 1.09%), K_2O varies between 1.89 and 3.86% (average 2.77%) and P_2O_5 varies between 0.06 and 0.50% (average 0.18%). Total iron is expressed as Fe_2O_3 .

Correlation coefficient values for major elements are given in Table 5.5. Al_2O_3 shows strong positive correlations with TiO_2 and MgO . This indicates that both titanium and magnesium reside primarily in clay minerals and are dominantly terrigenous components.

However TiO_2 also shows a somewhat weaker positive correlation with SiO_2 that can be attributed to the presence of anatase. Good positive correlation between Na_2O and Al_2O_3 can be related to the presence of smectite in illite-smectite. CaO shows negative correlation with SiO_2 . This indicates that calcium is dominantly a marine component. MnO shows good positive correlation with Fe_2O_3 indicating that Mn primarily resides in siderite. Negative correlation between SiO_2 and Fe_2O_3 (and also MnO) suggests that siderite is authigenic in origin. Correlation between CaO and P_2O_5 can be related to the presence of apatite. Correlation between K_2O and MgO can be attributed to the presence of chlorite.

Values of $\text{K}_2\text{O}/\text{Al}_2\text{O}_3$ ratio of the Cretaceous mudstone samples show variation between 0.12 and 0.25 (average of 0.16). These values are consistent with the preponderance of clay minerals over K-feldspar in these samples (Cox et al., 1995).

Values of Si/Al , K/Al and Na/Al show good correlation with QXRD established mineral abundances (Figure 5.17). Strong correlation of Na/Al with the plagioclase content indicates that sodium resides primarily in plagioclase feldspar (Figure 5.17c, d). This is in accordance with an illite dominated clay mineralogy in most wells (dominance of an illite-smectite population with >80% illite in illite-smectite). Correlation of K/Al and illite-smectite (Figure 5.17e, f) is obscured due to illitization and due the presence of considerable amount of detrital K-feldspar in some of the samples.

Calculated ICV values of the samples range from 0.68 to 1.65. Calculated CIA and CIW values range from 68 to 79 and 86 to 94 respectively. Correlation between the calculated CIA and CIW is shown in Figure 5.18. As can be seen in the figure the correlation is strong if solely core sample data is used. Correlation is obscured when using data from cuttings due to large variations of carbonate and total clay mineral content in these samples.

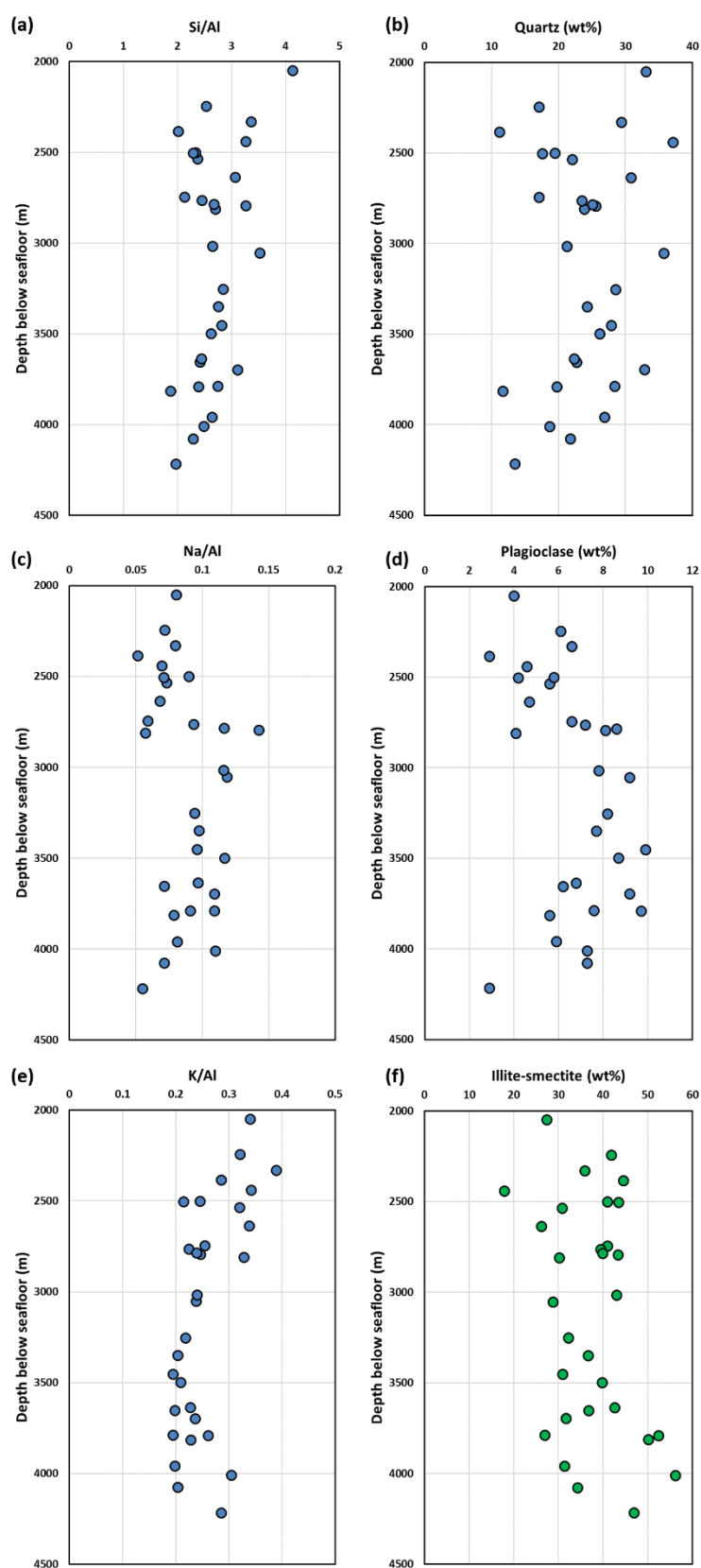


Figure 5.17. Variation of (a) Si/Al, (c) Na/Al and (e) K/Al with depth in comparison with the variation of (b) quartz, (d) plagioclase and (f) illite-smectite.

| | <i>SiO2</i> | <i>Al2O3</i> | <i>Fe2O3(T)</i> | <i>MnO</i> | <i>MgO</i> | <i>CaO</i> | <i>Na2O</i> | <i>K2O</i> | <i>TiO2</i> | <i>P2O5</i> |
|----------|-------------|--------------|-----------------|------------|------------|------------|-------------|------------|-------------|-------------|
| SiO2 | 1.00 | | | | | | | | | |
| Al2O3 | 0.28 | 1.00 | | | | | | | | |
| Fe2O3(T) | -0.63 | -0.04 | 1.00 | | | | | | | |
| MnO | -0.53 | -0.16 | 0.64 | 1.00 | | | | | | |
| MgO | 0.03 | 0.82 | 0.34 | 0.21 | 1.00 | | | | | |
| CaO | -0.49 | -0.36 | 0.15 | 0.44 | -0.18 | 1.00 | | | | |
| Na2O | 0.81 | 0.66 | -0.48 | -0.53 | 0.41 | -0.51 | 1.00 | | | |
| K2O | -0.13 | 0.28 | 0.24 | 0.16 | 0.54 | 0.08 | 0.06 | 1.00 | | |
| TiO2 | 0.57 | 0.84 | -0.30 | -0.47 | 0.53 | -0.58 | 0.79 | 0.13 | 1.00 | |
| P2O5 | -0.70 | -0.32 | 0.55 | 0.71 | 0.03 | 0.67 | -0.69 | 0.23 | -0.62 | 1.00 |

Table 5.5. Correlation matrix showing values of Pearson's correlation coefficient for major elements of Cretaceous mudstones.

| | <i>SiO2</i> | <i>Al2O3</i> | <i>CaO</i> | <i>TiO2</i> | <i>La</i> | <i>Ce</i> | <i>Pr</i> | <i>Nd</i> | <i>Sm</i> | <i>Eu</i> | <i>Gd</i> | <i>Tb</i> | <i>Dy</i> | <i>Ho</i> | <i>Er</i> | <i>Tm</i> | <i>Yb</i> |
|--------------|-------------|--------------|------------|-------------|-----------|-----------|-----------|-----------|-----------|-----------|-----------|-----------|-----------|-----------|-----------|-----------|-----------|
| SiO2 | 1.00 | | | | | | | | | | | | | | | | |
| Al2O3 | 0.28 | 1.00 | | | | | | | | | | | | | | | |
| CaO | -0.49 | -0.36 | 1.00 | | | | | | | | | | | | | | |
| TiO2 | 0.57 | 0.84 | -0.58 | 1.00 | | | | | | | | | | | | | |
| La | 0.20 | 0.79 | -0.09 | 0.61 | 1.00 | | | | | | | | | | | | |
| Ce | 0.02 | 0.64 | 0.08 | 0.39 | 0.96 | 1.00 | | | | | | | | | | | |
| Pr | 0.12 | 0.70 | 0.01 | 0.48 | 0.98 | 0.98 | 1.00 | | | | | | | | | | |
| Nd | 0.05 | 0.64 | 0.09 | 0.40 | 0.95 | 0.98 | 0.99 | 1.00 | | | | | | | | | |
| Sm | -0.14 | 0.43 | 0.21 | 0.16 | 0.80 | 0.90 | 0.89 | 0.93 | 1.00 | | | | | | | | |
| Eu | 0.43 | 0.73 | -0.38 | 0.77 | 0.81 | 0.69 | 0.76 | 0.72 | 0.57 | 1.00 | | | | | | | |
| Gd | -0.25 | 0.29 | 0.31 | 0.01 | 0.67 | 0.81 | 0.78 | 0.85 | 0.96 | 0.40 | 1.00 | | | | | | |
| Tb | -0.25 | 0.36 | 0.27 | 0.08 | 0.69 | 0.80 | 0.78 | 0.84 | 0.95 | 0.42 | 0.98 | 1.00 | | | | | |
| Dy | -0.10 | 0.44 | 0.17 | 0.19 | 0.75 | 0.84 | 0.83 | 0.87 | 0.93 | 0.49 | 0.95 | 0.97 | 1.00 | | | | |
| Ho | 0.01 | 0.60 | 0.07 | 0.38 | 0.84 | 0.87 | 0.87 | 0.89 | 0.88 | 0.61 | 0.87 | 0.90 | 0.95 | 1.00 | | | |
| Er | 0.10 | 0.66 | -0.08 | 0.50 | 0.86 | 0.86 | 0.87 | 0.87 | 0.83 | 0.68 | 0.79 | 0.84 | 0.92 | 0.95 | 1.00 | | |
| Tm | 0.23 | 0.78 | -0.18 | 0.67 | 0.86 | 0.80 | 0.82 | 0.80 | 0.70 | 0.75 | 0.63 | 0.69 | 0.79 | 0.87 | 0.96 | 1.00 | |
| Yb | 0.27 | 0.79 | -0.24 | 0.73 | 0.84 | 0.76 | 0.78 | 0.75 | 0.63 | 0.77 | 0.54 | 0.61 | 0.71 | 0.81 | 0.91 | 0.98 | 1.00 |

Table 5.6. Correlation matrix showing values of Pearson's correlation coefficient for REE of Cretaceous mudstones.

| | SiO2 | Al2O3 | CaO | TiO2 | Sc | V | Ba | Sr | Y | Zr | Cr | Co | Ni | Zn | Rb | Nb | Pb | Th | U |
|-------|-------|-------|-------|-------|-------|-------|-------|-------|-------|-------|-------|-------|-------|-------|-------|-------|-------|------|------|
| SiO2 | 1.00 | | | | | | | | | | | | | | | | | | |
| Al2O3 | 0.28 | 1.00 | | | | | | | | | | | | | | | | | |
| CaO | -0.49 | -0.36 | 1.00 | | | | | | | | | | | | | | | | |
| TiO2 | 0.57 | 0.84 | -0.58 | 1.00 | | | | | | | | | | | | | | | |
| Sc | 0.14 | 0.95 | -0.24 | 0.75 | 1.00 | | | | | | | | | | | | | | |
| V | 0.05 | 0.81 | -0.17 | 0.68 | 0.82 | 1.00 | | | | | | | | | | | | | |
| Ba | -0.59 | -0.43 | 0.13 | -0.52 | -0.45 | -0.33 | 1.00 | | | | | | | | | | | | |
| Sr | -0.53 | -0.36 | 0.09 | -0.44 | -0.41 | -0.29 | 0.99 | 1.00 | | | | | | | | | | | |
| Y | -0.14 | 0.45 | 0.20 | 0.20 | 0.52 | 0.51 | -0.33 | -0.34 | 1.00 | | | | | | | | | | |
| Zr | 0.71 | 0.45 | -0.59 | 0.76 | 0.29 | 0.38 | -0.53 | -0.47 | 0.02 | 1.00 | | | | | | | | | |
| Cr | 0.34 | 0.44 | -0.26 | 0.52 | 0.41 | 0.53 | -0.30 | -0.26 | 0.14 | 0.52 | 1.00 | | | | | | | | |
| Co | 0.00 | 0.56 | -0.07 | 0.45 | 0.58 | 0.51 | -0.32 | -0.31 | 0.56 | 0.20 | 0.41 | 1.00 | | | | | | | |
| Ni | -0.19 | 0.26 | 0.28 | -0.04 | 0.31 | 0.35 | -0.18 | -0.19 | 0.62 | -0.10 | 0.38 | 0.57 | 1.00 | | | | | | |
| Zn | -0.47 | -0.56 | 0.30 | -0.57 | -0.45 | -0.46 | 0.04 | -0.05 | -0.18 | -0.42 | -0.54 | -0.25 | -0.13 | 1.00 | | | | | |
| Rb | 0.47 | 0.87 | -0.51 | 0.81 | 0.83 | 0.68 | -0.45 | -0.38 | 0.23 | 0.50 | 0.49 | 0.41 | 0.17 | -0.57 | 1.00 | | | | |
| Nb | 0.51 | 0.52 | -0.44 | 0.63 | 0.38 | 0.57 | -0.47 | -0.42 | 0.29 | 0.86 | 0.49 | 0.24 | 0.19 | -0.45 | 0.50 | 1.00 | | | |
| Pb | -0.53 | -0.45 | 0.53 | -0.63 | -0.32 | -0.37 | 0.07 | -0.03 | 0.04 | -0.60 | -0.49 | -0.12 | 0.08 | 0.85 | -0.53 | -0.50 | 1.00 | | |
| Th | 0.28 | 0.89 | -0.27 | 0.81 | 0.86 | 0.89 | -0.57 | -0.52 | 0.60 | 0.59 | 0.53 | 0.63 | 0.37 | -0.52 | 0.77 | 0.72 | -0.43 | 1.00 | |
| U | 0.30 | 0.65 | -0.29 | 0.74 | 0.58 | 0.71 | -0.54 | -0.50 | 0.39 | 0.71 | 0.52 | 0.48 | 0.10 | -0.35 | 0.55 | 0.70 | -0.35 | 0.84 | 1.00 |

Table 5.7. Correlation matrix showing values of Pearson's correlation coefficient for selected trace elements of Cretaceous mudstones.

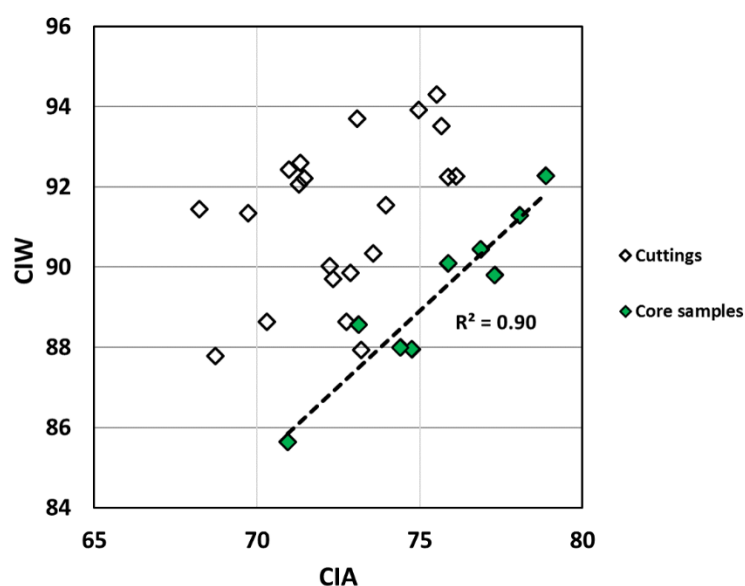


Figure 5.18. Correlation between calculated CIA and CIW values for cuttings and core samples.

Correlation coefficient values for selected trace elements and rare earth elements (REE) are shown in Tables 5.6 and 5.7 respectively. Among the analysed elements Sc, V, Rb, U and Th show strong positive correlation with Al_2O_3 indicating that they are closely related to clay minerals either as primary constituents or as adsorbed components on clay mineral surfaces. Zirconium show strong positive correlation with SiO_2 indicating the presence of zircon. Uranium and niobium show positive correlation with TiO_2 indicating likely association with anatase. Chromium, cobalt and nickel are most likely associated with mafic mineral components. Rare earth elements show strong positive correlations with TiO_2 and Al_2O_3 indicating that their mostly associated with clay minerals.

Th/Sc ratios of the samples range from 0.55 to 0.85 (average of 0.67). Zr/Sc ratios range from 6.24 to 15.58 (average of 10.29). La/Sc ratios of the samples range from 1.52 to 2.53 (average of 2.04). La/Th ratios range from 1.78 to 3.45 (average of 3.07). Zr/Cr ratios range from 0.84 to 2.30 (average of 1.43) and Y/Ni ratios range from 0.18 to 0.50 (average of 0.36).

5.4.5 Clay mineral fabric alignment

Quantitative assessment of the phyllosilicate alignment in the Cretaceous mudstone samples was carried out using high-resolution X-ray textural goniometry (HRXTG) as described in 3.3.10. Complete HRXTG data of individual samples (including the chosen 2theta angles) can be found in Appendix V.

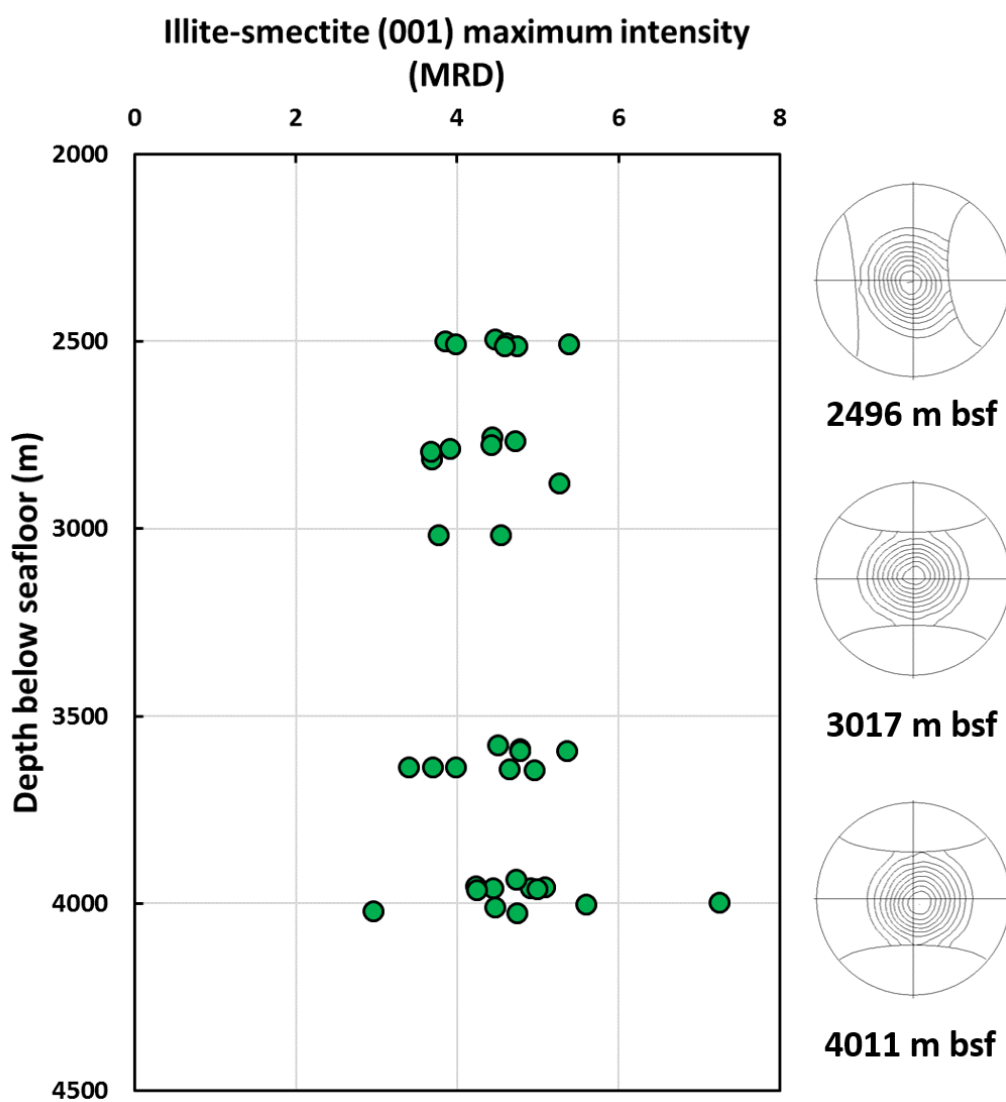


Figure 5.19. Measured illite-smectite (001) maximum intensity values of Cretaceous mudstone samples. Representative illite-smectite pole figures are displayed to the right.

Results displayed in Figure 5.19 indicate very strong alignment for illite-smectite throughout the whole studied interval. No trend can be seen when plotting the measured fabric intensity values against depth. Day-Stirrat et al. (2008) suggested a slight increase in the alignment of illite-smectite at depths and temperatures greater than the main phase of smectite to illite reaction (>80% illite in illite-smectite), perhaps as a result of continuing dissolution and re-precipitation of clay minerals. No evidence is found to support this suggestion with this dataset, but this might be due to sample selection issues, since the overall alignment is highly influenced by clay content and silt/clay ratio in the individual samples (Figure 5.22), so that a small increase in clay mineral alignment with depth/temperature cannot be ruled out.

The anomalously low pole density value of 2.96 MRD in a sample from 4020 m bsf in well 6406/2-3 is the result of post-depositional deformation (Figure 5.20).

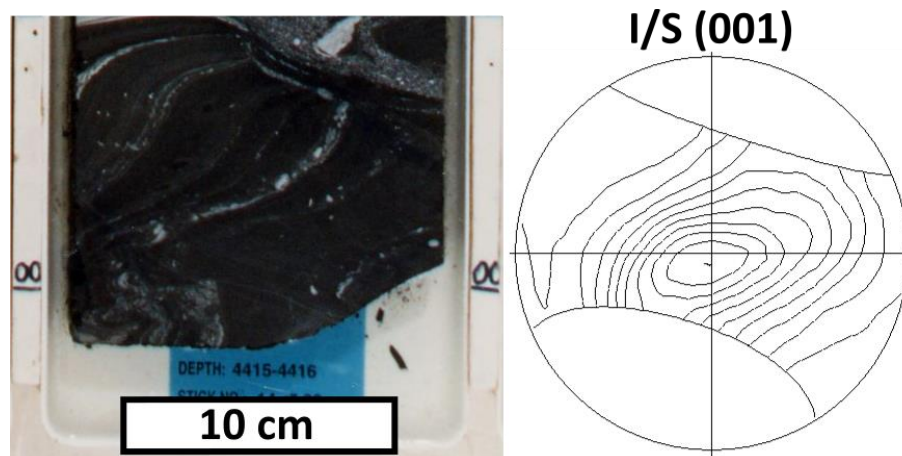


Figure 5.20. Post depositional, soft sediment deformation structure (slump) in a mudstone sample at 4020 m bsf in well 6406/2-3 and associated illite-smectite (001) pole figure. Picture source: Norwegian Petroleum Directorate (NPD).

As it is shown in Figure 5.21 there is very strong correlation between the measured illite-smectite (001) and chlorite (002) +kaolinite fabric intensity values. The strong correlation suggest that the whole clay mineral fabric (not just illite-smectite but also chlorite and kaolinite, both detrital and authigenic) was realigned normal to the maximum effective stress (parallel to bedding) in the Cretaceous mudstones.

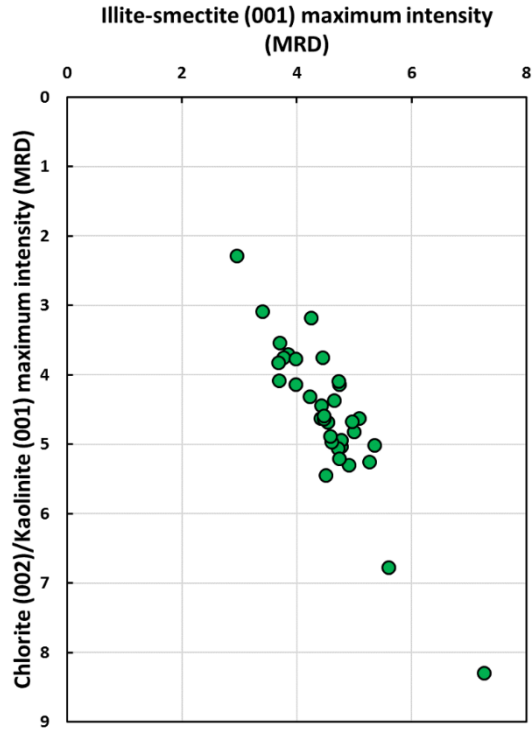


Figure 5.21. Illite-smectite (001) maximum intensity values shown in correlation with the maximum intensity values of chlorite (002) +kaolinite (001) for the Cretaceous mudstone samples.

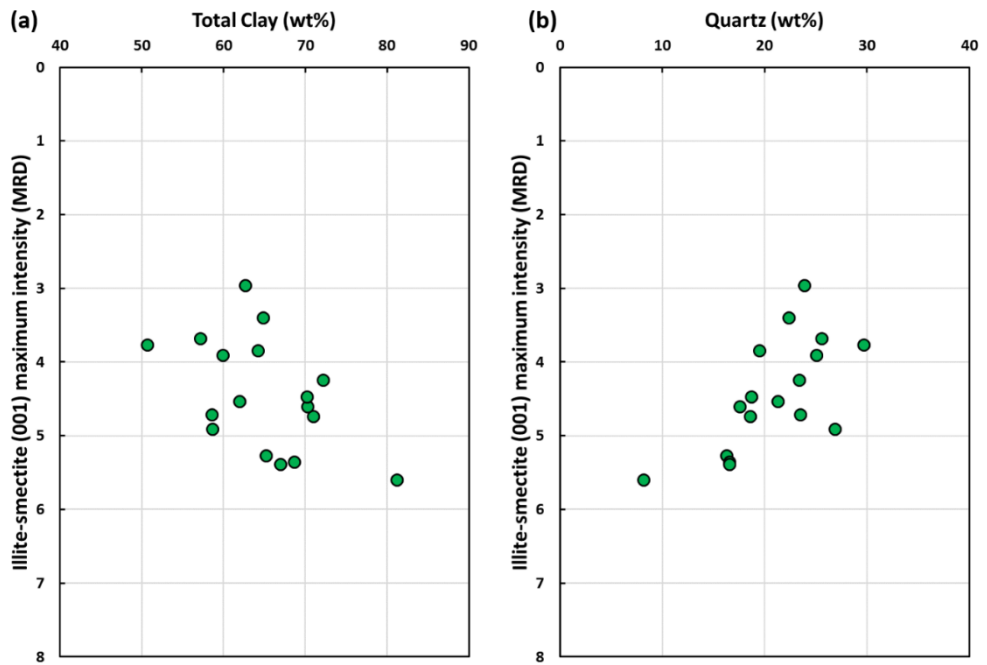


Figure 5.22. Illite-smectite maximum intensity values shown in correlation with (a) total clay and (b) quartz content of the Cretaceous mudstone samples.

At any depth, there is substantial scatter which is largely a reflection of variations in the clay:silt (i.e. plate:sphere) ratio of the samples. This is illustrated in Figure 5.22 by showing correlations between illite-smectite maximum intensity values, total clay content and quartz content of the mudstone samples.

5.4.6 Mudstone petrography

Support for the results shown in 5.4.5 is provided by petrographic observations made by SEM (Figure 5.23), which suggest an overall well-developed clay mineral fabric in the Cretaceous mudstone samples. However, SEM observations also revealed considerable variability of the clay mineral fabric on a micrometre-scale.

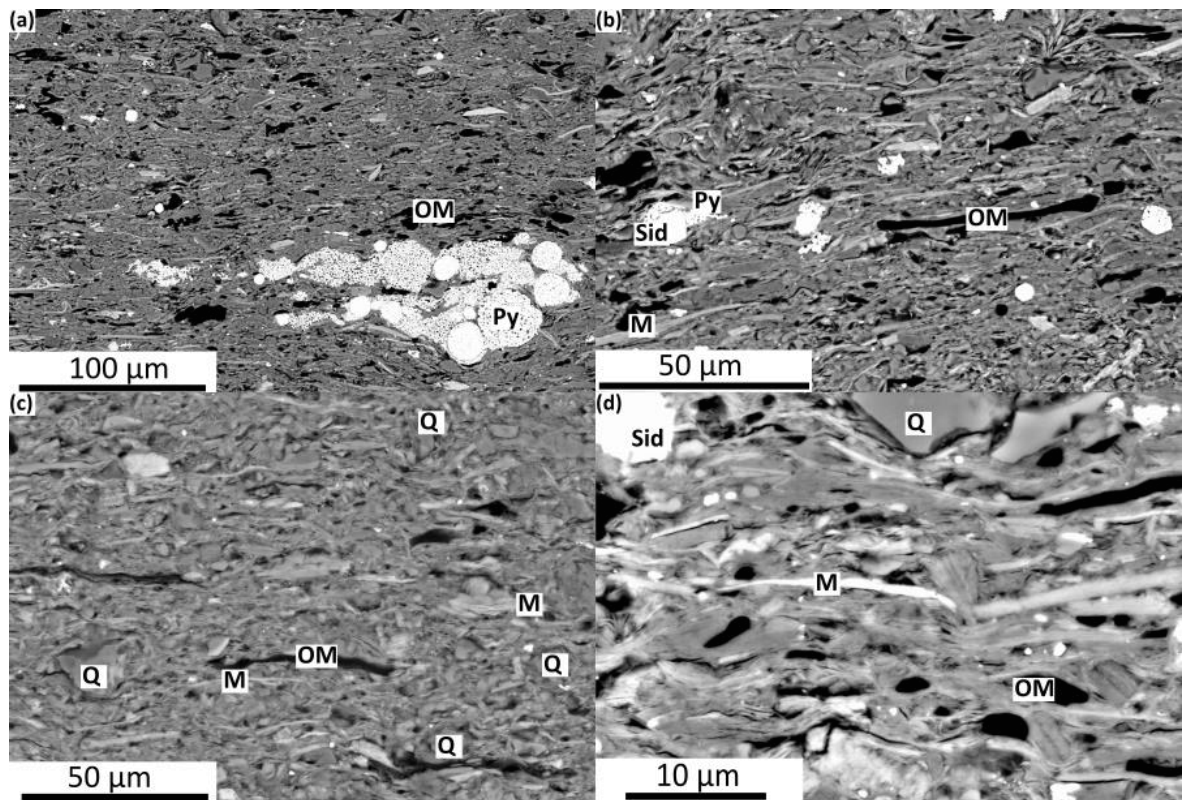


Figure 5.23. BSE images of Lower Cretaceous mudstone samples from wells (a)(b)(d) 6406/2-3 at 4003 m and (c) 6507/2-3 at 2878 m depths below seafloor, showing examples of well-developed clay mineral fabric. Q: quartz, M: mica, OM: organic matter, Py: pyrite, Sid: siderite. All sections imaged are perpendicular to the bedding

Overall BSEM observations suggest that the fine-grained clay mineral matrix is well aligned where quartz or other silt sized spherical grains (e.g. pyrite, siderite, feldspar etc)

do not disrupt the fabric. Where silt sized equidimensional grains are present the clay fabric is locally disrupted (Figure 5.24). These observations provide further support for the results shown in 5.4.5.

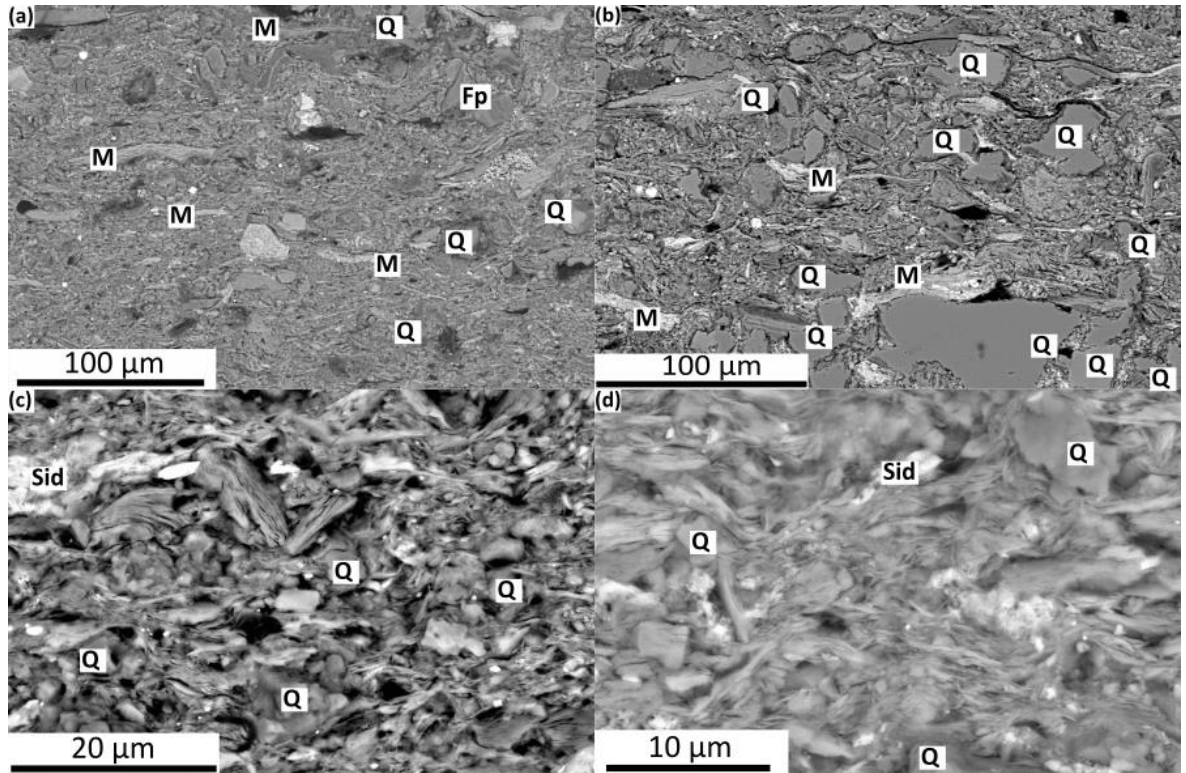


Figure 5.24. BSE images of Lower Cretaceous mudstone samples from well 6507/2-3 at 2508 (a)(c)(d) and 2878 m (b) depths below seafloor and, showing examples of poor sorting (a)(b) and of silt-sized quartz grains locally disturbing the clay mineral fabric (c)(d). Q: quartz, M: mica, Fp: detrital feldspar Sid: siderite. All sections imaged are perpendicular to the bedding

All samples contain a mixture of silt- and clay-sized particles and few samples also include sand-sized grains (Figure 5.25). Overall sorting of the samples is poor likely due to bioturbation and the silt particles are mixed with the clay-sized particles (Figure 5.24).

Silt-sized mineral grains are dominantly quartz and mica with lesser amounts of feldspar, carbonate grains, pyrite and organic matter. Carbonate grains include carbonate fossils (mostly foraminifers and bivalves) and authigenic minerals (dominantly siderite). Based on the observed arcuate shapes that reflect the cell structure typical of woody material (Figure 5.29b) (e.g. Milliken et al., 2012) the organic matter was likely derived from a terrestrial source region.

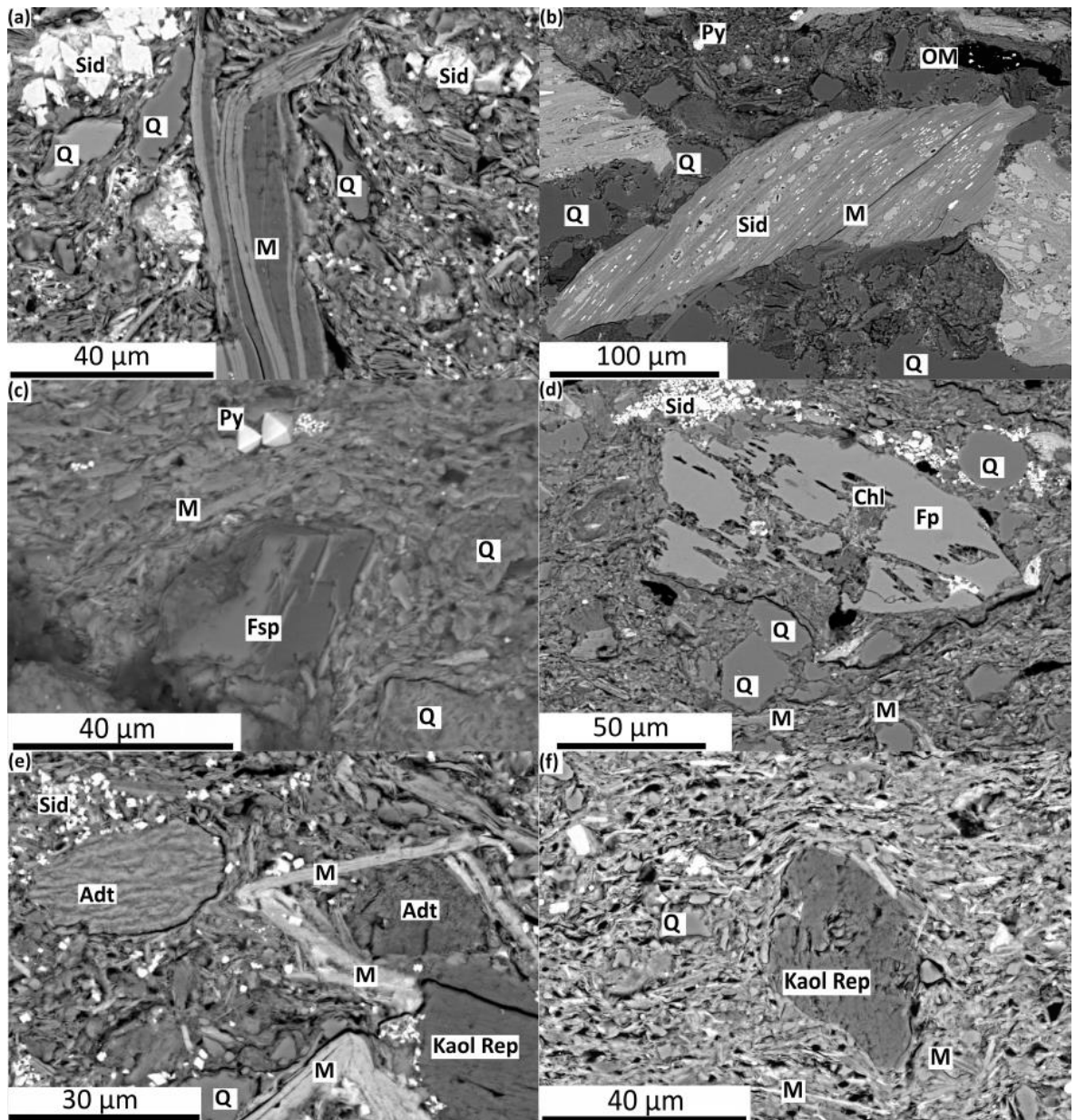


Figure 5.25. BSE images of Lower Cretaceous mudstone sample from wells 6406/2-3 at 4003 m (f) 6507/2-3 at 2508 (c) and 2878 m (a)(b)(d)(e) depths below seafloor showing examples of strongly altered and mechanically deformed detrital mica grains (a)(b); sand-sized detrital feldspar grain (c); partially dissolved detrital feldspar grain with authigenic chlorite inside its dissolution voids (d); Completely altered remnants of detrital grains of unknown origin (e) and detrital feldspar grains completely replaced by authigenic kaolinite (e)(f). Q: quartz, M: mica, Py: pyrite, Fp: detrital feldspar Sid: authigenic siderite, Kaol Rep: authigenic kaolinite replacing detrital feldspar, Chl: authigenic chlorite, Adt: completely altered remnants of detrital grains of unknown origin (likely feldspar). All sections imaged are perpendicular to the bedding.

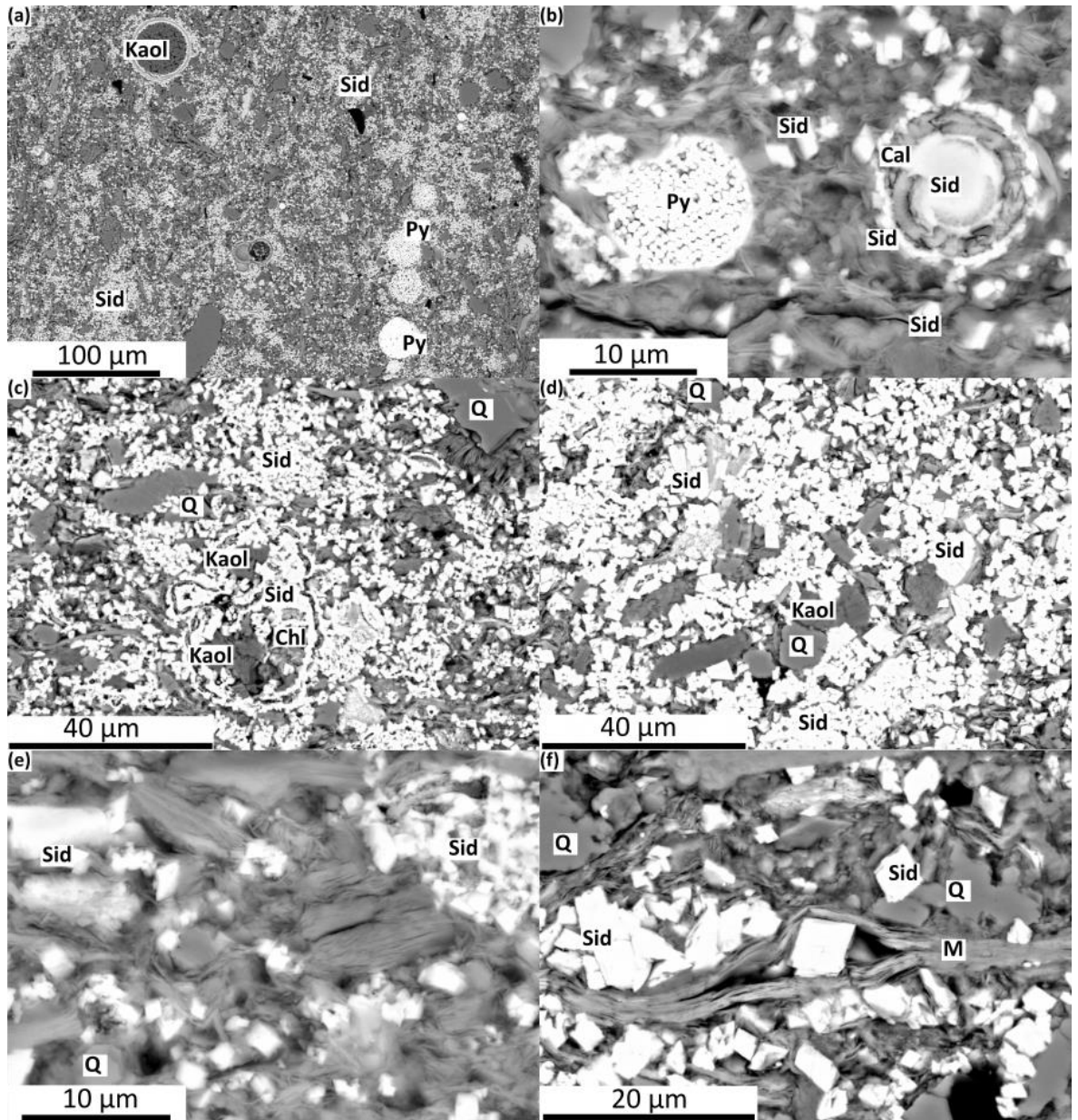


Figure 5.26. BSE images of a siderite concretion in Lower Cretaceous mudstone sample from well 6507/2-3 at 2878 m depth below seafloor with early diagenetic pore filling euhedral siderite cement and abundant foraminifer fossils, showing examples of early diagenetic kaolinite preserved inside foram fossil cavities (a,c), late diagenetic chlorite replacing early diagenetic kaolinite (c) and locally preserved isotropic clay fabrics (b,c,d,e,f). Cal: calcite, Py: pyrite, Sid: authigenic siderite Kaol: authigenic kaolinite Chl: authigenic chlorite. All sections imaged are perpendicular to the bedding.

The detected detrital mica and feldspar grains were commonly strongly altered (Figure 5.25). Partial dissolution of detrital feldspar grains was also observed in several samples (Figure 5.25d). In some cases detrital mineral grains (mostly feldspar, in some cases probably also rock fragments) were completely replaced by aluminosilicates (Figure 5.25e, f).

Mechanical features such as compactional bending of mica (Figure 5.25a) or bending of clays around more resistant mineral grains were also commonly observed features within these mudstones.

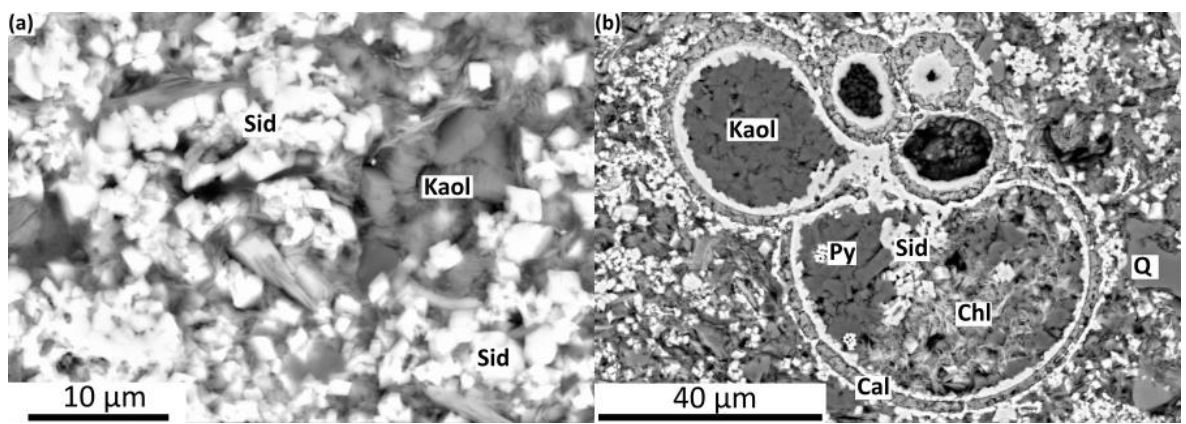


Figure 5.27. BSE images of a siderite concretion in Lower Cretaceous mudstone sample from well 6507/2-3 at 2878 m depth below seafloor with (a) abundant pore filling euhedral siderite and authigenic kaolinite, (b) example of a larger void inside a planktonic foraminifer fossil that has been filled by authigenic phases (pyrite, siderite, kaolinite and chlorite). Cal: calcite, Py: pyrite, Sid: siderite Kaol: kaolinite Chl: chlorite Q: quartz. All sections imaged are perpendicular to the bedding.

Figure 5.26 and 5.27 show BSEM images of an early-formed (see 5.4) siderite-cemented concretion from well 6507/2-3. Within the cemented zones petrographic observations reveal a high-volume percent of siderite cement occluding micrometre-scale pores. However, some porosity is preserved. It is apparent that calcitic grains are present in addition to the pore filling siderite cement. These grains are dominantly planktonic foraminiferal fragments which are in most cases completely or partially filled by authigenic siderite (Figures 5.26a, b,c and 5.27b). Phyllosilicate fabric inside the cemented zone is isotopic with common edge to face contacts (Figure 5.26b, e). This observation

clearly indicates that the early depositional fabric was isotropic and that most phyllosilicate grains were deposited as flocs.

Pyrite was present in both framboidal (Figure 5.23a, b and 5.26a,b) and euhedral (Figure 5.25c) forms and was commonly associated with organic matter (Figure 5.29).

Authigenic kaolinite with a well-developed vermiform habit was commonly observed filling shelter porosity within foraminifera tests (Figures 5.26a and 5.27b). In some cases, such kaolinite was also associated with pyrite (Figure 5.27b). Kaolinite was also present as grain replacement (likely replacing detrital K-feldspar) in patches within the clay matrix (Figure 5.25e, f).

Chlorite was also commonly observed as both detrital and authigenic component. Authigenic chlorite was commonly observed as replacement for kaolinite (Figure 5.26c and 5.27b) and detrital feldspar (Figure 5.25d).

Although SEM-CL observations have not been made in this study, the presence of euhedral terminations and edges to quartz grains –suggesting crystal growth into open pore space— clearly indicate that authigenic quartz is present in these samples as quartz overgrowth on detrital grains (Figure 5.28).

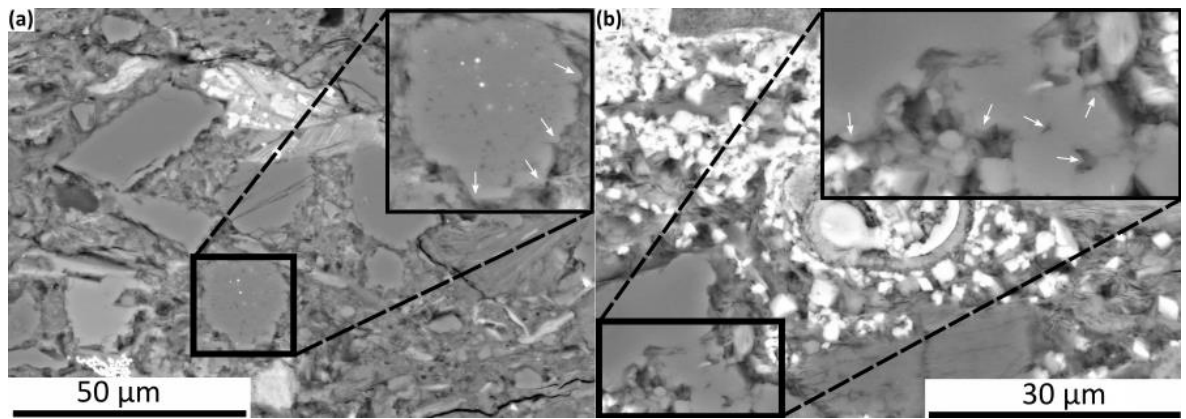


Figure 5.28. BSE images of a Lower Cretaceous mudstone sample from well 6507/2-3 at 2878 m depth below seafloor, showing examples of authigenic quartz overgrowth cement on detrital grains. White arrows denote euheedral crystal terminations resulting in inter-grown composite grains.

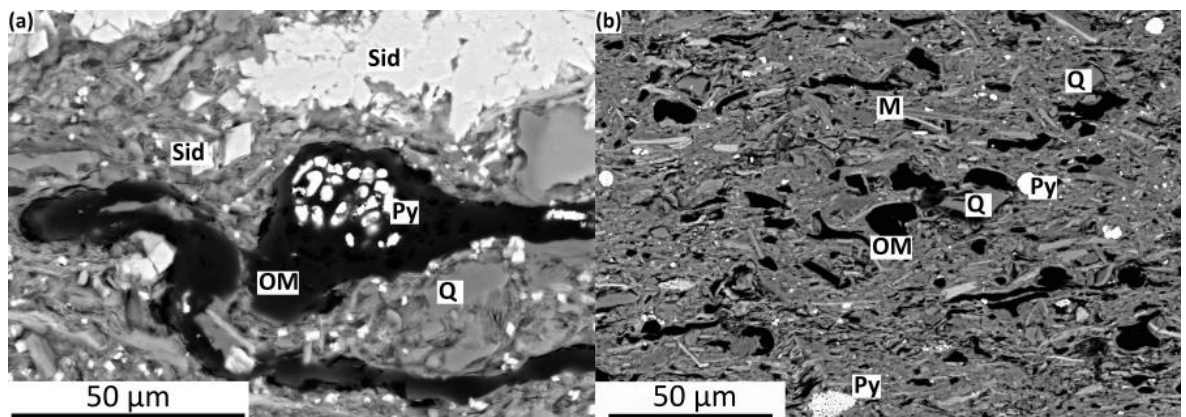


Figure 5.29. BSE images of Lower Cretaceous mudstone samples from wells (a) 6507/2-3 at 2878 m and (b) 6406/2-3 at 4003 m depths below seafloor, showing examples of (a) compactionally deformed organic matter (likely wood fragments) with abundant framboidal pyrite, (b) example of a mudstone sample with abundant detrital organic matter with characteristic arcuate shapes indicating continental origin and woody material.

5.4.7 Mudstone porosity and permeability

Grain density was measured for selected mudstone core samples (from wells 6406/2-3; 6506/11-3; 6506/11-4S; 6506/3-1 and 6507/2-3) using the “Small Pycnometer Method”, as it is described in 3.3.6. Measurements range from 2.60 to 2.94 g/cm³ (average 2.75 g/cm³) as it is shown in Figure 5.30a. No trend can be seen when plotting the data against depth. Relatively high values of particle density in samples from wells 6506/3-1 and 6506/11-4S are most likely related to the presence of iron bearing heavy minerals such as pyrite and siderite. In contrast the relatively low value of 2.60 g/cm³ in a mudstone sample from well 6406/2-3 can be attributed to the high organic matter content (5.17 wt% TOC) of the sample. High organic matter content in this sample is related to the presence of detrital plant fragments as it is shown in the BSEM image of the sample in Figure 5.29b. In overall, these results are in accordance with the QXRD determined bulk mineralogy and indicate fairly consistent particle densities within the Cretaceous mudstones.

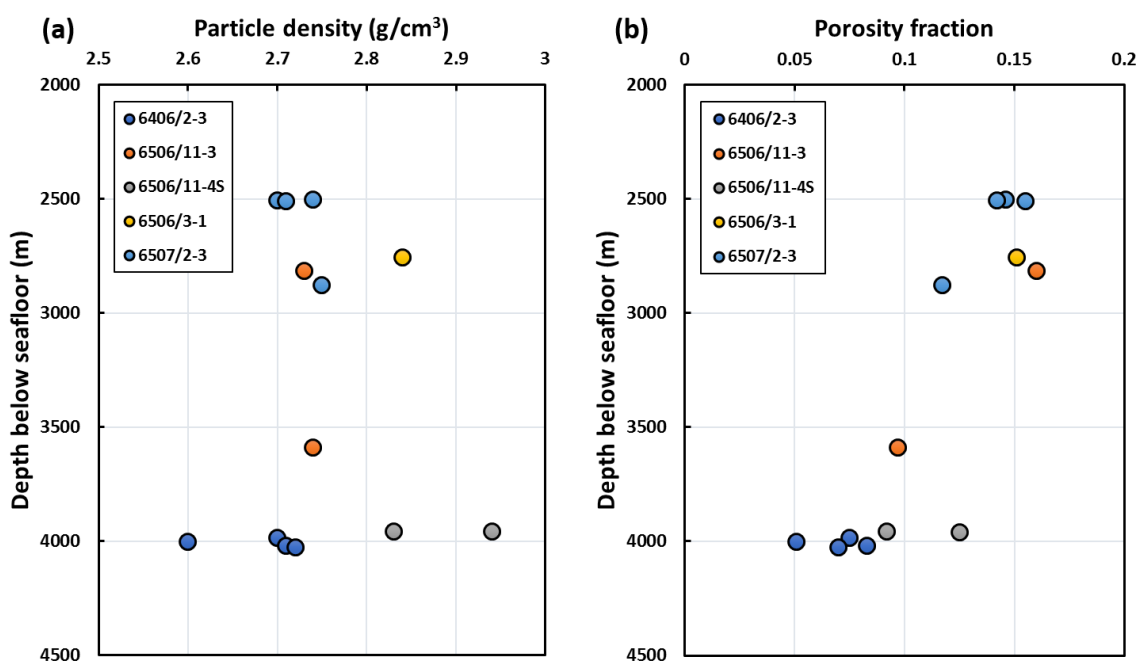


Figure 5.30. (a) Measured grain densities and (b) corrected total porosities of selected Cretaceous mudstone samples plotted against depth below seafloor.

Measured grain densities were used to determine the total porosity of the mudstone samples as it is described in 3.3.7. Corrected total porosity (refer to 3.3.8) values of the samples ranges from 5% to 16% as it is shown on Figure 5.30b. A clear decreasing trend can be seen when plotting the porosity data against depth (Figure 5.30b) which indicates ~10% porosity loss between 2500 and 4000 m bsf.

Figure 5.31a illustrate the relationship between illite-smectite (001) fabric intensity and porosity. Note the overall strong negative correlation. The only outlier data point corresponds to a sample which was affected by soft sediment deformation as it was shown in Figure 5.20. Figure 5.31b shows the relationship between mean pore throat radius (determined by MICP) and illite-smectite (001) fabric intensity. Similarly, an overall negative correlation can be seen. The two clear outlier data points correspond to a deformed and to a silty mudstone sample. The silt content has considerable effect on the mean pore throat radius of a given mudstone sample. This is because the largest pores in mudstones are usually associated with the boundary of larger silt sized particles, thus silty mudstones contain pores that are orders of magnitude larger than in clay-rich mudstones (e.g. Day-Stirrat et al., 2011).

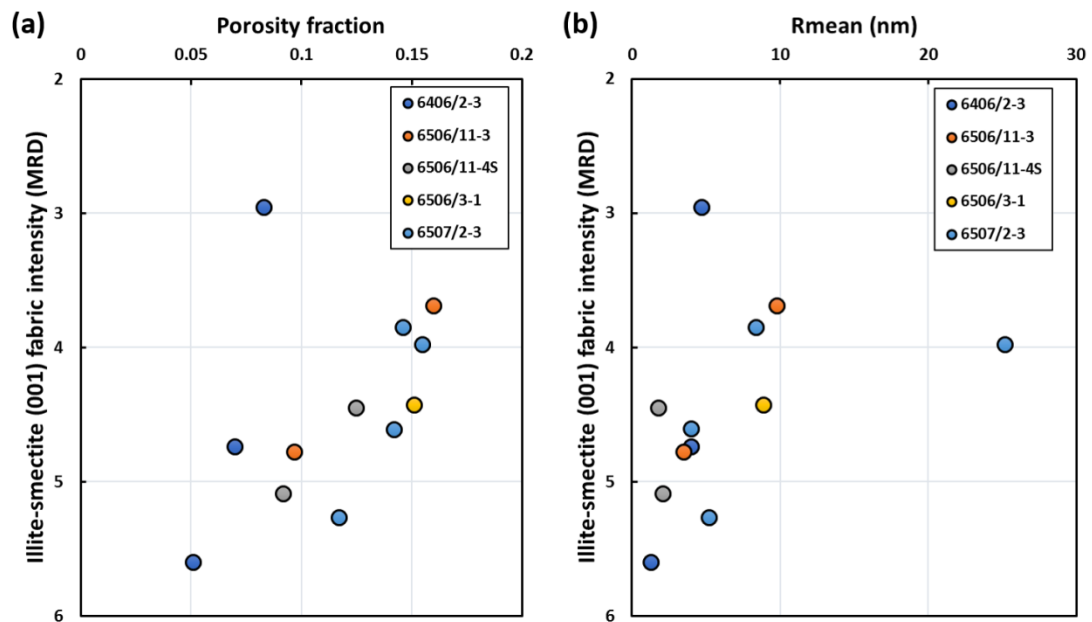


Figure 5.31. (a) Correlation between corrected total porosity and illite-smectite (001) fabric intensity; (b) correlation between mean pore throat radius and illite-smectite (001) fabric intensity.

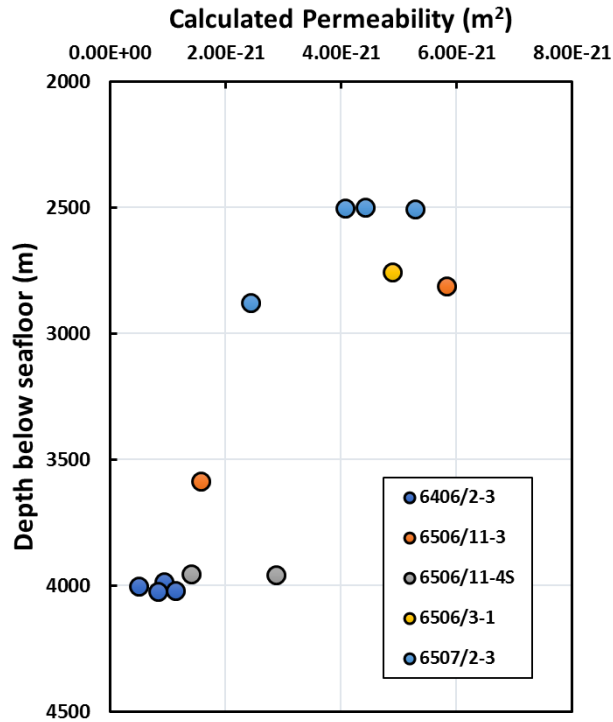


Figure 5.32. Calculated bedding perpendicular permeability (after Yang and Aplin, 2010) of selected Cretaceous mudstone samples.

Permeability of the mudstone samples was calculated based on the model of Yang and Aplin (2010) utilising bulk QXRD estimated total clay mineral content and estimated (corrected) total porosities. Total clay mineral content was used as a proxy for the mass fraction of particles less than two microns since no grain size distribution measurements have been made. The calculated permeabilities of the samples are very low (in the nD range) and show an overall decreasing permeability-depth trend (Figure 5.32).

Figure 5.33 shows corrected pore throat size distributions, corrected cumulative porosities and corrected mean pore throat radius of selected Cretaceous mudstone samples. These were all determined using Mercury Injection Core Porosimetry (MICP) as it was described in 3.3.8.

In overall, these results reveal very tight lithologies with mean pore throat sizes below 10nm and show an overall loss of the larger mesopores with increasing depth. Full grain density, total porosity, MICP and calculated permeability data can be found in Appendix VI.

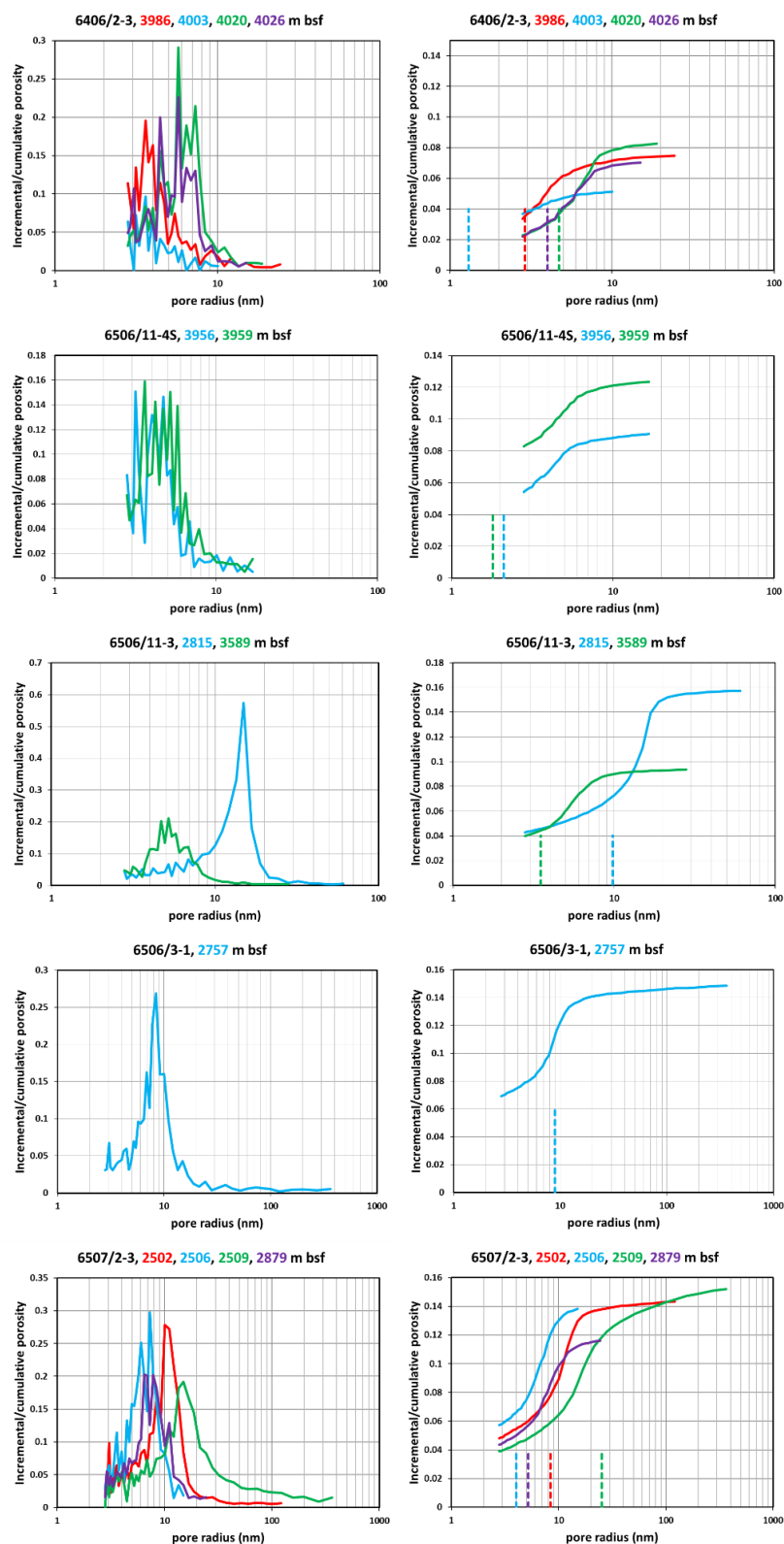


Figure 5.33. Corrected pore throat size distribution (left) and corrected cumulative porosity (right) (from MICP) of selected Cretaceous mudstone samples. Dashed lines on right figures denote mean pore throat radius.

5.5 One-dimensional basin modelling

One-dimensional modelling was carried out to estimate the magnitude of overpressure build-up by disequilibrium compaction in wells 6406/2-3 and 6507/2-3. Details of the modelling software and approach can be found in 3.5. Modelling parameters including estimated depositional periods, layer thicknesses and lithology are listed in Tables 5.8 and 5.9.

These two wells were selected based on previous work done by Cicchino et al. (2015) and Sargent et al. (2015) who showed that lateral variation in the efficacy of pore water escape following rapid Plio-Pleistocene burial resulted in considerable lateral porosity variation in the Cretaceous mudstones. Cicchino et al. (2015) denoted the wells high, intermediate and low porosity according to their calculated density porosity values at 2700 m depth (refer to 5.3 for more details). According to their classification 6406/2-3 is a high porosity well and 6507/2-3 is a low porosity well.

It should be emphasised that the main purpose of these models was to estimate the maximum magnitude of overpressure build-up by disequilibrium compaction in these wells and not to accurately model the present-day pore pressures in the Cretaceous mudstones. An additional aim was to further test the assumption, made by previous researchers (Skar et al., 1999; O'Connor et al., 2012), that the Cretaceous formations were hydrostatically pressured (or close to hydrostatic) prior to the deposition of the Naust Formation.

Porosity and permeability of the default PetroMod lithology types which were used in modelling the pore pressure evolution is shown in Figure 5.36. Note that the modelled porosities and permeabilities are in accordance with the measured porosities and calculated permeabilities of the Cretaceous mudstones.

The one-dimensional burial history models for wells 6406/2-3 and 6507/2-3 are shown in Figure 5.34. The Cretaceous Kvitnos and Lange Formations experienced an early rapid burial phase between deposition and ~85 Ma, followed by a long phase of slow burial until 2.8 Ma. This was followed by a phase of very rapid burial to its present burial depth. Overpressure build up in the Lange Formation in well 6406/2-3 started during the end of

the early rapid burial phase ~85 Ma. The model indicates minor overpressure build-up during the slow burial phase and predicts around 5 MPa overpressure in middle part of the Lange Formation (~9 MPa at the base of the formation) prior to the deposition of the Naust Formation (Figure 5.35). In 6507/2-3 the model predicts hydrostatic conditions in the Lange Formation throughout most of the slow burial phase and the build-up of only around 1 MPa overpressure (at the base of the formation ~ 3 MPa) prior to the deposition of the Naust Formation (Figure 5.35).

The model predicts the present-day top of overpressure at around 2 km below sea surface within the Paleogene formations which is consistent with the reported distribution of overpressure in the Halten Terrace area (Hermanrud et al., 1998; Skar et al., 1999; O'Connor et al., 2012) (Figure 5.37). However, the modelled build-up of overpressure caused by disequilibrium compaction is considerably lower than the reported RFT pressure measurements from the Lange Formation (Figure 5.37). As shown in Figure 5.37 the measured formation pressures in the Lange Formation are ~15 MPa higher at around 4600 m (bss) in well 6406/2-3 and ~5 MPa higher at around 3200 m (bss) in well 6507/2-3 respectively. This implies the presence of pressure generating mechanisms other than disequilibrium compaction in the Lange Formation mudstones which is consistent with the findings of O'Connor et al. (2012).

| Time (Ma) | | Group | Formation | Depth (m RKB) | | Thickness (m) | Lithology |
|-----------|-----|--------------|-------------|---------------|--------|---------------|-------------|
| Start | End | | | Top | Base | | |
| 16 | 0 | Nordland | | 396 | 1954 | 1558 | Siltstone |
| 2.8 | 0 | | Naust Fm | 396 | 1518 | 1122 | Siltstone |
| 2.8 | 16 | | Kai Fm | 1518 | 1954 | 436 | Siltstone |
| 55 | 16 | Hordaland | | 1954 | 2300 | 346 | Shale |
| 55 | 16 | | Brygge Fm | 1954 | 2300 | 346 | Shale |
| 65 | 55 | Rogaland | | 2300 | 2425 | 125 | Shale |
| 59 | 55 | | Tare Fm | 2300 | 2364 | 64 | Shale |
| 65 | 59 | | Tang Fm | 2364 | 2425 | 61 | Shale |
| 94 | 65 | Shetland | | 2425 | 3429 | 1004 | Shale |
| 83 | 65 | | Springar Fm | 2425 | 2549 | 124 | Shale |
| 86 | 83 | | Nise Fm | 2549 | 2838 | 289 | Shale |
| 94 | 86 | | Kvitnos Fm | 2838 | 3429 | 591 | Shale |
| 145 | 94 | Cromer Knoll | | 3429 | 4629 | 1200 | Shale |
| 96 | 94 | | Lysing Fm | 3429 | 3440 | 11 | Sandstone |
| 125 | 96 | | Lange Fm | 3440 | 4620 | 1180 | Shale |
| 140 | 125 | | Lyr Fm | 4620 | 4629 | 9 | Marl |
| 183 | 140 | Fangst | | 4629 | 4837 | 208 | Sandstone |
| 200 | 183 | Bat | | 4837 | 5255.9 | 418.9 | Sandy shale |

Table 5.8. Basic model parameters, with estimated depositional periods in millions of years, layer thicknesses and lithology for the 6406/2-3 1D burial history model. Based on Dalland et al. (1988) and Ottesen et al. (2009).

| Time (Ma) | | Group | Formation | Depth (m RKB) | | Thickness (m) | Lithology |
|-----------|-----|--------------|-------------|---------------|------|---------------|-----------|
| Start | End | | | Top | Base | | |
| 16 | 0 | Nordland | | 378 | 1835 | 1457 | Siltstone |
| 2.8 | 0 | | Naust Fm | 378 | 1375 | 997 | Siltstone |
| 2.8 | 16 | | Kai Fm | 1375 | 1835 | 460 | Siltstone |
| 55 | 16 | Hordaland | | 1835 | 1948 | 113 | Shale |
| 55 | 16 | | Brygge Fm | 1835 | 1948 | 113 | Shale |
| 65 | 55 | Rogaland | | 1948 | 2052 | 104 | Shale |
| 59 | 55 | | Tare Fm | 1948 | 2005 | 57 | Shale |
| 65 | 59 | | Tang Fm | 2005 | 2052 | 47 | Shale |
| 94 | 65 | Shetland | | 2052 | 2850 | 798 | Shale |
| 83 | 65 | | Springar Fm | 2052 | 2157 | 105 | Shale |
| 86 | 83 | | Nise Fm | 2157 | 2453 | 296 | Shale |
| 94 | 86 | | Kvitnos Fm | 2453 | 2850 | 397 | Shale |
| 145 | 94 | Cromer Knoll | | 2850 | 3843 | 993 | Shale |
| 96 | 94 | | Lysing Fm | 2850 | 2891 | 41 | Sandstone |
| 125 | 96 | | Lange Fm | 2891 | 3791 | 900 | Shale |
| 140 | 125 | | Lyr Fm | 3791 | 3843 | 52 | Marl |

Table 5.9. Basic model parameters, with estimated depositional periods in millions of years, layer thicknesses and lithology for the 6507/2-3 1D burial history model. Based on Dalland et al. (1988) and Ottesen et al. (2009).

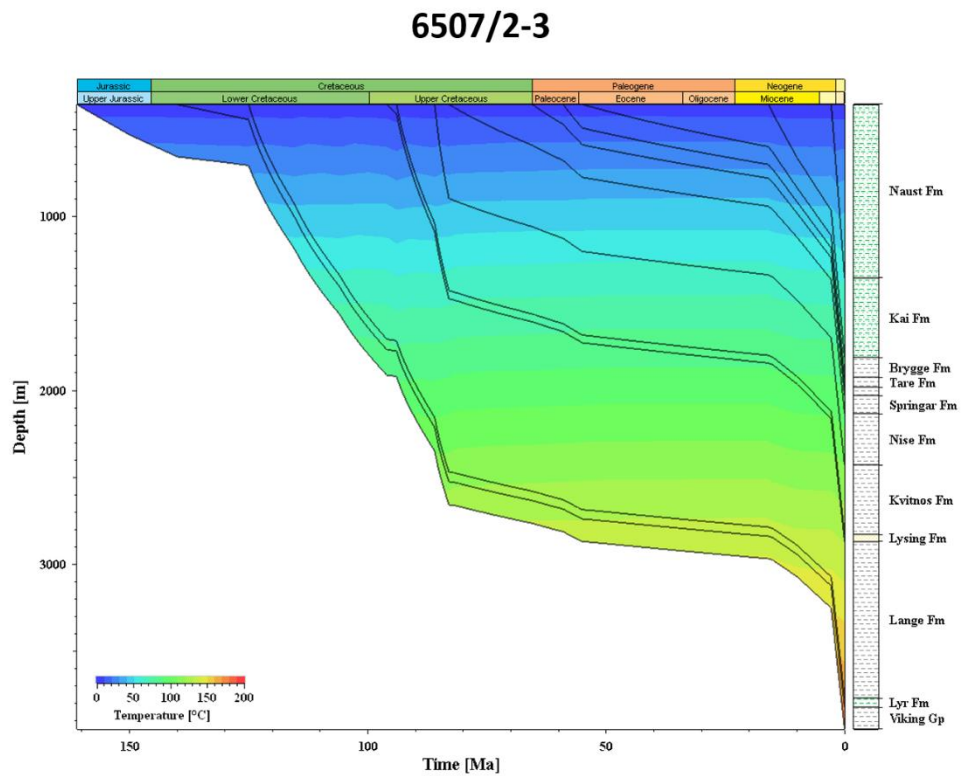
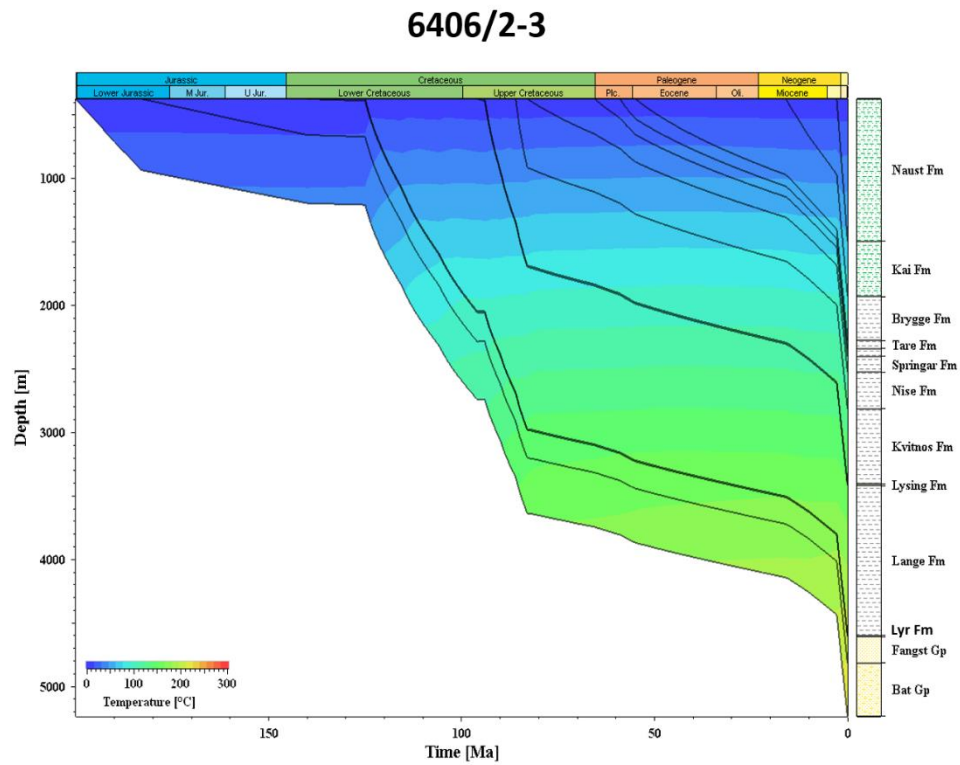
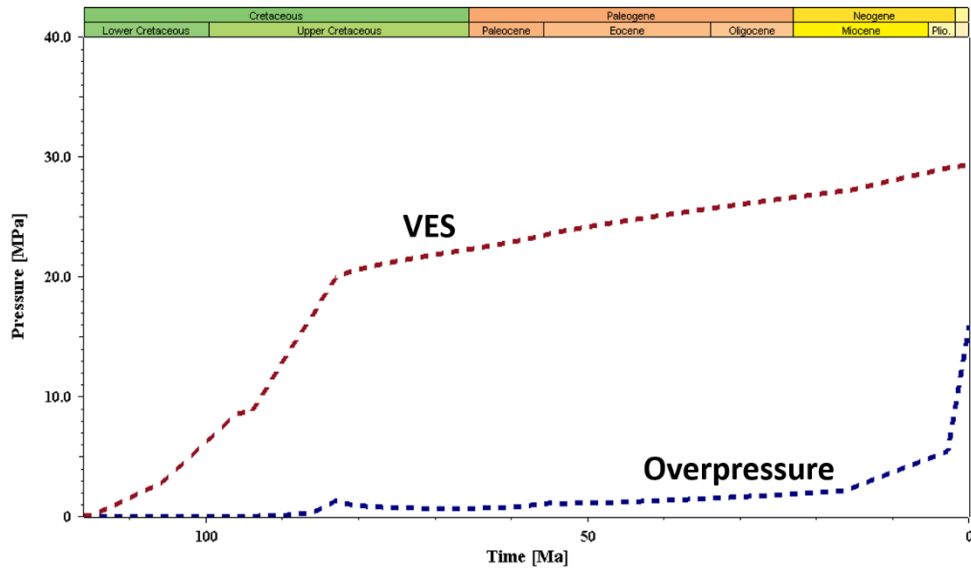


Figure 5.34. 1D burial-temperature history plot for wells 6406/2-3 and 6507/2-3. Depth is displayed relative to sea surface (m).

6406/2-3



6507/2-3

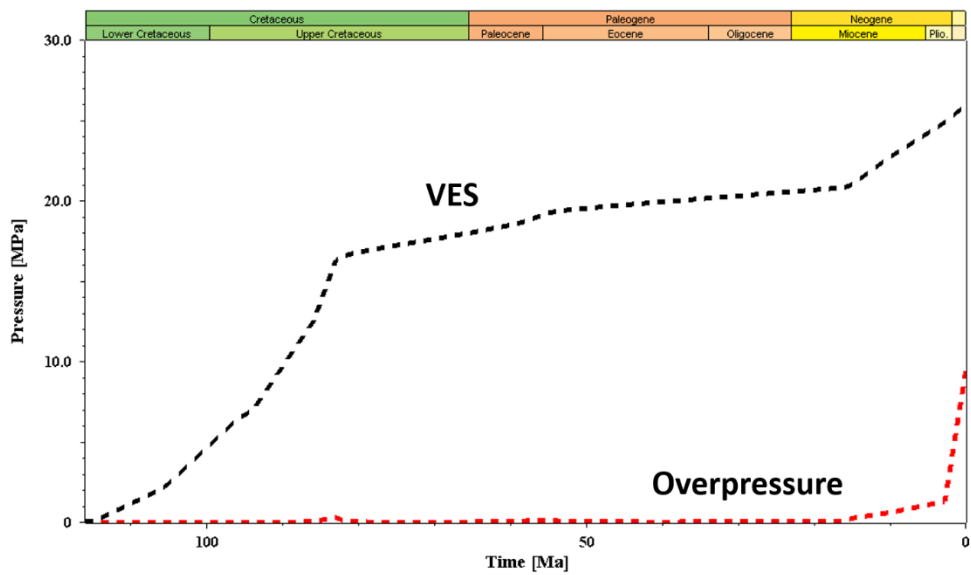
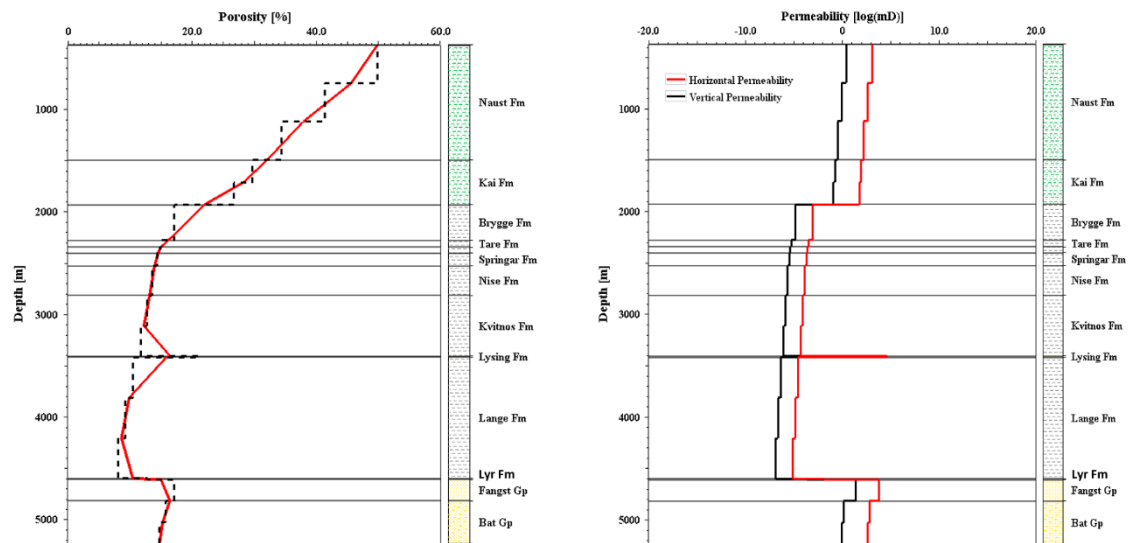


Figure 5.35. Pore fluid overpressure and vertical effective stress (VES) development for the Lower Cretaceous Lange Formation (middle part) in wells 6406/2-3 and 6507/2-3.

6406/2-3



6507/2-3

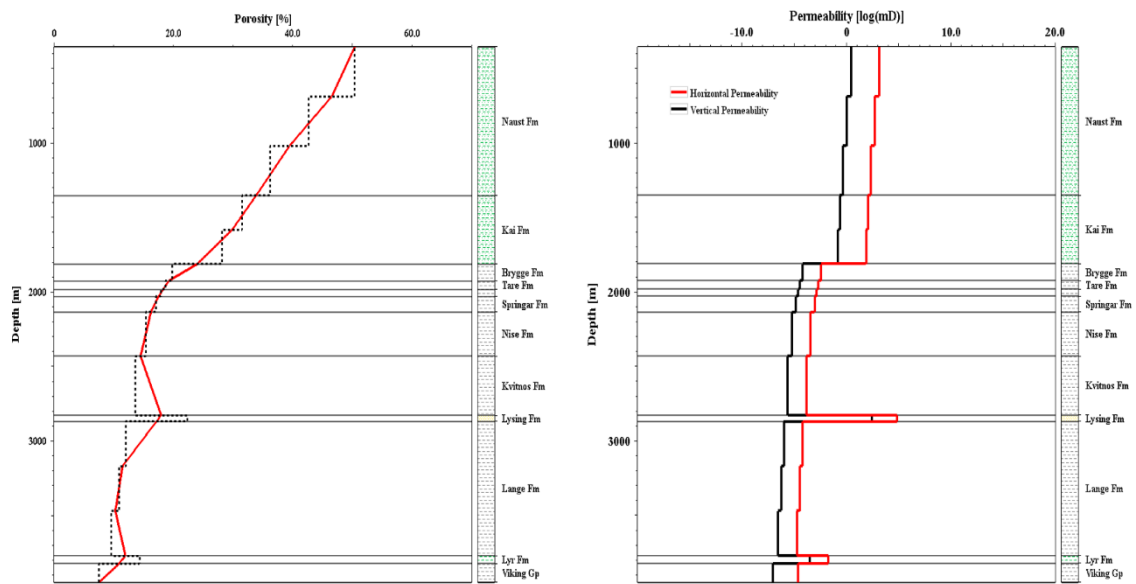
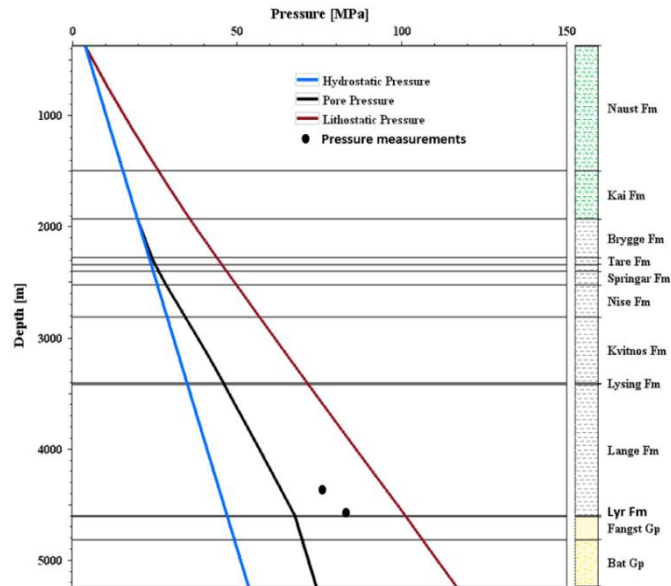


Figure 5.36. Porosity and permeability of the modelled formation units in wells 6406/2-3 and 6507/2-3. Depth is displayed relative to sea surface (m).

6406/2-3



6507/2-3

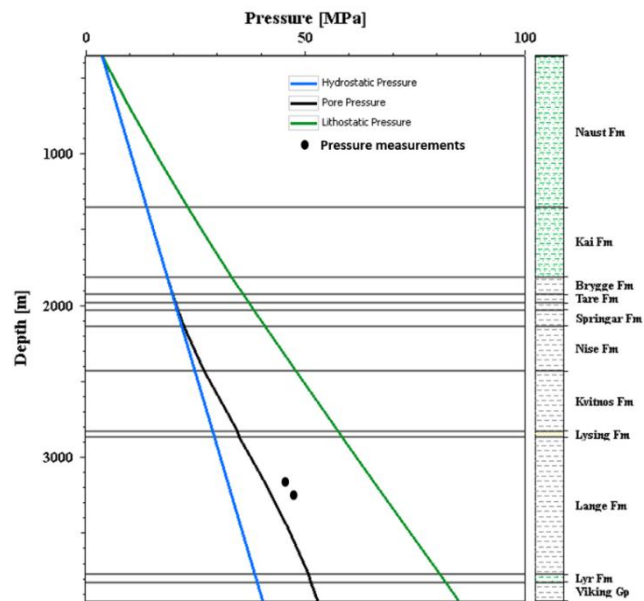


Figure 5.37. Modelled formation pressures caused by disequilibrium compaction and measured RFT pressures (from O'Connor et al., 2012) within the Lange Formation in wells 6406/2-3 and 6507/2-3. Pore pressure measurements exceed the modelled fluid pressures by 5-10 MPa which suggest the presence of pressure generating mechanisms other than disequilibrium compaction within the Cretaceous mudstones. Depth is displayed relative to sea surface (m).

5.6 Discussion

5.6.1 Sediment provenance and paleoweathering reconstruction from major and trace element geochemistry

Figure 5.38 shows major and trace elemental distributions of the Cretaceous mudstone samples normalized to post-Archaean Australian Shale (PAAS; from Taylor and McLennan, 1985). Elemental distributions of core samples and cuttings are displayed separately. Considerable differences can be seen between the elemental distributions of core samples and cuttings.

In comparison to PAAS the Cretaceous mudstone core samples appear to be depleted in Mn, Mg, Ca, K and P. Depletion of Mn, Mg and Ca in the Cretaceous mudstones can be attributed to lesser amount of carbonates (calcite, dolomite, siderite) in these samples compared to PAAS. Note the positive Mn anomaly in samples CH6 and CH8 which is most likely the result of relatively higher amounts of carbonate (calcite and siderite) in these samples. Depletion of K indicates lesser amounts of detrital mica and K-feldspar in these samples compared to PAAS. Phosphorus depletion is the result of lesser amount of accessory phases such as apatite compared to PAAS.

In contrast to the core samples mudstone cuttings show enrichment in Mn, Ca and P compared to PAAS. Mn and Ca enrichment is the result of the presence of considerable (and variable) amounts of carbonate in cuttings compared to core samples. This is because the core samples were mostly collected from homogeneous and uncemented mudstone intervals in contrast to cuttings which represent averaged composition of several meters of mudstone. Phosphorous enrichment in cuttings is the result of the presence of more abundant accessory phases such as apatite compared to PAAS.

Figure 5.39 shows major and trace elemental distributions of Cretaceous mudstone samples normalised to average upper continental crust (UCC; from McLennan, 2001). Similarly, to Figure 5.38 elemental distributions of core samples and cuttings are displayed separately due to the considerable differences between the elemental distributions of different types of samples.

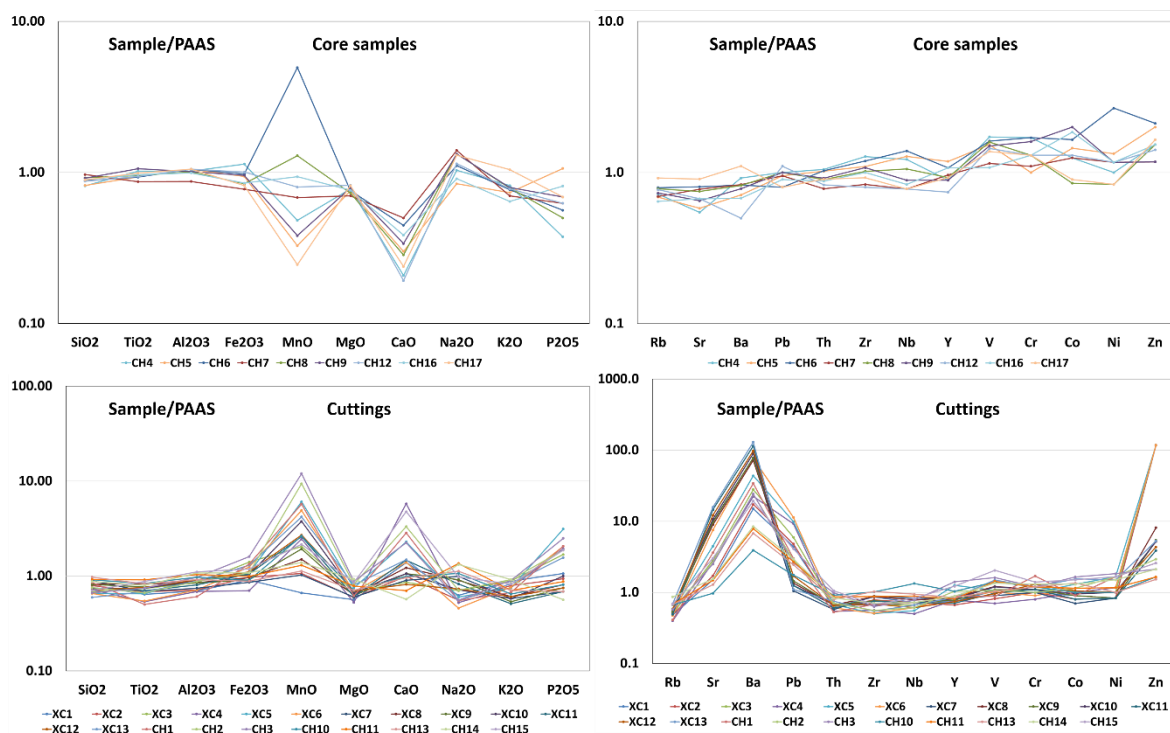


Figure 5.38. Multi element spider diagram for Cretaceous mudstones. Major and trace element composition is normalised to post-Australian average shale (PAAS; values of Taylor and McLennan 1985).

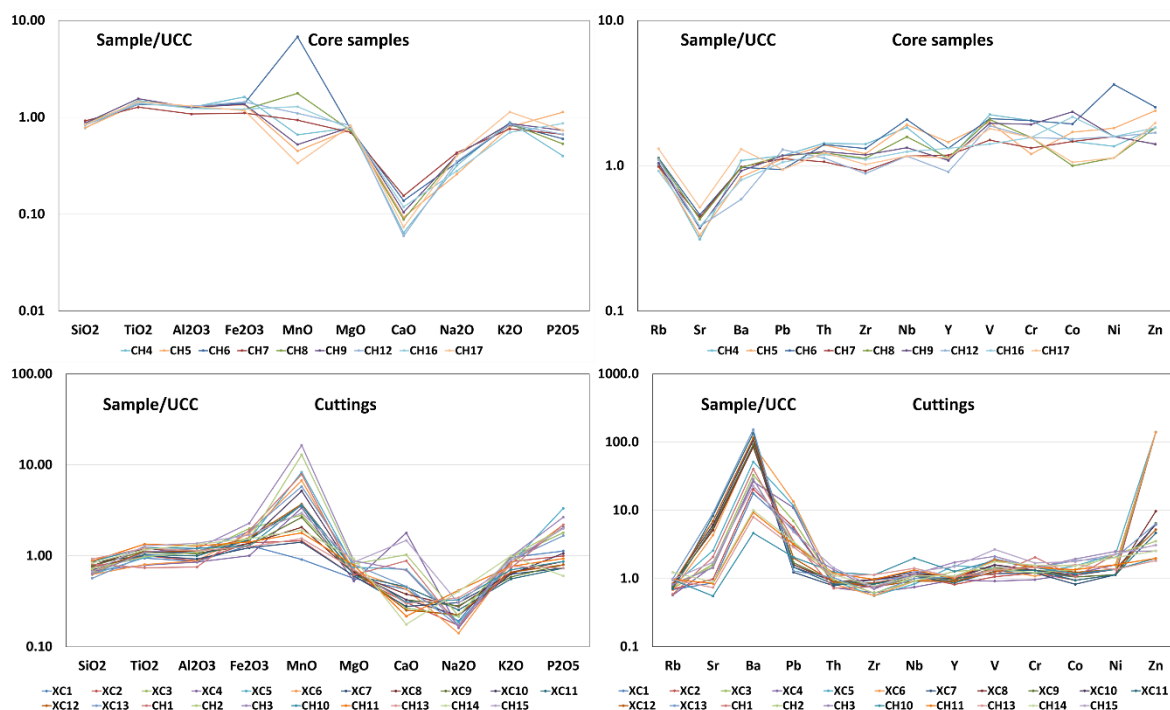


Figure 5.39. Multi element spider diagram for Cretaceous mudstones. Major and trace element composition is normalised to average upper continental crust (UCC; values from McLennan, 2001).

The plot of major elements normalized to UCC values indicate significant depletion of Ca and Na and slight depletion of Mg and K for both core samples and cuttings. Depletion of Ca (depletion is considerably less for cuttings due to higher carbonate content) and Na in the mudstone samples compared to UCC is clearly the result of chemical weathering of the source material during erosion, transport and deposition of these sediments (Nesbitt et al., 1980; Nesbitt and Young, 1982; McLennan et al., 1993a). Slight depletion of Mg and K compared to UCC can be attributed to lesser amounts of dolomite and detrital mica (and K-feldspar). Just as in Figure 5.38, Mn and P show positive anomaly for the cuttings and negative anomaly for the core samples. This is due to differences in carbonate and apatite content between them. Aluminium and titanium show slight enrichment compared to UCC which can be attributed to the high total clay mineral content in the Cretaceous mudstone samples. Slight enrichment of iron can be attributed to the presence of pyrite and siderite.

Trace elemental composition of the core samples is fairly similar to PAAS with the exception of minor depletions of Rb, Sr and Ba and minor enrichments of V, Cr, Co, Ni and Zn (Figure 5.38). Compared to UCC the core samples show Sr depletion and slight enrichments of Th, Nb, V, Cr, Co and Zn (Figure 103). Slight depletion of Sr and Ba can be attributed to weathering since strontium and Ba along with Ca and Na tend to be leached during chemical weathering (Nesbitt et al., 1980). Enrichments of Th and Nb is most likely the result of the high total clay mineral content in the Cretaceous mudstone samples. V, Cr, Co and Zn enrichments are likely related to more abundant mafic mineral components in the Cretaceous mudstone samples compared to PAAS.

In contrast to the core samples cuttings show significant enrichment in Ba, Pb, Zn and Sr compared to both PAAS and UCC. Enrichment in Ba, Pb and Zn in the cuttings is clearly the result of contamination by drilling mud. Barium can be attributed to barite. However, in addition to barite other weighting additives such as galena are also commonly used. Zinc can be attributed to drilling fluid components such as zinc bromide (ZnBr_2). Enrichment of Sr compared to both PAAS and UCC can be attributed to the relatively high carbonate content of the cutting samples.

Uniform K_2O/Al_2O_3 and TiO_2/Al_2O_3 ratios of the Cretaceous mudstone samples indicate a source area of similar bulk composition throughout their deposition. This is also supported by the relatively little variation in the ratios of low-solubility trace elements (such as Th, Hf, REEs etc.) which are generally considered inert during the sediment cycle (Taylor and McLennan, 1985).

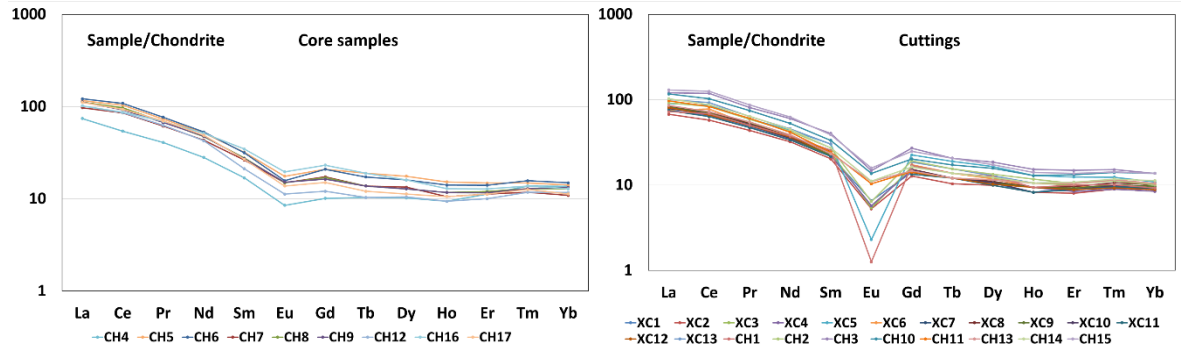


Figure 5.40. Chondrite-normalised (values of Taylor and McLennan, 1985) REE patterns for Cretaceous mudstones.

Figure 5.40 shows chondrite-normalised REE patterns of Cretaceous mudstone samples. REE patterns for both core samples and cuttings display LREE enrichments and variable degrees of development of a negative Eu anomaly. The chondrite normalised ratio of Eu/Eu^* of the mudstone samples range from 0.06 to 0.70 (average of 0.49). These values are close to but somewhat lower than PAAS (0.66). Since europium is not fractionated during weathering or diagenesis relative to other REE (McLennan, 1989) the size of the Eu anomaly reflects the Eu anomaly in the source rocks. The chondrite normalised La_N/Yb_N ratios vary from 5.43 to 9.82 (average of 8.51). Once again, these values are similar to that of PAAS (9.2). In overall, patterns like LREE enrichment, flat HREE and negative Eu anomaly indicate that these mudstones were derived from a dominantly felsic continental source region (Bhatia, 1985; McLennan et al., 1993a).

Similarly, ratios of La/Th (average of 3.07), Th/Sc (average of 0.67) and relatively large Hf contents (average of 4.35) of the mudstone samples indicate derivation from a continental crust of largely granitic or granodioritic composition (Bhatia and Taylor, 1981; McLennan et al., 1993a) (Figure 5.41).

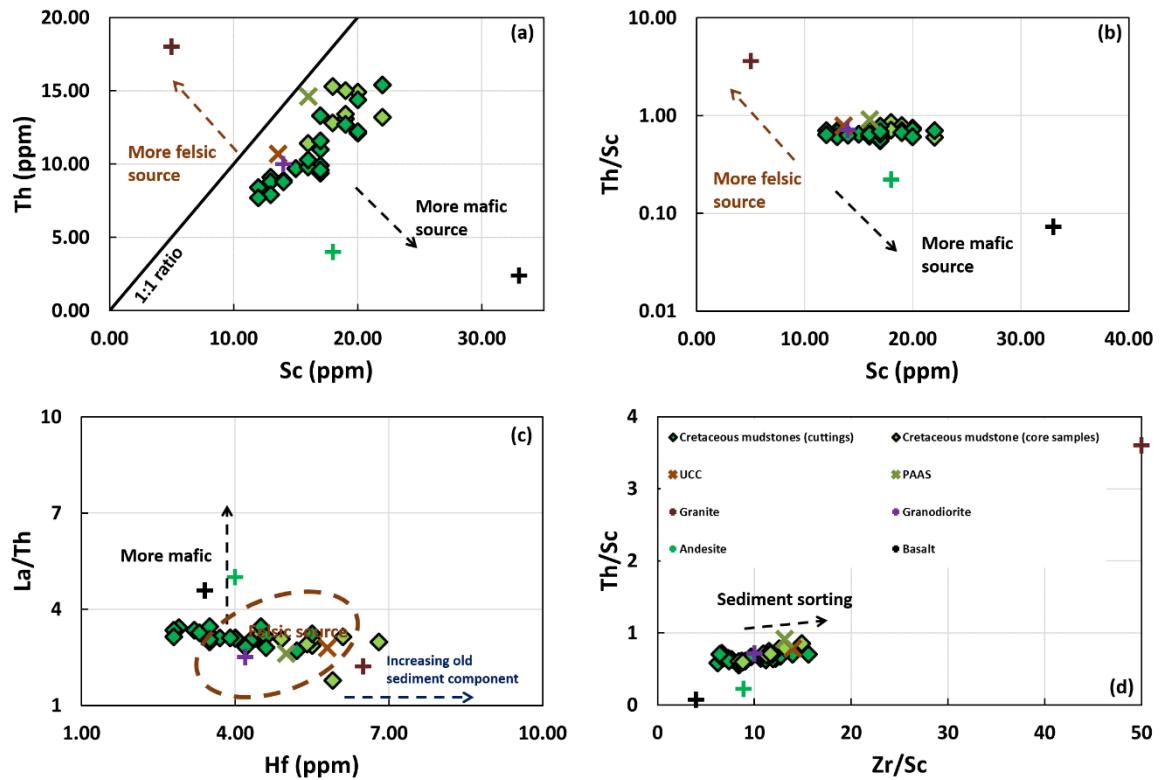


Figure 5.41. Selected trace element plots indicating the average composition of the source. (a) Th versus Sc (b) Th/Sc versus Sc (c) discrimination plot of La/Th versus Hf (after Floyd and Leveridge, 1987) (d) discrimination plot of Th/Sc versus Zr/Sc (after McLennan et al., 1993) monitoring sediment sorting and recycling processes. UCC, PAAS (values from Taylor and McLennan, 1985 and McLennan, 2001) and average Phanerozoic granite, granodiorite, andesite and basalt (values from Condie, 1993) are additionally plotted for reference.

Figure 5.41a,b show the ratios of Th/Sc in Cretaceous mudstones. The Th/Sc ratio of the samples is a sensitive index of average source composition (Taylor and McLennan, 1985). Rocks with mafic compositions tend to have considerably higher Sc than do rocks with felsic or intermediate compositions. This is illustrated in Figure 5.41 by showing the Th/Sc ratios for average Phanerozoic granite, granodiorite, andesite and basalt (values taken from Condie, 1993) and also for average upper continental crust (UCC, values from McLennan, 2001) and for post-Archean Australian average shale (PAAS, values from Taylor and McLennan, 1985). The average Th/Sc ratio in the Cretaceous mudstones (0.67) is close to that of granodiorite (0.71) and UCC (0.78) and is lower than that of PAAS (0.91). Figure 5.41c shows a plot of La/Th against Hf which also provides a useful discrimination between different source compositions. As shown in the figure, sediments derived from a

dominantly felsic source region have relatively low and uniform La/Th ratios and Hf contents in the range of approximately 3-7 ppm. Erosion of ancient metasedimentary rocks will result in an increase in the Hf content due to the release of zircon which is the main host mineral phase for this element (Floyd and Leveridge, 1987). Figure 5.41d shows a plot of Th/Sc versus Zr/Sc which can be used to monitor sediment recycling and sorting processes (McLennan et al., 1993a). In overall, the relatively low Zr/Sc ratio of the samples indicates no or only minor sediment recycling. Strong positive correlation between Zr/Sc and Si/Al ratio indicates that the zircon enrichment in samples with relatively higher Zr/Sc ratio is due to sediment sorting (more abundant coarse-grained material).

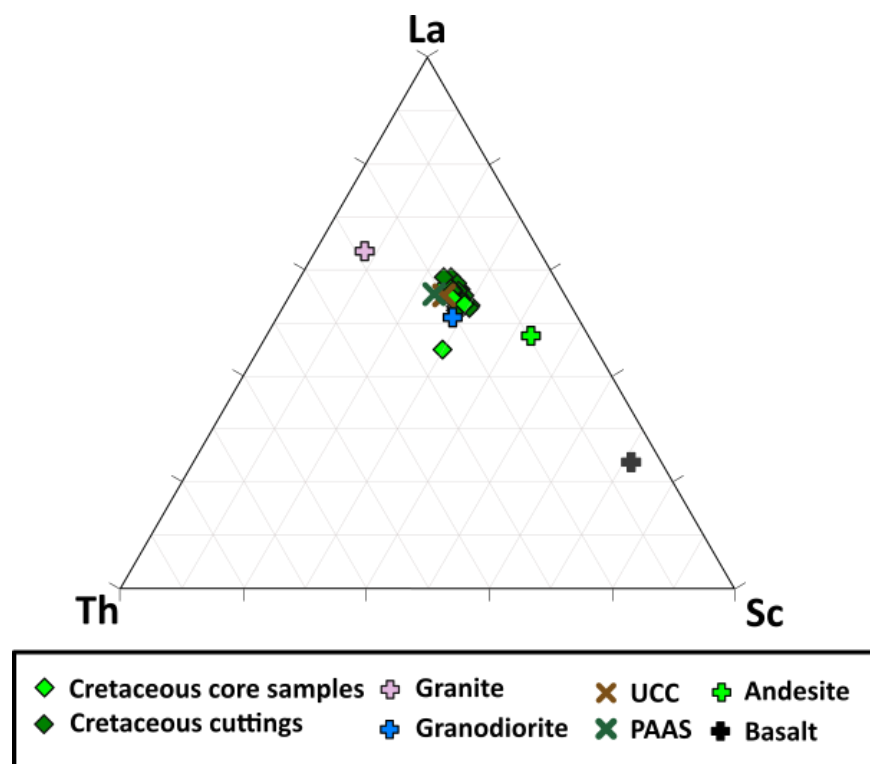


Figure 5.42. Discrimination plot of La-Th-Sc (after Bhatia and Crook, 1986) indicating the average bulk composition of the source. UCC, PAAS (values from Taylor and McLennan, 1985 and McLennan, 2001) and average Phanerozoic granite, granodiorite, andesite and basalt (values from Condie, 1993) are additionally plotted for reference.

On the discrimination plot of La-Th-Sc the samples plot close to the average composition of the upper continental crust (UCC) (Figure 5.42).

The degree of source area weathering was quantified using the chemical index of alteration (CIA) following the method of Nesbitt and Young (1982) as described in 3.3.5.

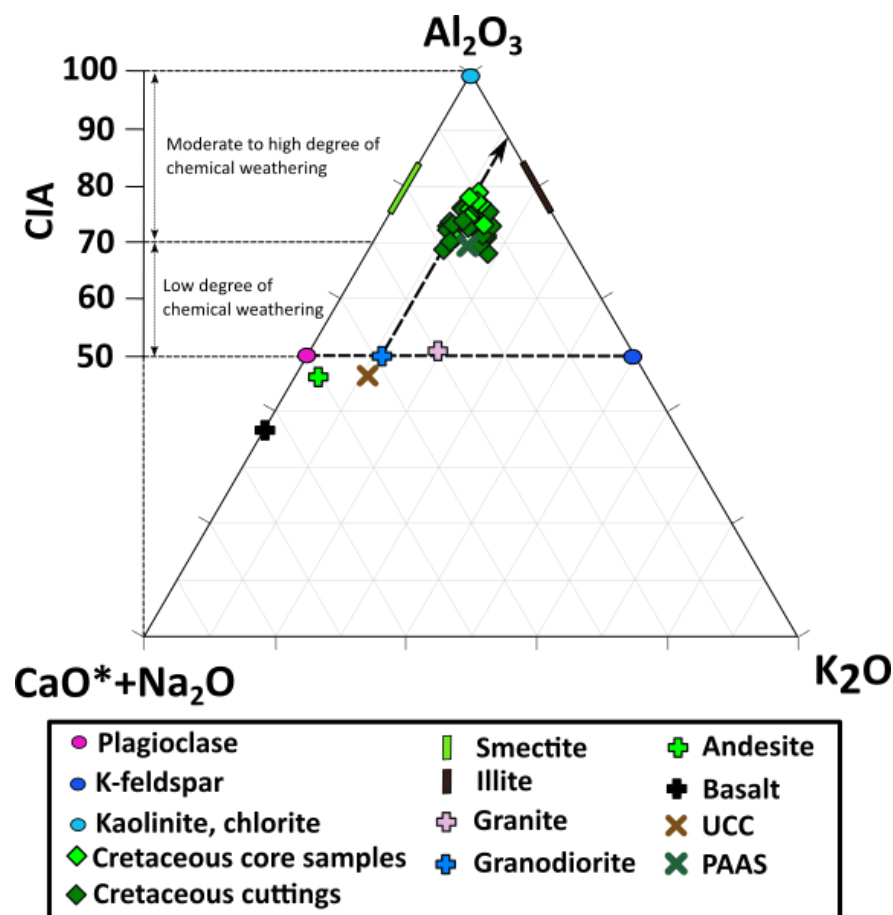


Figure 5.43. A-CN-K ($A=Al_2O_3$; $CN=CaO^*+Na_2O$; $K=K_2O$; all in molecular proportions; refer to 3.3.5 for more detail) ternary diagram of the Cretaceous mudstone sample set with associated chemical index of alteration (CIA) values (after Nesbitt and Young, 1982). Dashed arrow represents the estimated weathering trend. Average compositions of granite, granodiorite, andesite and basalt (values from Condie, 1993), post-Archean Australian average shale (PAAS, Taylor and McLennan, 1985), average upper continental crust (UCC, McLennan, 2001) and average composition of illites and smectites are additionally plotted for reference. Refer to text for further explanation.

CIA values for Cretaceous mudstone samples indicate moderate to high degree of chemical weathering (Figure 5.43). Cretaceous mudstone samples display considerable scatter when plotted in an A-CN-K space as shown in Figure 5.43. Several samples are inclined towards the K apex indicating considerable differences in K_2O content among the samples. These are related to differences in detrital mica and K-feldspar content. The estimated weathering trend shown in Figure 5.43 is subparallel to the A-CN join and is

marked by the dashed arrow. This was plotted as a straight line through the core sample data which showed considerable less variation. The trend projects onto the feldspar join at a point which indicates the proportion of plagioclase to K-feldspar in the source. This indicates an average composition of the source similar to that of the average upper continental crust or that of an average granodiorite (Figure 5.43).

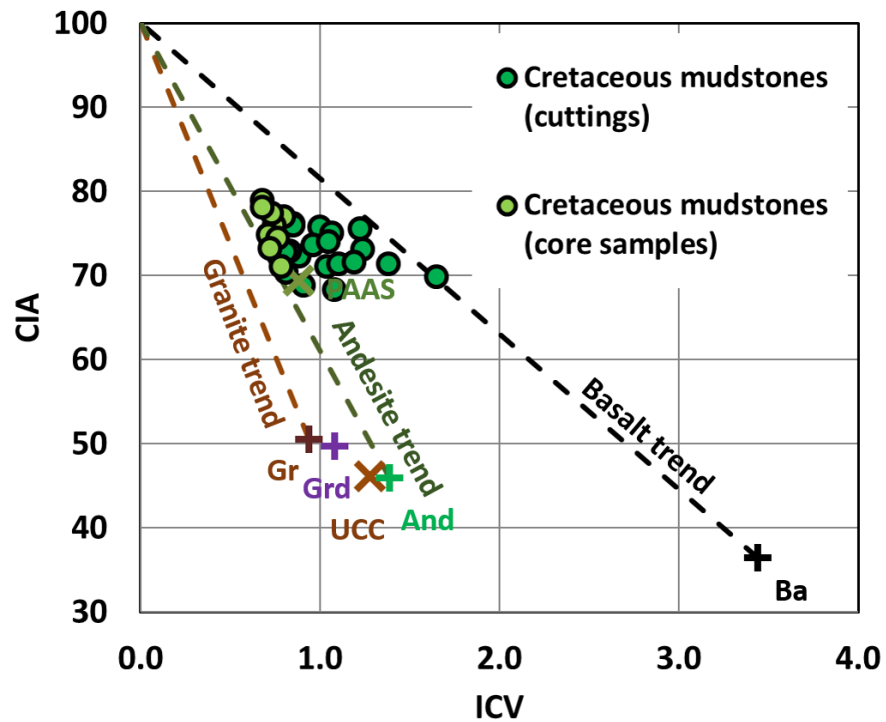


Figure 5.44. Plot of chemical index of alteration (CIA) against index of compositional variability (ICV) (after Potter et al., 2005) illustrating relationships between the degree of source area weathering and original detrital mineralogy in the Cretaceous mudstones. Dashed lines represent weathering trends. Average compositions of granite, granodiorite, andesite and basalt (values from Condie, 1993), post-Archean Australian average shale (PAAS, Taylor and McLennan, 1985), average upper continental crust (UCC, McLennan, 2001) are additionally plotted for reference. Refer to text for further explanation.

Figure 5.44 shows a crossplot of chemical index of alteration (CIA) against index of compositional variability (ICV). ICV values of cuttings show considerable variability which can be explained by the variable carbonate and detrital feldspar content of the cutting samples and associated variability of CaO, MnO, Fe₂O₃ and Na₂O (refer back to 3.3.5). ICV values of the core samples are more consistent and suggest evolution from an initial

composition close to that of an average andesite or that of the average upper continental crust.

In overall, inferences made from major and trace elements are in accordance with the findings of Fonneland et al. (2004) who analysed detrital zircons in order to determine the provenance of Cretaceous sandstones in the Norwegian Sea. According to their findings the eastern flank of the Norwegian Sea received sediments mainly from the Norwegian landmass which is mostly composed of Precambrian metamorphic rocks of dominantly felsic composition.

5.6.2 Mudstone mineralogy

The primary sediment composition and the early diagenetic reactions determine subsequent diagenetic pathways. Early diagenetic processes are contemporaneous with deposition and can locally affect the physical properties by cementing depositional porosity and make the mudstone locally resistant to mechanical compaction. These early diagenetic processes are typically redox processes where organic matter becomes oxidised by microbes (Aplin and Macquaker, 2011).

Sulphate reduction was locally important during early diagenesis in the Cretaceous mudstones as evidenced by the common occurrence of framboidal pyrite. Framboidal pyrite likely precipitated from iron-rich porewaters near sites of sulphide supply, usually near organic matter as a result of bacterial sulphate reduction, where sulphide production rates were high enough to reach supersaturation with respect to FeS. Euhedral pyrite precipitated directly from iron-rich porewaters when FeS₂ saturation was reached near sites where FeS saturation levels were not reached at the sites of sulphide supply due to lower sulphide production rates from organic matter (Taylor and Macquaker, 2000).

The presence of siderite indicates that Fe(III) reduction was also important (at least locally) during early diagenesis (Taylor, 1998). Cementation by siderite and formation of siderite concretions is likely to have occurred prior to compaction as a result of bacterially mediated respiratory processes. This indicates that sites of cementation were close to the sediment-water interface for prolonged periods of times in order to allow for

cementation to take place (e.g. Taylor and Macquaker, 2000, 2014). Although siderite (and also other carbonate cementing phases) precipitation had locally affected mudstone porosities its overall effect on porosity reduction in the studied Cretaceous mudstones is negligible.

Abundant early diagenetic kaolinite can be interpreted as the result of Al-mobilization by organic acids generated during organic matter oxidation reactions. The likely sources of Al were poorly crystalline detrital aluminium oxides and clay minerals (Foscolos, 1984; Taylor and Macquaker, 2014). In addition to this, kaolinite also formed by leaching of detrital feldspar and mica grains as evidenced by the presence of grain replacement kaolinite.

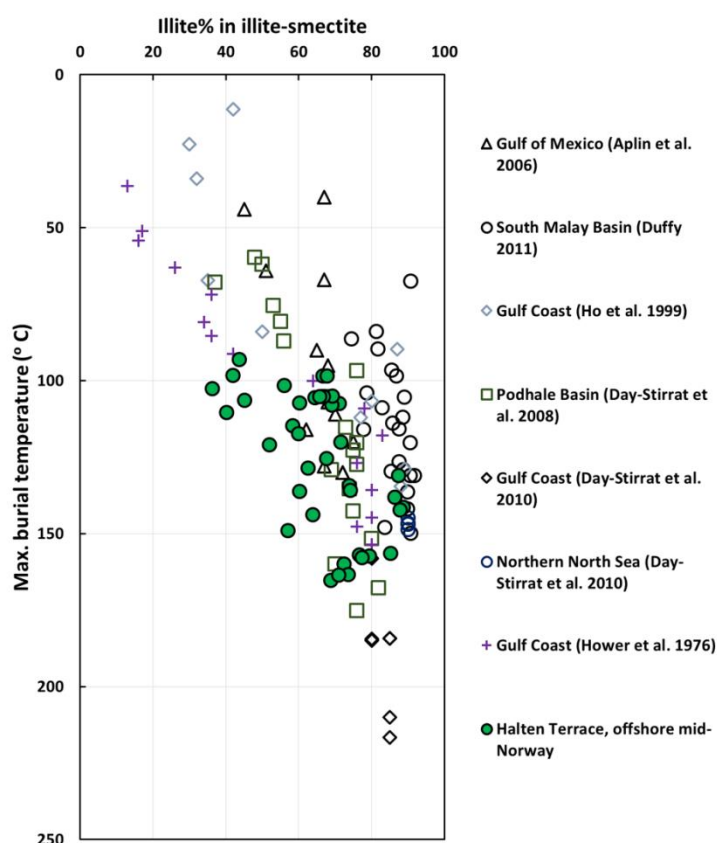


Figure 5.45. Published examples of illite % in illite-smectite with new results from Cretaceous mudstones of the Halten Terrace, offshore mid-Norway plotted against maximum burial temperature. Illite % in illite-smectite was calculated using the CEC results as described in 3.3.3.

Among the identified late diagenetic mineral phases chlorite formed diagenetically from kaolinite and likely also from smectite in the presence of Fe and Mg (Bjørlykke, 1998).

QXRD and CEC results showed clear evidence for ongoing illitization of smectite in the studied Cretaceous mudstones. Figure 5.45 shows % illite in mixed-layer illite-smectite trends from several published examples and new results from the Cretaceous mudstone from Halten Terrace, offshore mid-Norway plotted against burial temperature. In the Cretaceous mudstones illitization is still ongoing above 100°C because of the substantial recent burial as it is demonstrated in Figure 5.46. This observation is in accord with the understanding that illitization is a kinetic reaction controlled by both time and temperature (e.g. Huang et al., 1993) (see 2.4.1).

Possible sources for the identified quartz cement include dissolution and recrystallisation of biogenic silica (siliceous radiolaria or sponges) and smectite illitization (Peltonen et al., 2009; Thyberg et al., 2010; Thyberg and Jahren, 2011).

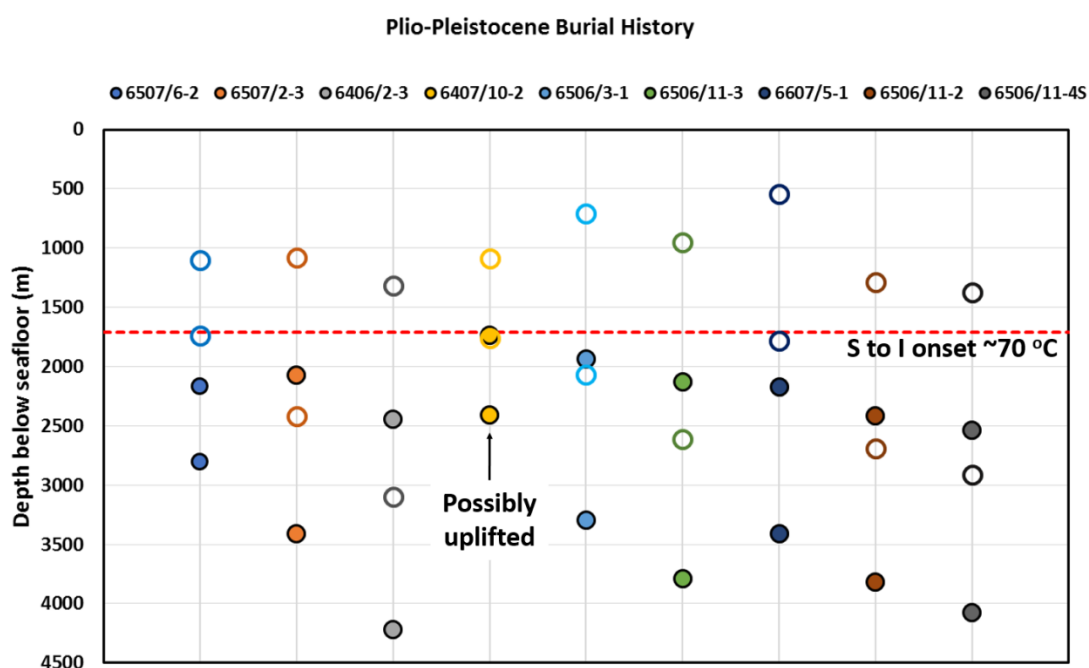


Figure 5.46. Depths of the top of the Kvitnos and base of the Lange formations at present day (filled circles) and prior to deposition of the Naust Formation (empty circles) in all studied wells. Red dashed line represents the 70°C isotherm which is the likely temperature of the onset of illitization. Temperature is calculated using a common linear geothermal gradient of 38°C/km from the seafloor which is assumed to be at 5°C.

5.6.3 The effect of rapid Plio-Pleistocene burial on the extent of smectite illitization

Figure 5.46 illustrates the Plio-Pleistocene burial history of the studied wells by showing the present-day depths of the top of the Kvitnos and base of the Lange formations and their depths prior to Naust deposition. These depths intervals are shown in relation to the likely depth of the onset of smectite illitization (~1700 m bsf; ~70°C). Note that prior to the deposition of the Naust Formation (prior to 2.8 Ma) illitization has likely not yet started in wells 6507/6-2, 6407/10-2 and 6607/5-1 and in the rest of the wells it has only started at greater depths in the Lange Formation. This recent substantial burial has the consequence that illitization is still ongoing in these mudstones at temperatures well above 100°C. This observation is in accord with the understanding that illitization is a kinetic reaction controlled by both time and temperature (see 2.4.1).

5.6.4 The role of rapid Plio-Pleistocene burial in overpressure development

Previous studies have suggested that pore pressures within the Cretaceous formations were hydrostatic at 2.8 Ma, prior to the deposition of the Naust Formation (Skar et al., 1999; O'Connor et al., 2012), because of the limited amount of Cenozoic burial up to 2.8 Ma (Figure 5.34). Note that this would suggest a laterally consistent porosity-depth trend (normal compaction trend) for the Cretaceous mudstones at that time. Interestingly, however Cicchino et al. (2015) reported large variation in the Cretaceous porosity-depth trends (inferred from density logs) across the Halten Terrace. They also showed that this variation is only slightly reduced when plotted against depth below the base of the Naust Formation. They concluded that lateral variation of the Cretaceous mudstone compaction trends can be attributed to lateral variations in the escape of porewater since 2.8 Ma while mudstone compaction was ongoing. Their proposal was later confirmed by the pore pressure interpretation of Sargent et al. (2015) and Goult et al. (2016). However Goult et al. (2016) also noted the possibility that there may have been some overpressure present in the Cretaceous mudstones in some of the high porosity wells when the Naust deposition began.

One-dimensional basin modelling carried out in this thesis indicates that the Cretaceous mudstones in wells 6406/2-3 and 6507/2-3 were likely to have been overpressured prior to the deposition of the Naust Formation. The pore pressure model predicts considerable amount of overpressure (~ 9 MPa) in the Lange Formation pre Naust in the high porosity well 6406/2-3 and minor overpressure (~ 3 MPa) in the low porosity well 6507/2-3. These overpressure values are considerably higher compared to the interpretation of Goulty et al. (2016) who estimated 3 MPa overpressure in 6406/2-3 and no overpressure in 6507/2-3 at 2.8 Ma (pre Naust).

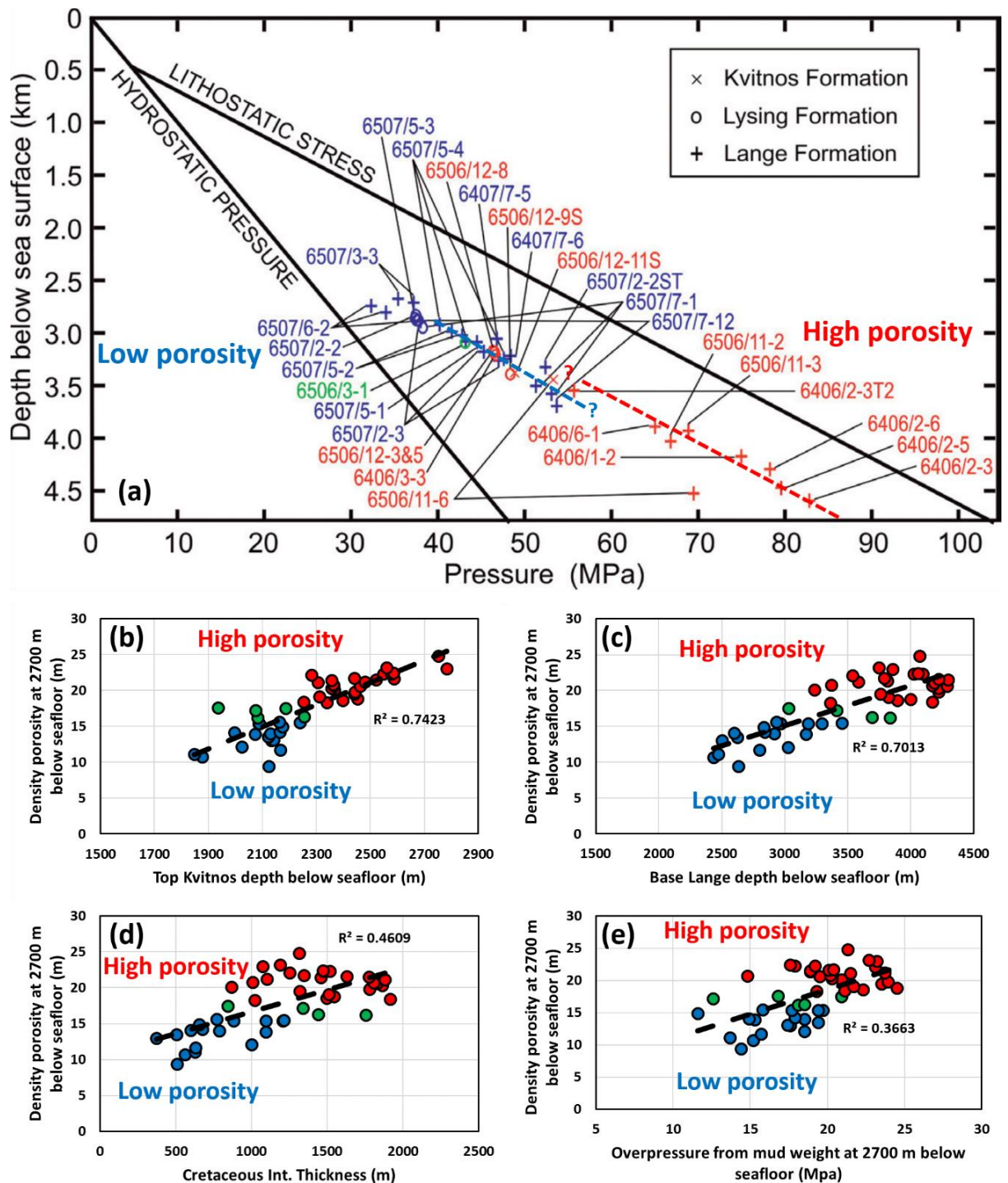


Figure 5.47. (a) Multi well pressure-depth plot of Figure 69 colour-coded according to the porosity classification of Cicchino et al. (2015). Separate trends are drawn through pressure measurements from the Lange Fm sands in the shallower low porosity wells and in the deeper high porosity wells (modified after Cicchino et al., 2015). Lateral variations in mudstone porosity show correlation with the (b) present day top Kvitnos depth, (c) base Lange depth, (d) Cretaceous interval thickness and (e) overpressure estimated from mud weight. Plots coloured according to the porosity

classification of Cicchino et al. (2015). Correlation plots were constructed using data presented by Cicchino et al. (2015).

These anomalously high values of overpressure are likely the result of simplistic model assumptions such as homogeneous fine-grained formation lithologies, continuous deposition (no gaps or erosion etc.) and uncertainties related to porosity-depth and porosity-permeability relationships used in the model.

One interesting feature of the modelling results is the striking difference between 6406/2-3 and 6507/2-3 in predicted pre Naust pore pressure magnitudes.

The considerably higher predicted overpressures in 6406/2-3 are likely due to the considerably thicker Cretaceous interval in this well. Also, the Cretaceous mudstones were buried to greater depths in 6406/2-3 compared to 6507/2-3 (Figures 5.34 and 5.46). This has the consequence that the Cretaceous mudstones in 6406/2-3 were more compacted and had lower porosities and permeabilities which allowed more effective fluid retention than in 6507/2-3. The more effective fluid retention in this well likely resulted in less compaction following the Naust deposition. This observation suggests that in the high porosity wells the porosity and permeability of the Cretaceous mudstones could have been low enough (even without considering the effect of clay diagenesis which was likely ongoing in the Lange Formation at that time; see Figure 5.46) to impede porewater escape and thereby generate at least few megapascals of overpressure by disequilibrium compaction pre 2.8 Ma. This observation is in agreement with the proposal of Goult et al. (2016) that there might have been some overpressure before the Naust deposition in the Cretaceous mudstones at least in some of the high porosity wells. Results are presented in Figure 5.47 to further support this hypothesis. Figure 5.47b-e was constructed using data presented by Cicchino et al. (2015). The authors have previously noted that the lateral variations in mudstone porosity show some correlation with overpressure as estimated from mud weight used in drilling (Figure 111e). In addition to this lateral variation in density porosity show strong correlation with the present day top of Kvitnos and base of Lange formations (Figure 5.47b, c). Density porosity at 2700m appears to be greater in wells where the present-day top of the Kvitnos Formation and the base of the Lange Formation is at greater depths. Lateral

porosity variation also correlates with the thickness of the Cretaceous interval (from top of Kvitnos to base of Lange Fm) with greater porosities being associated with wells having a thicker Cretaceous interval (Figure 5.47d). Note that on the multi-well pressure-depth plot in Figure 5.47a separate, roughly lithostatic parallel trends can be drawn through the pressure measurements from the Lange Formation sandstones in the low porosity and in the high porosity wells which would indicate a pore pressure difference of ~4 MPa when extrapolated to ~ 3500 m below sea surface (Cicchino et al., 2015).

These observations tend to support the hypothesis that Cretaceous mudstones in the high porosity wells were likely (slightly) overpressured whilst in the low porosity wells they were likely hydrostatically pressured prior to Naust deposition.

Basin modelling indicate an additional 11 MPa and 9 MPa overpressure build up in wells 6406/2-3 and 6507/2-3 respectively due to recent rapid burial of the Naust Formation (Figures 5.33 and 5.37). These overpressure magnitudes are in accordance with previous estimations of overpressure magnitudes which were generated by the Plio-Pleistocene sediment loading (Skar et al., 1999; O'Connor et al., 2012; Goulty et al., 2016).

Theoretically, the maximum amount of overpressure build-up is limited by the lithostatic pressure increase imposed by the weight of the Naust Formation (Skar et al., 1999). However, the hydrostatic pressure in the Cretaceous mudstones would have also increased by the same amount as its increase at the base of the Naust Formation. Thus, the maximum amount of overpressure that could have been generated by disequilibrium compaction equals the present day vertical effective stress at the base of the Naust Formation (C Sargent et al., 2015; Goulty et al., 2016). However, as it was shown by Goulty et al. (2016) the estimated values of overpressure at the estimated depths of the onset of unloading (see also 5.6.5) in the high porosity wells 6406/2-6, 6406/2-5, 6406/2-3 and 6506/11-6 are larger than the respective values of vertical effective stresses at the base of the Naust Formation. In contrast, in each of the studied low porosity wells (including 6507/2-3 and 6506/3-1) the estimated overpressures at the estimated depths of the onset of unloading is less than respective values of vertical effective stresses at the base of the Naust Formation. This means that the present day vertical effective stress in the high porosity wells is either equal or less than it was when the Naust deposition

started while in the low porosity wells the present day vertical effective stress is greater than it was when the Naust deposition begun (C Sargent et al., 2015; Goulty et al., 2016).

In overall, these results clearly show that the maximum amount of overpressure build-up by disequilibrium compaction is significantly smaller than the measured present-day overpressures in the Cretaceous mudstones. Even if one considers the likely overestimated pre Naust overpressure magnitude indicated by one-dimensional basin modelling, the predicted magnitude of disequilibrium compaction overpressure is minimum 15 MPa smaller than present day overpressures in 6406/2-3 (Figure 101). Similar findings have been presented by Nordgård Bolås et al. (2004) who showed that present day pore fluid pressures in deeply buried North Sea mudstones can only be accurately modelled when using unrealistic porosity vs. depth relationships.

A considerable amount of overpressure was created internally in the Cretaceous mudstones (they are unloaded) since the onset of the Naust burial. Since there are no source rocks in the studied Cretaceous interval, gas generation is unlikely to be a significant internal source of overpressure. Also, there is no evidence for lateral pressure transfer within the sandstones (refer to 5.3). There is however clear evidence for ongoing clay mineral diagenesis (illitization) in the Cretaceous mudstones, so clay diagenesis is a viable mechanism for generating overpressures within them.

Further evidence in support of this hypothesis is presented in the below sections.

5.6.5 Evaluation with wireline log-based compaction profiles and implications for the mechanisms of overpressure generation

Figure 5.48 shows smoothed cosine-weighted density and sonic log responses through the studied Cretaceous mudstone intervals for wells 6406/2-3 and 6507/2-3. These two wells were selected as representatives of the high porosity and low porosity wells respectively. Similar observations have been made in all the other studied wells.

Density increases substantially with increasing depth through the Kvitnos and Lange formations in both wells implying ongoing compaction. Note that there is comparatively small decrease in sonic transit time with increasing depth below ~3000 m in 6406/2-3 and

below ~2400 m in 6507/2-3 and that sonic transit time becomes approximately constant at greater depth in both wells (Figure 5.48). In 6406/2-3 the sonic log also shows a reversal below 4000 m (Figure 5.48a). These observations indicate unloading. Small fluctuations in the smoothed data are the result of changing lithology, most likely related to variations in grain size and/or clay mineral content.

Figure 5.49 shows crossplots of smoothed sonic transit time against smoothed density in the studied mudstone intervals for 6406/2-3 and 6507/2-3. Dutta's (2002) reference lines for smectite rich and illite rich mudstones are also shown.

In 6406/2-3, from a depth of around 2800 m below sea surface the crossplot trend parallels Dutta's (2002) trend for illitic mudstones. At a depth of about 3400 m below sea surface the trend abruptly turns upwards, indicating that unloading of the mudstones accompanies ongoing compaction (Figure 5.49a). In 6507/2-3, the crossplot trend parallels Dutta's (2002) illitic mudstone trend from 2400 m to a depth of around 2800 m below sea surface where it abruptly turns upwards. There are considerable lateral fluctuations on the crossplot trend in both wells which can be attributed to lithological variation.

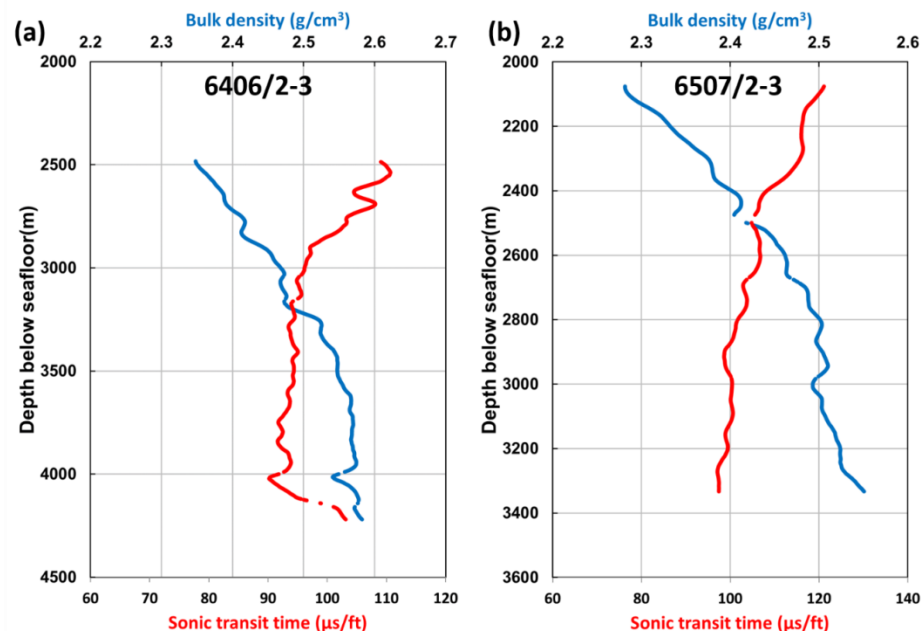


Figure 5.48. Smoothed density (blue) and sonic (red) logs through the mudstone intervals for (a) 6406/2-3 and (b) 6507/2-3.

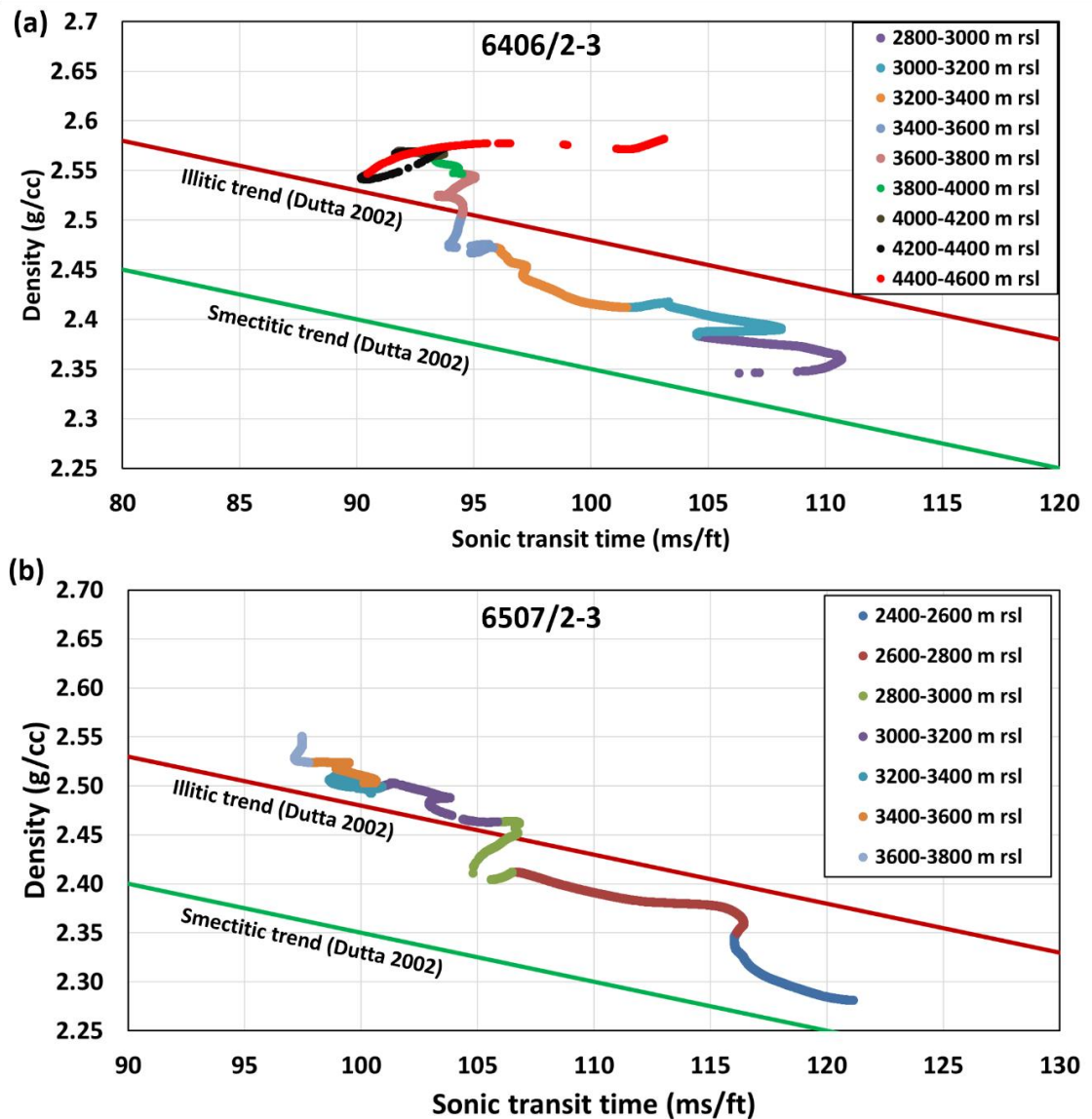


Figure 5.49. Sonic-density crossplots for 6406/2-3 (a) and 6507/2-3 (b). Colour coding is by depth relative to sea surface. Red and green line is the illitic and smectitic line from Dutta (2002).

Note that these observations (increasing density with constant or decreasing effective stress) are similar to that of Lahann et al. (2001) and Lahann and Swarbrick (2011) and are consistent with load transfer following clay diagenesis (refer to 2.7.2).

In overall, the following interpretation can be drawn based on the wireline logs. The Cretaceous mudstones were likely close to hydrostatically pressured immediately prior to Naust burial, as previously suggested by Skar et al. (1999) and O'Connor et al. (2012). However, in accordance with Goult et al. (2016) basin modelling suggests that there may have been at least a few megapascals of overpressure in the more distal high porosity

wells in the west where the Cretaceous formations were thicker and were buried to greater depth compared to the more proximal low porosity wells in the northeast.

The pre Naust overpressure in these wells was likely created by the combination of clay mineral diagenesis, which was likely ongoing in the Lange Formation at that time (Figure 5.46), and disequilibrium compaction. During the rapid Naust burial very little porewater could escape from the high porosity wells consequently mudstone compaction was limited. In contrast, Cretaceous mudstones in the low porosity wells were better able to drain immediately following Naust burial, so the amounts of overpressure generated by disequilibrium compaction was less (Goulty et al., 2016). Increased burial also resulted in warming which triggered further clay mineral diagenesis that unloaded the mudstones by load transfer as the normal compaction curve shifted to lower porosity for a given value of vertical effective stress (Lahann, 2002; Lahann and Swarbrick, 2011).

To further illustrate the plausibility of this interpretation, Figure 114 shows sonic-density crossplots as presented by Goulty et al. (2016) for nine wells with the picked onset of unloading in each well and Figure 5.51 shows the associated pressure-depth profiles based on pressure measurements in each well. Note that the sonic-density crossplots in Figure 5.50 were constructed using lithology-corrected sonic transit times. Corrections were made to the sonic logs to counter the effect of the variable clay content by making use of the gamma-ray log and the difference between the neutron porosity and density porosity (Goulty et al., 2016). For more details on this correction refer to Goulty et al. (2016).

The depths to the onsets of unloading are shallower in the north-eastern low porosity wells than in the high porosity wells. This is because the low porosity wells were better able to drain during the rapid Naust burial which resulted in lower porosities, less overpressure build up by disequilibrium compaction and relatively large amounts of unloading overpressure generated by clay diagenesis (Goulty et al., 2016).

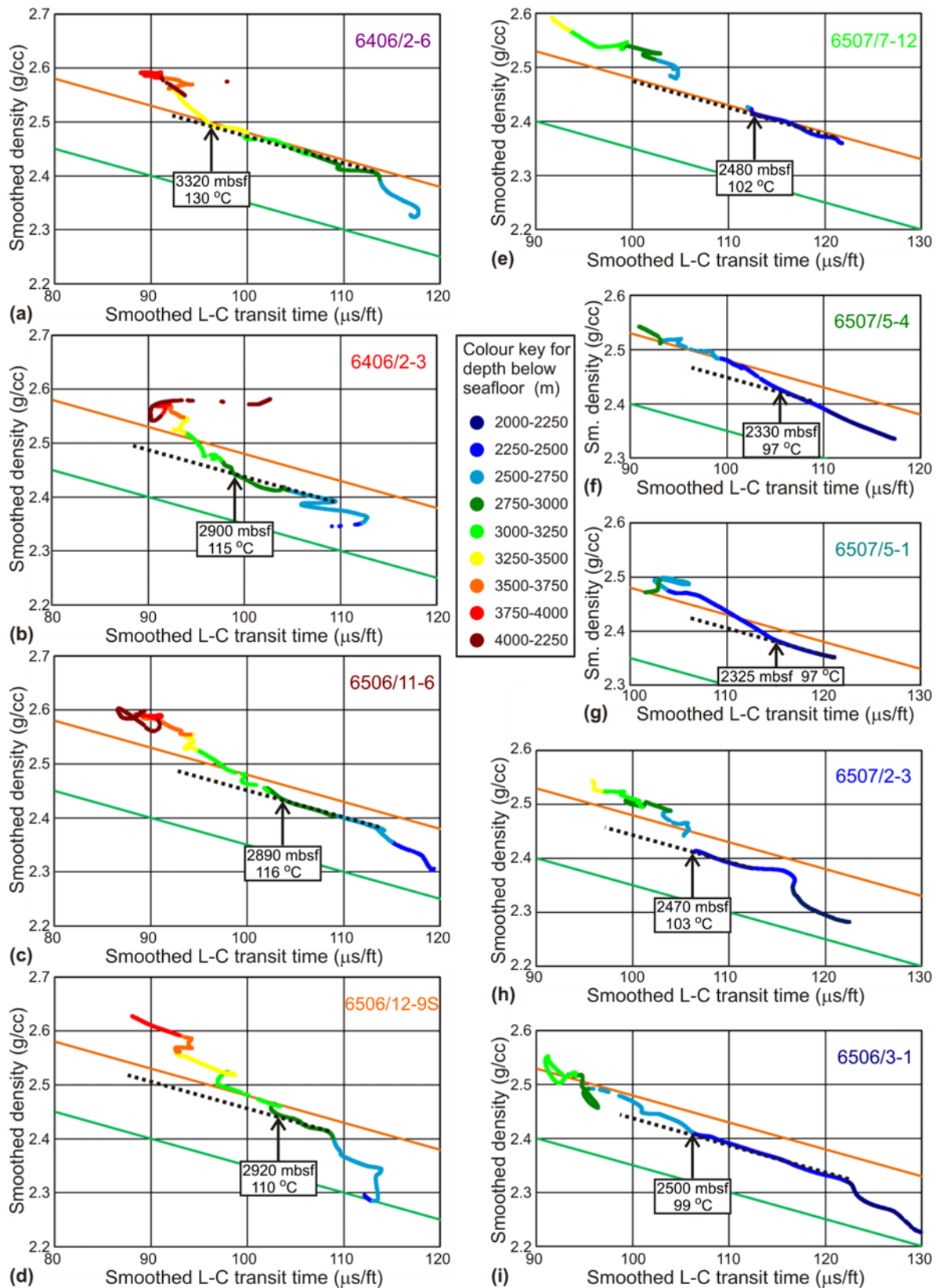


Figure 5.50. Sonic-density crossplots for nine wells (including 6406/2-3; 6507/2-3 and 6506/3-1; locations of the rest is shown in Goulty et al. 2016) using lithology-corrected sonic transit times

and smoothed logs. Vertical arrows denote picked onsets of unloading in each well (from Goulty et al., 2016).

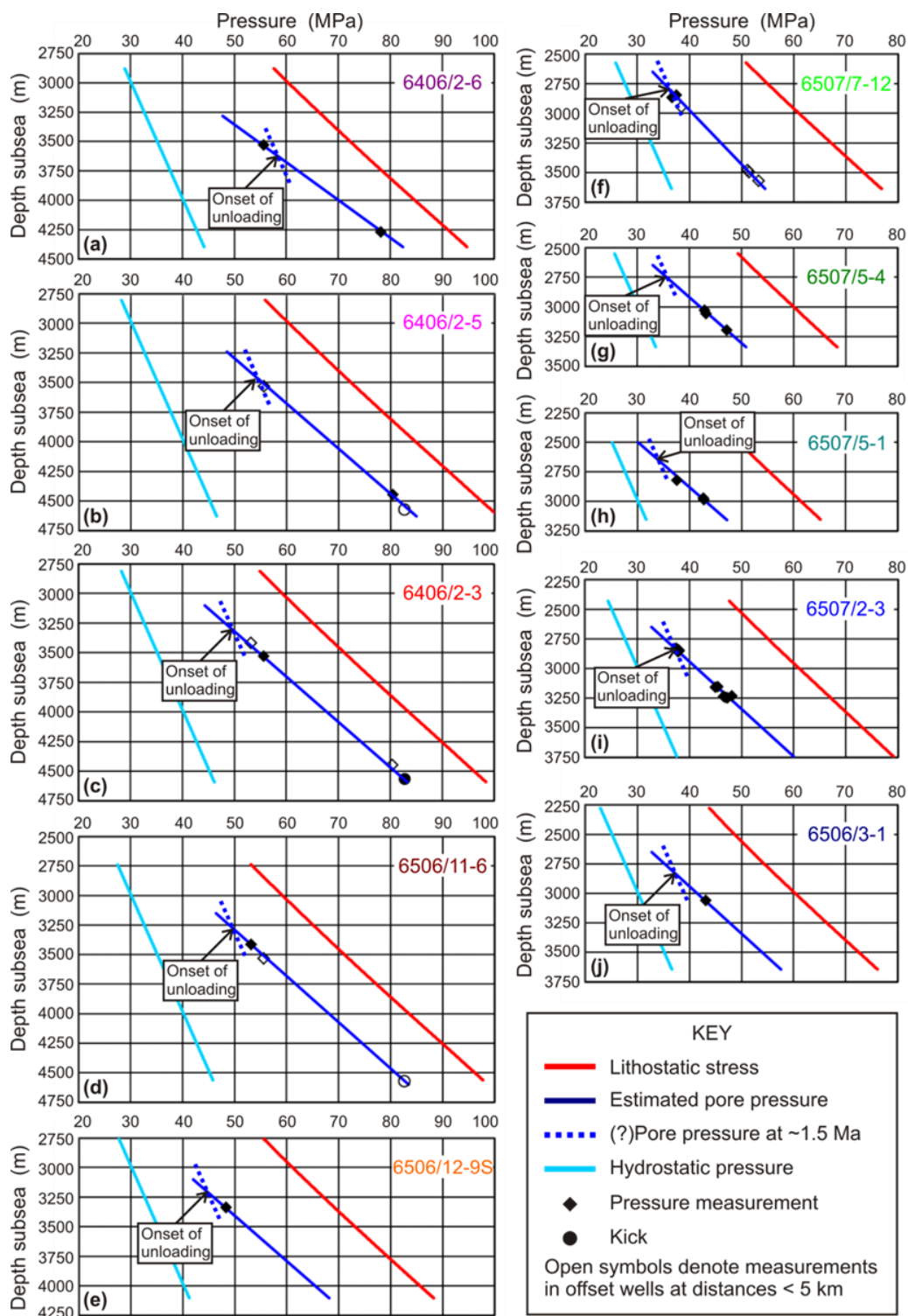


Figure 5.51. Pressure-depth profiles within the Cretaceous formations for ten wells (including 6406/2-3; 6507/2-3 and 6506/3-1; locations of the rest is shown in Goulty et al. 2016). Depths are displayed relative to mean sea level. Trends were estimated by fitting to direct measurements.

Dashed line denotes maximum disequilibrium compaction overpressure at ~ 1.5 Ma when bulk of the Naust Fm was deposited (Rise et al., 2005). The depths of unloading were picked on sonic-density crossplots as shown in Figure 5.50 (from Goult et al., 2016).

5.6.6 Implications for mudstone compaction processes

Figure 5.52a demonstrates the laterally consistent pressure-depth profile at the present day for the Cretaceous mudstones. Cicchino et al. (2015) found that porosities in these mudstones vary by a factor of two at depths of around 2700m below seafloor. They denoted the wells high, intermediate and low porosity according to their calculated density porosity values at that depth (refer to 5.3). Figure 5.52b shows corrected total porosities (from MICP-determined bulk density and grain density; see 3.3.7) and calculated density porosity (from smoothed logs, calculated as described in 3.4.3 using 2.75 g/cm^3 for grain density and 1.05 g/cm^3 for fluid density) for high porosity well 6406/2-3 and low porosity well 6507/2-3.

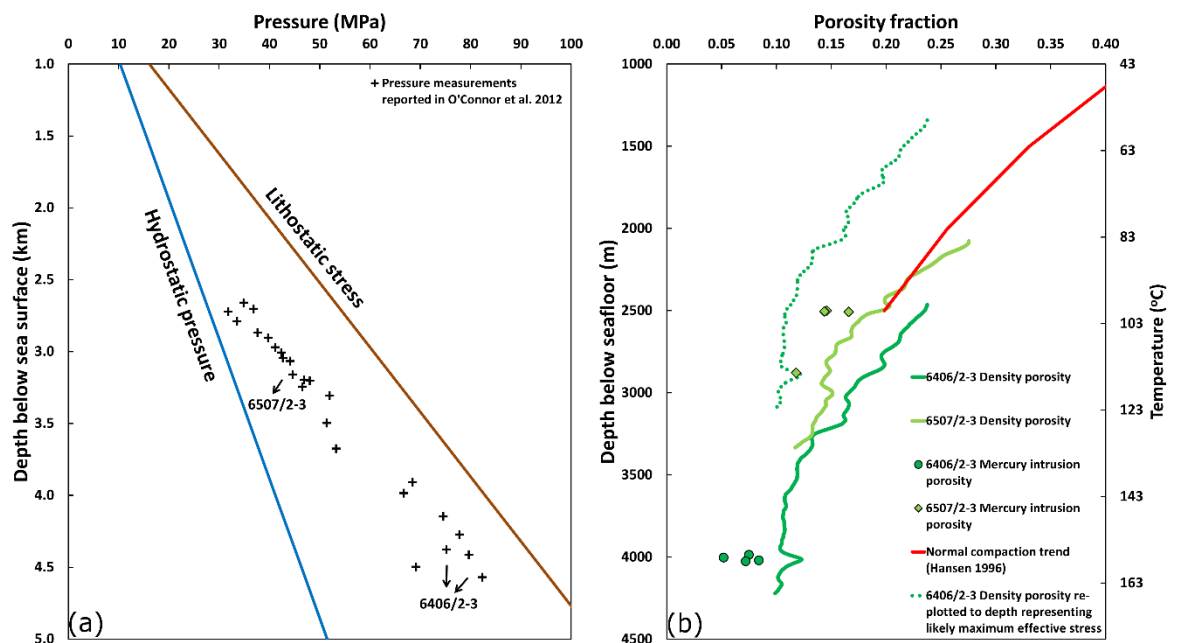


Figure 5.52. (a) Multi well pressure-depth plot showing pressure measurements from isolated turbidite sandstone bodies in the Cretaceous. (b) Evidence for continued compaction at reduced effective stresses associated with smectite illitization in the Cretaceous mudstones in well 6406/2-3. Density porosity was calculated from smoothed logs using 2.75 g/cm^3 for grain density and 1.05 g/cm^3 for fluid density. Mercury intrusion porosity denotes corrected total porosity which was determined according to 3.3.7. The exponential normal compaction trend of Hansen (1996) for

hydrostatically pressured Tertiary and Cretaceous mudstones on the Norwegian Shelf is shown here (from Andras et al., 2016).

The measured grain densities for the Cretaceous mudstone samples are consistent, mostly in the range 2.70-2.75 g/cm³ (average 2.75 g/cm³) confirming that the observed density increase is due to ongoing compaction. Measured total porosities are in accordance with the findings of Cicchino et al. (2015) and support the existence of considerably different porosity-depth trends (see 5.4.6 and Figure 5.30b).

The red compaction trend on Figure 5.52 is the superimposed porosity-depth trend from Hansen (1996) for hydrostatically pressured Cretaceous and Tertiary mudstones on the Norwegian Shelf. Hansen's (1996) compaction trend is the best available estimate of the maximum amount of compaction in the Cretaceous mudstones for their burial depth prior Naust deposition (at 2.8Ma).

Mudstones in the low-porosity well continue to compact along Hansen's (1996) trend (Figure 5.52) which suggest that they are close to being fully compacted for their depth of burial, even though they are overpressured. However, according to the pore pressure interpretation of Sargent et al. (2015) and Goult et al. (2016) the effective stress in this well temporarily increased after the onset of Naust burial, before falling towards its present-day trend when pore pressure built up as a result of clay diagenesis. Nevertheless, effective stress in the high porosity well has not subsequently exceeded its value immediately prior to the onset of Naust burial. As can be seen on Figure 5.52 the porosity-depth profile of the mudstones in the high porosity well can be matched to that of Hansen's (1996) normal compaction trend by an upward shift of ~300-400 m. However, they have been buried by 1122 m of Naust sediments. This is illustrated on Figure 5.52 by the dashed trend line which shows the density porosity of the high porosity well mudstones re-plotted relative to the base of the Naust Formation. Assuming that the maximum effective stress in the high porosity wells occurred at ~2.8 Ma when they were hydrostatically (or close to hydrostatic) pressured, further porosity loss since that time would not be expected as a result of purely mechanical processes. Furthermore, in accordance with Goult et al. (2016) one-dimensional basin modelling suggests that there may have been at least a few megapascals of overpressure in the Cretaceous mudstones

in the high porosity wells at ~2.8 Ma, so their porosity at that time might have been greater than defined by Hansen's (1996) normal compaction trend.

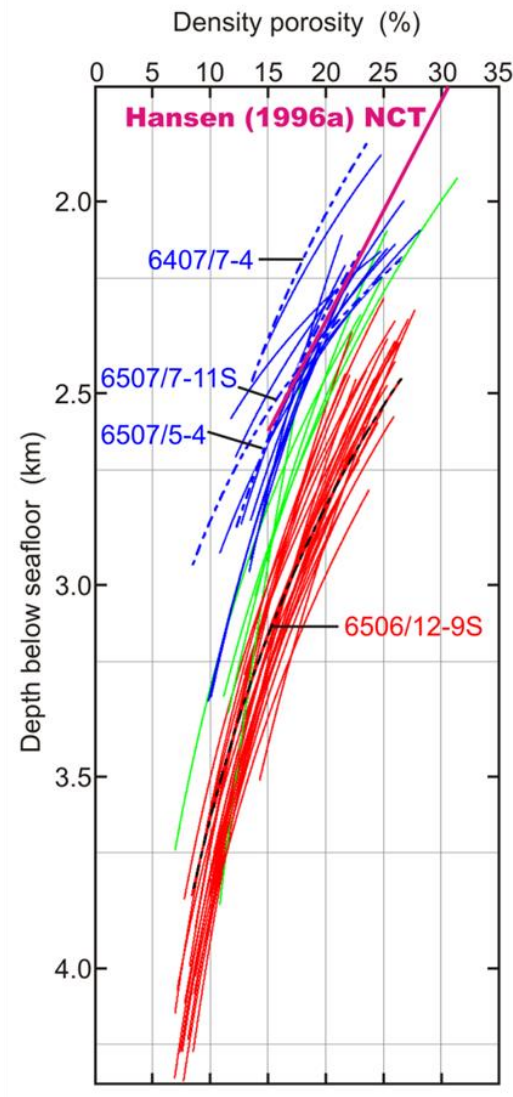


Figure 5.53. Best-fitting exponential trends for the density porosity values in the Kvitnos and Lange mudstones penetrated by 48 wells at Haltenbanken (locations shown in Cicchino et al. 2015), coloured according to the value of density porosity at 2700 m depth below seafloor: blue – low porosity of 9-16%; green – intermediate porosity of 16-18%; red – high porosity of 18-25%. Cuttings from the four named wells with dashed trend lines were sampled for XRD analysis, as reported by Cicchino et al. (2015). The linear normal compaction trend of Hansen (1996) for hydrostatically pressured Tertiary and Cretaceous mudstones on the Norwegian shelf is shown here. (From Cicchino et al., 2015).

It is clear that there has been a considerable amount of compaction since, concomitant with the illitization of smectite. Additional compaction that has taken place in the

Cretaceous mudstones since 2.8 Ma must be due to clay mineral diagenesis (smectite illitization) because the present day vertical effective stress above the onset of unloading is the maximum that these mudstones have experienced and it is less than that would have been in the same mudstone beds prior to Naust burial if the pore pressure had been hydrostatic (Goulty et al., 2016).

These results show strong evidence for porosity loss/volume reduction associated with smectite illitization. The porosity reduction appears to have taken place even as the effective stress reduced while pore pressure increased due to clay diagenesis (Goulty et al., 2016).

Figure 5.53 shows best fitting exponential trends for the density porosity values in the Kvitnos and Lange mudstones from 48 wells at the Halten Terrace, coloured according to the porosity classification of Cicchino et al. (2015). As it was shown in 5.6.5, Cretaceous mudstones in the low porosity wells (blue coloured trends in Figure 5.53) have been unloaded from vertical effective stress values closer to those corresponding to hydrostatic pore pressure at present day (Goulty et al., 2016). The cause for this is that less of the disequilibrium compaction overpressure generated by rapid Naust burial was retained in these wells (see 5.6.5). Present day pressure-depth profile is very similar in the Cretaceous mudstones across the Halten Terrace (Figure 5.52a) indicating that much of the present-day overpressure in the low porosity wells was generated by unloading process (Goulty et al., 2016). In overall, this clearly indicates that mudstones in the low porosity wells have lower porosity than those in the high porosity wells (red coloured trends in Figure 5.53) because they have experienced greater vertical effective stress in the past which resulted in greater amount of mechanical compaction.

These observations clearly contradict Bjørlykke and Høeg's (1997) and Bjørlykke's (1998) effective stress independent chemical compaction model (refer back to 2.6). Apologists for the stress-independent compaction model may argue that at a depth of 2700 m below seafloor at the Halten Terrace the temperature is around 105°C, only just within the temperature range where chemical compaction becomes stress-independent according to that model (Figure 2.9). Perhaps the greater compaction of the low-porosity mudstones occurred during the transition stage whilst they were still at temperatures

below 100°C? That suggestion is not supported by the porosity trends at greater depths in Figure 5.53. The trends look distinct throughout their common depth range, down to 3250m below seafloor (~130°C). In addition to this clay mineralogical data presented in 5.4.2 clearly shows that smectite illitization is in its final stages at these temperatures (>60% illite in illite-smectite; dominance of R1 ordered phase population) (Figure 5.45).

These observations are however entirely consistent with the chemically-enhanced mechanical compaction model (refer to 2.6), which can also explain porosity loss in overpressured mudstones (Dutta, 2002, 2016; Lahann, 2002), as shown by the cartoons in Figure 2.17.

In overall, these observations strongly suggest that the combination of porosity/volume loss and unloading are directly linked to clay mineral diagenesis (smectite illitization). Fabric alignment data for illite-smectite, measured by high-resolution X-ray textural goniometry, indicate strong fabric anisotropy. This is consistent with previously published fabric alignment data from diagenetically mature mudstones which showed that illitization leads to fabric realignment (Ho et al., 1999; Worden et al., 2005; Day-Stirrat et al., 2008). Strong realignment of the clay mineral fabric as a result of smectite illitization is further supported by petrographic observations made by SEM on the early diagenetic siderite concretion which indicate isotropic depositional fabric as it is shown in Figure 5.26. Furthermore, there is a very strong correlation between the alignment of illite-smectite (001) and chlorite (002) + kaolinite (001) (Figure 5.21). This observation strongly suggests that during illitization the whole clay fabric (both detrital and authigenic minerals; and not only illite-smectite but also kaolinite and chlorite) is realigned, normal to the maximum effective stress. Mechanical realignment thus appears to be driven by mineralogical changes. Strong correlation between the illite-smectite (001) fabric intensity and measured total porosity (Figure 5.31) clearly shows that fabric realignment causes additional porosity loss thus illitization results in enhanced compaction. This observation is in accordance with Lahann's (2002) original point that illitization reduces the equilibrium porosity associated with a given effective stress (makes the mudstone more compactable) (see 2.6). These results suggest that illitization result in the local destabilisation of clay mineral fabric, driving porosity loss and also transferring load from solid to fluid, thus generating pore pressure.

5.7 Summary and conclusions

Several previous studies have observed the apparent lack of a relationship between porosity and effective stress in mudstones buried to the diagenetic regime (Hermanrud et al., 1998; Teige et al., 1999) and reported density increases in mudstones which are not related to effective stress but are coincident with clay diagenesis (Peltonen et al., 2009; Lahann and Swarbrick, 2011). These observations confirm that chemical compaction may take place in association with clay diagenesis.

Additionally, clear evidence was presented here for chemical compaction (porosity loss/sediment volume reduction) associated with smectite illitization from Cretaceous mudstones at the Haltenbanken, offshore mid-Norway (Figure 5.52). Although chemical compaction associated with clay diagenesis is not a new idea, this is the first time it has been demonstrated in a single mudstone formation from several lines of evidence (measured physical, textural, mineralogical properties, plus log responses).

Cicchino et al. (2015) reported that porosities in Cretaceous mudstones on the Halten Terrace vary by a factor of two at a common depth of 2700 m below seafloor. The authors suggested that the observed lateral variation in porosity is the result of lateral variations in the efficacy of pore water escape following the recent rapid burial of Plio-Pleistocene sediments. They pointed out that although clay diagenesis takes place independently of effective stress, chemical compaction cannot be independent of the effective stress since likewise to mechanical compaction chemical compaction requires expulsion of pore water.

Complementing their findings, the evidence presented here shows that Cretaceous mudstones at the Haltenbanken, offshore mid-Norway continue to compact mechanically in response to increasing effective stress above 100 °C. Consideration of density logs in association with the pore pressure history suggests that overall compaction is still driven by effective stress (Goult et al., 2016); however, the extent of the compaction has been significantly enhanced by chemical processes.

These results are evidence that tends to refute the stress-independent chemical compaction model for diagenetically altered mudstones at temperatures above $\sim 100^{\circ}\text{C}$ and supports the chemically-enhanced mechanical compaction model.

In addition to this, coincident with clay mineral diagenesis, the presented 1D modelling results and pore pressure data from Cretaceous mudstones at the Haltenbanken, offshore mid-Norway clearly indicate that pore pressure increased, and effective stress decreased (“unloading”) during the illitization process. The presented results suggest that unloading is a direct result of clay mineral diagenesis and concomitant fabric destabilisation, due to the local transfer of load from dissolving detrital clay grains to fluid. Pore pressure is then a function of the rate at which it is generated by clay mineral diagenesis (and other mechanisms such as disequilibrium compaction) and the rate at which it is dissipated by compaction and fluid flow.

Chapter 6

Clay mineralogical control on compaction properties of Albian to Miocene mudstones of the Sergipe-Alagoas Basin, offshore eastern Brazil

6.1 Introduction

Several previous studies suggested that chemical diagenetic changes can cause further porosity loss in addition to the mechanical compaction processes (Bjørlykke, 1998). In addition, further evidence was shown in here from Miocene mudstones in the Central Malay Basin and from Cretaceous mudstones at the Haltenbanken, offshore mid-Norway in support of enhanced compaction due to mineral diagenesis in clastic mudstones. The newly presented evidence indicates that the overall compaction in the diagenetic regime is still driven by effective stress (Goult et al., 2016); however, the extent of the compaction has been significantly enhanced by chemical processes. A key question arises regarding the rates of porosity reduction due to diagenesis in different pore pressure regimes. However, both previously presented datasets represents overpressured basin settings where overpressure generation due to disequilibrium compaction significantly affected mudstone compaction.

To contrast the previous case studies, the Sergipe-Alagoas Basin was selected to represents a passive continental margin setting where deposition of fine grained siliciclastic sediments post-dating Aptian age took place at a slow average rate of around 35 m/Ma (De Souza et al., 1995). This has the consequence that overpressure generation due to disequilibrium compaction is not likely to be expected which would otherwise have considerable effect on the compaction properties of these mudstones. Thus, the Sergipe-Alagoas Basin provides the opportunity to study the effects of slow sedimentation rates on the compaction properties of siliciclastic mudstones.

Well log data and samples were provided by Petrobras from 8 wells (Wells A, B, C, D, E, F, G, H) in the Sergipe Sub-Basin out of which 4 wells (Wells A, C, D and E) were selected for this study. Mineralogical and chemical properties of the samples were analysed and compared with physical properties such as porosity, measured on the samples and derived from well log responses. The key aim was to assess the role of clay mineralogy and mineral diagenesis on the compaction properties of Albian to Miocene mudstones. In addition to this, the secondary objective was to evaluate the role of clay mineral diagenesis on pore pressure generation in the Sergipe-Alagoas Basin.

This chapter details these results following a brief introduction to the geological history of the Sergipe-Alagoas Basin.

6.2 Geological background

The Sergipe-Alagoas Basin is located along the coast of North-eastern Brazil. The basin setting is a passive continental margin. It straddles the coastline and covers an area of about 42000 km², including 12000 km² onshore (Figure 6.1). The seafloor gradient increases dramatically from around 200 m water depth to attain water depths of about 3000 m at the south-eastern margin of the basin (Cainelli, 1992). It is a prolific hydrocarbon province that includes 26 known oil fields and has hydrocarbon reserves of about 2.39 billion barrels of oil in place (Mello et al., 1994).

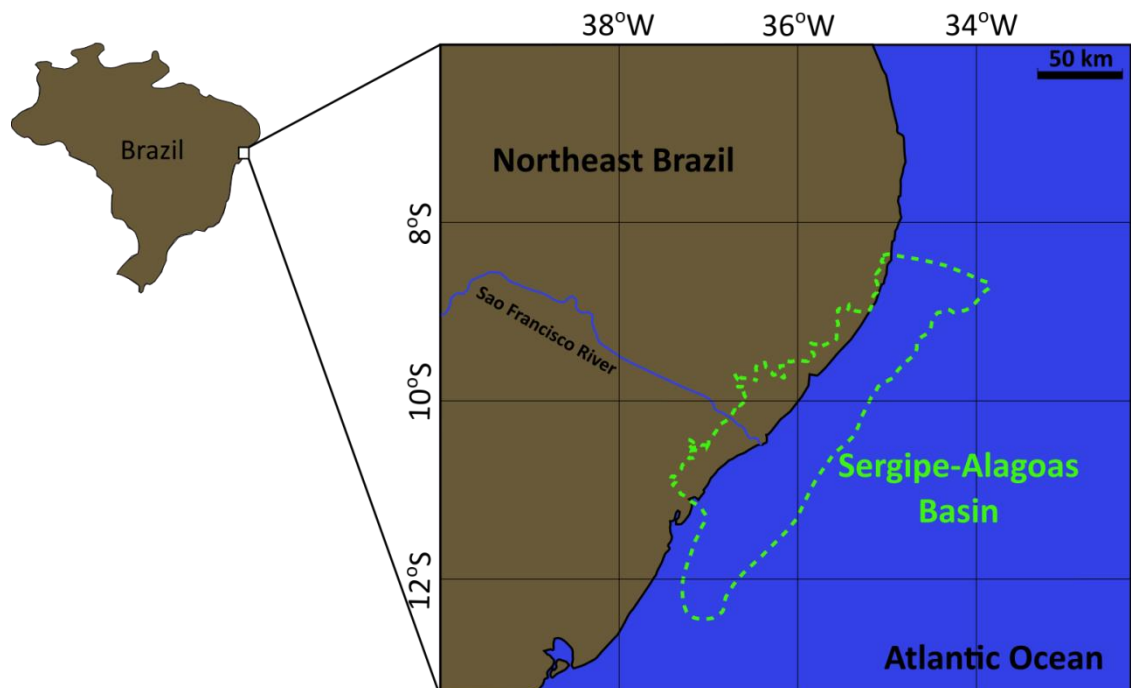


Figure 6.1. Location map of the Sergipe-Alagoas Basin.

The Sergipe-Alagoas Basin formed during the Late Jurassic to Early Cretaceous break-up of the Gondwana supercontinent (Hamsi, 2010). It contains up to 10 km of continental to deep-marine siliciclastic sediments, shallow marine carbonates and evaporites deposited from the Carboniferous to Quaternary (Figure 6.2). The structural evolution of the basin is subdivided into four phases: pre-rift, rift, transitional and post rift (Figures 6.2 and 6.4)

(Ojeda, 1982). The basin was developed on Precambrian metamorphic and igneous rocks, locally covered by Palaeozoic intracratonic sediments (Davison and Dos Santos, 1989).

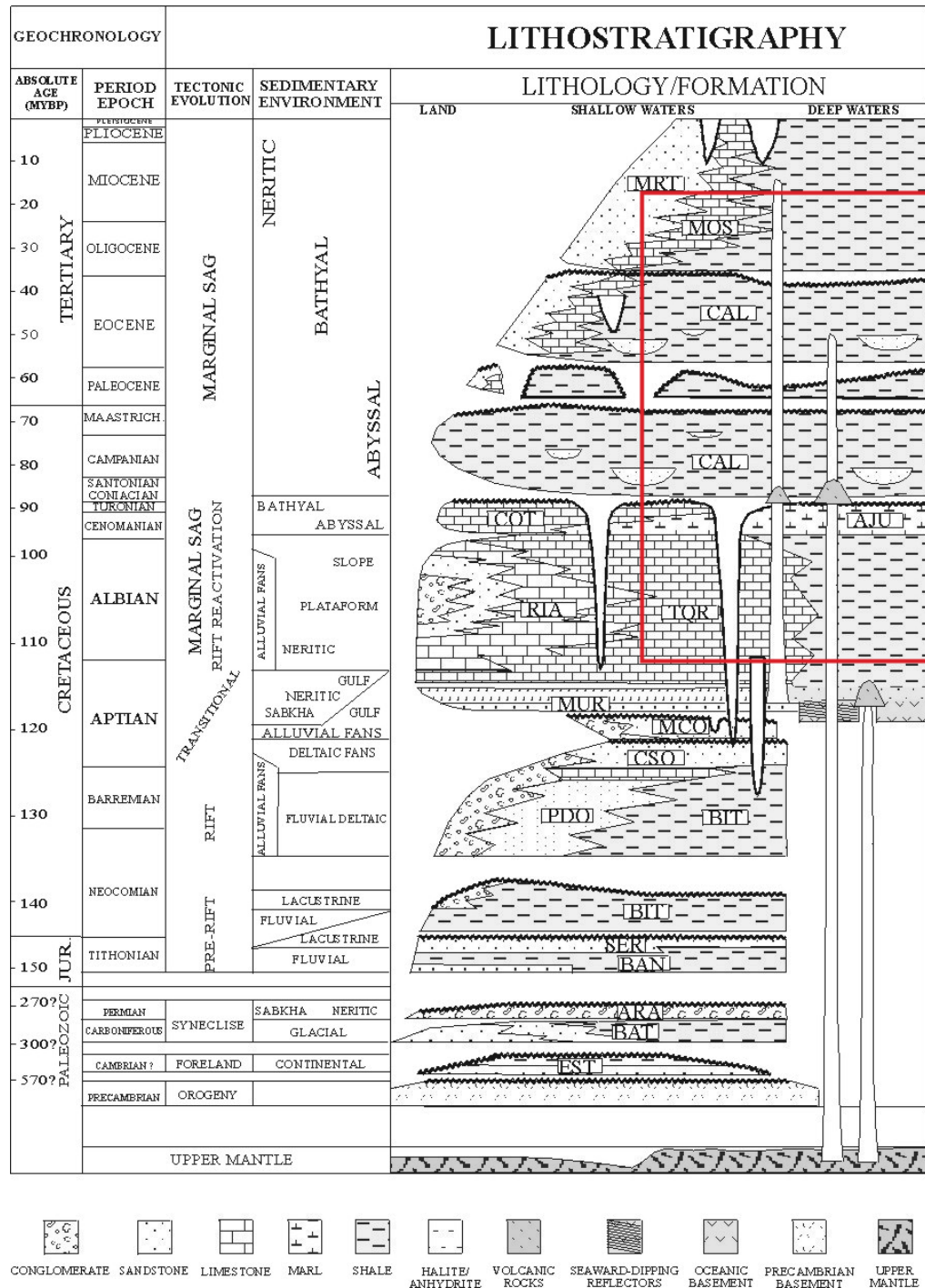


Figure 6.2. Stratigraphic framework and structural history of the Sergipe-Alagoas Basin (modified after Mohriak et al., 2000). Red square marks the study interval. Abbreviations of formation units: EST, Estância; BAT, Batinga; ARA, Aracaré; BAN, Bananeiras; SER, Serraria; BIT, Barra de Itiúba; PDO, Penedo; CSO, Coqueiro Seco; MAC, Maceió; MUR, Muribeca; RIA, Riachuelo; TQR, Taquari; COT, Cotinguiba; AJU, Aracaju; CAL, Calumbi; MOS, Mosquero; MRT, Marituba.

Incipient crustal thinning in the pre-rift phase prompted the deposition of fluvial-lacustrine sediments in low-amplitude regional depressions. Rock types of the Palaeozoic pre-rift sequence correlates with those in the African Gabon Basin (Mohriak et al., 2000).

Rupture of the Gondwana supercontinent started towards the Late Jurassic. Initial stretching and thinning of the lithosphere was followed by break-up during late Aptian-early Albian times which resulted in the formation of the South American and African plates (Mohriak et al., 2000). During the syn-rift phase a deep asymmetric rift basin developed in which alluvial, fluvial, deltaic and lacustrine sediments accumulated in half grabens. This syn-rift megasequence complex is approximately 5000 m thick. During the transitional phase in the Aptian a narrow proto-oceanic gulf developed where transitional marginal siliciclastics and evaporites were deposited (Cainelli, 1992). By the early Aptian, a hinge line had developed in the Sergipe-Alagoas Basin (Figure 6.4) where erosion was taking place on the upthrown, north-western side, whilst on the downthrown, south-eastern side deposition continued, mainly of evaporites interbedded with terrigenous clastics and carbonates. Salt remobilization resulted in listric faults that sole out in the Aptian sediments (Cainelli, 1992; Mohriak et al., 2000). With further thermal subsidence, by the late Aptian deposition of sediments had extended over the upthrown side of the hinge and a fully open marine depositional environment had developed. Initially, shallow marine carbonates were deposited during the post rift phase and over the time period from the Albian to the Santonian a carbonate platform and slope had developed. This was followed by the deposition of mudstones and turbidites during the Campanian, producing the overlapping shelf-slope basin wedge of the Calumbi Member of the Piaçabuçu Formation which is primarily composed of siliciclastic mudstones (Figure 6.2). The formation ranges in age from the Campanian to the Holocene. From the Palaeocene onwards it includes the Marituba Member which consists of shelf edge carbonates with more proximal sandstones. In the deeper water environment mudstones continued to be deposited from the Palaeocene onwards. By the Late Eocene, the palaeo-shelf edge was near to the present-day shelf break. Presently, the Piaçabuçu Formation is undergoing localised erosion by the formation of canyons, some of which cut down into the shelf-edge carbonates. The canyon formation and mass wasting associated with São Francisco River is currently developing a deep-sea fan. The Cenozoic sediments are both thicker and

muddier beneath the continental slope and in deep water than they are on the shelf (Cainelli, 1992).

The main source rocks in the Sergipe-Alagoas Basin are calcareous black shales of Aptian age (Ibura Member within the Muribeca Formation). These sediments reach the oil window around 2000 m below seafloor. Onshore oil fields are shallower than the oil window, whereas source rocks are within the oil window offshore. The main reservoirs are found in the coarse siliciclastics of Lower Cretaceous alluvial fans and fan deltas and in the fractured Precambrian basement (Mello et al., 1994).

6.3 Supplied data

The dataset provided by Petrobras included wireline data from eight wells out of which four (Wells A, C, D and E) has been selected for this study. The provided wireline data comprised density, sonic, gamma ray, resistivity, neutron and caliper logs. In addition to this, lithology interpretations, repeat formation tester (RFT) and drill stem test (DST) pressure and temperature measurements, mudweights and bottom-hole temperature measurements were also provided. Mudstone cuttings were provided from wells A, C, D and E and core samples were provided from wells A, C and E.

6.4 Well locations, local geology and overall lithology

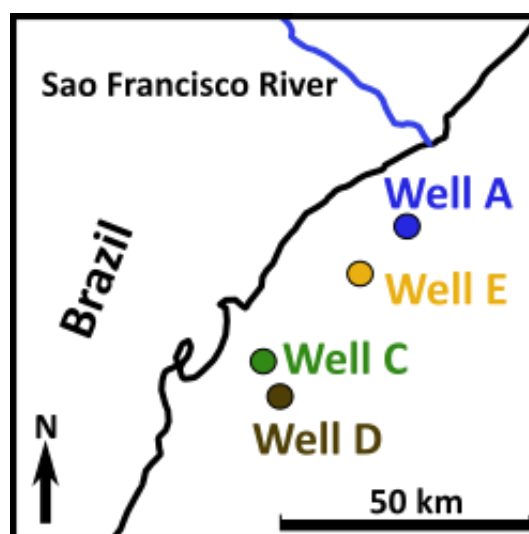


Figure 6.3. Location map for wells A, C, D and E in the Sergipe Sub-Basin.

Well locations are shown in Figure 6.3. All four wells are located in the Sergipe Sub-Basin. Wells A, C and E are on the narrow coastal shelf, where water depths are less than 100 m and well D is in deep water. Water depths in wells A, C, D and E are 29, 52, 1547 and 27 m respectively. A schematic NW-SE cross section through the Sergipe Sub-Basin is shown in Figure 6.4.

Provided wireline logs and samples cover mudstones of Albian to Miocene age corresponding to the Piaçabuçu, Cotinguiba and Riachuelo formations (Figure 6.2). Lithological information for each of the four wells was provided by Petrobras.

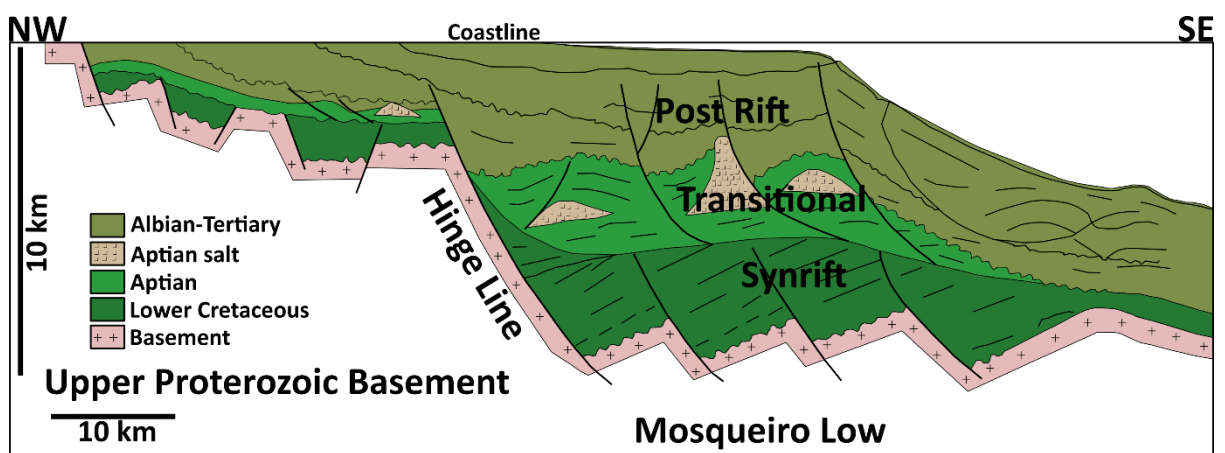


Figure 6.4. Schematic NW-SE cross section of the Sergipe Sub-Basin (Based on Feijo, 2014).

Lithology in the studied intervals consist of about 70% mudstones with some sandy and carbonaceous sections. Most of the carbonate-rich intervals are present in the top 1km of wells A and E corresponding to the shelf-edge Marituba Member of the Piaçabuçu Formation. Below 1 km siliciclastics dominate in all four wells, although some sections of calcarenite and calcilutite appears at greater depths within the mid-Cretaceous Cotinguiba and Riachuelo formations.

Based on the information provided by Petrobras, all sediments in these four wells are now at their maximum burial depth.

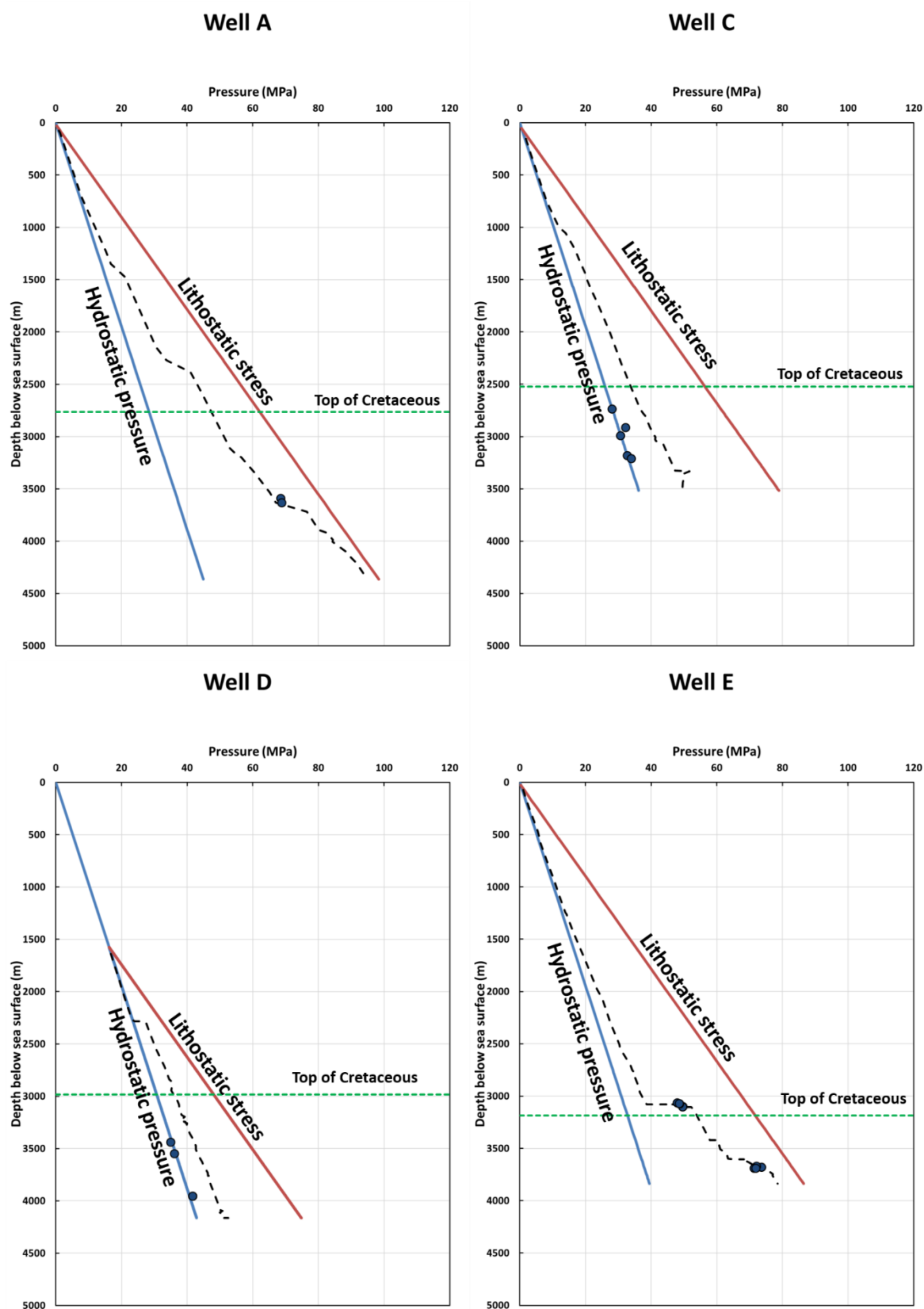


Figure 6.5. Pore pressure-depth profiles for wells A, C, D and E. Blue dots are direct formation pressure measurements and dashed lines denote mudweights.

6.5 Pore pressure-depth profiles and geothermal gradient

Drilling mudweights and pore pressure measurements are shown in Figure 6.5. Drilling mudweights used in Well A and E imply high overpressures towards the base of both wells which is confirmed by the limited number of direct pressure measurements. In contrast, all pressure measurements in Well C and D are hydrostatic (Figure 6.5).

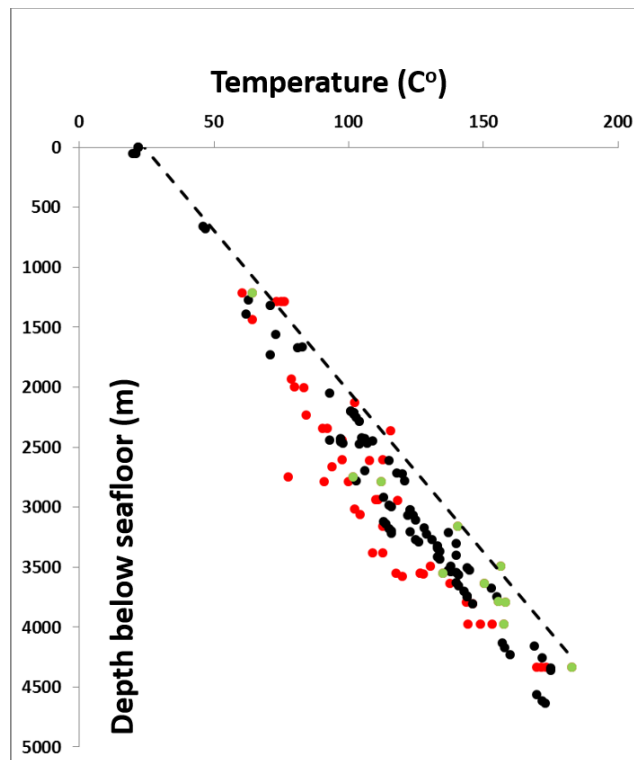


Figure 6.6. Measure formation temperatures in the shelfal wells. Red dots: direct readings; Green dots: extrapolated readings; and black dots: modelled temperatures (modified after Sargent et al., 2015).

Figure 6.6 shows modelled and measured formation temperatures in seven shelfal wells (including Well A, C and E). Water temperatures along the Sergipe-Alagoas coastline are in the range 18-20°C (Bischof et al., 2003), so seafloor temperature is estimated to be 20°C for the shelfal wells and 5°C for the deep water well D. A linear geothermal gradient of 37.3°C/km is plotted as an upper envelope to the raw, extrapolated and modelled temperature data (Figure 6.6). However, measured RFTs and BHTs underestimate true formation temperatures (Hermanrud et al., 1990) thus a common geothermal gradient of 40°C/km was assumed for all four wells. This value is within the typical range of geothermal gradients for passive continental margins.

| Well | Sample type | Depth below seafloor (m) | Temperature (°C) |
|--------|-------------|--------------------------|------------------|
| Well A | cuttings | 1026.0 (+/- 3m) | 65 |
| Well A | cuttings | 1098.0 (+/- 3m) | 68 |
| Well A | cuttings | 1245.0 (+/- 3m) | 74 |
| Well A | cuttings | 1521.0 (+/- 3m) | 85 |
| Well A | cuttings | 1776.0 (+/- 3m) | 95 |
| Well A | cuttings | 1995.0 (+/- 3m) | 104 |
| Well A | cuttings | 2085.0 (+/- 3m) | 107 |
| Well A | cuttings | 2304.0 (+/- 3m) | 116 |
| Well A | cuttings | 2448.0 (+/- 3m) | 122 |
| Well A | core | 2465.8 | 123 |
| Well A | core | 2466.4 | 123 |
| Well A | core | 2467.6 | 123 |
| Well A | core | 2468.5 | 123 |
| Well A | core | 2471.0 | 123 |
| Well A | core | 2471.9 | 123 |
| Well A | cuttings | 2691.0 (+/- 3m) | 132 |
| Well A | cuttings | 3012.0 (+/- 3m) | 144 |
| Well A | cuttings | 3270.0 (+/- 3m) | 155 |
| Well A | cuttings | 3900.0 (+/- 3m) | 180 |
| Well C | cuttings | 713.0 (+/- 3m) | 53 |
| Well C | cuttings | 971.0 (+/- 3m) | 63 |
| Well C | cuttings | 1181.0 (+/- 3m) | 71 |
| Well C | cuttings | 1424.0 (+/- 3m) | 81 |
| Well C | cuttings | 1664.0 (+/- 3m) | 91 |
| Well C | cuttings | 1928.0 (+/- 3m) | 101 |
| Well C | cuttings | 2168.0 (+/- 3m) | 111 |
| Well C | core | 2347.9 | 118 |
| Well C | core | 2352.6 | 118 |
| Well C | cuttings | 2414.0 (+/- 3m) | 121 |
| Well C | core | 2654.6 | 130 |
| Well C | core | 2655.4 | 130 |
| Well C | core | 2656.7 | 130 |
| Well C | cuttings | 2675.0 (+/- 3m) | 131 |
| Well C | core | 2753.4 | 134 |
| Well C | core | 2888.8 | 140 |
| Well C | core | 2911.8 | 140 |
| Well C | core | 2912.5 | 140 |
| Well C | cuttings | 2948.0 (+/- 3m) | 142 |
| Well C | cuttings | 3110.0 (+/- 3m) | 148 |
| Well D | cuttings | 743.0 (+/- 3m) | 35 |
| Well D | cuttings | 983.0 (+/- 3m) | 44 |
| Well D | cuttings | 1289.0 (+/- 3m) | 57 |
| Well D | cuttings | 1496.0 (+/- 3m) | 65 |
| Well D | cuttings | 1769.0 (+/- 3m) | 76 |
| Well D | cuttings | 2009.0 (+/- 3m) | 85 |
| Well D | cuttings | 2390.0 (+/- 3m) | 101 |

| Well | Sample type | Depth below seafloor (m) | Temperature (°C) |
|--------|-------------|--------------------------|------------------|
| Well D | cuttings | 2519.0 (+/- 3m) | 106 |
| Well E | cuttings | 1102.0 (+/- 3m) | 68 |
| Well E | cuttings | 1255.0 (+/- 3m) | 74 |
| Well E | cuttings | 1432.0 (+/- 3m) | 81 |
| Well E | cuttings | 1717.0 (+/- 3m) | 93 |
| Well E | cuttings | 2035.0 (+/- 3m) | 105 |
| Well E | cuttings | 2194.0 (+/- 3m) | 112 |
| Well E | cuttings | 2350.0 (+/- 3m) | 118 |
| Well E | cuttings | 2650.0 (+/- 3m) | 130 |
| Well E | core | 2751.2 | 134 |
| Well E | core | 2751.7 | 134 |
| Well E | core | 2752.9 | 134 |
| Well E | cuttings | 2923.0 (+/- 3m) | 141 |
| Well E | cuttings | 3259.0 (+/- 3m) | 154 |
| Well E | cuttings | 3466.0 (+/- 3m) | 163 |

Table 6.1. List of mudstone samples selected for study.

6.6 Mudstone sample characterization results

Petrobras provided both core samples and cuttings of variable size and quality. In total 61 samples (43 cuttings and 18 core) were selected for further study. The complete list of the studied samples is shown in Table 6.1. The selected samples were from depths in the range of 713-3900 m below seafloor, corresponding to the Piaçabuçu, Cotinguiba and Riachuelo formations.

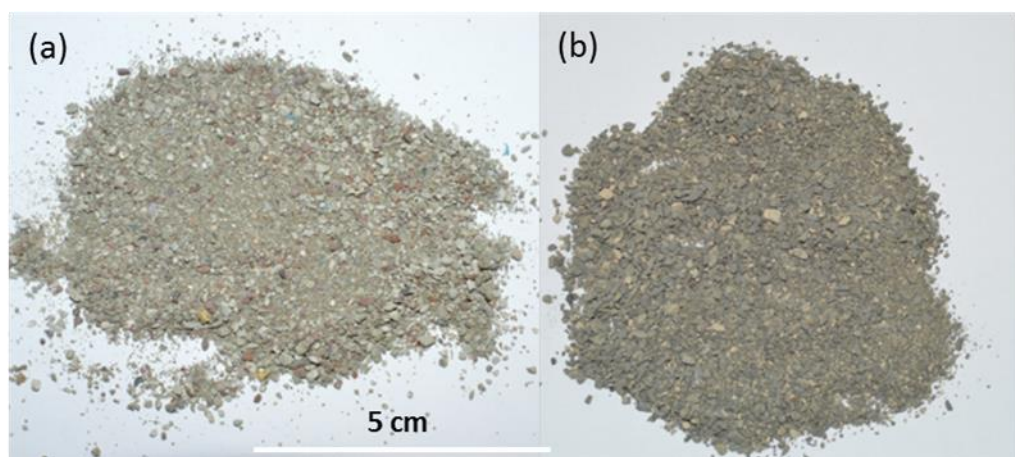


Figure 6.7. Washed cutting samples (a) Well A; 1098m bsf (b) Well E; 3259m bsf.

Cuttings were collected from depths intervals which were previously checked using the wireline logs (Gamma ray and NPHI-DPHI) to make sure these are made of dominantly mudstones. Care was taken to pick thick mudstone sections in order to minimise contamination from other lithologies.

Cuttings were mainly small (sub-millimetre to centimetre scale), dark grey pieces of sub-angular to sub-rounded material. In some cases, the cutting samples contained a more heterogenous assemblage with considerable amount of brown, yellow and white material (Figure 6.7).



Figure 6.8. Examples of mudstone lithology types from (a) Well C; ~2910-2913m bsf and (b) Well E; ~2752-53 m bsf.

Core samples were available from the mudstone intervals of the cored sandstone members. Representative mudstone samples were selected based on visual observation of the provided core photographs (Figure 6.8). Sampling covered visually recognisable volumetrically significant fine grained lithologies. Sampling points for dominant fine grained lithologies were selected based on the need to select a range of materials from the discernible heterogeneity; rock types that dominate over significant core intervals;

and core material that are homogeneous within the actual sample size so that analyses made on subsamples can be correlated. Care was taken to collect samples from homogeneous and uncemented mudstone-rich intervals (as far as it was possible based solely on visual observation of the core photographs).

6.6.1 Bulk mineralogical properties

Quantitative bulk XRD show consistent bulk mineral composition (Figure 6.9). Quartz, plagioclase, 2:1 clays (illite-smectite), and chlorite were detected in all of the samples. The average clay content (kaolinite + mica + illite + illite-smectite + chlorite) is ~53 wt%. The dominant components are quartz (average ~ 26 wt%) and 2:1 clay minerals (illite-smectite; average ~ 40 wt%). There is an average of ~6 wt% plagioclase, ~4 wt% K-feldspar, ~ 4 wt% chlorite, ~7 wt% calcite and minor amounts of pyrite in all of the samples. Kaolinite and minor, but variable amounts of dolomite and siderite were detected in most of the samples and in some of them traces of iron oxide (hematite + goethite), barite, anatase, anhydrite, amphibole and gypsum. Bulk quantitative XRD data of the studied samples can be found in Appendix I.

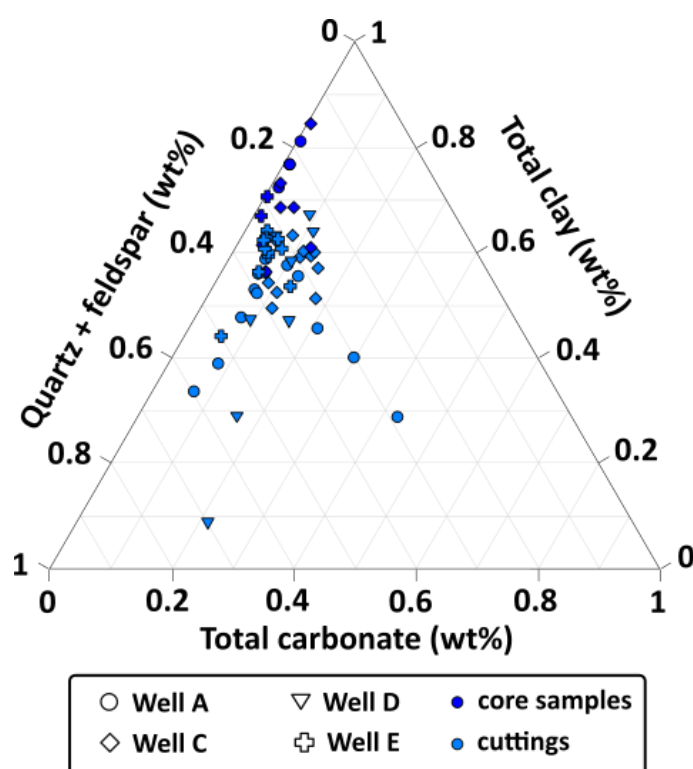


Figure 6.9. Bulk mineral composition of mudstone samples obtained from QXRD.

Figure 6.9 was constructed using the quantitative XRD determined mineral weight percentages. Total clay content is defined here as the sum of all the XRD determined clay minerals including all 2:1 clays (illite, mica and illite-smectite). Overall, mineralogy in the studied wells is fairly similar, however the quartz plus feldspar content and the total carbonate (calcite, dolomite, siderite, ankerite) content is highly variable. Core samples appear to be considerably more clay-rich and contain much less carbonate.

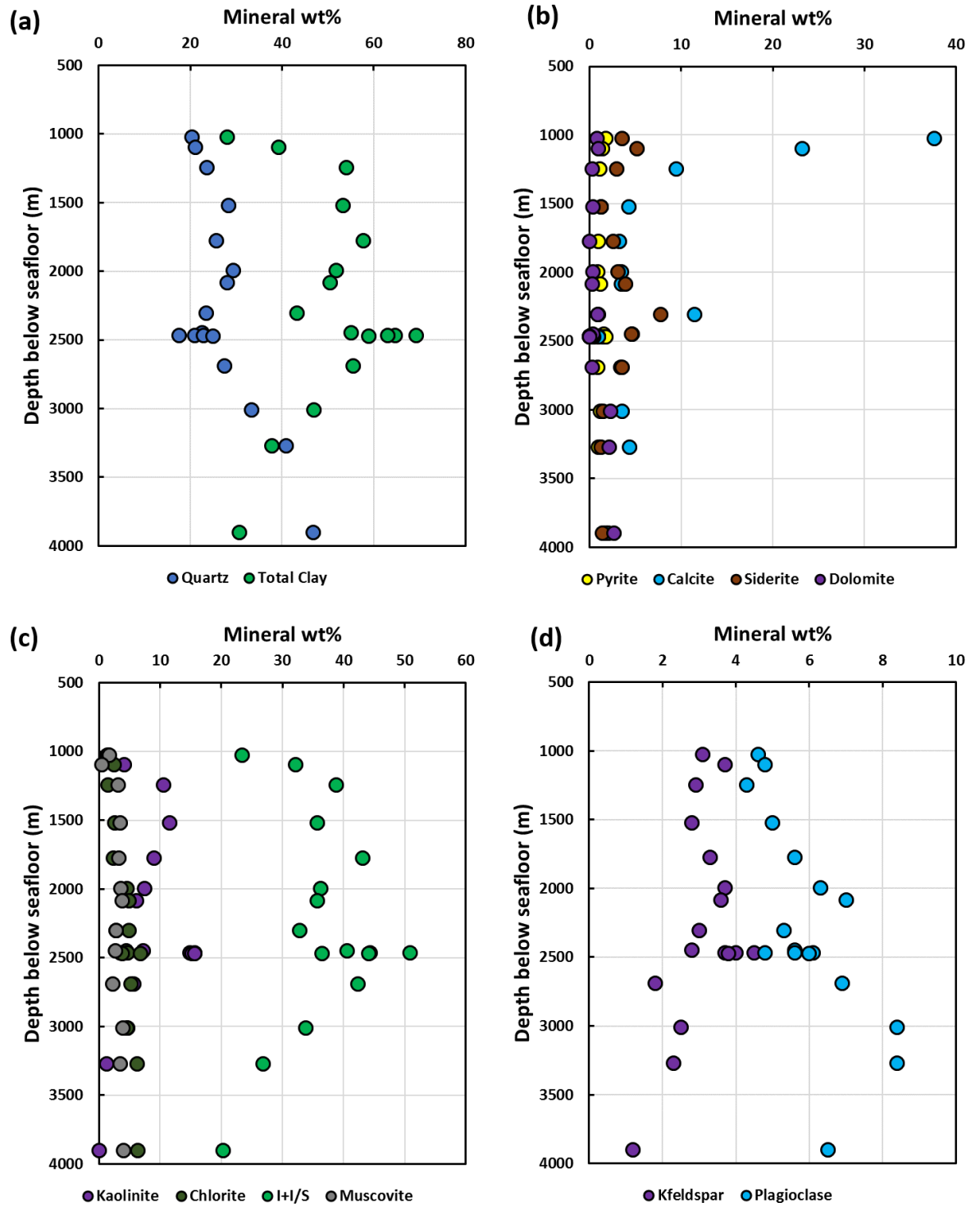


Figure 6.10. Bulk mineralogy versus depth trends for Well A mudstones.

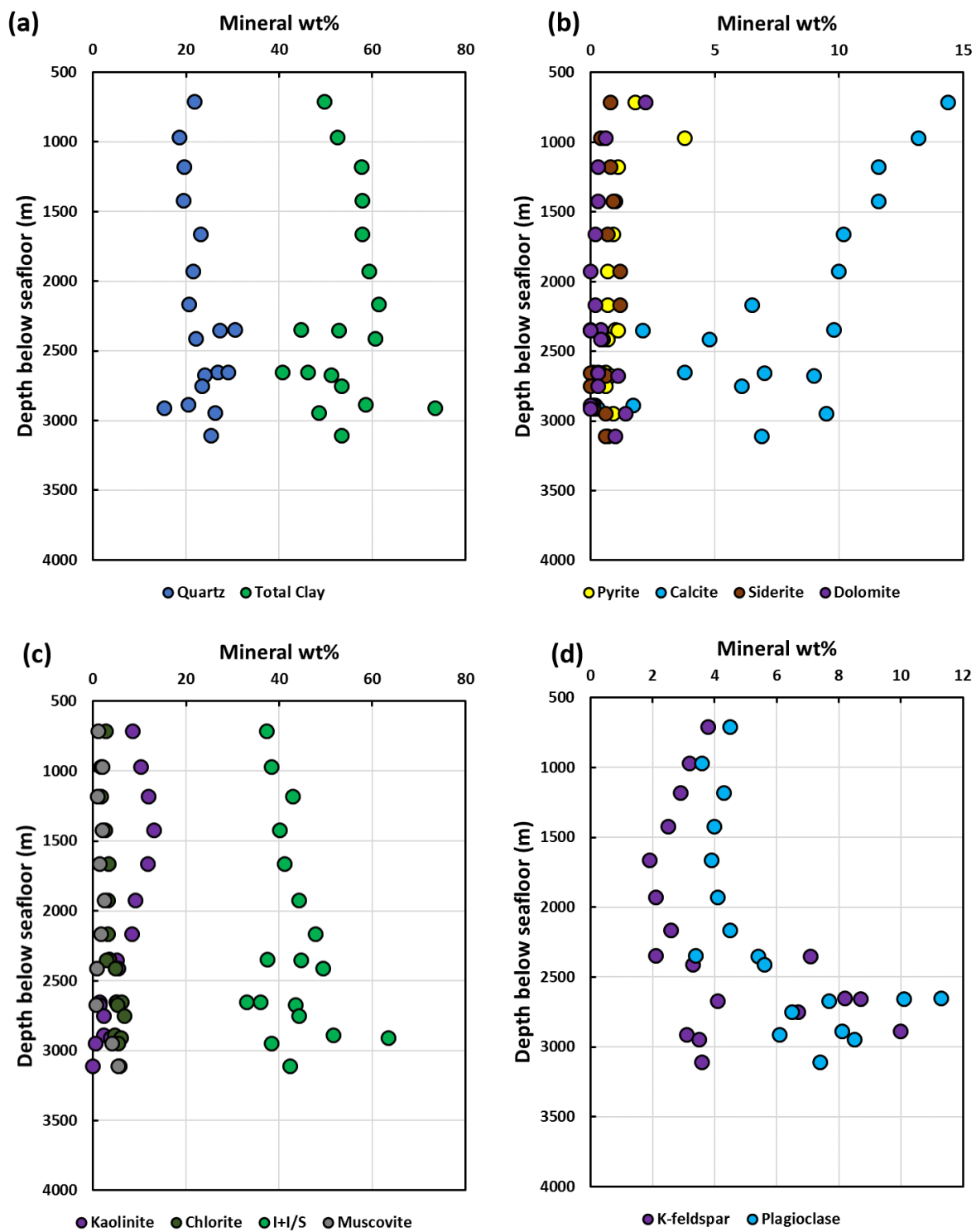


Figure 6.11. Bulk mineralogy versus depth trends for Well C mudstones.

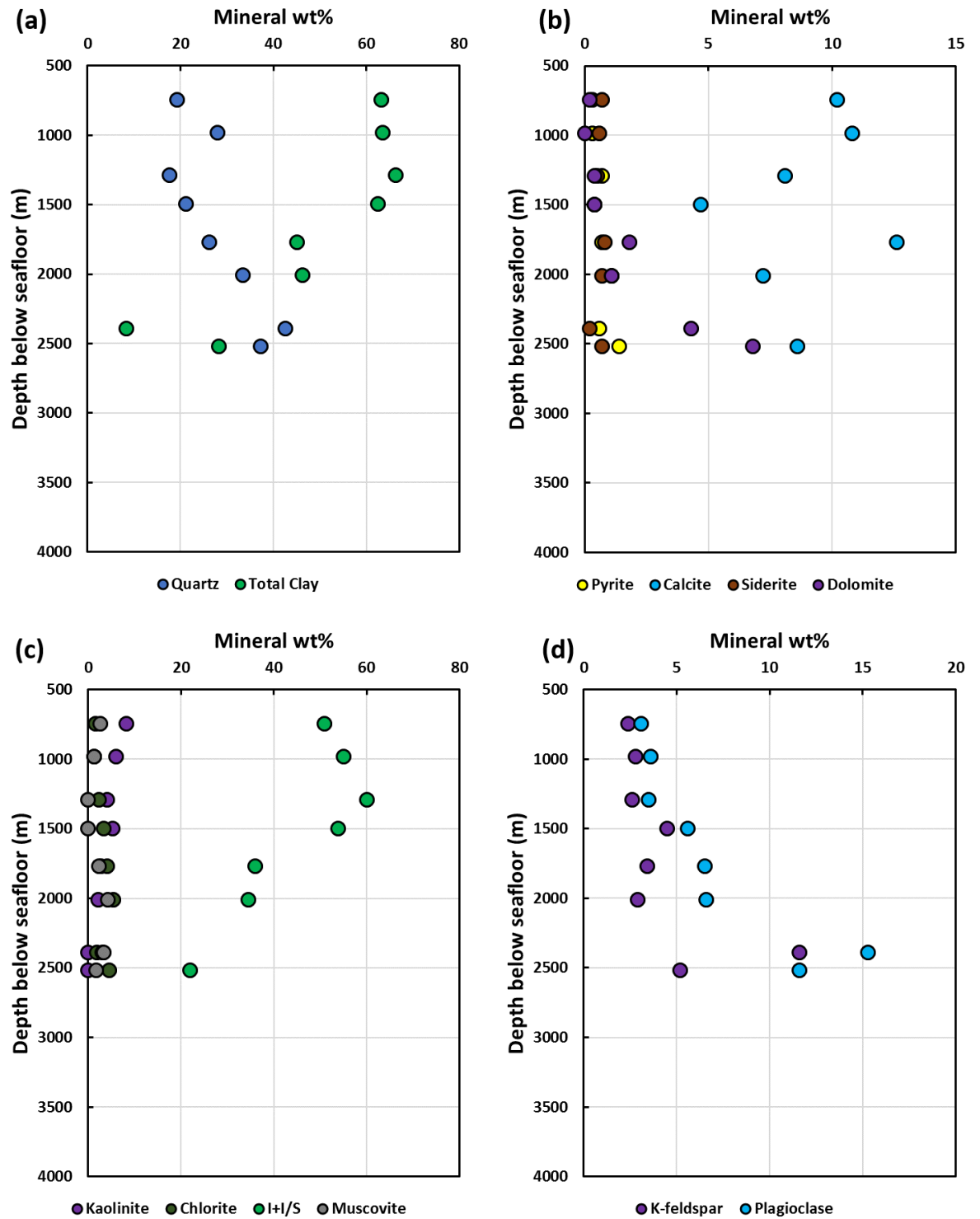


Figure 6.12. Bulk mineralogy versus depth trends for Well D mudstones.

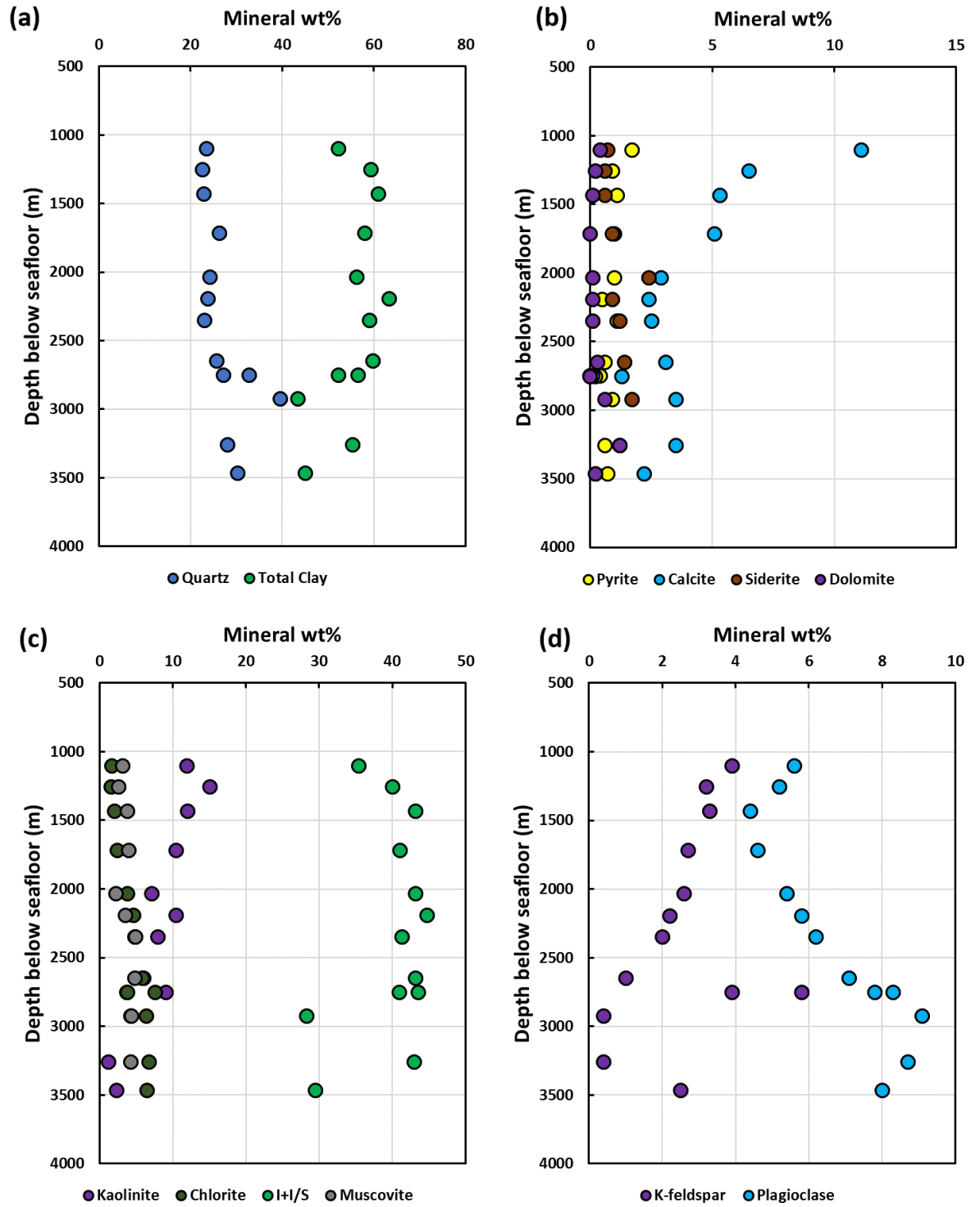


Figure 6.13. Bulk mineralogy versus depth trends for Well E mudstones.

| | <i>Quartz</i> | <i>Plagioclase</i> | <i>K-fspar</i> | <i>Calcite</i> | <i>Dolomite</i> | <i>Siderite</i> | <i>Pyrite</i> | <i>Anatase</i> | <i>Barite</i> | <i>Muscovite</i> | <i>I+I/S</i> | <i>Chlorite</i> | <i>Kaolinite</i> |
|--------------------|---------------|--------------------|----------------|----------------|-----------------|-----------------|---------------|----------------|---------------|------------------|--------------|-----------------|------------------|
| Quartz | 1.00 | | | | | | | | | | | | |
| Plagioclase | 0.65 | 1.00 | | | | | | | | | | | |
| K-fspar | -0.74 | -0.35 | 1.00 | | | | | | | | | | |
| Calcite | -0.30 | -0.43 | 0.01 | 1.00 | | | | | | | | | |
| Dolomite | 0.81 | 0.56 | -0.69 | 0.11 | 1.00 | | | | | | | | |
| Siderite | -0.18 | -0.22 | -0.15 | 0.49 | 0.03 | 1.00 | | | | | | | |
| Pyrite | 0.24 | -0.19 | -0.37 | 0.35 | 0.29 | 0.12 | 1.00 | | | | | | |
| Anatase | -0.40 | -0.22 | 0.48 | -0.29 | -0.37 | -0.52 | -0.36 | 1.00 | | | | | |
| Barite | 0.74 | 0.22 | -0.60 | -0.12 | 0.66 | 0.09 | 0.32 | -0.22 | 1.00 | | | | |
| Muscovite | 0.65 | 0.53 | -0.32 | -0.75 | 0.27 | -0.54 | -0.21 | | 0.36 | 1.00 | | | |
| I+I/S | -0.63 | -0.19 | 0.55 | -0.49 | -0.76 | -0.25 | -0.59 | 0.61 | -0.62 | -0.01 | 1.00 | | |
| Chlorite | 0.56 | 0.68 | -0.26 | -0.56 | 0.35 | -0.18 | 0.04 | -0.08 | 0.48 | 0.48 | -0.18 | 1.00 | |
| Kaolinite | -0.55 | -0.33 | 0.67 | -0.48 | -0.75 | -0.57 | -0.33 | 0.63 | -0.55 | 0.14 | 0.80 | -0.11 | 1.00 |

Table 6.2. Correlation matrix showing values of Pearson's correlation coefficient for Well A mineralogy.

| | Quartz | Plagioclase | K-fspar | Calcite | Dolomite | Siderite | Pyrite | Anatase | Barite | Muscovite | I+I/S | Chlorite | Kaolinite |
|-------------|--------|-------------|---------|---------|----------|----------|--------|---------|--------|-----------|-------|----------|-----------|
| Quartz | 1.00 | | | | | | | | | | | | |
| Plagioclase | 0.40 | 1.00 | | | | | | | | | | | |
| K-fspar | 0.31 | 0.73 | 1.00 | | | | | | | | | | |
| Calcite | -0.03 | -0.49 | -0.56 | 1.00 | | | | | | | | | |
| Dolomite | 0.14 | 0.06 | -0.19 | 0.54 | 1.00 | | | | | | | | |
| Siderite | -0.40 | -0.46 | -0.65 | 0.55 | 0.23 | 1.00 | | | | | | | |
| Pyrite | -0.19 | -0.45 | -0.29 | 0.62 | 0.33 | 0.13 | 1.00 | | | | | | |
| Anatase | 0.24 | 0.55 | 0.18 | -0.07 | 0.14 | -0.05 | -0.11 | 1.00 | | | | | |
| Barite | -0.33 | -0.23 | -0.35 | 0.44 | 0.19 | 0.50 | 0.14 | -0.07 | 1.00 | | | | |
| Muscovite | 0.55 | 0.51 | 0.11 | -0.21 | 0.17 | -0.08 | -0.13 | 0.64 | -0.45 | 1.00 | | | |
| I+I/S | -0.63 | -0.14 | -0.08 | -0.63 | -0.40 | -0.03 | -0.37 | -0.29 | -0.07 | -0.25 | 1.00 | | |
| Chlorite | 0.28 | 0.72 | 0.44 | -0.57 | 0.00 | -0.49 | -0.62 | 0.15 | -0.36 | 0.47 | 0.21 | 1.00 | |
| Kaolinite | -0.51 | -0.69 | -0.49 | 0.52 | -0.17 | 0.57 | 0.43 | -0.16 | 0.40 | -0.55 | -0.09 | -0.83 | 1.00 |

Table 6.3. Correlation matrix showing values of Pearson's correlation coefficient for Well C mineralogy.

| | <i>Quartz</i> | <i>Plagioclase</i> | <i>K-fspar</i> | <i>Calcite</i> | <i>Dolomite</i> | <i>Siderite</i> | <i>Pyrite</i> | <i>Anatase</i> | <i>Barite</i> | <i>Muscovite</i> | <i>I-I/S-ML</i> | <i>Chlorite</i> | <i>Kaolinite</i> |
|--------------------|---------------|--------------------|----------------|----------------|-----------------|-----------------|---------------|----------------|---------------|------------------|-----------------|-----------------|------------------|
| Quartz | 1.00 | | | | | | | | | | | | |
| Plagioclase | 0.89 | 1.00 | | | | | | | | | | | |
| K-fspar | 0.74 | 0.90 | 1.00 | | | | | | | | | | |
| Calcite | 0.52 | 0.54 | 0.65 | 1.00 | | | | | | | | | |
| Dolomite | 0.77 | 0.86 | 0.60 | 0.33 | 1.00 | | | | | | | | |
| Siderite | -0.25 | -0.46 | -0.75 | -0.27 | -0.09 | 1.00 | | | | | | | |
| Pyrite | 0.52 | 0.47 | 0.08 | -0.16 | 0.72 | 0.31 | 1.00 | | | | | | |
| Anatase | -0.08 | -0.27 | -0.27 | 0.30 | -0.25 | 0.39 | -0.30 | 1.00 | | | | | |
| Barite | -0.18 | -0.08 | -0.11 | 0.22 | -0.13 | 0.38 | -0.15 | 0.50 | 1.00 | | | | |
| Muscovite | 0.62 | 0.42 | 0.30 | 0.48 | 0.25 | 0.16 | 0.28 | -0.06 | 0.15 | 1.00 | | | |
| I-I/S-ML | -0.92 | -0.96 | -0.83 | -0.64 | -0.81 | 0.29 | -0.48 | 0.19 | -0.04 | -0.64 | 1.00 | | |
| Chlorite | 0.28 | 0.21 | -0.13 | -0.41 | 0.35 | 0.42 | 0.79 | -0.16 | 0.23 | 0.28 | -0.26 | 1.00 | |
| Kaolinite | -0.82 | -0.86 | -0.64 | -0.32 | -0.82 | 0.21 | -0.77 | 0.18 | 0.05 | -0.34 | 0.82 | -0.54 | 1.00 |

Table 6.4. Correlation matrix showing values of Pearson's correlation coefficient for Well D mineralogy.

| | <i>Quartz</i> | <i>Plagioclase</i> | <i>K-fspar</i> | <i>Calcite</i> | <i>Dolomite</i> | <i>Siderite</i> | <i>Pyrite</i> | <i>Anatase</i> | <i>Barite</i> | <i>Muscovite</i> | <i>I-I/S</i> | <i>Chlorite</i> | <i>Kaolinite</i> |
|--------------------|---------------|--------------------|----------------|----------------|-----------------|-----------------|---------------|----------------|---------------|------------------|--------------|-----------------|------------------|
| Quartz | 1.00 | | | | | | | | | | | | |
| Plagioclase | 0.76 | 1.00 | | | | | | | | | | | |
| K-fspar | -0.30 | -0.25 | 1.00 | | | | | | | | | | |
| Calcite | -0.34 | -0.51 | 0.02 | 1.00 | | | | | | | | | |
| Dolomite | 0.29 | 0.50 | -0.64 | 0.19 | 1.00 | | | | | | | | |
| Siderite | 0.00 | -0.10 | -0.65 | 0.07 | 0.30 | 1.00 | | | | | | | |
| Pyrite | -0.37 | -0.54 | -0.02 | 0.84 | 0.06 | 0.31 | 1.00 | | | | | | |
| Anatase | 0.57 | 0.70 | -0.34 | -0.33 | 0.49 | -0.10 | -0.30 | 1.00 | | | | | |
| Barite | 0.20 | 0.26 | -0.03 | -0.18 | -0.04 | -0.31 | -0.10 | 0.68 | 1.00 | | | | |
| Muscovite | 0.36 | 0.50 | -0.62 | -0.36 | 0.27 | -0.08 | -0.26 | 0.30 | 0.21 | 1.00 | | | |
| I-I/S | -0.64 | -0.40 | 0.22 | -0.21 | -0.21 | 0.03 | -0.27 | -0.58 | -0.57 | -0.11 | 1.00 | | |
| Chlorite | 0.68 | 0.81 | -0.46 | -0.65 | 0.35 | 0.03 | -0.66 | 0.55 | 0.30 | 0.60 | -0.23 | 1.00 | |
| Kaolinite | -0.66 | -0.79 | 0.48 | 0.54 | -0.48 | -0.13 | 0.47 | -0.63 | -0.40 | -0.51 | 0.30 | -0.92 | 1.00 |

Table 6.5. Correlation matrix showing values of Pearson's correlation coefficient for Well E mineralogy.

The detected mineral composition is monotonous, however illite-smectite, K-feldspar, plagioclase, calcite, siderite and dolomite contents show considerable variability among the studied mudstone samples (Figures 6.10-6.13). Core samples with abundant carbonates are all localised phenomena, likely local cementations. It should be noted however that collected samples included both cores and cuttings which also contributes to this variability. Cuttings represent sampled depth intervals in the range of 5 m and these results only show averaged mineralogy which may include some carbonatic material. However, all samples are considered to be composed of dominantly siliciclastic material.

Figures 6.10-6.13 show mineralogy-depth trends in individual wells. The variability of quartz with increasing depth shows a good negative correlation with the variability of the sum of clay minerals in all four wells indicating that quartz is predominantly sedimentary in origin. The K-feldspar content decreases with depth in wells A and E implying ongoing clay mineral diagenesis. Concomitant with the disappearance of K-feldspar, the plagioclase content appears to be increasing with depth in these two wells (Figures 6.10d and 6.13d). The overall trends of decreasing K-feldspar and increasing plagioclase are obscured in Wells C and D likely due to the variations of initial detrital mineralogy. Both the K-feldspar and the plagioclase content increases very sharply below ~2000 m in these wells indicating more abundant coarse-grained material (Figures 6.11d and 6.12d). In addition, kaolinite content shows an overall decrease and the chlorite content an overall increase in all four wells, which suggests ongoing clay diagenesis where kaolinite is being dissolved and authigenic chlorite is being precipitated.

Tables 6.2-6.5 show correlation coefficient values for individual mineral phases. Quartz shows a strong negative correlation with illite-smectite in all four wells. Plagioclase content correlates positively with quartz in all four wells. However, the correlation is much weaker in Well C compared to Wells A, D and E. The K-feldspar content shows positive correlation with quartz in Well D. Interestingly however, in Well A, it shows strong negative correlation with quartz and no clear correlation can be seen in Wells C and E. Such differences between samples from different wells can be attributed to local differences in depositional mineralogy and grain size (differences in the relative amounts of detrital and authigenic minerals). Negative correlation between kaolinite and quartz in

all four wells and positive correlation between kaolinite and illite-smectite in wells A and D indicates that kaolinite is mostly present in the clay fraction. Relatively weak negative correlation between quartz and kaolinite in Wells C and D suggests the presence of considerable amount of coarser grained detrital kaolinite in these wells. Positive correlation between the chlorite content and quartz in Wells A and E suggests the presence of considerable amounts of detrital chlorite in these two wells.

The origin of the detected barite is uncertain. Barite is commonly used in drilling muds as heavyweight additive. It occurs naturally in sedimentary environments; however, it is relatively uncommon in most settings. It was not detected in the core samples which clearly indicates contamination with drilling mud components, so it was assumed to have come from drilling mud, and barite free normalized mineral concentrations have been calculated. Traces of halite and sylvite are probably precipitates from pore solutions.

6.6.2 Clay mineralogical properties

Cation exchange capacity (CEC) measurements of the studied mudstone samples range from 0 to 31.9 meq/100g and show an overall decreasing CEC-depth trend. These results are consistent with ongoing smectite illitization. However, any contamination by clay components of the drilling fluid can affect the CEC results of cutting samples. Bentonite is one such component and could have influenced the CEC results. Organic matter from an organic-based drilling fluid is another possible source of contamination. The barite content is usually the best indicator of drilling mud contamination since it is the dominant component in most drilling muds. Small amounts of barite in most of the cuttings would indicate contamination, however the comparatively similar CEC of the core samples and the lack of any discernible correlation between the CEC and the barite content (Figure 6.16) suggest that the CEC results are largely unaffected.

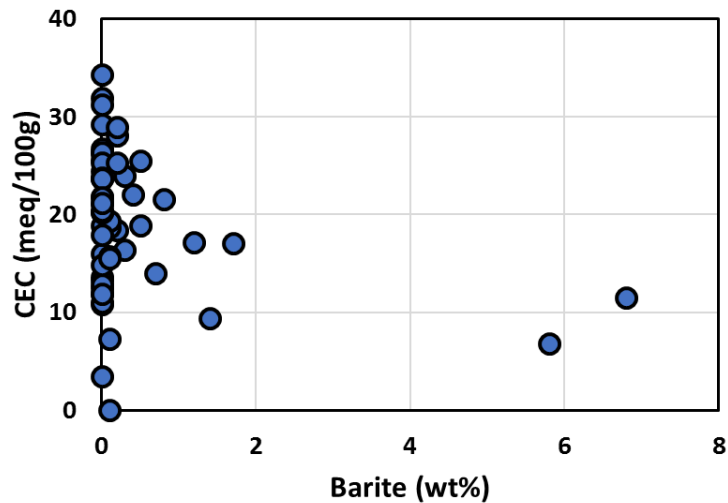


Figure 6.14. Bulk rock CEC plotted against QXRD measured barite content.

Figure 6.15a shows the calculated smectite equivalent contents in illite-smectite for the individual samples. Smectite content shows little variation with increasing depth until a depth of ~2500 m below seafloor in Wells A, C and E at which point a sharp decrease occurs in the smectite content. As it is shown in Figure 6.15b K-feldspar is decreasing concomitantly in wells A and E. In Well D, the smectite content in illite-smectite starts to decrease at a much shallower depth (~1500 m) than in the three shelfal wells. In overall, these results indicate ongoing illitization of smectite in the studied mudstones.

Complete CEC data and calculated smectite equivalent contents for individual samples can be found in Appendix I.

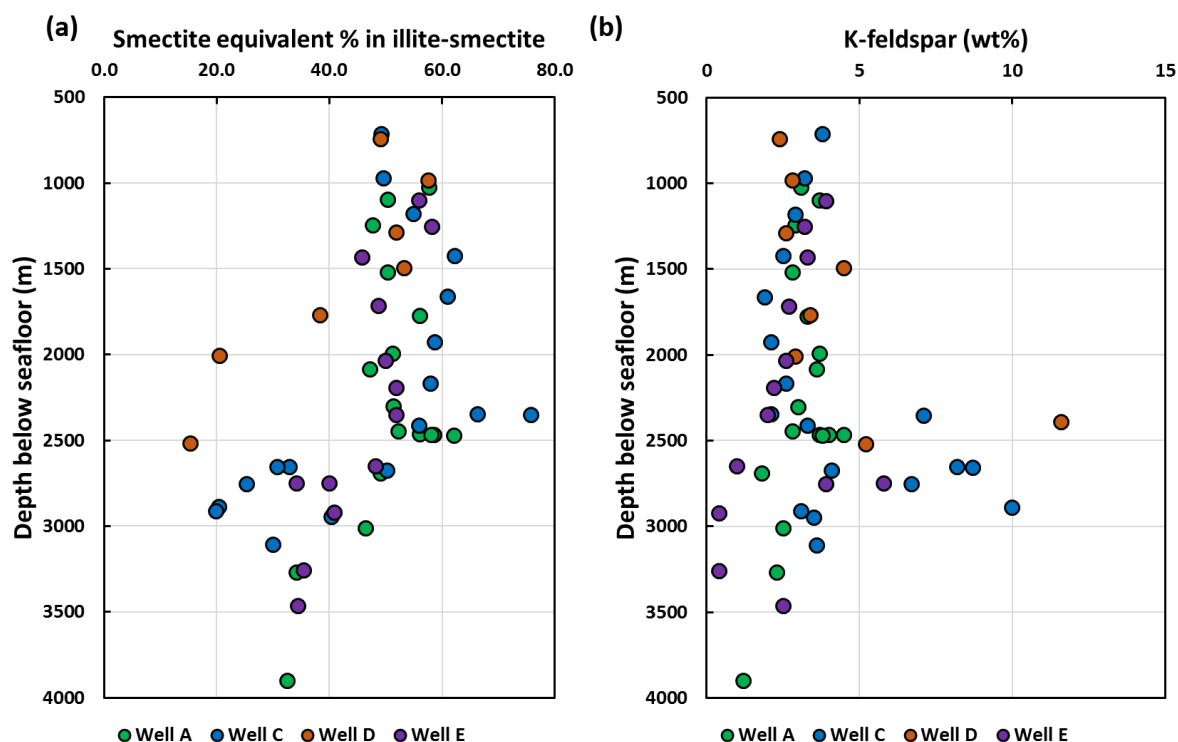


Figure 6.15. (a) Calculated smectite equivalent % in illite-smectite for the studied mudstone samples plotted against depth below seafloor. Smectite equivalent content was calculated using CEC results as described in 3.3.3. (b) QXRD measured K-feldspar content versus depth below seafloor.

The authigenic (<0.2 μm fraction) and clay fraction (<2 μm fraction) XRD results confirm ongoing illitization of smectite by showing decreasing smectite content with increasing depth (Figure 6.17). In overall the mudstone samples contain illite, illite-smectite, kaolinite and chlorite. The <2 μm clay fraction is dominated by mixed-layer illite-smectite in all samples (Figure 6.16). A disordered (R0) illite-smectite phase population with >50% smectite in illite-smectite has been detected in the shallower samples in all four wells (Figures 6.16 and 6.17).

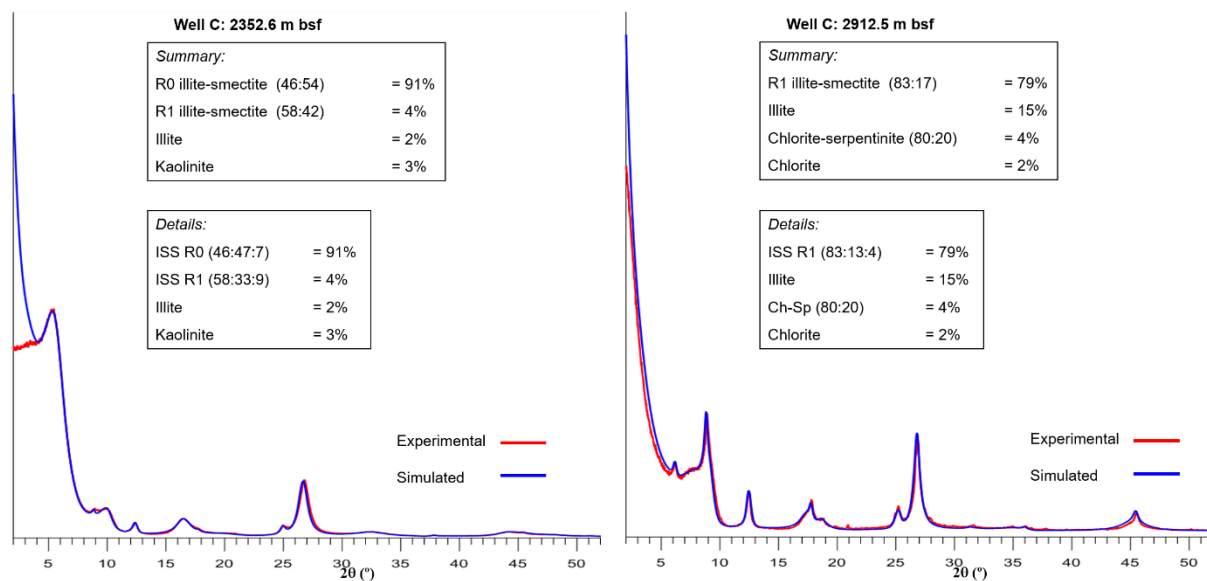


Figure 6.16. Experimental and simulated XRD patterns for ethylene glycol-saturated samples from Well C.

This smectitic illite-smectite population is dominant below 2500 m in wells A, C and E; and below 1500 m in the deep water Well D. However, this population disappears with increasing depth in all four wells. No disordered illite-smectite phase population was detected below 1500 m in Well D and below 2500 m in Wells A, C and E. Below these depths the <2 μm clay fraction is dominated by mixed-layer illite-smectite with ordered interstratification ($R>1$) (Figure 6.16). No pure smectite has been detected in the samples. Full <0.2 μm fraction XRD data and modelling results can be found in Appendix II.

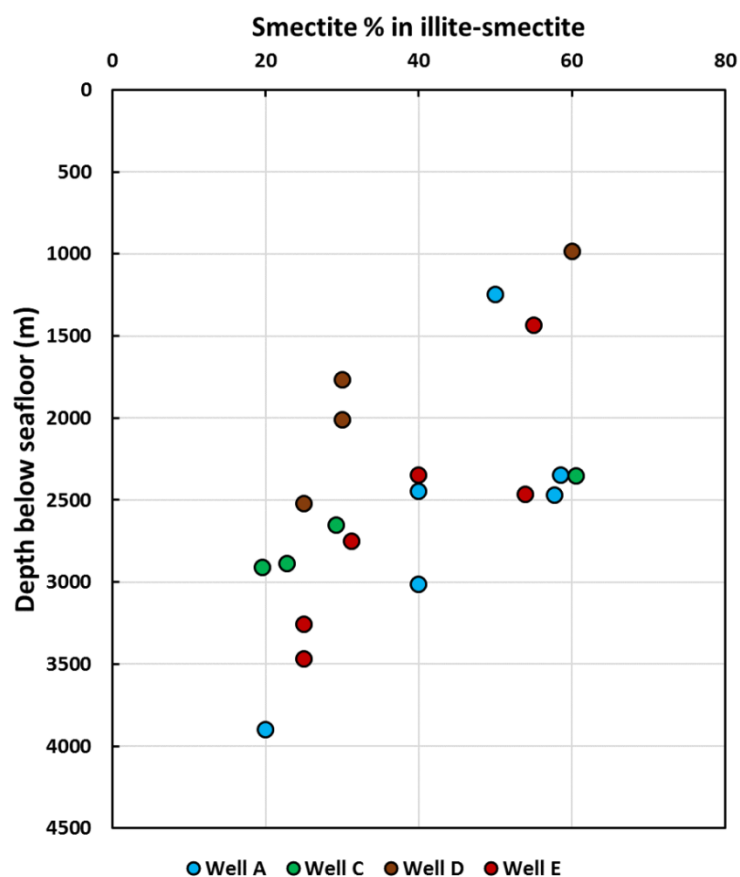


Figure 6.17. Smectite equivalent (%) in illite-smectite versus depth for the studied samples. Smectite equivalent content was calculated using the combination of the bulk QXRD, $<2\ \mu\text{m}$ and $<0.2\ \mu\text{m}$ fraction modelling results.

6.6.3 Total organic carbon content

Total organic carbon content (TOC) was estimated in mudstone samples from wells A, C and E. Complete TOC data and calculated organic matter contents for individual samples are given in Appendix III.

Figure 6.18 shows the measured TOC content of individual mudstone samples. The TOC values are consistent, mostly being less than 1 wt%. In overall, these TOC values are considered typical for siliciclastic mudstones.

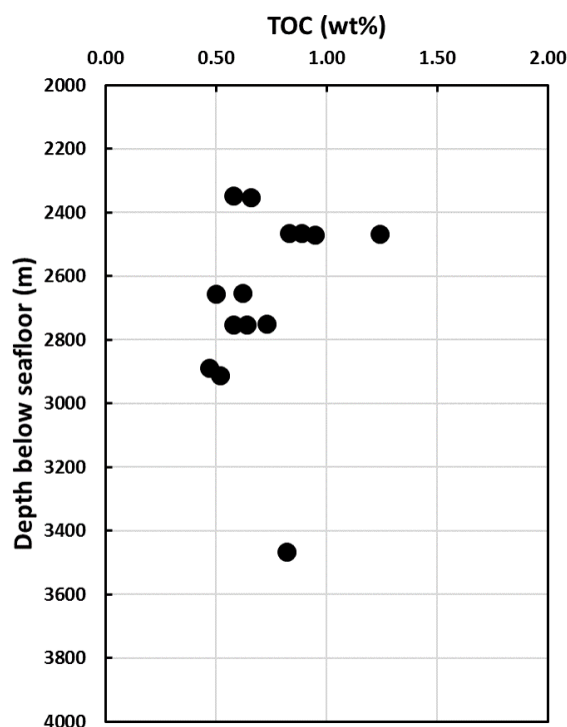


Figure 6.18. TOC (wt%) results for the studied mudstones.

6.6.4 Bulk inorganic chemical properties

Selected mudstone samples were analysed for their major and trace elemental composition. Complete major and trace element concentrations of the individual mudstone samples along with the ratios of selected pairs of major and trace elements and calculated weathering indices can be found in Appendix IV.

The amount of SiO_2 varies between 48.23 and 63.61% (average of 56.56%), Al_2O_3 varies between 11.40 and 19.91% (average 16.33%), TiO_2 varies between 0.49 and 0.91% (average 0.75%), Fe_2O_3 varies between 4.14 and 9.79% (average 6.20%), MnO varies between 0.03 and 0.08% (average 0.04%), MgO varies between 1.45 and 2.79% (average 2.05%), CaO varies between 0.35 and 12.49% (average 3.05%), Na_2O varies between 1.16 and 1.77% (average 1.49%), K_2O varies between 1.78 and 4.80% (average 3.02%) and P_2O_5 varies between 0.02 and 0.15% (average 0.08%). Total iron is expressed as Fe_2O_3 .

Correlation coefficient values for major elements are given in Table 6.6. Al_2O_3 shows strong positive correlations with TiO_2 . This indicates that titanium resides primarily in clay minerals and is dominantly terrigenous component. However, TiO_2 also shows weak

positive correlation with SiO_2 that can be attributed to the presence of anatase. Good positive correlation between Na_2O and SiO_2 can be related to the presence of plagioclase. CaO shows negative correlations with SiO_2 and Al_2O_3 . This indicates that calcium is dominantly a marine component. Weak positive correlation between Fe_2O_3 and Al_2O_3 indicates that some of the iron was transported to the basin with clay minerals either as primary constituents in the crystal structure or on crystal surfaces as oxides and oxyhydroxides (Carroll, 1958; Hofstetter et al., 2003). MnO shows weak positive correlation with Fe_2O_3 indicating that Mn partially resides in siderite. Correlation between K_2O and MgO can be attributed to the presence of chlorite.

Values of $\text{K}_2\text{O}/\text{Al}_2\text{O}_3$ ratio of the studied mudstone samples show variation between 0.14 and 0.26 (average of 0.19). These values are consistent with the preponderance of clay minerals over K-feldspar in these samples (Cox et al., 1995).

Values of Si/Al shows good correlation with QXRD established quartz abundances (Figure 6.14 a, b). Correlation between K/Al and illite-smectite (Figure 6.14 c, d) and between Na/Al and plagioclase (Figure 6.14 e,f) is obscured due to the presence of considerable amount of detrital K-feldspar and plagioclase in most of the samples.

Calculated ICV values of the samples range from 0.66 to 1.93. Calculated CIA and CIW values range from 60 to 74 and 83 to 90 respectively. Calculated CIA and CIW values show strong positive correlation indicating that the two indices are matchable (Figure 6.20).

Correlation coefficient values for selected trace elements and rare earth elements (REE) are shown in Tables 6.7 and 6.8 respectively. Among the analysed elements Sc, V, Y, Rb, Nb, U and Th show strong positive correlation with Al_2O_3 indicating that they are closely related to clay minerals either as primary constituents or as adsorbed components on clay mineral surfaces. Zirconium show strong positive correlation with SiO_2 indicating the presence of zircon. Uranium and niobium also show positive correlation with TiO_2 indicating likely association with anatase. Chromium, cobalt and nickel are most likely associated with mafic mineral components. Rare earth elements show strong positive correlations with TiO_2 and Al_2O_3 indicating that their mostly associated with clay minerals.

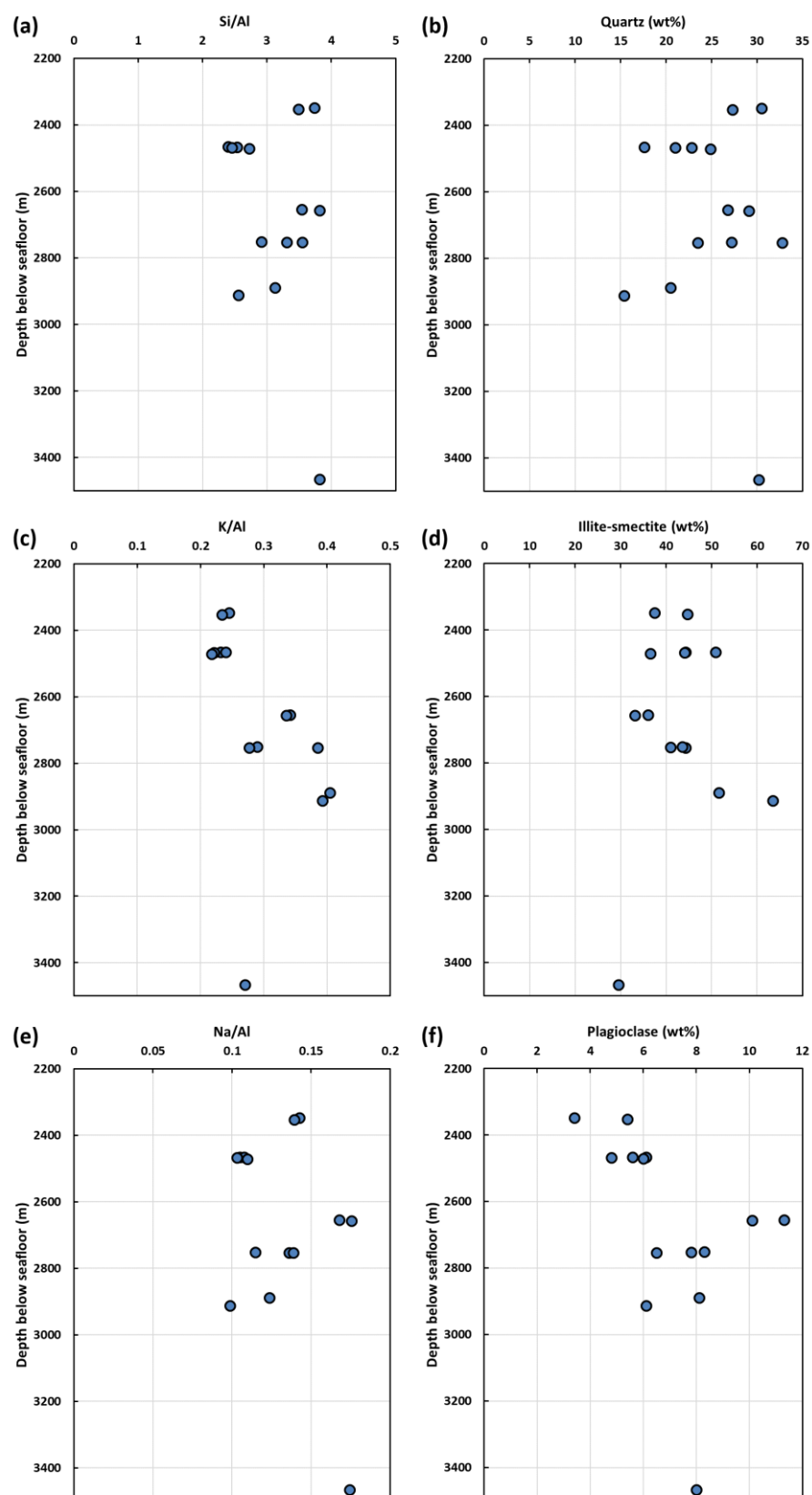


Figure 6.19. Variation of (a) Si/Al , (c) K/Al and (e) Na/Al with depth in comparison with the variation of (b) quartz, (d) illite-smectite and (f) plagioclase.

| | SiO2 | Al2O3 | Fe2O3(T) | MnO | MgO | CaO | Na2O | K2O | TiO2 | P2O5 |
|----------|-------|-------|----------|-------|-------|-------|------|------|------|------|
| SiO2 | 1.00 | | | | | | | | | |
| Al2O3 | 0.20 | 1.00 | | | | | | | | |
| Fe2O3(T) | -0.30 | 0.44 | 1.00 | | | | | | | |
| MnO | -0.05 | -0.34 | 0.37 | 1.00 | | | | | | |
| MgO | -0.12 | -0.15 | -0.15 | -0.35 | 1.00 | | | | | |
| CaO | -0.54 | -0.82 | -0.44 | -0.04 | 0.19 | 1.00 | | | | |
| Na2O | 0.66 | -0.03 | 0.00 | 0.24 | 0.06 | -0.33 | 1.00 | | | |
| K2O | 0.31 | 0.47 | -0.10 | -0.45 | 0.66 | -0.42 | 0.08 | 1.00 | | |
| TiO2 | 0.33 | 0.97 | 0.35 | -0.31 | -0.13 | -0.86 | 0.00 | 0.57 | 1.00 | |
| P2O5 | 0.17 | 0.16 | 0.05 | -0.27 | 0.86 | -0.24 | 0.28 | 0.81 | 0.20 | 1.00 |

Table 6.6. Correlation matrix showing values of Pearson's correlation coefficient for major elements of the studied mudstones.

| | SiO2 | Al2O3 | CaO | TiO2 | Sc | V | Ba | Sr | Y | Zr | Cr | Co | Ni | Zn | Rb | Nb | Pb | Th | U |
|-------|-------|-------|-------|-------|-------|-------|-------|-------|------|-------|-------|-------|------|-------|-------|------|-------|------|------|
| SiO2 | 1.00 | | | | | | | | | | | | | | | | | | |
| Al2O3 | 0.20 | 1.00 | | | | | | | | | | | | | | | | | |
| CaO | -0.54 | -0.82 | 1.00 | | | | | | | | | | | | | | | | |
| TiO2 | 0.33 | 0.97 | -0.86 | 1.00 | | | | | | | | | | | | | | | |
| Sc | 0.06 | 0.97 | -0.78 | 0.94 | 1.00 | | | | | | | | | | | | | | |
| V | 0.00 | 0.94 | -0.76 | 0.90 | 0.98 | 1.00 | | | | | | | | | | | | | |
| Ba | -0.16 | -0.39 | 0.03 | -0.36 | -0.29 | -0.27 | 1.00 | | | | | | | | | | | | |
| Sr | -0.50 | -0.74 | 0.64 | -0.76 | -0.68 | -0.67 | 0.69 | 1.00 | | | | | | | | | | | |
| Y | 0.37 | 0.83 | -0.86 | 0.89 | 0.85 | 0.82 | -0.05 | -0.62 | 1.00 | | | | | | | | | | |
| Zr | 0.79 | -0.03 | -0.24 | 0.11 | -0.21 | -0.31 | -0.06 | -0.07 | 0.08 | 1.00 | | | | | | | | | |
| Cr | 0.12 | 0.14 | -0.31 | 0.17 | 0.23 | 0.25 | 0.08 | -0.20 | 0.15 | -0.22 | 1.00 | | | | | | | | |
| Co | 0.02 | 0.42 | -0.31 | 0.41 | 0.41 | 0.45 | -0.06 | -0.21 | 0.51 | -0.08 | -0.16 | 1.00 | | | | | | | |
| Ni | -0.17 | 0.32 | -0.34 | 0.30 | 0.39 | 0.43 | 0.42 | 0.06 | 0.49 | -0.31 | 0.10 | 0.79 | 1.00 | | | | | | |
| Zn | 0.06 | -0.29 | -0.12 | -0.25 | -0.17 | -0.12 | 0.81 | 0.31 | 0.06 | -0.19 | 0.29 | -0.03 | 0.42 | 1.00 | | | | | |
| Rb | 0.31 | 0.87 | -0.76 | 0.94 | 0.91 | 0.86 | -0.32 | -0.77 | 0.88 | 0.00 | 0.24 | 0.30 | 0.22 | -0.13 | 1.00 | | | | |
| Nb | 0.25 | 0.93 | -0.86 | 0.95 | 0.94 | 0.91 | -0.14 | -0.63 | 0.93 | 0.01 | 0.12 | 0.47 | 0.47 | -0.04 | 0.91 | 1.00 | | | |
| Pb | -0.05 | 0.00 | -0.16 | 0.03 | 0.05 | 0.09 | 0.63 | 0.33 | 0.31 | -0.04 | -0.11 | 0.72 | 0.88 | 0.52 | -0.02 | 0.22 | 1.00 | | |
| Th | 0.26 | 0.97 | -0.84 | 0.98 | 0.95 | 0.91 | -0.36 | -0.71 | 0.87 | 0.08 | 0.16 | 0.38 | 0.26 | -0.31 | 0.90 | 0.94 | -0.02 | 1.00 | |
| U | 0.16 | 0.89 | -0.80 | 0.91 | 0.91 | 0.91 | -0.23 | -0.61 | 0.85 | -0.02 | 0.17 | 0.32 | 0.26 | -0.17 | 0.87 | 0.91 | 0.01 | 0.95 | 1.00 |

Table 6.7. Correlation matrix showing values of Pearson's correlation coefficient for selected trace elements of the studied mudstones.

| | SiO ₂ | Al ₂ O ₃ | CaO | TiO ₂ | La | Ce | Pr | Nd | Sm | Eu | Gd | Tb | Dy | Ho | Er | Tm | Yb |
|--------------------------------|------------------|--------------------------------|-------|------------------|------|------|------|------|------|------|------|------|------|------|------|------|------|
| SiO ₂ | 1.00 | | | | | | | | | | | | | | | | |
| Al ₂ O ₃ | 0.20 | 1.00 | | | | | | | | | | | | | | | |
| CaO | -0.54 | -0.82 | 1.00 | | | | | | | | | | | | | | |
| TiO ₂ | 0.33 | 0.97 | -0.86 | 1.00 | | | | | | | | | | | | | |
| La | 0.47 | 0.88 | -0.86 | 0.95 | 1.00 | | | | | | | | | | | | |
| Ce | 0.39 | 0.93 | -0.90 | 0.96 | 0.97 | 1.00 | | | | | | | | | | | |
| Pr | 0.43 | 0.90 | -0.89 | 0.96 | 0.99 | 0.99 | 1.00 | | | | | | | | | | |
| Nd | 0.43 | 0.90 | -0.87 | 0.96 | 0.98 | 0.98 | 1.00 | 1.00 | | | | | | | | | |
| Sm | 0.35 | 0.89 | -0.89 | 0.94 | 0.91 | 0.95 | 0.96 | 0.96 | 1.00 | | | | | | | | |
| Eu | 0.40 | 0.84 | -0.86 | 0.90 | 0.92 | 0.92 | 0.94 | 0.97 | 0.98 | 1.00 | | | | | | | |
| Gd | 0.39 | 0.85 | -0.86 | 0.91 | 0.90 | 0.92 | 0.94 | 0.96 | 0.99 | 0.99 | 1.00 | | | | | | |
| Tb | 0.20 | 0.87 | -0.81 | 0.88 | 0.83 | 0.90 | 0.89 | 0.90 | 0.97 | 0.93 | 0.95 | 1.00 | | | | | |
| Dy | 0.34 | 0.82 | -0.84 | 0.88 | 0.84 | 0.89 | 0.90 | 0.91 | 0.98 | 0.96 | 0.98 | 0.97 | 1.00 | | | | |
| Ho | 0.36 | 0.90 | -0.85 | 0.94 | 0.89 | 0.93 | 0.94 | 0.95 | 0.98 | 0.96 | 0.97 | 0.95 | 0.97 | 1.00 | | | |
| Er | 0.37 | 0.86 | -0.88 | 0.93 | 0.90 | 0.94 | 0.94 | 0.95 | 0.98 | 0.96 | 0.99 | 0.96 | 0.98 | 0.97 | 1.00 | | |
| Tm | 0.51 | 0.83 | -0.91 | 0.90 | 0.89 | 0.93 | 0.93 | 0.94 | 0.96 | 0.93 | 0.96 | 0.91 | 0.95 | 0.92 | 0.97 | 1.00 | |
| Yb | 0.41 | 0.87 | -0.89 | 0.94 | 0.91 | 0.95 | 0.95 | 0.95 | 0.96 | 0.93 | 0.95 | 0.92 | 0.96 | 0.95 | 0.98 | 0.96 | 1.00 |

Table 6.8. Correlation matrix showing values of Pearson's correlation coefficient for REE of the studied mudstones.

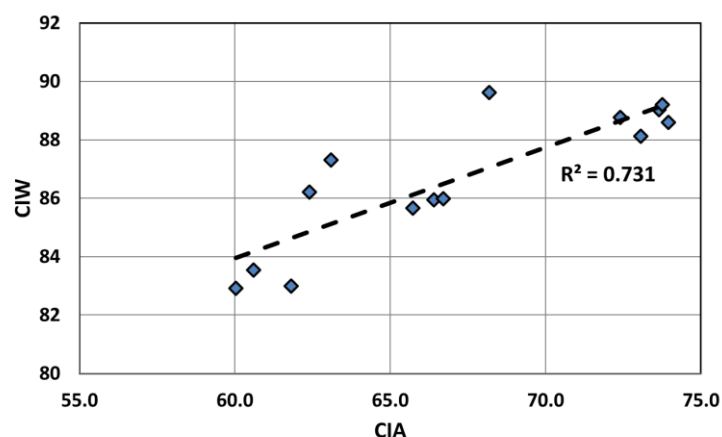


Figure 6.20. Strong positive correlation between calculated CIA and CIW values of the studied mudstones.

Th/Sc ratios of the samples range from 0.99 to 1.29 (average of 1.10). Zr/Sc ratios range from 8.89 to 24.09 (average of 14.90). La/Sc ratios of the samples range from 2.58 to 4.02 (average of 3.29). La/Th ratios range from 2.61 to 3.43 (average of 2.99). Zr/Cr ratios range from 0.92 to 2.38 (average of 1.52) and Y/Ni ratios range from 0.24 to 0.73 (average of 0.48).

6.6.5 Mudstone porosity and permeability

Grain density was measured for selected mudstone core samples (from wells A, C and E) using the “Small Pycnometer Method”, as it is described in 3.3.6. Measurements range from 2.63 to 2.89 g/cm³ (average 2.78 g/cm³) as it is shown in Figure 6.21a. No trend can be seen when plotting the data against depth. Relatively high values of particle density are most likely related to the presence of iron bearing heavy minerals such as pyrite and siderite. In contrast, the relatively low value of 2.63 g/cm³ in a mudstone sample from Well A can likely be attributed to the relatively high organic matter content of the sample. In overall, these results are in accordance with the QXRD determined bulk mineralogy and indicate fairly consistent particle densities within the studied mudstones.

Measured grain densities were used to determine the total porosity of the mudstone samples as it is described in 3.3.7. Corrected total porosity (refer to 3.3.8) values of the samples ranges from 8% to 17% as it is shown on Figure 6.21b. A clear decreasing trend

can be seen when plotting the porosity data against depth (Figure 6.21b) which indicates ~9% porosity loss between 2400 and 3000 m bsf.

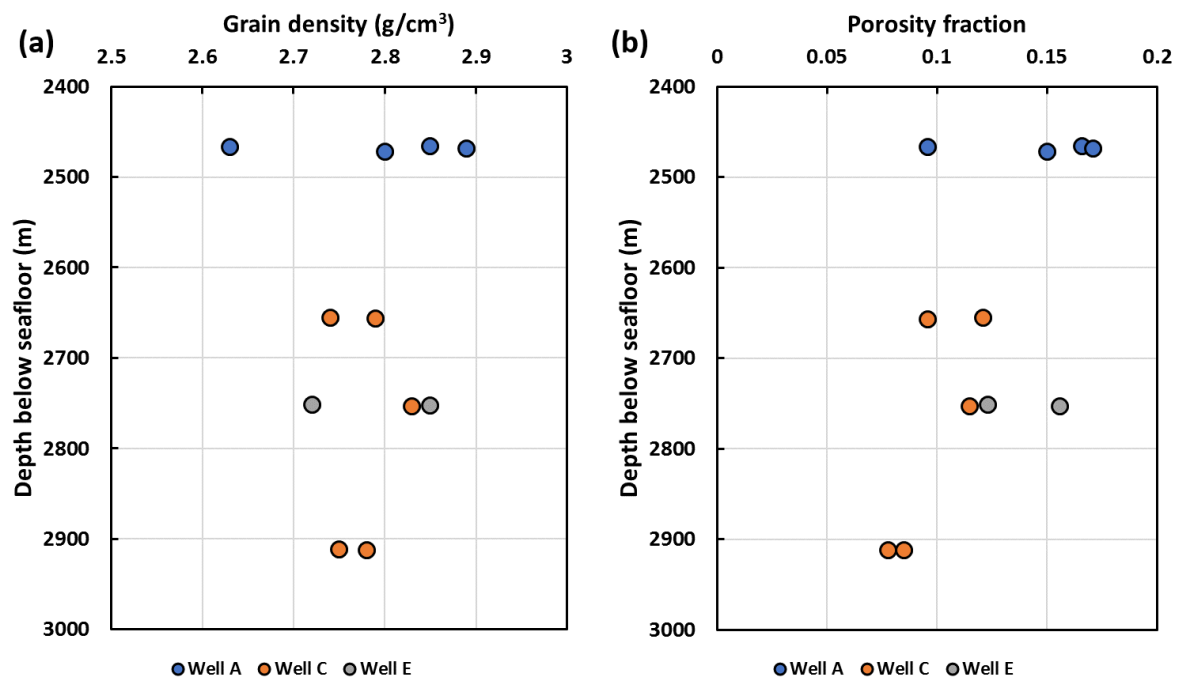


Figure 6.21. (a) Measured grain densities and (b) corrected total porosities of selected mudstone samples plotted against depth below seafloor.

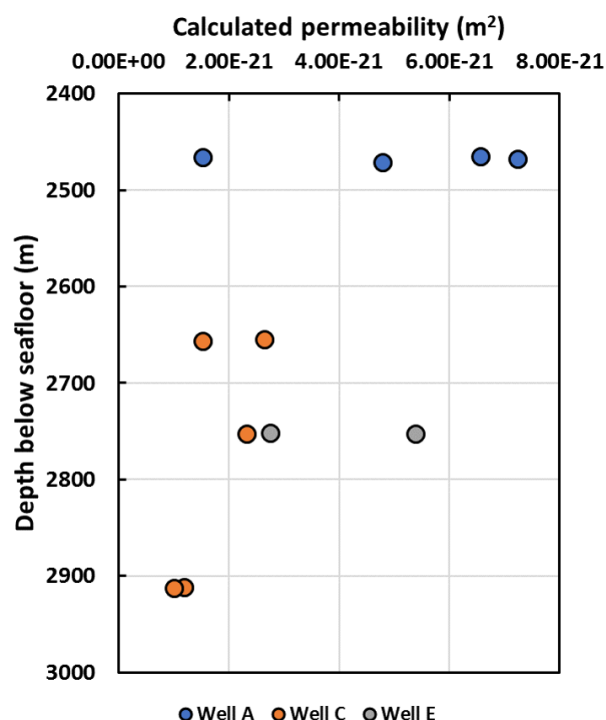


Figure 6.22. Calculated bedding perpendicular permeability (after Yang and Aplin, 2010) of selected mudstone samples.

Permeability of the mudstone samples was calculated based on the model of Yang and Aplin (2010) utilising bulk QXRD estimated total clay mineral content and estimated (corrected) total porosities. Total clay mineral content was used as a proxy for the mass fraction of particles less than two microns since no grain size distribution measurements have been made. The calculated permeabilities of the samples are very low (in the nD range) and show an overall decreasing permeability-depth trend (Figure 6.22).

Figure 6.23 shows corrected pore throat size distributions, corrected cumulative porosities and corrected mean pore throat radius of selected mudstone samples. These were all determined using Mercury Injection Core Porosimetry (MICP) as it was described in 3.3.8.

In overall, these results reveal tight lithologies with mean pore throat sizes below 100 nm and show an overall loss of the larger mesopores with increasing depth. Full grain density, total porosity, MICP and calculated permeability data can be found in Appendix VI.

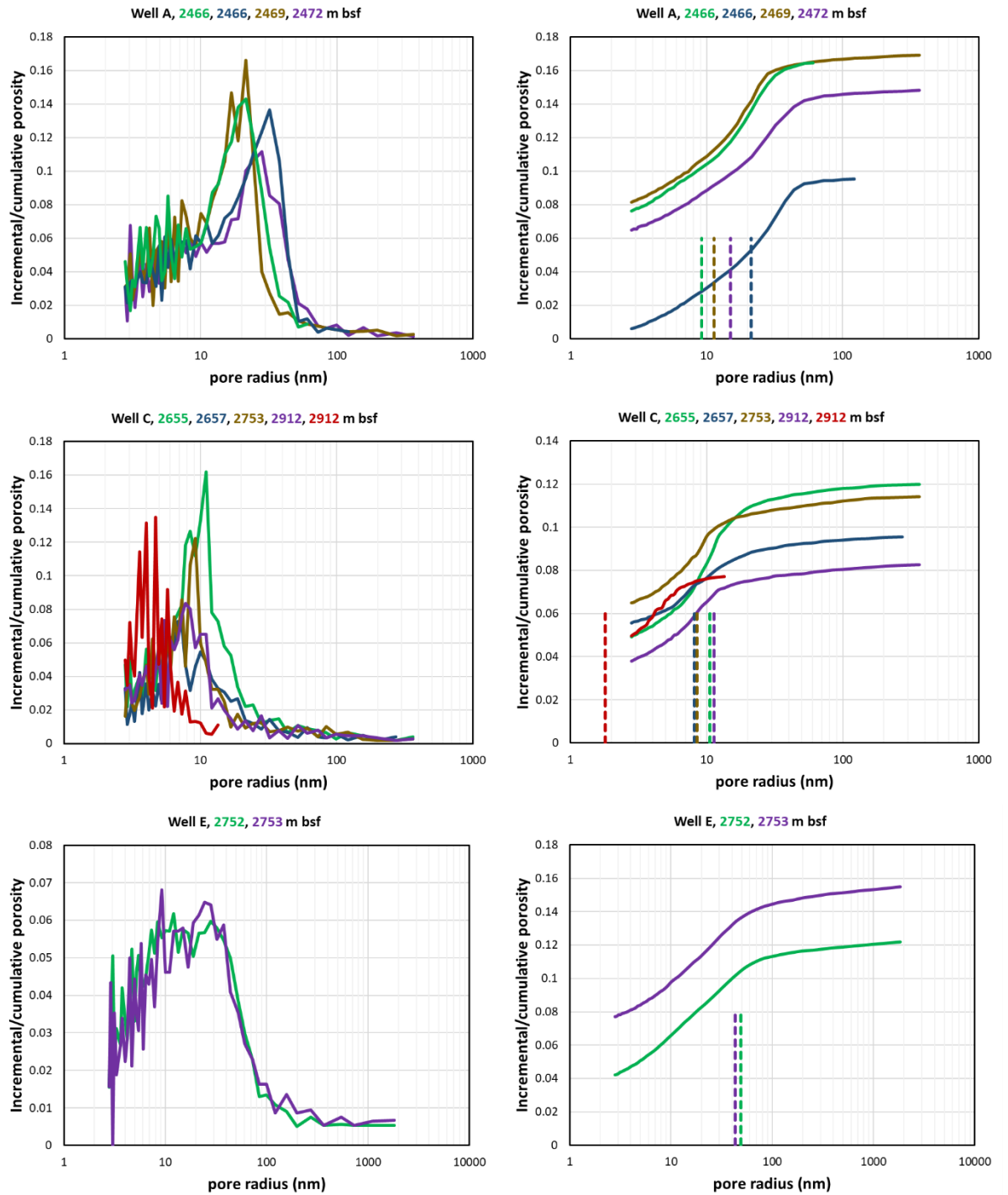


Figure 6.23. Corrected pore throat size distribution (left) and corrected cumulative porosity (right) (from MICP) of selected mudstone samples. Dashed lines on right figures denote mean pore throat radius.

6.7 Discussion

6.7.1 Sediment provenance and paleoweathering reconstruction from major and trace element geochemistry

Figure 6.24 shows major and trace elemental distributions of the Sergipe Alagoas Basin mudstone samples normalized to post-Archaean Australian Shale (PAAS; from Taylor and McLennan 1985) and to average upper continental crust (UCC; from McLennan 2001).

In comparison to PAAS the Sergipe mudstone samples appear to be slightly depleted in Ti, Al, Mn, K and P. Depletion of Ti, Al and K indicate lesser amount of clay minerals, mica and K-feldspar in these mudstones compared to PAAS. Phosphorus depletion is the result of lesser amount of accessory phases such as apatite compared to PAAS. Ca shows considerable variability among the studied mudstone samples due to the variable carbonate content. Variability in K content is related to the variable illite/mica and K-feldspar content of the samples.

The plot of major elements normalized to UCC values indicate depletion of Mn, Mg, Ca, Na, K and P. Iron show slight enrichment compared to UCC. Depletion of Ca and Na in the mudstone samples compared to UCC is clearly the result of chemical weathering of the source material during erosion, transport and deposition of these sediments (Nesbitt et al., 1980; Nesbitt and Young, 1982; McLennan et al., 1993a). Slight depletion of Mg and K compared to UCC can be attributed to lesser amounts of dolomite, chlorite, detrital mica and K-feldspar. Slight enrichment of iron can be attributed to the presence of pyrite and siderite. Variability of Ca among the studied mudstone samples is due to the variable carbonate content.

Trace elemental composition of the samples is fairly similar to both PAAS and UCC with the exception of minor enrichment of Cr. Compared to UCC mudstone samples show slight depletion of Sr and Ba and slight enrichments of Th and Nb. Slight depletion of Sr and Ba can be attributed to weathering since strontium and Ba along with Ca and Na tend to be leached during chemical weathering (Nesbitt et al., 1980). Enrichments of Th and Nb can likely be attributed to the high total clay mineral content of the mudstone samples

along with the presence of anatase in them. Cr enrichment can be likely attributed to the amphibole content of the mudstone samples.

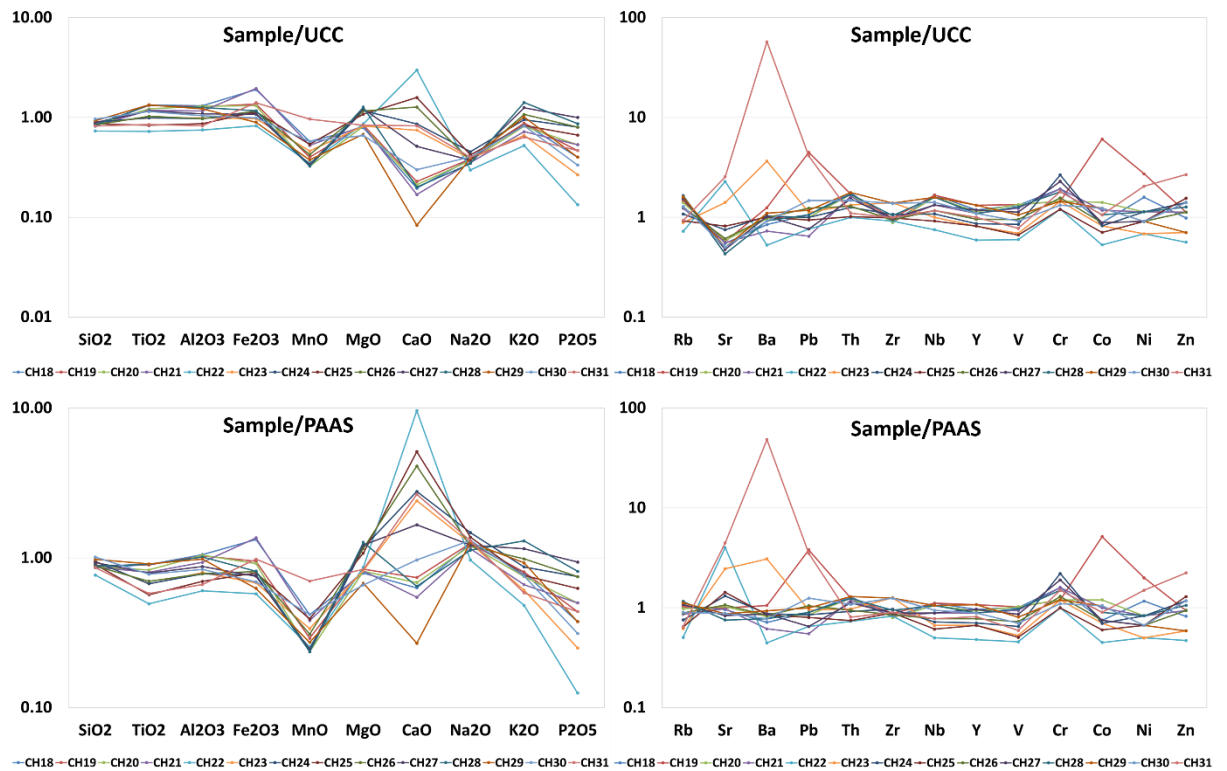


Figure 6.24. Multi element spider diagrams for Sergipe Alagoas Basin mudstones. Major and trace element composition normalised to post-Archean Australian average shale (PAAS; values of Taylor and McLennan 1985) and to average upper continental crust (UCC; values from McLennan 2001).

Significant enrichment in Ba, Pb and Zn and compared to both PAAS and UCC in the sole cutting sample (CH31) is clearly the result of contamination by drilling mud. Barium can be attributed to barite. However, in addition to barite other weighting additives such as galena are also commonly used. Zinc can be attributed to drilling fluid components such as zinc bromide (ZnBr_2).

Uniform $\text{TiO}_2/\text{Al}_2\text{O}_3$ ratios of the Sergipe mudstone samples indicate a source area of similar bulk composition throughout their deposition. This is also supported by the relatively little variation in the ratios of low-solubility trace elements (such as Th, Hf, REEs etc.) which are generally considered inert during the sediment cycle (Taylor and McLennan, 1985). Variability of $\text{K}_2\text{O}/\text{Al}_2\text{O}_3$ can be attributed to the variable illite/mica and K-feldspar content of the samples.

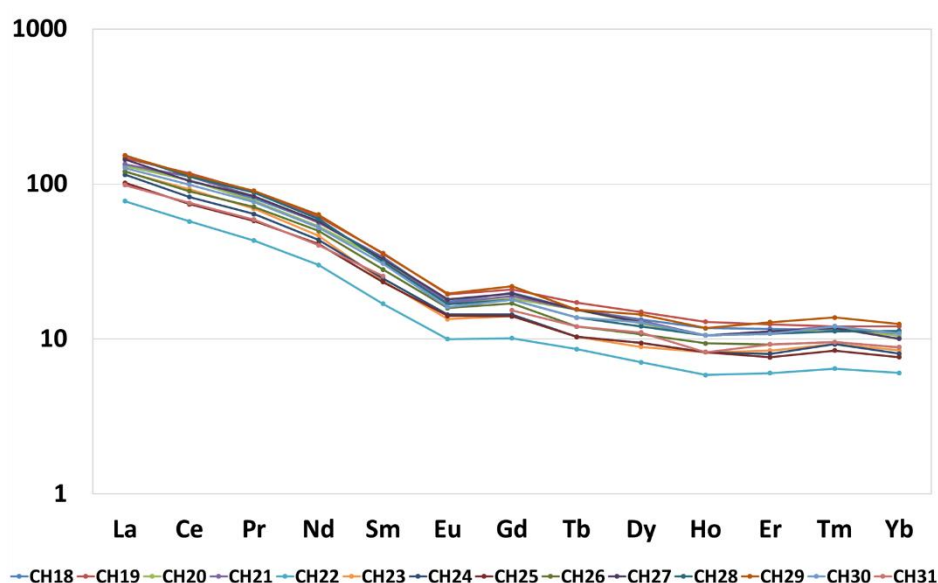


Figure 6.25. Chondrite-normalised (values of Taylor and McLennan, 1985) REE patterns for Sergipe Alagoas Basin mudstones.

Figure 6.25 shows chondrite-normalised REE patterns of the Sergipe mudstone samples. REE patterns display LREE enrichments and variable degrees of development of a negative Eu anomaly. The chondrite normalised ratio of Eu/Eu^* of the mudstone samples range from 0.65 to 0.76 (average of 0.69). These values are close to that of PAAS (0.66). Since europium is not fractionated during weathering or diagenesis relative to other REE (McLennan, 1989) the size of the Eu anomaly reflects the Eu anomaly in the source rocks. The chondrite normalised La_N/Yb_N ratios vary from 11.09 to 14.33 (average of 12.89). Once again, these values are close to but somewhat higher than that of PAAS (9.2). In overall, patterns like LREE enrichment, flat HREE and negative Eu anomaly indicate that these mudstones were derived from a dominantly felsic continental source region (Bhatia, 1985; McLennan et al., 1993a).

Similarly ratios of La/Th (average of 2.99), Th/Sc (average of 1.10) and relatively large Hf contents (average of 4.76) of the mudstone samples indicate derivation from a continental crust of largely granitic or granodioritic composition (Bhatia and Taylor, 1981; McLennan et al., 1993a) (Figure 143).

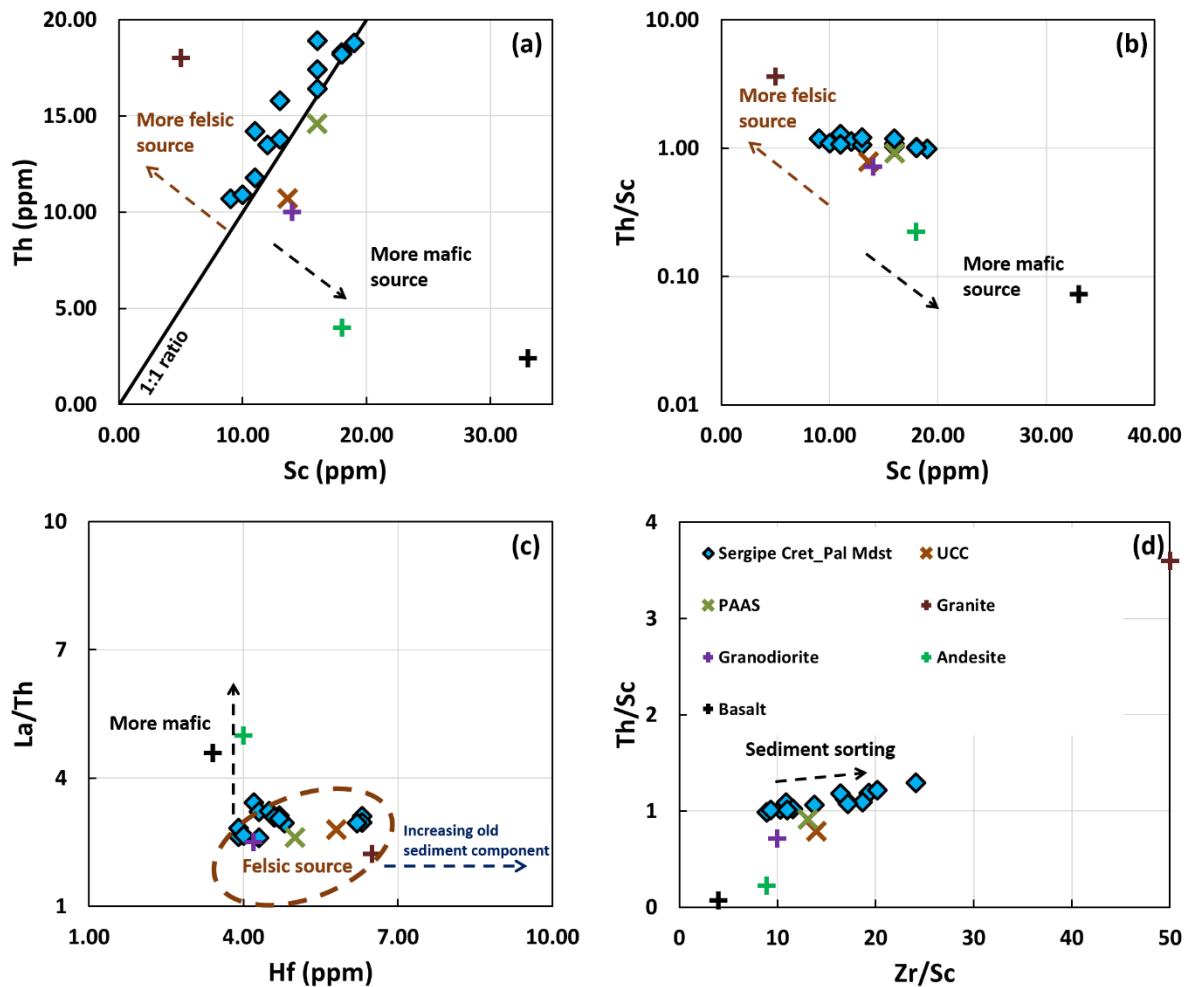


Figure 6.26. Selected trace element plots indicating the average composition of the source. (a) Th versus Sc (b) Th/Sc versus Sc (c) discrimination plot of La/Th versus Hf (after Floyd and Leveridge, 1987) (d) discrimination plot of Th/Sc versus Zr/Sc (after McLennan et al., 1993) monitoring sediment sorting and recycling processes. UCC, PAAS (values from Taylor and McLennan, 1985 and McLennan, 2001) and average Phanerozoic granite, granodiorite, andesite and basalt (values from Condie, 1993) are additionally plotted for reference.

Figure 6.26a,b show the ratios of Th/Sc in the Sergipe mudstone samples. The Th/Sc ratio of the samples is a sensitive index of average source composition (Taylor and McLennan, 1985). Rocks with mafic compositions tend to have considerably higher Sc than do rocks with felsic or intermediate compositions. This is illustrated in Figure 6.26 by showing the Th/Sc ratios for average Phanerozoic granite, granodiorite, andesite and basalt (values taken from Condie, 1993) and also for average upper continental crust (UCC, values from McLennan, 2001) and for post-Archean Australian average shale (PAAS, values from

Taylor and McLennan, 1985). The average Th/Sc ratio in the Sergipe mudstones (1.10) is close to that of PAAS (0.91) and higher than that of UCC (0.78) and that of granodiorite (0.71). Figure 6.26c shows a plot of La/Th against Hf which also provides a useful discrimination between different source compositions. As shown in the figure, sediments derived from a dominantly felsic source region have relatively low and uniform La/Th ratios and Hf contents in the range of approximately 3-7 ppm. Erosion of ancient metasedimentary rocks will result in an increase in the Hf content due to the release of zircon which is the main host mineral phase for this element (Floyd and Leveridge, 1987). Figure 6.26d shows a plot of Th/Sc versus Zr/Sc which can be used to monitor sediment recycling and sorting processes (McLennan et al., 1993a). In overall, the relatively low Zr/Sc ratio of the samples indicates no or only minor sediment recycling. Strong positive correlation between Zr/Sc and Si/Al ratio indicates that the zircon enrichment in samples with relatively higher Zr/Sc ratio is due to more abundant coarse-grained material (sediment sorting).

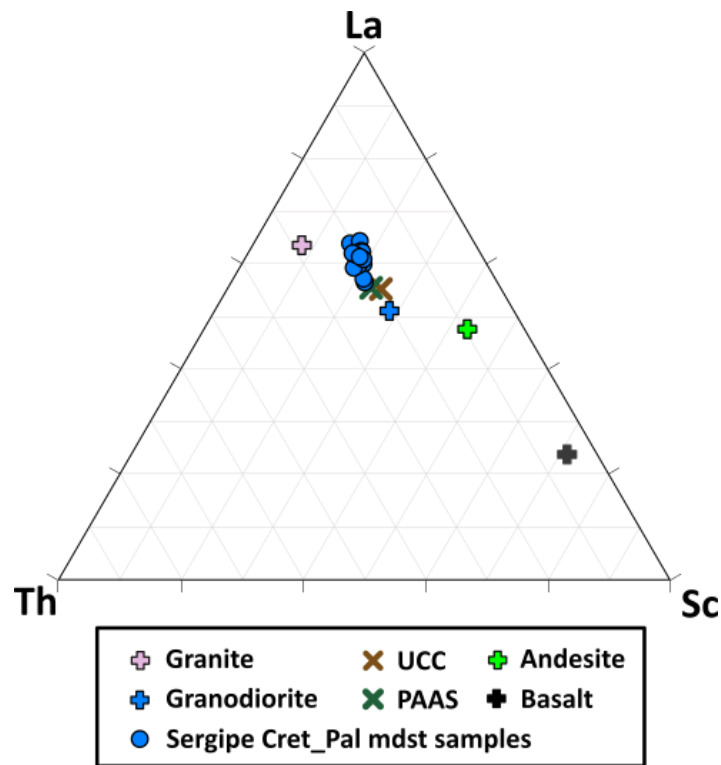


Figure 6.27. Discrimination plot of La-Th-Sc (after Bhatia and Crook, 1986) indicating the average bulk composition of the source. UCC, PAAS (values from Taylor and McLennan, 1985 and McLennan, 2001) and average Phanerozoic granite, granodiorite, andesite and basalt (values from Condie, 1993) are additionally plotted for reference.

On the discrimination plot of La-Th-Sc the samples plot close to the composition of the post-Archean Australian average shale (PAAS) (Figure 6.27).

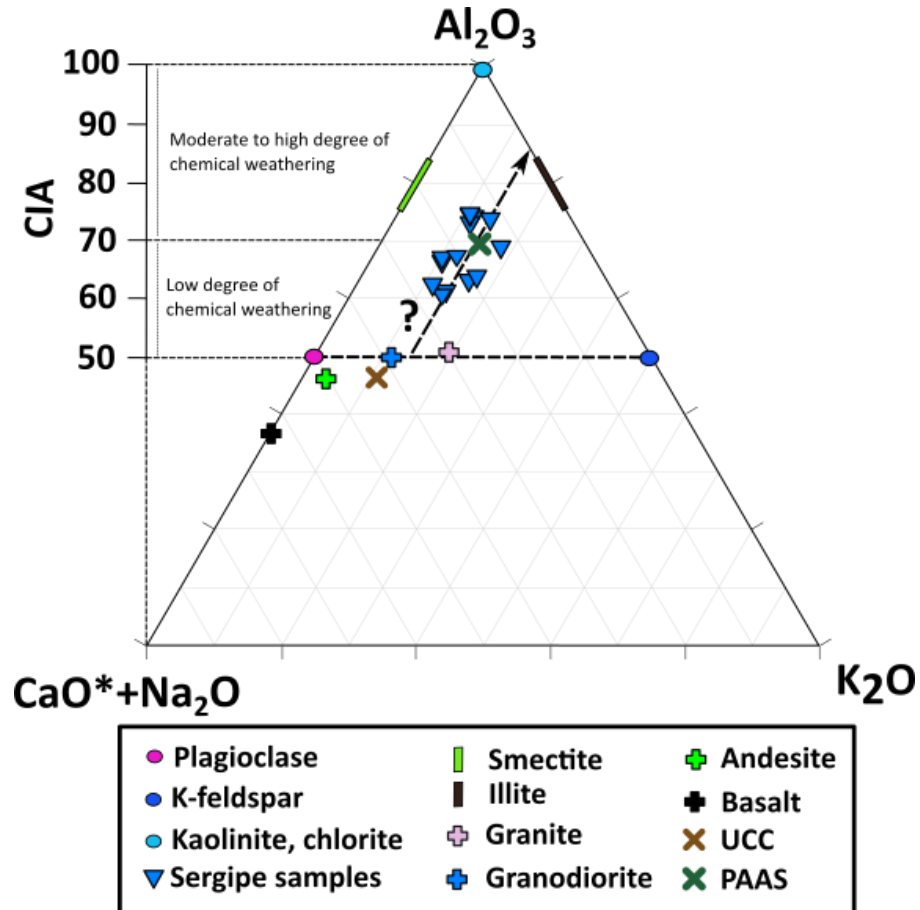


Figure 6.28. A-CN-K ($A = \text{Al}_2\text{O}_3$; $CN = \text{CaO}^* + \text{Na}_2\text{O}$; $K = \text{K}_2\text{O}$; all in molecular proportions; refer to 3.3.5 for more detail) ternary diagram of the Sergipe Alagoas Basin mudstone sample set with associated chemical index of alteration (CIA) values (after Nesbitt and Young, 1982). Dashed arrow represents the estimated weathering trend. Average compositions of granite, granodiorite, andesite and basalt (values from Condie, 1993), post-Archean Australian average shale (PAAS, Taylor and McLennan, 1985), average upper continental crust (UCC, McLennan, 2001) and average composition of illites and smectites are additionally plotted for reference. Refer to text for further explanation.

The degree of source area weathering was quantified using the chemical index of alteration (CIA) following the method of Nesbitt and Young (1982) as described in 3.3.5. CIA values for Sergipe mudstone samples indicate low to moderate degree of chemical weathering (Figure 6.28). The mudstone samples display considerable scatter when

Figure 6.29 shows a crossplot of chemical index of alteration (CIA) against index of compositional variability (ICV). ICV values of the samples show considerable variability which can be explained by the variable carbonate and detrital feldspar content of the mudstones and associated variability of CaO, MnO, Fe₂O₃ and Na₂O (refer to 3.3.5).

In overall, inferences from major and trace element geochemistry are in accordance with the geological setting and tectonic history of the Sergipe Sub Basin. The exact provenance region of the studied mudstones is not known. However, the most likely provenance area of these mudstones is the Sergipano Fold Belt in Northeast Brazil which consists of Precambrian granites and metamorphic rocks including granulites and amphibolites (Davison and Dos Santos, 1989).

6.7.2 Mudstone mineralogy

The primary sediment composition and the early diagenetic reactions determine subsequent diagenetic pathways. Early diagenetic processes are contemporaneous with deposition and can locally affect the physical properties by cementing depositional porosity and make the mudstone locally resistant to mechanical compaction. These early diagenetic processes are typically redox processes where organic matter becomes oxidised by microbes (Aplin and Macquaker, 2011).

No petrographic observations have been made on the samples. However, the combination of mineralogy results presented in 6.6.1 and 6.6.2 and bulk inorganic geochemistry results presented in 6.6.4 indicate the presence of authigenic pyrite, siderite, kaolinite and chlorite.

Pyrite likely precipitated from iron-rich porewaters near sites of sulphide supply, usually near organic matter as a result of bacterial sulphate reduction, where sulphide production rates were high enough to reach supersaturation with respect to FeS (Taylor and Macquaker, 2000). The presence of siderite indicates that Fe(III) reduction was also important (at least locally) during early diagenesis. Kaolinite is likely early diagenetic and can be interpreted as the result of Al-mobilization by organic acids generated during organic matter oxidation reactions or as the result of detrital feldspar or mica leaching. The likely sources of Al were poorly crystalline detrital aluminium oxides and clay

minerals (Foscolos, 1984; Taylor and Macquaker, 2014). Authigenic chlorite likely formed from kaolinite and likely also from smectite in the presence of Fe and Mg during late diagenesis (Bjørlykke, 1998).

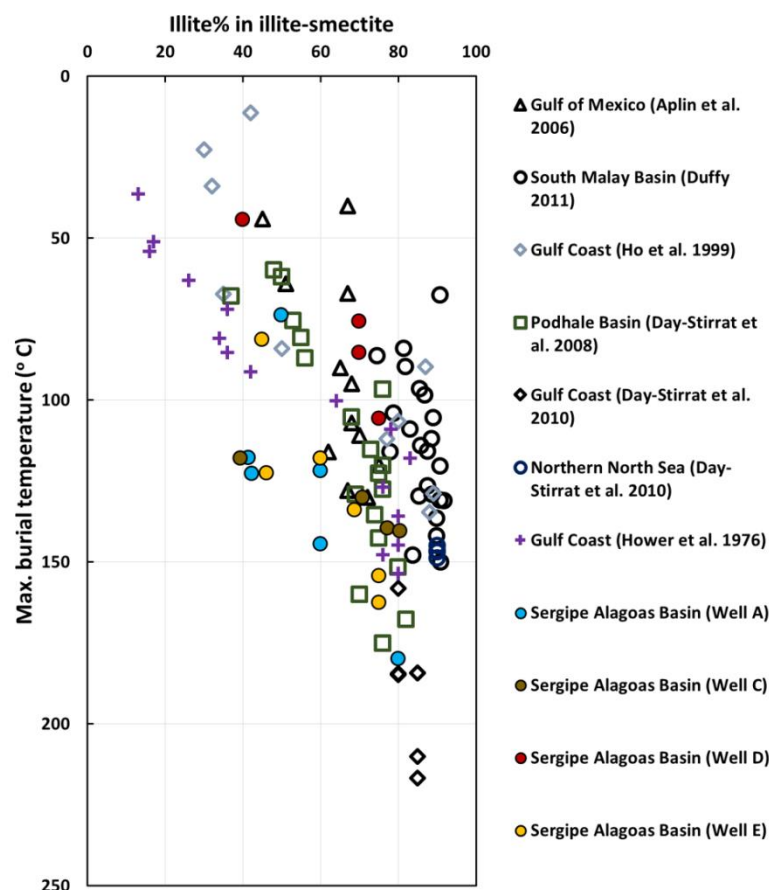


Figure 6.30. Published examples of illite % in illite-smectite with new results from the studied mudstones of the Sergipe Alagoas Basin, offshore Brazil plotted against maximum burial temperature. Illite % in illite-smectite was calculated using the combination of the bulk QXRD, $<2 \mu\text{m}$ and $<0.2 \mu\text{m}$ fraction modelling results.

Based on the QXRD and CEC results, there is evidence for ongoing illitization of smectite in all four wells from which mudstone samples were studied in this thesis. Figure 6.30 shows % illite in mixed-layer illite-smectite trends from several published examples and new results from the Sergipe Alagoas Basin, offshore Brazil plotted against burial temperature. Illitization trend in Well D fits in with other studies. However, in Wells A, C and E illitization is still ongoing above 100°C . The illitization trends in these shallower shelf wells (A, C and E) appear to be anomalous considering the slow burial rate and the estimated geothermal gradient for the shelf region (Figure 6.30). It is not likely that the

estimated geothermal gradient for the shelf wells would be significantly overestimated since measured temperatures generally underestimate true formation temperatures (Hermanrud et al., 1990). Conversely, the considerably different illitization trend in the deep water Well D cannot be due to uplift since based on the information provided by Petrobras the studied mudstones are at their maximum burial depth in all four wells. One possible explanation for the anomalous (“delayed”) illitization trend found in the shelf wells might be the presence of volcanic material. This would result in the formation of smectite and smectitic illite-smectite from volcanic glass simultaneously with the illitization of detrital smectite, as suggested for several other settings (e.g. Aplin et al., 2006). The authigenic (<0.2 µm) clay fraction modelling results indicate that an ordered (R1) authigenic illite-smectite phase population does coexist with the dominant smectitic (R0) illite-smectite population below ~2500 m in the shelf wells which support this hypothesis (Figure 6.16). However, this hypothesis is not supported by independent geological evidence based on the information provided by Petrobras. There is no evidence for nearby volcanic edifices and for considerable amount of volcanic material within these clastic sections. In addition to this, the geochemical results presented in 6.7.1 do not show clear evidence for an added volcanic component within these mudstones.

It should be noted that QXRD results presented in 6.6.1 indicate more abundant coarse-grained material below 1500 m in Well D and below 2500 m in the Well C. In addition to this, the top of the Cretaceous interval in these wells is at the depth where clay mineralogy changes from a dominantly smectitic to illitic (R0 to R1) illite-smectite. No such correlations exist in Wells A and E however, the possibility that the sharp change in mineralogy reflects a combination of marked change in the original depositional mineralogy and grain size in addition to diagenesis cannot be excluded.

In overall these observations are fairly similar to that presented from the Callovo-Oxfordian in the Paris Basin (Claret et al., 2004), from the Oligocene Frio Formation, offshore Gulf of Mexico (McCarty et al., 2008) and from Cretaceous to Eocene sediments in the Texas Gulf Coast (Lanson et al., 2009). However further research will be needed to decipher the origin of the illitization trends in the Sergipe Alagoas Basin.

6.7.3 Evaluation with wireline log-based compaction profiles and implication for overpressure development

Figure 6.31 shows smoothed cosine-weighted density and sonic log responses through the studied mudstone intervals for all four wells. Density increases, and sonic transit time decreases substantially with increasing depth through the studied intervals in all four wells implying ongoing compaction. Note that there is a marked increase in density and marked decrease in sonic transit time between 1500-2000 m in Well D and between 2500-3000 m in wells A, C and E (Figure 148). Small fluctuations in the smoothed data are the result of changing lithology, most likely related to variations in carbonate, grain size and/or clay mineral content. Missing sections of the smoothed density logs (within mudstones) represent log data samples that were rejected because density values lied outside of the chosen threshold limit (see 3.4). Large amounts of log data samples were rejected for wells A, C and E due to poor (rugose) borehole conditions. Rugose borehole conditions can likely be attributed to use of water-based drilling muds (Julio Garcia Carvalho, pers. comm.).

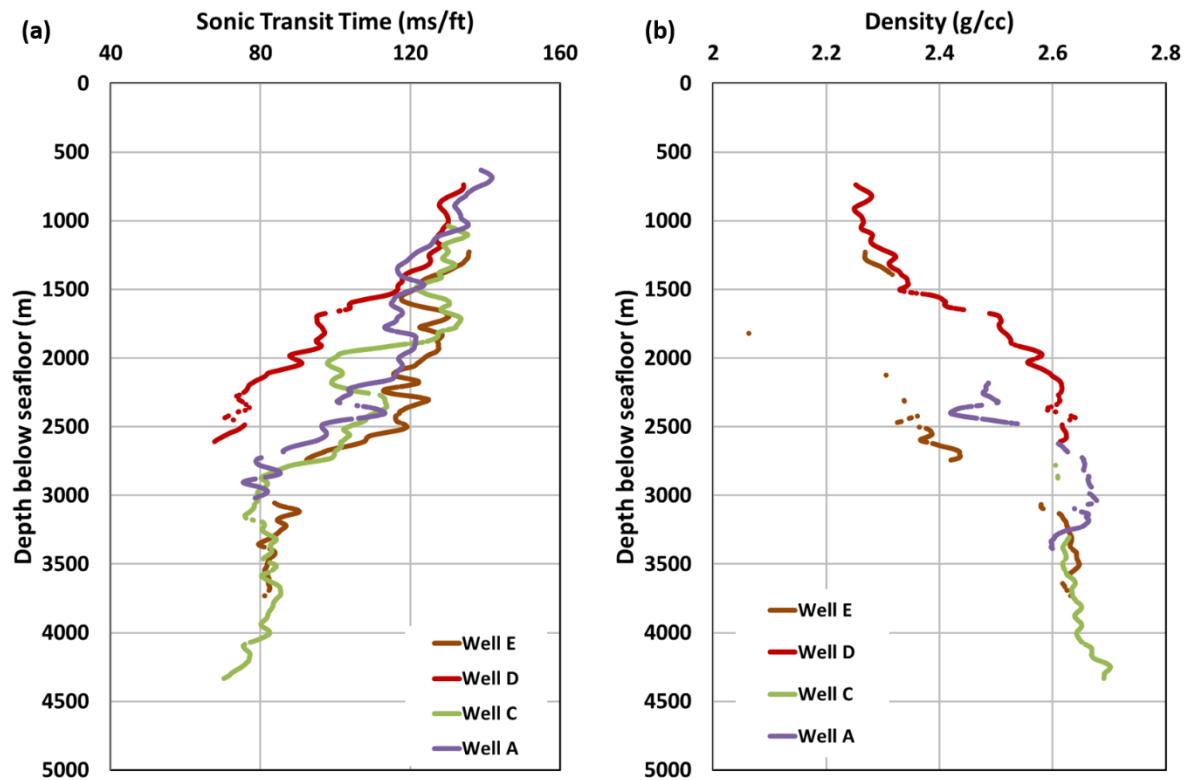


Figure 6.31. Smoothed (a) sonic and (b) density logs through the mudstone intervals for Wells A, C, D and E.

Figure 6.32 shows crossplot of smoothed sonic transit time against smoothed density in the studied mudstone intervals for Well D. Dutta's (2002) reference lines for smectite rich and illite rich mudstones are also shown. The sonic-density crossplot is only shown for Well D because this well had the best quality log data. Large amounts of density log data were rejected in wells A, C and E due to poor borehole conditions.

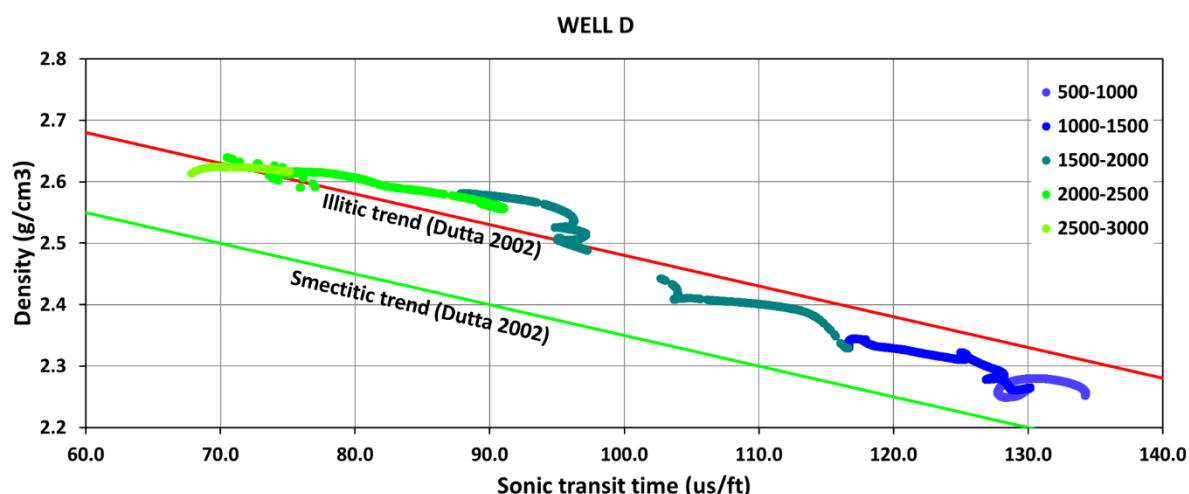


Figure 6.32. Sonic-density crossplot for Well D. Colour coding is by depth relative to seafloor. Red and green line is the illitic and smectitic line from Dutta (2002).

From a depth of around 500 m below seafloor the crossplot trend parallels Dutta's (2002) trend for smectitic mudstones. However, the sonic-density path in Well D is slightly above the smectitic line. This relatively high density may be due to the slow sedimentation rates and high carbonate content. Slow sedimentation rates and associated hydrostatic pore pressures might have resulted in more effective compaction (and higher density) in the Sergipe Alagoas Basin compared to the compaction of highly overpressured Gulf of Mexico mudstones.

At a depth of about 1500 m below seafloor the crossplot trend abruptly turns upwards (Figure 6.32). Since pore pressure measurements in Well D indicate hydrostatic conditions throughout the whole studied interval (Figure 6.5) the upward step in density from $\sim 2.40 \text{ g/cm}^3$ to $\sim 2.56 \text{ g/cm}^3$ seen on the crossplot is attributed to lithological change, most likely to the change in clay mineralogy from a disordered, (R0) smectitic illite-smectite to an ordered, (R1) illitic illite-smectite occurring at this depth. There are considerable lateral fluctuations on the crossplot trend which can be attributed to variations in carbonate and in clay mineral content.

In passive margin settings such as the Sergipe-Alagoas Basin, the most commonly encountered mechanism of overpressure generation is disequilibrium compaction with contributions from gas generation, load transfer and lateral transfer (Swarbrick et al., 2002). However, in the Sergipe Sub-basin at the Camorim oil field, Cretaceous sediments

post-dating the Aptian hinge line event (see 6.2) were deposited at an average rate of ~ 35 m/Ma, and since the end of the Cretaceous period deposition took place at the very slow rate of ~ 8 m/Ma (De Souza et al., 1995). As shown in Figure 6.33 sedimentation rates in the four studied wells were somewhat higher than in the Camorim oil field. However, these values of sedimentation rates are still considered to be too low to account for significant amounts of overpressure in these wells. In addition to this there is no evidence for disequilibrium compaction based on the wireline log responses (Figure 6.31).

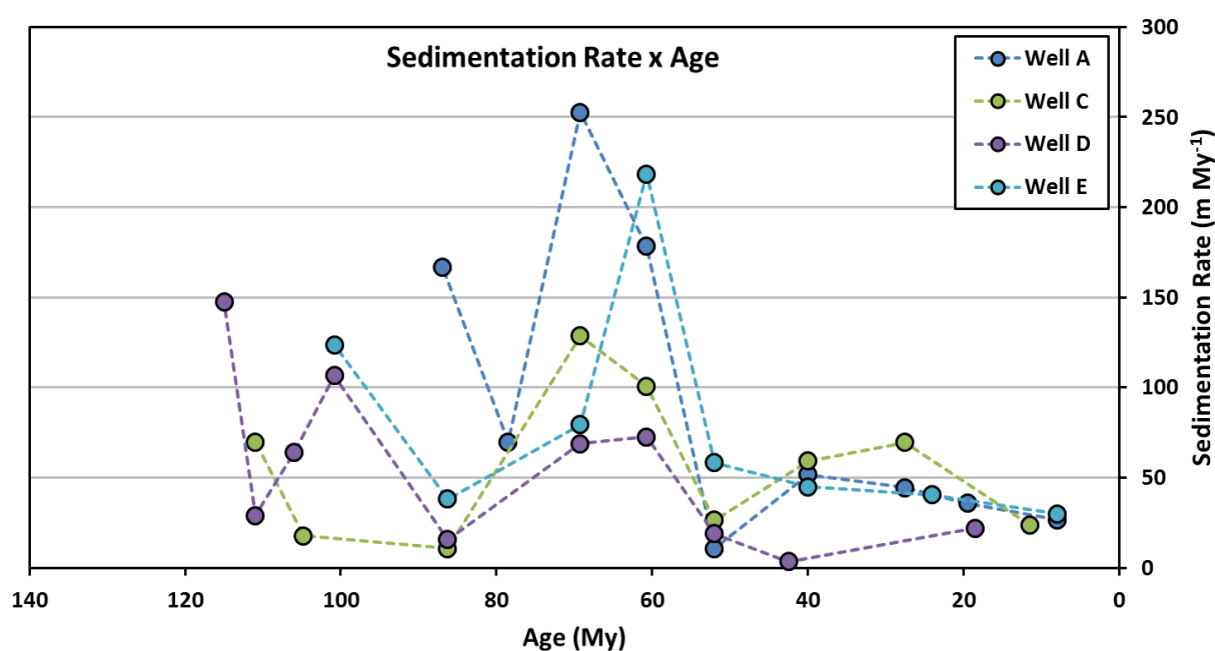


Figure 6.33. Sedimentation rate vs age in the four studied wells based on 1D basin modelling (courtesy of Petrobras).

Clay diagenesis and load transfer are not viable pressure generating mechanisms in the studied mudstones based on the observation that illitization of smectite is ongoing in the two hydrostatically pressured wells (Well D and C). Since there are no source rocks in the studied Cretaceous-Palaeogene interval and the total organic carbon contents of these mudstones are low ($< 1\%$ TOC), gas generation is unlikely to be a significant internal source of overpressure. In addition to this there is no evidence for unloading based on the wireline log responses. Note that other than small variations due to differences in mudstone lithology, the sonic log response of the mudstones in the hydrostatic and overpressured wells are not noticeably different (Figure 6.31).

In overall, these observations indicate that the measured overpressures in the sandstones in wells A and E may have arisen by lateral or vertical transfer of overpressure may be caused by gas generation, or oil cracking to gas, in the Aptian source rocks (Mello et al., 1994), enhanced by recent burial. The studied sequence in these four wells may have been hydrostatically pressured until recently, allowing the mudstones to compact; consequently, the sandstones are overpressured, but the mudstones are not. In addition to this, listric faults in the Sergipe Sub-basin may act as partial or complete seals to lateral fluid flow (Cainelli, 1992).

6.7.4 Implications for mudstone compaction processes

Figure 6.34 shows the variation of smectite equivalent (%) in illite-smectite with increasing depth in the studied mudstone samples in comparison with the variation of mudstone porosity with increasing depth. As can be seen the depth range over which clay mineralogy changes from a dominantly smectitic to illitic (R0 to R1) illite-smectite is also the depth range over which a marked reduction of porosity occurs in all four wells. This observation is consistent with Lahann's (2002) original point that illitization reduces the equilibrium porosity associated with a given effective stress (makes the mudstone more compactable) (see 2.6).

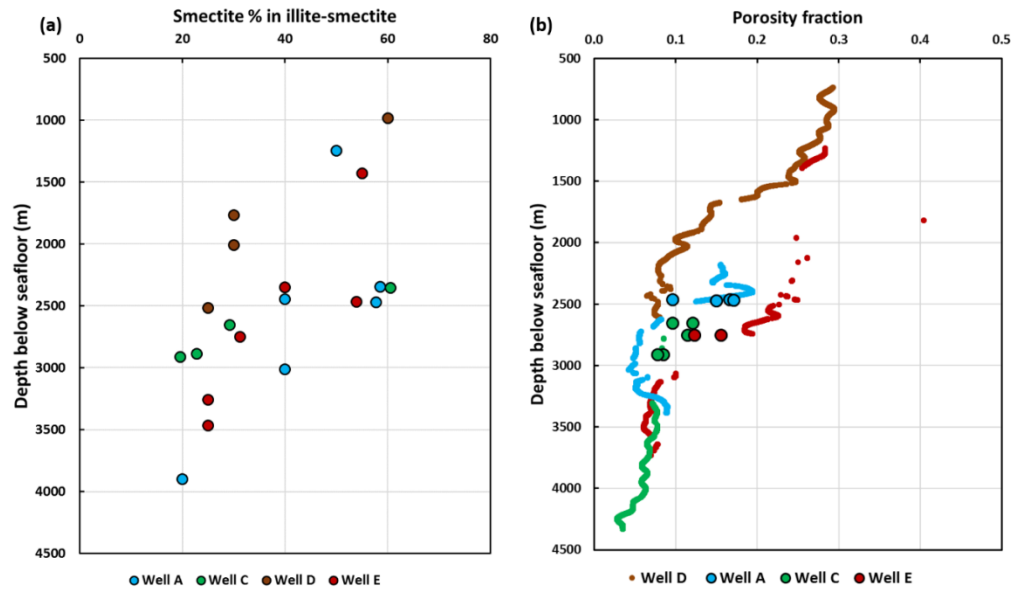


Figure 6.34. (a) Variation of smectite equivalent (%) in illite-smectite (calculated using the combination of the bulk QXRD, $<2\ \mu\text{m}$ and $<0.2\ \mu\text{m}$ fraction modelling results) with increasing depth for the studied samples in comparison with (b) the variation of mudstone porosity with depth. Smoothed lines are calculated density porosity (calculated from smoothed logs using $2.75\ \text{g/cm}^3$ for grain density and $1.05\ \text{g/cm}^3$ for fluid density) and coloured dots are corrected total porosity (determined according to 3.3.7).

Figure 6.35 shows the calculated density porosity of the studied Sergipe mudstones in comparison with Mondol et al's. (2007) experimental mechanical compaction curve for 100% kaolinite and with Yang and Aplin's (2004) compaction curve for mudstone with 50% clay content. The experimental compaction curve of pure kaolinite was selected since it represents the lowest porosities achieved by experimental mechanical compaction of clays and silt-clay mixtures. Pure illite or mixtures of silt and clays would be a closer representation of the Bravo-Y mudstone mineralogy however these all have considerably higher porosities than pure kaolinite (Mondol et al., 2007; Mondol, 2009a). Yang and Aplin's (2004) relationship between porosity and effective stress was chosen to represent real life mechanical compaction since it was derived from natural mudstone porosity data and it is based on solid soil mechanical principles. Total clay mineral content as estimated by QXRD was used as a proxy for the mass fraction of particles less than two microns and the average clay mineral content in the studied samples was chosen to represent the whole working interval. Note that porosities in the studied mudstones are

lower and porosity is lost considerably faster below the depths of the onset of smectite to illite transformation. This depth is considerably shallower in Well D ~ 1500 m than in the shelf wells in which this depth is ~ 2500 m (Figure 6.35).

In overall, these observations indicate that the illitization reaction is accompanied by considerable porosity loss and volume reduction. These findings are entirely consistent with previous studies which reported considerable density increases coincident with smectite illitization (Lahann et al., 2001; Dutta, 2002, 2016; Lahann and Swarbrick, 2011) and support the chemically-enhanced mechanical compaction model as described in 2.6.

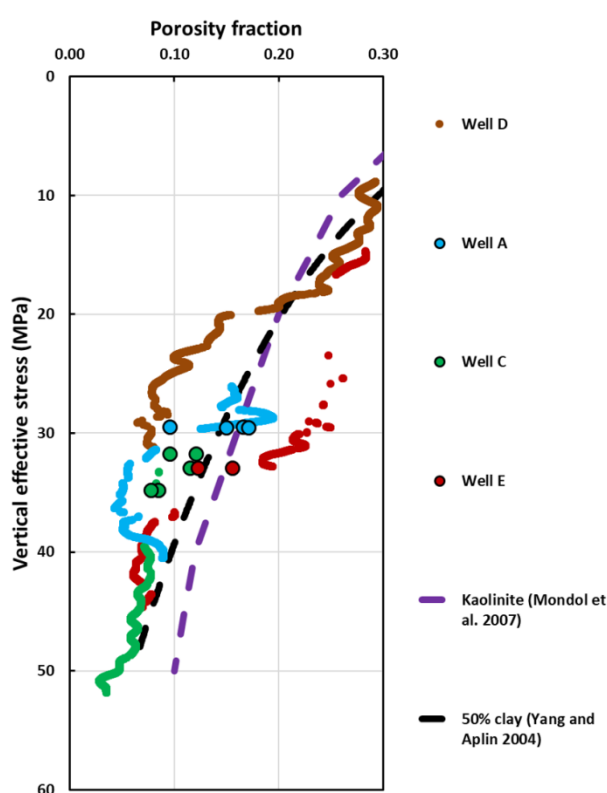


Figure 6.35. Calculated density porosity (calculated from smoothed logs using 2.75 g/cm^3 for grain density and 1.05 g/cm^3 for fluid density) for Sergipe-Alagoas Basin mudstones plotted against calculated hydrostatic vertical effective stress. Coloured dots are corrected total porosity (determined according to 3.3.7). Dashed purple and black trends – experimentally compacted kaolinite (from Mondol et al. 2007) and mechanically compacted mudstone with 50% clay content (from Yang and Aplin 2004).

6.8 Summary and conclusions

Previous studies have demonstrated that chemical diagenetic changes can cause further porosity loss in addition to the mechanical compaction processes (e.g. Bjørlykke 1998). According to Lahann (2002) illitization reduces the equilibrium porosity associated with a given effective stress hence it makes the mudstone more compactable. In contrast according to the compaction model of Bjørlykke and Høeg (1997) the main porosity reducing process during chemical compaction is cementation by authigenic minerals like quartz or illite (refer to 2.6). According to this model in diagenetically altered mudstones above $\sim 100^{\circ}\text{C}$ mechanical compaction does not take place since mudstones have become stronger through diagenesis (e.g. Draege et al., 2006; Thyberg et al., 2009). Note that this model would predict significant velocity increase (due to cementation of the connecting pores; refer to 2.7) and no or negligible density increase/porosity decrease during chemical compaction (Thyberg et al., 2010; Thyberg and Jahren, 2011). This is because mineralogical changes in a chemically closed system on their own (without any pressure/stress effect) would not result in net volume change.

Evidence presented here clearly shows that considerable amount of porosity is lost coincident with clay mineral diagenesis in Cretaceous-Palaeogene mudstones in the Sergipe-Alagoas Basin, offshore Brazil. The rate of porosity reduction in these (hydrostatically pressured) mudstones is considerably greater than what was observed in the highly overpressured Cretaceous mudstones at the Haltenbanken. Based on the available porosity measurements and density log data Cretaceous mudstones at the Haltenbanken loose $\sim 10\%$ porosity between 2500 – 4000 m below seafloor in contrast to the Cretaceous-Palaeogene mudstones in the Sergipe-Alagoas Basin, offshore Brazil which loose $\sim 15\%$ porosity between 2500 – 3000 m in the shelf wells and between 1500 – 2000 m in the deep water Well D. This observation is entirely consistent with Lahann's (2002) original proposal that illitization reduces the equilibrium porosity associated with a given effective stress.

These results are further evidence that tends to support the chemically-enhanced mechanical compaction model.

Chapter 7

Diagenesis and compaction of Triassic mudstones in the HPHT fields of the North Sea Central Graben

7.1 Introduction

Several previous studies reported on the lack of relationship between overpressure and (log based) porosity in deeply buried mudstones in the North Sea and at the Halten Terrace, offshore mid-Norway (Hermanrud et al., 1998; Teige et al., 1999). Hermanrud et al. (1998) showed that bulk density and neutron log responses of deeply buried intra-reservoir Jurassic shales on the Halten Terrace, offshore mid-Norway are not noticeably different in hydrostatically pressured and highly overpressured compartments. This lack of relationship led these authors conclude that porosity reduction in these mudstones proceeded independently of the effective stress and hence independently of overpressuring.

To further test these assumptions and to test the effect of high overpressures on the compaction properties of clastic mudstones the mudstone members of the Triassic HPHT reservoirs have been selected for study.

The mudstone members of the Triassic Skagerrak Formation in the North Sea Central Graben provide an ideal sample set with which to study the effects of high overpressures on the compaction properties of diagenetically mature siliciclastic mudstones. The Triassic Skagerrak Formation is one of the main reservoirs in the high pressure-high temperature (HPHT) regime in the Central Graben where present day pore pressures can exceed 80 MPa (in the upper part of the formation) and temperatures are above 100°C. The formation contains fluvial sandstones and mudstones representing floodplain, lacustrine and playa facies. Fluvial sandstones maintain anomalously high porosities at burial depth greater than 3200 m bsf from which hydrocarbons are currently being produced. Previous workers have suggested that shallow overpressure development by disequilibrium compaction played a key role in preserving such high porosities by arresting mechanical compaction (Nguyen et al., 2013; Stricker and Jones, 2016; Stricker et al., 2016). These findings provided the basis for further investigation.

Mudstone samples were provided by ConocoPhillips and the British Geological Survey (BGS) from six wells (22/29-1, 30/2c-04, 30/2c-J07, 30/7a-7, 30/7a-8, 6/3-1). Mineralogical and textural properties of the samples were analysed and compared with physical properties such as porosity measured on the samples. The key aim was to

investigate the effect of HPHT conditions on mudstone compaction and to test whether anomalously high porosities have been preserved in the mudstone members of the Skagerrak Formation.

This chapter details these results following a brief description of the geological background of the study area.

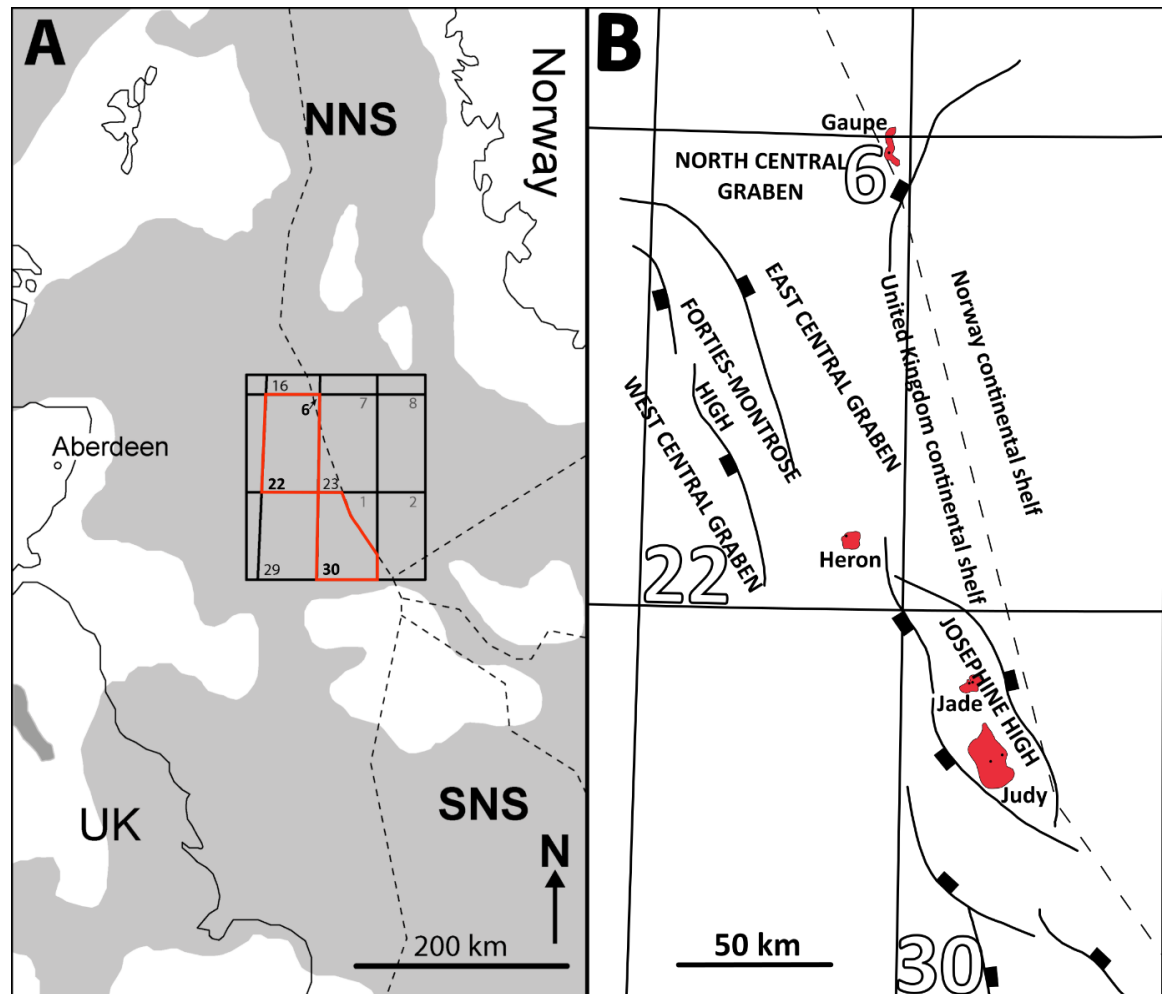


Figure 7.1. (A) Location map of the Central North Sea showing quad 30,22 and the Norwegian block 6 (red outline); grey colouring shows the distribution of the Triassic sediments. (B) Map of the Central Graben with major structures showing Triassic fields and well locations in UK quadrants 22 and 30 and Norwegian quadrant 6 (modified after Stricker, 2016).

7.2 Samples and geological setting

The Central Graben is 70 to 130 km wide and approximately 550 km long. It forms the southern arm of a trilete rift system in the North Sea (Figure 7.1). Present day structural configuration of the Central Graben is the combined result of at least two major rift events, one during the Permian-Triassic (290-210 Ma) and the second during the Late Jurassic (155-140 Ma) (e.g. Glennie, 1998).

The structural evolution of the Central North Sea basin is commonly subdivided into three phases: pre-rift, synrift and postrift phases (Clark et al., 1999). During the synrift phase in the Triassic and Jurassic period siliciclastic sediments deposited with a total thickness of 2000 m. Postrift sediments deposited between the Cretaceous and the Holocene period and have a total thickness of as much as 4500 m. These are mainly siliciclastic sediments dominated by mudstones, sandstones and a thick chalk section (Goldsmith et al., 2003) (Figure 7.2).

The Triassic stratigraphic nomenclature for the Central Graben that is used in this thesis was proposed by Goldsmith et al. (1995) and is based on the combination of biostratigraphy and lithostratigraphic methods, including wireline log correlations.

The Triassic Skagerrak Formation in the Central Graben contains fluvial sediments deposited in tectonically active half grabens. The formation was accumulated in a series of fault- and salt-controlled minibasins within the overall rift basin. The underlying Permian Zechstein salt strongly influenced sedimentation by developing salt withdrawal basins caused by structural extension and loading (Smith et al., 1993; Bishop, 1996). Fluvial sedimentation in Middle to Late Triassic times took place in coexisting braided and meandering channels together with playa and lacustrine deposition. The Skagerrak Formation contains three major sand-prone units; the Judy, Joanne and Josephine Sandstone Members. These are intercalated with fine-grained successions of the Julius, Jonathan and Joshua Mudstone Members (Figure 7.2). Sandstones include multistorey stacked channel sand-bodies, sheetflood and crevasse splay deposits and mudstones constitute floodplain, lacustrine and playa facies (Goldsmith et al., 1995, 2003).

Schematic stratigraphy of the wider Central graben area is shown in Figure 7.2.





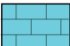


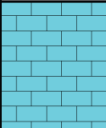











| Tectonics | System | Series | Group | Formation | Member | Lithology | | | |
|-----------|------------|--------------|--------------|-----------------|---|---|---|---|---|
| Postrift | Quaternary | | Nordland | | | |  | Shale | |
| | Neogene | Pliocene | Westray | Lark | | |  | Tuff | |
| | | Miocene | | | | | | | |
| | Paleogene | Oligocene | Stronesay | Horda | | |  | | |
| | | Eocene | | | Balder | |  | | |
| | | Paleocene | Moray | Sele | | Forties |  | Chalk | |
| | | | | Montrose | Lista | | Mey |  | |
| | | | | | Maureen | | |  | |
| | | | Cretaceous | Upper | Chalk | Ekofisk | | |  |
| | Tor | | | | | | | | |
| | Hod | | | | | | | | |
| | Herring | | | | | | | | |
| | Hidra | | | | | | | | |
| | Rodby | | | | | | | | |
| | Lower | Cromer Knoll | | Valhall | | |  | | |
| | | | | | | | | | |
| | Synrift | Jurassic | Upper | Humber | Kimmeridge Clay | |  | | |
| Heather | | | | | Fulmar |  | | | |
| | | | Middle | Fladen | Pentland | |  | | |
| Postrift | Triassic | Upper | Heron | Skagerrak | Jonathan Mdst |  | | | |
| | | | | | Joanne Sst |  | | | |
| | | | | | Julius Mdst |  | | | |
| | | Middle | | Judy Sst |  | | | | |
| Synrift | | Lower | | Smith Bank | |  | | | |
| Postrift | Permian | | Zechstein | Shearwater Salt | |  | | | |
| Synrift | | | Rotliegendes | Auk | | | | | |
| Synrift | Devonian | Upper | Old Red | Buchan | |  | | | |

Figure 7.2. Regional lithostratigraphy of the Central Graben, North Sea (from Stricker and Jones, 2016).

Mudstone samples were investigated from the fine-grained members of the Skagerrak Formation covering UK quadrants 22 and 30 and Norwegian quadrant 6 in the wider Central Graben area (Figure 153). Core samples were available from the mudstone intervals of the cored reservoir sandstone members of the Triassic Skagerrak Formation in wells 30/7a-7 (Judy Sandstone Member) and 30/7a-8 (Joanne Sandstone Member) from the Judy field; in wells 30/2c-4 (Joanne Sandstone Member) and 30/2c-J07 (Jonathan Mudstone Member) from Jade field; in well 22/29-1 (Skagerrak Fm undifferentiated) from

the Heron field; and in well 6/3-1 (Skagerrak Fm undifferentiated) from the Gaupe field (Figure 7.1).

Mudstone samples from the Judy, Jade and Gaupe fields were provided by ConocoPhillips. Samples from the Heron field were provided by the British Geological Survey (BGS) and have been collected from the BGS core store in Keyworth. In total 21 samples were selected for study. The complete list of the studied samples is shown in Table 7.1.

| Well | Sample type | Depth relative to kelly bushing (m) | Temperature (°C) |
|-----------|-------------|-------------------------------------|------------------|
| 6/3-1 | core | 3028.7 | 111 |
| 6/3-1 | core | 3041.5 | 111 |
| 6/3-1 | core | 3043.0 | 112 |
| 6/3-1 | core | 3059.7 | 112 |
| 6/3-1 | core | 3062.0 | 112 |
| 6/3-1 | core | 3092.1 | 113 |
| 22/29-1 | core | 4592.8 | 166 |
| 22/29-1 | core | 4594.3 | 166 |
| 22/29-1 | core | 4599.7 | 166 |
| 22/29-1 | core | 4718.3 | 170 |
| 22/29-1 | core | 4761.5 | 172 |
| 30/2c-04 | core | 4791.4 | 173 |
| 30/2c-04 | core | 4807.6 | 173 |
| 30/2c-J07 | core | 4972.3 | 179 |
| 30/2c-J07 | core | 4973.0 | 179 |
| 30/2c-J07 | core | 4988.2 | 180 |
| 30/2c-J07 | core | 5010.0 | 180 |
| 30/7a-7 | core | 3460.8 | 126 |
| 30/7a-7 | core | 3489.0 | 127 |
| 30/7a-8 | core | 3556.9 | 129 |
| 30/7a-8 | core | 3633.5 | 132 |

Table 7.1. List of Triassic mudstone samples selected for study.

Core samples from well 22/29-1 have been collected from the BGS core store. Sampling covered volumetrically significant fine grained lithologies. Sampling points for dominant fine grained lithologies were selected based on the need to select a range of materials from the discernible heterogeneity; rock types that dominate over significant core intervals; and core material that are homogeneous within the actual sample size so that analyses made on subsamples can be correlated. Care was taken to collect samples from homogeneous and uncemented mudstone-rich intervals.

7.2.1 Overpressure distribution

The Triassic Skagerrak Formation is in the high pressure-high temperature (HPHT) regime in the North Sea Central Graben where pore pressures can exceed 80 MPa at depths of around 4000 to 5000 m below seafloor where temperatures are in the range of 166°C to 200°C (Swarbrick et al., 2000; di Primio and Neumann, 2008). Overpressures are widespread across the Mesozoic reservoirs in the Central Graben due to continuous sedimentation of dominantly fine-grained lithologies since early Cretaceous times (Osborne and Swarbrick, 1999; Swarbrick et al., 2000; Yardley and Swarbrick, 2000).

Figure 7.3 shows measured pore pressures within the Skagerrak Formation from 41 wells in the UK quad 30. As it can be seen, overpressure magnitude varies considerably between different sandstone members and oil fields. Overpressure magnitude can even change within the same reservoir across faults or across mudstone beds (Jones et al., 2005; Nguyen et al., 2013). However, the Triassic reservoirs are overpressured all across the Central Graben area.

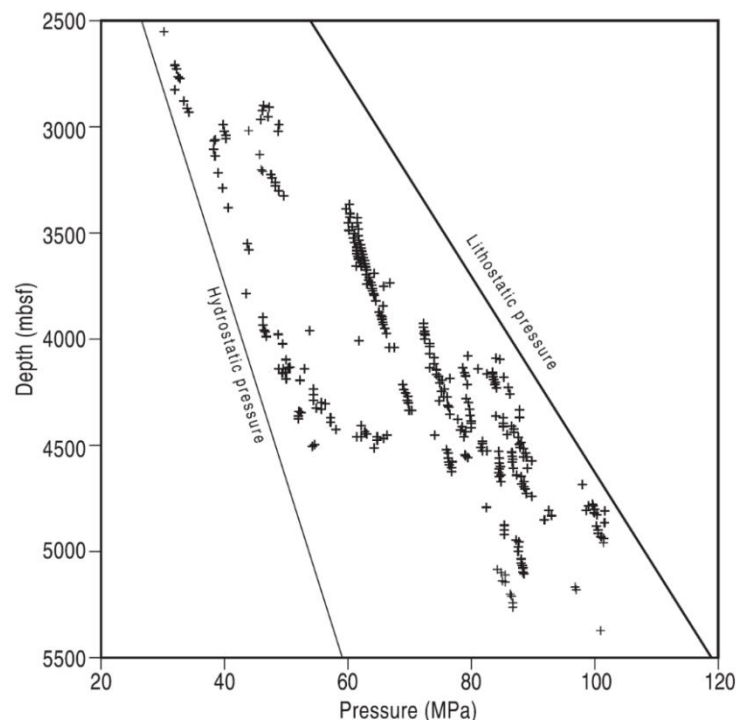


Figure 7.3. Multi well pressure-depth plot for Triassic formations in United Kingdom quad 30. Plotted data displays pressure measurements obtained from modular formation dynamics tester (MDT) and drill stem tests (DST) from 41 wells (from Nguyen et al., 2013).

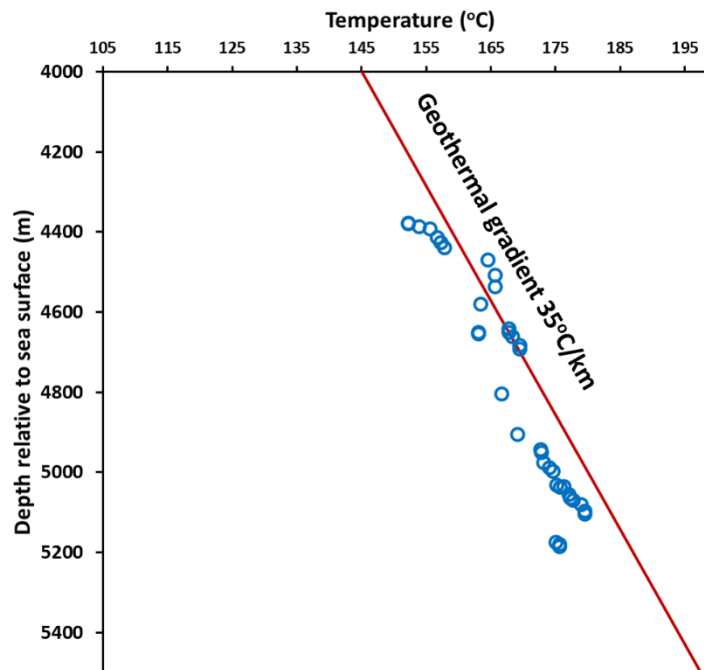


Figure 7.4. Temperature measurements (courtesy of ConocoPhillips) and estimated linear geothermal gradient plotted against depth for the Jade field in block 30.

Overpressure generation in the Triassic formations is mainly attributed to disequilibrium compaction caused by rapid burial during the late Neogene (Nguyen et al., 2013; Stricker and Jones, 2016) with possible contributions from hydrocarbon generation and lateral pressure transfer (Osborne and Swarbrick, 1999; Swarbrick et al., 2000; Yardley and Swarbrick, 2000; di Primio and Neumann, 2008).

Figure 7.4 shows temperature measurements from three wells from the Jade field (provided by ConocoPhillips). Following Hermanrud et al. (1990) who showed that measured temperatures underestimate the true formation temperatures due to cooling effect of the drilling mud; a line was taken through the upper envelope of the provided temperature values, yielding 35°C/km. This value is consistent with previously reported thermal gradients for the area (Swarbrick et al., 2000; di Primio and Neumann, 2008; Stricker, 2016) and was assumed to be the common geothermal gradient for all six studied wells.

Water depth in the study area is generally 70 to 90 m.

7.3 Mudstone sample characterization results

7.3.1 Bulk mineralogical properties

Quantitative bulk XRD show consistent bulk mineral composition (Figure 7.5). Quartz, K-feldspar, 2:1 clays (illite-smectite), kaolinite and chlorite were detected in all of the samples. The average clay content (kaolinite + mica + illite + illite-smectite + chlorite) is ~60 wt%. The dominant components are quartz (average ~ 14 wt%) and 2:1 clay minerals (illite-smectite; average ~ 47 wt%). There is an average of ~ 4 wt% kaolinite, ~ 9 wt % chlorite and ~ 8 wt% K-feldspar in all of the samples. Plagioclase (average ~5 wt%), pyrite (average ~1.2 wt%), dolomite (average ~2 wt%), ankerite (average ~2 wt%) and minor amounts of calcite were detected in most of the samples. There are traces of iron oxide (hematite + goethite), gypsum, and anatase in most of the samples, and in some of them traces of barite, anhydrite and halite. Bulk quantitative XRD data of the studied samples can be found in Appendix I.

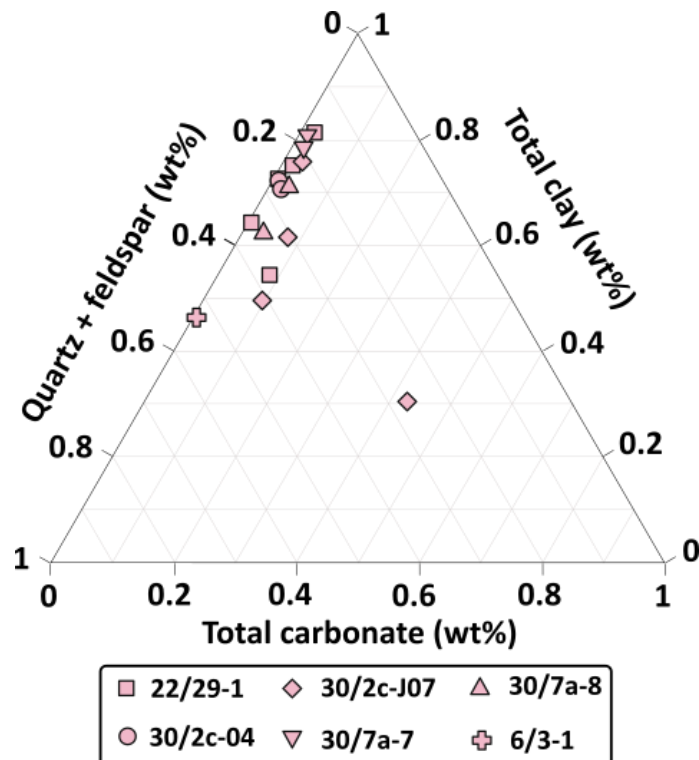


Figure 7.5. Bulk mineral composition of mudstone samples obtained from QXRD.

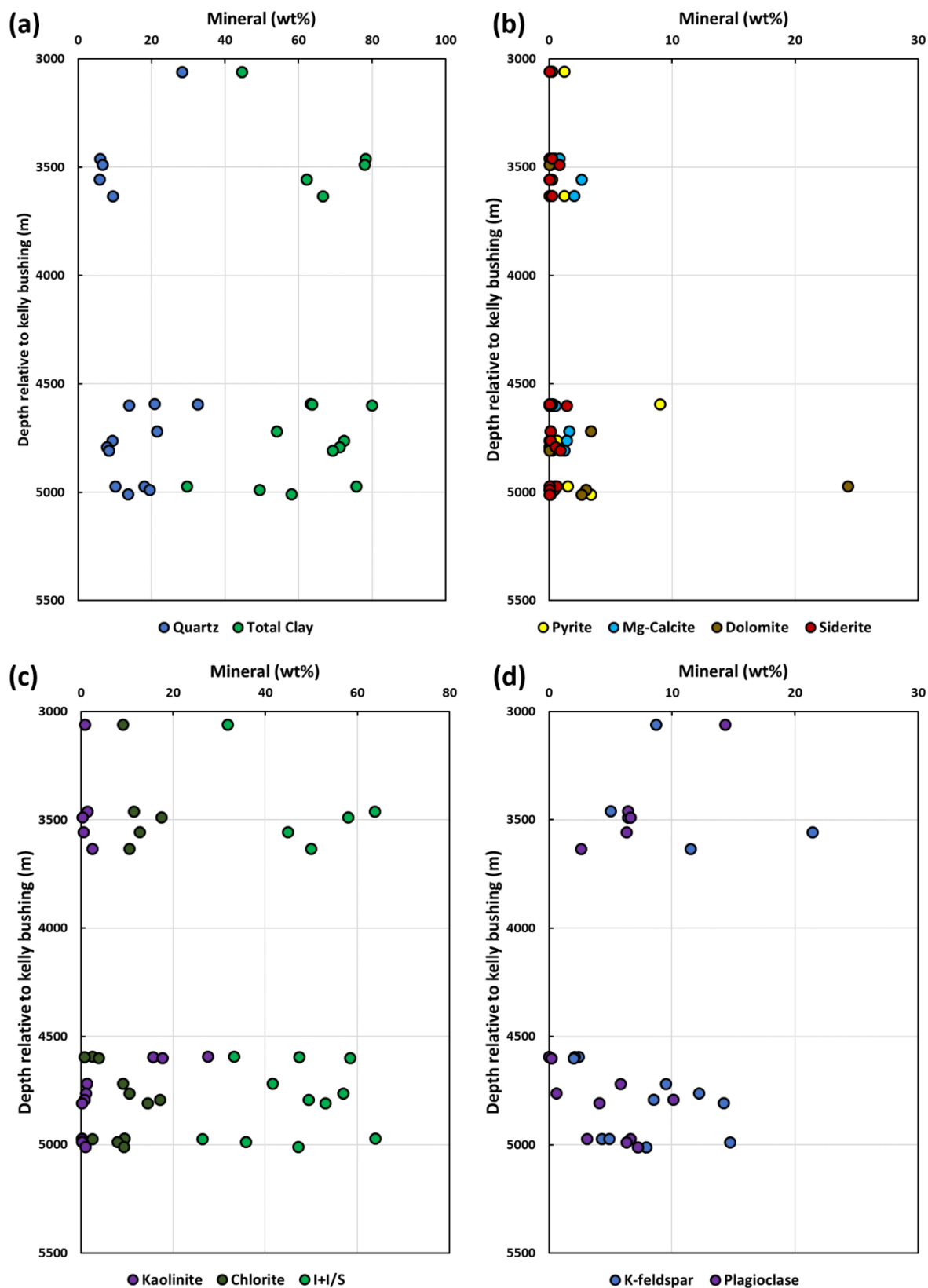


Figure 7.6. Bulk mineralogy versus depth trends in the studied Triassic mudstones.

| | Quartz | Kspar | Plagioclase | Calcite | Mg-Calcite | Dolomite | Pyrite | Siderite | Anhydrite | Ankerite | Kaolin | 2:1 Al Clay | Fe Chlorite | Tri 1:1 Clay |
|------------------|--------|-------|-------------|---------|------------|----------|--------|----------|-----------|----------|--------|-------------|-------------|--------------|
| Quartz | 1.00 | | | | | | | | | | | | | |
| Kspar | -0.36 | 1.00 | | | | | | | | | | | | |
| Plagioclase | -0.05 | 0.26 | 1.00 | | | | | | | | | | | |
| Calcite | -0.04 | -0.41 | 0.02 | 1.00 | | | | | | | | | | |
| Mg-Calcite | -0.50 | 0.66 | -0.12 | -0.29 | 1.00 | | | | | | | | | |
| Dolomite | 0.17 | -0.14 | -0.09 | -0.22 | -0.11 | 1.00 | | | | | | | | |
| Pyrite/Marcasite | 0.24 | -0.32 | -0.26 | 0.54 | -0.35 | 0.03 | 1.00 | | | | | | | |
| Siderite | -0.40 | -0.25 | -0.16 | 0.06 | -0.03 | -0.26 | -0.26 | 1.00 | | | | | | |
| Anhydrite | -0.20 | 0.02 | -0.01 | 0.32 | 0.08 | -0.28 | 0.41 | -0.08 | 1.00 | | | | | |
| Ankerite | 0.17 | -0.07 | -0.04 | -0.24 | -0.19 | 0.96 | 0.03 | -0.31 | -0.38 | 1.00 | | | | |
| Kaolin | 0.42 | -0.56 | -0.61 | 0.36 | -0.34 | -0.18 | 0.66 | 0.15 | 0.23 | -0.25 | 1.00 | | | |
| 2:1 Al Clay | -0.61 | -0.10 | -0.13 | 0.10 | 0.22 | -0.55 | -0.43 | 0.58 | 0.08 | -0.56 | -0.13 | 1.00 | | |
| Fe Chlorite | -0.72 | 0.51 | 0.55 | -0.07 | 0.39 | -0.38 | -0.41 | 0.25 | 0.16 | -0.37 | -0.65 | 0.44 | 1.00 | |
| Tri 1:1 Clay | -0.32 | 0.76 | 0.43 | -0.16 | 0.38 | -0.21 | -0.40 | -0.25 | -0.09 | -0.11 | -0.60 | -0.01 | 0.56 | 1.00 |

Table 7.2. Correlation matrix showing values of Pearson's correlation coefficient for Triassic mudstone mineralogy.

Figure 7.5 was constructed using the quantitative XRD determined mineral weight percentages. Total clay content is defined here as the sum of all the XRD determined clay minerals including all 2:1 clays (illite, mica and illite-smectite). Overall, mineralogy in the studied wells is fairly similar. The only outlier sample in Figure 7.6 is a carbonate cemented (dolomite and ankerite) mudstone from well 30/2c-J07.

The detected mineral composition is monotonous, however illite-smectite, K-feldspar, plagioclase, dolomite and ankerite shows considerable variability among the studied mudstone samples (Figure 7.6). Samples with abundant carbonates are all localised phenomena. No marls or extensive carbonate cemented layers (e.g. hardgrounds) have been sampled.

Figure 7.6 shows mineralogy-depth trends in the Triassic mudstones by using individual mineralogy data from all six wells. No trend can be seen when plotting individual mineralogy with depth (Figure 7.6). However, the variability of quartz with increasing depth shows weak negative correlation with the variability of the sum of clay minerals (Figure 7.6a) indicating that quartz is predominantly sedimentary in origin.

Table 7.2 shows correlation coefficient values for individual mineral phases. It was constructed by using mineralogy data from all six wells. Quartz shows weak negative correlation with illite-smectite. The relatively weak correlation suggests that there is considerable amount of silt-sized mica in the dioctahedral 2:1 mineral fraction. Note the lack of a clear correlation between quartz and the feldspars. K-feldspar shows a very weak negative correlation with quartz, but no discernible correlation exists with the plagioclase content. In addition to this the plagioclase content positively correlates with chlorite. This indicates that some of the original detrital K-feldspar was lost (likely because of clay mineral diagenesis) and that considerable amounts of authigenic plagioclase is present in these samples. Kaolinite shows weak positive correlation with quartz which indicates that at least a fraction of it is detrital in origin. In addition to this, kaolinite negatively correlates with chlorite which indicates that some of the original kaolinite was replaced by authigenic chlorite.

7.3.2 Clay mineralogical properties

Cation exchange capacity (CEC) measurements of the Triassic mudstone samples range from 2.5 to 10.9 meq/100g. These results are fairly consistent and indicate that the dioctahedral 2:1 mineral fraction is dominated by illite. Figure 7.7 shows the calculated smectite equivalent contents in illite-smectite for the individual samples. These results indicate an average of 12% smectite equivalent in illite-smectite in the Triassic mudstone samples.

Complete CEC data and calculated smectite equivalent contents for individual samples can be found in Appendix I.

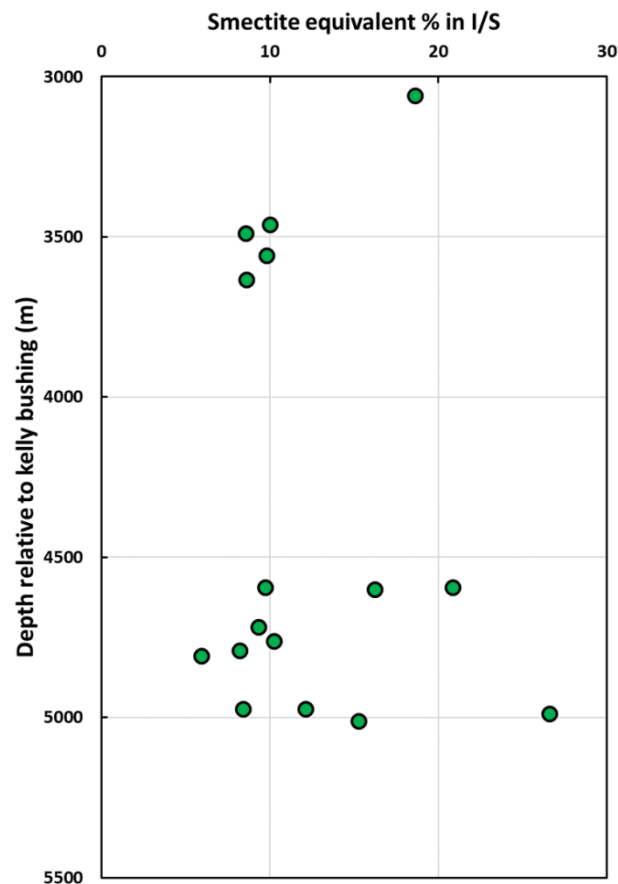


Figure 7.7. Calculated smectite equivalent % in illite-smectite for Triassic mudstone samples plotted against depth relative to Kelly bushing. Smectite equivalent content was calculated using the CEC results as described in 3.3.3.

7.3.3 Total organic carbon content

Total organic carbon content (TOC) was estimated in mudstone samples from all six wells. Complete TOC data and calculated organic matter contents for individual samples are given in Appendix III.

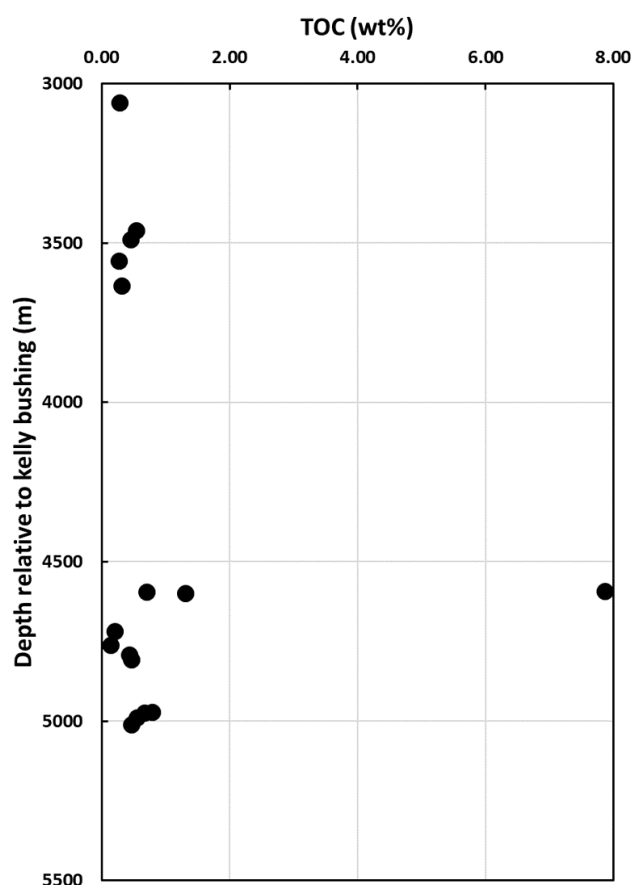


Figure 7.8. TOC (wt%) results for Triassic mudstones.

Figure 7.8 shows the measured TOC content of individual mudstone samples. The TOC values are consistent, mostly being less than 1 wt%. Anomalous high TOC value in a sample from 22/29-1 is likely the result of high amount of detrital plant material. In overall, these TOC values are considered typical for siliciclastic mudstones.

7.3.4 Clay mineral fabric alignment

Quantitative assessment of the phyllosilicate alignment in the Triassic mudstone samples was carried out using high-resolution X-ray textural goniometry (HRXTG) as described in 3.3.10. Complete HRXTG data of individual samples (including the chosen 2theta angles) can be found in Appendix V.

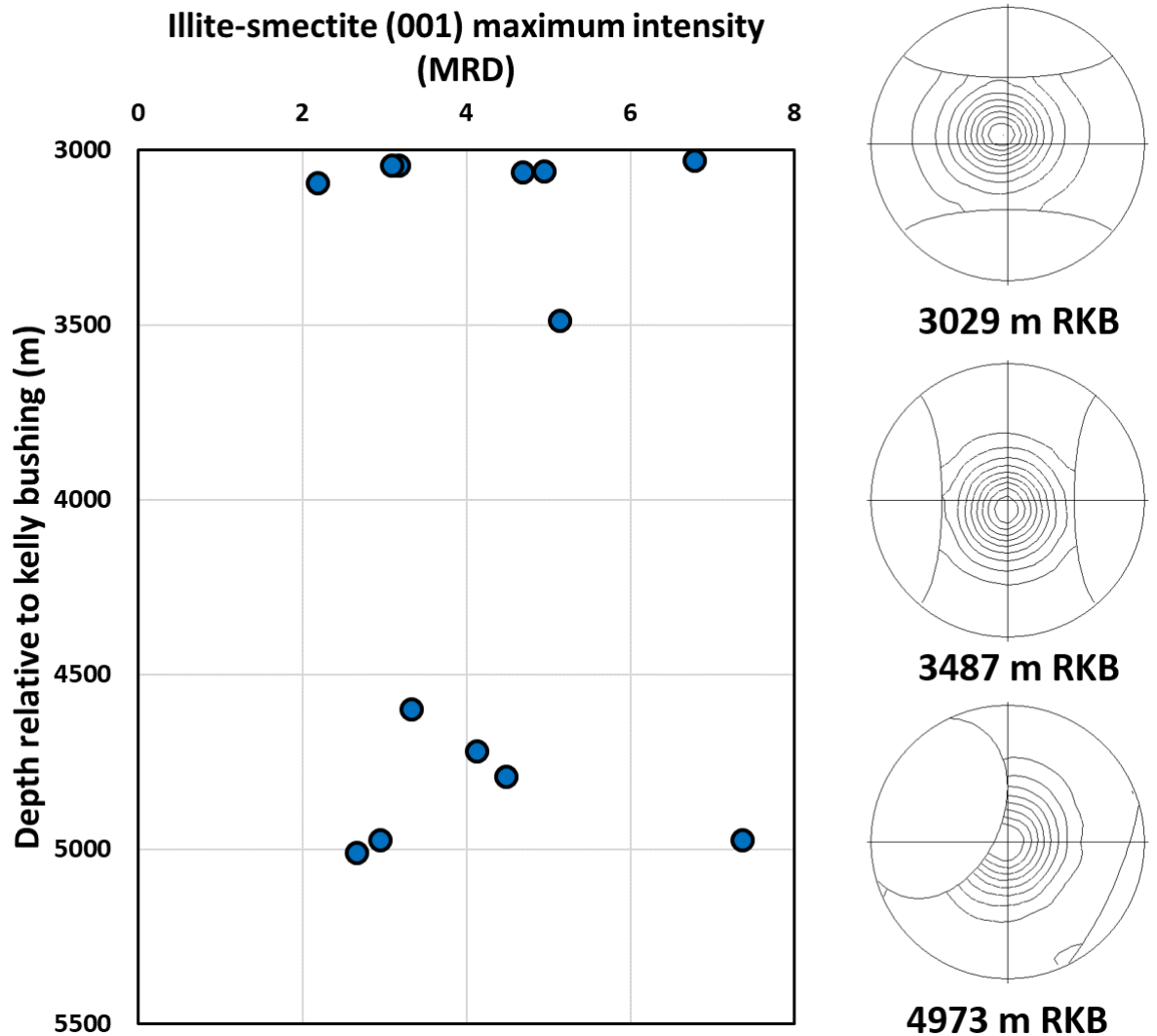


Figure 7.9. Measured illite-smectite (001) maximum intensity values of Triassic mudstone samples. Representative illite-smectite pole figures are displayed to the right.

Results displayed in Figure 7.9 show substantial scatter however indicate an overall strong alignment for illite-smectite throughout the whole studied Triassic interval. No trend can be seen when plotting the measured fabric intensity values against depth. At any depth, there is substantial scatter which is largely a reflection of variations in the clay:silt (i.e. plate:sphere) ratio of the samples (Day-Stirrat, Dutton, et al., 2010). However, as it is shown in Figure 7.10 there is no discernible correlation between the measured illite-smectite maximum intensity values and the QXRD estimated total clay mineral and quartz content. This is likely due to the variability of sand- and silt-sized mineral components within the studied samples and due to the limited number of samples used for this study from individual wells and formation members.

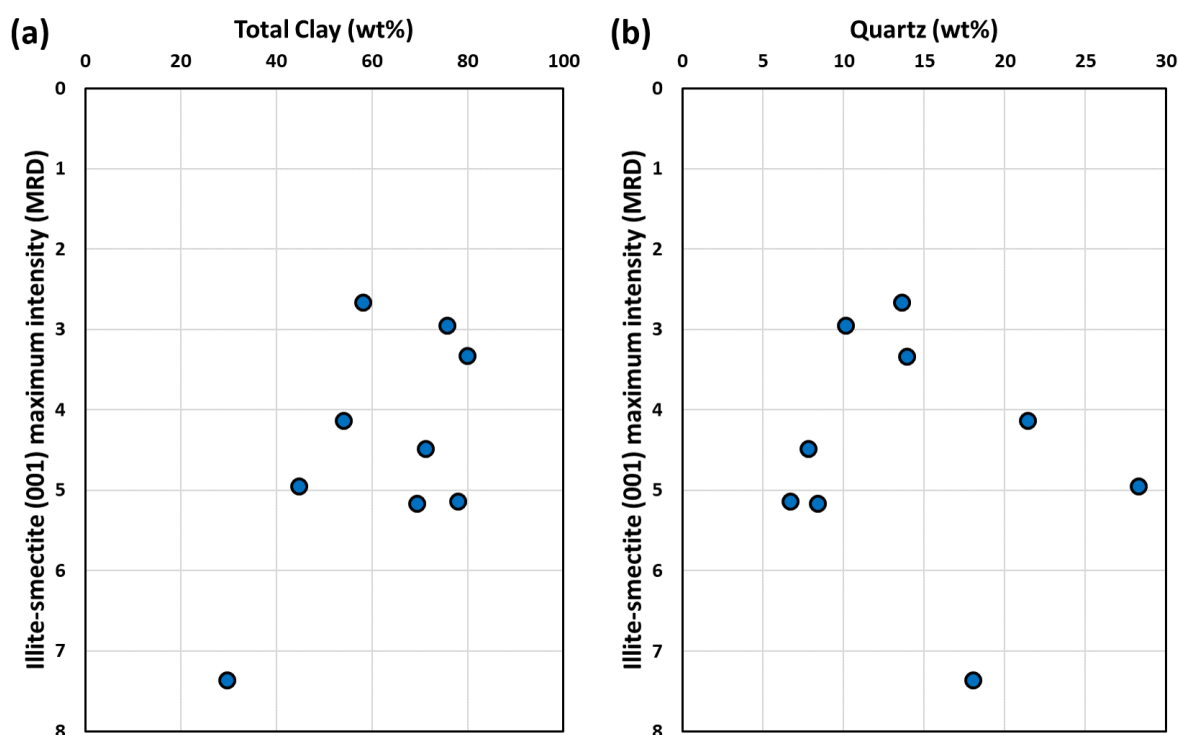


Figure 7.10. Illite-smectite (001) maximum intensity values shown in correlation with (a) total clay and (b) quartz content of the Triassic mudstone samples.

As it is shown in Figure 7.11 there is very strong correlation between the measured illite-smectite (001) and chlorite (002) +kaolinite (001) fabric intensity values. The strong correlation suggests that the whole clay mineral fabric (not just illite-smectite but also chlorite and kaolinite, both detrital and authigenic) was realigned normal to the maximum effective stress (parallel to bedding) in the Triassic mudstones.

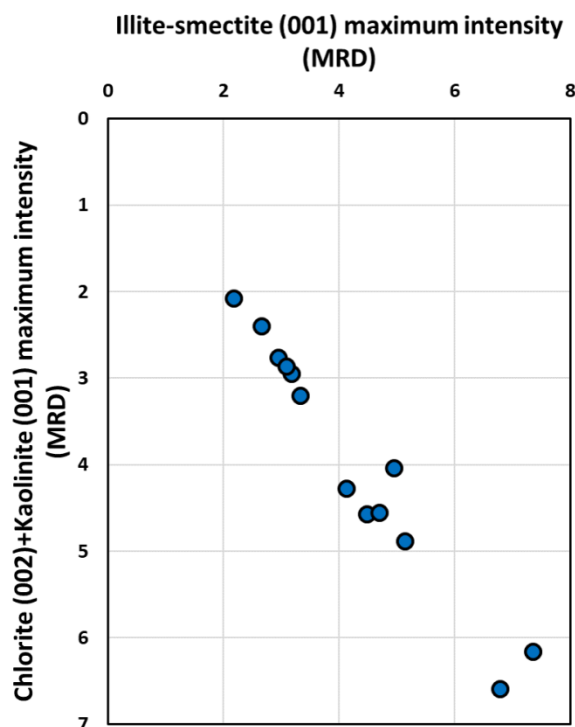


Figure 7.11. Illite-smectite (001) maximum intensity values shown in correlation with the maximum intensity values of chlorite (002)+kaolinite (001) for the Triassic mudstone samples.

7.3.5 Mudstone petrography

Support for the results shown in 7.3.4 is provided by petrographic observations made by SEM (Figure 7.12), which suggest an overall well-developed clay mineral fabric in the Triassic mudstone samples. However, SEM observations also revealed considerable variability of the clay mineral fabric on a micrometre-scale.

Overall SEM observations suggest that the fine-grained clay mineral matrix is well aligned where quartz or other silt sized spherical grains (e.g. feldspar, pyrite etc) do not disrupt the fabric. Where silt sized equidimensional grains are present the clay fabric is locally disrupted (Figure 7.12e, f). These observations provide further support for the results shown in 7.3.4.

All samples contain a mixture of sand- silt- and clay-sized particles (Figure 7.12). Overall sorting of the samples is poor, and the silt particles are mixed with the clay-sized particles (Figure 7.12).

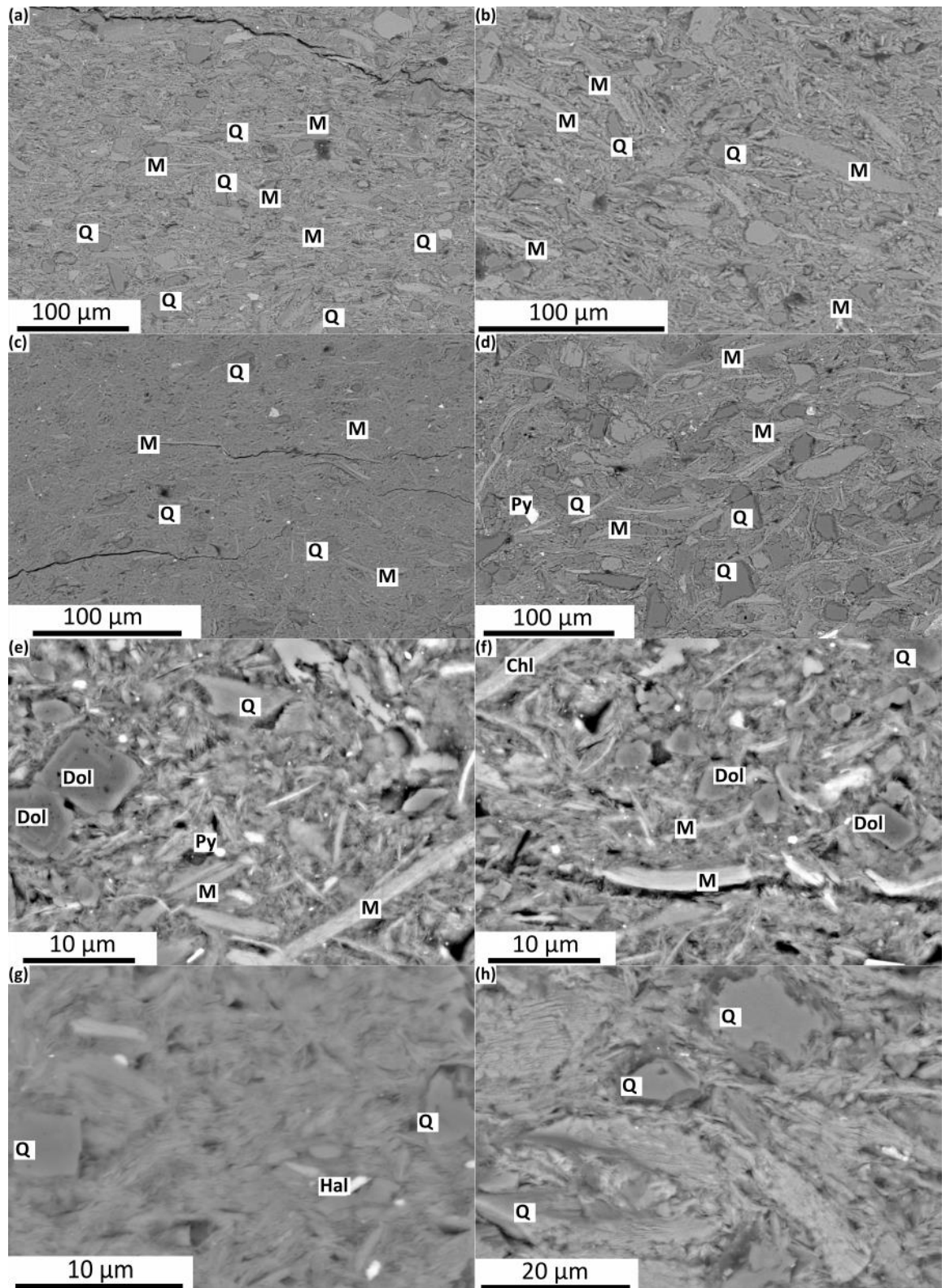


Figure 7.12. BSE images of Triassic mudstone samples from wells 22/29-1 (c)(d)(e)(f)(g) and 30/7a-7 (a)(b)(h) at 4624 m and 3414 m depths below seafloor respectively, showing examples of poor sorting and of silt-sized mineral grains locally disturbing the clay mineral fabric (d)(e)(f), and

examples of locally well-developed clay mineral fabric (g). Q: quartz, M: mica, Dol: dolomite, Chl: chlorite, Py: pyrite and Hal: halite. All sections imaged are perpendicular to the bedding.

Silt-sized mineral grains are dominantly quartz, mica, feldspar and carbonate (dolomite and ankerite). The detected detrital mica grains were commonly strongly altered (Figure 7.12c, d). Mechanical features such as compactional bending of mica or bending of clays around more resistant mineral grains were commonly observed features within these mudstones (Figure 7.12b, d).

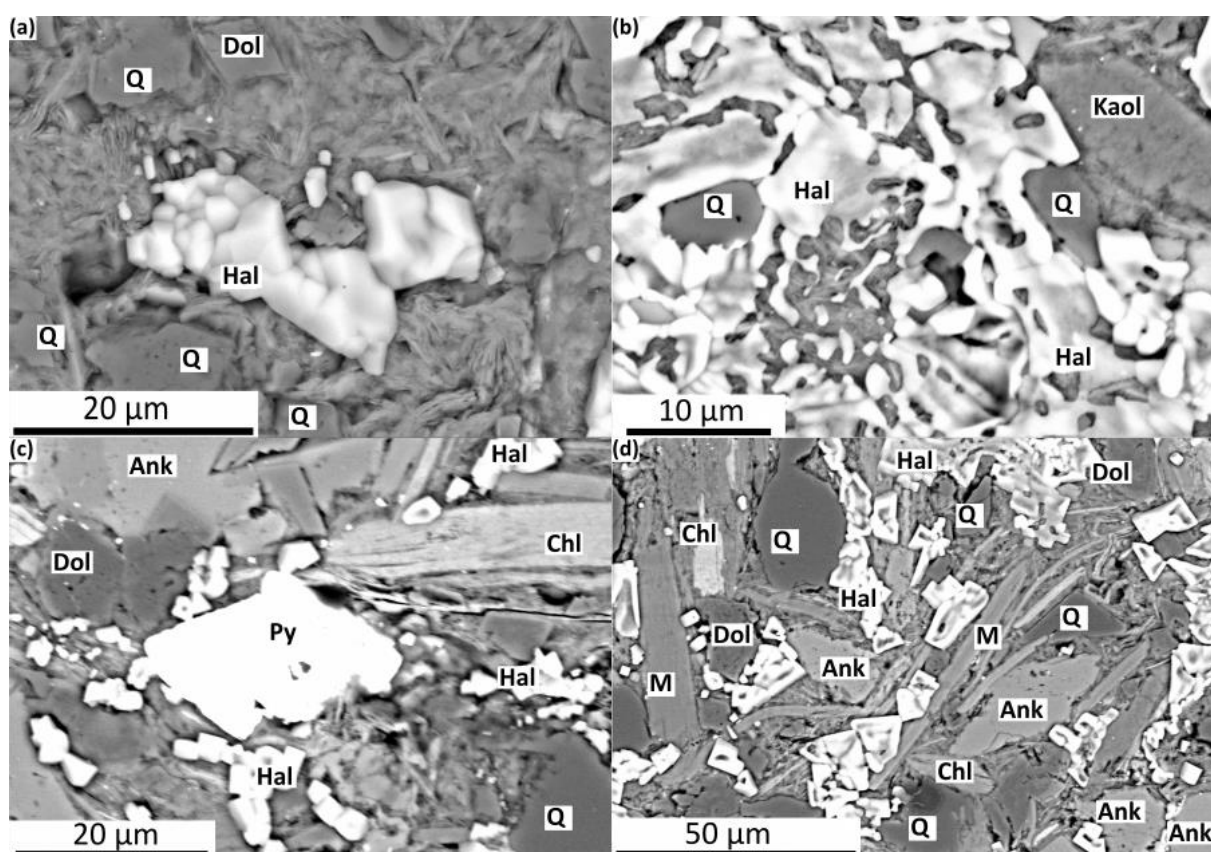


Figure 7.13. BSEI images showing examples for pore filling euhedral and poikilitic halite cement in Well 22/29-1 at 4624 m. Q: quartz, M: mica, Dol: dolomite, Chl: chlorite, Py: pyrite, Ank: ankerite, Hal: halite and Kaol: kaolinite. All sections imaged are perpendicular to the bedding.

Petrographic observations revealed the presence of dolomite and ankerite cements occluding micrometre-scale pores (Figure 7.13c, d). Pyrite was observed in euhedral form (Figure 7.13c).

Halite has been found as cement in mudstone samples from Well 22/29-1. It is present as intergranular poikilitic cement (Figure 7.13b) and euhedral micron-sized pore filling halite cement (Figure 7.13a).

Kaolinite was found as grain replacement (likely replacing detrital K-feldspar) in patches within the clay matrix (Figure 7.13b). Chlorite was observed as both detrital component and as grain replacement for detrital mica (Figures 7.13c, d).

Although SEM-CL observations have not been made in this study, the presence of euhedral terminations and edges to quartz grains –suggesting crystal growth into open pore space— clearly indicate that authigenic quartz is present in these samples as quartz overgrowth on detrital grains (Figure 7.14).

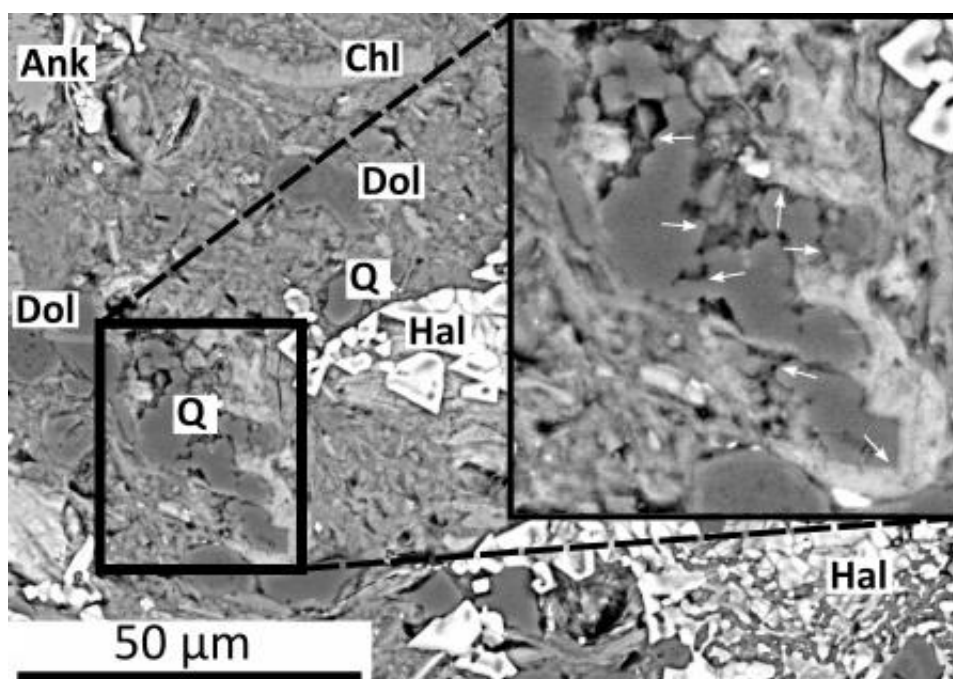


Figure 7.14. BSE image of a Triassic mudstone sample from Well 22/29-1 at 4624 m depth below seafloor, showing example of authigenic quartz overgrowth cement on detrital grains. White arrows denote euhedral crystal terminations resulting in inter-grown composite grains. Q: quartz, Dol: dolomite, Chl: chlorite, Ank: ankerite, Hal: halite. Imaged section is perpendicular to the bedding.

7.3.6 Mudstone porosity and permeability

Grain density was measured for selected mudstone core samples (from wells 22/29-1, 30/2c-J07, 30/2c-4 and 30/7a-7) using the “Small Pyknometer Method”, as it is described in 3.3.6. Measurements range from 2.60 to 2.83 g/cm³ (average 2.75 g/cm³) as it is shown in Figure 7.15a. No trend can be seen when plotting the data against depth. The relatively low value of 2.60 g/cm³ in a mudstone sample from well 22/29-1 can likely be attributed to the high organic matter content of the sample. In overall, these results are in accordance with the QXRD determined bulk mineralogy and indicate fairly consistent particle densities within the Triassic mudstones.

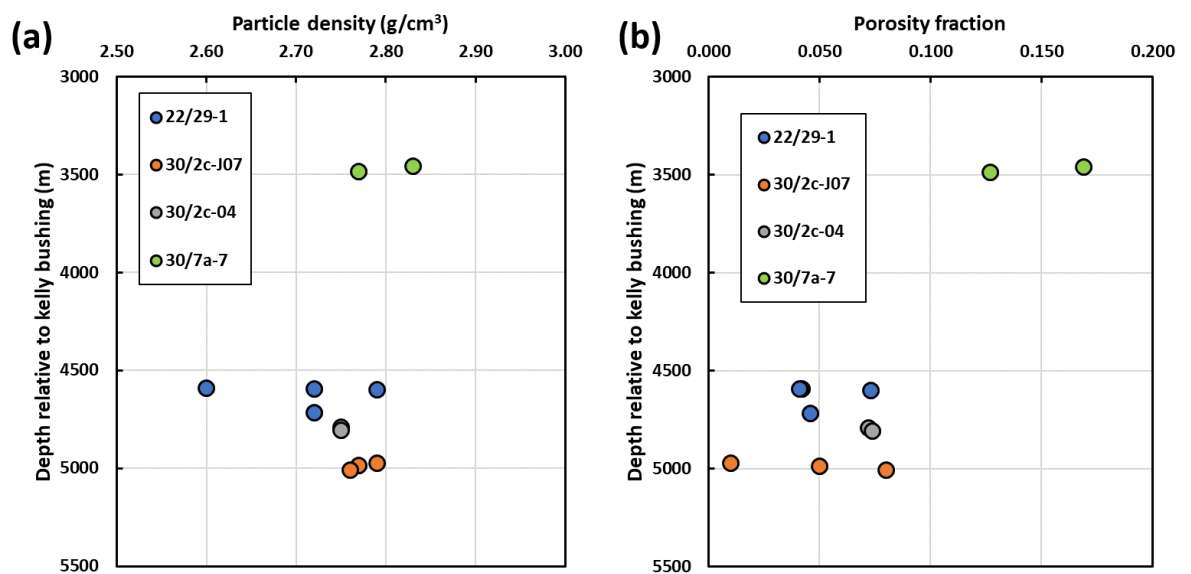


Figure 7.15. (a) Measured grain densities and (b) corrected total porosities of selected Triassic mudstone samples plotted against depth relative to Kelly bushing.

Measured grain densities were used to determine the total porosity of the mudstone samples as it is described in 3.3.7. Corrected total porosity (refer to 3.3.8) values of the samples ranges from 1% to 17% as it is shown on Figure 7.15b. A clear decreasing trend can be seen when plotting the porosity data against depth (Figure 7.15b) which indicates ~10% porosity loss between 3500 and 5000 m RKB.

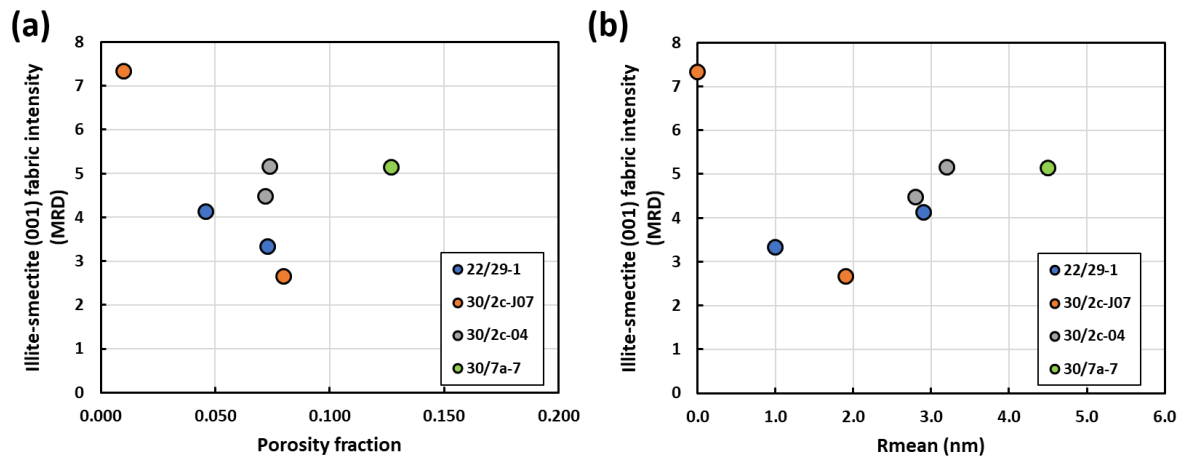


Figure 7.16. (a) Correlation between corrected total porosity and illite-smectite (001) fabric intensity; (b) correlation between mean pore throat radius and illite-smectite (001) fabric intensity.

Figure 7.16a illustrate the relationship between illite-smectite (001) fabric intensity and porosity. Note the weak overall negative correlation. Figure 7.16b shows the relationship between mean pore throat radius (determined by MICP) and illite-smectite (001) fabric intensity. No clear correlation can be seen.

The weak correlation of illite-smectite (001) fabric intensity with porosity and the lack of correlation with mean pore throat radius can be attributed to the variability of sand- and silt-sized mineral components within the studied samples. The silt content has considerable effect on the mean pore throat radius of a given mudstone sample. This is because the largest pores in mudstones are usually associated with the boundary of larger silt sized particles, thus silty mudstones contain pores that are orders of magnitude larger than in clay-rich mudstones (e.g. Day-Stirrat et al., 2011).

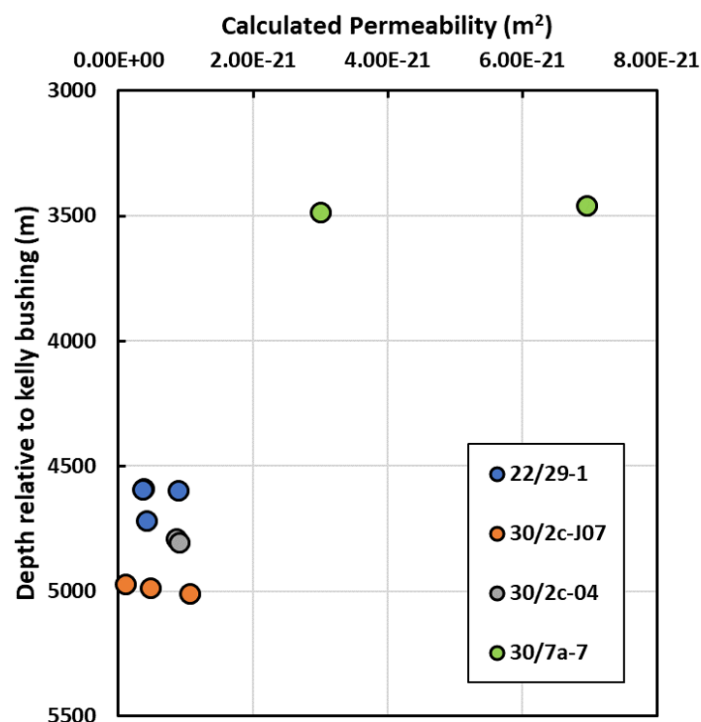


Figure 7.17. Calculated bedding perpendicular permeability (after Yang and Aplin, 2010) of selected Triassic mudstone samples.

Permeability of the mudstone samples was calculated based on the model of Yang and Aplin (2010) utilising bulk QXRD estimated total clay mineral content and estimated (corrected) total porosities. Total clay mineral content was used as a proxy for the mass fraction of particles less than two microns since no grain size distribution measurements have been made. The calculated permeabilities of the samples are very low (in the nD range) and show an overall decreasing permeability-depth trend (Figure 169).

Figure 7.18 shows corrected pore throat size distributions, corrected cumulative porosities and corrected mean pore throat radius of selected Triassic mudstone samples. These were all determined using Mercury Injection Core Porosimetry (MICP) as it was described in 3.3.8.

In overall, these results reveal very tight lithologies with mean pore throat sizes below 10 nm and show an overall loss of the larger mesopores with increasing depth. Full grain density, total porosity, MICP and calculated permeability data can be found in Appendix VI.

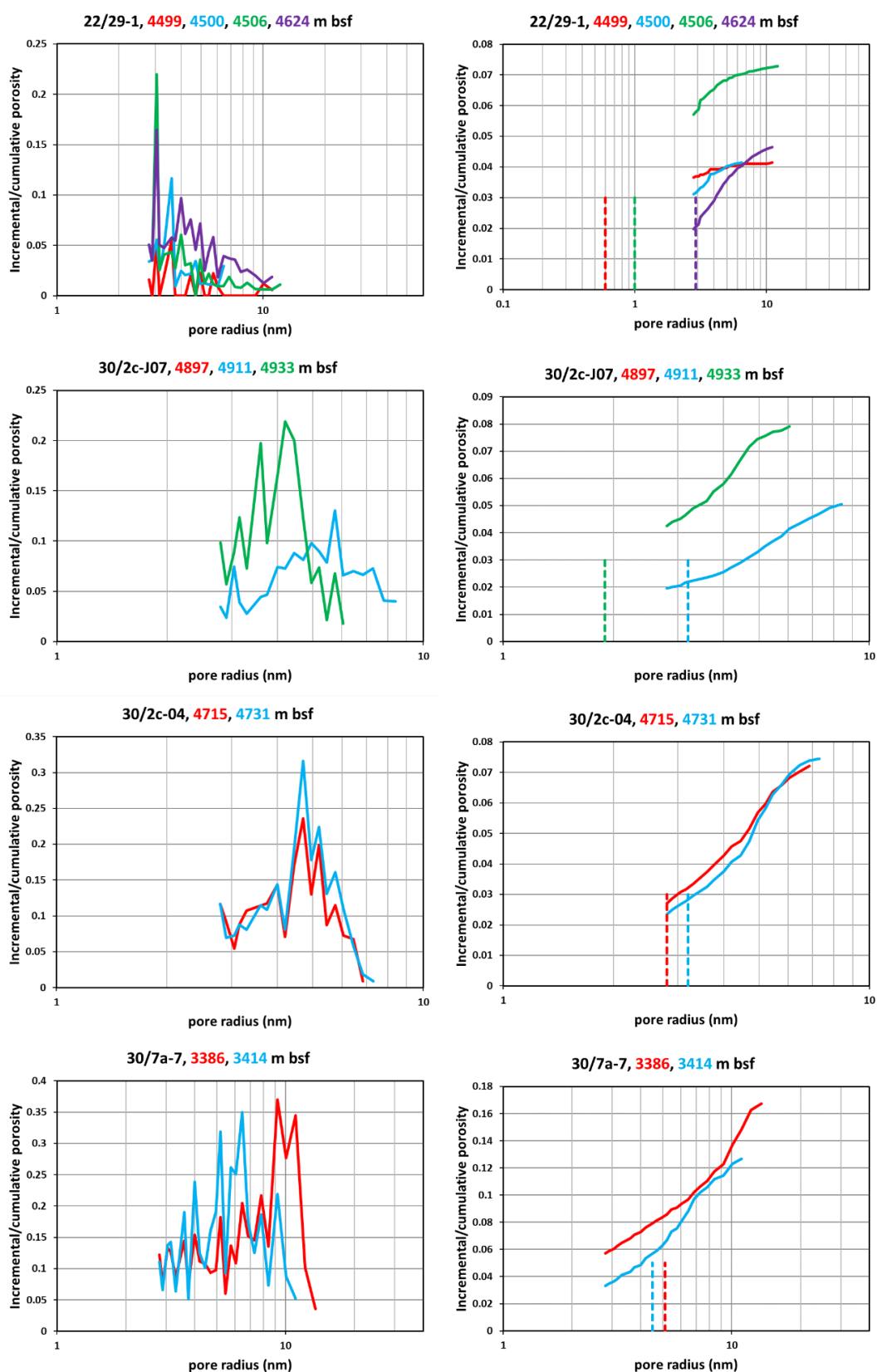


Figure 7.18. Corrected pore throat size distribution (left) and corrected cumulative porosity (right) (from MICP) of selected Triassic mudstone samples. Dashed lines on right figures denote mean pore throat radius.

7.4 Discussion

7.4.1 Mudstone mineralogy

The primary sediment composition and the early diagenetic reactions determine subsequent diagenetic pathways. Early diagenetic processes are contemporaneous with deposition and can locally affect the physical properties by cementing depositional porosity and make the mudstone locally resistant to mechanical compaction. These early diagenetic processes are typically redox processes where organic matter becomes oxidised by microbes (Aplin and Macquaker, 2011).

The identified halite cement is likely syndepositional and precipitated directly from the highly saline brines (Nguyen et al., 2013). It has filled much of the remaining porosity in the affected samples which likely contributed to the observed anomalously low porosities shown in Figure 7.18.

Euhedral pyrite likely precipitated directly from iron-rich porewaters when FeS_2 saturation was reached near sites where FeS saturation levels were not reached at the sites of sulphide supply due to lower sulphide production rates from organic matter (Taylor and Macquaker, 2000).

Cementation by dolomite and ankerite is likely to have occurred prior to compaction as a result of pedogenic and/or bacterially mediated respiratory processes (e.g. Taylor and Macquaker, 2000, 2014). Although carbonate precipitation had locally affected mudstone porosities its overall effect on porosity reduction in the studied Triassic mudstone samples is negligible. No extensive carbonate cemented layers have been sampled, however these might exist and might have locally affected the porosity and could have also affected the pore pressure by acting as early diagenetic seal.

Kaolinite can be interpreted as the result of Al-mobilization by organic acids generated during organic matter oxidation reactions. It has likely formed by leaching of detrital feldspar and mica grains as evidenced by the presence of grain replacement kaolinite. The likely sources of Al were poorly crystalline detrital aluminium oxides and clay minerals (Foscolos, 1984; Taylor and Macquaker, 2014).

Among the identified late diagenetic mineral phases chlorite may have formed diagenetically from kaolinite and also from smectite in the presence of Fe and Mg (Bjørlykke, 1998).

CEC and QXRD results reveal a diagenetically mature clay mineral assemblage with >80% illite in illite-smectite consistent with the high formation temperature (Figure 7.19). It should be noted that the question whether the illitic nature of the samples is depositional or diagenetic in origin cannot be comprehensively answered by this study as shallower samples were not available. However, the lack of a clear correlation between quartz and plagioclase and between K-feldspar and plagioclase and the positive correlation of plagioclase with chlorite indicate a diagenetically mature clay mineral assemblage where smectite has been illitized.

Possible source for the identified quartz cement is the illitization of smectite (Peltonen et al., 2009; Thyberg et al., 2010; Thyberg and Jahren, 2011).

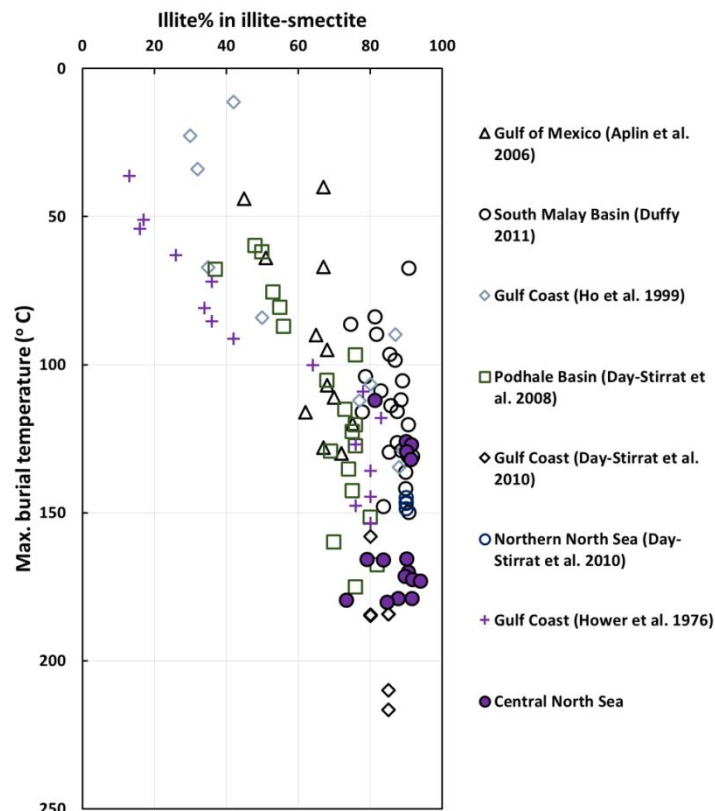


Figure 7.19. Published examples of illite % in illite-smectite with new results from Triassic mudstones of the North Sea Central Graben plotted against maximum burial temperature.

7.4.2 Implications for mudstone compaction processes

Figure 7.20 shows corrected total porosities (from MICP-determined bulk density and grain density; see 3.3.7) for the Triassic mudstone samples plotted against depth below seafloor. The green compaction trend on Figure 7.20 is the superimposed porosity-depth trend from Hansen (1996) for hydrostatically pressured Cretaceous and Tertiary mudstones on the Norwegian Shelf. Hansen's (1996) compaction trend is used here as an estimate of the maximum amount of compaction in the Triassic mudstones for their burial depth assuming hydrostatic conditions. It should be noted that Hansen (1996) cautioned against applying his trend for mudstones buried deeper than 2600 m therefore his trend is only used here as a reference for mechanical compaction at hydrostatic conditions. The measured porosities fall on trend with Hansen's (1996) compaction model indicating that Triassic mudstones continue to compact along Hansen's (1996) trend which suggest that they are close to being fully compacted for their depth of burial, even though they are highly overpressured.

According to Nguyen et al. (2013), Stricker and Jones (2016) and Stricker et al. (2016) shallow overpressure development by disequilibrium compaction played a key role in preserving anomalously high porosities in the Skagerrak Formation sandstones by arresting mechanical compaction. Stricker and Jones (2016) presented pore fluid overpressure development and effective stress history modelling results for the Judy Sandstone Member in the Heron Field and for the Joanne Sandstone Member in the Judy Field. Their estimated values of maximum vertical effective stress for these two fields were used in combination with the QXRD estimated total clay mineral content of the mudstone samples to recalculate the porosities of the samples from these two fields using Yang and Aplin's (2004) relationship between porosity and vertical effective stress (Figure 7.20). Total clay mineral content as estimated by QXRD was used as a proxy for the mass fraction of particles less than two microns. As can be seen on Figure 7.20, Yang and Aplin's (2004) mechanical compaction model would suggest considerably higher porosity than the measured porosities of the Triassic mudstones in these two fields.

Similar findings have been presented by Hermanrud et al. (1998), Teige et al. (1999) and Nordgård Bolås et al. (2004) who showed that deeply buried mudstone formations at the

Halten Terrace and in the North Sea have been individually compacted according to burial depth, seemingly independently of pressure regimes.

These results suggest porosity loss/volume reduction associated with the illitization reaction which cannot be explained by classical mechanical compaction models, suggesting that the mineralogical changes also result in overall porosity loss. Porosity reduction appears to have taken place even as the effective stress reduced while pore pressure increased due to disequilibrium compaction.

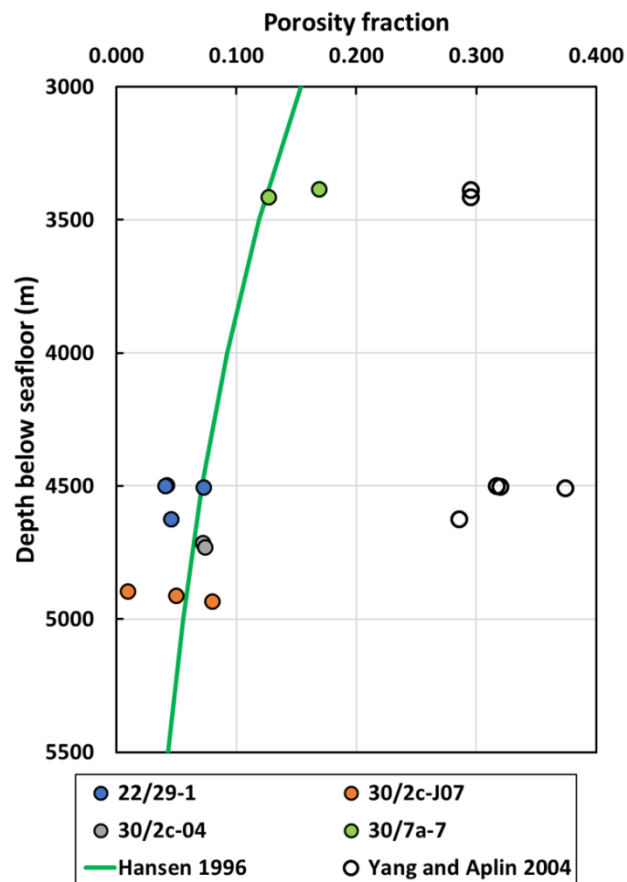


Figure 7.20. Corrected total porosities (coloured dots; determined according to 3.3.7) plotted against burial depth below seafloor. The exponential normal compaction trend of Hansen (1996) for hydrostatically pressured Tertiary and Cretaceous mudstones on the Norwegian Shelf is shown here. Empty dots denote mudstone porosities recalculated using the combination of the model of Yang and Aplin (2004) and the maximum effective stress values estimated by Stricker and Jones (2016).

7.5 Summary and conclusions

The lack of a clear relationship between porosity and effective stress in deeply buried North Sea mudstones led several previous researchers to conclude that chemical compaction in these mudstones have taken place independently of overpressuring (independent of the effective stress) (Hermanrud et al., 1998; Teige et al., 1999; Nordgård Bolås et al., 2004).

Triassic mudstones in the North Sea Central Graben have considerably lower porosities than what could be inferred from the compaction model of Yang and Aplin (2004) based on the modelled effective stress history. Bulk QXRD results indicate diagenetically mature (illitized) mudstone assemblage in the studied North Sea wells. These results suggest that illitization during ongoing compaction results in anomalously low porosity compared to solely mechanical compaction. Porosity reduction appears to have taken place even as the effective stress reduced while pore pressure increased due to disequilibrium compaction.

The new evidence presented here is in accordance with the previous findings of Hermanrud et al. (1998), Teige et al. (1999) and Nordgård Bolås et al. (2004) and suggest that these deeply buried Triassic mudstones have been individually compacted according to burial depth, seemingly independently of pressure regimes. However, it should be noted that these observations are not inconsistent with the chemically enhanced mechanical compaction model (refer to 2.6) which can also explain porosity loss in overpressured mudstones (Figure 2.17).

In overall these results show evidence for porosity loss (volume reduction) associated with illitization of smectite and confirm that chemical compaction may take place in association with clay diagenesis.

Chapter 8

Chemical compaction or chemically enhanced mechanical compaction:

a discussion on compaction processes in diagenetically altered mudstones

8.1 Evidence for chemical compaction

As it was pointed out by Bjørlykke (1998) experimental mechanical compaction models seriously underestimate real-life (observed) mudstone porosities below ~2 km depth (Figure 2.2). This suggests that chemical diagenetic changes –which usually start to operate at these depths— can cause further porosity loss in addition to the mechanical compaction processes.

Bjørlykke and Høeg (1997) and Bjørlykke (1998) coined the term chemical compaction to refer to this compaction process. However, as it was already mentioned in 2.6, the term chemical compaction (sometimes also called ‘non-mechanical compaction’) is misleading since it was originally established to describe the dissolution of quartz or carbonate at grain-to-grain contacts in sandstones and limestones, with concomitant mineral precipitation and porosity loss. This is an inappropriate conceptual model for mudstones, in which the main diagenetic reactions involve clay mineral transformations, classically but not solely the conversion of smectite to illite. In spite of this, the term is commonly used by many researchers when referring to the observed or sometimes only inferred (usually from wireline logs) physical effects of chemical diagenesis in mudstones (e.g. Peltonen et al., 2009; Thyberg et al., 2010; Thyberg and Jahren, 2011; Goult et al., 2012; Bruijn and Almqvist, 2015). This has the consequence that the term chemical compaction does not have a well-defined and precise meaning as for sandstones or carbonates when it is used for mudstones.

Figure 8.1 was constructed to further illustrate Bjørlykke's (1998) original point by showing measured mudstone (total) porosities from several published examples, previously unpublished results from GeoPOP Phase 2 and new results from this study (Halten Terrace, Central North Sea and Sergipe Alagoas Basin). All plotted porosity data in this figure represents total porosities measured using MICP according to 3.3.7 so the results are comparable. Measured porosities are shown in comparison with Mondol et al.'s. (2007) experimental mechanical compaction curve for 100% smectite and 100% kaolinite. These experimental compaction curves were selected as end-members since they represent the highest and lowest porosities achieved by experimental mechanical compaction of clays and silt-clay mixtures.

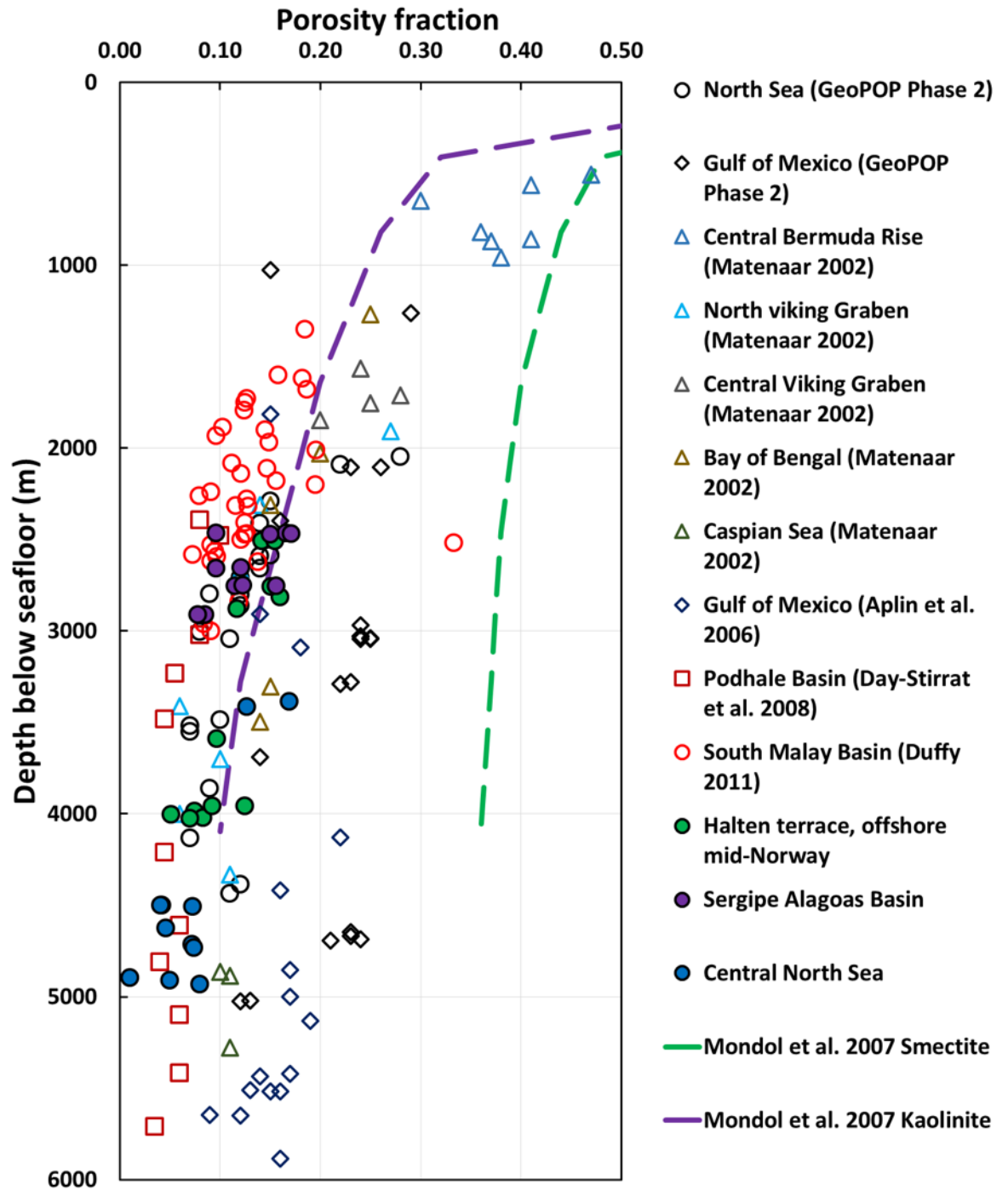


Figure 8.1. Published examples of measured total porosities with new results from Halten Terrace, offshore mid-Norway, Sergipe Alagoas Basin and the Central North Sea plotted against maximum burial depth. Experimental compaction curves for brine-saturated smectite and kaolinite (from Mondol et al., 2007) are plotted in comparison. All depths are measured relative to sea floor.

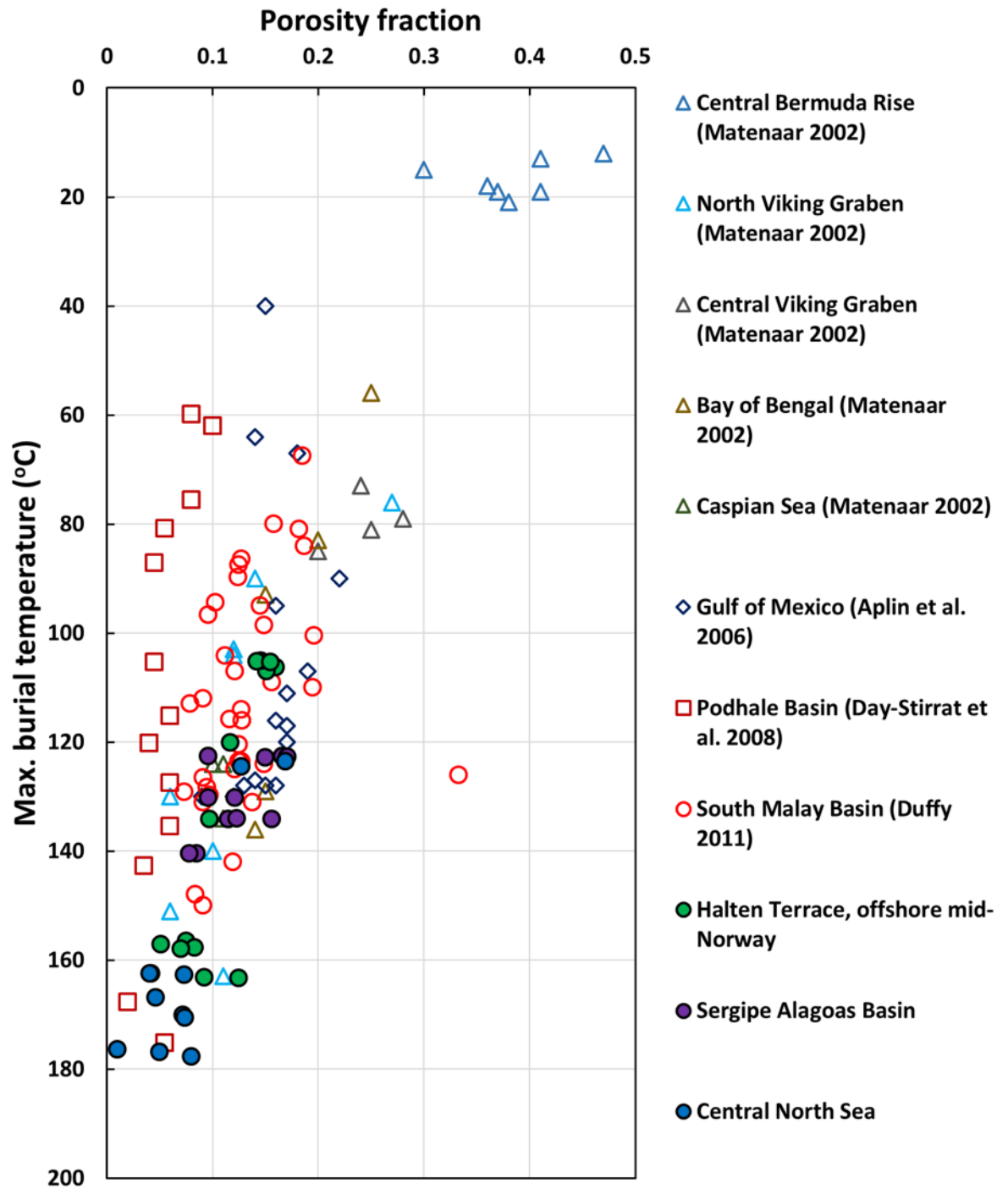


Figure 8.2. Published examples of measured total porosities with new results from Halten Terrace, offshore mid-Norway, Sergipe Alagoas Basin and the Central North Sea plotted against maximum burial temperature.

Pure illite or mixtures of silt and clays would be a closer representation of real-life mudstone mineralogy however those would all have porosities considerably less than pure smectite and considerably higher than pure kaolinite (Mondol et al., 2007; Mondol, 2009a). Note that below ~ 2 km mudstone porosities in the North Viking Graben, Podhale Basin, Malay Basin, Sergipe Alagoas Basin and Halten Terrace, offshore mid-Norway are considerably lower than what would be predicted by the experimental compaction curve for 100% kaolinite, which is Mondol et al.'s (2007) lowest porosity curve. Considering that Mondol et al.'s (2007) compaction curves were plotted assuming hydrostatic conditions and that most of the plotted porosity measurement data is from overpressured mudstone successions this clearly illustrates that there are compaction mechanisms at work at higher temperatures that are not included in these purely mechanical compaction models. Anomalously high porosities in Gulf of Mexico are interpreted as the result of the highly overpressured setting and the presence of pure smectite in those mudstones (Aplin et al., 2006) Figure 8.2 shows most of the same porosity data replotted against maximum burial temperatures (where temperature information was available). As can be seen, much of the scatter is reduced especially at higher temperatures which further supports the hypothesis that mudstone compaction is affected by chemical diagenesis. The only dataset that appears anomalous is that of Day-Stirrat et al. (2008) from the Podhale Basin. It should be noted however that the maximum burial depth and temperature for the Podhale sample set was estimated from smectite% in illite-smectite mineralogy data (these mudstone beds have been uplifted) thus it might be erroneous.

In accordance with Bjørlykke and Høeg's (1997) and Bjørlykke's (1998) chemical compaction model (refer back to 2.6) several previous studies have observed the apparent lack of a relationship between porosity and effective stress in mudstones buried into the diagenetic regime (e.g. Hermanrud et al., 1998; Teige et al., 1999) and also density increases in mudstones which are not related to effective stress but are coincident with smectite illitization (e.g. Peltonen et al., 2009; Lahann and Swarbrick, 2011).

New evidence was shown in this thesis from Miocene mudstones in the Central Malay Basin (Chapter 4) which had considerably lower porosities than the experimentally compacted kaolinite-smectite and silt-kaolinite mixtures of Mondol et al. (2007) and

Mondol (2009), respectively. These porosities are also low compared to the compaction trend of Yang and Aplin (2004) for mechanically compacted mudstones with similar clay content (Figure 4.33).

Duffy (2011) reported similar anomalously low porosities from two South Malay Basin wells. XRD results show a diagenetically mature (illitized) mudstone assemblage in both Central Malay Basin and South Malay Basin wells (Figure 4.30), which suggests that illitization during ongoing compaction resulted in anomalously low porosities compared to solely mechanically compacted mudstones.

Further evidence was shown from diagenetically mature Triassic mudstones in the North Sea Central Graben (Chapter 7) which had considerably lower porosities than what could be inferred from the compaction model of Yang and Aplin (2004) based on the modelled effective stress history.

Illitization of smectite resulted in enhanced porosity loss in hydrostatically pressured Cretaceous-Tertiary mudstones in the Sergipe-Alagoas Basin, offshore Brazil as it is described in Chapter 6.

Key evidence in favour of chemical compaction was found in Lower Cretaceous mudstones at Haltenbanken, offshore mid-Norway as described in Chapter 5. These results show clear evidence of porosity loss/volume reduction associated with smectite illitization which cannot be explained by classical mechanical compaction models, suggesting that the mineralogical changes also result in overall porosity loss. Porosity reduction appears to have taken place even as the effective stress reduced while pore pressure increased due to clay mineral diagenesis (Goult et al., 2016).

In overall these results show strong evidence for porosity loss (volume reduction) associated with illitization of smectite and confirm that chemical compaction may take place in association with clay diagenesis.

8.2 Clay diagenetic control on mudstone microfabric revealed by High Resolution X-ray Texture Goniometry

Following the work of Ho et al. (1999), Matenaar (2002) Worden et al. (2005) Day-Stirrat (2006) Aplin et al. (2006) Day-Stirrat et al. (2008, 2010) and Duffy (2011) linking the preferred orientation of phyllosilicates with illitization and chemical compaction (refer back to 2.5), phyllosilicate alignment was quantitatively assessed in Miocene (Central Malay Basin), Lower Cretaceous (offshore mid-Norway) and Triassic (Central North Sea) mudstone samples using HRXTG.

Figure 8.3 is a composite plot showing the measured fabric intensity (MRD) values for 2:1 Al clays (illite plus mixed-layer illite/smectite) (001) of the Miocene mudstones from the Central Malay Basin, Lower Cretaceous mudstone assemblage from offshore mid-Norway and the Triassic mudstone assemblage from Central North Sea. The new data are superimposed on published HRXTG data from several different basin settings. The three new datasets represent diagenetically mature mudstones where clay diagenesis is ongoing or is in the final stages (>50% illite in mixed-layer illite-smectite) with high overall clay fabric alignment (MRD values of 3–8). The vertical axis is in temperature rather than depth in order to show the effect of illitization, which is in reality a function of thermal history. Although the alignment of clay minerals (illite and mixed-layer illite/smectite in this case) is influenced by several other factors, most obviously the silt/clay ratio of the mudstone (Day-Stirrat et al., 2010), it is clear that at temperatures usually associated with the onset of smectite illitization (70–100°C) there is a sharp increase in the clay fabric anisotropy values (marked by double-headed dashed green arrow in Figure 8.3). Day-Stirrat et al. (2008) suggested a slight increase in the alignment of illite at depths and temperatures greater than the smectite-to-illite reaction, perhaps as a result of continuing dissolution and re-precipitation of illite. We found no evidence to support this suggestion in our datasets, but that might be due to sample selection issues, since the overall alignment is highly influenced by clay content and silt/clay ratio in the individual samples, so that a small increase in clay mineral alignment with depth/temperature cannot be ruled out. The only anomalous dataset which does not show this abrupt change is that of Aplin et al. (2006), which is interpreted as the result of the highly overpressured

slope setting and the presence of pure smectite in those mudstones. The sole anomalous data point that has a very high fabric intensity value at a relatively shallow depth/low temperature is that of a deep sea clay sample deposited with extremely slow sedimentation rate (< 5 m/Ma) (Matenaar, 2002).

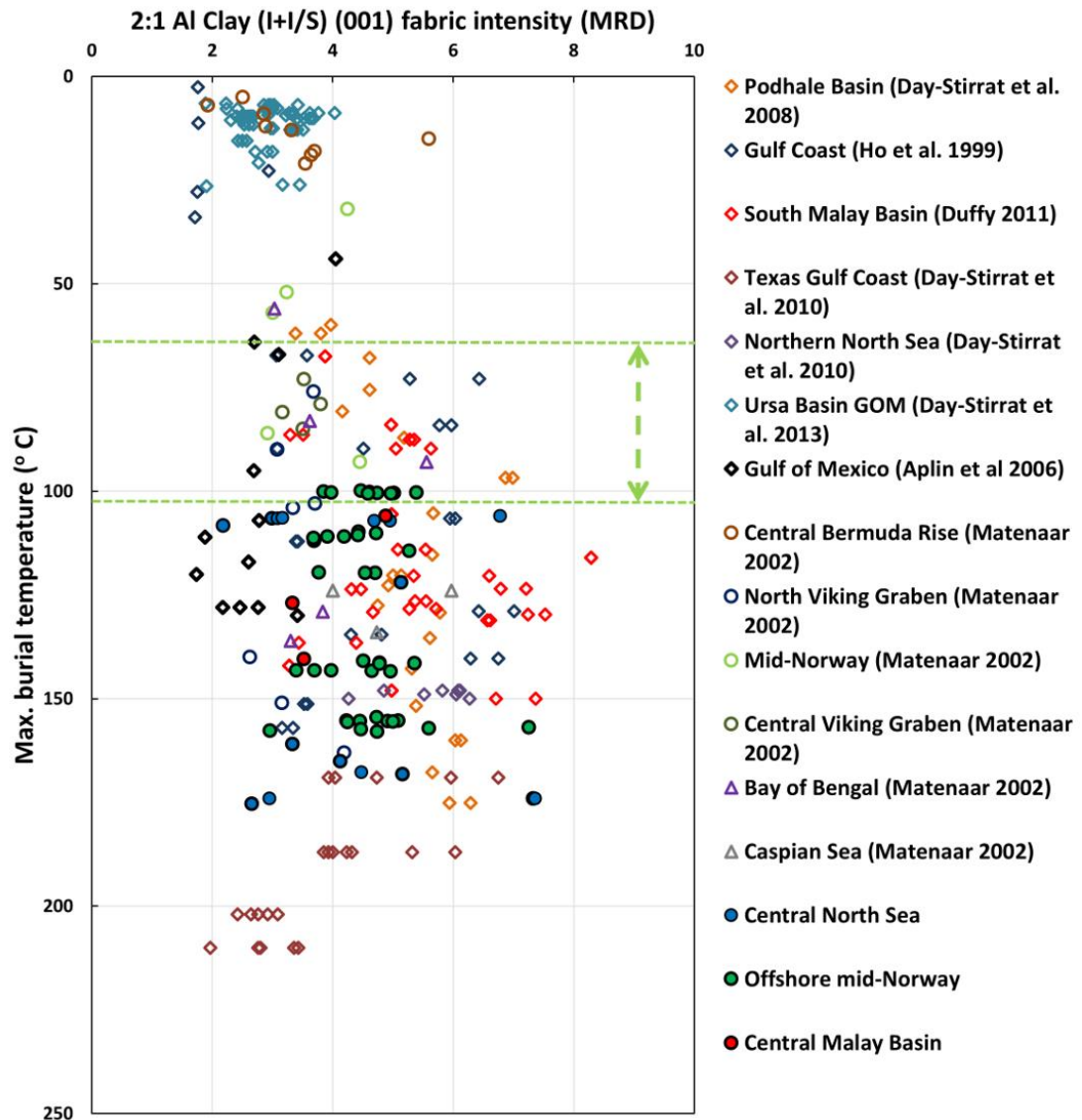


Figure 8.3. 2:1 Al clay (illite + illite-smectite) (001) fabric alignment in MRD plotted against temperature for samples from the mid-Norwegian, Central Malay Basin and Central North Sea case studies and previous studies. At any temperature, there is substantial scatter which is at least partly a reflection of variations in the clay:silt (i.e. plate:sphere) ratio of the samples. Note the sharp increase in alignment at temperatures associated with the onset of illitization (70–100°C). The only anomalous dataset which does not show this abrupt change is that of Aplin et al. (2006), which is interpreted as the result of the highly overpressured slope setting and the presence of pure smectite in those mudstones.

These datasets strongly imply that the conversion of smectite to illite is a dissolution-precipitation process rather than a solid-state transformation, with the reaction being controlled by temperature and reactant availability and being independent of effective stress. It is also apparent that during illitization the whole clay fabric is realigned normal to the maximum effective stress. Figure 8.4 shows measured fabric intensity values for chlorite (002) + kaolinite (001) in correlation with illite/smectite (001) fabric intensity values from the Gulf Coast, South Malay Basin, Podhale Basin and from the new datasets. These sample sets represent diagenetically altered mudstones where clay diagenesis is either still ongoing or is in the final stages (80% illite in illite-smectite). Note the nearly perfect correlation, which shows that during illitization other clay phases, both authigenic and detrital, realign. This observation strongly suggests at least a partial mechanical (grain rotation) effect associated with the clay fabric realignment. This interpretation is in good agreement with the model of Śródoń et al. (2000) (refer to 2.4.1 and Figure 2.5) and it also implies small-scale fabric destabilization during illitization of smectite.

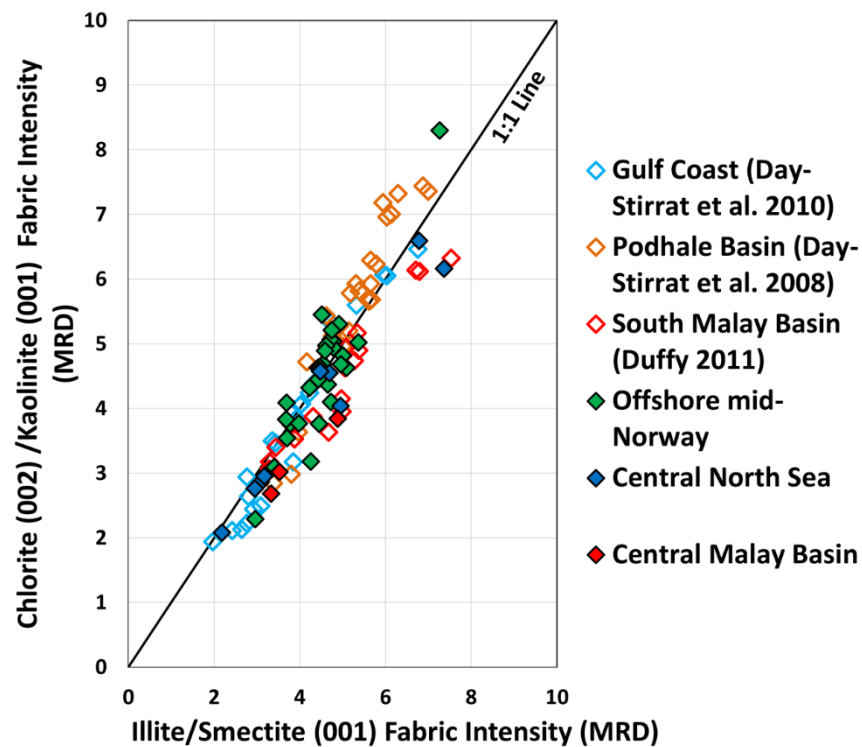


Figure 8.4. Illite-smectite (001) fabric alignment shown in correlation with chlorite (002)+kaolinite (001) fabric alignment. Alignment is given in MRD. The strong correlation suggests at least partial mechanical realignment of the clay matrix during clay diagenesis.

Increasing fabric anisotropy has a considerable effect on the physical properties of mudstones, e.g., by changing the pore structure (Bowers and Katsube, 2002) and creating permeability anisotropy. Johnston and Christensen (1995) reported compressional-wave and shear-wave velocities to change by as much as 20% with increase in the preferred orientation of the clay minerals. Banik (1984) investigated mudstone anisotropy data by comparison of wireline sonic data and interval velocities and by comparison of seismic and well-log depths in the North Sea Basin. He found a sharp increase in anisotropy below approximately 2700 m depth below seafloor (e.g., Figure 5 in Banik, 1983). His findings are strikingly similar to those which were presented in this thesis.

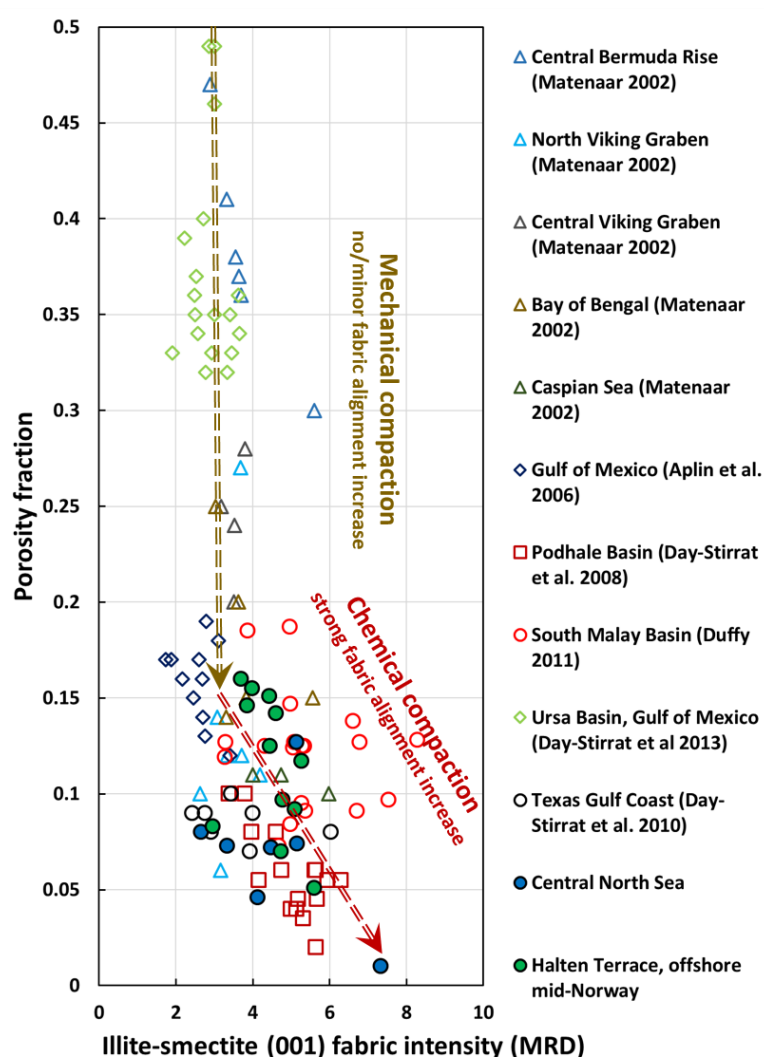


Figure 8.5. Alignment of illite-smectite (001), measured by HRXTG, as a function of porosity. At any porosity, there is substantial scatter which is at least partly a reflection of variations in the clay:silt (i.e. plate:sphere) ratio of the samples.

The relationship between illite-smectite (001) fabric anisotropy and mudstone porosity is illustrated in Figure 8.5. No clear correlation can be seen when considering all plotted data points. At any porosity, there is substantial scatter which is at least partly a reflection of variations in the clay:silt (i.e. plate:sphere) ratio of the samples. However, at lower porosity values (below ~15% porosity) fabric intensity appears to be increasing with decreasing porosity. The overall correlation is obscured by variations in the clay:silt ratio of the different mudstones sample sets nevertheless the correlation is clear for individual sample sets where lithological variation between the samples was negligible. One example where this was the case is shown in this thesis from Cretaceous mudstones at the Halten Terrace, offshore mid-Norway (Chapter 5). Another good example was shown by Day-Stirrat et al. (2008) from the Podhale Basin. These observations are in good agreement with previous experimental compaction results. Mechanical compaction experiments of clay-rich sediments have demonstrated that porosity decreases with increasing effective stress to minimum values close to ~10-15% (e.g. Rieke and Chilingarian, 1974; Mondol et al., 2007). It was also shown that mechanical compaction can reduce the porosities of fine-grained sediments without significant reorientation of the phyllosilicate minerals (Aplin et al., 2006; Voltolini et al., 2009; Day-Stirrat et al., 2011b).

In overall results presented in Figure 8.3-8.5 clearly indicate that the dominant clay mineral reaction in siliciclastic mudstones, the conversion of smectite to illite, involves a series of dissolution and reprecipitation reactions which result in a significant change in the orientation of the whole clay mineral fabric (both detrital and authigenic). Chemical compaction (porosity loss/volume reduction) is a direct result of clay mineral diagenesis and concomitant (small scale) fabric destabilisation.

Petrographic observations made by SEM provide further evidence for destabilization of the small-scale fabric and at least some dependence of chemical compaction on effective stress. Figures 8.-8.8 show back-scattered electron (BSE) images of a selected Lower Cretaceous mudstone sample from offshore mid-Norway. This sample has high alignment with a measured MRD value of 5.3 for both illite-smectite and chlorite (002)+kaolinite (001). Figure 8.6 shows the effect of small variations in the amounts of silt and clay, which has an observable effect on the overall clay fabric alignment. As can be seen on Figure

8.6, silt-sized quartz grains in contact locally created pressure shadows in which the phyllosilicates are uncompacted and have an isotropic fabric. Figure 8.9 is an example of a larger void inside a planktonic foraminifer fossil that has been filled by authigenic phases (siderite, pyrite, kaolinite and chlorite). Note the isotropic chlorite fabric inside the fossil, which locally created a pressure shadow during clay diagenesis. Figure 8.8 shows a partially dissolved K-feldspar crystal with authigenic chlorite precipitated inside its dissolution voids. Note the lack of any preferred alignment for the authigenic chlorite which precipitated inside the feldspar grain. In contrast, the clay matrix surrounding the grain is well compacted and shows a well-developed fabric alignment. These observations illustrate possible ways in which the small-scale fabric may be destabilized during diagenesis and show clear evidence that chemical changes do not affect the porosity without at least some influence of the effective stress.

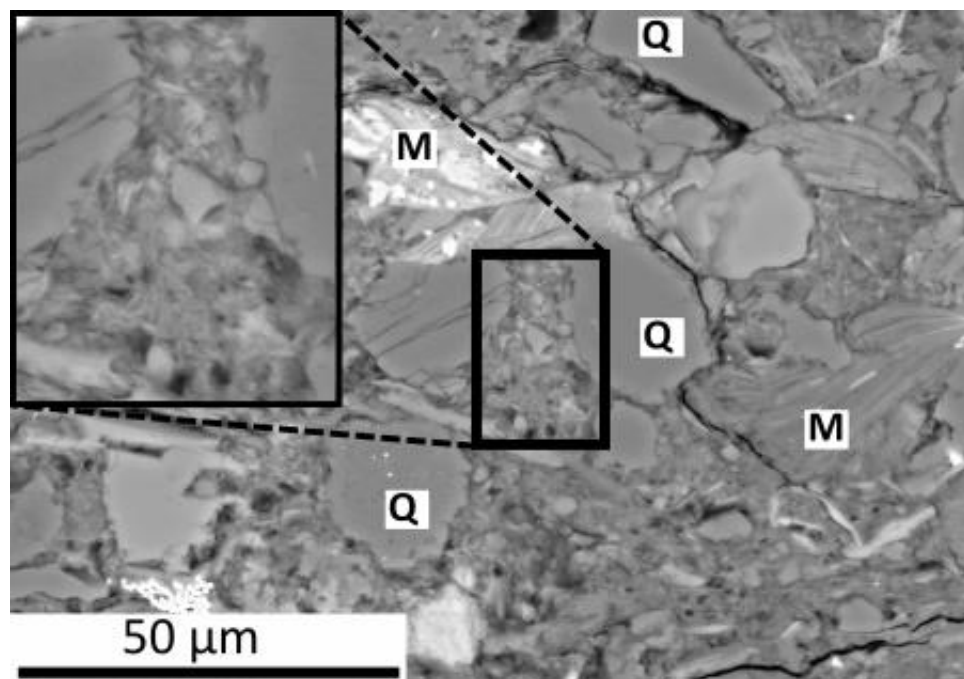


Figure 8.6. BSE image of a Lower Cretaceous mudstone sample, from well from 6507/2-3 at 2878 m depth below seafloor, showing an example of silt-sized quartz grains in contact creating pressure shadows in which the phyllosilicates are uncompacted and locally have an isotropic fabric. The section imaged is perpendicular to the bedding.

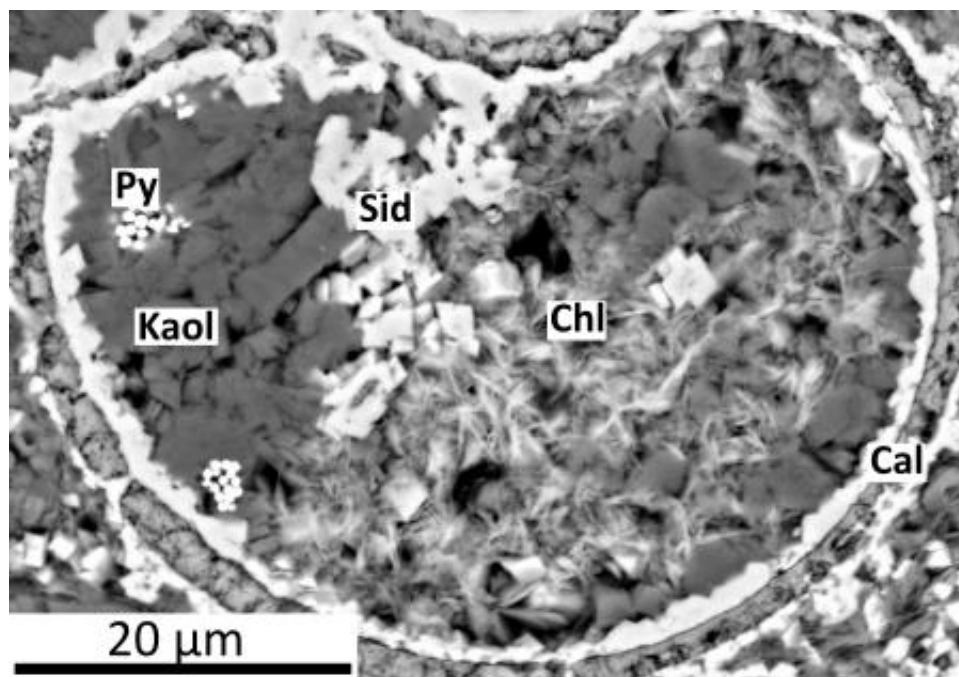


Figure 8.7. BSE image of a Lower Cretaceous mudstone sample, from well 6507/2-3 at 2878 m depth below seafloor, showing an example of local isotropic chlorite fabric inside a foraminifer fossil. The section imaged is perpendicular to the bedding.

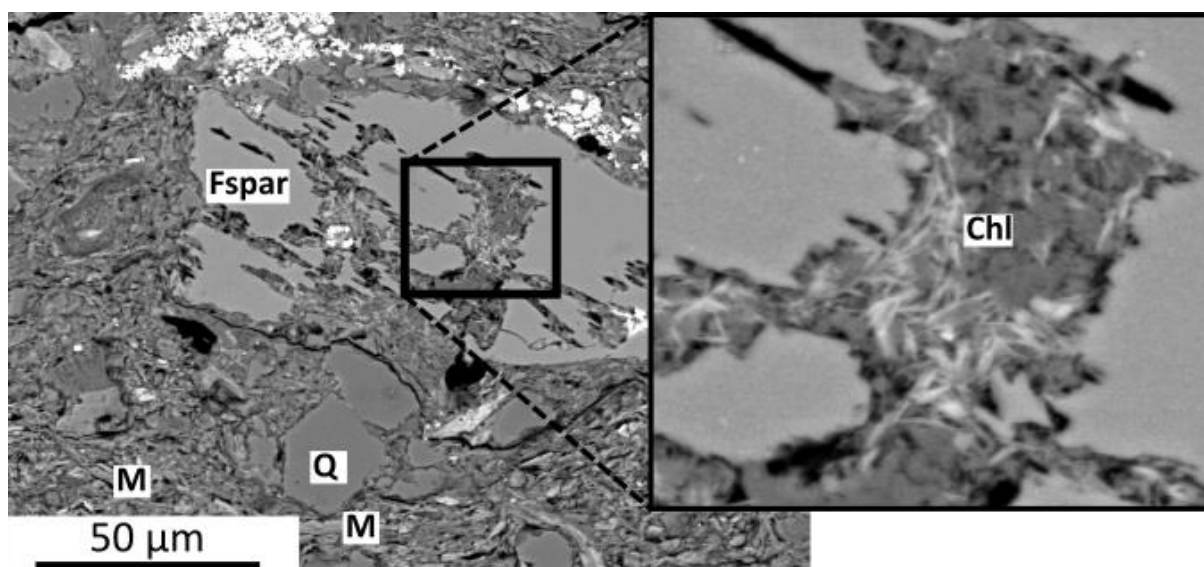


Figure 8.8. BSE image of a Lower Cretaceous mudstone sample, from well from 6507/2-3 at 2878 m depth below seafloor, showing an example of isotropic chlorite fabric inside a partially dissolved feldspar grain. The section imaged is perpendicular to the bedding.

These results are evidence that tends to refute the idea that compaction associated with clay mineral diagenesis is non-mechanical and thus independent of effective stress. Compaction in diagenetically-altered mudstones appears to be driven mainly by mechanical processes, although porosity loss is enhanced by small-scale fabric destabilization as a result of clay diagenesis.

8.3 Discriminating between compaction models

As it was already mentioned in 2.6 chemical compaction cannot be completely independent of the effective stress since porosity reduction/volume loss can only proceed, if pore water can escape (Cicchino et al., 2015). Nevertheless, according to the effective stress independent chemical compaction model of Bjørlykke and Høeg, (1997), Bjørlykke (1998) and Bjørlykke (1999) in diagenetically altered mudstones above ~100 °C mechanical compaction does not take place since mudstones have become stronger through diagenesis and their stress state lies inside the yield envelope even, if pore pressure is hydrostatic (e.g. Draege et al., 2006). This model implies that the main porosity reducing process during chemical compaction is cementation by authigenic minerals like quartz or illite (e.g. Draege et al., 2006; Thyberg et al., 2009). Unfortunately however dissolution and reprecipitation of authigenic minerals in a chemically closed system –which is assumed for this model (e.g. Bjørlykke, 1999)— on its own (without the effect of the overburden pressure; e.g. pressure solution or mechanical effects like pore collapse) would not result in porosity loss/volume reduction. This was illustrated by showing selected BSEM images from diagenetically altered Cretaceous mudstones in 8.2 (Figures 8.6-8.8). Precipitation of newly formed authigenic minerals would likely have considerable effect on the textural properties and would probably reduce the permeability by reprecipitating pore bridging illite (Nadeau et al., 2002). Note that this model would predict significant velocity increase (due to cementation of the connecting pores; refer to 2.7) and negligible density increase during chemical compaction (Thyberg et al., 2010; Thyberg and Jahren, 2011).

As it was shown in 2.7.1 several previous studies observed considerable density increases coincident with smectite illitization (Lahann et al., 2001; Dutta, 2002, 2016; Lahann and Swarbrick, 2011) indicating porosity loss and volume reduction concomitant with the

chemical changes. Complementing these observations strong evidence was presented in this thesis for porosity loss (volume reduction) associated with illitization of smectite in Miocene mudstones from the Central Malay Basin (Chapter 4), in Cretaceous mudstones from offshore mid-Norway (Chapter 5), in Cretaceous to Paleogene mudstones from the Sergipe Alagoas Basin (Chapter 6) and in Triassic mudstones from the North Sea Central Graben (Chapter 7).

In addition to this new evidence was presented in this thesis which showed that Miocene mudstones in the Central Malay Basin and Cretaceous mudstones at the Halten Terrace, offshore mid-Norway continue to compact mechanically in response to increasing effective stress up to at least 130°C (e.g. Goult et al., 2016).

In overall these results falsify the hypothesis that porosity in siliciclastic mudstones undergoing clay mineral diagenesis at temperatures above 100 °C is a function only of chemical processes and independent of the effective stress. These findings are entirely consistent with the chemically-enhanced mechanical compaction model as described in 2.6 and illustrated in Figure 8.9. Chemical reactions drive changes in the mechanical properties of the mudstones, thus porosity loss is dependent on time and temperature as well as on effective stress. Mechanical compaction continues to be viable in diagenetically mature siliciclastic mudstones because grain contacts are still predominantly clay-clay contacts and porosity loss is enhanced by small-scale fabric destabilization as a result of clay diagenesis.

It should be noted that although chemical diagenetic changes drive local, grain scale weakening of the mudstone (it becomes “more compactable”) by dissolution and shrinking (loss of interlayer water) of mineral grains (Lahann, 2002) the overall effect is strengthening the material by cementation and increasing the grain-grain contacts. The overall strengthening effect of mineral diagenesis was clearly demonstrated by previous studies using wireline log responses (e.g. Storvoll and Brevik, 2008).

The overall evolution of mudstone porosity and clay mineral fabric alignment during burial diagenesis is illustrated in Figure 8.9. As it can be seen mudstone compaction can be subdivided into three stages based on the relative contributions of different compaction processes. The first stage corresponds to mechanical compaction where

porosity is a function of the effective stress and lithology. Here compaction is dominated by mechanical processes such as grain rotation and breakage which result in closer packing of the particles and in minor increase of the clay fabric alignment.

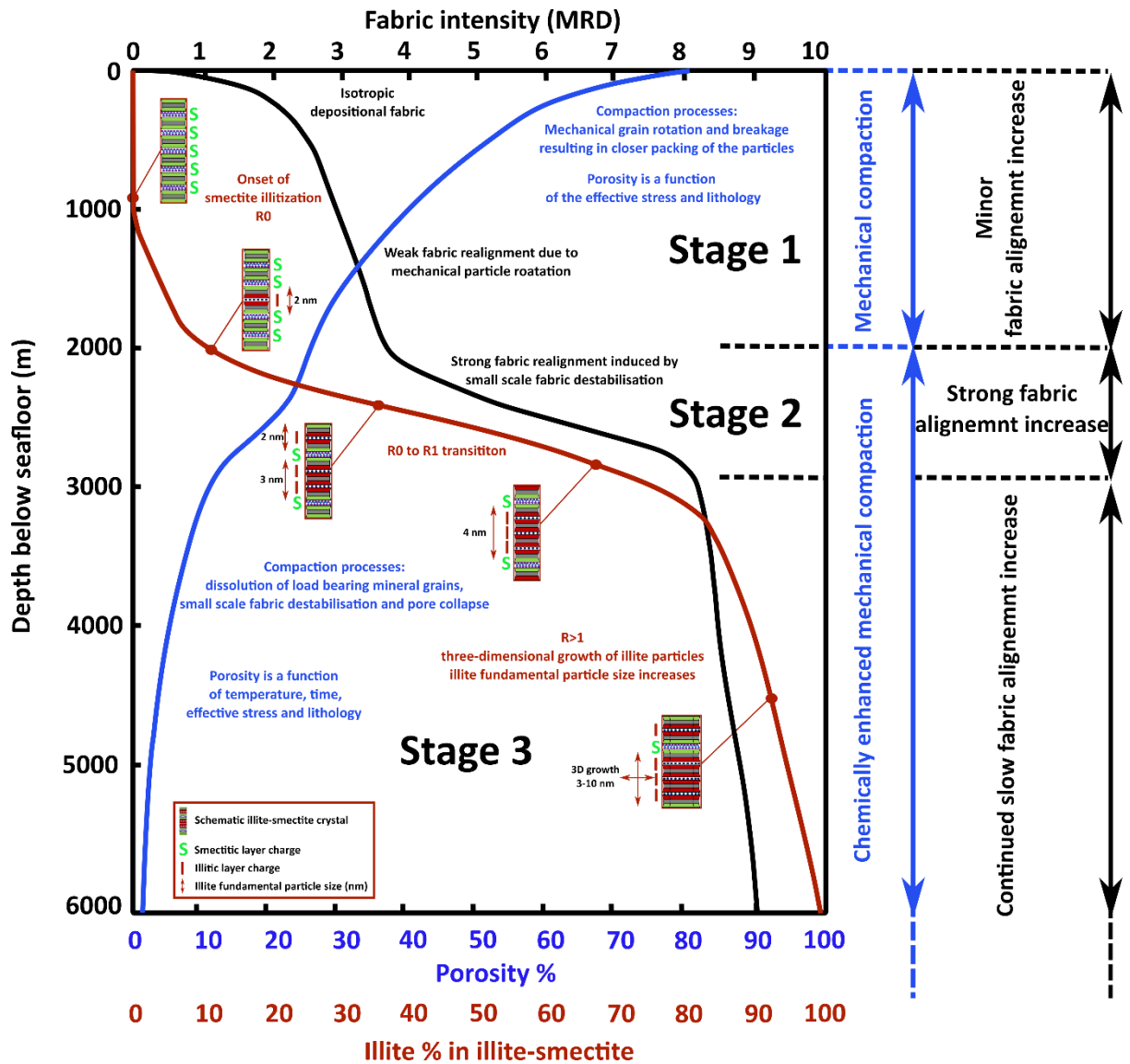


Figure 8.9. Schematic illustration of the evolution of mudstone porosity (blue), clay mineral fabric (black) and illite-smectite mineralogy (reddish brown) during burial diagenesis as inferred from natural data presented in this thesis. Refer to text for further explanation.

The second and third stages both correspond to chemically enhanced mechanical compaction where porosity is a function of temperature, time, effective stress and lithology. However, the most pronounced porosity and fabric change is associated with the second stage corresponding to the main phase of smectite illitization (R0 to R1 transition). Here compaction is enhanced by chemical processes such as dissolution and

shrinking of load bearing mineral grains and authigenic mineral growth. The overall results of these processes are enhanced mechanical particle reorientation and strong fabric alignment increase. The second stage was seen most clearly in Cretaceous to Paleogene mudstones from the Sergipe Alagoas Basin as described in Chapter 6. The third stage corresponds to the late stages of smectite illitization (>80% illite in illite-smectite). Here further compaction can be attributed to continued dissolution and reprecipitation related to the three dimensional growth of illite fundamental particles (Środoń et al., 2000). The third stage was seen most clearly in Miocene mudstones from the Central Malay Basin as described in Chapter 4 and in Cretaceous mudstones at the Halten Terrace, offshore mid-Norway as described in Chapter 5.

It should be noted that as mudstone porosities approach minimum values the role of mechanical compaction processes will become increasingly less important, thus a chemical compaction stage is reached at some point in the metamorphism of mudstone to slate. However even in metasedimentary rocks, textural features such as cleavage and phyllosilicate preferred orientation are related to compactional and/or tectonic stresses (e.g. Jacob et al., 2000).

8.4 Implications for pore pressure prediction in diagenetically altered mudstones

As it was shown in 8.3 diagenetically altered mudstones continue to compact mechanically, consequently their normal compaction trend depends upon their time-temperature history as well as on the maximum effective stress they have experienced.

A commonly applied method of pore pressure estimation within mudstones in the mechanical compaction regime, at temperatures below ~70°C, is the equivalent depth method (see 2.7). This method can account for overpressure generated by disequilibrium compaction (Mouchet and Mitchell, 1989) and has been modified to also take account of the tectonic stress (e.g. Goult, 2004). Key assumption here is that porosity is a single-valued function of vertical effective stress for a given mudstone lithology (e.g. Yang and Aplin, 2004). This has the consequence that equivalent depth methods do not account for overpressure generated by unloading. Also, they are not viable in diagenetically altered

mudstones because they do not account for the time-temperature dependence of mudstone compaction (Dutta, 2002, 2016; Lahann, 2002).

Lahann (2002) introduced separate smectitic and illitic compaction models to account for the effect of clay diagenesis which makes mudstones more compactable and shifts the normal compaction curve towards lower porosity for a given value of effective stress (see 2.7.2). This method is empirical and needs additional information about clay mineralogy to accurately determine the depths where the smectitic and the illitic compaction model should be used. However, porosity on both the smectitic and the illitic compaction model is a single-valued function of vertical effective stress. In this sense, this model also fits in with the “equivalent depth method” category. Therefore, this method does not directly account for overpressure generated by unloading. In spite of this, since this method is empirical the established smectitic and illitic normal compaction trends can be fitted to match pressure measurements from offset wells (Lahann, 2002).

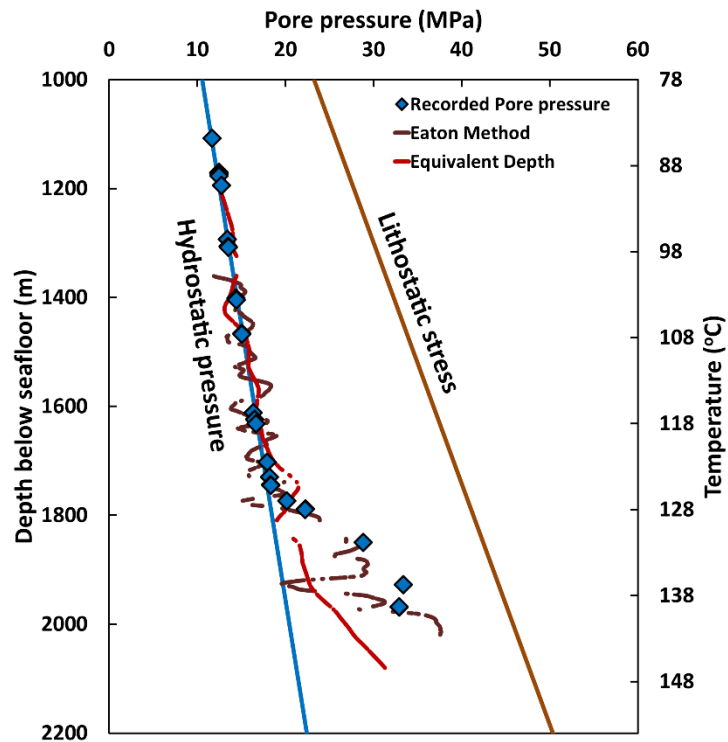


Figure 8.10. Pore pressure estimation for Bravo-Y in the Central Malay Basin using the equivalent depth method (red line) and Eaton’s method (brown line) with measured pore pressures (blue diamonds). The equivalent depth method uses the exponential normal compaction trend fitted to the smoothed density porosity log as shown in Figure 4.33. Eaton’s method uses a linear normal

compaction trend fitted to the sonic log data in the hydrostatically pressured shallower section and a standard exponent of three.

Another widely applied empirical method of pore pressure estimation is the method of Eaton (1975) using the sonic transit time (see 2.7). This method can give satisfactory results even in diagenetically altered mudstones when calibrated with neighbouring wells that are good analogues or when the hydrostatic normal compaction curve is known. An example of the latter case is shown in Figure 8.10 from the Bravo-Y well in the Central Malay Basin. As can be seen on Figure 8.10, in contrast to the equivalent depth method which seriously underestimates the overpressure, Eaton's method with a standard exponent of three provides accurate prediction. Calculated pore pressure is in fair agreement with the measured pore pressures with some discrepancies attributed to lithological variations (high velocity layer; see Chapter 4).

A further complication for pore pressure prediction in diagenetically altered mudstones is that they are commonly overpressured where clay diagenesis occurs, as it was shown in Chapter 5, which prevents direct observation of the hydrostatic normal compaction trend. Goultly and Sargent (2016) showed that when Eaton's method is used in reverse for Cretaceous mudstones at the Haltenbanken, offshore mid-Norway, to calculate the sonic normal compaction curve in wells with a known pressure-depth profile and then to estimate pore pressures in offset wells using Eaton's method normally, it will give inconsistent results. This is because the sonic log responds differently to overpressures generated by disequilibrium compaction and by unloading and their relative contributions vary across the Halten Terrace (Goultly and Sargent, 2016) as it was shown in Chapter 5. The increase in velocity due to increasing vertical effective stress during compaction is comparatively much smaller than its reduction due to unloading (assuming the same increment of vertical effective stress during both compaction and unloading) (Bowers, 2001; Goultly and Sargent, 2016).

As a possible solution to this problem, Bowers (2001) suggested that the combination of sonic log and density log data can be used to estimate the vertical effective stress unambiguously (see 2.7; and Figure 2.14). According to his model, values of sonic transit time and density in a given mudstone should correspond to a single point on the

unloading surface (Figure 2.14) thus determine the vertical effective stress. Bowers's (2001) method is appropriate for pore pressure estimation in diagenetically altered mudstones when the normal compaction trends relating the sonic velocity and density to the maximum vertical effective stress experienced by the mudstone are known for hydrostatic pore pressures (Goult and Sargent, 2016). This is because the method does not explicitly account for the time-temperature dependence of mudstone compaction (Dutta, 2002, 2016; Lahann, 2002). As it was shown in this thesis, clay diagenesis makes the mudstones more compactable thereby shifting the normal compaction trend towards lower porosity and, therefore, towards higher density and sonic velocity. Mudstone porosity can be reduced by clay mineral diagenesis with no increase in vertical effective stress as it was shown for Cretaceous mudstones at the Haltenbanken, offshore mid-Norway as described in Chapter five. Note that such mudstones are still normally compacted for the ambient confining stress and pore pressure ("normally consolidated" mudstone; Terzaghi 1943, Skempton 1969) because they have not experienced any unloading. This has the consequence that normal compaction trends established using sonic vs density crossplots do not necessarily correspond to the hydrostatic normal compaction trend as it is assumed for Bowers's (2001) method (Goult and Sargent, 2016).

A partial solution to this problem was offered by the method of Sargent et al. (2015) and Goult and Sargent (2016) at the expense of not providing an entirely deterministic solution. Their method is applicable to mudstones at temperatures above 100°C, and makes use of the crossplot between sonic transit time and density (Figure 8.11).

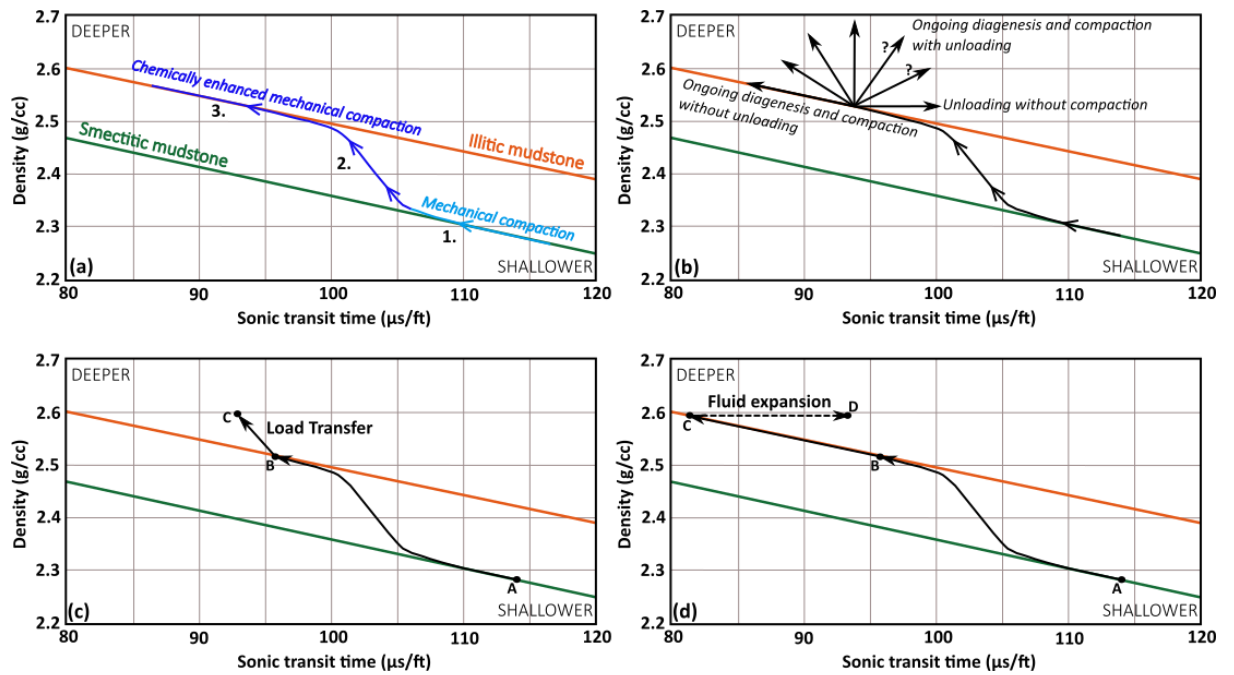


Figure 8.11. (a) Interpretation of the mudstone compaction trend (arrowed curve) on a sonic-density crossplot based on results presented in this thesis. Numbers correspond to three stages of mudstone compaction displayed on Figure 8.9. The green and orange lines are Dutta's (2002) trends for smectite-rich and illite-rich mudstones, respectively. (b) The fan of arrows illustrates possible depth trends for a specific mudstone lithology undergoing diagenesis accompanied by unloading. Different models of velocity-stress and density-velocity dependence of mudstones during illitization is displayed on the bottom figures. Letters show the evolutionary pathway of an arbitrary chosen mudstone bed reaching the same density/porosity value (c) via load transfer and (d) via fluid expansion. Refer to text for more explanation.

The use of sonic vs density crossplot in pore pressure interpretation was originally introduced by Dutta (2002). He identified two bounding linear compaction trends, one for early mechanical compaction of smectite-rich mudstones, and one for the compaction of diagenetically altered illitic mudstones. Diagenesis causes an increase in bulk density for a given transit time and shifts the overall compaction trend of a given mudstone from the smectitic trend towards the illitic trend (see 2.7.1), resulting in the overall sigmoidal shape of the normal compaction trend in sonic-density space (Figure 8.11). In view of new evidence presented in this thesis about the nature of the chemical compaction process (see 8.3), the following interpretation can be given for the three sections of the mudstone compaction curve on a sonic-density crossplot. The first section of the curve corresponds to mechanical compaction and to the first stage of mudstone compaction displayed one

on Figure 8.9; the steep second section corresponds to the main stage of smectite illitization at temperatures in the range of $\sim 70\text{-}100^\circ\text{C}$ and to the second stage of mudstone compaction displayed on Figure 8.9; and the third section corresponds to continued chemically enhanced mechanical compaction at temperatures above $\sim 100^\circ\text{C}$ and to the third stage of mudstone compaction displayed on Figure 8.9 (Figure 8.11a). Clay diagenetic reactions are kinetic in nature thus depend on both temperature and time, so the onset of the steep transitional section of the compaction curve would be displaced to greater sonic travel time and lower density in a basin with a higher geothermal gradient or a slower burial rate, and vice versa.

The fundamental assumption underlying the pore pressure prediction method of Sargent et al. (2015) and Goult and Sargent (2016) is that there is a unique, linear sonic-density trend for mudstones of a given lithology on the third section of the compaction curve, for temperatures above 100°C , provided that they are not unloaded, and mudstones which fall on this linear late diagenetic compaction curve are at the maximum vertical effective stress they have experienced. That assumption permits estimation of the amount of unloading overpressure present in the mudstones using Bowers' (2001) unloading relation (C Sargent et al., 2015). The limitation is that the maximum effective stress experienced by the mudstones must be estimated in an independent operation.

As it was shown in 2.7, unloading (reduction in effective stress) can result from fluid expansion. In such cases porosity only increases slightly due to elastic rebound, while velocity reduces significantly and an increase in effective stress after unloading should result in a return to the virgin compaction curve via a reloading pathway (Bowers, 1995, 2001). This behaviour is illustrated on Figure 8.11d. According to Lahann et al. (2001), Katahara (2006) and Lahann and Swarbrick (2011) the observed increase in density within the unloading-reloading interval that is associated with the velocity reduction due to smectite illitization is not consistent with a fluid expansion mechanism, as poro-elastic behaviour should lead to a small or no decrease in density. Katahara (2006) suggested that unloading which occurs because of the illitization reaction is inelastic, because it involves dissolution and shrinking of some load bearing mineral grains. According to this model smectite illitization can entail contraction of the yield surface –on a mean stress - shear stress diagram— such that the resulting stress state remains on the yield surface

even if the effective stress decreases (Katahara, 2006). This has the consequence that the mudstone is allowed to be on a unique stress-velocity trend and on a unique velocity-density trend during illitization. Lahann and Swarbrick (2011) suggested that this interpretation is consistent with unloading due to framework weakening and load transfer (see 2.7.2). This behaviour is illustrated on Figure 8.11c. However Katahara (2006) also suggested that the kind of interpretation which uses the combination of the elements of these two models (inelastic unloading/load transfer plus elastic unloading/fluid expansion) might be closer to the truth. This interpretation is illustrated on Figure 8.11b.

Observations presented in this thesis from Cretaceous mudstones on the Halten Terrace, offshore mid-Norway (Chapter 5) suggest that unloading is a direct result of clay mineral diagenesis and concomitant fabric destabilisation, due to the local transfer of load from dissolving detrital clay grains to fluid. Pore pressure is then a function of the rate at which it is generated by clay mineral diagenesis (and other mechanisms such as disequilibrium compaction) and the rate at which it is dissipated by compaction and fluid flow. This interpretation is consistent with load transfer as proposed by Lahann and Swarbrick (2011). However, without independent geomechanical evidence the observations made from Cretaceous mudstones on the Halten Terrace, offshore mid-Norway (Chapter 5) on their own, cannot prove the validity of an inelastic unloading model as proposed by Katahara (2006).

More recently Dutta et al. (2014) and Dutta (2016) presented a generalised compaction model for mudstones (refer to 2.7.2) which is applicable in the diagenetic regime. Similarly Yang and Aplin's (2004) compaction model could be modified to incorporate a temperature dependent term accounting for the effects of mineral diagenesis. The data presented in this thesis could potentially serve as the basis for such an empirical model, however much more well-characterized data is needed from mudstone samples buried into the diagenetic regime in well known basin settings where there is enough information regarding burial and pore pressure history. Nevertheless, this method would still have the disadvantage of not being able to account for overpressure generated by unloading.

8.5 Project conclusions

This thesis details the combined analysis of mudstone sample material and wireline log data to evaluate the role of clay mineral diagenesis on porosity loss and overpressure generation in siliciclastic mudstones.

It has been demonstrated that clay diagenesis has a considerable effect on the physical properties of siliciclastic mudstones, with important implications for pore pressure prediction. The dominant clay mineral reaction, the conversion of smectite to illite, involves a series of dissolution and reprecipitation reactions which results in a significant change in the orientation of the whole clay fabric; not only illite-smectite but also kaolinite and chlorite.

New evidence was presented from Miocene mudstones in the Central Malay Basin which showed that illitization during ongoing compaction results in anomalously low porosity compared to solely mechanical compaction. In addition to this, these diagenetically mature, illitized mudstones continue to compact mechanically with increasing effective stress at temperatures above 100°C.

Observations presented in this thesis from Cretaceous mudstones on the Halten Terrace, offshore mid-Norway showed clear evidence for chemical compaction (porosity loss/sediment volume reduction) associated with smectite illitization. Although chemical compaction associated with clay diagenesis is not a new idea, this is the first time it has been demonstrated in a single mudstone formation from several lines of evidence (measured physical, textural, mineralogical properties, plus wireline log responses). Coincident with clay mineral diagenesis, pore pressure data from the Cretaceous in Haltenbanken clearly indicate that pore pressure increased, and effective stress decreased (“unloading”) during the illitization process. This suggests that the unloading is a direct result of clay mineral diagenesis and concomitant fabric destabilisation, due to the local transfer of load from dissolving detrital clay grains to fluid. Pore pressure is then a function of the rate at which it is generated by clay mineral diagenesis (and other mechanisms such as disequilibrium compaction) and the rate at which it is dissipated by compaction and fluid flow. Quantification of the pore pressure response to clay mineral diagenesis remains a key question.

New evidence presented from Cretaceous-Tertiary mudstones in the Sergipe-Alagoas Basin, offshore Brazil showed that illitization of smectite results in enhanced porosity loss in hydrostatically pressured mudstones.

Further evidence was shown from diagenetically mature Triassic mudstones in the North Sea Central Graben which suggests that illitization during ongoing compaction results in anomalously low porosity compared to solely mechanical compaction. Porosity reduction appears to have taken place even as the effective stress reduced while pore pressure increased due to disequilibrium compaction.

These results are evidence that tends to refute the stress-independent chemical compaction model for diagenetically altered mudstones at temperatures above $\sim 100^{\circ}\text{C}$, and supports the chemically-enhanced mechanical compaction model (Dutta, 2002; Lahann, 2002). A key question that remains is how to quantify the contributions of increasing effective stress and diagenesis to porosity reduction in mudstones at these higher temperatures.

8.6 Recommendations for future work

This study utilised a wide variety of rock property analyses to study the compaction properties of natural mudstone samples. The remaining sample material used as part of this study is currently stored in the Department of Earth Sciences at Durham University. Although the main research objectives set out in this thesis have been achieved, many questions and avenues of research have arisen which could not be answered in the given time constraint of the project. Recommendation for future investigations based on the remaining unanswered questions are outlined in the below section.

- Analysis of diagenetic change in the Central Malay Basin would be improved through further quantitative XRD analysis of the clay fraction, along with measurements of physical properties in shallower sections of the Formation E mudstones from other wells, similar to Bravo-Y.
- Analysis of mudstone samples from the Central Malay Basin Bravo-X well and from additional wells would improve our understanding of the role played by the mineralogy on affecting the physical properties of these mudstones.

- Analysis of samples from the depth intervals of the anomalous “high velocity layers” in the Central Malay Basin wells would help to unravel nature of these mudstone layers.
- Focused ion beam (FIB SEM) techniques could allow better interpretation of the textural features of Cretaceous mudstone samples from the Halten Terrace, offshore mid-Norway.
- TEM analysis of Cretaceous mudstone samples from the Halten Terrace, offshore mid-Norway could provide additional evidence for a link between illite-smectite ordering and clay mineral alignment.
- BSEM and HRXTG analysis of the Sergipe mudstone samples would allow interpretation of the textural features and would improve our understanding of the role played by the mineralogy on affecting the physical properties of these mudstones.
- TEM analysis of the Sergipe mudstone samples would improve our understanding of the diagenetic changes and would help to unravel the nature of the observed illitization profiles.
- Ultimate test of the role played by the effective stress in the realignment of the clay mineral fabric during diagenesis would be BSEM, HRXTG and TEM analysis of mudstone samples from tectonic/compressional regimes where the magnitude of the horizontal stress surpasses the magnitude of vertical/overburden stress. Such observations would further test the validity chemically enhanced mechanical compaction model proposed in this thesis.
- Experimental modelling and laboratory experiments of clay mineral diagenesis in mudstone samples would greatly enhance our knowledge of how diagenesis affects the geomechanical properties of siliciclastic mudstones.
- Data presented in this thesis could serve as a basis for a modified version of Yang and Aplin's (2004) compaction model which incorporates the effect of temperature and mineral diagenesis.

Appendix I

Bulk QXRD and CEC data

| Sample | Well | Depth below seafloor (m) | Quartz | Plagioclase | K-feldspar | Calcite | Dolomite | Siderite | Pyrite | Anatase | Barite | Halite | Sylvite |
|--------|---------|--------------------------|--------|-------------|------------|---------|----------|----------|--------|---------|--------|--------|---------|
| XL1 | Bravo-L | 1525,5 | 33,3 | 2,9 | 0,6 | 0 | 0 | 7,6 | 0,2 | 0,1 | 1,9 | 0,1 | |
| XL2 | Bravo-L | 1620,5 | 36,6 | 2,3 | 0,8 | 0,1 | 0 | 9 | 0,1 | 0,1 | 3,4 | 0,1 | |
| XL3 | Bravo-L | 1765,5 | 41,4 | 1,4 | 0,5 | 0 | 1,3 | 7,5 | 0,4 | 0,2 | 0,8 | 0 | |
| XL4 | Bravo-L | 1865,5 | 34,1 | 2,7 | 1 | 0 | 0,1 | 4,6 | 1,7 | 0,2 | 2,6 | 0 | |
| XL5 | Bravo-L | 1930,5 | 34,2 | 4,1 | 0,4 | 0 | 0,2 | 8,8 | 0,3 | 0,2 | 2,1 | 0 | |
| XL6 | Bravo-L | 2000,5 | 31,4 | 5,1 | 0 | 0 | 3,3 | 4,8 | 0,6 | 0,1 | 1,2 | 0 | |
| XM1 | Bravo-Y | 1460,5 | 43,3 | 5,8 | 2 | 1,4 | 0 | 6,6 | 0,4 | 0,3 | 2 | | 0 |
| XM2 | Bravo-Y | 1515,5 | 35,9 | 3,6 | 1,8 | 0,6 | 0 | 9,7 | 0 | 0,3 | 1,2 | | 0 |
| XM3 | Bravo-Y | 1633,0 | 42,9 | 3,1 | 0,9 | 0,6 | 0 | 9,1 | 0 | 0,5 | 1,5 | | 0 |
| XM4 | Bravo-Y | 1683,0 | 38,8 | 1,9 | 0,9 | 0,5 | 0 | 7,7 | 0,1 | 0,4 | 1,1 | | 0,1 |
| XM5 | Bravo-Y | 1725,5 | 44,4 | 3,5 | 1,8 | 0,3 | 0 | 8,4 | 0 | 0,1 | 0,8 | | 0 |
| XM6 | Bravo-Y | 1755,5 | 42,8 | 2,5 | 0,7 | 0,2 | 0 | 7 | 0,8 | 0,4 | 0,4 | | 0 |
| XM7 | Bravo-Y | 1865,5 | 37,6 | 2 | 0,9 | 0,9 | 0 | 9,6 | 0,7 | 0,3 | 1,7 | | 0 |
| XM8 | Bravo-Y | 1945,5 | 46,9 | 3,8 | 0,9 | 0,8 | 0,5 | 11,6 | 0,7 | 0,3 | 2,2 | | 0,1 |
| XM9 | Bravo-Y | 2015,5 | 39 | 4,7 | 0,9 | 0,9 | 2,9 | 7,4 | 0,6 | 0,4 | 1,4 | | 0 |
| XM10 | Bravo-Y | 2090,5 | 43,7 | 6,1 | 0,9 | 0,7 | 0,7 | 11 | 0,5 | 0 | 2,1 | | 0 |

| Sample | Well | Depth below seafloor (m) | Gypsum | Hematite+ Goethite | Muscovite | I-I/S-ML | I-I/S | Chlorite | Kaolinite | Total | H2O@200 (mg/g) | CEC (meq/100g) | Calculated smectite equivalent in I/S (%) |
|--------|---------|--------------------------|--------|--------------------|-----------|----------|-------|----------|-----------|-------|----------------|----------------|---|
| XL1 | Bravo-L | 1525,5 | | | 9,7 | 32,4 | | 1 | 10,4 | 100 | | | |
| XL2 | Bravo-L | 1620,5 | | | 7,4 | 28,8 | | 0,2 | 11,2 | 100 | | | |
| XL3 | Bravo-L | 1765,5 | | | 10,5 | 21,4 | | 0 | 14,7 | 100 | | | |
| XL4 | Bravo-L | 1865,5 | | | 10,9 | 30,6 | | 0 | 11,4 | 100 | | | |
| XL5 | Bravo-L | 1930,5 | | | 11,4 | 28,2 | | 0,4 | 9,5 | 100 | | | |
| XL6 | Bravo-L | 2000,5 | | | 11,7 | 31,9 | | 0 | 9,7 | 100 | | | |
| XM1 | Bravo-Y | 1460,5 | 0 | 0,1 | | | 25,5 | 2,2 | 10,3 | 99,9 | 16,0 | | |
| XM2 | Bravo-Y | 1515,5 | 0 | 0,4 | | | 36,8 | 0,9 | 8,9 | 100,1 | 24,9 | 10,7 | 28,1 |
| XM3 | Bravo-Y | 1633,0 | 0,1 | 0,2 | | | 27,8 | 1,5 | 12,1 | 100,3 | 13,3 | 6,2 | 20,8 |
| XM4 | Bravo-Y | 1683,0 | 0 | 0 | | | 34,2 | 1,4 | 12,9 | 100 | 9,1 | 9,3 | 26,0 |
| XM5 | Bravo-Y | 1725,5 | 0,5 | 0,3 | | | 28,4 | 0,7 | 10,7 | 99,9 | 11,3 | 5,4 | 18,0 |
| XM6 | Bravo-Y | 1755,5 | 0,8 | 0 | | | 30,2 | 1,3 | 12,9 | 100 | 9,8 | 7,2 | 22,5 |
| XM7 | Bravo-Y | 1865,5 | 0,4 | 0 | | | 38,3 | 0,7 | 6,9 | 100 | 12,9 | 7,8 | 19,7 |
| XM8 | Bravo-Y | 1945,5 | 0,7 | 0 | | | 23,6 | 0,5 | 7,2 | 99,8 | 13,3 | 9,4 | 39,0 |
| XM9 | Bravo-Y | 2015,5 | 0 | 0 | | | 32,6 | 0,4 | 8,9 | 100,1 | 13,0 | 7,2 | 21,1 |
| XM10 | Bravo-Y | 2090,5 | 0 | 0 | | | 25,5 | 1,3 | 7,3 | 99,8 | 12,0 | 10,1 | 38,5 |

Table 1.1 Bulk QXRD and CEC data for the Central Malay Basin samples.

| Sample | Well | Depth below seafloor (m) | Quartz | Kspar | Plagioclase | Calcite | Mg-Calcite | Dolomite | Halite | Sylvite | Pyrite/Marcasite | Siderite | Barite | Anhydrite | Ankerite | Gypsum | Opal C |
|--------|------------|--------------------------|--------|-------|-------------|---------|------------|----------|--------|---------|------------------|----------|--------|-----------|----------|--------|--------|
| XC-7 | 6406/2-3 | 3054,0 | 35,8 | 1,3 | 9,2 | 0,6 | | | | 0 | 1,5 | 0,2 | 11,3 | | | 0 | 0 |
| XC-8 | 6406/2-3 | 3254,0 | 28,6 | 1,5 | 8,2 | 1,4 | | | | 0 | 1,6 | 1,7 | 10,6 | | | 0 | 0 |
| XC-9 | 6406/2-3 | 3454,0 | 27,9 | 0,6 | 9,9 | 1,1 | | | | 0 | 1,1 | 1,3 | 11,4 | | | 0 | 0 |
| XC-10 | 6406/2-3 | 3655,0 | 22,7 | 0 | 6,2 | 0,8 | | | | 0,1 | 1 | 1,2 | 13,2 | | | 0 | 0 |
| XC-11 | 6406/2-3 | 3790,0 | 28,4 | 0 | 7,6 | 2,2 | | | | 0 | 0,6 | 1,5 | 16,9 | | | 0,2 | 0 |
| XKC-1 | 6406/2-3 | 3986,0 | 6,9 | 0,6 | 5,8 | 0,1 | 0,1 | 0 | 0 | | 1,2 | 0 | 0,1 | 0,3 | 0,3 | 0,2 | |
| XKC-2 | 6406/2-3 | 4002,7 | 8,2 | 0 | 3,6 | 0,4 | 0,4 | 0 | 0,6 | | 2,6 | 0 | 0 | 0,3 | 0,1 | 0,5 | |
| XKC-18 | 6406/2-3 | 4010,8 | 18,7 | 0,1 | 7,3 | 0,1 | 0 | 0 | 0 | | 1,7 | 0 | 0 | 0,1 | 0 | 0,1 | |
| XKC-3 | 6406/2-3 | 4020,0 | 23,9 | 0 | 9,4 | 0,2 | 0 | 0 | 0,1 | | 0,9 | 0,3 | 0 | 0 | 0 | 0,4 | |
| XKC-4 | 6406/2-3 | 4025,9 | 18,6 | 0,5 | 7,1 | 0 | 0 | 0,1 | 0 | | 1,2 | 0 | 0 | 0 | 0 | 0 | |
| XC-12 | 6406/2-3 | 4078,0 | 21,8 | 0 | 7,3 | 0,6 | | | | 0,1 | 0,9 | 3,1 | 12,5 | | | 0 | 0 |
| XC-13 | 6406/2-3 | 4218,0 | 13,5 | 0 | 2,9 | 1,5 | | | | 0 | 1,4 | 2,8 | 21,9 | | | 0 | 0,5 |
| XK-1 | 6407/10-2 | 2051,0 | 33,1 | 2,7 | 4 | 3,3 | 0,7 | 0 | 0 | | 1,1 | 1,7 | 6,3 | 0 | 0,3 | 0 | |
| XK-7 | 6407/10-2 | 2246,0 | 17,1 | 1,8 | 6,1 | 4,8 | 0,2 | 0,5 | 0 | | 0 | 0,7 | 4,5 | 0,1 | 0,5 | 0,2 | |
| XK-2 | 6407/10-2 | 2386,0 | 11,2 | 0,1 | 2,9 | 1,3 | 1,7 | 0 | 0,2 | | 1,2 | 1,4 | 3,8 | 0,5 | 1 | 0,3 | |
| XK-3 | 6506/11-2 | 3350,0 | 24,3 | 2,7 | 7,7 | 1,1 | 0,3 | 0,2 | 0,8 | | 0,9 | 0,2 | 1,2 | 0,1 | 0,1 | 0 | |
| XK-8 | 6506/11-2 | 3500,0 | 26,2 | 4,2 | 8,7 | 1 | 0,9 | 0 | 0 | | 0,1 | 0 | 2 | 0 | 0,5 | 0,1 | |
| XK-4 | 6506/11-2 | 3698,0 | 32,9 | 3,1 | 9,2 | 0,8 | 1,8 | 0 | 0 | | 0,2 | 0 | 2,1 | 0 | 0,8 | 0,4 | |
| XK-6 | 6506/11-2 | 3791,0 | 19,8 | 1,8 | 9,7 | 0,6 | 0,4 | 0 | 0 | | 0,9 | 0 | 2,3 | 0 | 0,7 | 0 | |
| XK-5 | 6506/11-2 | 3815,0 | 11,7 | 3 | 5,6 | 6,2 | 0,5 | 0,1 | 0 | | 1,4 | 0,4 | 4,1 | 0,2 | 0,6 | 0,2 | |
| XKC-14 | 6506/11-3 | 2795,4 | 25,6 | 4,2 | 8,1 | 0,4 | 0 | 0 | 0 | | 1,7 | 0 | 0,4 | 0 | 0,1 | 0,3 | |
| XKC-16 | 6506/11-3 | 3592,5 | 16,6 | 0 | 6,1 | 0 | 0 | 0 | 0 | | 5,4 | 0,1 | 0,1 | 0,5 | 0 | 0 | |
| XKC-15 | 6506/11-3 | 3637,5 | 22,4 | 0 | 6,8 | 0,1 | 0,4 | 0 | 0,1 | | 3 | 0,1 | 0 | 0,5 | 0 | 0,1 | |
| XKC-12 | 6506/11-4S | 3959,8 | 26,9 | 0,5 | 5,9 | 0,1 | 0,4 | 0,1 | 0,5 | | 2,5 | 0,5 | 0,4 | 0,5 | 0,1 | 0,2 | |
| XKC-13 | 6506/11-4S | 3964,9 | 23,4 | 0 | 4,1 | 0 | 0 | 0 | 0 | | 0 | 0 | 0 | 0 | 0 | 0 | |
| XKC-11 | 6506/3-1 | 2765,6 | 23,5 | 4,1 | 7,2 | 0,1 | 0 | 0,1 | 0 | | 1,2 | 0,2 | 0,2 | 0,2 | 0,9 | 0,2 | |
| XKC-10 | 6506/3-1 | 2786,8 | 25,1 | 3,1 | 8,6 | 0,1 | 0,2 | 0,1 | 0,1 | | 0,1 | 0,2 | 0,3 | 0,1 | 0,1 | 0,2 | |
| XKC-6 | 6507/2-3 | 2501,8 | 19,5 | 2,6 | 5,8 | 0,2 | 0 | 0 | 0 | | 3 | 0 | 0,4 | 0 | 0 | 0 | |
| XKC-7 | 6507/2-3 | 2505,8 | 17,6 | 1,1 | 4,2 | 0,2 | 0,7 | 0 | 0 | | 2,1 | 0,1 | 0,4 | 0,2 | 0,1 | 0,2 | |
| XKC-5 | 6507/2-3 | 2507,6 | 16,6 | 1,9 | 4,3 | 0,6 | 0,2 | 0 | 0 | | 3 | 0 | 0,8 | 0 | 0,2 | 0,2 | |
| XKC-8 | 6507/2-3 | 2878,6 | 16,3 | 0,1 | 5,8 | 0,3 | 0 | 0 | 0 | | 0 | 3,7 | 0 | 0,1 | 0,1 | 0,6 | |
| XC-1 | 6507/6-2 | 2332,0 | 29,4 | 2 | 6,6 | 2,4 | | | | 0,7 | 2,8 | 1,2 | 2,8 | | | 0,9 | 0 |
| XC-2 | 6507/6-2 | 2442,0 | 37,1 | 6,8 | 4,6 | 1,8 | | | | 0,7 | 0,8 | 3,1 | 2,7 | | | 0,1 | 0 |
| XC-3 | 6507/6-2 | 2537,0 | 22,1 | 2,8 | 5,6 | 1,2 | | | | 0,6 | 0,7 | 8,5 | 4,4 | | | 0 | 0 |
| XC-4 | 6507/6-2 | 2637,0 | 30,9 | 3,5 | 4,7 | 12,3 | | | | 0,5 | 0,1 | 1,1 | 3,5 | | | 0 | 0 |
| XC-5 | 6507/6-2 | 2747,0 | 17,1 | 1,5 | 6,6 | 3,3 | | | | 0,1 | 0,4 | 1,9 | 6,7 | | | 0 | 0 |
| XC-6 | 6507/6-2 | 2812,0 | 23,9 | 2,4 | 4,1 | 4 | | | | 0,1 | 0,2 | 4,8 | 10,8 | | | 0 | 0 |
| XKC-9 | 6607/5-1 | 3016,0 | 29,7 | 3,6 | 10,9 | 0,2 | 0,7 | 0 | 0 | | 0,3 | 0 | 0,5 | 0,5 | 0,4 | 0,7 | |
| XKC-17 | 6607/5-1 | 3017,4 | 21,3 | 3,7 | 7,8 | 0,5 | 0,4 | 0 | 0,6 | | 0,7 | 0 | 0,4 | 0,3 | 0 | 0,1 | |

| Sample | Well | Depth below seafloor (m) | Sulphates | Fe (oxy-) hydroxide | Brucite | Fluoro-apatite | Anatase | Al (oxy-) hydroxide | Fluorite | Kaolin | 2:1 Al Clay | 2:1 Fe Clay | Fe Chlorite | Tri 1:1 Clay | Total | CEC (meq/100g) | Calculated smectite equivalent in I/S (%) |
|--------|------------|--------------------------|-----------|---------------------|---------|----------------|---------|---------------------|----------|--------|-------------|-------------|-------------|--------------|-------|----------------|---|
| XC-7 | 6406/2-3 | 3054,0 | | 0,2 | | | 0,4 | | | 6,8 | 28,8 | | 4 | | 100,1 | 14,13 | 47,9 |
| XC-8 | 6406/2-3 | 3254,0 | | 1,3 | | | 0,8 | | | 7,4 | 32,3 | | 4,6 | | 100 | 12,43 | 37,4 |
| XC-9 | 6406/2-3 | 3454,0 | | 1,1 | | | 0,9 | | | 8,7 | 31 | | 4,9 | | 99,9 | 12,72 | 39,7 |
| XC-10 | 6406/2-3 | 3655,0 | | 1,6 | | | 0,9 | | | 11,2 | 36,8 | | 4,4 | | 100,1 | 13,76 | 36,1 |
| XC-11 | 6406/2-3 | 3790,0 | | 1,7 | | | 0,8 | | | 7,7 | 27 | | 5,5 | | 100,1 | 11,97 | 42,9 |
| XKC-1 | 6406/2-3 | 3986,0 | 0 | 0,3 | 0 | 0,9 | 0,7 | 0 | 0 | 8,7 | 67,3 | 0 | 6,3 | 0 | 99,8 | 10,67 | 15,9 |
| XKC-2 | 6406/2-3 | 4002,7 | 0 | 0,4 | 0 | 0,6 | 1,1 | 0 | 0 | 24,6 | 49,9 | 0 | 6,7 | 0 | 100 | 12,75 | 25,6 |
| XKC-18 | 6406/2-3 | 4010,8 | 0,3 | 0,7 | 0 | 0,1 | 0,7 | 0 | 0 | 7,5 | 56,3 | 0 | 3,5 | 2,9 | 100,1 | 12,32 | 21,9 |
| XKC-3 | 6406/2-3 | 4020,0 | 0,1 | 0,5 | 0,5 | 0 | 0,6 | 0,3 | 0 | 9,9 | 48,8 | 0 | 4 | 0 | 99,9 | | |
| XKC-4 | 6406/2-3 | 4025,9 | 0 | 0,3 | 0 | 0 | 0,8 | 0,5 | 0 | 8,2 | 57,1 | 0 | 5,7 | 0 | 100,1 | 13,63 | 23,9 |
| XC-12 | 6406/2-3 | 4078,0 | | 1,3 | | | 0,8 | | | 11,9 | 34,3 | | 5,2 | | 99,8 | 9,93 | 27,5 |
| XC-13 | 6406/2-3 | 4218,0 | | 1,5 | | | 1,6 | | | 0,4 | 47 | | 4,8 | | 99,8 | 14,8 | 31,2 |
| XK-1 | 6407/10-2 | 2051,0 | 0 | 3 | 0,6 | 2,3 | 0,1 | 0,8 | 0,1 | 7 | 27,4 | 0 | 1,8 | 3,8 | 100,1 | 16,1 | 58,8 |
| XK-7 | 6407/10-2 | 2246,0 | 0 | 1,8 | 0 | 0 | 0 | 0 | 0 | 13,5 | 41,9 | 0 | 1,1 | 5 | 99,8 | 19,28 | 46,0 |
| XK-2 | 6407/10-2 | 2386,0 | 0 | 0,4 | 0 | 0 | 0,7 | 0 | 0 | 18 | 44,6 | 0 | 4,9 | 5,8 | 100 | 14,31 | 32,1 |
| XK-3 | 6506/11-2 | 3350,0 | 0 | 0,9 | 0 | 0,4 | 0,4 | 0 | 0 | 10,6 | 36,7 | 0 | 5 | 6,5 | 100,1 | 13,22 | 36,0 |
| XK-8 | 6506/11-2 | 3500,0 | 0 | 1,7 | 0 | 0,7 | 0,3 | 0 | 0 | 5,6 | 39,8 | 0 | 3,1 | 5,1 | 100 | 5,94 | 14,9 |
| XK-4 | 6506/11-2 | 3698,0 | 0 | 1,7 | 0 | 1,4 | 0,6 | 0 | 0 | 4,9 | 31,7 | 0 | 4,9 | 3,5 | 100 | 5,24 | 16,5 |
| XK-6 | 6506/11-2 | 3791,0 | 0 | 1,1 | 0 | 0 | 0,4 | 0 | 0 | 4,2 | 52,5 | 0 | 2,3 | 3,3 | 100 | 6,52 | 12,4 |
| XK-5 | 6506/11-2 | 3815,0 | 0 | 0,8 | 0 | 1,1 | 0,7 | 0 | 0 | 6,6 | 50,2 | 0 | 3,9 | 2,7 | 100 | 6,89 | 13,7 |
| XKC-14 | 6506/11-3 | 2795,4 | 0 | 0,9 | 0 | 0,4 | 0,5 | 0 | 0 | 10,5 | 43,4 | 0 | 3,3 | 0 | 99,8 | 15,95 | 36,8 |
| XKC-16 | 6506/11-3 | 3592,5 | 0,6 | 1,1 | 0 | 0 | 0,8 | 0 | 0 | 14,3 | 47,3 | 0 | 7,1 | 0 | 100 | 13,34 | 28,2 |
| XKC-15 | 6506/11-3 | 3637,5 | 0 | 0,3 | 0 | 0,1 | 1 | 0 | 0 | 17 | 42,7 | 0 | 5,2 | 0 | 99,8 | 11,84 | 27,7 |
| XKC-12 | 6506/11-4S | 3959,8 | 0,4 | 0,2 | 0,3 | 0,5 | 0,6 | 0,9 | 0 | 20,3 | 31,4 | 0 | 7 | 0 | 100,2 | 9,39 | 29,9 |
| XKC-13 | 6506/11-4S | 3964,9 | 0 | 0,3 | 0 | 0 | 0 | 0 | 0 | 4,3 | 44,9 | 0 | 6,4 | 16,6 | 100 | 15,4 | 34,3 |
| XKC-11 | 6506/3-1 | 2765,6 | 0,8 | 1 | 0 | 0,9 | 0,7 | 0 | 0 | 13,7 | 39,5 | 0 | 5,4 | 0 | 99,9 | 16,49 | 41,7 |
| XKC-10 | 6506/3-1 | 2786,8 | 0 | 0,3 | 0 | 0,5 | 0,9 | 0 | 0 | 14 | 39,9 | 0 | 6 | 0 | 99,9 | 13,17 | 33,0 |
| XKC-6 | 6507/2-3 | 2501,8 | 2,2 | 1,1 | 0 | 0,6 | 0,4 | 0 | 0 | 21,1 | 41 | 0 | 2,1 | 0 | 100 | 13,24 | 32,3 |
| XKC-7 | 6507/2-3 | 2505,8 | 1 | 0,8 | 0 | 0,7 | 0,4 | 0 | 0 | 21,8 | 43,5 | 0 | 5 | 0 | 100,1 | 15,37 | 35,3 |
| XKC-5 | 6507/2-3 | 2507,6 | 3,1 | 0,9 | 0 | 0,7 | 0,4 | 0 | 0 | 21,1 | 41,4 | 0 | 4,5 | 0 | 99,9 | 15 | 36,2 |
| XKC-8 | 6507/2-3 | 2878,6 | 0,2 | 1,2 | 0,7 | 1,7 | 0,6 | 3,3 | 0 | 21,2 | 39,1 | 0 | 4,9 | 0 | 99,9 | 12,03 | 30,8 |
| XC-1 | 6507/6-2 | 2332,0 | | 1 | | | 0,4 | | | 9,8 | 35,9 | | 4,1 | | | 21,24 | 58,0 |
| XC-2 | 6507/6-2 | 2442,0 | | 0 | | | 0,5 | | | 20,3 | 17,9 | | 3,5 | | 99,9 | 12,12 | 63,7 |
| XC-3 | 6507/6-2 | 2537,0 | | 0 | | | 0,7 | | | 16,8 | 30,9 | | 5,7 | | 100 | 17,61 | 54,8 |
| XC-4 | 6507/6-2 | 2637,0 | | 0,4 | | | 0,5 | | | 12,7 | 26,2 | | 3,6 | | 100 | 16,15 | 59,8 |
| XC-5 | 6507/6-2 | 2747,0 | | 0 | | | 0,6 | | | 17,3 | 41 | | 3,5 | | 100 | 17,69 | 41,6 |
| XC-6 | 6507/6-2 | 2812,0 | | 0 | | | 0,2 | | | 15,5 | 30,2 | | 3,6 | | 99,8 | 12,67 | 40,1 |
| XKC-9 | 6607/5-1 | 3016,0 | 0 | 1 | 0 | 0,4 | 0,6 | 0 | 0 | 9,7 | 36,4 | 0 | 4,6 | 0 | 100,2 | 12,78 | 35,1 |
| XKC-17 | 6607/5-1 | 3017,4 | 0,1 | 1,4 | 0 | 0,2 | 0,7 | 0 | 0 | 13,1 | 43,1 | 0 | 5,8 | 0 | 100,2 | 14,71 | 34,1 |

Table 1.2 Bulk QXRD and CEC data for the Haltenbanken mudstone samples

| Sample | Well | Depth below seafloor (m) | Quartz w% | Plagioclase w% | K-fspar w% | Calcite w% | Mg-Calcite | Dolomite w% | Siderite w% | Ankerite | Pyrite w% | Anatase w% | Barite w% | Jarosite w% | Gypsum w% | Anhydrite | Halite w% | Fe (oxy-) hydroxide | Brucite | Amphibole | Flour Apatite | Muscovite w% | H/S-ML w% | 2:1 Al Clay (illite-smectite group) | Chlorite w% | Tri 1:1 Clay | Kaolinite w% | Total | CEC (meq/100g) | Calculated smectite equivalent in I/S (%) |
|--------|--------|--------------------------|-----------|----------------|------------|------------|------------|-------------|-------------|----------|-----------|------------|-----------|-------------|-----------|-----------|-----------|---------------------|---------|-----------|---------------|--------------|-----------|-------------------------------------|-------------|--------------|--------------|--------|----------------|---|
| ASA1 | Well A | 1026,00 | 20,40 | 4,60 | 3,10 | 37,60 | | 0,80 | 3,60 | | 1,80 | 0,00 | 0,00 | 0,00 | trace | | 0,10 | | | | | 1,70 | 23,40 | | 1,60 | | 1,40 | 100,00 | 13,60 | 57,74 |
| ASA2 | Well A | 1098,00 | 21,10 | 4,80 | 3,70 | 23,20 | | 1,00 | 5,20 | | 1,40 | 0,00 | 0,30 | 0,00 | trace | | trace | | | | | 0,50 | 32,20 | | 2,50 | | 4,10 | 100,00 | 16,40 | 50,32 |
| ASA3 | Well A | 1245,00 | 23,60 | 4,30 | 2,90 | 9,50 | | 0,30 | 3,00 | | 1,10 | 0,00 | 0,00 | 0,00 | 0,90 | | 0,30 | | | | | 3,10 | 38,80 | | 1,50 | | 10,60 | 100,00 | 18,90 | 47,78 |
| ASA4 | Well A | 1521,00 | 28,30 | 5,00 | 2,80 | 4,30 | | 0,40 | 1,30 | | 1,30 | 0,00 | 0,20 | 0,00 | 3,20 | | 0,00 | | | | | 3,50 | 35,70 | | 2,60 | | 11,50 | 100,00 | 18,40 | 50,36 |
| ASA5 | Well A | 1776,00 | 25,70 | 5,60 | 3,30 | 3,30 | | 0,00 | 2,60 | | 1,00 | 0,00 | 0,00 | 0,00 | 0,60 | | 0,20 | | | | | 3,20 | 43,10 | | 2,40 | | 9,00 | 100,00 | 24,50 | 56,05 |
| ASA6 | Well A | 1995,00 | 29,30 | 6,30 | 3,70 | 3,50 | | 0,40 | 3,10 | | 0,90 | 0,00 | 0,50 | 0,00 | 0,40 | | 0,00 | | | | | 3,60 | 36,20 | | 4,60 | | 7,40 | 100,00 | 18,90 | 51,22 |
| ASA7 | Well A | 2085,00 | 28,10 | 7,00 | 3,60 | 3,50 | | 0,30 | 3,90 | | 1,20 | 0,00 | 1,20 | 0,00 | 0,70 | | 0,00 | | | | | 3,80 | 35,70 | | 4,90 | | 6,10 | 100,00 | 17,20 | 47,25 |
| ASA8 | Well A | 2304,00 | 23,50 | 5,30 | 3,00 | 11,50 | | 0,90 | 7,80 | | 1,00 | 0,00 | 1,70 | 0,00 | 1,00 | | 1,00 | | | | | 2,80 | 32,80 | | 4,90 | | 2,80 | 100,00 | 17,10 | 51,43 |
| ASA9 | Well A | 2448,00 | 22,60 | 5,60 | 2,80 | 4,70 | | 0,40 | 4,60 | | 1,60 | 0,00 | 0,80 | 0,00 | 1,00 | | 0,70 | | | | | 2,70 | 40,60 | | 4,50 | | 7,20 | 100,00 | 21,60 | 52,34 |
| XSA-8 | Well A | 2465,80 | 17,60 | 5,60 | 4,00 | 1,00 | 0,00 | 0,00 | 0,00 | 0,00 | 0,50 | 0,40 | 0,00 | | 0,00 | 0,00 | 0,00 | 1,30 | 0,00 | 0,30 | 0,00 | | | 50,90 | 3,50 | | 14,90 | 100,00 | 29,21 | 56,11 |
| XSA-1 | Well A | 2466,40 | 21,00 | 6,10 | 4,50 | 1,00 | 0,10 | 0,00 | 0,30 | 0,00 | 0,20 | 0,20 | 0,00 | | 0,20 | 0,30 | 0,00 | 0,70 | 0,00 | 0,00 | 0,70 | | | | 44,30 | 4,70 | 15,60 | 99,90 | 26,73 | 58,57 |
| XSA-11 | Well A | 2467,60 | 22,80 | 4,80 | 3,70 | 0,50 | 0,60 | 0,00 | 0,30 | 0,10 | 1,50 | 0,40 | 0,00 | | 0,70 | 0,50 | 0,00 | 1,00 | 0,00 | 0,00 | 0,00 | | | 44,10 | 3,80 | | 15,20 | 100,00 | 26,29 | 58,06 |
| XSA-5 | Well A | 2471,00 | 24,90 | 6,00 | 3,80 | 0,20 | 1,40 | 0,00 | 0,30 | 0,00 | 1,80 | 0,00 | 0,00 | | 0,50 | 0,50 | 0,00 | 1,00 | 0,00 | 0,50 | 0,20 | | | 36,50 | 6,80 | | 15,60 | 100,00 | 23,67 | 62,13 |
| ASA10 | Well A | 2691,00 | 27,50 | 6,90 | 1,80 | 3,40 | | 0,30 | 3,60 | | 0,90 | 0,00 | 0,00 | 0,00 | trace | | 0,30 | | | | | 2,30 | 42,30 | | 5,20 | | 5,70 | 100,00 | 21,10 | 49,11 |
| ASA11 | Well A | 3012,00 | 33,30 | 8,40 | 2,50 | 3,60 | | 2,30 | 1,50 | | 1,20 | 0,00 | 0,00 | 0,00 | trace | | trace | | | | | 3,90 | 33,80 | | 4,60 | | 4,70 | 100,00 | 16,00 | 46,51 |
| ASA12 | Well A | 3270,00 | 40,90 | 8,40 | 2,30 | 4,40 | | 2,20 | 1,30 | | 1,00 | 0,00 | 1,40 | 0,00 | 0,40 | | trace | | | | | 3,50 | 26,80 | | 6,20 | | 1,30 | 100,00 | 9,40 | 34,24 |
| ASA13 | Well A | 3900,00 | 46,80 | 6,50 | 1,20 | 2,10 | | 2,70 | 1,40 | | 1,80 | 0,00 | 5,80 | 0,00 | 1,00 | | trace | | | | | 4,00 | 20,30 | | 6,40 | | 0,00 | 100,00 | 6,80 | 32,55 |
| ASC1 | Well C | 713,00 | 21,80 | 4,50 | 3,80 | 14,40 | | 2,20 | 0,80 | | 1,80 | 0,00 | 0,10 | 0,00 | 0,70 | | 0,20 | | | | | 1,20 | 37,30 | | 2,80 | | 8,50 | 100,00 | 18,70 | 49,23 |
| ASC2 | Well C | 971,00 | 18,60 | 3,60 | 3,20 | 13,20 | | 0,60 | 0,40 | | 3,80 | 0,00 | 0,10 | 2,20 | 1,70 | | 0,20 | | | | | 2,00 | 38,40 | | 1,80 | | 10,30 | 100,00 | 19,40 | 49,58 |
| ASC3 | Well C | 1181,00 | 19,60 | 4,30 | 2,90 | 11,60 | | 0,30 | 0,80 | | 1,10 | 0,10 | 0,30 | 0,00 | 1,10 | | 0,20 | | | | | 1,10 | 42,90 | | 1,80 | | 100,00 | 24,00 | 54,99 | |
| ASC4 | Well C | 1424,00 | 19,40 | 4,00 | 2,50 | 11,60 | | 0,30 | 0,90 | | 1,00 | 0,00 | 0,50 | 0,00 | 0,80 | | 1,10 | | | | | 2,00 | 40,20 | | 2,60 | | 13,10 | 100,00 | 25,50 | 62,26 |
| ASC5 | Well C | 1664,00 | 23,10 | 3,90 | 1,90 | 10,20 | | 0,20 | 0,70 | | 0,90 | 0,00 | 0,00 | 0,00 | 0,70 | | 0,70 | | | | | 1,40 | 41,20 | | 3,40 | | 11,80 | 100,00 | 25,60 | 61,03 |
| ASC6 | Well C | 1928,00 | 21,50 | 4,10 | 2,10 | 10,00 | | 0,00 | 1,20 | | 0,70 | 0,00 | 0,00 | 0,00 | 0,60 | | 0,60 | | | | | 2,50 | 44,30 | | 3,30 | | 9,20 | 100,00 | 26,40 | 58,75 |
| ASC7 | Well C | 2168,00 | 20,70 | 4,50 | 2,60 | 6,50 | | 0,20 | 1,20 | | 0,70 | 0,00 | 0,20 | 0,00 | 0,80 | | 1,10 | | | | | 1,80 | 47,90 | | 3,30 | | 8,40 | 100,00 | 28,10 | 57,93 |
| XSA-2 | Well C | 2347,90 | 30,50 | 3,40 | 2,10 | 9,80 | 5,80 | 0,40 | 0,00 | 0,40 | 1,00 | 0,00 | 0,00 | | 0,00 | 0,10 | 0,10 | 0,80 | 0,70 | 0,00 | 0,00 | | | 37,50 | 3,60 | | 3,60 | 99,80 | 25,31 | 66,34 |
| XSA-13 | Well C | 2352,60 | 27,30 | 5,40 | 7,10 | 2,10 | 2,30 | 0,00 | 0,00 | 0,50 | 1,10 | 0,00 | 0,00 | | 0,40 | 0,00 | 0,00 | 0,80 | 0,00 | 0,00 | 0,20 | | | 44,70 | 2,90 | | 5,20 | 100,00 | 34,28 | 75,81 |
| ASC8 | Well C | 2414,00 | 22,20 | 5,60 | 3,30 | 4,80 | | 0,40 | 0,50 | | 0,70 | 0,00 | trace | 0,00 | 0,70 | | 1,10 | | | | | 0,90 | 49,50 | | 4,90 | | 5,40 | 100,00 | 28,00 | 55,94 |
| XSA-10 | Well C | 2654,57 | 26,80 | 11,30 | 8,20 | 3,80 | 0,40 | 0,30 | 0,10 | 0,80 | 0,60 | 0,20 | 0,00 | | 0,00 | 0,00 | 0,00 | 1,20 | 0,00 | 0,00 | 0,00 | | | 36,00 | 5,20 | | 5,00 | 99,90 | 12,49 | 32,97 |
| XSA-3 | Well C | 2656,68 | 29,10 | 10,10 | 8,70 | 7,00 | 1,30 | 0,30 | 0,00 | 1,00 | 0,40 | 0,00 | 0,00 | | 0,20 | 0,20 | 0,10 | 0,70 | 0,00 | 0,00 | 0,00 | | | 33,10 | 6,20 | | 1,50 | 99,90 | 10,85 | 30,82 |
| ASC9 | Well C | 2675,00 | 24,10 | 7,70 | 4,10 | 9,00 | | 1,10 | 0,60 | | 0,80 | 0,00 | 0,40 | 0,00 | 0,70 | | 0,30 | | | | | 0,80 | 43,60 | | 5,30 | | 1,50 | 100,00 | 22,10 | 50,22 |
| XSA-9 | Well C | 2753,35 | 23,50 | 6,50 | 6,70 | 6,10 | 1,10 | 0,30 | 0,00 | 0,40 | 0,60 | 0,00 | 0,00 | | 0,00 | 0,00 | 0,00 | 1,10 | 0,00 | 0,00 | 0,00 | | | 44,30 | 6,80 | | 2,40 | 99,80 | 11,94 | 25,31 |
| XSA-6 | Well C | 2888,80 | 20,50 | 8,10 | 10,00 | 1,70 | 0,00 | 0,00 | 0,10 | 0,00 | 0,20 | 0,00 | 0,00 | | 0,00 | 0,00 | 0,00 | 0,60 | 0,00 | 0,00 | 0,10 | | | 51,60 | 4,70 | | 2,30 | 99,90 | 11,01 | 20,34 |
| XSA-7 | Well C | 2912,45 | 15,40 | 6,10 | 3,10 | 0,30 | 0,00 | 0,00 | 0,10 | 0,30 | 0,20 | 0,00 | 0,00 | | 0,10 | 0,20 | 0,00 | 0,40 | 0,00 | 0,00 | 0,20 | | | 63,50 | 6,10 | | 3,90 | 99,90 | 13,34 | 19,92 |
| ASC10 | Well C | 2948,00 | 26,20 | 8,50 | 3,50 | 9,50 | | 1,40 | 0,60 | | 0,90 | 0,10 | 0,10 | 0,00 | 0,30 | | 0,20 | | | | | 4,20 | 38,40 | | 5,40 | | 0,60 | 100,00 | 15,70 | 40,42 |
| ASC11 | Well C | 3110,00 | 25,40 | 7,40 | 3,60 | 6,90 | | 1,00 | 0,60 | | 0,70 | 0,10 | 0,00 | 0,00 | 0,40 | | 0,30 | | | | | 5,40 | 42,40 | | 5,70 | | 0,00 | 100,00 | 12,90 | 30,02 |
| ASD1 | Well D | 743,00 | 19,30 | 3,10 | 2,40 | 10,20 | | 0,20 | 0,70 | | 0,30 | 0,00 | 0,20 | 0,00 | 0,40 | | 0,10 | | | | | 2,60 | 50,90 | | 1,50 | | 8,20 | 100,00 | 25,30 | 49,13 |
| ASD2 | Well D | 983,00 | 28,00 | 3,60 | 2,80 | 10,80 | | 0,00 | 0,60 | | 0,30 | 0,10 | 0,70 | 0,00 | 0,00 | | 0,20 | | | | | 1,30 | 55,00 | | 1,30 | | 6,00 | 100,00 | 31,90 | 57,60 |
| ASD3 | Well D | 1289,00 | 17,60 | 3,50 | 2,60 | 8,10 | | 0,40 | 0,50 | | 0,70 | 0,00 | 0,00 | 0,00 | 0,00 | | 0,20 | | | | | 0,00 | 60,00 | | 2,30 | | 4,00 | 100,00 | 31,30 | 51,85 |
| ASD4 | Well D | 1496,00 | 21,20 | 5,60 | 4,50 | 4,70 | | 0,40 | 0,40 | | 0,40 | 0,00 | 0,20 | 0,00 | 0,10 | | 0,10 | | | | | 0,00 | 53,90 | | 3,40 | | 5,20 | 100,00 | 29,00 | 53,32 |
| ASD5 | Well D | 1769,00 | 26,20 | 6,50 | 3,40 | 12,60 | | 1,80 | 0,80 | | 0,70 | 0,10 | 0,70 | 0,00 | 2,10 | | 0,10 | | | | | 2,30 | 36,00 | | 4,00 | | 2,80 | 100,00 | 14,00 | 38,32 |
| ASD6 | Well D | 2009,00 | 33,50 | 6,60 | 2,90 | 7,20 | | 1,10 | 0,70 | | 1,10 | 0,00 | 0,10 | 0,00 | 0,40 | | 0,20 | | | | | 4,20 | 34,50 | | 5,40 | | 2,10 | 100,00 | 7,30 | 20,51 |
| ASD7 | Well D | 2390,00 | 42,60 | 15,30 | 11,60 | 16,90 | | 4,30 | 0,20 | | 0,60 | 0,00 | 0,10 | 0,00 | 0,00 | | 0,00 | | | | | 3,40 | 3,10 | | 1,90 | | 0,00 | 100,00 | 0,00 | |
| ASD8 | Well D | 2519,00 | 37,30 | 11,60 | 5,20 | 8,60 | | 6,80 | 0,70 | | 1,40 | 0,00 | 0,00 | 0,00 | 0,00 | | 0,10 | | | | | 1,70 | 22,00 | | 4,50 | | 0,00 | 100,00 | 3,50 | 15,30 |
| ASE1 | Well E | 1102,00 | 23,50 | 5,60 | 3,90 | 11,10 | | 0,40 | 0,70 | | 1,70 | 0,00 | 0,00 | 0,00 | 0,70 | | 0,10 | | | | | 3,20 | 35,40 | | 1,70 | | 11,90 | 100,00 | 20,20 | 55,91 |
| ASE2 | Well E | 1255,00 | 22,60 | 5,20 | 3,20 | 6,50 | | 0,20 | 0,60 | | 0,90 | 0,00 | 0,00 | 0,00 | 0,90 | | 0,60 | | | | | 2,60 | 40,00 | | 1,60 | | 15,10 | 100,00 | 23,80 | 58,25 |
| ASE3 | Well E | 1432,00 | 22,90 | 4,40 | 3,30 | 5,30 | | 0,10 | 0,60 | | 1,10 | 0,00 | 0,00 | 0,00 | 1,00 | | 0,20 | | | | | 3,80 | 43,20 | | 2,00 | | 12,00 | 100,00 | 20,20 | 45,79 |
| ASE4 | Well E | 1717,00 | 26,30 | 4,60 | 2,70 | 5,10 | | 0,00 | 0,90 | | 1,00 | 0,00 | 0,00 | 0,00 | 0,90 | | 0,40 | | | | | 4,00 | 41,10 | | 2,40 | | 10,50 | 100,00 | 20,40 | 48,69 |
| ASE5 | Well E | 2035,00 | 24,20 | 5,40 | 2,60 | 2,90 | | 0,10 | 2,40 | | 1,00 | 0,00 | 0,00 | 2,20 | 2,00 | | 0,60 | | | | | 2,20 | 43,20 | | 3,80 | | 7,10 | 100,00 | 21,90 | 49,94 |
| ASE6 | Well E | 2194,00 | 23,80 | 5,80 | 2,20 | 2,40 | | 0,10 | | | | | | | | | | | | | | | | | | | | | | |

| Sample | Well | Depthrelative to kelly bushing (m) | Quartz | Kspar | Plagioclase | Calcite | Mg- Calcite | Dolomite | Halite | Pyrite / Marcasite | Siderite | Barite | Anhydrite | Ankerite | Gypsum | Sulphates | Fe (oxy-) hydroxide |
|--------|-----------|------------------------------------|--------|-------|-------------|---------|-------------|----------|--------|--------------------|----------|--------|-----------|----------|--------|-----------|---------------------|
| XT-5 | 22/29-1 | 4592,75 | 20,80 | 2,40 | 0,00 | 0,40 | 0,00 | 0,00 | 0,00 | 9,00 | 0,10 | 0,20 | 0,20 | 0,00 | 1,00 | 0,00 | 1,60 |
| XT-4 | 22/29-1 | 4594,25 | 32,60 | 2,10 | 0,00 | 0,00 | 0,10 | 0,20 | 0,00 | 0,30 | 0,00 | 0,00 | 0,00 | 0,00 | 0,10 | 0,00 | 0,30 |
| XT-2 | 22/29-1 | 4599,73 | 13,90 | 2,00 | 0,20 | 0,00 | 0,50 | 0,00 | 0,20 | 0,30 | 1,40 | 0,10 | 0,00 | 0,20 | 0,30 | 0,00 | 0,10 |
| XT-3 | 22/29-1 | 4718,30 | 21,40 | 9,50 | 5,80 | 0,00 | 1,60 | 3,40 | 0,10 | 0,10 | 0,10 | 0,00 | 0,00 | 3,20 | 0,10 | 0,00 | 0,10 |
| XT-1 | 22/29-1 | 4761,49 | 9,30 | 12,20 | 0,60 | 0,00 | 1,40 | 0,00 | 0,10 | 0,60 | 0,10 | 0,60 | 0,10 | 0,00 | 0,00 | 0,00 | 2,70 |
| XT-6 | 30/2c-04 | 4791,44 | 7,80 | 8,50 | 10,10 | 0,10 | 0,30 | 0,00 | 0,10 | 0,30 | 0,50 | 0,00 | 0,00 | 0,10 | 0,10 | 0,00 | 0,80 |
| XT-7 | 30/2c-04 | 4807,58 | 8,40 | 14,20 | 4,10 | 0,00 | 1,20 | 0,00 | 0,20 | 0,20 | 0,90 | 0,10 | 0,10 | 0,10 | 0,20 | 0,00 | 0,40 |
| XT-15 | 30/2c-J07 | 4972,31 | 10,10 | 4,30 | 6,60 | 0,40 | 0,40 | 0,10 | 0,20 | 0,10 | 0,60 | 0,10 | 0,00 | 1,40 | 0,00 | 0,00 | 0,00 |
| XT-13 | 30/2c-J07 | 4973,02 | 18,00 | 4,90 | 3,10 | 0,00 | 0,50 | 24,30 | 0,40 | 1,50 | 0,00 | 0,10 | 0,00 | 16,80 | 0,10 | 0,00 | 0,50 |
| XT-14 | 30/2c-J07 | 4988,16 | 19,40 | 14,70 | 6,30 | 0,00 | 0,00 | 3,00 | 0,00 | 0,40 | 0,00 | 0,00 | 0,00 | 6,40 | 0,10 | 0,00 | 0,20 |
| XT-12 | 30/2c-J07 | 5009,97 | 13,60 | 7,90 | 7,20 | 0,00 | 0,10 | 2,60 | 0,10 | 3,40 | 0,00 | 0,00 | 0,00 | 4,50 | 0,30 | 0,00 | 0,80 |
| XT-10 | 30/7a-7 | 3460,80 | 6,00 | 5,00 | 6,40 | 0,10 | 0,80 | 0,00 | 0,60 | 0,40 | 0,20 | 0,20 | 0,20 | 0,30 | 0,50 | 0,00 | 1,00 |
| XT-11 | 30/7a-7 | 3489,00 | 6,70 | 6,40 | 6,60 | 0,10 | 0,80 | 0,00 | 0,00 | 0,10 | 0,80 | 0,00 | 0,10 | 0,30 | 0,10 | 0,00 | 0,00 |
| XT-8 | 30/7a-8 | 3556,90 | 5,90 | 21,40 | 6,30 | 0,00 | 2,60 | 0,20 | 0,00 | 0,00 | 0,00 | 0,40 | 0,10 | 0,30 | 0,50 | 0,00 | 0,20 |
| XT-9 | 30/7a-8 | 3633,45 | 9,40 | 11,50 | 2,60 | 0,10 | 2,00 | 0,00 | 0,00 | 1,20 | 0,20 | 0,00 | 0,00 | 0,40 | 0,40 | 0,00 | 5,00 |
| XT-16 | 6/3-1 | 3059,65 | 28,30 | 8,70 | 14,30 | 0,10 | 0,10 | 0,20 | 0,30 | 1,20 | 0,00 | 0,30 | 0,10 | 0,00 | 0,00 | 0,00 | 1,60 |

Table 1.4 Bulk QXRD and CEC data for the Central North SeaTriassic mudstone samples (Above and below).

| Sample | Well | Depthrelative to kelly bushing (m) | Brucite | Fluoroapatite | Anatase | Al (oxy-) hydroxide | Amphibole | Fluorite | Kaolin | 2:1 Al Clay | 2:1 Fe Clay | Fe Chlorite | Tri 1:1 Clay | SUM | CEC (meq/100g) | Calculated smectite equivalent in I/S (%) |
|--------|-----------|------------------------------------|---------|---------------|---------|---------------------|-----------|----------|--------|-------------|-------------|-------------|--------------|--------|----------------|---|
| XT-5 | 22/29-1 | 4592,75 | 0,00 | 0,00 | 1,00 | 0,00 | 0,00 | 0,00 | 27,50 | 33,20 | 0,00 | 2,50 | 0,00 | 99,90 | 4,03 | 9,73 |
| XT-4 | 22/29-1 | 4594,25 | 0,00 | 0,00 | 0,50 | 0,00 | 0,00 | 0,00 | 15,60 | 47,40 | 0,00 | 0,70 | 0,00 | 99,90 | 10,26 | 20,84 |
| XT-2 | 22/29-1 | 4599,73 | 0,00 | 0,00 | 0,70 | 0,00 | 0,00 | 0,00 | 17,70 | 58,40 | 0,00 | 3,80 | 0,00 | 99,80 | 10,21 | 16,23 |
| XT-3 | 22/29-1 | 4718,30 | 0,00 | 0,40 | 0,20 | 0,00 | 0,00 | 0,00 | 1,30 | 41,60 | 0,00 | 9,10 | 2,00 | 100,00 | 5,01 | 9,31 |
| XT-1 | 22/29-1 | 4761,49 | 0,00 | 0,00 | 0,00 | 0,00 | 0,00 | 0,00 | 1,10 | 56,90 | 0,00 | 10,50 | 3,80 | 100,00 | 7,28 | 10,24 |
| XT-6 | 30/2c-04 | 4791,44 | 0,00 | 0,00 | 0,10 | 0,00 | 0,00 | 0,00 | 0,70 | 49,40 | 0,00 | 17,10 | 3,90 | 99,90 | 6,17 | 8,21 |
| XT-7 | 30/2c-04 | 4807,58 | 0,00 | 0,20 | 0,40 | 0,00 | 0,00 | 0,00 | 0,20 | 53,00 | 0,00 | 14,50 | 1,60 | 100,00 | 4,75 | 5,92 |
| XT-15 | 30/2c-J07 | 4972,31 | 0,00 | 0,10 | 0,00 | 0,00 | 0,00 | 0,00 | 0,20 | 63,90 | 0,00 | 9,40 | 2,10 | 100,00 | 8,88 | 12,09 |
| XT-13 | 30/2c-J07 | 4973,02 | 0,00 | 0,20 | 0,20 | 0,00 | 0,00 | 0,00 | 0,20 | 26,40 | 0,00 | 2,40 | 0,60 | 100,20 | 2,52 | 8,39 |
| XT-14 | 30/2c-J07 | 4988,16 | 0,00 | 0,00 | 0,00 | 0,00 | 0,00 | 0,00 | 0,20 | 35,80 | 0,00 | 7,90 | 5,40 | 99,80 | 10,86 | 26,61 |
| XT-12 | 30/2c-J07 | 5009,97 | 0,00 | 1,20 | 0,20 | 0,00 | 0,00 | 0,00 | 0,90 | 47,10 | 0,00 | 9,30 | 0,70 | 99,90 | 8,21 | 15,27 |
| XT-10 | 30/7a-7 | 3460,80 | 0,00 | 0,00 | 0,20 | 0,00 | 0,00 | 0,00 | 1,40 | 63,70 | 0,00 | 11,50 | 1,60 | 100,10 | 7,70 | 9,99 |
| XT-11 | 30/7a-7 | 3489,00 | 0,00 | 0,00 | 0,00 | 0,00 | 0,00 | 0,00 | 0,30 | 58,00 | 0,00 | 17,50 | 2,10 | 99,90 | 6,92 | 8,54 |
| XT-8 | 30/7a-8 | 3556,90 | 0,00 | 0,00 | 0,00 | 0,00 | 0,00 | 0,00 | 0,50 | 44,90 | 0,00 | 12,70 | 4,10 | 100,10 | 6,08 | 9,78 |
| XT-9 | 30/7a-8 | 3633,45 | 0,00 | 0,60 | 0,10 | 0,00 | 0,00 | 0,00 | 2,50 | 49,90 | 0,00 | 10,50 | 3,70 | 100,10 | 5,75 | 8,58 |
| XT-16 | 6/3-1 | 3059,65 | 0,00 | 0,00 | 0,20 | 0,00 | 0,00 | 0,00 | 0,80 | 31,80 | 0,00 | 9,10 | 2,90 | 100,00 | 7,13 | 18,60 |

Appendix II

Clay fraction QXRD data

| Detailed clay analysis, <0.2 micron fraction | | | | | | | | | | | | | Total illite+smectite clay in a bulk rock (based on QXRD & <2 mm data) | | | |
|--|---------|-----------------------------|-----------------------------|------|------------------------------|------|--------|----------|------------------------------|------|----------------------------------|------|---|--------|----------|-----------------------|
| | | | Total illite+smectite R0 | | Total Illite-Smectite R≥1 | | Illite | Smectite | Total Chlorite- type clay | | Total Kaolinite- type clay | | Total I-S | Illite | Smectite | Total S equivalent |
| Sample | Well | Depth below seafloor (m) | %S | Amt. | %S | Amt. | Amt. | Amt. | %S | Amt. | %S | Amt. | Amt. | Amt. | Amt. | Amt. |
| XM-1 | Bravo-Y | 1460,5 | - | 0 | 20 | 63 | 12 | 0 | 0 | 8 | 0 | 17 | 21 | 4 | 0 | 5 |
| XM-3 | Bravo-Y | 1633,0 | - | 0 | 23 | 65 | 15 | 0 | 0 | 4 | 0 | 16 | 30 | 7 | 0 | 8 |
| XM-4 | Bravo-Y | 1683,0 | - | 0 | 19 | 60 | 16 | 0 | 0 | 3 | 0 | 21 | 22 | 6 | 0 | 5 |
| XM-8 | Bravo-Y | 1945,5 | - | 0 | 17 | 69 | 11 | 0 | 0 | 3 | 0 | 17 | 29 | 5 | 0 | 6 |

Table 2.1 Clay fraction QXRD modelling results for Central Malay Basin mudstone samples.

| Detailed clay analysis, < 0.2 micron fraction | | | | | | | | | | | | Total illite+smectite clay in a bulk rock (based on QXRD & <2 mm data) | | | | |
|---|----------|--------------------------|--------------------------|------|---------------------------|------|--------|----------|--------------------------|------|---------------------------|--|-----------|--------|----------|--------------------|
| Sample | Well | Depth below seafloor (m) | Total illite+smectite R0 | | Total Illite-Smectite R≥1 | | Illite | Smectite | Total Chlorite-type clay | | Total Kaolinite-type clay | | Total I-S | Illite | Smectite | Total S equivalent |
| | | | %S | Amt. | %S | Amt. | Amt. | Amt. | %S | Amt. | %S | Amt. | Amt. | Amt. | Amt. | Amt. |
| XC-1 | 6507/6-2 | 2332 | 76,1 | 9 | 30 | 73 | 2 | 0 | 0 | 4 | 0 | 12 | 35,05 | 0,85 | 0,00 | 12,43 |
| XC-2 | 6507/6-2 | 2442 | 62,3 | 2 | 27 | 61 | 5 | 0 | 0 | 9 | 0 | 23 | 16,58 | 1,32 | 0,00 | 4,89 |
| XC-3 | 6507/6-2 | 2537 | 70,6 | 1 | 29 | 66 | 3 | 0 | 0 | 8 | 0 | 22 | 29,58 | 1,32 | 0,00 | 8,99 |
| XC-4 | 6507/6-2 | 2637 | 70,3 | 2 | 31 | 73 | 4 | 0 | 0 | 9 | 0 | 12 | 24,87 | 1,33 | 0,00 | 8,20 |
| XC-5 | 6507/6-2 | 2747 | - | 0 | 23 | 65 | 9 | 0 | 0 | 10 | 0 | 16 | 36,01 | 4,99 | 0,00 | 9,16 |
| XC-6 | 6507/6-2 | 2812 | - | 0 | 23 | 63 | 13 | 0 | 0 | 10 | 0 | 14 | 25,03 | 5,17 | 0,00 | 6,66 |
| XC-7 | 6406/2-3 | 3054 | 71 | 14 | 28 | 56 | 8 | 0 | 0 | 12 | 0 | 10 | 25,85 | 2,95 | 0,00 | 9,98 |
| XC-8 | 6406/2-3 | 3254 | 80,1 | 5 | 25 | 65 | 7 | 0 | 0 | 10 | 0 | 13 | 29,36 | 2,94 | 0,00 | 9,01 |
| XC-12 | 6406/2-3 | 4078 | - | 0 | 23 | 65 | 10 | 0 | 0 | 12 | 0 | 13 | 29,73 | 4,57 | 0,00 | 7,64 |
| XC-13 | 6406/2-3 | 4218 | - | 0 | 16 | 74 | 4 | 0 | 0 | 19 | 0 | 3 | 44,59 | 2,41 | 0,00 | 7,56 |

Table 2.2 Clay fraction QXRD modelling results for Haltenbanken mudstone samples.

| Clay fraction calc | | | | | Total illite+smectite clay (2:1 layer clay: IS + illite + smectite) | | | | | | Total chlorite-type clay (trioctahedral 2:1+1 + 1:1) | | | | | | Total kaolinite-type clay (dioctahedral 1:1 clay) | | | |
|--------------------|--------|-----------------------------|--------------------------|--------------------------------------|--|------|-------------------------------|------|--------|----------|---|------|----------|-------------------------------|------|------------|--|------|-----------|--|
| Sample | Well | Depth below seafloor (m) | Sum of 2:1 Clay | Calculated CEC for 2:1 clay | Total Illite- Smectite R0 | | Total Illite- Smectite R≥1 | | Illite | Smectite | Total Chlorite- Smectite | | Chlorite | Total Chlorite- Serpentine | | Serpentine | Total Kaolinite-Smectite | | Kaolinite | |
| | | | | | %S | Amt. | %S | Amt. | Amt. | Amt. | %S | Amt. | Amt. | %Serp | Amt. | Amt. | %S | Amt. | Amt. | |
| XSA-2 | Well A | 2347,9 | 96 | 59 | 57 | 81 | 19 | 24 | 3 | 0 | 0 | 0 | 0 | 20 | 2 | 0 | 0 | 0 | 2 | |
| XSA-5 | Well A | 2471,0 | 85 | 58 | 53 | 76 | 35 | 10 | 4 | 0 | 0 | 0 | 0 | 0 | 0 | 0 | 0 | 0 | 15 | |
| XSA-13 | Well C | 2352,6 | 97 | 61 | 54 | 91 | 42 | 8 | 2 | 0 | 0 | 0 | 0 | 0 | 0 | 0 | 0 | 0 | 3 | |
| XSA-10 | Well C | 2654,6 | 90 | 29 | 0 | 0 | 26 | 168 | 6 | 0 | 0 | 0 | 0 | 20 | 5 | 0 | 0 | 0 | 5 | |
| XSA-6 | Well C | 2888,8 | 96 | 23 | 0 | 0 | 20 | 170 | 11 | 0 | 0 | 0 | 3 | 20 | 1 | 0 | 0 | 0 | 0 | |
| XSA-7 | Well C | 2912,5 | 94 | 20 | 0 | 0 | 17 | 158 | 15 | 0 | 0 | 0 | 2 | 20 | 4 | 0 | 0 | 0 | 0 | |
| XSA-1 | Well E | 2466,4 | 89 | 54 | 50 | 74 | 37 | 22 | 4 | 0 | 0 | 0 | 0 | 0 | 0 | 0 | 0 | 0 | 11 | |
| XSA-4 | Well E | 2751,2 | 97 | 31 | 0 | 0 | 27 | 188 | 3 | 0 | 0 | 0 | 0 | 0 | 0 | 0 | 0 | 0 | 3 | |

Table 2.3 Clay fraction QXRD modelling results for Sergipe mudstone samples (<0.2-micron fraction).

| Sample | Well | Depth below seafloor (m) | Chlorite (Tri) | Kaolinite | Illite | I/S-ML | %Exp |
|--------|--------|--------------------------|----------------|-----------|--------|--------|------|
| ASA3 | Well A | 1245,0 | 6 | 20 | 12 | 62 | 50 |
| ASA9 | Well A | 2448,0 | 7 | 10 | 7 | 76 | 40 |
| ASA11 | Well A | 3012,0 | 5 | 8 | 6 | 81 | 40 |
| ASA13 | Well A | 3900,0 | 6 | 4 | 15 | 75 | 20 |
| ASD2 | Well D | 983,0 | 4 | 4 | 4 | 88 | 60 |
| ASD5 | Well D | 1769,0 | 5 | 6 | 5 | 84 | 30 |
| ASD6 | Well D | 2009,0 | 7 | 4 | 7 | 82 | 30 |
| ASD8 | Well D | 2519,0 | 12 | 6 | 11 | 71 | 25 |
| ASE3 | Well E | 1432,0 | 5 | 21 | 6 | 68 | 55 |
| ASE7 | Well E | 2350,0 | 6 | 5 | 3 | 86 | 40 |
| ASE10 | Well E | 3259,0 | 4 | 3 | 5 | 88 | 25 |
| XSC-1 | Well E | 3466,0 | 6 | 5 | 8 | 81 | 25 |

Table 2.4 Clay fraction QXRD modelling results for Sergipe mudstone samples (<2-micron fraction).

Appendix III

TOC data

| Sample | Well | Depth below seafloor (m) | Total Carbon (wt.%) | Total Sulfur (wt.%) | Total Inorganic Carbon (wt.%) | TOC (wt.%) | Calculated Organic Matter content (wt.%) |
|--------|---------|--------------------------|---------------------|---------------------|-------------------------------|------------|--|
| XM1 | Bravo-Y | 1460,5 | 12,96 | 0,35 | 0,94 | 12,01 | 15,02 |
| XM2 | Bravo-Y | 1515,5 | 2,71 | 0,25 | 0,99 | 1,71 | 2,14 |
| XM3 | Bravo-Y | 1633,0 | 10,09 | 0,22 | 0,77 | 9,32 | 11,65 |
| XM4 | Bravo-Y | 1683,0 | 4,27 | 0,20 | 1,08 | 3,19 | 3,99 |
| XM5 | Bravo-Y | 1725,5 | 3,80 | 0,24 | 0,98 | 2,82 | 3,52 |
| XM6 | Bravo-Y | 1755,5 | 4,78 | 0,60 | 0,60 | 4,18 | 5,23 |
| XM7 | Bravo-Y | 1865,5 | 2,75 | 0,48 | 1,08 | 1,67 | 2,09 |
| XM8 | Bravo-Y | 1945,5 | 4,11 | 0,61 | 1,24 | 2,87 | 3,59 |
| XM9 | Bravo-Y | 2015,5 | 2,45 | 0,60 | 1,37 | 1,08 | 1,35 |
| XM10 | Bravo-Y | 2090,5 | 2,70 | 0,54 | 0,71 | 1,98 | 2,48 |

Table 3.1 TOC data for Central Malay Basin mudstone samples.

| Sample | Well | Depth below seafloor (m) | Total Carbon (wt.%) | Total Sulfur (wt.%) | Total Inorganic Carbon (wt.%) | TOC (wt.%) | Calculated Organic Matter content (wt.%) |
|--------|------------|--------------------------|---------------------|---------------------|-------------------------------|------------|--|
| XC-7 | 6406/2-3 | 3054 | 1,90 | 2,04 | 0,05 | 1,84 | 2,30 |
| XC-8 | 6406/2-3 | 3254 | 2,29 | 1,84 | 0,29 | 1,99 | 2,49 |
| XC-9 | 6406/2-3 | 3454 | 2,16 | 1,62 | 0,01 | 2,15 | 2,69 |
| XC-10 | 6406/2-3 | 3655 | 2,25 | 1,85 | 0,22 | 2,03 | 2,54 |
| XC-11 | 6406/2-3 | 3790 | 2,10 | 1,67 | 0,37 | 1,72 | 2,16 |
| XKC-1 | 6406/2-3 | 3985,98 | 2,55 | 0,71 | 0,00 | 2,55 | 3,19 |
| XKC-2 | 6406/2-3 | 4002,7 | 5,17 | 1,52 | 0,00 | 5,17 | 6,46 |
| XKC-18 | 6406/2-3 | 4010,75 | 2,36 | 0,58 | 0,00 | 2,36 | 2,95 |
| XKC-4 | 6406/2-3 | 4025,9 | 1,56 | 0,37 | 0,00 | 1,56 | 1,95 |
| XC-12 | 6406/2-3 | 4078 | 2,45 | 1,64 | 0,50 | 1,95 | 2,44 |
| XC-13 | 6406/2-3 | 4218 | 2,90 | 1,89 | 0,34 | 2,57 | 3,21 |
| XK-1 | 6407/10-2 | 2051 | 2,34 | 1,53 | 1,44 | 0,89 | 1,11 |
| XK-7 | 6407/10-2 | 2246 | 2,43 | 0,63 | 1,16 | 1,27 | 1,59 |
| XK-2 | 6407/10-2 | 2386 | 3,04 | 1,03 | 1,28 | 1,76 | 2,20 |
| XK-3 | 6506/11-2 | 3350 | 1,29 | 0,55 | 0,23 | 1,06 | 1,33 |
| XK-8 | 6506/11-2 | 3500 | 1,03 | 0,45 | 0,06 | 0,97 | 1,21 |
| XK-4 | 6506/11-2 | 3698 | 1,07 | 0,40 | 0,02 | 1,05 | 1,31 |
| XK-6 | 6506/11-2 | 3791 | 0,75 | 0,41 | 0,01 | 0,74 | 0,93 |
| XK-5 | 6506/11-2 | 3815 | 2,64 | 0,95 | 0,77 | 1,87 | 2,34 |
| XKC-14 | 6506/11-3 | 2795,4 | 1,44 | 0,97 | 0,02 | 1,42 | 1,78 |
| XKC-16 | 6506/11-3 | 3592,5 | 0,71 | 2,42 | 0,00 | 0,71 | 0,89 |
| XKC-15 | 6506/11-3 | 3637,5 | 1,08 | 1,67 | 0,00 | 1,08 | 1,35 |
| XKC-12 | 6506/11-4S | 3959,8 | 3,30 | 1,19 | 0,02 | 3,28 | 4,10 |
| XKC-13 | 6506/11-4S | 3964,9 | 0,23 | 0,02 | 0,00 | 0,23 | 0,29 |
| XKC-11 | 6506/3-1 | 2765,6 | 1,89 | 0,55 | 0,23 | 1,66 | 2,08 |
| XKC-10 | 6506/3-1 | 2786,8 | 1,69 | 0,09 | 0,03 | 1,66 | 2,08 |
| XKC-6 | 6507/2-3 | 2501,8 | 1,86 | 2,16 | 0,00 | 1,86 | 2,33 |
| XKC-7 | 6507/2-3 | 2505,8 | 2,88 | 1,79 | 0,00 | 2,88 | 3,60 |
| XKC-5 | 6507/2-3 | 2507,55 | 4,95 | 2,43 | 0,00 | 4,95 | 6,19 |
| XKC-8 | 6507/2-3 | 2878,6 | 3,30 | 0,23 | 1,77 | 1,53 | 1,91 |
| XC-1 | 6507/6-2 | 2332 | 1,75 | 2,35 | 0,48 | 1,27 | 1,59 |
| XC-2 | 6507/6-2 | 2442 | 2,15 | 0,77 | 0,83 | 1,32 | 1,65 |
| XC-3 | 6507/6-2 | 2537 | 1,93 | 0,90 | 0,96 | 0,97 | 1,21 |
| XC-4 | 6507/6-2 | 2637 | 2,57 | 0,52 | 1,70 | 0,86 | 1,08 |
| XC-5 | 6507/6-2 | 2747 | 2,00 | 0,72 | 0,70 | 1,30 | 1,62 |
| XC-6 | 6507/6-2 | 2812 | 2,40 | 1,23 | 0,90 | 1,49 | 1,87 |
| XKC-9 | 6607/5-1 | 3016 | 1,17 | 0,26 | 0,00 | 1,16 | 1,45 |
| XKC-17 | 6607/5-1 | 3017,4 | 1,43 | 0,34 | 0,06 | 1,38 | 1,73 |

Table 3.2 TOC data for Haltenbanken mudstone samples.

| Sample | Well | Depth below seafloor (m) | Total Carbon (wt.%) | Total Sulfur (wt.%) | Total Inorganic Carbon (wt.%) | TOC (wt.%) | Calculated Organic Matter content (wt.%) |
|--------|--------|--------------------------|---------------------|---------------------|-------------------------------|------------|--|
| XSA-8 | Well A | 2465,8 | 0,95 | 0,27 | 0,12 | 0,83 | 1,04 |
| XSA-1 | Well A | 2466,4 | 0,99 | 0,35 | 0,10 | 0,89 | 1,11 |
| XSA-11 | Well A | 2467,6 | 1,25 | 0,85 | 0,01 | 1,24 | 1,55 |
| XSA-5 | Well A | 2471,0 | 0,95 | 1,58 | 0,00 | 0,95 | 1,19 |
| XSA-2 | Well C | 2347,9 | 3,44 | 0,57 | 2,85 | 0,58 | 0,73 |
| XSA-13 | Well C | 2352,6 | 1,32 | 0,65 | 0,65 | 0,66 | 0,83 |
| XSA-10 | Well C | 2654,6 | 1,23 | 0,44 | 0,61 | 0,62 | 0,78 |
| XSA-3 | Well C | 2656,7 | 1,90 | 0,36 | 1,40 | 0,50 | 0,63 |
| XSA-9 | Well C | 2753,4 | 1,61 | 0,55 | 1,03 | 0,58 | 0,73 |
| XSA-6 | Well C | 2888,8 | 0,79 | 0,30 | 0,32 | 0,47 | 0,59 |
| XSA-7 | Well C | 2912,5 | 0,52 | 0,27 | 0,00 | 0,52 | 0,65 |
| XSA-4 | Well E | 2751,2 | 0,73 | 0,19 | 0,00 | 0,73 | 0,91 |
| XSA-12 | Well E | 2752,9 | 0,85 | 0,10 | 0,21 | 0,64 | 0,80 |
| XSC-1 | Well E | 3466,0 | 1,50 | 1,43 | 0,68 | 0,82 | 1,03 |

Table 3.3 TOC data for Sergipe mudstone samples.

| Sample | Well | Depth relative to kelly bushing (m) | Total Carbon (wt.%) | Total Sulfur (wt.%) | Total Inorganic Carbon (wt.%) | TOC (wt.%) | Calculated Organic Matter content (wt.%) |
|--------|-----------|-------------------------------------|---------------------|---------------------|-------------------------------|------------|--|
| XT-5 | 22/29-1 | 4592,75 | 7,87 | 4,82 | 0,00 | 7,87 | 9,84 |
| XT-4 | 22/29-1 | 4594,25 | 0,70 | 0,03 | 0,00 | 0,70 | 0,88 |
| XT-2 | 22/29-1 | 4599,73 | 1,32 | 0,15 | 0,01 | 1,31 | 1,64 |
| XT-3 | 22/29-1 | 4718,304 | 1,15 | 0,05 | 0,94 | 0,20 | 0,25 |
| XT-1 | 22/29-1 | 4761,49 | 0,14 | 0,01 | 0,00 | 0,14 | 0,18 |
| XT-6 | 30/2c-04 | 4791,44 | 0,43 | 0,11 | 0,00 | 0,43 | 0,54 |
| XT-7 | 30/2c-04 | 4807,58 | 0,47 | 0,10 | 0,00 | 0,46 | 0,58 |
| XT-15 | 30/2c-J07 | 4972,31 | 0,99 | 0,01 | 0,21 | 0,78 | 0,98 |
| XT-13 | 30/2c-J07 | 4973,02 | 6,73 | 0,58 | 6,05 | 0,67 | 0,84 |
| XT-14 | 30/2c-J07 | 4988,16 | 1,97 | 0,01 | 1,42 | 0,55 | 0,69 |
| XT-12 | 30/2c-J07 | 5009,97 | 1,39 | 1,44 | 0,93 | 0,46 | 0,58 |
| XT-10 | 30/7a-7 | 3460,8 | 0,54 | 0,16 | 0,00 | 0,54 | 0,68 |
| XT-11 | 30/7a-7 | 3489 | 0,45 | 0,01 | 0,00 | 0,45 | 0,56 |
| XT-8 | 30/7a-8 | 3556,9 | 0,27 | 0,04 | 0,00 | 0,27 | 0,34 |
| XT-9 | 30/7a-8 | 3633,45 | 0,31 | 0,01 | 0,00 | 0,31 | 0,39 |
| XT-16 | 6/3-1 | 3059,65 | 0,31 | 0,01 | 0,03 | 0,28 | 0,35 |

Table 3.4 TOC data for Central North Sea Triassic mudstone samples.

Appendix IV

ICP OES and ICP MS data

| Sample | Well | Analysis Method | FUS-ICP | FUS-ICP | FUS-ICP | FUS-ICP | FUS-ICP | FUS-ICP | FUS-ICP | FUS-ICP | FUS-ICP | FUS-ICP | FUS-ICP | FUS-ICP |
|--------|---------|--------------------------|----------|-----------|--------------|---------|---------|---------|----------|---------|----------|----------|---------|-----------|
| | | Detection Limit | 0,01 | 0,01 | 0,01 | 0,001 | 0,01 | 0,01 | 0,01 | 0,01 | 0,001 | 0,01 | | |
| | | Depth below seafloor (m) | SiO2 (%) | Al2O3 (%) | Fe2O3(T) (%) | MnO (%) | MgO (%) | CaO (%) | Na2O (%) | K2O (%) | TiO2 (%) | P2O5 (%) | LOI (%) | Total (%) |
| XM1 | Bravo-Y | 1460,5 | 48,88 | 12,38 | 6,2 | 0,132 | 1,39 | 0,64 | 0,8 | 1,93 | 0,587 | 0,1 | 24,82 | 97,87 |
| XM2 | Bravo-Y | 1515,5 | 56,99 | 17,01 | 6,59 | 0,136 | 1,62 | 0,74 | 0,72 | 2,61 | 0,735 | 0,11 | 11,79 | 99,05 |
| XM3 | Bravo-Y | 1633,0 | 53,17 | 13,72 | 5,86 | 0,116 | 1,29 | 0,56 | 0,63 | 2,16 | 0,645 | 0,09 | 21,02 | 99,25 |
| XM4 | Bravo-Y | 1683,0 | 54,75 | 17,5 | 6,46 | 0,137 | 1,44 | 0,71 | 0,5 | 2,59 | 0,787 | 0,11 | 13,55 | 98,53 |
| XM5 | Bravo-Y | 1725,5 | 62,83 | 14,07 | 6,16 | 0,111 | 1,23 | 0,66 | 0,6 | 2,39 | 0,734 | 0,09 | 10,5 | 99,37 |
| XM6 | Bravo-Y | 1755,5 | 59,32 | 14,98 | 5,64 | 0,097 | 1,22 | 0,52 | 0,54 | 2,35 | 0,733 | 0,08 | 13,59 | 99,08 |
| XM7 | Bravo-Y | 1865,5 | 54,44 | 18,48 | 7,09 | 0,117 | 1,83 | 1,01 | 0,58 | 2,93 | 0,774 | 0,12 | 12,13 | 99,5 |
| XM8 | Bravo-Y | 1945,5 | 53,1 | 17,25 | 7,18 | 0,134 | 1,6 | 1,02 | 0,71 | 2,43 | 0,727 | 0,12 | 14,8 | 99,08 |
| XM9 | Bravo-Y | 2015,5 | 57,26 | 14,58 | 5,41 | 0,082 | 2,02 | 2,05 | 0,79 | 2,66 | 0,691 | 0,09 | 11,54 | 97,16 |
| XM10 | Bravo-Y | 2090,5 | 55,76 | 17,84 | 6,17 | 0,084 | 2,09 | 0,94 | 0,94 | 2,86 | 0,704 | 0,1 | 11,24 | 98,72 |

| Sample | Well | Analysis Method | FUS-ICP | FUS-ICP | FUS-ICP | FUS-ICP | FUS-ICP | FUS-ICP | FUS-ICP | FUS-ICP | FUS-MS | FUS-MS | FUS-MS | FUS-MS | FUS-MS |
|--------|---------|--------------------------|----------|----------|---------|----------|----------|---------|----------|----------|----------|----------|----------|----------|--------|
| | | Detection Limit | 1 | 1 | 5 | 3 | 2 | 2 | 4 | 20 | 1 | 20 | 10 | 30 | |
| | | Depth below seafloor (m) | Sc (ppm) | Be (ppm) | V (ppm) | Ba (ppm) | Sr (ppm) | Y (ppm) | Zr (ppm) | Cr (ppm) | Co (ppm) | Ni (ppm) | Cu (ppm) | Zn (ppm) | |
| XM1 | Bravo-Y | 1460,5 | 12 | 3 | 86 | 6736 | 133 | 24 | 119 | 130 | 14 | 40 | 100 | 290 | |
| XM2 | Bravo-Y | 1515,5 | 16 | 3 | 112 | 9567 | 187 | 30 | 155 | 100 | 18 | 50 | 80 | 260 | |
| XM3 | Bravo-Y | 1633,0 | 13 | 3 | 96 | 5886 | 131 | 26 | 139 | 130 | 14 | 40 | 100 | 110 | |
| XM4 | Bravo-Y | 1683,0 | 16 | 3 | 113 | 5170 | 138 | 29 | 149 | 110 | 15 | 50 | 110 | 240 | |
| XM5 | Bravo-Y | 1725,5 | 13 | 3 | 93 | 4323 | 114 | 30 | 228 | 60 | 13 | 30 | 70 | 180 | |
| XM6 | Bravo-Y | 1755,5 | 13 | 3 | 95 | 4645 | 124 | 29 | 178 | 90 | 12 | 30 | 60 | 200 | |
| XM7 | Bravo-Y | 1865,5 | 16 | 3 | 119 | 10440 | 156 | 28 | 145 | 120 | 15 | 40 | 120 | 290 | |
| XM8 | Bravo-Y | 1945,5 | 15 | 3 | 109 | 9460 | 134 | 29 | 149 | 80 | 15 | 30 | 70 | 200 | |
| XM9 | Bravo-Y | 2015,5 | 15 | 3 | 110 | 10810 | 172 | 23 | 152 | 110 | 15 | 40 | 50 | 210 | |
| XM10 | Bravo-Y | 2090,5 | 16 | 3 | 121 | 9534 | 144 | 25 | 143 | 110 | 16 | 40 | 90 | 190 | |

| Sample | Well | Analysis Method | FUS-MS | FUS-MS | FUS-MS | FUS-MS | FUS-MS | FUS-MS | FUS-MS | FUS-MS | FUS-MS | FUS-MS | FUS-MS | FUS-MS | FUS-MS |
|--------|---------|--------------------------|----------|----------|----------|----------|----------|----------|----------|----------|----------|----------|----------|----------|----------|
| | | Detection Limit | 1 | 1 | 5 | 2 | 1 | 2 | 0,5 | 0,2 | 1 | 0,5 | 0,5 | 0,04 | 0,2 |
| | | Depth below seafloor (m) | Ga (ppm) | Ge (ppm) | As (ppm) | Rb (ppm) | Nb (ppm) | Mo (ppm) | Ag (ppm) | In (ppm) | Sn (ppm) | Sb (ppm) | Cs (ppm) | Lu (ppm) | Hf (ppm) |
| XM1 | Bravo-Y | 1460,5 | 15 | 3 | 10 | 106 | 8 | < 2 | < 0.5 | < 0.2 | 32 | 1,1 | 9,6 | 0,36 | 3,2 |
| XM2 | Bravo-Y | 1515,5 | 22 | 2 | 11 | 152 | 13 | 2 | < 0.5 | < 0.2 | 5 | 1,3 | 14,2 | 0,44 | 4,3 |
| XM3 | Bravo-Y | 1633,0 | 17 | 3 | 12 | 124 | 11 | < 2 | 0,5 | < 0.2 | 27 | 1,3 | 11,4 | 0,38 | 3,7 |
| XM4 | Bravo-Y | 1683,0 | 23 | 1 | 13 | 158 | 13 | 3 | 0,5 | < 0.2 | 17 | 1,2 | 15 | 0,46 | 4 |
| XM5 | Bravo-Y | 1725,5 | 16 | < 1 | 8 | 128 | 12 | < 2 | < 0.5 | < 0.2 | 7 | 6 | 10,6 | 0,5 | 5,5 |
| XM6 | Bravo-Y | 1755,5 | 17 | < 1 | 12 | 128 | 15 | < 2 | < 0.5 | < 0.2 | 19 | 2,7 | 10,9 | 0,48 | 4,4 |
| XM7 | Bravo-Y | 1865,5 | 23 | 1 | 14 | 169 | 14 | 5 | < 0.5 | 0,5 | 145 | 1,3 | 16,2 | 0,44 | 3,9 |
| XM8 | Bravo-Y | 1945,5 | 20 | 1 | 11 | 141 | 12 | 2 | < 0.5 | < 0.2 | 6 | 1,4 | 12,8 | 0,47 | 3,7 |
| XM9 | Bravo-Y | 2015,5 | 21 | 2 | 7 | 152 | 13 | 3 | < 0.5 | < 0.2 | 3 | 1,1 | 13,8 | 0,41 | 3,9 |
| XM10 | Bravo-Y | 2090,5 | 23 | 1 | 9 | 164 | 12 | 2 | < 0.5 | < 0.2 | 5 | 1,1 | 16,1 | 0,42 | 3,7 |

| Sample | Well | Analysis Method | FUS-MS | FUS-MS | FUS-MS | FUS-MS | FUS-MS | FUS-MS | FUS-MS | FUS-MS | FUS-MS | FUS-MS | FUS-MS | FUS-MS | FUS-MS |
|--------|---------|--------------------------|----------|----------|----------|----------|----------|----------|----------|----------|----------|----------|----------|----------|----------|
| | | Detection Limit | 0,1 | 0,1 | 0,05 | 0,1 | 0,1 | 0,05 | 0,1 | 0,1 | 0,1 | 0,1 | 0,1 | 0,05 | 0,1 |
| | | Depth below seafloor (m) | La (ppm) | Ce (ppm) | Pr (ppm) | Nd (ppm) | Sm (ppm) | Eu (ppm) | Gd (ppm) | Tb (ppm) | Dy (ppm) | Ho (ppm) | Er (ppm) | Tm (ppm) | Yb (ppm) |
| XM1 | Bravo-Y | 1460,5 | 29,7 | 58,9 | 6,66 | 24,9 | 5,1 | 0,71 | 4,6 | 0,7 | 4,3 | 0,8 | 2,4 | 0,36 | 2,4 |
| XM2 | Bravo-Y | 1515,5 | 37,2 | 74,2 | 8,35 | 30,5 | 6,4 | 0,75 | 5,6 | 0,8 | 5,2 | 1 | 2,9 | 0,44 | 2,9 |
| XM3 | Bravo-Y | 1633,0 | 33 | 65,6 | 7,44 | 28 | 5,8 | 0,82 | 4,8 | 0,8 | 4,7 | 0,9 | 2,6 | 0,4 | 2,5 |
| XM4 | Bravo-Y | 1683,0 | 40,6 | 80,8 | 9 | 33,7 | 6,8 | 1,17 | 6,1 | 0,9 | 5,2 | 1 | 3,1 | 0,45 | 3 |
| XM5 | Bravo-Y | 1725,5 | 39,4 | 79,5 | 8,73 | 33 | 6,4 | 1,33 | 5,4 | 0,9 | 5,7 | 1,1 | 3,2 | 0,46 | 3,1 |
| XM6 | Bravo-Y | 1755,5 | 37,5 | 75,7 | 8,58 | 30,9 | 6,7 | 1,28 | 5,6 | 0,9 | 5,3 | 1 | 2,9 | 0,45 | 3 |
| XM7 | Bravo-Y | 1865,5 | 39,9 | 79,4 | 8,98 | 33,7 | 6,7 | 0,79 | 6 | 0,9 | 5,3 | 1,1 | 3,1 | 0,46 | 3 |
| XM8 | Bravo-Y | 1945,5 | 38 | 76,8 | 8,57 | 32,2 | 6,4 | 1,31 | 5,6 | 0,9 | 5,4 | 1 | 3,1 | 0,44 | 2,8 |
| XM9 | Bravo-Y | 2015,5 | 35,9 | 70,9 | 8,01 | 29,4 | 5,9 | 0,63 | 5,1 | 0,8 | 4,7 | 0,9 | 2,6 | 0,41 | 2,7 |
| XM10 | Bravo-Y | 2090,5 | 36,8 | 73,2 | 8,2 | 30,3 | 6,2 | 0,74 | 5,1 | 0,8 | 4,7 | 0,9 | 2,7 | 0,42 | 2,7 |

| Sample | Well | Analysis Method | FUS-MS | FUS-MS | FUS-MS | FUS-MS | FUS-MS | FUS-MS | FUS-MS |
|--------|---------|--------------------------|----------|---------|----------|----------|----------|----------|---------|
| | | Detection Limit | 0,1 | 1 | 0,1 | 5 | 0,4 | 0,1 | 0,1 |
| | | Depth below seafloor (m) | Ta (ppm) | W (ppm) | Tl (ppm) | Pb (ppm) | Bi (ppm) | Th (ppm) | U (ppm) |
| XM1 | Bravo-Y | 1460,5 | 1 | 3 | 0,6 | 23 | < 0.4 | 12,4 | 2,5 |
| XM2 | Bravo-Y | 1515,5 | 1,3 | 4 | 0,7 | 35 | < 0.4 | 16,5 | 3,1 |
| XM3 | Bravo-Y | 1633,0 | 1,2 | 3 | 0,5 | < 5 | < 0.4 | 14,2 | 2,8 |
| XM4 | Bravo-Y | 1683,0 | 1,4 | 4 | 0,8 | 58 | < 0.4 | 18,1 | 3,3 |
| XM5 | Bravo-Y | 1725,5 | 1,3 | 4 | 0,9 | 24 | < 0.4 | 15,7 | 3,6 |
| XM6 | Bravo-Y | 1755,5 | 1,6 | 5 | 0,8 | 23 | < 0.4 | 15,3 | 3,3 |
| XM7 | Bravo-Y | 1865,5 | 1,3 | 4 | 0,8 | 240 | < 0.4 | 17,6 | 3,1 |
| XM8 | Bravo-Y | 1945,5 | 1,2 | 3 | 0,7 | 21 | < 0.4 | 16,5 | 3,5 |
| XM9 | Bravo-Y | 2015,5 | 1,3 | 4 | 0,7 | 29 | < 0.4 | 14,7 | 3 |
| XM10 | Bravo-Y | 2090,5 | 1,2 | 3 | 0,8 | 29 | < 0.4 | 15,9 | 3 |

Table 4.1 ICP OES and ICP MS data (major and trace elements) for Central Malay Basin mudstone samples (pages:363-365).

| Sample | Well | Analysis Method Detection Limit Depth below seafloor (m) | FUS-ICP 0,01 SiO2 (%) | FUS-ICP 0,01 Al2O3 (%) | FUS-ICP 0,01 Fe2O3(T) (%) | FUS-ICP 0,001 MnO (%) | FUS-ICP 0,01 MgO (%) | FUS-ICP 0,01 CaO (%) | FUS-ICP 0,01 Na2O (%) | FUS-ICP 0,01 K2O (%) | FUS-ICP 0,001 TiO2 (%) | FUS-ICP 0,01 P2O5 (%) | FUS-ICP LOI (%) | FUS-ICP 0,01 Total (%) |
|--------|------------|---|-----------------------------|------------------------------|------------------------------------|-----------------------------|----------------------------|----------------------------|-----------------------------|----------------------------|------------------------------|-----------------------------|--------------------|------------------------------|
| XC7 | 6406/2-3 | 3054,0 | 56,05 | 14,06 | 6,18 | 0,113 | 1,32 | 1,17 | 1,19 | 2,14 | 0,689 | 0,11 | 11,47 | 94,49 |
| XC8 | 6406/2-3 | 3254,0 | 51,62 | 16,04 | 6,94 | 0,165 | 1,4 | 1,59 | 1,08 | 2,24 | 0,825 | 0,13 | 13,01 | 95,04 |
| XC9 | 6406/2-3 | 3454,0 | 51,1 | 16,02 | 6,57 | 0,212 | 1,37 | 1,38 | 1,1 | 1,99 | 0,767 | 0,12 | 12,69 | 93,31 |
| XC10 | 6406/2-3 | 3655,0 | 46,18 | 16,88 | 7,46 | 0,414 | 1,46 | 1,38 | 0,86 | 2,14 | 0,745 | 0,16 | 14,55 | 92,22 |
| XC11 | 6406/2-3 | 3790,0 | 47,34 | 15,23 | 7,58 | 0,287 | 1,34 | 1,91 | 0,99 | 1,89 | 0,702 | 0,11 | 12,83 | 90,22 |
| CH17 | 6406/2-3 | 4010,8 | 56 | 19,88 | 5,91 | 0,027 | 1,8 | 0,31 | 1,56 | 3,86 | 0,989 | 0,11 | 9,29 | 99,73 |
| XC12 | 6406/2-3 | 4078,0 | 44,67 | 17,21 | 7,97 | 0,297 | 1,53 | 1,06 | 0,88 | 2,24 | 0,759 | 0,12 | 14,38 | 91,11 |
| XC13 | 6406/2-3 | 4218,0 | 37,48 | 16,77 | 9,36 | 0,462 | 1,77 | 1,93 | 0,66 | 3,06 | 0,679 | 0,25 | 16,73 | 89,14 |
| CH1 | 6407/10-2 | 2051,0 | 53,66 | 11,47 | 9,61 | 0,631 | 1,36 | 3,7 | 0,66 | 2,49 | 0,503 | 0,33 | 11,82 | 96,24 |
| CH2 | 6407/10-2 | 2246,0 | 47,5 | 16,58 | 7,76 | 1,035 | 1,8 | 4,32 | 0,85 | 3,4 | 0,665 | 0,3 | 13,01 | 97,24 |
| CH3 | 6407/10-2 | 2386,0 | 41,69 | 18,24 | 11,52 | 1,319 | 1,93 | 2,92 | 0,67 | 3,32 | 0,747 | 0,4 | 14,36 | 97,12 |
| CH10 | 6506/11-2 | 3350,0 | 57,37 | 18,35 | 6,51 | 0,29 | 1,55 | 1,29 | 1,28 | 2,39 | 0,837 | 0,13 | 8,86 | 98,86 |
| CH11 | 6506/11-2 | 3500,0 | 58,01 | 19,55 | 7,16 | 0,143 | 1,73 | 0,91 | 1,63 | 2,61 | 0,914 | 0,14 | 7,03 | 99,83 |
| CH13 | 6506/11-2 | 3698,0 | 61,13 | 17,32 | 6,37 | 0,124 | 1,56 | 1,25 | 1,35 | 2,61 | 0,829 | 0,11 | 5,99 | 98,64 |
| CH14 | 6506/11-2 | 3791,0 | 55,11 | 20,39 | 7,8 | 0,153 | 2,04 | 0,74 | 1,59 | 3,4 | 0,797 | 0,09 | 7,08 | 99,18 |
| CH15 | 6506/11-2 | 3815,0 | 44,33 | 20,86 | 8,53 | 0,237 | 1,88 | 6,2 | 1,17 | 3,04 | 0,876 | 0,3 | 11,44 | 98,86 |
| CH7 | 6506/11-3 | 2795,4 | 60,88 | 16,48 | 5,58 | 0,075 | 1,54 | 0,65 | 1,68 | 2,59 | 0,868 | 0,1 | 8,39 | 98,82 |
| CH12 | 6506/11-3 | 3637,5 | 54,97 | 19,84 | 7,24 | 0,088 | 1,81 | 0,25 | 1,37 | 2,88 | 0,941 | 0,1 | 9,45 | 98,94 |
| CH16 | 6506/11-4S | 3959,8 | 56,16 | 18,79 | 6,12 | 0,103 | 1,68 | 0,5 | 1,09 | 2,38 | 0,967 | 0,13 | 11 | 98,92 |
| CH6 | 6506/3-1 | 2765,6 | 55,26 | 19,9 | 7,03 | 0,544 | 1,67 | 0,58 | 1,33 | 2,85 | 0,93 | 0,09 | 10,16 | 100,3 |
| CH8 | 6506/3-1 | 2786,8 | 57,85 | 19,1 | 6,06 | 0,142 | 1,61 | 0,37 | 1,59 | 2,92 | 0,954 | 0,08 | 8,99 | 99,67 |
| CH4 | 6507/2-3 | 2501,8 | 51,21 | 19,31 | 8,18 | 0,053 | 1,71 | 0,27 | 1,24 | 3,03 | 1,019 | 0,06 | 12,4 | 98,47 |
| CH5 | 6507/2-3 | 2505,8 | 51,53 | 19,85 | 6,78 | 0,036 | 1,66 | 0,39 | 1,01 | 2,72 | 0,934 | 0,17 | 13,83 | 98,9 |
| XC1 | 6507/6-2 | 2332,0 | 50,23 | 13,18 | 6,53 | 0,073 | 1,24 | 1,8 | 0,75 | 3,27 | 0,641 | 0,17 | | 77,88 |
| XC2 | 6507/6-2 | 2442,0 | 49,74 | 13,46 | 7,01 | 0,117 | 1,31 | 1,29 | 0,67 | 2,94 | 0,682 | 0,15 | | 77,38 |
| XC3 | 6507/6-2 | 2537,0 | 43,05 | 16,04 | 10,08 | 0,225 | 1,51 | 1,12 | 0,84 | 3,28 | 0,74 | 0,27 | | 77,15 |
| XC4 | 6507/6-2 | 2637,0 | 45,07 | 12,97 | 5,05 | 0,27 | 1,16 | 7,51 | 0,63 | 2,8 | 0,537 | 0,31 | | 76,3 |
| XC5 | 6507/6-2 | 2747,0 | 41,36 | 17,11 | 7,72 | 0,666 | 1,65 | 2,98 | 0,72 | 2,78 | 0,651 | 0,5 | | 76,14 |
| XC6 | 6507/6-2 | 2812,0 | 41,13 | 13,45 | 8,94 | 0,54 | 1,5 | 1,81 | 0,55 | 2,82 | 0,546 | 0,33 | | 71,63 |
| CH9 | 6607/5-1 | 3017,4 | 57,53 | 19,18 | 6,89 | 0,042 | 1,74 | 0,44 | 1,59 | 2,94 | 1,06 | 0,11 | 9,15 | 100,7 |

| Sample | Well | Analysis Method | FUS-ICP | FUS-ICP | FUS-ICP | FUS-ICP | FUS-ICP | FUS-ICP | FUS-ICP | FUS-MS | FUS-MS | FUS-MS | FUS-MS | FUS-MS |
|--------|------------|--------------------------|----------|----------|---------|----------|----------|---------|----------|----------|----------|----------|----------|----------|
| | | Detection Limit | 1 | 1 | 5 | 3 | 2 | 2 | 4 | 20 | 1 | 20 | 10 | 30 |
| | | Depth below seafloor (m) | Sc (ppm) | Be (ppm) | V (ppm) | Ba (ppm) | Sr (ppm) | Y (ppm) | Zr (ppm) | Cr (ppm) | Co (ppm) | Ni (ppm) | Cu (ppm) | Zn (ppm) |
| XC7 | 6406/2-3 | 3054,0 | 12 | 2 | 126 | 50700 | 1976 | 22 | 187 | 100 | 14 | 50 | 120 | 450 |
| XC8 | 6406/2-3 | 3254,0 | 15 | 3 | 170 | 46910 | 1796 | 23 | 183 | 110 | 18 | 50 | 100 | 690 |
| XC9 | 6406/2-3 | 3454,0 | 15 | 2 | 153 | 50670 | 1939 | 21 | 160 | 110 | 18 | 50 | 140 | 460 |
| XC10 | 6406/2-3 | 3655,0 | 16 | 3 | 168 | 58670 | 2148 | 22 | 139 | 110 | 19 | 60 | 90 | 440 |
| XC11 | 6406/2-3 | 3790,0 | 14 | 2 | 137 | 74370 | 2913 | 19 | 157 | 110 | 16 | 50 | 100 | 330 |
| CH17 | 6406/2-3 | 4010,8 | 22 | 4 | 193 | 716 | 181 | 25 | 194 | 130 | 18 | 50 | 40 | 140 |
| XC12 | 6406/2-3 | 4078,0 | 17 | 2 | 134 | 63540 | 2430 | 20 | 144 | 130 | 21 | 60 | 90 | 370 |
| XC13 | 6406/2-3 | 4218,0 | 17 | 3 | 209 | 84410 | 3156 | 23 | 115 | 120 | 31 | 90 | 180 | 450 |
| CH1 | 6407/10-2 | 2051,0 | 12 | 2 | 123 | 22190 | 726 | 24 | 143 | 170 | 18 | 100 | 50 | 220 |
| CH2 | 6407/10-2 | 2246,0 | 16 | 3 | 149 | 15580 | 525 | 28 | 117 | 100 | 23 | 100 | 90 | 250 |
| CH3 | 6407/10-2 | 2386,0 | 20 | 3 | 226 | 15740 | 502 | 38 | 133 | 120 | 33 | 110 | 120 | 180 |
| CH10 | 6506/11-2 | 3350,0 | 17 | 3 | 196 | 2545 | 194 | 28 | 214 | 120 | 20 | 60 | 30 | 140 |
| CH11 | 6506/11-2 | 3500,0 | 19 | 3 | 201 | 5127 | 297 | 22 | 184 | 120 | 23 | 70 | 40 | 140 |
| CH13 | 6506/11-2 | 3698,0 | 17 | 3 | 145 | 4410 | 258 | 23 | 216 | 120 | 27 | 60 | 50 | 130 |
| CH14 | 6506/11-2 | 3791,0 | 20 | 3 | 189 | 5488 | 310 | 24 | 148 | 130 | 26 | 90 | 60 | 180 |
| CH15 | 6506/11-2 | 3815,0 | 22 | 4 | 286 | 12560 | 605 | 33 | 142 | 140 | 30 | 100 | 100 | 220 |
| CH7 | 6506/11-3 | 2795,4 | 16 | 4 | 161 | 541 | 155 | 26 | 175 | 110 | 25 | 70 | 30 | 100 |
| CH12 | 6506/11-3 | 3637,5 | 20 | 3 | 202 | 324 | 134 | 20 | 168 | 130 | 26 | 70 | 40 | 120 |
| CH16 | 6506/11-4S | 3959,8 | 18 | 3 | 151 | 439 | 134 | 29 | 210 | 130 | 37 | 70 | 50 | 130 |
| CH6 | 6506/3-1 | 2765,6 | 19 | 4 | 226 | 537 | 161 | 29 | 250 | 170 | 33 | 160 | 40 | 180 |
| CH8 | 6506/3-1 | 2786,8 | 19 | 3 | 223 | 534 | 150 | 25 | 214 | 130 | 17 | 50 | 40 | 130 |
| CH4 | 6507/2-3 | 2501,8 | 18 | 4 | 241 | 598 | 109 | 24 | 268 | 170 | 25 | 60 | 50 | 130 |
| CH5 | 6507/2-3 | 2505,8 | 20 | 4 | 214 | 461 | 116 | 32 | 230 | 100 | 29 | 80 | 50 | 170 |
| XC1 | 6507/6-2 | 2332,0 | 13 | 2 | 148 | 9768 | 302 | 20 | 181 | 100 | 18 | 50 | 60 | 10000 |
| XC2 | 6507/6-2 | 2442,0 | 13 | 2 | 114 | 11220 | 343 | 18 | 165 | 100 | 16 | 50 | 60 | 10000 |
| XC3 | 6507/6-2 | 2537,0 | 17 | 3 | 169 | 18170 | 570 | 23 | 143 | 110 | 21 | 60 | 70 | 10000 |
| XC4 | 6507/6-2 | 2637,0 | 13 | 2 | 98 | 14540 | 534 | 21 | 118 | 80 | 20 | 70 | 120 | 10000 |
| XC5 | 6507/6-2 | 2747,0 | 17 | 2 | 150 | 28400 | 897 | 34 | 106 | 100 | 26 | 100 | 150 | 10000 |
| XC6 | 6507/6-2 | 2812,0 | 14 | 2 | 142 | 50150 | 1511 | 23 | 107 | 90 | 23 | 70 | 150 | 10000 |
| CH9 | 6607/5-1 | 3017,4 | 19 | 3 | 210 | 508 | 130 | 24 | 226 | 160 | 40 | 70 | 40 | 100 |

| Sample | Well | Analysis Method | FUS-MS | FUS-MS | FUS-MS | FUS-MS | FUS-MS | FUS-MS | FUS-MS | FUS-MS | FUS-MS | FUS-MS | FUS-MS | FUS-MS |
|--------|------------|--------------------------|----------|----------|----------|----------|----------|----------|----------|----------|----------|----------|----------|----------|
| | | Detection Limit | 1 | 1 | 5 | 2 | 1 | 2 | 0,5 | 0,2 | 1 | 0,5 | 0,5 | 0,04 |
| | | Depth below seafloor (m) | Ga (ppm) | Ge (ppm) | As (ppm) | Rb (ppm) | Nb (ppm) | Mo (ppm) | Ag (ppm) | In (ppm) | Sn (ppm) | Sb (ppm) | Cs (ppm) | Lu (ppm) |
| XC7 | 6406/2-3 | 3054,0 | 18 | 1 | 5 | 82 | 15 | < 2 | 0,8 | < 0.2 | 3 | 0,7 | 4,5 | 0,35 |
| XC8 | 6406/2-3 | 3254,0 | 21 | 2 | 11 | 91 | 14 | < 2 | 0,7 | < 0.2 | 2 | 0,7 | 5,3 | 0,37 |
| XC9 | 6406/2-3 | 3454,0 | 21 | 2 | 13 | 85 | 13 | 2 | 0,5 | < 0.2 | 5 | 0,8 | 5,4 | 0,38 |
| XC10 | 6406/2-3 | 3655,0 | 22 | 2 | 15 | 94 | 13 | 2 | 0,5 | < 0.2 | 2 | 0,7 | 6 | 0,34 |
| XC11 | 6406/2-3 | 3790,0 | 20 | 2 | 14 | 79 | 13 | 2 | 0,6 | < 0.2 | 2 | 0,9 | 4,9 | 0,33 |
| CH17 | 6406/2-3 | 4010,8 | 26 | 1 | 12 | 147 | 14 | < 2 | 0,5 | < 0.2 | 3 | 0,7 | 8,1 | 0,47 |
| XC12 | 6406/2-3 | 4078,0 | 22 | 2 | 8 | 94 | 11 | < 2 | 0,5 | < 0.2 | 2 | 0,8 | 5,4 | 0,35 |
| XC13 | 6406/2-3 | 4218,0 | 22 | 2 | 10 | 111 | 12 | 5 | < 0.5 | < 0.2 | 2 | 0,7 | 6,8 | 0,39 |
| CH1 | 6407/10-2 | 2051,0 | 17 | 2 | 17 | 66 | 13 | 4 | 0,5 | < 0.2 | 2 | 2,3 | 3,9 | 0,36 |
| CH2 | 6407/10-2 | 2246,0 | 22 | 2 | 11 | 92 | 11 | 2 | < 0.5 | < 0.2 | 2 | 1,7 | 5,6 | 0,38 |
| CH3 | 6407/10-2 | 2386,0 | 26 | 2 | 38 | 92 | 14 | 3 | < 0.5 | < 0.2 | 3 | 1,8 | 5,2 | 0,52 |
| CH10 | 6506/11-2 | 3350,0 | 27 | 2 | 18 | 107 | 24 | 2 | 0,7 | < 0.2 | 3 | 1,3 | 6,6 | 0,49 |
| CH11 | 6506/11-2 | 3500,0 | 26 | 2 | 14 | 109 | 16 | < 2 | 0,6 | < 0.2 | 3 | 1,1 | 6,9 | 0,42 |
| CH13 | 6506/11-2 | 3698,0 | 24 | 2 | 9 | 108 | 17 | 2 | 0,7 | < 0.2 | 3 | 0,9 | 5,7 | 0,39 |
| CH14 | 6506/11-2 | 3791,0 | 26 | 2 | 7 | 138 | 13 | 3 | 0,6 | < 0.2 | 3 | 1,3 | 8,6 | 0,44 |
| CH15 | 6506/11-2 | 3815,0 | 26 | 2 | 39 | 110 | 15 | 5 | 0,5 | < 0.2 | 3 | 2,1 | 7 | 0,5 |
| CH7 | 6506/11-3 | 2795,4 | 22 | 2 | 12 | 111 | 14 | 2 | 0,6 | < 0.2 | 3 | 0,8 | 6,4 | 0,42 |
| CH12 | 6506/11-3 | 3637,5 | 27 | 2 | 27 | 123 | 14 | < 2 | 0,5 | < 0.2 | 3 | 1,2 | 7,6 | 0,44 |
| CH16 | 6506/11-4S | 3959,8 | 23 | 1 | 22 | 103 | 15 | < 2 | 0,6 | < 0.2 | 3 | 0,8 | 5,1 | 0,49 |
| CH6 | 6506/3-1 | 2765,6 | 28 | 2 | 25 | 127 | 25 | 5 | 0,8 | < 0.2 | 4 | 0,8 | 7,6 | 0,58 |
| CH8 | 6506/3-1 | 2786,8 | 27 | 2 | 9 | 125 | 19 | < 2 | 0,7 | < 0.2 | 3 | 0,8 | 7,2 | 0,51 |
| CH4 | 6507/2-3 | 2501,8 | 30 | 2 | 23 | 115 | 22 | 7 | 0,8 | < 0.2 | 4 | 0,8 | 7,2 | 0,54 |
| CH5 | 6507/2-3 | 2505,8 | 28 | 2 | 14 | 110 | 23 | < 2 | < 0.5 | < 0.2 | 3 | 0,7 | 6,9 | 0,56 |
| XC1 | 6507/6-2 | 2332,0 | 18 | < 1 | 11 | 77 | 13 | 5 | 0,7 | < 0.2 | 2 | 0,9 | 4,8 | 0,35 |
| XC2 | 6507/6-2 | 2442,0 | 19 | 1 | 10 | 79 | 13 | 2 | 0,6 | < 0.2 | 3 | 0,9 | 4,2 | 0,32 |
| XC3 | 6507/6-2 | 2537,0 | 21 | 2 | 18 | 80 | 12 | 3 | 0,6 | < 0.2 | 2 | 1,1 | 5,3 | 0,38 |
| XC4 | 6507/6-2 | 2637,0 | 17 | 2 | 11 | 64 | 9 | 3 | 0,6 | < 0.2 | 2 | 1,2 | 3,6 | 0,32 |
| XC5 | 6507/6-2 | 2747,0 | 22 | 2 | 13 | 88 | 10 | 3 | 0,6 | < 0.2 | 2 | 1,5 | 5,4 | 0,4 |
| XC6 | 6507/6-2 | 2812,0 | 18 | 2 | 55 | 76 | 11 | 4 | 1 | < 0.2 | 3 | 3,2 | 4,5 | 0,34 |
| CH9 | 6607/5-1 | 3017,4 | 25 | 2 | 13 | 117 | 16 | 3 | 0,6 | < 0.2 | 3 | 0,7 | 7,1 | 0,49 |

| Sample | Well | Analysis Method | FUS-MS | FUS-MS | FUS-MS | FUS-MS | FUS-MS | FUS-MS | FUS-MS | FUS-MS | FUS-MS | FUS-MS | FUS-MS | FUS-MS | FUS-MS |
|--------|------------|--------------------------|----------|----------|----------|----------|----------|----------|----------|----------|----------|----------|----------|----------|----------|
| | | Detection Limit | 0,1 | 0,1 | 0,05 | 0,1 | 0,1 | 0,05 | 0,1 | 0,1 | 0,1 | 0,1 | 0,1 | 0,05 | 0,1 |
| | | Depth below seafloor (m) | La (ppm) | Ce (ppm) | Pr (ppm) | Nd (ppm) | Sm (ppm) | Eu (ppm) | Gd (ppm) | Tb (ppm) | Dy (ppm) | Ho (ppm) | Er (ppm) | Tm (ppm) | Yb (ppm) |
| XC7 | 6406/2-3 | 3054,0 | 29 | 65,6 | 6,83 | 25,3 | 5,6 | < 0,05 | 4,5 | 0,7 | 4,2 | 0,8 | 2,2 | 0,33 | 2,3 |
| XC8 | 6406/2-3 | 3254,0 | 30,4 | 69,2 | 7,17 | 26,4 | 5,7 | < 0,05 | 4,7 | 0,7 | 4,2 | 0,8 | 2,4 | 0,38 | 2,5 |
| XC9 | 6406/2-3 | 3454,0 | 30,2 | 66,8 | 7 | 25,3 | 5,2 | < 0,05 | 4,3 | 0,7 | 4,1 | 0,8 | 2,3 | 0,36 | 2,4 |
| XC10 | 6406/2-3 | 3655,0 | 29,2 | 65,4 | 6,96 | 25,3 | 5,5 | < 0,05 | 4,6 | 0,7 | 4,1 | 0,7 | 2,2 | 0,35 | 2,3 |
| XC11 | 6406/2-3 | 3790,0 | 27,4 | 60,8 | 6,44 | 24 | 5 | < 0,05 | 4,1 | 0,7 | 3,8 | 0,7 | 2,2 | 0,34 | 2,3 |
| CH17 | 6406/2-3 | 4010,8 | 40,7 | 89,4 | 9,56 | 34,8 | 6,2 | 1,2 | 4,6 | 0,7 | 4,3 | 0,9 | 2,8 | 0,45 | 2,8 |
| XC12 | 6406/2-3 | 4078,0 | 29,8 | 63,5 | 6,85 | 26 | 5,4 | < 0,05 | 4,3 | 0,7 | 3,9 | 0,8 | 2,2 | 0,33 | 2,2 |
| XC13 | 6406/2-3 | 4218,0 | 36,9 | 88,3 | 8,74 | 32,5 | 7 | < 0,05 | 5,7 | 0,9 | 4,9 | 0,9 | 2,7 | 0,4 | 2,6 |
| CH1 | 6407/10-2 | 2051,0 | 26,6 | 65,7 | 6,87 | 26,6 | 5,9 | 0,11 | 5,2 | 0,8 | 4,8 | 0,8 | 2,5 | 0,36 | 2,3 |
| CH2 | 6407/10-2 | 2246,0 | 33,7 | 79,9 | 8,09 | 30,5 | 6,3 | 0,56 | 5,9 | 0,9 | 5,1 | 1 | 2,6 | 0,4 | 2,5 |
| CH3 | 6407/10-2 | 2386,0 | 44,1 | 114 | 11,1 | 42,8 | 9,3 | 1,29 | 8,3 | 1,2 | 7,1 | 1,3 | 3,7 | 0,54 | 3,4 |
| CH10 | 6506/11-2 | 3350,0 | 43 | 98 | 10,2 | 37,5 | 7,7 | 1,19 | 6,2 | 1 | 6 | 1,1 | 3,3 | 0,5 | 3,4 |
| CH11 | 6506/11-2 | 3500,0 | 35,7 | 79,6 | 8,3 | 29,6 | 5,6 | 0,9 | 4,4 | 0,7 | 4,4 | 0,9 | 2,6 | 0,41 | 2,6 |
| CH13 | 6506/11-2 | 3698,0 | 31,5 | 69,6 | 7,52 | 27,7 | 5,4 | 0,96 | 4,5 | 0,7 | 4,4 | 0,9 | 2,6 | 0,41 | 2,6 |
| CH14 | 6506/11-2 | 3791,0 | 37,7 | 83,7 | 8,76 | 32 | 6,3 | 0,97 | 5 | 0,8 | 4,7 | 0,9 | 2,7 | 0,42 | 2,8 |
| CH15 | 6506/11-2 | 3815,0 | 47,8 | 120 | 11,9 | 44,5 | 9 | 1,38 | 7,6 | 1,2 | 6,6 | 1,2 | 3,4 | 0,51 | 3,4 |
| CH7 | 6506/11-3 | 2795,4 | 35,7 | 82 | 8,42 | 30,8 | 6,1 | 1,3 | 5,3 | 0,8 | 5,1 | 0,9 | 2,8 | 0,42 | 2,7 |
| CH12 | 6506/11-3 | 3637,5 | 37,4 | 82,3 | 8,59 | 30,3 | 4,9 | 0,98 | 3,7 | 0,6 | 4 | 0,8 | 2,5 | 0,42 | 2,9 |
| CH16 | 6506/11-4S | 3959,8 | 37,3 | 83,1 | 9,49 | 36,5 | 8 | 1,71 | 7,1 | 1,1 | 6,1 | 1,1 | 3,2 | 0,49 | 3,2 |
| CH6 | 6506/3-1 | 2765,6 | 44,6 | 104 | 10,5 | 37,7 | 7,3 | 1,37 | 6,4 | 1 | 6,1 | 1,2 | 3,5 | 0,56 | 3,7 |
| CH8 | 6506/3-1 | 2786,8 | 41,1 | 92,9 | 9,35 | 33,7 | 6,4 | 1,3 | 5,2 | 0,8 | 4,9 | 1 | 3 | 0,46 | 3,2 |
| CH4 | 6507/2-3 | 2501,8 | 27,3 | 51,8 | 5,59 | 20 | 3,9 | 0,74 | 3,1 | 0,6 | 3,9 | 0,8 | 2,8 | 0,49 | 3,4 |
| CH5 | 6507/2-3 | 2505,8 | 42,8 | 99 | 10 | 36,9 | 7,4 | 1,53 | 6,4 | 1,1 | 6,7 | 1,3 | 3,7 | 0,53 | 3,5 |
| XC1 | 6507/6-2 | 2332,0 | 27,6 | 63,8 | 6,61 | 24,2 | 5,1 | 0,57 | 4,3 | 0,7 | 4 | 0,7 | 2,3 | 0,34 | 2,2 |
| XC2 | 6507/6-2 | 2442,0 | 24,8 | 55,2 | 5,98 | 22,9 | 4,7 | 0,46 | 3,9 | 0,6 | 3,8 | 0,7 | 2 | 0,32 | 2,1 |
| XC3 | 6507/6-2 | 2537,0 | 30,1 | 68,3 | 7,28 | 27,3 | 5,6 | 0,47 | 5 | 0,8 | 4,6 | 0,9 | 2,5 | 0,36 | 2,4 |
| XC4 | 6507/6-2 | 2637,0 | 27,1 | 62,2 | 6,46 | 24,9 | 5,1 | 0,5 | 4,6 | 0,7 | 4,1 | 0,8 | 2,1 | 0,32 | 2,1 |
| XC5 | 6507/6-2 | 2747,0 | 33,2 | 82,1 | 8,11 | 31,4 | 7 | 0,2 | 6,9 | 1,1 | 6,3 | 1,1 | 3,1 | 0,44 | 2,7 |
| XC6 | 6507/6-2 | 2812,0 | 27,9 | 74,4 | 7,01 | 26,5 | 5,9 | < 0,05 | 5,3 | 0,8 | 4,5 | 0,8 | 2,4 | 0,34 | 2,3 |
| CH9 | 6607/5-1 | 3017,4 | 41,1 | 88,4 | 9,2 | 34 | 6,3 | 1,32 | 5 | 0,8 | 4,9 | 1 | 2,9 | 0,46 | 3,3 |

| Sample | Well | Analysis Method | FUS-MS | FUS-MS | FUS-MS | FUS-MS | FUS-MS | FUS-MS | FUS-MS | FUS-MS |
|--------|------------|--------------------------|----------|----------|---------|----------|----------|----------|----------|---------|
| | | Detection Limit | 0,2 | 0,1 | 1 | 0,1 | 5 | 0,4 | 0,1 | 0,1 |
| | | Depth below seafloor (m) | Hf (ppm) | Ta (ppm) | W (ppm) | Ti (ppm) | Pb (ppm) | Bi (ppm) | Th (ppm) | U (ppm) |
| XC7 | 6406/2-3 | 3054,0 | 4,5 | 1,3 | 3 | 0,4 | 21 | < 0,4 | 8,4 | 2 |
| XC8 | 6406/2-3 | 3254,0 | 4,6 | 1,3 | 4 | 0,4 | 27 | < 0,4 | 9,7 | 2 |
| XC9 | 6406/2-3 | 3454,0 | 4 | 1,1 | 3 | 0,4 | 29 | < 0,4 | 9,7 | 2 |
| XC10 | 6406/2-3 | 3655,0 | 3,5 | 1 | 3 | 0,4 | 25 | < 0,4 | 9,8 | 2 |
| XC11 | 6406/2-3 | 3790,0 | 4 | 1,1 | 3 | 0,3 | 25 | < 0,4 | 8,8 | 1,9 |
| CH17 | 6406/2-3 | 4010,8 | 4,9 | 1,1 | 2 | 0,6 | 16 | < 0,4 | 13,2 | 2,6 |
| XC12 | 6406/2-3 | 4078,0 | 3,7 | 1 | 4 | 0,4 | 34 | < 0,4 | 9,6 | 2 |
| XC13 | 6406/2-3 | 4218,0 | 3,2 | 1 | 3 | 0,5 | 22 | < 0,4 | 11 | 2,2 |
| CH1 | 6407/10-2 | 2051,0 | 3,5 | 1,1 | 6 | 0,4 | 60 | < 0,4 | 7,7 | 1,7 |
| CH2 | 6407/10-2 | 2246,0 | 3,3 | 0,9 | 19 | 0,5 | 57 | < 0,4 | 10,3 | 2 |
| CH3 | 6407/10-2 | 2386,0 | 3,5 | 1,1 | 4 | 0,6 | 52 | < 0,4 | 14,4 | 2,5 |
| CH10 | 6506/11-2 | 3350,0 | 5,5 | 1,8 | 3 | 0,7 | 35 | < 0,4 | 13,3 | 2,9 |
| CH11 | 6506/11-2 | 3500,0 | 4,6 | 1,2 | 5 | 2 | 54 | < 0,4 | 12,7 | 2,5 |
| CH13 | 6506/11-2 | 3698,0 | 5,2 | 1,3 | 50 | 1,3 | 49 | < 0,4 | 11,6 | 2,6 |
| CH14 | 6506/11-2 | 3791,0 | 4 | 1,1 | 6 | 1 | 59 | < 0,4 | 12,2 | 2,3 |
| CH15 | 6506/11-2 | 3815,0 | 3,9 | 1,2 | 6 | 2,2 | 82 | < 0,4 | 15,4 | 3,5 |
| CH7 | 6506/11-3 | 2795,4 | 4,5 | 1,3 | 2 | 0,5 | 19 | < 0,4 | 11,4 | 2,6 |
| CH12 | 6506/11-3 | 3637,5 | 4,4 | 1,1 | 2 | 0,6 | 22 | < 0,4 | 12,1 | 2,5 |
| CH16 | 6506/11-4S | 3959,8 | 5,4 | 1,3 | 2 | 0,5 | 18 | < 0,4 | 12,8 | 3,4 |
| CH6 | 6506/3-1 | 2765,6 | 6,8 | 1,9 | 3 | 0,5 | 16 | < 0,4 | 15 | 2,9 |
| CH8 | 6506/3-1 | 2786,8 | 6,1 | 1,4 | 2 | 0,5 | 20 | < 0,4 | 13,1 | 2,9 |
| CH4 | 6507/2-3 | 2501,8 | 5,9 | 2 | 2 | 0,5 | 20 | < 0,4 | 15,3 | 4,7 |
| CH5 | 6507/2-3 | 2505,8 | 5,5 | 1,9 | 3 | 0,6 | 19 | < 0,4 | 14,9 | 3,3 |
| XC1 | 6507/6-2 | 2332,0 | 4,3 | 1,1 | 6 | 0,5 | 88 | < 0,4 | 9,1 | 2,5 |
| XC2 | 6507/6-2 | 2442,0 | 4,2 | 1,1 | 11 | 0,4 | 96 | < 0,4 | 8,8 | 2 |
| XC3 | 6507/6-2 | 2537,0 | 3,5 | 1,1 | 7 | 0,4 | 119 | < 0,4 | 9,4 | 2 |
| XC4 | 6507/6-2 | 2637,0 | 2,9 | 0,8 | 5 | 0,4 | 185 | < 0,4 | 7,9 | 1,7 |
| XC5 | 6507/6-2 | 2747,0 | 2,8 | 0,8 | 4 | 0,6 | 198 | < 0,4 | 9,9 | 2,1 |
| XC6 | 6507/6-2 | 2812,0 | 2,8 | 0,9 | 22 | 0,6 | 227 | < 0,4 | 8,9 | 2 |
| CH9 | 6607/5-1 | 3017,4 | 5,5 | 1,3 | 2 | 0,5 | 20 | < 0,4 | 13,4 | 2,8 |

Table 4.2 ICP OES and ICP MS data (major and trace elements) for Haltenbanken mudstone samples (pages:366-370).

| Sample | Well | Analysis Method Detection Limit Depth below seafloor (m) | FUS-ICP 0,01 | FUS-ICP 0,01 | FUS-ICP 0,01 | FUS-ICP 0,001 | FUS-ICP 0,01 | FUS-ICP 0,01 | FUS-ICP 0,01 | FUS-ICP 0,01 | FUS-ICP 0,001 | FUS-ICP 0,01 | FUS-ICP 0,01 | FUS-ICP 0,01 |
|--------|--------|---|-----------------|-----------------|-----------------|------------------|-----------------|-----------------|-----------------|-----------------|------------------|-----------------|-----------------|-----------------|
| | | | SiO2 (%) | Al2O3 (%) | Fe2O3(T) (%) | MnO (%) | MgO (%) | CaO (%) | Na2O (%) | K2O (%) | TiO2 (%) | P2O5 (%) | LOI (%) | Total (%) |
| CH18 | Well A | 2465,8 | 54,04 | 19,91 | 9,56 | 0,046 | 1,74 | 0,82 | 1,49 | 2,94 | 0,901 | 0,06 | 8,85 | 100,4 |
| CH19 | Well A | 2466,4 | 55,97 | 19,51 | 6,85 | 0,032 | 1,85 | 0,96 | 1,5 | 2,98 | 0,898 | 0,07 | 10 | 100,6 |
| CH20 | Well A | 2467,6 | 54,8 | 19,7 | 6,6 | 0,026 | 1,79 | 0,89 | 1,45 | 2,78 | 0,829 | 0,08 | 11,08 | 100 |
| CH21 | Well A | 2471,0 | 54,47 | 17,64 | 9,79 | 0,042 | 1,8 | 0,71 | 1,38 | 2,45 | 0,8 | 0,08 | 10,16 | 99,32 |
| CH22 | Well C | 2347,9 | 48,23 | 11,4 | 4,14 | 0,028 | 1,9 | 12,49 | 1,16 | 1,78 | 0,493 | 0,02 | 17,14 | 98,78 |
| CH23 | Well C | 2352,6 | 59,6 | 15,08 | 4,91 | 0,037 | 1,81 | 3,13 | 1,5 | 2,25 | 0,67 | 0,04 | 10,88 | 99,91 |
| CH24 | Well C | 2654,6 | 59,33 | 14,79 | 5,53 | 0,026 | 2,57 | 3,61 | 1,77 | 3,22 | 0,673 | 0,12 | 8,74 | 100,4 |
| CH25 | Well C | 2656,7 | 56,91 | 13,17 | 5,72 | 0,043 | 2,37 | 6,65 | 1,65 | 2,82 | 0,567 | 0,1 | 10,27 | 100,3 |
| CH26 | Well C | 2753,4 | 55,49 | 14,82 | 5,83 | 0,034 | 2,55 | 5,33 | 1,44 | 3,64 | 0,698 | 0,12 | 10,27 | 100,2 |
| CH27 | Well C | 2888,8 | 58,5 | 16,53 | 5,43 | 0,027 | 2,68 | 2,16 | 1,46 | 4,26 | 0,791 | 0,15 | 7,62 | 99,6 |
| CH28 | Well C | 2912,5 | 55,46 | 19,16 | 5,87 | 0,026 | 2,79 | 0,84 | 1,35 | 4,8 | 0,906 | 0,13 | 7,54 | 98,88 |
| CH29 | Well E | 2751,2 | 61,27 | 18,57 | 4,5 | 0,03 | 1,49 | 0,35 | 1,52 | 3,43 | 0,911 | 0,06 | 7,45 | 99,6 |
| CH30 | Well E | 2752,9 | 63,61 | 15,84 | 4,98 | 0,046 | 1,45 | 1,26 | 1,57 | 2,8 | 0,778 | 0,05 | 6,7 | 99,08 |
| CH31 | Well E | 3466,0 | 54,19 | 12,53 | 7,06 | 0,077 | 1,84 | 3,46 | 1,56 | 2,16 | 0,578 | 0,07 | 11,35 | 94,88 |

| Sample | Well | Analysis Method Detection Limit Depth below seafloor (m) | FUS-ICP 1 | FUS-ICP 1 | FUS-ICP 5 | FUS-ICP 3 | FUS-ICP 2 | FUS-ICP 2 | FUS-ICP 4 | FUS-MS 20 | FUS-MS 1 | FUS-MS 20 | FUS-MS 10 | FUS-MS 30 |
|--------|--------|---|--------------|--------------|--------------|--------------|--------------|--------------|--------------|--------------|-------------|--------------|--------------|--------------|
| | | | Sc (ppm) | Be (ppm) | V (ppm) | Ba (ppm) | Sr (ppm) | Y (ppm) | Zr (ppm) | Cr (ppm) | Co (ppm) | Ni (ppm) | Cu (ppm) | Zn (ppm) |
| CH18 | Well A | 2465,8 | 19 | 4 | 141 | 465 | 192 | 26 | 169 | 160 | 15 | 70 | 50 | 70 |
| CH19 | Well A | 2466,4 | 18 | 4 | 143 | 687 | 200 | 29 | 186 | 120 | 103 | 120 | 40 | 80 |
| CH20 | Well A | 2467,6 | 18 | 4 | 144 | 531 | 206 | 25 | 168 | 120 | 24 | 50 | 30 | 80 |
| CH21 | Well A | 2471,0 | 16 | 3 | 132 | 400 | 196 | 24 | 174 | 160 | 20 | 50 | 40 | 80 |
| CH22 | Well C | 2347,9 | 9 | 2 | 64 | 290 | 800 | 13 | 174 | 100 | 9 | 30 | 20 | 40 |
| CH23 | Well C | 2352,6 | 11 | 2 | 74 | 2011 | 492 | 18 | 265 | 120 | 14 | 30 | 20 | 50 |
| CH24 | Well C | 2654,6 | 12 | 2 | 91 | 567 | 263 | 19 | 203 | 220 | 14 | 50 | 40 | 100 |
| CH25 | Well C | 2656,7 | 10 | 2 | 71 | 552 | 286 | 18 | 187 | 100 | 12 | 40 | 30 | 110 |
| CH26 | Well C | 2753,4 | 13 | 3 | 102 | 546 | 214 | 21 | 179 | 130 | 15 | 40 | 30 | 80 |
| CH27 | Well C | 2888,8 | 16 | 3 | 121 | 563 | 167 | 26 | 185 | 190 | 15 | 40 | 30 | 100 |
| CH28 | Well C | 2912,5 | 18 | 4 | 136 | 506 | 151 | 24 | 198 | 150 | 18 | 50 | 30 | 90 |
| CH29 | Well E | 2751,2 | 16 | 4 | 113 | 605 | 175 | 29 | 263 | 120 | 21 | 40 | 30 | 50 |
| CH30 | Well E | 2752,9 | 13 | 3 | 98 | 504 | 176 | 24 | 262 | 110 | 21 | 40 | 30 | 100 |
| CH31 | Well E | 3466,0 | 11 | 2 | 83 | 31460 | 890 | 22 | 189 | 150 | 18 | 90 | 50 | 190 |

| Sample | Well | Analysis Method | FUS-MS | FUS-MS | FUS-MS | FUS-MS | FUS-MS | FUS-MS | FUS-MS | FUS-MS | FUS-MS | FUS-MS | FUS-MS | FUS-MS |
|--------|--------|--------------------------|----------|----------|----------|----------|----------|----------|----------|----------|----------|----------|----------|----------|
| | | Detection Limit | 1 | 1 | 5 | 2 | 1 | 2 | 0,5 | 0,2 | 1 | 0,5 | 0,5 | 0,04 |
| | | Depth below seafloor (m) | Ga (ppm) | Ge (ppm) | As (ppm) | Rb (ppm) | Nb (ppm) | Mo (ppm) | Ag (ppm) | In (ppm) | Sn (ppm) | Sb (ppm) | Cs (ppm) | Lu (ppm) |
| CH18 | Well A | 2465,8 | 28 | 2 | < 5 | 168 | 20 | 3 | < 0.5 | < 0.2 | 4 | 0,7 | 7,6 | 0,41 |
| CH19 | Well A | 2466,4 | 26 | 2 | < 5 | 164 | 20 | < 2 | 0,5 | < 0.2 | 4 | 0,6 | 7,2 | 0,44 |
| CH20 | Well A | 2467,6 | 28 | 1 | < 5 | 157 | 19 | < 2 | < 0.5 | < 0.2 | 3 | < 0.5 | 7,5 | 0,38 |
| CH21 | Well A | 2471,0 | 26 | < 1 | < 5 | 138 | 16 | 3 | < 0.5 | < 0.2 | 2 | < 0.5 | 6,5 | 0,41 |
| CH22 | Well C | 2347,9 | 16 | 1 | < 5 | 81 | 9 | < 2 | < 0.5 | < 0.2 | 2 | < 0.5 | 3,4 | 0,22 |
| CH23 | Well C | 2352,6 | 21 | 1 | < 5 | 99 | 12 | < 2 | < 0.5 | < 0.2 | 2 | < 0.5 | 3,8 | 0,3 |
| CH24 | Well C | 2654,6 | 21 | 1 | < 5 | 121 | 13 | 3 | < 0.5 | < 0.2 | 2 | < 0.5 | 4 | 0,31 |
| CH25 | Well C | 2656,7 | 18 | 1 | < 5 | 103 | 11 | < 2 | < 0.5 | < 0.2 | 2 | < 0.5 | 3,3 | 0,28 |
| CH26 | Well C | 2753,4 | 22 | 1 | < 5 | 142 | 14 | < 2 | < 0.5 | < 0.2 | 2 | < 0.5 | 5,2 | 0,34 |
| CH27 | Well C | 2888,8 | 24 | 2 | < 5 | 173 | 16 | 2 | < 0.5 | < 0.2 | 3 | < 0.5 | 6,9 | 0,38 |
| CH28 | Well C | 2912,5 | 31 | 2 | < 5 | 185 | 19 | < 2 | < 0.5 | < 0.2 | 3 | < 0.5 | 8 | 0,41 |
| CH29 | Well E | 2751,2 | 27 | 2 | < 5 | 179 | 19 | < 2 | < 0.5 | < 0.2 | 3 | < 0.5 | 6,7 | 0,45 |
| CH30 | Well E | 2752,9 | 23 | 2 | < 5 | 144 | 17 | < 2 | < 0.5 | < 0.2 | 3 | < 0.5 | 5,2 | 0,41 |
| CH31 | Well E | 3466,0 | 18 | 2 | 6 | 104 | 14 | 7 | 0,6 | < 0.2 | 3 | 0,7 | 3,8 | 0,33 |

| Sample | Well | Analysis Method | FUS-MS | FUS-MS | FUS-MS | FUS-MS | FUS-MS | FUS-MS | FUS-MS | FUS-MS | FUS-MS | FUS-MS | FUS-MS | FUS-MS | FUS-MS |
|--------|--------|--------------------------|----------|----------|----------|----------|----------|----------|----------|----------|----------|----------|----------|----------|----------|
| | | Detection Limit | 0,1 | 0,1 | 0,05 | 0,1 | 0,1 | 0,05 | 0,1 | 0,1 | 0,1 | 0,1 | 0,1 | 0,05 | 0,1 |
| | | Depth below seafloor (m) | La (ppm) | Ce (ppm) | Pr (ppm) | Nd (ppm) | Sm (ppm) | Eu (ppm) | Gd (ppm) | Tb (ppm) | Dy (ppm) | Ho (ppm) | Er (ppm) | Tm (ppm) | Yb (ppm) |
| CH18 | Well A | 2465,8 | 49 | 101 | 11,1 | 40,4 | 7,8 | 1,51 | 6,1 | 0,9 | 5,1 | 1 | 2,9 | 0,41 | 2,7 |
| CH19 | Well A | 2466,4 | 54 | 112 | 12,2 | 43,8 | 8,3 | 1,69 | 6,4 | 1 | 5,7 | 1,1 | 3,1 | 0,43 | 3 |
| CH20 | Well A | 2467,6 | 48 | 101 | 10,7 | 38 | 7,5 | 1,46 | 5,6 | 0,9 | 4,8 | 0,9 | 2,7 | 0,42 | 2,6 |
| CH21 | Well A | 2471,0 | 49,3 | 107 | 11,4 | 40,1 | 7,7 | 1,49 | 5,8 | 0,9 | 5 | 0,9 | 2,8 | 0,43 | 2,7 |
| CH22 | Well C | 2347,9 | 28,5 | 54,9 | 5,93 | 21,4 | 3,9 | 0,87 | 3,1 | 0,5 | 2,7 | 0,5 | 1,5 | 0,23 | 1,5 |
| CH23 | Well C | 2352,6 | 44,2 | 88,8 | 9,49 | 33,1 | 5,5 | 1,17 | 4,3 | 0,6 | 3,4 | 0,7 | 2,1 | 0,33 | 2,1 |
| CH24 | Well C | 2654,6 | 42,2 | 79,1 | 8,77 | 31 | 5,7 | 1,25 | 4,4 | 0,6 | 3,6 | 0,7 | 2 | 0,33 | 2 |
| CH25 | Well C | 2656,7 | 37,4 | 71,1 | 7,95 | 29,3 | 5,4 | 1,23 | 4,3 | 0,6 | 3,6 | 0,7 | 1,9 | 0,3 | 1,9 |
| CH26 | Well C | 2753,4 | 44,4 | 85,9 | 9,76 | 35,5 | 6,5 | 1,38 | 5,2 | 0,7 | 4,1 | 0,8 | 2,3 | 0,34 | 2,2 |
| CH27 | Well C | 2888,8 | 53 | 100 | 11,4 | 41 | 7,6 | 1,57 | 6 | 0,9 | 4,9 | 0,9 | 2,8 | 0,42 | 2,5 |
| CH28 | Well C | 2912,5 | 56,2 | 107 | 12,1 | 42,3 | 7,3 | 1,46 | 5,5 | 0,8 | 4,6 | 0,9 | 2,7 | 0,4 | 2,8 |
| CH29 | Well E | 2751,2 | 56,1 | 110 | 12,4 | 45,2 | 8,2 | 1,71 | 6,7 | 0,9 | 5,5 | 1 | 3,2 | 0,49 | 3,1 |
| CH30 | Well E | 2752,9 | 46,7 | 94,8 | 10,5 | 37,3 | 7,1 | 1,4 | 5,5 | 0,8 | 4,9 | 0,9 | 2,7 | 0,43 | 2,7 |
| CH31 | Well E | 3466,0 | 36,1 | 72,2 | 8,08 | 28,7 | 5,9 | < 0.05 | 4,7 | 0,7 | 4,2 | 0,7 | 2,3 | 0,34 | 2,2 |

| Sample | Well | Analysis Method | FUS-MS | FUS-MS | FUS-MS | FUS-MS | FUS-MS | FUS-MS | FUS-MS | FUS-MS |
|--------|--------|--------------------------|----------|----------|---------|----------|----------|----------|----------|---------|
| | | Detection Limit | 0,2 | 0,1 | 1 | 0,1 | 5 | 0,4 | 0,1 | 0,1 |
| | | Depth below seafloor (m) | Hf (ppm) | Ta (ppm) | W (ppm) | Tl (ppm) | Pb (ppm) | Bi (ppm) | Th (ppm) | U (ppm) |
| CH18 | Well A | 2465,8 | 4,3 | 1,6 | 2 | 0,7 | 18 | < 0.4 | 18,8 | 2,9 |
| CH19 | Well A | 2466,4 | 4,8 | 1,6 | 2 | 0,8 | 76 | < 0.4 | 18,3 | 2,9 |
| CH20 | Well A | 2467,6 | 3,9 | 1,4 | < 1 | 0,5 | 17 | < 0.4 | 18,2 | 3,1 |
| CH21 | Well A | 2471,0 | 3,9 | 1,5 | 2 | 0,6 | 11 | < 0.4 | 17,4 | 3 |
| CH22 | Well C | 2347,9 | 4 | 0,8 | < 1 | 0,3 | 13 | < 0.4 | 10,7 | 2,2 |
| CH23 | Well C | 2352,6 | 6,3 | 1 | < 1 | 0,3 | 19 | < 0.4 | 14,2 | 2,3 |
| CH24 | Well C | 2654,6 | 4,7 | 1,1 | < 1 | 0,5 | 17 | < 0.4 | 13,5 | 2,4 |
| CH25 | Well C | 2656,7 | 4,2 | 0,9 | < 1 | 0,4 | 16 | < 0.4 | 10,9 | 2 |
| CH26 | Well C | 2753,4 | 4,3 | 1,1 | < 1 | 0,5 | 21 | < 0.4 | 13,8 | 2,5 |
| CH27 | Well C | 2888,8 | 4,5 | 1,3 | < 1 | 0,7 | 13 | < 0.4 | 16,4 | 2,8 |
| CH28 | Well C | 2912,5 | 4,6 | 1,5 | < 1 | 0,7 | 18 | < 0.4 | 18,2 | 3 |
| CH29 | Well E | 2751,2 | 6,3 | 1,5 | < 1 | 0,7 | 20 | < 0.4 | 18,9 | 3 |
| CH30 | Well E | 2752,9 | 6,2 | 1,4 | < 1 | 0,6 | 25 | < 0.4 | 15,8 | 2,8 |
| CH31 | Well E | 3466,0 | 4,7 | 1,4 | 7 | 0,5 | 70 | < 0.4 | 11,8 | 2,4 |

Table 4.3 ICP OES and ICP MS data (major and trace elements) for Sergipe mudstone samples (pages:371-373).

| Sample | Depth | Si/Al | K/Al | Na/Al | ICV | CaO* | CIA | CIW | LaN/YbN | Eu/Eu* |
|--------|--------|-------|-------|-------|-------|-------|--------|--------|---------|--------|
| XM1 | 1460,5 | 3,487 | 0,244 | 0,091 | 0,943 | 0,011 | 73,043 | 90,391 | 8,362 | 0,440 |
| XM2 | 1515,5 | 2,959 | 0,241 | 0,059 | 0,773 | 0,013 | 76,180 | 93,490 | 8,668 | 0,375 |
| XM3 | 1633 | 3,423 | 0,247 | 0,064 | 0,821 | 0,010 | 75,748 | 92,977 | 8,920 | 0,462 |
| XM4 | 1683 | 2,763 | 0,232 | 0,040 | 0,721 | 0,009 | 79,418 | 95,511 | 9,145 | 0,545 |
| XM5 | 1725,5 | 3,944 | 0,266 | 0,060 | 0,845 | 0,011 | 75,100 | 93,445 | 8,589 | 0,674 |
| XM6 | 1755,5 | 3,498 | 0,246 | 0,051 | 0,741 | 0,009 | 77,386 | 94,402 | 8,447 | 0,622 |
| XM7 | 1865,5 | 2,602 | 0,249 | 0,044 | 0,775 | 0,010 | 78,106 | 95,090 | 8,987 | 0,374 |
| XM8 | 1945,5 | 2,719 | 0,221 | 0,058 | 0,800 | 0,013 | 77,218 | 93,658 | 9,171 | 0,655 |
| XM9 | 2015,5 | 3,469 | 0,286 | 0,076 | 0,940 | 0,014 | 72,195 | 91,816 | 8,985 | 0,343 |
| XM10 | 2090,5 | 2,761 | 0,251 | 0,074 | 0,773 | 0,017 | 73,745 | 92,023 | 9,210 | 0,391 |

Table 4.4 Ratios of selected pairs of major and trace elements and calculated weathering indices for Central Malay Basin mudstone samples.

| Sample | Depth | Si/Al | K/Al | Na/Al | ICV | CaO* | CIA | CIW | LaN/YbN | Eu/Eu* |
|--------|---------|-------|-------|-------|-------|-------|--------|--------|---------|--------|
| XC1 | 2332 | 3,366 | 0,389 | 0,080 | 1,085 | 0,013 | 68,230 | 91,440 | 8,478 | 0,363 |
| XC2 | 2442 | 3,264 | 0,343 | 0,070 | 1,042 | 0,012 | 70,981 | 92,431 | 7,980 | 0,320 |
| XC3 | 2537 | 2,371 | 0,321 | 0,073 | 1,109 | 0,015 | 71,290 | 92,068 | 8,475 | 0,266 |
| XC4 | 2637 | 3,069 | 0,339 | 0,068 | 1,385 | 0,011 | 71,331 | 92,600 | 8,720 | 0,310 |
| XC5 | 2747 | 2,135 | 0,255 | 0,059 | 1,003 | 0,013 | 75,665 | 93,526 | 8,309 | 0,087 |
| XC6 | 2812 | 2,701 | 0,329 | 0,057 | 1,242 | 0,010 | 73,069 | 93,697 | 8,197 | |
| XC7 | 3054 | 3,521 | 0,239 | 0,119 | 0,911 | 0,021 | 68,715 | 87,778 | 8,520 | |
| XC8 | 3254 | 2,842 | 0,219 | 0,094 | 0,888 | 0,019 | 72,236 | 90,028 | 8,217 | |
| XC9 | 3454 | 2,817 | 0,195 | 0,096 | 0,836 | 0,020 | 72,872 | 89,851 | 8,503 | |
| XC10 | 3655 | 2,416 | 0,199 | 0,071 | 0,857 | 0,015 | 76,122 | 92,267 | 8,579 | |
| XC11 | 3790 | 2,745 | 0,195 | 0,091 | 0,965 | 0,018 | 73,559 | 90,339 | 8,050 | |
| XC12 | 4078 | 2,293 | 0,204 | 0,072 | 0,856 | 0,016 | 75,874 | 92,241 | 9,153 | |
| XC13 | 4218 | 1,974 | 0,286 | 0,055 | 1,069 | 0,012 | 74,973 | 93,919 | 9,590 | |
| CH1 | 2051 | 4,132 | 0,340 | 0,081 | 1,652 | 0,012 | 69,722 | 91,353 | 7,815 | 0,059 |
| CH2 | 2246 | 2,530 | 0,322 | 0,072 | 1,196 | 0,015 | 71,453 | 92,222 | 9,109 | 0,277 |
| CH3 | 2386 | 2,019 | 0,285 | 0,051 | 1,229 | 0,012 | 75,515 | 94,302 | 8,765 | 0,440 |
| CH4 | 2501,8 | 2,342 | 0,246 | 0,090 | 0,803 | 0,005 | 76,869 | 90,445 | 5,426 | 0,630 |
| CH5 | 2505,8 | 2,293 | 0,215 | 0,071 | 0,682 | 0,007 | 78,880 | 92,276 | 8,263 | 0,664 |
| CH6 | 2765,6 | 2,453 | 0,225 | 0,094 | 0,750 | 0,010 | 75,875 | 90,094 | 8,146 | 0,600 |
| CH7 | 2795,4 | 3,263 | 0,246 | 0,143 | 0,788 | 0,012 | 70,945 | 85,638 | 8,935 | 0,683 |
| CH8 | 2786,8 | 2,675 | 0,240 | 0,117 | 0,714 | 0,007 | 74,758 | 87,955 | 8,679 | 0,669 |
| CH9 | 3017,4 | 2,649 | 0,240 | 0,116 | 0,767 | 0,008 | 74,404 | 87,999 | 8,416 | 0,696 |
| CH10 | 3350 | 2,761 | 0,204 | 0,098 | 0,771 | 0,023 | 72,329 | 89,706 | 8,546 | 0,510 |
| CH11 | 3500 | 2,621 | 0,209 | 0,117 | 0,772 | 0,016 | 73,190 | 87,938 | 9,279 | 0,536 |
| CH12 | 3637,5 | 2,447 | 0,228 | 0,097 | 0,735 | 0,004 | 77,301 | 89,799 | 8,715 | 0,676 |
| CH13 | 3698 | 3,117 | 0,236 | 0,109 | 0,814 | 0,022 | 70,296 | 88,635 | 8,187 | 0,580 |
| CH14 | 3791 | 2,387 | 0,262 | 0,109 | 0,810 | 0,013 | 72,740 | 88,630 | 9,098 | 0,511 |
| CH15 | 3815 | 1,877 | 0,229 | 0,079 | 1,051 | 0,021 | 73,964 | 91,552 | 9,500 | 0,497 |
| CH16 | 3959,8 | 2,640 | 0,199 | 0,081 | 0,683 | 0,009 | 78,069 | 91,288 | 7,877 | 0,680 |
| CH17 | 4010,75 | 2,488 | 0,305 | 0,110 | 0,727 | 0,006 | 73,120 | 88,567 | 9,822 | 0,659 |

Table 4.5 Ratios of selected pairs of major and trace elements and calculated weathering indices for Haltenbanken mudstone samples.

| Sample | Depth | Si/Al | K/Al | Na/Al | ICV | CaO* | CIA | CIW | LaN/YbN | Eu/Eu* |
|--------|---------|-------|-------|-------|-------|-------|--------|--------|---------|--------|
| CH18 | 2465,8 | 2,397 | 0,232 | 0,105 | 0,879 | 0,015 | 73,647 | 89,038 | 12,264 | 0,646 |
| CH19 | 2466,4 | 2,534 | 0,240 | 0,108 | 0,772 | 0,017 | 72,396 | 88,772 | 12,163 | 0,683 |
| CH20 | 2467,6 | 2,457 | 0,221 | 0,103 | 0,729 | 0,016 | 73,747 | 89,199 | 12,475 | 0,661 |
| CH21 | 2471 | 2,727 | 0,218 | 0,110 | 0,962 | 0,013 | 73,952 | 88,598 | 12,339 | 0,655 |
| CH22 | 2347,9 | 3,737 | 0,245 | 0,143 | 1,929 | 0,021 | 65,728 | 85,661 | 12,839 | 0,740 |
| CH23 | 2352,6 | 3,491 | 0,234 | 0,139 | 0,949 | 0,027 | 66,401 | 85,938 | 14,223 | 0,710 |
| CH24 | 2654,57 | 3,543 | 0,341 | 0,168 | 1,176 | 0,032 | 60,601 | 83,551 | 14,258 | 0,736 |
| CH25 | 2656,68 | 3,817 | 0,336 | 0,176 | 1,505 | 0,029 | 60,036 | 82,912 | 13,302 | 0,755 |
| CH26 | 2753,35 | 3,307 | 0,385 | 0,136 | 1,317 | 0,026 | 62,407 | 86,218 | 13,638 | 0,703 |
| CH27 | 2888,8 | 3,126 | 0,404 | 0,124 | 1,017 | 0,026 | 63,097 | 87,313 | 14,326 | 0,687 |
| CH28 | 2912,45 | 2,557 | 0,393 | 0,099 | 0,865 | 0,015 | 68,176 | 89,613 | 13,563 | 0,677 |
| CH29 | 2751,2 | 2,914 | 0,290 | 0,115 | 0,659 | 0,006 | 73,054 | 88,133 | 12,229 | 0,685 |
| CH30 | 2752,9 | 3,547 | 0,277 | 0,139 | 0,813 | 0,022 | 66,710 | 85,980 | 11,688 | 0,661 |
| CH31 | 3466 | 3,820 | 0,270 | 0,175 | 1,336 | 0,028 | 61,813 | 83,000 | 11,088 | |

Table 4.6 Ratios of selected pairs of major and trace elements and calculated weathering indices for Sergipe mudstone samples.

Appendix V

HRXTG data

| Sample | Well | Depth below seafloor (m) | Illite(001; 10 Angs.) | | Illite/smectite (001) | | Chlorite(002)/kaolinite | | Chlorite(001) | |
|--------|---------|--------------------------|-----------------------|--------|-----------------------|--------|-------------------------|--------|---------------|--------|
| | | | MRD | 2Theta | MRD | 2Theta | MRD | 2Theta | MRD | 2Theta |
| XM-2 | Bravo-Y | 1515,5 | 4,88 | 4,06 | | | 3,84 | 5,74 | | |
| XM-7 | Bravo-Y | 1865,5 | 3,33 | 4,06 | | | 2,68 | 5,74 | | |
| XM-10 | Bravo-Y | 2090,5 | 3,52 | 4,06 | | | 3,02 | 5,74 | | |

Table 5.1 HRXTG data for Central Malay Basin mudstone samples.

| Sample | Well | Depth below seafloor (m) | Illite(001; 10 Angs.) | | Illite/smectite (001) | | Chlorite(002)/kaolinite | | Chlorite(001) | |
|--------|------------|--------------------------|-----------------------|--------|-----------------------|--------|-------------------------|--------|---------------|--------|
| | | | MRD | 2Theta | MRD | 2Theta | MRD | 2Theta | MRD | 2Theta |
| xl35 | 6406/2-3 | 3997,8 | | | 7,26 | 3,86 | 8,3 | 5,64 | | |
| xl1 | 6406/2-3 | 4003,0 | 5,6 | 4,06 | 5,6 | | 6,78 | 5,74 | | |
| xl36 | 6406/2-3 | 4010,8 | | | 4,47 | 3,86 | 4,59 | 5,77 | | |
| xl37 | 6406/2-3 | 4020,0 | | | 2,96 | 3,86 | 2,29 | 5,82 | | |
| xl2 | 6406/2-3 | 4025,0 | 4,74 | 4,06 | 4,74 | | 4,14 | 5,74 | | |
| xl21 | 6506/11-3 | 2795,4 | | | 3,68 | 3,54 | 3,83 | 5,64 | | |
| xl16 | 6506/11-3 | 2815,0 | | | 3,69 | 3,54 | 4,09 | 5,74 | | |
| xl23 | 6506/11-3 | 3576,9 | | | 4,51 | 3,73 | 5,45 | 5,74 | | |
| xl15 | 6506/11-3 | 3588,6 | | | 4,78 | 3,73 | 5,04 | 5,74 | | |
| xl19 | 6506/11-3 | 3592,5 | | | 5,36 | 3,89 | 5,02 | 5,74 | | |
| xl25 | 6506/11-3 | 3593,4 | | | 4,78 | 3,86 | 4,94 | 5,64 | | |
| xl22 | 6506/11-3 | 3636,5 | | | 3,98 | 3,89 | 3,77 | 5,8 | | |
| xl18 | 6506/11-3 | 3636,7 | | | 3,7 | 3,86 | 3,54 | 5,74 | | |
| xl17 | 6506/11-3 | 3637,5 | | | 3,4 | 3,95 | 3,09 | 5,74 | | |
| xl24 | 6506/11-3 | 3640,9 | | | 4,65 | 3,86 | 4,37 | 5,74 | | |
| xl20 | 6506/11-3 | 3644,0 | | | 4,96 | 3,95 | 4,68 | 5,74 | | |
| xl13 | 6506/11-4S | 3935,3 | | | 4,73 | 3,86 | 4,1 | 5,74 | | |
| xl10 | 6506/11-4S | 3954,8 | | | 4,23 | 3,76 | 4,32 | 5,74 | | |
| xl11 | 6506/11-4S | 3955,8 | | | 5,09 | 3,73 | 4,63 | 5,74 | | |
| xl8 | 6506/11-4S | 3958,6 | | | 4,45 | 3,67 | 3,76 | 5,74 | | |
| xl9 | 6506/11-4S | 3959,8 | | | 4,91 | 3,89 | 5,3 | 5,74 | | |
| xl14 | 6506/11-4S | 3962,0 | | | 5 | 3,86 | 4,82 | 5,8 | | |
| xl12 | 6506/11-4S | 3964,9 | | | 4,25 | 3,86 | 3,18 | 5,74 | | |
| xl26 | 6506/3-1 | 2756,9 | | | 4,43 | 3,73 | 4,45 | 5,74 | | |
| xl27 | 6506/3-1 | 2765,6 | | | 4,72 | 3,86 | 5,06 | 5,64 | | |
| xl28 | 6506/3-1 | 2777,2 | | | 4,42 | 3,64 | 4,63 | 5,64 | | |
| xl29 | 6506/3-1 | 2786,8 | 4,19 | 3,86 | 3,91 | 3,54 | | | | |
| xl30 | 6507/2-3 | 2495,6 | | | 4,47 | 3,86 | 4,64 | 5,74 | | |
| xl3 | 6507/2-3 | 2501,0 | 3,85 | 4,06 | 3,85 | | 3,71 | 5,74 | | |
| xl31 | 6507/2-3 | 2505,8 | | | 4,61 | 3,86 | 4,97 | 5,64 | | |
| xl32 | 6507/2-3 | 2507,6 | | | 5,39 | 3,8 | | | 5,24 | 3,04 |
| xl4 | 6507/2-3 | 2508,0 | 3,98 | 4,06 | 3,98 | | 4,14 | 5,74 | | |
| xl33 | 6507/2-3 | 2512,9 | 5,02 | 3,86 | 4,74 | 3,36 | 5,21 | 5,68 | | |
| xl34 | 6507/2-3 | 2513,8 | 4,97 | 3,86 | 4,59 | 3,54 | 4,89 | 5,74 | 4,59 | 3,14 |
| xl5 | 6507/2-3 | 2878,0 | 5,27 | 4,06 | 5,27 | | 5,26 | 5,74 | | |
| xl7 | 6607/5-1 | 3016,0 | | | 3,77 | 3,64 | 3,76 | 5,64 | | |
| xl6 | 6607/5-1 | 3017,4 | 4,71 | 4,06 | 4,54 | 3,86 | 4,69 | 5,74 | | |

Table 5.2 HRXTG data for Haltenbanken mudstone samples.

| Sample | Well | Depthrelative to kelly bushing (m) | Illite(001; 10 Angs.) | | Illite/smectite (001) | | Chlorite(002)/kaolinite | | Chlorite(001) | |
|--------|-----------|---------------------------------------|-----------------------|--------|-----------------------|--------|-------------------------|--------|---------------|--------|
| | | | MRD | 2Theta | MRD | 2Theta | MRD | 2Theta | MRD | 2Theta |
| msk3 | 22/29-1 | 4599 | 3,33 | 4,06 | | | 3,2 | 5,74 | | |
| msk4 | 22/29-1 | 4718 | 4,13 | 4,06 | | | 4,27 | 5,74 | | |
| sk12 | 30/2c-04 | 4791,44 | | | 4,48 | 3,75 | 4,57 | 5,64 | | |
| mcsk5 | 30/2c-4 | 4807 | 5,16 | 4,06 | | | 5,16 | 5,74 | | |
| sk11 | 30/2c-J07 | 4972,31 | | | 2,95 | 3,94 | 2,76 | 5,64 | | |
| sk8 | 30/2c-J07 | 4973,02 | 7,33 | 4,05 | 7,36 | 3,86 | 6,16 | 5,68 | | |
| mcsk3 | 30/2c-J07 | 5009 | 2,66 | 4,06 | | | 2,4 | 5,74 | | |
| mcsk7 | 30/7a-7 | 3487 | 5,14 | 4,06 | | | 4,88 | 5,74 | | |
| sk6 | 6/3-1 | 3028,65 | | | 6,78 | 3,86 | 6,59 | 5,96 | | |
| sk5 | 6/3-1 | 3041,5 | | | 3,17 | 3,95 | 2,95 | 5,68 | | |
| sk4 | 6/3-1 | 3043 | 2,99 | 4,08 | 3,09 | 3,73 | 2,86 | 5,8 | | |
| sk3 | 6/3-1 | 3059,65 | | | 4,95 | 3,92 | 4,04 | 5,93 | | |
| sk1 | 6/3-1 | 3061,95 | | | 4,69 | 3,92 | 4,55 | 5,74 | | |
| sk7 | 6/3-1 | 3092,07 | 2,18 | 4,05 | 2,18 | 3,86 | 2,08 | 5,74 | | |

Table 5.3 HRXTG data for Central North Sea Triassic mudstone samples.

Appendix VI

MICP data

| Sample | Well | Depth below seafloor (m) | grain density | total porosity | corrected porosity | cut off radius (nm) | Rmean (nm) | calculated permeability (m ²) |
|--------|------------|--------------------------|---------------|----------------|--------------------|---------------------|------------|---|
| ML1 | 6406/2-3 | 3986,0 | 2,70 | 0,084 | 0,075 | 28,05 | 2,90 | 9,36E-22 |
| ML2 | 6406/2-3 | 4002,7 | 2,60 | 0,062 | 0,051 | 11,05 | 1,30 | 4,96E-22 |
| ML3 | 6406/2-3 | 4020,0 | 2,71 | 0,089 | 0,083 | 21,45 | 4,70 | 1,14E-21 |
| ML4 | 6406/2-3 | 4025,9 | 2,72 | 0,081 | 0,070 | 16,80 | 4,00 | 8,26E-22 |
| XL16 | 6506/11-3 | 2815,0 | 2,73 | 0,170 | 0,160 | 72,90 | 9,80 | 5,84E-21 |
| XL15 | 6506/11-3 | 3588,6 | 2,74 | 0,130 | 0,097 | 32,15 | 3,50 | 1,57E-21 |
| XL11 | 6506/11-4S | 3955,8 | 2,83 | 0,103 | 0,092 | 18,85 | 2,10 | 1,40E-21 |
| XL8 | 6506/11-4S | 3958,6 | 2,94 | 0,132 | 0,125 | 18,85 | 1,80 | 2,88E-21 |
| XL26 | 6506/3-1 | 2756,9 | 2,84 | 0,168 | 0,151 | 546,65 | 8,90 | 4,89E-21 |
| ML5 | 6507/2-3 | 2501,8 | 2,74 | 0,163 | 0,146 | 156,20 | 8,40 | 4,42E-21 |
| ML6 | 6507/2-3 | 2505,8 | 2,70 | 0,166 | 0,142 | 16,80 | 4,00 | 4,08E-21 |
| ML7 | 6507/2-3 | 2508,8 | 2,71 | 0,172 | 0,155 | 546,65 | 25,20 | 5,29E-21 |
| ML8 | 6507/2-3 | 2878,6 | 2,75 | 0,124 | 0,117 | 28,05 | 5,20 | 2,43E-21 |

Table 6.1 Grain density, total porosity and MICP data for Haltenbanken mudstone samples.

| Sample | Well | Depth below seafloor (m) | grain density | total porosity | corrected porosity | cut off radius (nm) | Rmean (nm) | calculated permeability (m ²) |
|--------|--------|--------------------------|---------------|----------------|--------------------|---------------------|------------|---|
| XSA8 | Well A | 2465,8 | 2,85 | 0,175 | 0,166 | 72,90 | 9,2 | 6,57E-21 |
| XSA1 | Well A | 2466,4 | 2,63 | 0,102 | 0,096 | 156,20 | 21,2 | 1,54E-21 |
| SA5 | Well A | 2468,5 | 2,89 | 0,182 | 0,171 | 546,65 | 11,3 | 7,24E-21 |
| SA1 | Well A | 2471,9 | 2,8 | 0,158 | 0,15 | 546,65 | 15 | 4,79E-21 |
| SA4 | Well C | 2655,4 | 2,74 | 0,132 | 0,121 | 546,65 | 10,6 | 2,65E-21 |
| XSA3 | Well C | 2656,7 | 2,79 | 0,102 | 0,096 | 364,45 | 8,1 | 1,54E-21 |
| XSA9 | Well C | 2753,4 | 2,83 | 0,129 | 0,115 | 546,65 | 8,5 | 2,33E-21 |
| SA3 | Well C | 2911,8 | 2,75 | 0,112 | 0,085 | 546,65 | 11,3 | 1,19E-21 |
| XSA7 | Well C | 2912,5 | 2,78 | 0,091 | 0,078 | 15,00 | 1,8 | 1,01E-21 |
| SA2 | Well E | 2751,7 | 2,72 | 0,135 | 0,123 | 2733,35 | 48,8 | 2,76E-21 |
| XSA12 | Well E | 2752,9 | 2,85 | 0,167 | 0,156 | 2733,35 | 43,2 | 5,40E-21 |

Table 6.2 Grain density, total porosity and MICP data for Sergipe mudstone samples.

| Sample | Well | Depth relative to kelly bushing (m) | grain density | total porosity | corrected porosity | cut off radius (nm) | Rmean (nm) | calculated permeability (m ²) |
|--------|-----------|-------------------------------------|---------------|----------------|--------------------|---------------------|------------|---|
| MSK1 | 22/29-1 | 4592.8 | 2,60 | 0,057 | 0,042 | 12,15 | 0,6 | 3,79E-22 |
| MSK2 | 22/29-1 | 4594.3 | 2,72 | 0,048 | 0,041 | 6,85 | 1,0 | 3,67E-22 |
| MSK3 | 22/29-1 | 4599.7 | 2,79 | 0,080 | 0,073 | 13,50 | 1,0 | 8,91E-22 |
| MSK4 | 22/29-1 | 4718.3 | 2,72 | 0,057 | 0,046 | 12,15 | 2,9 | 4,28E-22 |
| MCSK1 | 30/2c-J07 | 4973.0 | 2,79 | 0,014 | 0,010 | 2,90 | 0,0 | 1,03E-22 |
| MCSK2 | 30/2c-J07 | 4987.4 | 2,77 | 0,055 | 0,050 | 9,20 | 3,2 | 4,82E-22 |
| MCSK3 | 30/2c-J07 | 5009.4 | 2,76 | 0,096 | 0,080 | 6,45 | 1,9 | 1,06E-21 |
| MCSK4 | 30/2c-04 | 4791.2 | 2,75 | 0,079 | 0,072 | 7,30 | 2,8 | 8,69E-22 |
| MCSK5 | 30/2c-04 | 4806.7 | 2,75 | 0,078 | 0,074 | 7,80 | 3,2 | 9,14E-22 |
| MCSK6 | 30/7a-7 | 3460.1 | 2,83 | 0,177 | 0,169 | 15,00 | 5,1 | 6,96E-21 |
| MCSK7 | 30/7a-7 | 3487.5 | 2,77 | 0,132 | 0,127 | 12,15 | 4,5 | 3,00E-21 |

Table 6.3 Grain density, total porosity and MICP data for Central North Sea Triassic mudstone samples.

Raw data from MICP and the QXRD modelling is considerable in size and is therefore included with this thesis in Excel files and ppts on a separate disc (CD appendix), along with other raw data.

References

- Ahn, J. H., and D. R. Peacor, 1986, Transmission and analytical electron microscopy of the smectite-to-illite transition: *Clays and Clay Minerals*, v. 34, no. 2, p. 165–179.
- Ahn, J. H., and D. R. Peacor, 1986, Transmission electron microscope data for rectorite: Implications for the origin and structure of “fundamental particles”: *Clays Clay Miner.*, v. 34, no. 2, p. 180–186.
- Altaner, S. P., C. A. Weiss, and R. J. Kirkpatrick, 1988, Evidence from ²⁹Si NMR for the structure of mixed-layer illite/smectite clay minerals: *Nature*, v. 331, no. 6158, p. 699–702, doi:10.1038/331699a0.
- Altaner, S. S. P., and R. R. F. Ylagan, 1997, Comparison of structural models of mixed-layer illite/smectite and reaction mechanisms of smectite illitization: *Clays and Clay Minerals*, v. 45, no. 4, p. 517–533, doi:10.1346/CCMN.1997.0450404.
- Andras, P., A. C. Aplin, N. R. Goult, C. Sargent, A. Derkowski, and B. A. van der Pluijm, 2016, Clay Mineral Transformations and Associated Compaction of Siliciclastic Mudstones, *in* Fifth EAGE Shale Workshop: doi:10.3997/2214-4609.201600396.
- Anjos, S. M. C., 1986, Absence of Clay Diagenesis in Cretaceous-Tertiary Marine Shales, Campos Basin, Brazil: *Clays and Clay Minerals*, v. 34, no. 4, p. 424–434, doi:10.1346/CCMN.1986.0340409.
- Aplin, A. C., A. J. Fleet, and J. H. S. Macquaker, 1999, Muds and mudstones: physical and fluid-flow properties: Geological Society, London, Special Publications, v. 158, no. 1, p. 1–8, doi:10.1144/GSL.SP.1999.158.01.01.
- Aplin, A. C., and J. H. S. Macquaker, 2011, Mudstone diversity: Origin and implications for source, seal, and reservoir properties in petroleum systems: *AAPG Bulletin*, v. 95, no. 12, p. 2031–2059, doi:10.1306/03281110162.
- Aplin, A. C., I. F. Matenaar, D. K. McCarty, and B. A. van der Pluijm, 2006, Influence of mechanical compaction and clay mineral diagenesis on the microfabric and pore-scale properties of deep-water Gulf of Mexico mudstones: *Clays and Clay Minerals*, v. 54, no. 4, p. 500–514, doi:10.1346/CCMN.2006.0540411.
- Aplin, A. C., Y. Yang, and S. Hansen, 1995, Assessment of β the compression coefficient of mudstones and its relationship with detailed lithology: *Marine and Petroleum Geology*, v. 12, no. 8, p. 955–963, doi:10.1016/0264-8172(95)98858-3.

- Armitage, P. J., R. H. Worden, D. R. Faulkner, A. C. Aplin, A. R. Butcher, and J. Iliffe, 2010, Diagenetic and sedimentary controls on porosity in Lower Carboniferous fine-grained lithologies, Krechba field, Algeria: A petrological study of a caprock to a carbon capture site: *Marine and Petroleum Geology*, v. 27, no. 7, p. 1395–1410, doi:10.1016/j.marpetgeo.2010.03.018.
- Aronson, J. L., and J. Hower, 1976, Mechanism of burial metamorphism of argillaceous sediment: 2. Radiogenic argon evidence: *Geological Society of America Bulletin*, v. 87, no. 5, p. 738, doi:10.1130/0016-7606(1976)87<738:MOBMOA>2.0.CO;2.
- Athy, L. F., 1930, Density, Porosity, and Compaction of Sedimentary Rocks: *AAPG Bulletin*, v. 14, no. 1, p. 194–200, doi:10.1306/3D93289E-16B1-11D7-8645000102C1865D.
- Atterberg, A. M., 1911, Die plastizität der tone: *Internationale Mitteilungen für Bodenkunde*, v. 1, p. 4–37.
- Audet, D. M., 1995, Mathematical modelling of gravitational compaction and clay dehydration in thick sediment layers: *Geophysical Journal International*, v. 122, no. 1, p. 283–298, doi:10.1111/j.1365-246X.1995.tb03554.x.
- Awwiller, D., 1993, Illite/smectite formation and potassium mass transfer during burial diagenesis of mudrocks: a study from the Texas Gulf Coast Paleocene-Eocene: *Journal of Sedimentary Research*, v. 63, no. 3, p. 501–512.
- Bailey, S. W., 1980, Summary of recommendations of AIPEA Nomenclature Committee on clay minerals: *American Mineralogist*, v. 65, no. 1–2, p. 1–7.
- Banik, N. C., 1983, Velocity Anisotropy of Shales And Depth Anomalies In the North Sea: *Society of Exploration Geophysicists*, p. 540–542.
- Banik, N. C., 1984, Velocity anisotropy of shales and depth estimation in the North Sea basin: *GEOPHYSICS*, v. 49, no. 9, p. 1411–1419, doi:10.1190/1.1441770.
- Bardon, C. et al., 1983, Recommandations pour la détermination expérimentale de la capacité d'échange de cations des milieux argileux: *Revue de l'Institut Français du Pétrole*, v. 38, no. 5, p. 621–626, doi:10.2516/ogst:1983037.
- Bennett, R. H., W. R. Bryant, and G. H. Keller, 1981, Clay Fabric of Selected Submarine Sediments: Fundamental Properties and Models: *Journal of Sedimentary Research*, v. 51, no. 1.
- Bennett, R., N. O'Brien, and H. Hulbert, 1991, Determinants of clay and shale microfabric signatures: Processes and mechanisms, *in* R. Bennett, W. Bryant, and M. Hulbert,

- eds., *Microstructure of Fine-Grained Sediments*: Berlin, Springer Verlag, p. 5–33.
- Berg, R. R., and M. F. Habeck, 1982, Abnormal Pressures in the Lower Vicksburg, McAllen Ranch Field, South Texas: *Association of Geological Sciences*, v. 32, p. 247–253.
- Berger, G., B. Velde, and T. Aigouy, 1999, Potassium sources and illitization in Texas Gulf Coast shale diagenesis: *Journal of Sedimentary Research*, v. 69, no. 1, p. 151–157, doi:10.2110/jsr.69.151.
- Bhatia, M. R., 1985, Rare earth element geochemistry of Australian Paleozoic graywackes and mudrocks: Provenance and tectonic control: *Sedimentary Geology*, v. 45, no. 1, p. 97–113, doi:10.1016/0037-0738(85)90025-9.
- Bhatia, M. R., and K. A. W. Crook, 1986, Trace element characteristics of graywackes and tectonic setting discrimination of sedimentary basins: *Contributions to Mineralogy and Petrology*, v. 92, no. 2, p. 181–193, doi:10.1007/BF00375292.
- Bhatia, M. R., and S. R. Taylor, 1981, Trace-element geochemistry and sedimentary provinces: A study from the Tasman Geosyncline, Australia: *Chemical Geology*, v. 33, no. 1–4, p. 115–125, doi:10.1016/0009-2541(81)90089-9.
- Bischof, B., A. J. Mariano, and E. H. Ryan, 2003, “The North Brazil Current.” *Ocean Surface Currents*: <http://oceancurrents.rsmas.miami.edu/atlantic/north-brazil.html> (accessed July 8, 2017).
- Bishop, M. G., 2002, *Petroleum systems of the Malay Basin Province, Malaysia*.
- Bishop, D. J., 1996, Regional distribution and geometry of salt diapirs and supra-Zechstein Group faults in the western and central North Sea: *Marine and Petroleum Geology*, v. 13, no. 4, p. 355–364, doi:10.1016/0264-8172(95)00081-X.
- Bjorkum, P. A., and P. H. Nadeau, 1998, Temperature controlled porosity/ permeability reduction, fluid migration, and petroleum exploration in sedimentary basins: *Australian Petroleum Exploration Association Journal*, v. 38, no. DECEMBER 1995, p. 453–464.
- Bjørlykke, K., 1997, Mineral/Water Interaction, Fluid Flow, and Frio Sandstone Diagenesis: Evidence from the Rocks: Discussion: *AAPG Bulletin*, v. 81, no. 9, p. 1534–1535.
- Bjørlykke, K., 1999, Principal aspects of compaction and fluid flow in mudstones: *Geological Society, London, Special Publications*, v. 158, no. 1, p. 73–78, doi:10.1144/GSL.SP.1999.158.01.06.
- Bjørlykke, K., 1998, *Clay Mineral Diagenesis in Sedimentary Basins — A Key to the*

- Prediction of Rock Properties. Examples from the North Sea Basin: *Clay Minerals*, v. 33, no. 1, p. 15–34, doi:10.1180/000985598545390.
- Bjørlykke, K., 2014, Relationships between depositional environments, burial history and rock properties. Some principal aspects of diagenetic process in sedimentary basins: *Sedimentary Geology*, v. 301, p. 1–14, doi:10.1016/j.sedgeo.2013.12.002.
- Bjørlykke, K., and K. Høeg, 1997, Effects of burial diagenesis on stresses, compaction and fluid flow in sedimentary basins: *Marine and Petroleum Geology*, v. 14, no. 3, p. 267–276, doi:10.1016/S0264-8172(96)00051-7.
- Bjørlykke, K., and J. Jahren, 2012, Open or closed geochemical systems during diagenesis in sedimentary basins: Constraints on mass transfer during diagenesis and the prediction of porosity in sandstone and carbonate reservoirs: *AAPG Bulletin*, v. 96, no. 12, p. 2193–2214, doi:10.1306/04301211139.
- Blystad, P., H. Brekke, R. B. Færseth, B. T. Larsen, J. Skogseid, and B. Tørudbakken, 1995, Structural elements of the Norwegian Continental Shelf. Part 2. The Norwegian Sea Region.: *Norwegian Petroleum Directorate Bulletin*, v. 8.
- Boles, J., and S. Franks, 1979, Clay diagenesis in Wilcox sandstones of southwest Texas: implications of smectite diagenesis on sandstone cementation: *Journal of Sedimentary Petrology*, v. 49, p. 55–70.
- Bowers, G. L., 2001, Determining an Appropriate Pore-Pressure Estimation Strategy, *in* Offshore Technology Conference: Offshore Technology Conference, doi:10.4043/13042-MS.
- Bowers, G. L., 1995, Pore pressure estimation from velocity data: Accounting for overpressure mechanisms besides undercompaction: *SPE Drilling & Completion*, v. 10, no. 2, p. 89–95, doi:10.2118/27488-PA.
- Bowers, G., and T. Katsube, 2002, The Role of Shale Pore Structure on the Sensitivity of Wire-Line Logs to Overpressure, *in* A. R. Huffmann, and B. G. L., eds., *Pressure Regimes in Sedimentary Basins and their Prediction*: AAPG Memoir, p. 43–60.
- Brekke, H., S. Dahlgren, B. Nyland, and C. Magnus, 1999, The prospectivity of the Vøring and Møre Basins on the Norwegian Sea continental margin, *in* A. J. Fleet, and S. A. Boldy, eds., *Petroleum Geology of the Northwest Europe: Proceedings of the 5th Conference*: Geological Society of London, p. 271–283.
- Bruce, C. H., 1973, Pressured Shale and Related Sediment Deformation: Mechanism for

- Development of Regional Contemporaneous Faults: AAPG Bulletin, v. 57, no. 5, p. 878–886.
- Bruce, C. H., 1984, Smectite Dehydration--Its Relation to Structural Development and Hydrocarbon Accumulation in Northern Gulf of Mexico Basin: AAPG Bulletin, v. 68, no. 6, p. 673–683.
- Bruijn, R. H. C., and B. S. G. Almqvist, 2015, The role of stress on chemical compaction of illite shale powder: Geological Society, London, Special Publications, v. 409, no. 1.
- Burland, J. B., 1990, On the compressibility and shear strength of natural clays: *Géotechnique*, v. 40, no. 3, p. 329–378, doi:10.1680/geot.1990.40.3.329.
- Burst, J. F., 1959, Post diagenetic clay mineral-environmental relationships in the Gulf Coast Eocene, *in* A. Swineford, ed., *Clays and Clay Minerals: 6th National Clays and Clay Minerals Conference Proceedings*: Pergamon Press.
- Cainelli, C., 1992, Sequence stratigraphy, canyons, and gravity mass-flow deposits in the Piaçabuçu Formation, Sergipe-Alagoas Basin, Brazil: University of Texas.
- Carroll, D., 1958, Role of clay minerals in the transportation of iron: *Geochimica et Cosmochimica Acta*, v. 14, no. 1, p. 1–28, doi:10.1016/0016-7037(58)90090-5.
- Cartwright, J. A., 1994, Episodic basin-wide fluid expulsion from geopressured shale sequences in the North Sea basin: *Geology*, v. 22, no. 5, p. 447–450, doi:10.1130/0091-7613(1994)022.
- Casagrande, A., 1932, Research on the Atterberg limits of soils: *Public roads*, v. 13, p. 121–131.
- Chilingar, G. V., and L. Knight, 1960, Relationship between pressure and moisture content of kaolinite, illite and montmorillonite clays: *Bulletin of the American Association of Petroleum Geologists*, v. 44, no. 1, p. 101–106.
- Cicchino, A. M. P., C. Sargent, N. R. Goult, and A. M. Ramdhan, 2015, Regional variation in Cretaceous mudstone compaction trends across Haltenbanken, offshore mid-Norway: *Petroleum Geoscience*, v. 21, no. 1, p. 17–34, doi:10.1144/petgeo2014-035.
- Claret, F., B. Sakharov, V. Drits, B. Velde, A. Meunier, L. Griffault, and B. Lanson, 2004, Clay minerals in the Meuse-Haute Marne underground laboratory (France): Possible influence of organic matter on clay mineral evolution: *Clays and Clay Minerals*, v. 53, p. 515–532.
- Clark, J. A., J. A. Cartwright, and S. A. Stewart, 1999, Mesozoic dissolution tectonics on the

- West Central shelf, UK Central North Sea: *Marine and Petroleum Geology*, v. 16, no. 3, p. 283–300, doi:10.1016/S0264-8172(98)00040-3.
- Clauer, N., J. Środoń, J. Francu, and V. Šucha, 1997, K-Ar dating of illite fundamental particles separated from illite-smectite: *Clay Minerals*, v. 32, p. 181–196.
- Colten-Bradley, V. A., 1987, Role of Pressure in Smectite Dehydration--Effects on Geopressure and Smectite-to-Illite Transformation: *AAPG Bulletin*, v. 71, no. 11, p. 1414–1427, doi:10.1306/703C8092-1707-11D7-8645000102C1865D.
- Condie, K. C., 1993, Chemical composition and evolution of the upper continental crust: Contrasting results from surface samples and shales: *Chemical Geology*, v. 104, no. 1–4, p. 1–37, doi:10.1016/0009-2541(93)90140-E.
- Corbet, T. F., and C. M. Bethke, 1992, Disequilibrium fluid pressures and groundwater flow in the western Canada sedimentary basin: *Journal of Geophysical Research*, v. 97, no. B5, p. 7203, doi:10.1029/91JB02993.
- Cox, R., D. R. Lowe, and R. L. Cullers, 1995, The influence of sediment recycling and basement composition on evolution of mudrock chemistry in the southwestern United States: *Geochimica et Cosmochimica Acta*, v. 59, no. 14, p. 2919–2940, doi:10.1016/0016-7037(95)00185-9.
- Cuadros, J., 2006, Modeling of smectite illitization in burial diagenesis environments: *Geochimica et Cosmochimica Acta*, v. 70, no. 16, p. 4181–4195, doi:10.1016/j.gca.2006.06.1372.
- Cuadros, J., and J. Linares, 1996, Experimental kinetic study of the smectite-to-illite transformation: *Geochimica et Cosmochimica Acta*, v. 60, no. 3, p. 439–453, doi:10.1016/0016-7037(95)00407-6.
- Cullers, R. L., 1994, The controls on the major and trace element variation of shales, siltstones, and sandstones of Pennsylvanian-Permian age from uplifted continental blocks in Colorado to platform sediment in Kansas, USA: *Geochimica et Cosmochimica Acta*, v. 58, no. 22, p. 4955–4972, doi:10.1016/0016-7037(94)90224-0.
- Cullers, R. L., 2000, The geochemistry of shales, siltstones and sandstones of Pennsylvanian–Permian age, Colorado, USA: implications for provenance and metamorphic studies: *Lithos*, v. 51, no. 3, p. 181–203, doi:10.1016/S0024-4937(99)00063-8.

- Dalland, A., D. Worsley, and K. Ofstad, 1988, A lithostratigraphic scheme for the Mesozoic and Cenozoic succession offshore mid and northern Norway: Norwegian Petroleum Directorate Bulletin, v. 4.
- Davison, I., and R. A. Dos Santos, 1989, Tectonic evolution of the Sergipano Fold Belt, NE Brazil, during the Brasiliano orogeny: *Precambrian Research*, v. 45, no. 4, p. 319–342, doi:10.1016/0301-9268(89)90068-5.
- Day-Stirrat, R., 2006, Diagenetic controls on the phyllosilicate fabric of mudstones: University of Newcastle-upon-Tyne.
- Day-Stirrat, R. J., A. C. Aplin, J. Środoń, and B. A. van der Pluijm, 2008, Diagenetic Reorientation of Phyllosilicate Minerals in Paleogene Mudstones of the Podhale Basin, Southern Poland: *Clays and Clay Minerals*, v. 56, no. 1, p. 100–111, doi:10.1346/CCMN.2008.0560109.
- Day-Stirrat, R. J., S. P. Dutton, K. L. Milliken, R. G. Loucks, A. C. Aplin, S. Hillier, and B. A. van der Pluijm, 2010, Fabric anisotropy induced by primary depositional variations in the silt: clay ratio in two fine-grained slope fan complexes: Texas Gulf Coast and northern North Sea: *Sedimentary Geology*, v. 226, no. 1–4, p. 42–53, doi:10.1016/j.sedgeo.2010.02.007.
- Day-Stirrat, R. J., K. L. Milliken, S. P. Dutton, R. G. Loucks, S. Hillier, A. C. Aplin, and A. M. Schleicher, 2010, Open-system chemical behavior in deep Wilcox Group mudstones, Texas Gulf Coast, USA: *Marine and Petroleum Geology*, v. 27, no. 9, p. 1804–1818, doi:10.1016/j.marpetgeo.2010.08.006.
- Day-Stirrat, R. J., A. M. Schleicher, J. Schneider, P. B. Flemings, J. T. Germaine, and B. A. van der Pluijm, 2011a, Preferred orientation of phyllosilicates: Effects of composition and stress on resedimented mudstone microfabrics: *Journal of Structural Geology*, v. 33, no. 9, p. 1347–1358, doi:10.1016/j.jsg.2011.06.007.
- Day-Stirrat, R. J., A. M. Schleicher, J. Schneider, P. B. Flemings, J. T. Germaine, and B. A. van der Pluijm, 2011b, Preferred orientation of phyllosilicates: Effects of composition and stress on resedimented mudstone microfabrics: *Journal of Structural Geology*, v. 33, no. 9, p. 1347–1358, doi:10.1016/j.jsg.2011.06.007.
- Derkowski, A., and T. F. Bristow, 2012, On the problems of total specific surface area and cation exchange capacity measurements in organic-rich sedimentary rocks: *Clays and Clay Minerals*, v. 60, no. 4, p. 348–362, doi:10.1346/CCMN.2012.0600402.

- Derkowski, A., and L. Marynowski, 2016, Reactivation of cation exchange properties in black shales: *International Journal of Coal Geology*, v. 158, p. 65–77, doi:10.1016/j.coal.2016.03.002.
- Dewhurst, D. N., A. C. Aplin, J.-P. Sarda, and Y. Yang, 1998, Compaction-driven evolution of porosity and permeability in natural mudstones: An experimental study: *Journal of Geophysical Research: Solid Earth*, v. 103, p. 651–661, doi:10.1029/97JB02540.
- Dickinson, G., 1953, Geological Aspects of Abnormal Reservoir Pressures in Gulf Coast Louisiana: *AAPG Bulletin*, v. 37, no. 2, p. 410–432.
- Dong, H., 2005, Interstratified Illite-Smectite: A Review of Contributions of TEM Data to Crystal Chemical Relations and Reaction Mechanisms: *Clay Science*, v. 12, no. Supplement 1, p. 6–12.
- Doust, H., and H. S. Sumner, 2007, Petroleum systems in rift basins - a collective approach in Southeast Asian basins: *Petroleum Geoscience*, v. 13, no. 2, p. 127–144, doi:10.1144/1354-079307-746.
- Draege, A., M. Jakobsen, and T. A. Johansen, 2006, Rock physics modelling of shale diagenesis: *Petroleum Geoscience*, v. 12, no. 1, p. 49–57, doi:10.1144/1354-079305-665.
- Drits, V., B. Sakharov, H. Lindgreen, and A. Salyn, 1997, Sequential structure transformation of illite-smectite-vermiculite during diagenesis of Upper Jurassic shales from the North Sea and Denmark: *Clay Minerals*, v. 32, p. 351–371.
- Drits, V., and C. Tchoubar, 1990, X-ray diffraction by disordered lamellar structures: Theory and applications to microdivided silicates and carbons: Berlin, Springer-Verlag, 371 p.
- Duffy, L. L. M., 2011, Compaction mechanisms in mudstones and shales : implications from the laboratory and nature: Newcastle University.
- Dutta, N. C., 2002, Deepwater geohazard prediction using prestack inversion of large offset P -wave data and rock model: *The Leading Edge*, v. 21, no. 2, p. 193–198, doi:10.1190/1.1452612.
- Dutta, N. C., 2016, Effect of chemical diagenesis on pore pressure in argillaceous sediment: *The Leading Edge*, v. 35, no. 6, p. 523–527, doi:10.1190/tle35060523.1.
- Dutta, N. C., 1988, Fluid Flow in Low Permeable, Porous Media: *Revue de l'Institut Français du Pétrole*, v. 43, no. 2, p. 165–180.

- Dutta, N. C., 1986, Shale Compaction, Burial Diagenesis, and Geopressures: A dynamic Model, solution and some results, *in* Burrus J, ed., Thermal Modelling of Sedimentary Basins: Paris, Technip, p. 149–172.
- Dutta, N. C., and J. Khazanehdari, 2006, Estimation of formation fluid pressure using high-resolution velocity from inversion of seismic data and a rock physics model based on compaction and burial diagenesis of shales: *The Leading Edge*, v. 25, no. 12, p. 1528–1539, doi:10.1190/1.2405339.
- Dutta, N. C., S. Yang, J. Dai, S. Chandrasekhar, F. Dotiwala, and C. V. Rao, 2014, Earth-model building using rock physics and geology for depth imaging: *The Leading Edge*, v. 33, no. 10, p. 1136–1152, doi:10.1190/tle33101136.1.
- Eaton, B. A., 1975, The Equation for Geopressure Prediction from Well Logs, *in* Fall Meeting of the Society of Petroleum Engineers of AIME: Society of Petroleum Engineers, doi:10.2118/5544-MS.
- Eberl, D. D., J. Sacuterodonacute, M. Kralik, B. E. Taylor, and Z. E. Peterman, 1990, Ostwald ripening of clays and metamorphic minerals.: *Science* (New York, N.Y.), v. 248, no. 4954, p. 474–7, doi:10.1126/science.248.4954.474.
- Eberl, D., and J. Srodon, 1988, Ostwald ripening and interparticle-diffraction effects for illite crystals: *American Mineralogist*, v. 73, p. 1335–1345.
- Eberl, D. D., J. Środoń, and H. R. Northrop, 1987, Potassium Fixation in Smectite by Wetting and Drying: p. 296–326, doi:10.1021/bk-1987-0323.ch014.
- Eslinger, E., and D. Pevear, 1988, Clay minerals for petroleum geologists and engineers: Tulsa, USA, SEPM.
- Færseth, R. B., and T. Lien, 2002, Cretaceous evolution in the Norwegian Sea - A period characterized by tectonic quiescence: *Marine and Petroleum Geology*, v. 19, no. 8, p. 1005–1027, doi:10.1016/S0264-8172(02)00112-5.
- Fedo, C. M., H. Wayne Nesbitt, and G. M. Young, 1995, Unraveling the effects of potassium metasomatism in sedimentary rocks and paleosols, with implications for paleoweathering conditions and provenance: *Geology*, v. 23, no. 10, p. 921, doi:10.1130/0091-7613(1995)023<0921:UTEOPM>2.3.CO;2.
- Feijo, F. J., 2014, Sergipe Basin, Old Oil Province Reborn: Search and Discovery Article #110174.
- Floyd, P. A., and B. E. Leveridge, 1987, Tectonic environment of the Devonian Gramscatho

- basin, south Cornwall: framework mode and geochemical evidence from turbiditic sandstones: *Journal of the Geological Society*, v. 144, no. 4, p. 531–542, doi:10.1144/gsjgs.144.4.0531.
- Folk, R. L., 1974, *Petrology of Sedimentary Rocks*: Hemphill Publishing Company, 182 p.
- Fonneland, H. C., T. Lien, O. J. Martinsen, R. B. Pedersen, and J. Košler, 2004, Detrital zircon ages: A key to understanding the deposition of deep marine sandstones in the Norwegian Sea: *Sedimentary Geology*, v. 164, no. 1–2, p. 147–159, doi:10.1016/j.sedgeo.2003.09.005.
- Foscolos, A. E., 1984, Diagenesis 7. Catagenesis of argillaceous sedimentary rocks: *Geoscience Canada*, v. 11, p. 67–74.
- Freed, R. L., and D. R. Peacor, 1989, Geopressured shale and sealing effect of smectite to illite transition: *American Association of Petroleum Geologists Bulletin*, v. 73, no. 10, p. 1223–1232, doi:10.1306/44B4AA0A-170A-11D7-8645000102C1865D.
- Garrels, R., and F. Mackenzie, 1971, *Evolution of sedimentary rocks*: New York, W.W. Norton.
- Ghosh, D., M. F. A. Halim, M. Brewer, B. Viratno, and N. Darman, 2010, Geophysical issues and challenges in Malay and adjacent basins from an E and P perspective: *The Leading Edge*, v. 29, no. 4, p. 436–449, doi:10.1190/1.3378307.
- Giesche, H., 2006, Mercury Porosimetry: A General (Practical) Overview: *Particle & Particle Systems Characterization*, v. 23, no. 1, p. 9–19, doi:10.1002/ppsc.200601009.
- Giles, M. R., S. L. Indrelid, and D. M. D. James, 1998, Compaction -- the great unknown in basin modelling: *Geological Society, London, Special Publications*, v. 141, no. 1, p. 15–43, doi:10.1144/GSL.SP.1998.141.01.02.
- Glennie, K. W., 1998, *Petroleum geology of the North Sea: Basic concepts and recent advances*, 4th ed.: Oxford, United Kingdom, Blackwell Publishing Ltd., 636 p.
- Goldsmith, P., G. Hudson, and P. Van Veen, 2003, Triassic, *in* D. Evans, C. Graham, A. Armour, and P. Bathurst, eds., *The Millenium Atlas: Petroleum geology of the central and northern North Sea*: London, United Kingdom, Geological Society (London), p. 105–127.
- Goldsmith, P. J., B. Rich, and J. Standring, 1995, Triassic correlation and stratigraphy in the South Central Graben, UK North Sea: *Geological Society, London, Special Publications*, v. 91, no. 1, p. 123–143, doi:10.1144/GSL.SP.1995.091.01.07.

- Goult, N. R., 2004, Mechanical compaction behaviour of natural clays and implications for pore pressure estimation: *Petroleum Geoscience*, v. 10, no. 1, p. 73–79, doi:10.1144/1354-079302-552.
- Goult, N. R., 2015, Revised Bowers' method of pore pressure estimation, *in* GeoPOP3 Final Report: Durham, p. 269–278.
- Goult, N. R., and A. M. Ramdhan, 2012, The challenge of pore pressure estimation in diagenetically consolidated mudrocks: *First Break*, v. 30, no. 12, p. 67–72.
- Goult, N. R., A. M. Ramdhan, and S. J. Jones, 2012, Chemical compaction of mudrocks in the presence of overpressure: *Petroleum Geoscience*, v. 18, no. 4, p. 471–479, doi:10.1144/petgeo2012-018.
- Goult, N. R., and C. Sargent, 2016, Compaction of diagenetically altered mudstones – Part 2: Implications for pore pressure estimation: *Marine and Petroleum Geology*, v. 77, p. 806–818, doi:10.1016/j.marpetgeo.2016.07.018.
- Goult, N. R., C. Sargent, P. Andras, and A. C. Aplin, 2016, Compaction of diagenetically altered mudstones – Part 1: Mechanical and chemical contributions: *Marine and Petroleum Geology*, doi:10.1016/j.marpetgeo.2016.07.015.
- Guggenheim, S., J. M. Adams, D. C. Bain, F. Bergaya, M. F. Brigatti, V. A. Drits, M. L. L. Formoso, E. Galán, T. Kogure, and H. Stanjek, 2006, Summary of recommendations of nomenclature committees relevant to clay mineralogy: report of the Association Internationale pour l'Etude des Argiles (AIPEA) Nomenclature Committee for 2006: *Clay Minerals*, v. 41, no. 4, p. 863–877, doi:10.1180/0009855064140225.
- Haines, S. H., B. A. van der Pluijm, M. J. Ikari, D. M. Saffer, and C. Marone, 2009, Clay fabric intensity in natural and artificial fault gouges: Implications for brittle fault zone processes and sedimentary basin clay fabric evolution: *Journal of Geophysical Research*, v. 114, no. B5, p. B05406, doi:10.1029/2008JB005866.
- Halim, M., 1994, Geothermics of the Malaysian sedimentary basins: *Bulletin of the Geological Society of Malaysia*, v. 36, p. 163–174.
- Hamsi, G. P., 2010, *The Ocean-Continent Transition Along The Northeast Brazilian Rifted Margin*: University of Liverpool.
- Hansen, S., 1996, A compaction trend for Cretaceous and Tertiary shales on the Norwegian shelf based on sonic transit times: *Petroleum Geoscience*, v. 2, no. 2, p. 159–166, doi:10.1144/petgeo.2.2.159.

- Harrison, W. J., and L. L. Summa, 1991, Paleohydrology of the Gulf of Mexico basin: American Journal of Science, v. 291, no. 2, p. 109–176, doi:10.2475/ajs.291.2.109.
- Hart, B., P. Flemings, and A. Deshpande, 1995, Porosity and pressure: Role of compaction disequilibrium in the development of geopressures in a Gulf Coast Pleistocene basin: Geology, v. 23, no. 1, doi:10.1130/0091-7613(1995)023<0045.
- Hedberg, H., 1936, Gravitational compaction of clays and shales: American Journal of Science.
- Hendricks, S., and E. Teller, 1942, X-Ray Interference in Partially Ordered Layer Lattices: The Journal of Chemical Physics, v. 10, no. 3, p. 147–167, doi:10.1063/1.1723678.
- Hermanrud, C., S. Cao, and I. Lerche, 1990, Estimates of virgin rock temperature derived from BHT measurements: Bias and error: GEOPHYSICS, v. 55, no. 7, p. 924–931, doi:10.1190/1.1442908.
- Hermanrud, C., L. Wensaas, G. M. G. Teige, H. M. N. Bolas, S. Hansen, and E. Vik, 1998, Shale porosities from well logs on haltenbanken (offshore mid-Norway) show no influence of overpressuring: Abnormal Pressures in Hydrocarbon Environments, v. 70, no. 1959, p. 65–85.
- Heslop, A., 1974, Gamma-ray Log Response Of Shaly Sandstones: The Log Analyst, v. 15, no. 5.
- Hillier, S., 2000, Accurate quantitative analysis of clay and other minerals in sandstones by XRD: comparison of a Rietveld and a reference intensity ratio (RIR) method and the importance of sample preparation: Clay Minerals, v. 35, no. 1, p. 291–291, doi:10.1180/000985500546666.
- Hillier, S., 2003, Quantitative analysis of clay and other minerals in sandstones by X-ray powder diffraction (XRPD), *in* R. Worden, and S. Morad, eds., Clay Minerals Cements in Sandstones: International Association of Sedimentologists, p. 213–251.
- Ho, N.-C., D. R. Peacor, and B. A. van der Pluijm, 1999, Preferred Orientation of Phyllosilicates in Gulf Coast Mudstones and Relation to the Smectite-Illite Transition: Clays and Clay Minerals, v. 47, no. 4, p. 495–504, doi:10.1346/CCMN.1999.0470412.
- Hoesni, M. J., 2004, Origins of overpressure in the Malay Basin and its influence on petroleum systems: University of Durham, 268 p.
- Hoesni, M. J., 2015, Thermally-induced Pressure Ramp in the Malay Basin: Insight from Basin Modelling, *in* APGCE 2015.

- Hofer, G., M. Wagreich, and S. Neuhuber, 2013, Geochemistry of fine-grained sediments of the upper Cretaceous to Paleogene Gosau Group (Austria, Slovakia): Implications for paleoenvironmental and provenance studies: *Geoscience Frontiers*, v. 4, no. 4, p. 449–468, doi:10.1016/j.gsf.2012.11.009.
- Hofmann, P., W. Ricken, L. Schwark, and D. Leythaeuser, 2001, Geochemical signature and related climatic-oceanographic processes for early Albian black shales: Site 417D, North Atlantic Ocean: *Cretaceous Research*, v. 22, no. 2, p. 243–257, doi:10.1006/cres.2001.0253.
- Hofstetter, T. B., R. P. Schwarzenbach, and S. B. Haderlein, 2003, Reactivity of Fe(II) Species Associated with Clay Minerals: *Environ. Sci. Technol.*, v. 37, no. 3, p. 519–528, doi:10.1021/ES025955R.
- Hower, J., E. V. Eslinger, M. E. Hower, and E. A. Perry, 1976, Mechanism of burial metamorphism of argillaceous sediment: *Geological Society Of America Bulletin*, v. 87, p. 725–737, doi:10.1130/0016-7606(1976)87<725.
- Huang, W.-L., J. M. Longo, and D. R. Pevear, 1993, An Experimentally Derived Kinetic Model for Smectite-to-Illite Conversion and Its Use as a Geothermometer: *Clays and Clay Minerals*, v. 41, no. 2, p. 162–177, doi:10.1346/CCMN.1993.0410205.
- Huffman, A., and G. Bowers, 2002, Pressure Regimes in Sedimentary Basins and Their Prediction: *AAPG Memoir* 76.
- Hunt, J. M., 1990, Generation and Migration of Petroleum from Abnormally Pressured Fluid Compartments: *AAPG Bulletin*, v. 74, no. 1, p. 1–12.
- Hutcheon, I., J. Bloch, P. De Caritat, M. Shevalier, H. Abercrombie, and F. Longstaffe, 1998, What is the cause of potassium enrichment in shales?, *in* J. Schieber, W. Zimmerle, and P. Sethi, eds., *Shales and Mudstones, part II: Petrography, Petrophysics, geochemistry, and Economic Geology*: Stuttgart, E. Schweizerbart'sche Verlagsbuchhandlung (Nägele u. Obermiller), p. 107–128.
- Inoue, A., and R. Kitagawa, 1994, Morphological characteristics of illitic clay minerals from a hydrothermal system: *American Mineralogist*, v. 79, no. 7–8, p. 700–711.
- Inoue, A., B. Velde, A. Meunier, and G. Touchard, 1988, Mechanism of illite formation during smectite-to-illite conversion in a hydrothermal system: *American Mineralogist*, v. 73, no. 11–12, p. 1325–1334.
- Issler, D. R., 1992, A New Approach to Shale Compaction and Stratigraphic Restoration,

- Beaufort-Mackenzie Basin and Mackenzie Corridor, Northern Canada: AAPG Bulletin, v. 76, no. 8, p. 1170–1189.
- Jackson, M., 1969, Soil Chemical Analysis: Advanced Course: Wisconsin, USA, Published by the author, University of Madison.
- Jacob, G., H. J. Kisch, and B. A. van der Pluijm, 2000, The relationship of phyllosilicate orientation, X-ray diffraction intensity ratios, and c/b fissility ratios in metasedimentary rocks of the Helvetic zone of the Swiss Alps and the Caledonides of Jämtland, central western Sweden: *Journal of Structural Geology*, v. 22, no. 2, p. 245–258, doi:10.1016/S0191-8141(99)00149-2.
- Jagodzinski, H., 1949, Eindimensionale Fehlordnung in Kristallen und ihr Einfluss auf die Röntgeninterferenzen. I. Berechnung des Fehlordnungsgrades aus den Röntgenintensitäten: *Acta Crystallographica*, v. 2, no. 4, p. 201–207, doi:10.1107/S0365110X49000552.
- Jennings, S., and G. Thompson, 1986, Diagenesis of Plio-Pleistocene Sediments of the Colorado River Delta, Southern California: *Journal of Sedimentary Research*, v. 56, no. 1.
- Johnston, J. E., and N. I. Christensen, 1995, Seismic anisotropy of shales: *Journal of Geophysical Research: Solid Earth*, v. 100, no. B4, p. 5991–6003, doi:10.1029/95JB00031.
- Jones, A. D., H. A. Auld, T. J. Carpenter, E. Fetkovich, I. A. Palmer, E. N. RIGATOS, and M. W. Thompson, 2005, Jade Field: an innovative approach to high-pressure, high-temperature field development: Geological Society, London, Petroleum Geology Conference series, v. 6, no. 1.
- van de Kamp, P. C., 2008, Smectite-Illite-Muscovite Transformations, Quartz Dissolution, and Silica Release in Shales: *Clays and Clay Minerals*, v. 56, no. 1, p. 66–81, doi:10.1346/CCMN.2008.0560106.
- Katahara, K., 2006a, Overpressure And Shale Properties: Stress Unloading Or Smectite-illite Transformation? Society of Exploration Geophysicists.
- Katahara, K., 2006b, Overpressure and shale properties: Stress unloading or smectite-illite transformation?, *in* SEG Technical Program Expanded Abstracts 2006: Society of Exploration Geophysicists, p. 1520–1524, doi:10.1190/1.2369809.
- Katahara, K., 2008, What is shale to a petrophysicist? *The Leading Edge*, v. 27, no. 6, p.

738–741, doi:10.1190/1.2944158.

Kingston, D., C. Dishroon, and P. Williams, 1983, Global Basin Classification System: AAPG Bulletin, v. 67, no. 12, p. 2175–2193.

Kranck, K., and T. G. Milligan, 1985, Origin of grain size spectra of suspension deposited sediment: Geo-Marine Letters, v. 5, no. 1, p. 61–66, doi:10.1007/BF02629800.

Kranck, K., P. C. Smith, and T. G. Milligan, 1996, Grain-size characteristics of fine -grained unflocculated sediments I: “one-round” distributions.: Sedimentology, v. 43, no. 3, p. 589–596.

Kuila, U., and M. Prasad, 2013, Specific surface area and pore-size distribution in clays and shales: Geophysical Prospecting, v. 61, no. 2, p. 341–362, doi:10.1111/1365-2478.12028.

Lahann, R., 2002, Impact of Smectite Diagenesis on Compaction Modeling and Compaction Equilibrium: AAPG Memoir 76: Pressure Regimes in Sedimentary Basins and Their Prediction, no. 2, p. 61–72.

Lahann, R. W., W. Lahann, D. K. McCarty, and J. C. C. Hsieh, 2001, Influence of Clay Diagenesis on Shale Velocities and Fluid-Pressure, *in* Offshore Technology Conference: Offshore Technology Conference, doi:10.4043/13046-MS.

Lahann, R. W., and R. E. Swarbrick, 2011, Overpressure generation by load transfer following shale framework weakening due to smectite diagenesis: Geofluids, v. 11, no. 4, p. 362–375, doi:10.1111/j.1468-8123.2011.00350.x.

Lanson, B., B. Sakharov, F. Claret, and V. Drits, 2005, Diagenetic evolution of clay minerals in Gulf Coast shales: New insights from X-ray diffraction profile modelling, *in* 13th International Clay Conference: p. 39.

Lanson, B., B. A. Sakharov, F. Claret, and V. A. Drits, 2009, Diagenetic smectite-to-illite transition in clay-rich sediments: A reappraisal of X-ray diffraction results using the multi-specimen method: American Journal of Science, v. 309, no. 6, p. 476–516, doi:10.2475/06.2009.03.

Leonards, G. H., 1962, Engineering properties of soils: New York.

Loucks, R. G., R. M. Reed, S. C. Ruppel, and U. Hammes, 2012, Spectrum of pore types and networks in mudrocks and a descriptive classification for matrix-related mudrock pores: AAPG Bulletin, v. 96, no. 6, p. 1071–1098, doi:10.1306/08171111061.

Loucks, R. G., R. M. Reed, S. C. Ruppel, and D. M. Jarvie, 2009, Morphology, Genesis, and

- Distribution of Nanometer-Scale Pores in Siliceous Mudstones of the Mississippian Barnett Shale: *Journal of Sedimentary Research*, v. 79, no. 12, p. 848–861, doi:10.2110/jsr.2009.092.
- Lynch, F. L., 1997, Frio shale mineralogy and the stoichiometry of the smectite-to-illite reaction: the most important reaction in clastic sedimentary diagenesis: *Clays and Clay Minerals*, v. 45, p. 618–631.
- MacEwan, D. M. C., 1956, Fourier transform methods for studying scattering from lamellar systems: *Kolloid-Zeitschrift*, v. 149, no. 2–3, p. 96–108, doi:10.1007/BF01511475.
- MacEwan, D. M. C., 1958, Fourier transform methods for studying x-ray scattering from lamellar systems: *Kolloid-Zeitschrift*, v. 156, no. 1, p. 61–67, doi:10.1007/BF01812363.
- Macquaker, J. H. S., M. A. Keller, and S. J. Davies, 2010, Algal Blooms and “Marine Snow”: Mechanisms That Enhance Preservation of Organic Carbon in Ancient Fine-Grained Sediments: *Journal of Sedimentary Research*, v. 80, no. 11, p. 934–942, doi:10.2110/jsr.2010.085.
- Madon, M., 2007, Overpressure development in rift basins: an example from the Malay Basin, offshore Peninsular Malaysia: *Petroleum Geoscience*, v. 13, no. 2, p. 169–180, doi:10.1144/1354-079307-744.
- Madon, M. B., and A. B. Watts, 1998, Gravity anomalies, subsidence history and the tectonic evolution of the Malay and Penyu Basins (offshore Peninsular Malaysia): *Basin Research*, v. 10, no. 4, p. 375–392.
- Mann, D. M., and A. S. Mackenzie, 1990, Prediction of pore fluid pressures in sedimentary basins: *Marine and Petroleum Geology*, v. 7, no. 1, p. 55–65, doi:10.1016/0264-8172(90)90056-M.
- Matenaar, I., 2002, *Compaction and Microfabric Rearrangement of Fine-Grained Siliciclastic Sediments*: University of Newcastle-Upon-Tyne.
- McCarty, D., 2002, Quantitative mineral analysis of clay bearing mixtures: The Reynolds Cup contest: *IUCr CPD Newsletter*, v. 27, p. 12–16.
- McCarty, D. K., B. A. Sakharov, and V. A. Drits, 2008, Early clay diagenesis in gulf coast sediments: New insights from XRD profile modeling: *Clays and Clay Minerals*, v. 56, no. 3, p. 359–379, doi:10.1346/CCMN.2008.0560306.

- McCarty, D. K., B. A. Sakharov, and V. A. Drits, 2009, New insights into smectite illitization: A zoned K-bentonite revisited: *American Mineralogist*, v. 94, no. 11–12, p. 1653–1671, doi:10.2138/am.2009.3260.
- McLennan, M. S., 1989, Rare earth elements in sedimentary rocks: Influence of provenance and sedimentary processes: *Review of Mineralogy*, v. 21, p. 169–200.
- McLennan, S. M., 2001, Relationships between the trace element composition of sedimentary rocks and upper continental crust: *Geochemistry, Geophysics, Geosystems*, v. 2, no. 4, p. 24, doi:10.1029/2000GC000109.
- McLennan, S. M., S. Hemming, D. K. McDaniel, and G. N. Hanson, 1993a, Geochemical approaches to sedimentation, provenance, and tectonics, *in* Geological Society of America Special Papers: Geological Society of America, p. 21–40, doi:10.1130/SPE284-p21.
- McLennan, S. M., S. Hemming, D. K. McDaniel, and G. N. Hanson, 1993b, Processes Controlling the Composition of Clastic Sediments: Geological Society of America, Geological Society of America Special Papers, 21-40 p., doi:10.1130/SPE284.
- McLennan, S. M., and S. R. Taylor, 1991, Sedimentary Rocks and Crustal Evolution: Tectonic Setting and Secular Trends: *The Journal of Geology*, v. 99, no. 1, p. 1–21, doi:10.1086/629470.
- Meade, R. H., 1966, Factors Influencing the Early Stages of the Compaction of Clays and Sands--Review: *Journal of Sedimentary Research*, v. 36, no. 4.
- Mello, M., E. Koutsoukos, W. Mohriak, and G. Bacoccoli, 1994, Selected petroleum systems in Brazil, *in* L. B. Magoon, and W. G. Dow, eds., *The petroleum system-from source to trap*: AAPG Memoir 60: p. 499–512.
- Milliken, K. K. L., 1992, Chemical Behavior of Detrital Feldspars in Mudrocks Versus Sandstones, Frio Formation (Oligocene), South Texas: *Journal of Sedimentary Petrology*, v. 62, no. 5, p. 790–801, doi:10.1306/D42679DD-2B26-11D7-8648000102C1865D.
- Milliken, K. L., W. L. Esch, R. M. Reed, and T. Zhang, 2012, Grain assemblages and strong diagenetic overprinting in siliceous mudrocks, Barnett Shale (Mississippian), Fort Worth Basin, Texas: *AAPG Bulletin*, v. 96, no. 8, p. 1553–1578, doi:10.1306/12011111129.
- Milliken, K. L., M. Rudnicki, D. N. Awwiller, and T. Zhang, 2013, Organic matter-hosted

- pore system, Marcellus Formation (Devonian), Pennsylvania: AAPG Bulletin, v. 97, no. 2, p. 177–200, doi:10.1306/072312I2O48.
- Milner, M., R. McLin, and J. Petriello, 2010, Imaging Texture and Porosity in Mudstones and Shales: Comparison of Secondary and Ion-Milled Backscatter SEM Methods, *in* Canadian Unconventional Resources and International Petroleum Conference: Society of Petroleum Engineers, p. 1–10, doi:10.2118/138975-MS.
- Mohriak, W. U., M. R. Mello, M. Bassetto, I. S. Vieira, and E. A. M. Koutsoukos, 2000, Crustal Architecture, Sedimentation, and Petroleum Systems in the Sergipe-Alagoas Basin, Northeastern Brazil, *in* M. R. Mello, and B. J. Katz, eds., Petroleum systems of South Atlantic margins: AAPG Memoir 73, : AAPG Special Volumes, p. 273–300.
- Mondol, N. H., 2009a, Porosity and permeability development in mechanically compacted silt-kaolinite mixtures: p. 2139–2143.
- Mondol, N. H., 2009b, Porosity and permeability development in mechanically compacted silt-kaolinite mixtures, *in* SEG Technical Program Expanded Abstracts 2009: Society of Exploration Geophysicists, p. 2139–2143, doi:10.1190/1.3255280.
- Mondol, N. H., K. Bjørlykke, J. Jahren, and K. Høeg, 2007, Experimental mechanical compaction of clay mineral aggregates—Changes in physical properties of mudstones during burial: Marine and Petroleum Geology, v. 24, no. 5, p. 289–311, doi:10.1016/j.marpetgeo.2007.03.006.
- Moore, D. M., and R. C. J. Reynolds, 1997, X-ray Diffraction and the Identification and Analysis of Clay Minerals: Oxford University Press, 378 p.
- Morley, C. K., 2001, Combined escape tectonics and subduction rollback-back arc extension: a model for the evolution of Tertiary rift basins in Thailand, Malaysia and Laos: Journal of the Geological Society, v. 158, no. 3, p. 461–474, doi:10.1144/jgs.158.3.461.
- Mouchet, J.-P., and A. Mitchell, 1989, Abnormal Pressures While Drilling: Origins, Prediction, Detection, Evaluation: Editions TECHNIP, 255 p.
- Mystkowski, K., J. Srodon, and D. McCarty, 2002, Application of evolutionary programming to auto-matic XRD quantitative analysis of clay-bearing rocks, *in* Abstracts with Programs, The Clay Minerals Society 39th Annual Meeting: p. 134.
- Nadeau, P., and D. Bain, 1986, Composition of some smectites and diagenetic illitic clays and implications for their origin: Clays and Clay Minerals, v. 34, p. 455–464.

- Nadeau, P. H., D. R. Peacor, J. Yan, and S. Hillier, 2002, I-S precipitation in pore space as the cause of geopressuring in Mesozoic mudstones, Egersund Basin, Norwegian continental shelf: *American Mineralogist*, v. 87, no. 11–12, p. 1580–1589, doi:10.2138/am-2002-11-1208.
- Nadeau, P., J. Tait, W. McHardy, and M. Wilson, 1984, Interstratified XRD characteristics of physical mixtures of elementary clay particles: *Clay Minerals*, v. 19, p. 67–76.
- Nadeau, P. H. P., M. Wilson, W. McHardy, and J. Tait, 1984, Interparticle Diffraction: A New Concept for Interstratified Clays: *Clay Minerals*, v. 19, no. 5, p. 757–769, doi:10.1180/claymin.1984.019.5.06.
- Nadeau, P. H., M. J. Wilson, W. J. McHardy, and J. M. Tait, 1984, Interstratified clays as fundamental particles: *Science (New York, N.Y.)*, v. 225, no. 4665, p. 923–925, doi:10.1346/CCMN.1985.0330612.
- Nadeau, P., M. Wilson, W. McHardy, and J. Tait, 1985, The conversion of smectite to illite during diagenesis: evidence from some illitic clays from bentonites and sandstones: *Mineralogical Magazine*, v. 49, p. 393–400.
- Nesbitt, H. W., and G. Markovics, 1997, Weathering of granodioritic crust, long-term storage of elements in weathering profiles, and petrogenesis of siliciclastic sediments: *Geochimica et Cosmochimica Acta*, v. 61, no. 8, p. 1653–1670, doi:10.1016/S0016-7037(97)00031-8.
- Nesbitt, H. W., G. Markovics, and R. C. Price, 1980, Chemical processes affecting alkalis and alkaline earths during continental weathering: *Geochimica et Cosmochimica Acta*, v. 44, no. 11, p. 1659–1666, doi:10.1016/0016-7037(80)90218-5.
- Nesbitt, H. W., and G. M. Young, 1982, Early Proterozoic climates and plate motions inferred from major element chemistry of lutites: *Nature*, v. 299, no. 5885, p. 715–717, doi:10.1038/299715a0.
- Neuzil, C. E., 1994, How permeable are clays and shales? *Water Resources Research*, v. 30, no. 2, p. 145–150, doi:10.1029/93WR02930.
- Ngah, K., M. Madon, and H. D. Tjia, 1996, Role of pre-Tertiary fractures in formation and development of the Malay and Penyu basins: *Geological Society, London, Special Publications*, v. 106, no. 1, p. 281–289, doi:10.1144/GSL.SP.1996.106.01.18.
- Nguyen, B. T. T., S. J. Jones, N. R. Goult, A. J. Middleton, N. Grant, A. Ferguson, and L. Bowen, 2013, The role of fluid pressure and diagenetic cements for porosity

- preservation in Triassic fluvial reservoirs of the Central Graben, North Sea: AAPG Bulletin, v. 97, no. 8, p. 1273–1302, doi:10.130e/01151311163.
- Nordgård Bolås, H. M., C. Hermanrud, and G. M. G. Teige, 2004, Origin of overpressures in shales: Constraints from basin modeling: AAPG Bulletin, v. 88, no. 2, p. 193–211, doi:10.1306/10060302042.
- O'Connor, S., R. Lahann, R. Swarbrick, P. Clegg, P. Kelly, J. Long, M. Diaz, and R. Labrum, 2012, Mid-Norway Pressure Study: Ikon GeoPressure and IHS.
- Oertel, G., 1983, The relationship of strain and preferred orientation of phyllosilicate grains in rocks—a review: Tectonophysics, v. 100, no. 1–3, p. 413–447, doi:10.1016/0040-1951(83)90197-X.
- Ojeda, H. A. O., 1982, Structural framework, stratigraphy, and evolution of Brazilian marginal basins: AAPG Bulletin, v. 66, no. 6, p. 732–749.
- Omotoso, O., D. K. McCarty, S. Hillier, and R. Kleeberg, 2006, Some successful approaches to quantitative mineral analysis as revealed by the 3rd Reynolds Cup contest: Clays and Clay Minerals, v. 54, p. 751–763.
- Orsini, L., and J. Remy, 1976, Utilisation du chlorure de cobaltihexammine pour la determination simultanee de la capacite d'échange et des bases échangeables des sols: Science du Sol, v. 4, p. 269–275.
- Osborne, M. J., and R. E. Swarbrick, 1999, Diagenesis in North Sea HPHT clastic reservoirs — consequences for porosity and overpressure prediction: Marine and Petroleum Geology, v. 16, no. 4, p. 337–353, doi:10.1016/S0264-8172(98)00043-9.
- Osborne, M. J., and R. E. Swarbrick, 1997, Mechanisms for Generating Overpressure in Sedimentary Basins: A Reevaluation: AAPG Bulletin, v. 81, no. 6, p. 1023–1041.
- Ottesen, D., L. Rise, E. S. Andersen, T. Bugge, and T. Eidvin, 2009, Geological evolution of the Norwegian continental shelf between 61 degrees N and 68 degrees N during the last 3 million years: Norwegian Journal of Geology, v. 89, no. 4, p. 251–265.
- Passey, Q. R., K. M. Bohacs, W. L. Esch, R. Klimentidis, S. Sinha, and E. Upstream, 2010, From Oil-Prone Source Rock to Gas-Producing Shale Reservoir – Geologic and Petrophysical Characterization of Unconventional Shale-Gas Reservoirs: CPS/SPE International Oil & Gas Conference and Exhibition in China 2010, p. 1707–1735, doi:131350.
- Pearson, F. J., 1999, What is the porosity of a mudrock? Geological Society, London,

- Special Publications, v. 158, no. 1, p. 9–21, doi:10.1144/GSL.SP.1999.158.01.02.
- Peltonen, C., Ø. Marcussen, K. Bjørlykke, and J. Jahren, 2009, Clay mineral diagenesis and quartz cementation in mudstones: The effects of smectite to illite reaction on rock properties: *Marine and Petroleum Geology*, v. 26, no. 6, p. 887–898, doi:10.1016/j.marpetgeo.2008.01.021.
- Peltonen, C., Ø. Marcussen, K. Bjørlykke, and J. Jahren, 2008, Mineralogical control on mudstone compaction: a study of Late Cretaceous to Early Tertiary mudstones of the Vøring and Møre basins, Norwegian Sea: *Petroleum Geoscience*, v. 14, no. 2, p. 127–138 ST–Mineralogical control on mudstone co, doi:10.1144/1354-079308-758.
- Perry, E., and J. Hower, 1972, Late-Stage Dehydration in Deeply Buried Pelitic Sediments: *AAPG Bulletin*, v. 56, no. 10, p. 2013–2021.
- van der Pluijm, B. A., N. C. Ho, and D. R. Peacor, 1994, High-resolution X-ray texture goniometry: *Journal of Structural Geology*, v. 16, no. 7, p. 1029–1032, doi:10.1016/0191-8141(94)90084-1.
- Plumley, W. J., 1980, Abnormally High Fluid Pressure: Survey of Some Basic Principles: *AAPG Bulletin*, v. 64, no. 3, p. 414–422, doi:10.1306/2F919409-16CE-11D7-8645000102C1865D.
- Pollastro, R., 1993, Considerations and applications of the illite/smectite geothermometer in hydrocarbon-bearing rocks of Miocene to Mississippian age: *Clays and Clay minerals*, v. 41, no. 2, p. 119–133.
- Potter, P. E., J. B. Maynard, and P. J. Depetris, 2005, *Mud and Mudstones: Introduction and Overview*: Springer Science & Business Media, 297 p.
- Potter, P., J. Maynard, and P. Depetris, 2005, Provenance of Mudstones: *Mud and Mudstones: Introduction and ...*, p. 157–174, doi:10.1007/3-540-27082-5_7.
- Potter, P. E., J. B. Maynard, and W. A. Pryor, 1980, *Sedimentology of Shale*: New York, NY, Springer New York, 310 p., doi:10.1007/978-1-4612-9981-3.
- Powers, M. C., 1967, Fluid-Release Mechanisms in Compacting Marine Mudrocks and Their Importance in Oil Exploration: *AAPG Bulletin*, v. 51, no. 7, p. 1240–1254.
- di Primio, R., and V. Neumann, 2008, HPHT reservoir evolution: a case study from Jade and Judy fields, Central Graben, UK North Sea: *International Journal of Earth Sciences*, v. 97, no. 5, p. 1101–1114, doi:10.1007/s00531-007-0206-y.
- Ramdhan, A. M., and N. R. Goult, 2010, Overpressure-generating mechanisms in the

- Peciko Field, Lower Kutai Basin, Indonesia: *Petroleum Geoscience*, v. 16, no. 4, p. 367–376, doi:10.1144/1354-079309-027.
- Ramadhan, A. M., and N. R. Goult, 2011, Overpressure and mudrock compaction in the Lower Kutai Basin, Indonesia: A radical reappraisal: *AAPG Bulletin*, v. 95, no. 10, p. 1725–1744, doi:10.1306/02221110094.
- Reynolds, R., 1980, Interstratified clay minerals, *in* G. Brindley, and G. Brown, eds., *Crystal structures of clay minerals and their X-ray identification*: London, Mineralogical Society, p. 249–303.
- Reynolds, R. C., and J. Hower, 1970, The Nature of Interlayering in Mixed-Layer Illite-Montmorillonites: *Clays and Clay Minerals*, v. 18, no. 1, p. 25–36, doi:10.1346/CCMN.1970.0180104.
- Rieke, H., and G. Chilingarian, 1974, *Compaction of argillaceous sediments*: Amsterdam, Elsevier.
- Rise, L., D. Ottesen, K. Berg, and E. Lundin, 2005, Large-scale development of the mid-Norwegian margin during the last 3 million years: *Marine and Petroleum Geology*, v. 22, no. 1–2 SPEC. ISS., p. 33–44, doi:10.1016/j.marpetgeo.2004.10.010.
- Ritter, U., G. W. Zielinski, H. M. Weiss, R. L. B. Zielinski, and J. Sættem, 2004, Heat flow in the Vøring Basin, Mid-Norwegian Shelf: *Petroleum Geoscience*, v. 10, no. 4.
- Rouchet, J. du, 1981, Stress Fields, A Key to Oil Migration: *AAPG Bulletin*, v. 65, no. 1, p. 74–85.
- Rouquerol, J., D. Avnir, C. W. Fairbridge, D. H. Everett, J. M. Haynes, N. Pernicone, J. D. F. Ramsay, K. S. W. Sing, and K. K. Unger, 1994, Recommendations for the characterization of porous solids (Technical Report): *Pure and Applied Chemistry*, v. 66, no. 8, p. 1739–1758, doi:10.1351/pac199466081739.
- Rubey, W. W., and K. M. Hubbert, 1959, Role of fluid pressure in mechanics of overthrust faulting II. Overthrust belt in geosynclinal area of western Wyoming in light of fluid-pressure hypothesis: *Geological Society of America Bulletin*, v. 70, no. 2, p. 167, doi:10.1130/0016-7606(1959)70[167:ROFPIM]2.0.CO;2.
- Sakharov, B., H. Lindgreen, A. Salyn, and V. Drits, 1999, Determination of illite-smectite structures using multispecimen X-ray diffraction profile fitting: *Clays and Clay minerals*, v. 47, p. 555–566.
- Sargent, C., P. Andras, N. R. Goult, and A. C. Aplin, 2015, Compaction and overpressure in

- the Sergipe-Alagoas Basin, *in* GeoPOP3 Final Report: Durham, p. 199–232.
- Sargent, C., N. R. Goult, A. M. P. Cicchino, and A. M. Ramdhan, 2015, Budge–Fudge method of pore-pressure estimation from wireline logs with application to Cretaceous mudstones at Haltenbanken: *Petroleum Geoscience*, v. 21, no. 4, p. 219–232, doi:10.1144/petgeo2014-088.
- Schieber, J., 1998, Deposition of mudstones and shales: Overview, problems, and challenges, *in* J. Schieber, W. Zimmerle, and P. Sethi, eds., *Shales and mudstones* (vol. 1): Basin studies, sedimentology and paleontology: Schweizerbart'sche Verlagsbuchhandlung, p. 131–146.
- Schieber, J., and W. Zimmerle, 1998, The history and promise of shale research: *Shales and Mudstones: Basin Studies, Sedimentology and Paleontology*, v. 1, p. 1–10.
- Schlumberger Oilfield Glossary, 2016: <<http://www.glossary.oilfield.slb.com/>>.
- Sclater, J., and P. Christie, 1980, Continental stretching: an explanation of the post-mid-Cretaceous subsidence of the central North Sea basin: *Journal of Geophysical Research*, v. 85, no. B7, p. 3711–3739.
- Shing, C. Y., 1992, Petrographic and diagenetic studies of the reservoir sandstone of the Malay Basin: *Geological Society of Malaysia Bulletin*, p. 261–283.
- Skar, T., R. T. Van Balen, L. Arnesen, and S. Cloetingh, 1999, Origin of overpressure on the Haltenbanken Terrace, offshore mid-Norway: the potential role of mechanical compaction, pressure transfer and stress, *in* A. C. Aplin, A. J. Fleet, and J. H. S. Macquaker, eds., *Muds and Mudstones: Physical and Fluid Properties. Special Publication vol.158.*: Geological Society of London, p. 137–156.
- Skempton, A. W., 1969, The consolidation of clays by gravitational compaction: *Quarterly Journal of the Geological Society*, v. 125, no. 1–4, p. 373–411, doi:10.1144/gsjgs.125.1.0373.
- Smith, R. I., N. Hodgson, and M. Fulton, 1993, Salt control on Triassic reservoir distribution , UKCS Central North Sea, *in* J. R. Parker, ed., *Petroleum Geology of Northwest Europe: Proceedings of the 4th Conference on Petroleum Geology of NW. Europe*: London, United Kingdom, Geological Society, p. 547–557, doi:10.1144/0040547.
- De Souza, R. S., L. F. De Ros, and S. Morad, 1995, Dolomite diagenesis and porosity preservation in lithic reservoirs: Carmopolis Member, Sergipe-Alagoas Basin,

- northeastern Brazil: *American Association of Petroleum Geologists Bulletin*, v. 79, no. 5, p. 725–748, doi:10.1306/8D2B1B88-171E-11D7-8645000102C1865D.
- Środoń, J., 1999, Nature of mixed-layer clays and mechanisms of their formation and alteration: *Annual Review of Earth and Planetary Sciences*, v. 27, no. 1, p. 19–53, doi:10.1146/annurev.earth.27.1.19.
- Środoń, J., 2009, Quantification of illite and smectite and their layer charges in sandstones and shales from shallow burial depth: *Clay Minerals*, v. 44, no. 4, p. 421–434.
- Srodon, J., C. Andreoli, F. Elsass, and M. Robert, 1990, Direct high-resolution transmission electron microscopic measurement of expandability of mixed-layer illite/smectite in bentonite rock: *Clays and Clay Minerals*, v. 38, p. 373–379.
- Środoń, J., V. A. Drits, D. K. McCarty, J. C. C. Hsieh, and D. D. Eberl, 2001, Quantitative X-Ray Diffraction Analysis of Clay-Bearing Rocks from Random Preparations: *Clays and Clay Minerals*, v. 49, no. 6, p. 514–528, doi:10.1346/CCMN.2001.0490604.
- Srodon, J., and D. D. Eberl, 1984, Illite: *Reviews in Mineralogy and Geochemistry*, v. 13, no. 1, p. 495–544.
- Środoń, J., D. D. Eberl, and V. A. Drits, 2000, Evolution of Fundamental-Particle Size during Illitization of Smectite and Implications for Reaction Mechanism: *Clays and Clay Minerals*, v. 48, no. 4, p. 446–458, doi:10.1346/CCMN.2000.0480405.
- Srodon, J., F. Elsass, W. McHardy, and D. Morgan, 1992, Chemistry of illite-smectite inferred from TEM measurements of fundamental particles: *Clay Minerals*, v. 27, p. 137–158.
- Środoń, J., and D. K. MaCarty, 2008, Surface area and layer charge of smectite from CEC and EGME/H₂O-retention measurements: *Clays and Clay Minerals*, v. 56, no. 2, p. 155–174, doi:10.1346/CCMN.2008.0560203.
- Środoń, J., E. Zeelmaekers, and A. Derkowski, 2009, The charge of component layers of illite-smectite in bentonites and the nature of end-member illite: *Clays and Clay Minerals*, v. 57, no. 5, p. 649–671, doi:10.1346/CCMN.2009.0570511.
- Storvoll, V., and I. Brevik, 2008, Identifying time, temperature, and mineralogical effects on chemical compaction in shales by rock physics relations: *The Leading Edge*, v. 27, no. 6, p. 750–756, doi:10.1190/1.2944160.
- Stricker, S., 2016, Influence of fluid pressure on the diagenesis of clastic sediments: University of Durham, 328 p.

- Stricker, S., and S. J. Jones, 2016, Enhanced porosity preservation by pore fluid overpressure and chlorite grain coatings in the Triassic Skagerrak, Central Graben, North Sea, UK: Geological Society, London, Special Publications, v. 435.
- Stricker, S., S. J. Jones, S. Sathar, L. Bowen, and N. Oxtoby, 2016, Exceptional reservoir quality in HPHT reservoir settings: Examples from the Skagerrak Formation of the Heron Cluster, North Sea, UK: Marine and Petroleum Geology, v. 77, p. 198–215, doi:10.1016/j.marpetgeo.2016.02.003.
- Stuevold, L. M., and O. Eldholm, 1996, Cenozoic uplift of Fennoscandia inferred from a study of the mid-Norwegian margin: Global and Planetary Change, v. 12, no. 1, p. 359–386, doi:10.1016/0921-8181(95)00028-3.
- Swarbrick, R. E., 2012, Review of pore-pressure prediction challenges in high-temperature areas: The Leading Edge, v. 31, no. 11, p. 1288–1294, doi:10.1190/tle31111288.1.
- Swarbrick, R. E., and M. J. Osborne, 1998, Mechanisms that Generate Abnormal Pressures: an Overview, *in* B. E. Law, G. F. Ulmishek, and U. I. Slavin, eds., Abnormal pressures in hydrocarbon environments: AAPG Memoir 70: AAPG Special Volumes, p. 13–34.
- Swarbrick, R. ., M. . Osborne, D. Grunberger, G. . Yardley, G. Macleod, A. . Aplin, S. . Larter, I. Knight, and H. . Auld, 2000, Integrated study of the Judy Field (Block 30/7a) — an overpressured Central North Sea oil/gas field: Marine and Petroleum Geology, v. 17, no. 9, p. 993–1010, doi:10.1016/S0264-8172(00)00050-7.
- Swarbrick, R. E., M. J. Osborne, and G. S. Yardley, 2002, Comparison of Overpressure Magnitude Resulting from the Main Generating Mechanisms: AAPG Memoirs, v. 76, p. 1–12.
- Tapponnier, P., G. Peltzer, A. Y. Le Dain, R. Armijo, and P. Cobbold, 1982, Propagating extrusion tectonics in Asia: New insights from simple experiments with plasticine: Geology, v. 10, no. 12, p. 611, doi:10.1130/0091-7613(1982)10<611:PETIAN>2.0.CO;2.
- Taylor, K. G., 1998, Spatial and temporal variations in early diagenetic organic matter oxidation pathways in Lower Jurassic mudstones of eastern England: Chemical Geology, v. 145, no. 1, p. 47–60, doi:10.1016/S0009-2541(97)00119-8.
- Taylor, K. G., and J. H. S. Macquaker, 2014, Diagenetic alterations in a silt- and clay-rich mudstone succession: an example from the Upper Cretaceous Mancos Shale of Utah,

- USA: *Clay Minerals*, v. 49, no. 2, p. 213–227, doi:10.1180/claymin.2014.049.2.05.
- Taylor, K., and J. Macquaker, 2000, Early diagenetic pyrite morphology in a mudstone-dominated succession: the Lower Jurassic Cleveland Ironstone Formation, eastern England: *Sedimentary Geology*, v. 131, p. 77–86.
- Taylor, S. R., and S. M. McLennan, 1985, *The continental crust: Its composition and evolution*: Blackwell Scientific Pub., Palo Alto, CA, 312 p.
- Teige, G. M. G., C. Hermanrud, L. Wensaas, and H. M. Nordgård Bolas, 1999, The lack of relationship between overpressure and porosity in North Sea and Haltenbanken shales: *Marine and Petroleum Geology*, v. 16, no. 4, p. 321–335, doi:10.1016/S0264-8172(98)00035-X.
- Terzaghi, K., 1925, *Erdbaumechanik auf bodenphysikalischer grundlage*: Leipzig, F. Deuticke, 399 p.
- Terzaghi, K., 1943, *Theoretical Soil Mechanics*: Hoboken, NJ, USA, John Wiley & Sons, Inc., doi:10.1002/9780470172766.
- Thyberg, B., and J. Jahren, 2011, Quartz cementation in mudstones: sheet-like quartz cement from clay mineral reactions during burial: *Petroleum Geoscience*, v. 17, no. 1, p. 53–63, doi:10.1144/1354-079310-028.
- Thyberg, B., J. Jahren, T. Winje, K. Bjørlykke, and J. I. Faleide, 2009, From mud to shale : rock stiffening by micro-quartz cementation: *First Break*, v. 27, no. 316, p. 53–59.
- Thyberg, B., J. Jahren, T. Winje, K. Bjørlykke, J. I. Faleide, and Ø. Marcussen, 2010, Quartz cementation in Late Cretaceous mudstones, northern North Sea: Changes in rock properties due to dissolution of smectite and precipitation of micro-quartz crystals: *Marine and Petroleum Geology*, v. 27, no. 8, p. 1752–1764, doi:10.1016/j.marpetgeo.2009.07.005.
- Thyberg, B. I., H. Jordt, K. Bjørlykke, and J. I. Faleide, 2000, Relationships between sequence stratigraphy, mineralogy and geochemistry in Cenozoic sediments of the northern North Sea: *Geological Society, London, Special Publications*, v. 167, no. 1.
- Tingay, M. R. P., C. K. Morley, A. Laird, O. Limpornpipat, K. Krisadasima, S. Pabchanda, and H. R. Macintyre, 2013, Evidence for overpressure generation by kerogen-to-gas maturation in the northern Malay Basin: *AAPG Bulletin*, v. 97, no. 4, p. 639–672, doi:10.1306/09041212032.
- Tingay, M. R., C. Morley, A. P. Laird, O. Limpornpipat, K. Krisadasima, S. Pabchanda, and H.

- Macintyre, 2011, Overpressures in the Northern Malay Basin: Part 1 - Origin and Distribution, *in* International Petroleum Technology Conference: International Petroleum Technology Conference, doi:10.2523/IPTC-15345-MS.
- Tjia, H., 1998, Origin and tectonic development of Malay-Penyu-West Natuna basins: *Geol. Soc Malaysia Bulletin*, v. 42, p. 147–160.
- Tosaya, C. A., 1982, *Acoustical Properties of Clay Bearing Rocks*: Stanford University.
- Veblen, D. R., G. D. J. Guthrie, K. J. T. Livi, and R. C. Reynolds, 1990, High-resolution transmission electron microscopy and electron diffraction of mixed-layer illite/smectite: Experimental results: *Clays and Clay Minerals*, v. 38, no. 1, p. 1–13.
- Velde, B., 1995, *Origin and Mineralogy of Clays*: Berlin, Heidelberg, Springer Berlin Heidelberg, doi:10.1007/978-3-662-12648-6.
- Velde, B., and G. Vasseur, 1992, Estimation of the diagenetic smectite to illite transformation in time-temperature space: *American Mineralogist*, v. 77, no. 9–10, p. 967–976.
- Vik, E., O. R. Heum, and K. G. Amalixsen, 1991, Geological Society , London , Special Publications Leakage from deep reservoirs : possible mechanisms and relationship to shallow gas in the Haltenbanken area , mid-Norwegian Shelf service Leakage from deep reservoirs : possible mechanisms and relationshi: Geological Society, London, no. June 2007, doi:10.1144/GSL.SP.1991.059.01.18.
- Voltolini, M., H.-R. Wenk, N. H. Mondol, K. Bjørlykke, and J. Jahren, 2009, Anisotropy of experimentally compressed kaolinite-illite-quartz mixtures: *GEOPHYSICS*, v. 74, no. 1, p. D13–D23, doi:10.1190/1.3002557.
- Wardlaw, N. C., and M. McKellar, 1981, Mercury porosimetry and the interpretation of pore geometry in sedimentary rocks and artificial models: *Powder Technology*, v. 29, no. 1, p. 127–143, doi:10.1016/0032-5910(81)85011-5.
- Washburn, E., 1921, Note on a method of determining the distribution of pore sizes in a porous material: *Proceedings of the National Academy of*, v. 63, p. 723–760.
- Weaver, C. C. E., 1989, *Clays, Muds, and Shales*: Elsevier, 818 p.
- Weaver, C., 1989, *Clays, muds, and shales: Developments in sedimentology*: Elsevier, 819 p.
- Wenk, H. R., 1985, Measurement of pole figures, *in* H. R. Wenk, ed., *Preferred Orientation in Deformed Metals and Rocks: An Introduction to Modern Texture*

- Analysis: London, Academic Press, p. 11–48.
- Whitney, G., 1990, Role of water in the smectite-to-illite reaction: *Clays and Clay Minerals*, v. 38, p. 343–350.
- Worden, R. H., and S. D. Burley, 2003, Sandstone Diagenesis: The Evolution of Sand to Stone, *in* R. H. Worden, and S. D. Burley, eds., *Sandstone Diagenesis*: Oxford, UK, Blackwell Publishing Ltd., p. 3–44, doi:10.1002/9781444304459.ch.
- Worden, R. H., D. Charpentier, Q. J. Fisher, and A. C. Aplin, 2005, Fabric development and the smectite to illite transition in Upper Cretaceous mudstones from the North Sea: an image Analysis Approach: Geological Society, London, Special Publications, v. 249, no. 1, p. 103–114, doi:10.1144/GSL.SP.2005.249.01.09.
- Worden, R. H., and S. Morad, 2003, Clay Minerals in Sandstones: Controls on Formation, Distribution and Evolution, *in* R. H. Worden, and S. Morad, eds., *Clay Mineral Cements in Sandstones*: Oxford, UK, Blackwell Publishing Ltd., p. 1–41, doi:10.1002/9781444304336.ch1.
- Yang, Y., and A. C. Aplin, 2010, A permeability-porosity relationship for mudstones: *Marine and Petroleum Geology*, v. 27, no. 8, p. 1692–1697, doi:10.1016/j.marpetgeo.2009.07.001.
- Yang, Y., and A. C. Aplin, 2004, Definition and practical application of mudstone porosity-effective stress relationships: *Petroleum Geoscience*, v. 10, no. 2, p. 153–162, doi:10.1144/1354-079302-567.
- Yang, Y., and A. C. Aplin, 1998, Influence of lithology and compaction on the pore size distribution and modelled permeability of some mudstones from the Norwegian margin: *Marine and Petroleum Geology*, v. 15, no. 2, p. 163–175, doi:10.1016/S0264-8172(98)00008-7.
- Yang, Y., and A. C. Aplin, 2007, Permeability and petrophysical properties of 30 natural mudstones: *Journal of Geophysical Research*, v. 112, no. B3, p. B03206, doi:10.1029/2005JB004243.
- Yardley, G. S., and R. E. Swarbrick, 2000, Lateral transfer: a source of additional overpressure? *Marine and Petroleum Geology*, v. 17, no. 4, p. 523–537, doi:10.1016/S0264-8172(00)00007-6.
- Yassir, N., and M. Addis, 2002, Relationships between pore pressure and stress in different tectonic settings, *in* A. R. Huffman, and G. L. Bowers, eds., *Pressure*

- Regimes in Sedimentary Basins and their Prediction: Tulsa, American Association of Petroleum Geologists, p. 79–88.
- Yeh, H.-W., and S. M. Savin, 1977, Mechanism of burial metamorphism of argillaceous sediments: 3. O-isotope evidence: Geological Society of America Bulletin, v. 88, no. 9, p. 1321, doi:10.1130/0016-7606(1977)88<1321:MOBMOA>2.0.CO;2.
- Yusoff, W., 1993, Geothermics of the Malay Basin, offshore Malaysia: University of Durham, 213 p.
- Zainul, A., R. Misman, and A. Ali, 1999, Overview of petroleum resources of Malaysia, *in* K. Leong, ed., The Petroleum Geology and Resources of Malaysia: Petronas, p. 33–58.
- Zinszner, B., and F. Pellerin, 2007, A Geoscientist's Guide to Petrophysics: Paris, Editions Technip.
- Zoback, M. D., 2010, Reservoir Geomechanics: Cambridge University Press, 449 p.